Doctoral theses at NTNU, 2024:43

Jon Ivar Belghaug Knarud

Hygrothermal Modeling of Masonry with Interior Insulation Retrofit

Perspectives on hygrothermal performance and modeling-uncertainty

Doctoral thesis

NTNU
Norwegian University of Science and Technology
Thesis for the Degree of
Philosophiae Doctor
Faculty of Engineering
Department of Civil and Environmental
Engineering

NTNU
Norwegian University of
Science and Technology

Jon Ivar Belghaug Knarud

Hygrothermal Modeling of Masonry with Interior Insulation Retrofit

Perspectives on hygrothermal performance and modeling-uncertainty

Thesis for the Degree of Philosophiae Doctor

Trondheim, January 2024

Norwegian University of Science and Technology
Faculty of Engineering
Department of Civil and Environmental Engineering

NTNU
Norwegian University of
Science and Technology

NTNU
Norwegian University of Science and Technology

Thesis for the Degree of Philosophiae Doctor

Faculty of Engineering
Department of Civil and Environmental Engineering

ISBN 978-82-326-7688-0 (printed ver.)
ISBN 978-82-326-7687-3 (electronic ver.)
ISSN 1503-8181 (printed ver.)
ISSN 2703-8084 (online ver.)

Doctoral theses at NTNU, 2024:43

Printed by NTNU Grafisk senter

Summary

Energy retrofit of existing buildings is mainly an endeavor to reduce energy consumption. Interior insulation retrofit of masonry falls among retrofit measures in this regard. However, interior insulation of masonry may give rise to hygrothermal risks in the structure. Thus, hygrothermal analysis of solutions for such retrofit becomes paramount. Such analysis often involves hygrothermal simulations of models that represent the retrofit scenario. Unfortunately, analysis of this kind can be complex and often suffers from lack of information, like limited access to the material properties involved, or it suffers from inaccurate understanding of the acting moisture transfer mechanisms. Uncertainties thus exist that practitioners should be aware of.

The objective of this thesis is to provide a contribution to modeling techniques and to provide an insight that highlights modeling uncertainty. This with a focus on modeling bare brick masonry exposed to driving rain in the context of interior insulation retrofit.

The work spans small- and large-scale experiments, analytical work on material property modeling methods, and hygrothermal modeling and simulation. In the experiment work, a focus is given moisture absorption along the brick-mortar interface, which is an important aspect of rain absorption of bare brick masonry. The information gathered on such absorption is further investigated by hygrothermal simulation.

The work includes establishing a hygrothermal model for 2D and 3D analysis, where different parameters and modeling choices are investigated. A 3D analysis is of particular interest regarding beam ends embedded in the masonry, a detail vulnerable to moisture damage in interior insulation retrofitting of masonry.

A smart vapor barrier (SVB), which provides an inward drying potential during warm weather, while preventing interstitial condensation during cold weather, is given special attention since little data has previously been gathered on the performance of SVB as a measure in combination with interior insulated masonry.

Simplified modeling of hydraulic conductivity (liquid permeability) is explored to ease engineering applicability through prediction based on the capillary absorption coefficient and retention curve. This is done in the framework of a bundle of tubes model that is supplemented with a liquid film model, with the latter covering surface diffusion.

A large-scale laboratory experiment, including varying configurations of interior insulated masonry wall structures, is presented, and assessed for performance by the varying of parameters. In addition, it provides a scenario with accompanying performance results with which to compare hygrothermal simulations against, for a check of realism of simulation results.

Specifically, the work provides:

- Experiment-based results from large-scale testing of interior insulated masonry, exposed to severe wetting through driving rain events in a cold climate and to subsequent drying in a warm climate.
- Insights into analytical derivation of a prediction expression for the capillary absorption coefficient of an imbibition setting.
- A novel prediction expression of the capillary conductivity at capillary saturation.
- A simplified practical conductivity model for the full moisture range that is assessed for a wide range of porous building materials.
- An assessment of modeling choices and their impact on hygrothermal simulation results, which underpins perspectives on uncertainty and sensitivity.

The work culminates in the following findings:

- The proposed model for hydraulic conductivity is on par with a method of calculating the conductivity from simplified prediction of capillary diffusivity. However, the proposed model is believed to be more realistic in form, not risking unphysical trends in the conductivity curve.
- SVB is seen to provide a significant contribution to the drying potential registered at the interior masonry (masonry-insulation interface). For the beam end, on the other hand, the contribution of SVB seems insignificant.
- Brick-mortar interfaces are found to significantly increase absorption along the interface planes of bare brick masonry, and to enable substantial localized leak-like infiltrations or permeations in the masonry. This can lead to rapid distribution of moisture to the interior masonry surface of one-brick-thick masonry, when the masonry is exposed to severe rain events.

The work highlights perspectives on complexity, uncertainty, and sensitivity that can support practitioners and researchers in hygrothermal modeling of bare brick masonry, smart vapor barriers, embedded beam ends, and interior insulation retrofit of masonry.

Preface

This thesis presents the outcome of my PhD research work carried out from August 2013 to August 2023 at the Department of Civil and Environmental Engineering. at the Norwegian University of Science and Technology (NTNU), The research has been conducted in a stand-alone PhD position titled Energy Efficient Buildings, with the position being financed by the Faculty of Engineering under its strategic research area (Forskningsområde 15) on Energy Efficient and Functional Buildings (Energieffektive og funksjonelle bygninger). Although the position has not been part of any larger research project, the accompanied laboratory investigations have been supported by The Research Council of Norway through the Center for Research-based Innovation “Klima 2050” (Grant No 237859).

The path towards this thesis has not been straightforward. Originally intended as a four-year project, including one year of scientific/teaching assistance work, the work ended up spanning ten years mostly due to a pressing need at the department to man the teaching of courses in fire safety engineering. Since I in 2013 already was the scientific assistant within fire safety engineering in buildings, my mandatory teaching was assigned to take over the parts having been taught by professor Per Jostein Hovde, who retired at that time. The teaching load that followed showed to be much more than the one year assigned in the PhD plan. In 2017, with the untimely passing of Professor Harald Landrø, who was responsible for the fire safety courses, the department made me a temporary assistant professor for two years, having the sole responsibility for administrating and teaching the fire safety courses at the department, teaching a course at NTNU in Ålesund and supervising master students in the field of fire safety. Although the work was very rewarding, it led to a corresponding extension to the PhD plan. At the same time over these years the focus of the PhD research had somewhat shifted. The original intention of the research had been to investigate hygrothermal performance of interior insulation retrofit, with an aim of arriving at advice on best practice to avoid moisture damage issues. However, I early on started to realize the difficulty in achieving novelty in research with such a focus, with the principles already well known, and furthermore with the difficulty in arriving at somewhat generalized advice. Overall, there are too many highly scenario-specific parameters that impact hygrothermal performance for such a focus to be very fruitful. Instead, the focus turned towards research into improvements of methods and tools, and input to such, used to analyze hygrothermal scenarios of interior insulation retrofit. Such a fucus could be less scenario specific. This included a focus on hygrothermal simulation tools and their “practical” use. Nevertheless, the context continued to be energy-efficient and moisture-safe retrofitting of brick buildings with interior insulation.

I extend a deep gratitude to my supervisors, Professor Stig Geving and Professor Tore Kvande, both of whom having been my main supervisor at some point. Stig Geving was my main supervisor up to September 2021 when he handed the torch to Tore as a result of changing job position from NTNU to SINTEF Community. I thank Stig for his effort in establishing the PhD position thereby enabling my research. I am also grateful that Stig from the very start pushed me to write conference papers, in so forcing extra effort into hygrothermal simulations, and managing tight deadlines, thereby being able to present papers at international conferences. Tore Kvande was my 2nd supervisor from the beginning up to becoming my main supervisor. I thank Tore for providing insight into masonry structures and practical issues regarding their hygrothermal behavior. Furthermore, for the helpful guidance that ensured completion of the last publication and the thesis itself. I am especially grateful to Tore and Stig for making it possible to finance and conduct large-scale laboratory testing of masonry wall elements, in a climate simulator at the NTNU/SINTEF building physics laboratory.

Great thanks go to lab-engineer Ole Aunrønning for all the help he provided with the laboratory testing. The contribution Ole provided, including wall and equipment assembly, various material property testing, and not least, measurement monitoring, has been invaluable.

I will also thank laboratory manager Einar Bergheim and senior engineer Egil Rognvik at SINTEF for their help with the access to and use of the climate simulator.

Thanks also go to Pär Johansson for helpfully having provided some material property data, and for establishing experience at NTNU through his own research prior to mine with use of the climate simulator on masonry.

I have also appreciated all my colleagues over the years, with whom I have had interesting and pleasant conversations.

Special thanks go to my father Ernst Ivar Knarud who has shown great interest in my research and endless patience in listening when I have recounted my ideas and work. His questions also helped me to see different perspectives.

Finally, I want to heartfully acknowledge Professor Harald Landrø who sadly passed away in 2017. He helped me to get employed at NTNU as a scientific assistant in 2011, and he encouraged me to do research and pursue my capabilities in academia. Before that he was my master thesis supervisor. Between 2012 and 2017 we had a great cooperation while sharing the teaching responsibility for the fire safety engineering courses and the supervision of master students at the department.

Guide for the reader

Article-based thesis

This thesis is article-based; thus, it centers on the enclosed collection of articles, while providing context, expanded methodology, and additional scrutiny. Even though the thesis to some extent can be read independently of the articles, it heavily refers to them. That is, the thesis tries to avoid repeating the articles, except for the essentials and the main findings. Thus, the thesis is not an alternative to the articles. It is recommended that one glance at or read the articles when they are referred to in the thesis for the more precise account of the specific topics they address. For an overview of the articles and the relation between the articles please refer to Section 3.

Accounts of the process

The thesis is not a traditional research report, although it in part has that purpose. The thesis also includes accounts of the processes or background leading up to the choices that have been made and the work that has been done. The reason this is included is because the thesis is also viewed as a documentation of the educational process and function of the PhD work. Furthermore, the processes have not always been optimal for the research paths, and consciously documenting this as well can give room for additional learning. The thesis reflects that knowledge and understanding have been acquired as the work has progressed, and the thesis also reflects the accumulation of insight from the beginning of the thesis and onwards, especially with the progression through Section 1 (Introduction), followed by Section 2 (Theoretical background), and subsequently Section 3 (Research questions). Due to this, the objectives in Section 1 are formulated to be wider, while the research questions in Section 3 are more precise.

Abandoned path of research

In addition to the article topics the thesis summarizes an abandoned path of research (Section 4.2.3-4.2.5). This is included to explain a detour in the research that did not lead to findings that were substantial enough to publish in an article. Furthermore, it is to provide the conclusions of that work, and to explain why it did not lead to substantial enough findings, so that if someone attempts something similar in the future, they can draw on some lessons and hopefully avoid a repeat of associated pitfalls.

Parameters in expressions

Many physics expressions are included in the thesis. Parameters are explained, with units, where they first appear.

Appendixes

The thesis' appendixes explain the hygrothermal model that was established for the research, in addition to document validation benchmark results for the model.

[This page is left blank]

Contents

List of articles

I. J. I. Belghaug Knarud, T. Kvande, S. Geving. Experimental investigation of capillary absorption along mortar-brick interface plane. in: J. Grunewald (Ed.), Proceedings CESBP 2016 BauSIM 2016, Central European Symposium on Building Physics / BauSIM, Fraunhofer IRB Verlag, Dresden, Germany (2016) 117-124 ISBN (E-Book): 978-3-8167-9798-2

II. J. I. Knarud, S. Geving, T. Kvande. Moisture performance of interior insulated brick wall segments subjected to wetting and drying – A laboratory investigation. Building and Environment 188 (2021) 107488 https://doi.org/10.1016/j.buildenv.2020.107488

III. J. I. Knarud, S. Geving. Implementation and benchmarking of a 3D hygrothermal model in the COMSOL Multiphysics software. 6th International Building Physics Conference, IBPC 2015, Energy Procedia 78 (2015) 3440-3445 http://dx.doi.org/10.1016/j.egypro.2015.12.327

IV. J. I. Knarud, S. Geving. Comparative study of hygrothermal simulations of a masonry wall. 11th Nordic Symposium on Building Physics, NSB2017, 11-14 June 2017, Trondheim, Norway, Energy Procedia 132 (2017) 771-776 https://doi.org/10.1016/j.egypro.2017.10.027

V. J. I. Knarud, T. Kvande, S. Geving. Modelling hydraulic conductivity for porous building materials based on a prediction of capillary conductivity at capillary saturation. International Journal of Heat and Mass Transfer 186 (2022) 122457 https://doi.org/10.1016/j.ijheatmasstransfer.2021.122457

VI. J. I. Knarud, T. Kvande, S. Geving. Hygrothermal simulation of interior insulated brick wall – Perspectives on uncertainty and sensitivity. Buildings 13(7) (2023) 1701 https://doi.org/10.3390/buildings13071701

Authorship clarification for articles

Applying the CRediT author statement methodology. Reiterating statements included in Article V and VI.

Article	J.I. Knarud	S. Geving	T. Kvande
I	Methodology, Formal analysis, Writing - Original Draft, Writing - Review & Editing, Visualization	Supervision	Conceptualization, Methodology, Resources, Supervision, Project administration, Funding acquisition
II	Conceptualization, Methodology, Validation, Formal analysis, Investigation, Data Curation, Writing - Original Draft, Writing - Review & Editing, Visualization, Project administration	Conceptualization, Writing - Review & Editing, Supervision, Project administration, Funding acquisition	Conceptualization, Resources, Writing - Review & Editing, Supervision, Project administration, Funding acquisition
III	Conceptualization, Methodology, Software, Validation, Formal analysis, Writing - Original Draft, Writing - Review & Editing, Visualization	Conceptualization, Writing - Review & Editing, Supervision	-
IV	Conceptualization, Methodology, Software, Validation, Formal analysis, Writing - Original Draft, Writing - Review & Editing, Visualization	Conceptualization, Writing - Review & Editing, Supervision	-
V	Conceptualization, Methodology, Validation, Formal analysis, Investigation, Writing - Original Draft, Writing - Review & Editing[a], Visualization.	Writing - Review & Editing, Supervision.	Writing - Review & Editing, Supervision.

VI	Conceptualization, Methodology, Software, Validation, Formal analysis, Investigation, Data Curation, Writing - Original Draft, Writing - Review & Editing, Visualization.	Writing - Review & Editing, Supervision.	Writing - Review & Editing, Supervision.

[a] By mistake not included in the published article's CRediT author statement.

Explanations in accordance with CRediT [1, 2]:

Conceptualization: Ideas; formulation or evolution of overarching research goals and aims
Methodology: Development or design of methodology; creation of models
Software: Programming, software development; designing computer programs; implementation of the computer code and supporting algorithms; testing of existing code components
Validation: Verification, whether as a part of the activity or separate, of the overall replication/ reproducibility of results/experiments and other research outputs
Formal analysis: Application of statistical, mathematical, computational, or other formal techniques to analyze or synthesize study data
Investigation: Conducting a research and investigation process, specifically performing the experiments, or data/evidence collection
Resources: Provision of study materials, reagents, materials, patients, laboratory samples, animals, instrumentation, computing resources, or other analysis tools
Data Curation: Management activities to annotate (produce metadata), scrub data and maintain research data (including software code, where it is necessary for interpreting the data itself) for initial use and later reuse
Writing - Original Draft: Preparation, creation and/or presentation of the published work, specifically writing the initial draft (including substantive translation)
Writing - Review & Editing: Preparation, creation and/or presentation of the published work by those from the original research group, specifically critical review, commentary or revision – including pre- or post-publication stages
Visualization: Preparation, creation and/or presentation of the published work, specifically visualization/ data presentation
Supervision: Oversight and leadership responsibility for the research activity planning and execution, including mentorship external to the core team
Project administration: Management and coordination responsibility for the research activity planning and execution
Funding acquisition: Acquisition of the financial support for the project leading to this publication

[This page is left blank]

1. Introduction

1.1. General context

In a world that struggles with climate and environmental issues related to energy production and consumption, a reduction in certain energy needs could slow down the ever-growing demand for more energy, smooth transitions between energy production forms, and alleviate markets that are often strained from demands and politics. Heating of buildings constitutes one area in which reduction of energy needs can provide a significant contribution in this regard [3, 4]. Especially in the Nordics, the building stock has a high heating requirement during the winter-half of the year. To remedy this, newer building regulations have continuously been incorporating stricter requirements for reducing and avoiding heat losses in new buildings. Simultaneously one gets a "side-effect" where non-energy-renovated older buildings seemingly pose a great potential for reducing energy consumption [4], that is, when comparing to what theoretically can be achieved with added insulation thickness, improvement of windows, increased airtightness, and installment of ventilation with heat recovery, to mention a few key measures. In practice, however, renovation of an existing building is often not a straightforward process but rather complex, e.g., [5, 6]. Depending on how much of the existing building and its appearance that is protected, or which should be kept or preserved, technically ideal or low risk energy-saving measures are often not applicable, for instance, measures like adding exterior insulation, airtightness, and weather protection, including eliminating heat bridges. Thus, higher risk and more technically complicated solutions must be considered, measures like interior insulation and moisture handling concepts. Nevertheless, a significant potential for reducing energy consumption persists [5, 7, 8]. Improving indoor comfort and the standard of the building space, thereby improving the utilization and market value of the building, also drives a demand for renovation. This includes removing cold drafts from surfaces, ventilation, and air leakages, as well as modernizing otherwise inconvenient or outdated building space.

Reuse of buildings also ensures preservation of buildings, as an alternative to them becoming obsolete and neglected, or abandoned to the point of deteriorating [9], or ultimately being torn down. Energy-renovation can also avoid additional energy-consumption associated with new construction, compared to reuse and preservation, as well as potentially having a beneficial financial and environmental dimension.

1.1.1. Retrofit of masonry buildings

A significant portion of buildings that are candidates for energy renovation consists of masonry buildings built in the period 1850-1950 [5, 10]. Many of these masonry buildings constitute city environments, architectural styles, aesthetical expressions, and historical heritage that are to different degrees given status of preservation and protection. Preserving heritage value is an important consideration in energy renovation projects [6, 11].

Interior insulation retrofit is often considered in energy renovation of existing buildings with protected facades. However, even though considered, interior wall insulation may not always be an imperative measure [12], with other measures being easier and less risky to implement when considered in combination with an overall assessment of energy saving, comfort, and health potentials. Hygrothermally, in cold temperate climates, interior insulation of masonry is a much riskier solution than exterior insulation design. With interior insulation, the masonry temperature is lowered, which can change the frequency and consequences of freeze-thaw cycles experienced by the masonry, and lead to frost damage [13, 14]. Furthermore, the added insulation decreases the U-value of the building envelope, lowering the outward heat flux, which reduces the evaporation potential of moisture from the masonry [15]. The moisture content of the masonry can therefore be significantly higher than before interior insulation was applied [16]. A higher moisture content may result in more frequent exceedance of critical moisture contents for frost damage and, furthermore, increase the thermal conductivity of the masonry, letting cold creep deeper into the structure by lowering its thermal resistance [16]. With interior insulation, embedded wooden beam ends that support building floors will experience colder temperatures and higher relative humidity (RH) conditions, causing increased risk of deterioration [17]. Adding interior insulation also adds interior vapor resistance, especially since the insulation is not applied alone but is accompanied with an interior finish with or without a vapor retarder or barrier. With increased interior vapor resistance, a drying potential to the interior during warm exterior climate conditions is also decreased [18]. As a result, high RH may also be experienced in the interior structure, for instance heightening the risk of mold [19]. Interior insulation might also make thermal bridges susceptible to increased condensation risk [11].

Consequently, if interior insulation retrofit is considered, there is a great need for making sure that the solution being chosen is on the safe side of what otherwise could result in moisture- and frost-related damage.

1.1.2. Research into interior insulation retrofit

Hygrothermal performance studies have received much scientific attention. These studies often involve monitoring in situ performance [19-26] or constructed field test performance [27-33] to local climate exposure. Assessment of performance in relation to damage criteria, e.g., by means of damage indexes (frost index, mold index), has also become common among such studies [19, 21, 22, 25, 28-30, 32, 33].

A limitation with hygrothermal performance studies is that it is often difficult to generalize the results. There are many influential parameters or factors that impact hygrothermal performance, which from a non-detailed perspective include: local climate, building design, building surroundings, façade orientation, façade design and weather exposure, masonry wall design, brick and mortar materials, masonry condition and craftmanship, insulation material, and retrofit solution design. Furthermore, execution of retrofit measures depends on the overall (societal) context of the specific renovation project [11]. Delving into details, regarding the substance, behavior, physics, and modeling of all these aspects adds even more complexity, e.g. [34-37].

Nevertheless, hygrothermal performance studies provide important case studies that in sum generate understanding of how to approach interior insulation retrofit. Furthermore, case studies can be used as measurement datasets to which validate and improve hygrothermal simulation efforts.

Another set of studies are laboratory studies. These studies either address specific aspects of moisture transport mechanisms in an investigation of a specific masonry wall structure [38], in context of applying interior insulation, or they address the more holistic performance of interior insulated masonry [39, 40]. Different from the field and in situ studies that are exposed to real world exterior climate, the laboratory studies are often exposed to more simple, synthetic climate sequences. However, there are exceptions where real-world climate exposure is imitated in the laboratory [40, 41]. With a simpler climate exposure, wall performance behavior or detailed behavior might be easier to interpret. However, actual performance in existing buildings is not revealed.

Hygrothermal simulation studies can approach performance prediction, or attempt confirmation or replication of in situ or field studies [21, 32, 42], or prediction or replication of laboratory studies [39-41]. Additionally, simulation studies can investigate variability or sensitivity by varying inputs [18], or investigate performance differences between solution alternatives [43, 44]. To accommodate similar aims, such studies can be expanded with probabilistic studies to more extensively investigate result sensitivity to parameter variation [45-47]. Some simulation studies also address the impact of model simplifications, for instance, differences between 1D, 2D and 3D [48-50]. Hygrothermal simulation, if the models prove reliable, can provide valuable help in analyzing what kind of interior insulation solution that should be chosen in an interior insulation retrofit project. However, although hygrothermal simulation has become easy to execute, it remains somewhat difficult to achieve quality (e.g., trustworthy accuracy) and to avoid challenging uncertainty. While simulation models are simplified to some ideal structure buildup and material interaction, the conditions in existing buildings are far from ideal. This due to imperfect craftmanship, complicated geometric details or geometric unevenness, in addition to complex material properties and interactions. It is therefore often difficult to replicate structure behavior in a simplified model, e.g., [42]. In such a perspective it is of interest to point out that many, if not most, simulation studies are conducted post-measurements (a posteriori) and thus often include some model calibration to measurement results. Far fewer simulation studies are conducted prior (a priori) to measurements, although there are a few, e.g., [39].

1.2. Contextual background of the thesis

This section includes a more specific background to underpin the thesis research trajectory and focuses therein. The background is written from a perspective of what scientific literature was available in the years 2015-2016 when the origins of the thesis' focus (scenario of Article II, IV and VI) were formed.

1.2.1. Interior insulation options

Stopp et al. [51] laid out the four principal options for interior insulation:

1. vapor barrier on warm side of insulation (vapor open, non-capillary insulation material)
2. humidity dependent vapor retarder/barrier on warm side of insulation (vapor open, non-capillary insulation material)
3. capillary active insulation material
4. vapor tight insulation material

A humidity-dependent or smart vapor barrier (SVB) functions by providing low vapor permeability at low RH conditions and high permeability at high RH conditions. It can thereby utilize the seasonal changes to the thermal gradient through a building envelope. An illustration of SVB functionality is provided in Fig. 1. Cold exterior weather causes a substantial positive thermal gradient towards the interior, thus causing decreasing RH in direction of the interior, putting the SVB at low RH conditions. This due to the RH's relation to saturation vapor pressure, which increases greatly with temperature. Warm exterior weather will lessen, remove, or reverse the thermal gradient, thus putting the SVB at moderate to high RH conditions dependent on exterior temperature and whether moisture is present in the building envelope. SVB functionality and performance are very product dependent, with several products existing on the market.

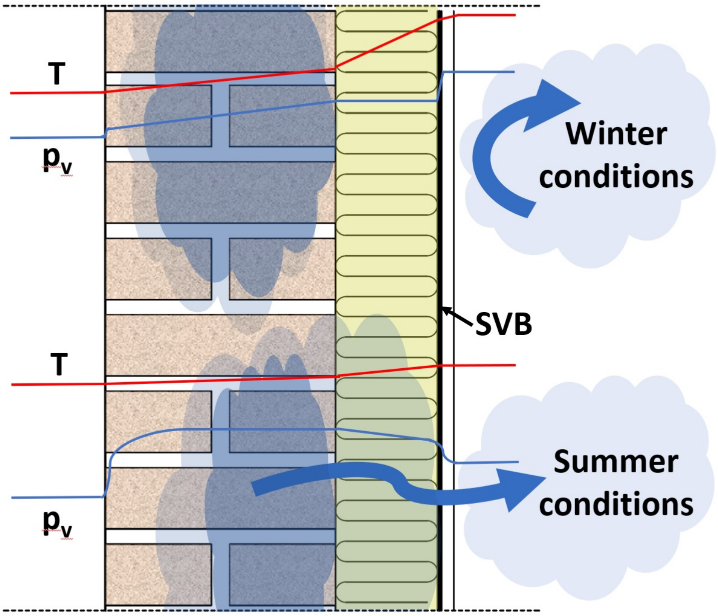

Fig. 1 SVB functionality when applied to interior insulated masonry. Vapor tight during winter and vapor open during summer. Typical illustrative profiles for vapor pressure and temperature are included. Figure assumptions include a significant over-hygroscopic saturation of the masonry, and a temperate climate with summer temperature close to but below indoor temperature.

A capillary active material utilizes a difference in capillary pressure over its thickness to enable capillary transport of moisture in the opposite direction of vapor transport during winter conditions. That is, with an interior surface that dries out, thereby providing high capillary suction, it can draw moisture from the exterior of the insulation material, which experiences increased moisture content or interstitial condensation with resultant lower capillary suction. More detailed description can be found in [36, 52].

All the four options have potential advantages and disadvantages that are dependent on the circumstances of the setting in which they are applied. This is elaborated a bit further in the next four paragraphs, while Table 1 summarizes general issues and the expected functionality of the four insulation options.

The traditional vapor barrier avoids interstitial condensation; however, at the same time it prevents inward drying, thus risking moisture issues from driving rain and other infiltration moisture sources. Furthermore, it can be susceptible to summer condensation or high RH conditions exterior of the barrier during warm summer conditions [53, 54].

SVB reduces or avoids interstitial condensation during winter conditions, while it allows some inward drying during summer conditions [55]. However, for masonry the inward drying might be insufficient if the masonry absorbs too much wind driven rain or is susceptible to other infiltration moisture sources. Furthermore, during cold exterior climates (winter) SVB utilization may experience challenging moisture issues, for instance at wooden beam ends [45], when the SVB behaves relatively vapor tight, since the measure itself does not contribute in improving the moisture conditions under such circumstances. Additionally, SVB requires an interior finish with low vapor resistance.

The capillary active insulation material aims at countering vapor diffusion from the indoors with inward capillary moisture transport, while simultaneously alleviating moisture accumulation from wind driven rain, by evaporation to the interior. However, since its functionality facilitates a moisture content in the insulation layer that is substantially higher than for the dry state, the thermal resistance becomes reduced [36, 45]. Furthermore, increased humidity can be experienced at the interior wall surface and indoors, which can be potentially problematic [36], and it gives limitations to interior-finish solutions [43].

A vapor tight insulation material avoids interstitial condensation; although, for rigid panels it can be vulnerable to air and vapor leaks if not properly sealed [39, 51]. It prevents inward drying, and thereby risks moisture issues in the masonry structure and is risky if wooden beam ends are present. Some typical closed cell materials benefit from not adsorbing moisture, thereby keeping a near dry thermal resistance [45].

Solutions without inward drying capability might perform sufficiently for structures not exposed to or with minimal exposure to driving rain [36], whereas inward drying capability could be needed when there is significant rain exposure, e.g., [56]. Driving rain exposure has been found to be a significant challenge in several interior insulation retrofit assessments [17, 21, 57, 58]. Assessing the scientific literature, accounts of SVB performance seem to be lacking in context of interior insulation retrofit of masonry. A smart vapor retarder (SVR) (SVRs having less vapor resistance than SVBs) is partially addressed in a probabilistic simulation study [45]; however, the study only addresses cold exterior conditions (heating season), and thus does not capture SVR performance for inward drying. Capillary active insulation is, on the other hand, given much attention, including in ongoing research [36, 43, 56, 59-63] (2016 perspective). It can, of course, be that the scientific community deems capillary active insulation to be a more viable or capable solution than smart vapor barriers; however, it is hard to find studies having conclusively discarded smart vapor barriers as a solution of merit. Furthermore, there is also a technological development that plausibly will provide even better SVR/SVB products in the future. Thus, it would be of interest to have more studies incorporating smart barrier functionality and performance to acquire more data. For reference, on fictitious interior insulation retrofit solutions, the current author did conduct a simple 1D simulation / sensitivity study [64]. This included simulations with both mineral wool (MW) + SVB and calcium silicate (CS), the latter as a capillary active insulation material. The results of that study indicated that CS outperformed MW + SVB; however, SVB also indicated some benefit by lowering RH during winter compared to MW with and without a traditional vapor barrier. Still, the study was neither much sophisticated in modeling the SVB and masonry, nor in addressing the ramifications of differences in thermal resistance between MW and CS.

Table 1 Principal interior insulation options – Expected functionality.

Issues	Vapor barrier	Smart vapor barrier/retarder	Capillary active	Vapor-closed
Thermal resistance	preserves	preserves	diminishes	preserves
Inward drying	prevents	allows	allows	prevents
Interstitial condensation	avoids	avoids/reduces	allows/handles	avoids
Summer condensation	may appear	avoids	avoids	depends
Humid interior surface	avoids	avoids	may appear	avoids
Interior finish and furnishment	minimal issue	gives limitation	gives limitation	minimal issue

1.2.2. Masonry structures and hygrothermal simulation challenges

Masonry from the period 1850-1950 typically implies load bearing masonry, with walls in this category being one brick thick or more. A great variety exists in design, from massive walls to hollow walls containing different cavity patterns.

Driving rain is a well-known challenge for masonry walls [57], either in form of regular moisture absorption, or in form of leaks through cracks or imperfect bonding in the masonry. Protection against rain penetration or infiltration has traditionally included:

- Increasing wall thickness, which implicitly adds internally a mortar collar joint that provides capillary and vapor resistance [65].
- Adding air cavities, which reduce penetration/infiltration pathways, and which potentially can provide some venting air circulation if allowed for by design.
- Providing external render [57, 62], which can act like a capillary retarder and remove infiltration pathways.
- Designing cornices, ornated sills and parapets [66], which act as overhanging cover.

Modern efforts to improve protection against rain typically involve replacing old exterior render with water repellent render with low vapor resistance, or applying hydrophobization treatment [57]. Bare brick masonry is, however, challenging due to infiltration pathways that can follow porous, poorly bonded, or cracked brick-mortar interfaces. Rain penetration has been observed to worsen by leakage through brick-mortar interfaces in [65]. Additionally, the bricks can have a quite large capillary absorption capacity, capable of absorbing and distributing large amounts of moisture during rain events. The masonry may therefore struggle to dry out between periods of rain; a situation which becomes worse with interior insulation.

Although infiltration pathways along the brick-mortar interface constitute a known issue, few studies have investigated this. More extensively studied is the brick-mortar transverse interface resistance [48, 67-69], in contrast to the increased permeability along the interface [65]. A question also arises on how to model such moisture infiltration.

A complicated detail in masonry structures is the embedded beam end that is due to its position especially susceptible to moisture risk. Direct attention to the beam end performance has been given in several studies [17, 20, 21, 57, 62, 70] when it comes to interior insulation retrofit. These studies include 2D hygrothermal simulations and assessments. However, the beam end is an inherent 3D detail and a 3D hygrothermal problem [17]. Although thermal simulations of the beam end have been done in 3D [71], the combined heat and moisture (hygrothermal) simulations are more demanding and difficult in 3D.

1.2.3. Material properties

Access to sufficient material property data is a challenge for hygrothermal simulation efforts. The data need to be representative for the specific physical retrofit project in focus, which simulations are applied to for analysis and support. A hygrothermal model requires several fundamental properties such as vapor permeability, capillary conductivity, moisture retention, density, specific heat capacity, and thermal conductivity [72]. Among these, all except density are moisture dependent. Nevertheless, heat capacity is usually approached with a simple weighing relation of the heat capacity of the bulk dry material and the contained water (moisture content) [73]. For the remaining properties, moisture dependence can be quite complex (further visited in Section 2.1). Temperature dependence is also an issue; however, it can be largely accounted for by temperature dependence in more fundamental physical parameters of water and gas kinetics, and the residual material-specific temperature dependence is often neglected. Physical identification of properties involves test procedures and use of laboratory equipment of varying sophistication. This can limit widespread availability of testing, especially at the high end of sophistication. It thereby limits a more thorough/advanced identification of material properties to well-equipped laboratories with experienced personnel, something only research projects or a select few retrofit projects have resources for.

Depending on access to laboratory resources, experience, and time, the different options available for identifying material properties for use in hygrothermal simulation can be listed as follows.

1. Measure material properties.
2. Find similar materials in material databases or in scientific studies, and assume they are representative for materials in a project.
3. Predict properties through property models.
4. Approximate or calibrate properties through an iterative simulation effort or parametric sweep, and evaluate against “goodness of fit” to experiment measurements.
5. Combinations of 1-4.

An alternative to finding similar materials, can be to apply generic materials that are synthesized from clustering techniques and parameter correlation assessments; comprehensively described by Zhao et al. [74, 75]. Generic materials can help in situations with limited knowledge of specific materials [75].

Iterative simulation or parametric sweep, evaluated against experimental measurements, is of course only applicable if experimental measurements are available, either in situ monitoring prior to a retrofit project or if a limited experiment is conducted with material samples from the set-for-retrofit building or by non-destructive measurement means on the building. For instance, simulating a masonry structure, Panico et al. [76] conducted a parametric sweep to optimize/identify material data by calibration to in situ monitoring. The parametric sweep calibration was further supplied with validation to different, more recent monitoring data.

Due to an often lack of ease in gathering property data by laboratory measurements, much attention has been given to simplify prediction and approximation of property values by means of different modeling approaches, e.g., [77-79]. Such modeling can identify "hard-to-come-by" properties by applying easier available property parameters as input. There can be benefits to further develop such modeling. On one hand, this can further simplify or ease model implementation, while on the other hand, it can improve accuracy or even include more advanced features, e.g., account for more dependences. Depending on intended use of material property models, requirements of accuracy and complexity may vary.

1.3. Problem formulation

On the background of Section 1.2, the scope of the present thesis will be limited to vapor open insulation with SVB, modeling of bare brick masonry with beam ends, and possible simplifications regarding identifying material properties for hygrothermal simulation.

Unknown issues and questions are elaborated in the following. However, not all of the following are included in the subsequent objective(s).

1.3.1. Smart vapor barrier

As already mentioned, scientific accounts of SVB are lacking for interior insulation retrofit of masonry. Not much is documented regarding SVB performance regarding the inward drying potential. Will an SVB both improve drying at the interior masonry surface and at the beam end? How to model the SVB and its functionality? Is the SVB a promising or sufficient measure for interior insulation retrofit?

1.3.2. Bare brick masonry and beam ends

It can be especially challenging to assess bare brick masonry due to the possibility of increased permeability or presence of infiltration pathways along brick-mortar interfaces. What is the performance of bare brick masonry exposed to driving rain? Which rates of absorption can be expected in joints due to the brick-mortar interface? What are the indications of poor brick-mortar interfaces? Does joint finish affect absorption? How to model bare brick masonry with increased permeability and presence of infiltration pathways? How does the beam end fare regarding moisture content, when embedded in severely wetted masonry, concerning wetting and drying? Is it practical to model beam ends in 3D? What is the impact on results when modeling beam ends in 3D compared to 2D?

1.3.3. Simplifications in identifying difficult material properties

With certain material properties being difficult and resource demanding to gather, then property modeling for property prediction is one approach. However, even with modeling there likely are assumptions, guesses, estimates, or simplifications that must be made to keep laboratory measurements or simulation efforts within practical reason. Are there simplifications that reasonably can be made? How reliable is property modeling compared to measurements? What uncertainties are introduced with property modeling? How do uncertainties impact hygrothermal simulation results? Is hygrothermal simulation reliable enough with the uncertainty of not having all properties measured?

1.4. Objectives

Inspired by the problem formulation in Section 1.3, more precise objectives are formulated. This is outlined by an aim of future usefulness of the work, a main objective to specify the overarching pursued production output of the work, and sub-objectives to specify pursued deliveries. All is intended to be in context of interior insulation retrofit of masonry, although there might be wider applications. The following objective and sub-objectives are intended to cover the overall objectives and pursuits of the thesis, whereas the more specific research questions that are answered by the enclosed journal articles are summarized in Section 3.

1.4.1. Aim

Provide scrutiny, insight, and methodology that can improve understanding, and ease and improve application of analysis and hygrothermal simulation tools.

1.4.2. Main objective

Provide contribution to modeling techniques in support of hygrothermal simulation. Furthermore, provide insight that highlights modeling uncertainty, and which guides the ability to more confidently predict experimental results of bare brick masonry exposed to driving rain.

1.4.3. Sub-objectives

Based on the problem formulation in Section 1.3 sub-objectives have been narrowed down to:

Smart vapor barrier

1) Gather more information on the performance of SVB through experiment and simulation efforts.

Brick-mortar interface

2) Determine contribution to moisture uptake by the brick-mortar interface in bare brick masonry.

Hygrothermal modeling

3) Establish a hygrothermal simulation model in a multi-physics software, providing the option of controlling all hygrothermal physics formulas, climate boundary formulas, and material property formulas.
4) Assess determination of the liquid transport property of masonry materials, as input for hygrothermal modeling, when direct measurements are not an available option.

1.5. Scope in context, and limitations

The larger context of hygrothermal performance related to interior insulation retrofit of masonry is illustrated in Fig. 2, wherein the thesis focus areas are highlighted in bold.

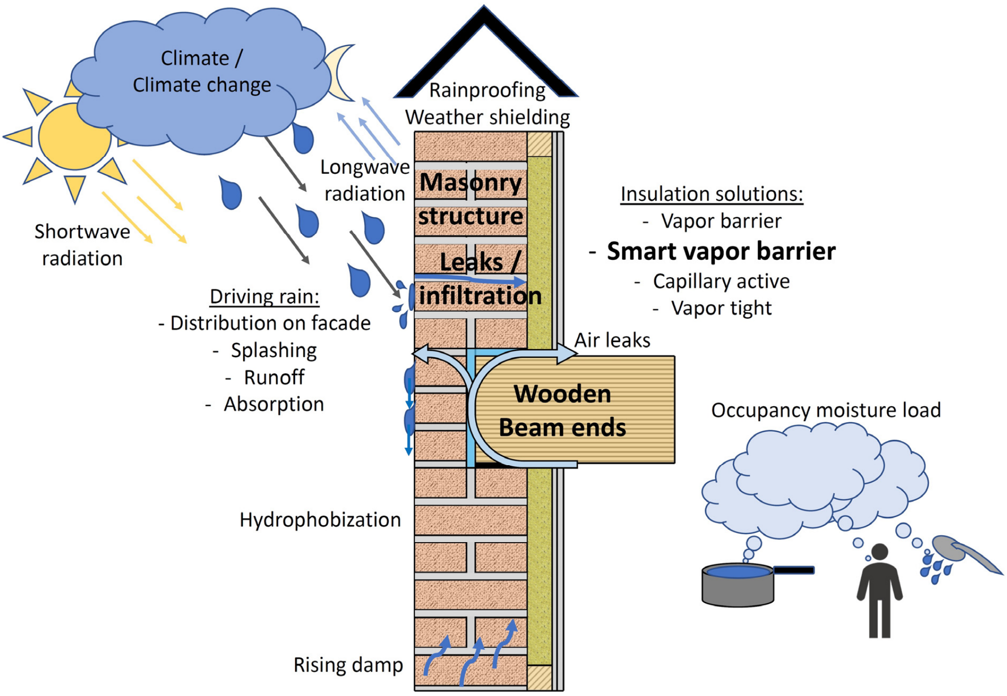

Fig. 2 Scope in context - Scope focus marked in bold.

Including an embedded beam end, makes what is illustrated in Fig. 2 a clear 3D problem regarding heat and moisture transport. Additionally, the brick-mortar system is also a 3D composition of head joints, bed joints, and collar joints. Thus, pursuit of 3D functionality should be an aim regarding hygrothermal modeling. Furthermore, the central moisture source in focus for bare brick masonry is driving rain. Although rain intensity can vary greatly, a hygrothermal model should also handle heavy rain exposure, which can create sharp moisture front propagation into the masonry. This can be numerically demanding in 2D and 3D models, which therefore warrants attention.

1.5.1. A comment on the starting point and development of scope

Energy efficient and moisture safe retrofitting of brick buildings with internal insulation has been the working title of the research. However, the research direction and focus have evolved over time. It was early on perceived that there are too many influential parameters, or combinations of parameters, to generalize what would entail moisture safe retrofitting. With numerous parameters affecting climate environment and exposure, and furthermore constituting structure design, material use and interaction, hygrothermal strategy, and workmanship, including additional uncertainty of existing buildings, then moisture safe retrofitting is more easily approachable when addressed case specific, i.e., when many of the parameters can be narrowed down. Consequently, the focus shifted. It became more interesting to address how to improve tools and understanding, which can be applied when analyzing (case specific) hygrothermal designs.

1.5.2. Topics not included in the scope

A few topics that are not included in the scope, but which are central in an overall context of interior insulation retrofit of masonry, are for clarity and reference listed in Table 2.

Table 2 Central topics not included in the scope, with references to where more on these topics can be found

Topic	Refer to, e.g.:
Considerations on decision making for energy renovation and interior insulation retrofit.	[11]
Probabilistic hygrothermal analysis of interior insulation retrofit.	[47]
Rain exposure of masonry facades, including deposition, adherence, and absorption.	[66, 80]
Future climate – changing climate exposure of masonry buildings.	[81]
Damage mechanisms (frost or mold) and damage indexes.	[13, 82, 83]
Hysteresis of masonry materials.	[84, 85]

1.6. Terms, abbreviations, and definitions

Regarding definitions and distinctions, the following terms require some comments on their use and intended meaning. The terms (moisture) infiltration, penetration and permeation might seem like synonyms, and sometimes they are indeed used to explain each other in dictionaries, specifically when describing the process of something passing into or through a substance. Nevertheless, the thesis tries to uphold the following subtle distinction (while knowing it is not following any standard convention).

Infiltration – A process of moisture moving into the structure, without specifically addressing how this process occurs. Furthermore, structure here implies the masonry wall with an interior insulation system. Here, the infiltration mainly addresses moisture appearing inside the structure, interior of the masonry, implying that one or more infiltration pathways exist through the masonry.

Penetration – A process of moisture passing through a structure entity. Here, mainly attributed to moisture penetrating the masonry, but without description of how the penetration appears.

Interpenetration – A process of moisture passing through a part of the structure entity (the masonry) up to a point where the conditions for penetration or ease of penetration changes.

Permeation – A process of moisture passing through a substance with the implicit understanding of moisture diffusion or diffusive spread of the moisture, thereby increasing the material moisture content (in the masonry) and with the moisture appearing as damp patches on the interior masonry surface when it reaches that far.

Several abbreviations are used in the current thesis. Corresponding terms and definitions are listed in Table 3.

Table 3 Definitions of terms and abbreviations

Term	Abbreviation	Definition	Based on or inspired by source
Calcium silicate	CS	Insulation material of calcium silicate, a highly capillary active insulation material. Must not be confused with calcium silicate bricks (sand-based bricks).	
Effective thermal conductivity	ETC	Thermal conductivity dependent on level of saturation. Units: [J/(m·K)]	
Initial rate of absorption	IRA	Measured absorbed water through a surface area for the first minute of partial immersion. Units: [kg/(m^{2}min)]	[86]
Lime-cement	LC	Lime-cement mortar, a type of mortar consisting of specified portions of lime and cement.	
Moisture design reference year	MDRY	Typically, the 90th percentile of year severity in terms of moist climate exposure. I.e., severe climate with 10-year return period. No fully agreed upon determination exists. Synonyms include “moisture reference year” (MRY) or “hygrothermal reference year” (HRY).	[87, 88]
Mineral wool	MW	Glass or stone wool. Can span a wide range of densities.	
Partial differential equation	PDE	Differential equation being multivariable, containing partial derivatives with respect to the temporal and spatial variables: t,x,y,z.	
Relative humidity	RH	Ratio of vapor pressure to saturation vapor pressure. Units: [-]	
Smart vapor barrier	SVB	Vapor barrier with resistance dependence on RH, with s_d > 10 m at low but realistic RH.	[89]
Smart vapor retarder	SVR	Vapor retarder with resistance dependence on RH, with s_d < 10 m at low but realistic RH.	[89]

2. Theoretical background

Regarding interior insulation retrofit of masonry buildings, several PhD theses [90-98] have been published over the last few years. These include a range of extensive literature reviews, in addition to descriptions of the research and findings of the theses. Extensive repetition or overlap of these reviews does not elicit much purpose. Instead, the literature review of this chapter will focus on the three main topics identified and condensed through sections: 1.2 Background, 1.3 Problem formulation and 1.4 Objective. For reference, a list of the recent relevant theses on interior insulation of masonry is provided in Table 4, with the focus of each highlighted.

Table 4 Recent theses on interior insulation of masonry

Author of thesis	Ref.	Year	Country	Title and focus
Kloseiko, Paul	[98]	2022	Estonia	*Hygrothermal performance of masonry walls retrofitted with interior insulation in cold climate* **Thesis focus:** Capillary active insulation, properties and modeling, including in situ monitoring and simulation. **Review focuses:** Performance and damage criteria.
Gutland, Michael	[97]	2022	Canada	*Evaluating uncertainty in hygrothermal modelling of heritage masonry buildings* **Thesis focus:** Hygrothermal masonry modeling and uncertainties, including spatially stochastic and fracture modeling. **Review focuses:** Hygrothermal modeling in general, damage mechanisms, fracture modeling.
Soulios, Vasilis	[96]	2021	Denmark	*Hygrothermal performance of hydrophobized brick and mortar – Energy renovation through internal insulation – Can hydrophobization improve moisture safety?* **Thesis focus:** Hydrophobization, material testing and hygrothermal performance. **Review focuses:** Hydrophobization.
Jensen, Nickolaj	[95]	2021	Denmark	*Robust solutions for internal retrofitting solid masonry walls in historic buildings with regards to hygrothermal performance* **Thesis focus:** Field measurements, simulation calibration, fungal growth. **Review focuses:** Heat, air and moisture transport, interior insulation solutions, measures improving hygrothermal performance, decay and risk assessment, categorized state-of-the-art overview.

Marincioni, Valentina	[94]	2020	UK	*A probabilistic approach for the moisture risk assessment of internally insulated solid walls* **Thesis focus:** probabilistic assessment of capillary active wood fiber insulation performance, including case studies and simulations. **Review focuses:** Interior insulation in general, probabilistic moisture risk assessment, probabilistic methods, material property function models.
Calle, Klaas	[93]	2020	Belgium	*Renovation of historical facades: the rescue or the kiss of death?* **Thesis focus:** Material variability and clustering, absorption and interface resistance, rainwater infiltration, probabilistic sensitivity analysis. **Review focuses:** Historic brick and mortar production and quality, material properties and hygrothermal simulation in general.
Ruisinger, Ulrich	[92]	2019	Germany	*The hygrothermal behaviour of joist ends in internally insulated buildings* **Thesis focus:** In situ measurements, hygrothermal simulation in 2D and 3D, determination of material properties. **Review focus:** Beam ends in masonry, including airtightness at beam end.
Hansen, Tessa	[91]	2019	Denmark	*Hygrothermal performance of internal insulation in historic buildings* **Thesis focus:** In situ hygrothermal performance, quantification of wind driven rain and absorption, hydrophobization, material characterization. **Review focuses:** Risk assessment, wind driven rain quantification, hydrophobization.
Odgaard, Tommy	[90]	2019	Denmark	*Challenges when retrofitting multi-storey buildings with interior thermal insulation* **Thesis focus:** Potential for energy reduction, hygrothermal performance in field and in situ experiments. **Review focuses:** Historic Danish masonry buildings, hygrothermal conditions, damage models.

2.1. Hygrothermal material properties – moisture dependence

The following review will not be exhaustive in terms of covering all expressions or models that have been proposed for description of material properties. Instead, it will focus on the modeling paths perceived to have the largest consensus/application in scientific works (on building physics, regarding masonry or porous materials, with inputs from soil physics), while simultaneously being simple enough for widespread application. More advanced modeling approaches or significant alternative approaches will only be briefly mentioned for reference.

Vapor permeability and thermal conductivity are not given much attention in the thesis research; nevertheless, they will be addressed for better overview and "completion" of the topic.

2.1.1. Sorption isotherms and retention curves

Moisture retention can be expressed in form of several different cumulative distribution functions, including for instance log-logistic, Weibull, lognormal and Van Genuchten form [99]. Use of Van Genuchten has become widespread in building physics, e.g. [49, 100, 101]; nevertheless, a weighed sum of Gauss distributions has also been proposed [77] to be similar in performance to Van Genuchten [84]. Only Van Genuchten will be further described. In its general form the Van Genuchten expression is given as Eq. (1); however, it is more often expressed as Eq. (2) thereby becoming a two- instead of three-parameter expression. This change was proposed by Van Genuchten [102] to obtain closed-form estimates of capillary conductivity [103]. The change is not needed unless the retention function is applied to the analytical Van Genuchten - Mualem conductivity model [102].

$$w = w_{cap}\left[1+\left(c_w p_c\right)^{n_w}\right]^{(-m_w)} \tag{1}$$

$$w = w_{cap}\left[1+\left(c_w p_c\right)^{n_w}\right]^{\left(\frac{1-n_w}{n_w}\right)} \tag{2}$$

where w [kg/m^3] is moisture content, w_{cap} moisture content at capillary saturation, c_w [Pa^{-1}] a characteristic coefficient related to pore size, p_c [Pa] capillary pressure, and n_w and m_w distribution shape coefficients [99].

The simplification from Eq. (1) to (2) comes at the expense of some flexibility loss in describing distributions [99]; however, with the benefit of having fewer parameters to identify. Nevertheless, unimodal Van Genuchten expressions like Eq. (1) and (2) are inaccurate in describing hygroscopic and capillary moisture retention for materials [104, 105]. Expressing the Van Genuchten expression as multi-modal, Eq. (3) [103], instead of unimodal, can mitigate some of the flexibility loss and inherent inaccuracy.

$$w = w_{cap}\sum_{i=1}^{N}\left(l_{w,i}\left[1+\left(c_{w,i}\cdot p_c\right)^{n_{w,i}}\right]^{\left(\frac{1-n_{w,i}}{n_{w,i}}\right)}\right) \tag{3}$$

where $l_{w,i}$ is a weighing coefficient equal to the share of pores associated with corresponding inflection point in the cumulative pore size distribution, i.e. $\Sigma\, l_{w,i} = 1$, $c_{w,i}$ inverse of p_c at the inflection point, where pore size and capillary pressure is related through the Young-Laplace equation [85].

A beneficial property of the Van Genuchten model is that its derivative is continuous and goes asymptotically towards zero at higher and lower capillary pressures [103].

Carmeliet and Roels [106] proposed an additional simple fitting term to be combined with the Van Genuchten expression, Eq. (4), to better account for adsorption in the hygroscopic region.

$$w = w_{lim}\phi^{n_{w,0}} + \left(w_{cap} - w_{lim}\right)\left[1 + \left(c_{w,i} \cdot P_{suc}\right)^{n_{w,i}}\right]^{\left(\frac{1-n_{w,i}}{n_{w,i}}\right)} \tag{4}$$

where w_{lim} would be the limiting, critical water content between the hygroscopic and over-hygroscopic region; however, the actual w_{lim} value could be expected to deviate from the critical moisture content, being a more arbitrary fitting parameter [106]. Furthermore, $\phi = \exp(-p_c/(\rho_w \cdot R_w \cdot T))$ and $n_{w,0}$ is a fitting exponent.

The first term in Eq. (4) is a Freundlich type expression, a better fit to be combined with the Van Genuchten term than the Brunauer, Emmett, and Teller (BET) theory that is often used to describe sorption and desorption in the hygroscopic region [107]. Numerous other expressions for sorption in the hygroscopic range also exist, some summarized by Feng et al. [108]. In contrast to the Freundlich type expression in Eq. (4), which has one fitting parameter $n_{w,0}$ (not counting w_{lim}), it is likely other expression variants, having more fitting parameters, could generate more accurate fits in the hygroscopic region. However, since highly detailed expressions for the hygroscopic region are seldom used in combination with the retention curve, and since the multi-modal retention curve can be given (extra) modality to cover the hygroscopic region, no further detail on expressions for sorption curves in the hygroscopic region will be provided here.

Combining Eq. (4) with multi-modality gives Eq. (5). Illustration is provided in Fig. 3.

$$w = w_{lim}\left[exp\left(-\frac{P_{suc}}{\rho_w R_w T}\right)\right]^{n_{w,0}} + \left(w_{cap} - w_{lim}\right) \cdot \sum_{i=1}^{N}\left(l_{w,i}\left[1 + \left(c_{w,i} \cdot P_{suc}\right)^{n_{w,i}}\right]^{\left(\frac{1-n_{w,i}}{n_{w,i}}\right)}\right) \tag{5}$$

It is widely accepted that not only is the capillary moisture content mobile, but also the adsorbed moisture that gives rise to a surface film [99]. Thus, in order to distinguish between moisture content associated with different forms of liquid transport, which occur simultaneously (surface and capillary diffusion), there is a need to separate moisture content into two parts. Basically, at low to moderate moisture contents, small pores are filled, enabling capillary transport, while larger pores are non-filled but do have adsorbed water films ensuring film flow (surface diffusion) [109, 110]. Since Eq. (4) and (5) are expressions to be empirically fitted to measurement data [102, 107], they are not readily separated into an adsorptive part and a capillary part. Many expressions have been proposed for splitting moisture content into parts for use in transport models. Lebeau and Konrad [109] separated the two:

$$\theta = \theta_c + \left(1 - \frac{\theta_c}{\theta_{sat}}\right)\theta_a \tag{6}$$

where θ [m^3/m^3] is the volumetric water content separated into capillary θ_c and adsorptive θ_a parts. The adsorptive expression is given as [109]:

$$\theta_a = \theta_0 \left[1 - \frac{ln|h_m|}{ln|h_{m,dry}|}\right] \tag{7}$$

where θ_0 is the adsorptive moisture content at a matric head of -1 m, h_m [m] is the matric head and $h_{m,dry}$ is the matric head at oven dryness, often assumed to be -10^5 m [109].

In combination, Eq. (6) and (7) ensure that adsorbed moisture is replaced by capillary moisture at lower capillary pressures, see Fig. 3 a) where the capillary moisture content is taken as the retention curve with the adsorptive moisture content subtracted. The curve that Eq. (7) provides is logarithmic-linear, where presumably θ_0 can be treated as a fitting parameter as implied in [109]. However, Eq. (7) may be difficult to align with multimodal versions of Eq. (3) or Eq. (5) , or for certain ranges of $n_{w,0}$ in Eq. (5).

Some retention models, e.g., [111, 112], uphold the adsorptive moisture content for the whole capillary pressure range, that is, the film-bound moisture content is not replaced by capillary moisture as capillaries are filled. Instead, in saturated pores, the film and the remaining volume (then being the "free" capillary moisture content) are summated, see Fig. 3 b). Whether such a model is applied instead of a model that replaces adsorbed moisture with capillary moisture, [109, 113], depends on choice of hydraulic conductivity model. For instance, in addition to the forementioned models [111, 112], some fractal models [110, 114] apply summated adsorbed film and "free" capillary moisture for a saturated pore structure.

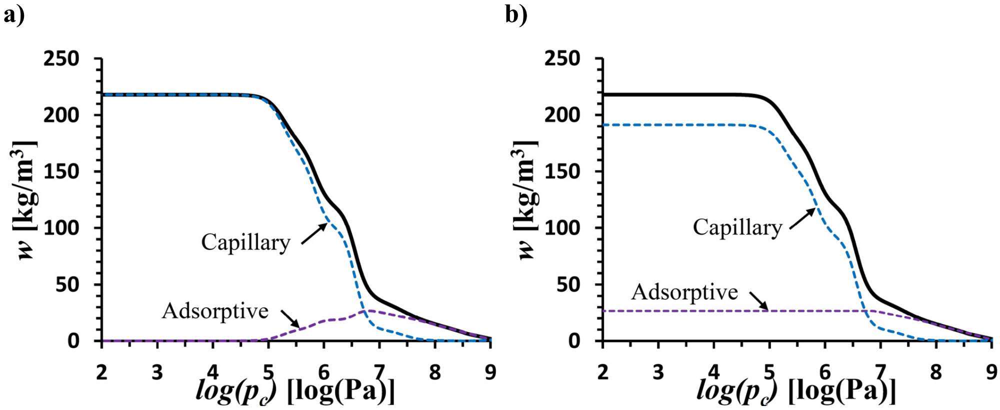

Fig. 3 Illustration of alternative handling of adsorptive and capillary retention contributions with a) capillary moisture replacing adsorbed moisture in saturated capillaries, and b) summated adsorptive and "free" capillary moisture content in saturated capillaries. Overall retention (black line) illustrates Eq. (5).

2.1.2. Vapor permeability

Some researchers [115] have in an isothermal setting [104] accounted for vapor transport as a vapor conductivity contribution to unsaturated moisture permeability, i.e., added it to hydraulic conductivity as function of capillary pressure. However, more commonly vapor transport is handled separately from liquid transport, expressed as vapor diffusivity. This is more straightforward since diffusive vapor flow is governed by gradients in vapor pressure. Still, such an approach must account for dependence to material moisture content, as vapor flow will be replaced by liquid flow as pores become filled with water. In soil science, vapor permeability has been scaled to a moisture dependent empirical tortuosity for air content in the pore space [104], whereas, in building physics, the most popular expression (e.g. [48, 73, 83, 116]) for such dependence stems from a mechanistic pore model proposed by Grunewald and Häupl [77, 117], given by Eq. (8).

$$\delta_v = \frac{\delta_{v,a}}{\mu_{dry}} \frac{1-\theta_r}{p+\left(1-\theta_r\right)^2\left(1-p\right)} \tag{8}$$

where $\delta_{v,a}$ [kg/(m·sPa)] is the vapor permeability for vapor in stagnant air, μ_{dry} [-] vapor resistance coefficient, θ relative moisture content $\theta_r = (w - w_{dry}) / (w_{sat} - w_{dry}) \approx w/w_{sat}$, p volumetric fraction that is parallel pore domain [79], i.e., theoretically $0 \leq p \leq 1$.

Eq. (8) combines Schirmer's equation [118], see Eq. (122), and a scaling expression from the serial-parallel pore model [77]. Derivation and principles of the pore model can be found in [77, 79, 84]. In Eq. (8), vapor permeability of a porous material is correlated to vapor permeability of stagnant air by the vapor resistance coefficient. The parameter p is material dependent [77]. Grunewald et al. [77] provides a procedure for calculating p, Eq. (9), from the premise that the maximum vapor permeability occurs at a (moisture content) transition point whereafter the liquid moisture flux exceeds the vapor diffusion flux. Furthermore, this involves setting the derivative of Eq. (8) equal to zero, to find its maximum, which leads to Eq. (9) [77].

$$p = \frac{\left(1-\theta_{r,tran}\right)^2}{1+\left(1-\theta_{r,tran}\right)^2} \tag{9}$$

where $\theta_{r,tran}$ is the relative moisture content at a transition where liquid moisture flux equals vapor diffusion flux. The transition point can be found by iteration [77]. This approach limits p to values $0 < p \leq 0.5$ since values above 0.5 will not for any $\theta_{r,tran}$ give a curve maximum. $\theta_{r,tran} = 0$ gives $p = 0.5$, and $\theta_{r,tran} = 1$, which is implausible, gives $p = 0$.

After following the ramifications of the serial-parallel pore model for liquid conductivity Scheffler and Plagge [79, 119] disputed that p could be a constant. They instead argued it should be a function of moisture content and proposed Eq. (10) to be used. In doing so a material will hardly have any parallel liquid transport at low moisture content when there is virtually no liquid continuity, and parallel transport will increase with higher moisture content [119].

$$p = \theta_r^{\eta_{sp}} \tag{10}$$

where η_{sp} is a parameter to adjust the serial-parallel relation of the pore model. The parameter is material dependent and should be calibrated to an experimental drying test [119].

Consequently, Scheffler and Plagge arrive at Eq. (11) [79] for representing vapor permeability as dependent of moisture content.

$$\delta_v = \frac{\delta_{v,a}}{\mu_{dry}} \frac{1-\theta_r}{\theta_r^{\eta_{sp}} + \left(1-\theta_r\right)^2 \left(1-\theta_r^{\eta_{sp}}\right)} \tag{11}$$

Among identified simulation studies on masonry, only Zhao and Plagge [120] are found to apply the Scheffler and Plagge model, which they apply for vapor permeability of sandstones. The Grunewald and Häupl model is generally applied, although most often without specific determination of p, instead applying the same values as are used in Hamstad benchmark 1 and 4 [121] with p = 0.497. One exception is Vereecken and Roels [48], who apply p = 1 for mortar, while p = 0.497 is still applied for brick. They provide no details on how p was determined for mortar. Hamstad benchmark 3 and 5 apply p = 0.2 for different materials.

To put these approaches into perspective, p is calculated according to the Grunewald and Häupl approach in Table 5 for three bricks and one mortar. Results for two bricks are fairly close to the p = 0.497 stemming from the Hamstad benchmarks. One brick is a bit lower with p = 0.480. Mortar is lower with p = 0.333. Effects of different p-values can be seen in Fig. 4 a).

Table 5 Calculation of p from the source data used in Article V, one iteration

Step	Parameter	Brick Scheffler	Brick Carmeliet	Brick Derluyn	Mortar Derluyn
	μ_{dry}	13.5	48.3	31.5	379
Step1	Guess p	0.5	0.5	0.5	0.5
	Guess $\theta_{r,tran}$	0.04	0.04	0.04	0.04
	Resultant ϕ**	0.988	0.989	0.9923	0.82
Step 2	Calc. $2xK_v$*	4.9E-16	1.37E-16	2.11E-16	1.45E-17
Step 3	$\theta_{r,tran}$**	0.040	0.010	0.012	0.33
	Resultant ϕ**	0.988	0.916	0.94	0.77
Step 4	p	0.480	0.495	0.494	0.310
Step 5	Calc. $2xK_v$*	4.9E-16	1.27E.16	2.0E-16	1.36E-17
Step 6	$\theta_{r,tran}$**	0.040	0.010	0.012	0.32
Step 7	p	0.480	0.496	0.495	0.333

* $2xK_v$ to compare to material total conductivity whereat the phase dividing function equals 0.5, see [77]; the expression for K_v can be found in Article V.

** Readings from similar spread sheet setup as used to calculate the hydraulic conductivity in Article V.

Following the Scheffler and Plagge approach, p is no longer a constant to be identified. Instead, the serial-parallel functions can be compared graphically in Fig. 4 b). Scheffler and Plagge [79] explain that the maximum of the function is a consequence of serial liquid shortcuts for the vapor transport, in addition to local higher vapor pressures in the pore space. They furthermore point out that varying η_{sp} (for this expression) has minor influence, especially seen in context of the fact that liquid conductivity spans a logarithmic scale while the scale (axis) in Fig. 4 is linear. Although Scheffler [84] identifies η_{sp} values ranging up towards 3 [79] to be applied in the serial-parallel model for capillary conductivity, Scheffler suspects such high values make the vapor permeability unreliable or gives maximum vapor permeability at too high moisture contents, thereby bringing inconsistency to the serial-parallel model. Consequently, Scheffler [79] made a choice to set $\eta_{sp} = 1$ for vapor permeability. Zhao and Plagge [120] do not reveal what η_{sp}-values they applied for different sandstones.

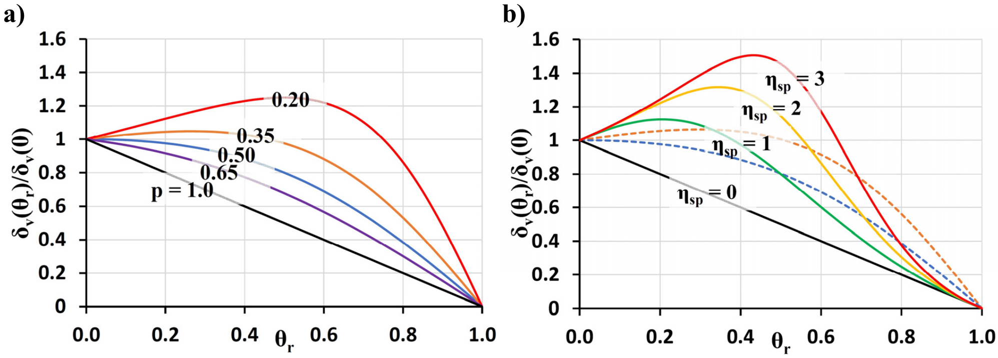

Fig. 4 Relative vapor permeability as function of relative moisture content for values of p, a), and for p replaced with Eq. (10) for values of η_{sp}, b). Dashed lines give p = 0.497 and p = 0.33, respectively.

2.1.3. Liquid conductivity

The term hydraulic conductivity is interchangeable with liquid conductivity. While hydraulic conductivity is widely used in the field of soil physics, the field of building physics more commonly applies liquid permeability. However, for the latter K_l needs to be specified with units [kg/(m·sPa)] or equivalently [s] not to be confused with liquid permeability k_l [m^2], see Appendix A.2.

Among moisture transport mechanisms hydraulic conductivity is significant or dominant in non-dry, unsaturated to saturated porous materials. Hydraulic conductivity consists of film flow (surface diffusion), typically dominant at lower moisture contents, and capillary flow, dominant at intermediate to higher moisture contents, e.g. [109].

In the building physics community, determination of hydraulic conductivity has mainly involved combining capillary conductivity with a liquid contribution in the hygroscopic region, implicitly seen from a decline in vapor resistance. Vapor conductivity can be calculated according to Eq. (12) [79, 115]. Thus, the liquid contribution to hydraulic conductivity can be calculated as the difference in wet and dry vapor conductivity found from respectively applying μ_{wet}, ϕ_{wet} and μ_{dry}, ϕ_{dry} in Eq. (12). The parameters correspond to the measurements and setup of the cup-tests (dry-cup and wet-cup). Scheffler and Plagge [79] provide a clear illustration of the process.

$$K_v = \frac{\delta_{v,a}}{\mu} \cdot \frac{\phi p_{v,sat}}{\rho_w R_w T} \tag{12}$$

In the soil physics community, capillary conductivity is combined with film conductivity. Thus, models respectively for capillary and film conductivity are combined, e.g., [109].

Capillary conductivity over the unsaturated range can be determined generally in two principal ways: 1) modeled and scaled to saturated conductivity [77], or 2) calculated from moisture diffusivity [122]. The latter is either calculated from measurements of moisture front profiles with, for instance, the Boltzmann transform method [123], or with models calculating the liquid diffusivity function from the capillary absorption coefficient [78, 124].

Liquid conductivity calculated from moisture diffusivity

An extensive and detailed review of liquid diffusivity models is provided by Scheffler [84]. Only a brief description will therefore be provided here.

A simple approximation to the liquid diffusivity is often taken as Eq. (13) [124]. This expression is generalized with the constant 3.8 and with the assumption that the diffusivity is exponentially linear and spans three orders of magnitude (the number 1000). Thus, the expression is not very precise for every material.

$$D_{w,abs} = 3.8\left(\frac{A_w}{w_{cap}}\right)^2 1000^{\frac{w}{w_{cap}}-1} \tag{13}$$

where $D_{w,abs}$ [m^2/s] is the liquid diffusivity function aligning with an absorption (imbibition) experiment, A_w [kg/(m^{2}s$^{1/2}$)] capillary absorption coefficient. In extension, Ramirez et al. [125] applied Eq. (14).

$$D_{w,abs} = \gamma\left(\frac{A_w}{w_{cap}}\right)^2 1000^{\frac{w}{w_{cap}}-1} \tag{14}$$

where the γ [-] coefficient was identified by matching moisture transport simulation, with Eq. (14) as input, to the imbibition experiment from which A_w was determined. For brick and mortar, Ramirez et al. [125] found support for the coefficient being 3.8 during absorption, while it could deviate from this in a desorption scenario.

A similar expression that is incorporating more material dependence was proposed by Carmeliet et al. [78], with Eq. (15) and Eq. (16) [78, 84, 126]. Similarities can be seen between Eq. (13) and the right hand side version of Eq. (16).

$$D_{w,cap} = f(F)\cdot\left(\frac{A_w}{w_{cap}}\right)^2 \tag{15}$$

$$D_{w,II} = D_{w,cap}\cdot exp\left[F\left(\frac{w}{w_{cap}}-1\right)\right] \Leftrightarrow D_{w,abs} = f(F)\cdot\left(\frac{A_w}{w_{cap}}\right)^2\cdot 10^{\frac{F}{ln(10)}\bullet\left(\frac{w}{w_{cap}}-1\right)} \tag{16}$$

where f(F) is a function of F, where F is a material dependent parameter, $D_{w,II}$ refers to the second regime of liquid diffusivity corresponding to capillary diffusivity (based on capillary absorption experiment) while a first regime corresponds to diffusivity in the hygroscopic and intermediate range (based on drying and vapor resistance experiments) [78].

The relation between liquid conductivity and diffusivity is given by Eq. (17) [122].

$$K = -D_w\frac{dw}{dp_c} \tag{17}$$

where dw/dp_c is the moisture capacity, i.e., the gradient of the retention curve.

Liquid conductivity

Modeling of capillary conductivity can be approached with different sophistication. The most applied approaches are bundle of tubes models and network models. A plausible alternative to modeling the conductivity is to train artificial neural networks to predict the conductivity from sets of input data [127, 128].

With simplistic representation of the pore system, bundle of tubes models have been widely applied [77, 79, 129]. These models envision simple parallel capillaries of different radii traversing a porous medium, for which an overall conductivity is calculated. To arrive at realistic values for the unsaturated range, the models are typically corrected for tortuosity [130] and scaled to measured saturated conductivity [77], to circumvent the complexity of the true pore system.

Network models adopt a more realistic representation of the pore system by allowing interconnectivity between capillaries in either a 2D or 3D lattice [131] or a node network [132, 133] system. The pore system is represented with different scales of lattice that are interconnected [131], creating pore throats and dead ends [133]. Percolation theory is applied to calculate or simulate the conductivity at different capillary pressures [134]. Despite improved realism, a drawback with network models is the laborious process of mapping the pore structure, determining scales, and conditionally simulating permeabilities [84]. Network models for porous building materials have been proposed in [115, 133].

Only bundle of tubes models will be further described due to the thesis objective of approaching simple methods. Furthermore, more elaborate background or historical development of such models is described in [84], and will not be addressed here.

Grunewald et al. [77] established a hydraulic conductivity model on the basis of the bundle of tubes model by Burdine [135]. The basics involve that flow in a capillary can be approximated with the Hagen-Poiseuille equation (see Article V for details). The total flow of a bundle of capillaries can be found from integrating over the pore radius distribution or, with help of the Young-Laplace equation, integrating over the moisture retention curve. However, since the true pore structure is much more complex than the bundle-of-tubes simplification, such an integration would not give the flow seen in practice for a real material. Therefore, it is necessary to include a relation to a measured value. With a measurement of the saturated (effective) conductivity, $K_{eff,sat}$, it is then possible to scale the unsaturated capillary conductivity as [77]:

$$K_c(\theta) = K_{rel}(\theta) K_{eff,sat} \tag{18}$$

where the relative function K_{rel}, Eq. (19), provides a way to circumvent the unknown correction that otherwise must accompany the integral of the Hagen-Poiseuille equation over the bundle of tubes. Thus, as a relative function only the integrals remain, which integrate a function of the capillary pressure [77]:

$$K_{rel} = \frac{K_c(\theta)}{K_{eff,sat}(\theta_{eff})} = \frac{\int_{\theta_{dry}}^{\theta} \left(\frac{1}{p_c(\theta)} \right)^2 d\theta}{\int_{\theta_{dry}}^{\theta_{eff}} \left(\frac{1}{p_c(\theta)} \right)^2 d\theta} \tag{19}$$

Scheffler [84] argued that a serial-parallel mechanistic model derived in Grunewald et al. [77] for vapor diffusion, with dependence to moisture content, should also be incorporated for the capillary conductivity, thus causing a change to Eq. (18). Additionally, Scheffler pointed out that $K_{eff,sat}$ is not equal to $K_{c,sat}$, thus a correction coefficient is required to scale down the effective conductivity determined in the over-capillary range to become the conductivity at capillary saturation. These two changes to Eq. (18) results in [84]:

$$K_c = f_l(\theta)\eta_{cap} K_{eff,sat} K_{rel}(\theta), \quad for\ \theta \leq \theta_{c,sat} \tag{20}$$

where η_{cap} is a correction factor, $f_l(\theta)$ the mechanistic serial-parallel pore model, with $\theta = w/w_{sat}$, given as:

$$f_l = \frac{\left(\frac{w}{w_{sat}} \right)^{\eta_{sp}}}{\left(\frac{w}{w_{sat}} \right)^{\eta_{sp}} + \left(1 - \frac{w}{w_{sat}} \right)^2 \left(1 - \left(\frac{w}{w_{sat}} \right)^{\eta_{sp}} \right)} \tag{21}$$

While Eq. (21) is associated with the liquid transport of the serial-parallel pore system behavior, the vapor counterpart is found as part of Eq. (11).

Scheffler [84] proposed and demonstrated procedures to determine η_{cap} and η_{sp}, which are acting on Eq. (20).

In addition to Scheffler [79, 84], Zhao and Plagge [120] provide another study in where the Scheffler model is applied on heavy materials (sandstone masonry).

Film models

Carmeliet and Roels [115] observed that their proposed multiscale network model did not accurately predict the liquid conductivity in the (upper) hygroscopic range. It should have been higher than what was determined from reduction in measured vapor resistance factors in this range. They ascribed the deviation to surface diffusion, effective pore cross section reduction (for capillary flow) due to molecular adsorption, and microscopic phase change phenomena.

Lebeau and Konrad [109] established a film model to account for surface diffusion. Their model is derived from assessing the forces that bind moisture to pore walls, in so creating a liquid film. From addressing the ionic-electrostatic and molecular disjoining pressure components, a film thickness can be derived for input into the Navier-Stokes equation used for a volumetric flow rate over a film cross section. From this volumetric flow rate, a moisture flux can be calculated when integrating over the bundle of tubes pore structure, resulting in an expression wherein the film conductivity can be identified.

Peters [111] argued that the approach of Lebeau and Konrad would not account for all the soil and fluid properties involved, such as surface roughness, surface charge, ionic strength of fluid and more. Thus, a material dependent correction might be needed. Instead of trying to solve the exact physics, Peters proposed that the conductivity trend can be approximated since it is highly linear on a log-log scale of conductivity vs. matric head. Resultantly the film conductivity can follow a function of matric head, adsorptive saturation degree, and the material dependent gradient coefficient. Overall, this amounts to a simplification when the gradient coefficient can be assumed to be -1.5.

Diamantopoulos and Durner [136] addressed the importance of corner flow (as a surface flow, neglecting general surface flow), and provided a hydraulic conductivity model for inclusion of corner flow in equilateral triangular capillaries. Similarly, Zheng et al. [113] combined capillary-, film- and corner-flow in determination of the hydraulic conductivity, while additionally attempting to compensate for impact on flow from pore surface roughness.

Absorption, redistribution and drying

A complicating aspect with accurate determination of hydraulic conductivity is the phenomenological difference between absorption, redistribution and drying of moisture in porous materials. For instance, absorption tests usually involve putting a dry porous material in contact with free liquid water, which gives radically more sudden wetting than that typically experienced by driving rain. With few exceptions, absorption events on building facades typically have slower wetting, or the porous materials already have some degree of wetting by initial moisture content. Such a difference in absorption may, for instance, affect microscale temperatures, dynamic contact angles (including curvature of the capillary meniscus), and air entrapment.

Dynamic effects were investigated by Janetti and Jansen [137] in terms of operating with dynamic contact angles in imbibition scenarios. They pointed to experience from experimental investigations having shown an increase in contact angle with increasing meniscus velocities. Furthermore, when applying dynamic contact angles in simulation of imbibition processes, it became possible to approach material behavior that deviate from traditional diffusion theory expressed with a single function of the Boltzmann variable $\lambda = xt^{-0.5}$. They noted that accurate understanding and representation of dynamic effects could be relevant for wind-driven rain on building facades [137]. For ceramic and calcium silicate bricks Carmeliet and Roels [115] found significant difference between drainage and wetting permeability in the high saturation range, and they ascribed it to air-entrapment phenomena.

It has been postulated and demonstrated for some materials that hydraulic conductivity can be approximated with a single curve with reasonable accuracy for both absorption and drying [115]. Carmeliet and Roels [115] demonstrated that hydraulic conductivity can be approximated to a single curve (log-log, conductivity as function of capillary pressure). Their results showed good prediction in simulating both drying and absorption moisture fronts in ceramic brick and calcium silicate. Applying one curve appears to have become conventional wisdom, e.g., [85]. Feng and Janssen [85] state that liquid diffusivity calculated from a single liquid conductivity curve can become process dependent (implying accounting for hysteresis) by respectively applying the adsorption and desorption retention function. Nevertheless, there are also examples of experiment measurements that seemingly are difficult to bring to agreement with one single curve. For instance, through simulation, Van Belleghem et al. [138] found that an adjusted (lowered) conductivity curve provided a better fit to moisture distribution profiles for a drying experiment than the original conductivity curve. The original curve was established from x-ray measurements of capillary uptake [139]. However, such deviation could perhaps be attributed to uncertainty related to material heterogeneity, and measurement methods and protocols, something that has been reported to cause a significant spread in measured properties of the same material [72].

Nevertheless, another phenomenon might also be involved. Inconsistencies between absorption, redistribution and drying might be closely linked to hysteresis. Hysteresis, which comes from Latin for "coming short", with the essence meaning of lagging behind, addresses when a system state is dependent on situational history. In building physics, hysteresis primarily addresses differences in the moisture retention during adsorption and desorption, where the desorption "lags" behind, i.e., moisture is drained at higher capillary pressures or at lower RH than observed when wetting a material. Whereas, regarding liquid conductivity, hysteresis has been attributed to air-entrapment during absorption [115], geometric non-uniformity of pores [136], (unspecified) dynamic hysteresis effects [115], and contact angle hysteresis [84, 115, 136], i.e., differing advancing and receding contact angles.

However, hysteresis is fairly complicated to implement into hygrothermal simulation programs for simulation of dynamic conditions, see Scheffler [84].

Regarding the drying phenomena, drying progresses along a two-phase drying curve. In the first phase, liquid moisture is continuously provided to the evaporation surface by capillary action, in so sustaining a saturated vapor pressure at the surface. Transition to the second phase occurs when this is no longer sustained, where vapor diffusion gradually takes over as the governing transfer mechanism [140] over a growing distance from the surface. The first phase is accompanied with surface cooling from the evaporation, providing significant decrease in surface temperature, whereas for the second phase evaporation slows down giving less decrease in surface temperature [140]. Moisture flux from the surface in the first phase is linear under constant conditions (vapor transfer coefficient and surface temperature), whereas in the second phase it is non-linear governed by the diffusion process.

Comparing to a drying experiment, Van Belleghem et al. [138] observed that simulation results deviated when concerning moisture content and moisture distribution profiles after when drying entered the second drying phase (decreasing drying rate period [72], when exterior surface RH falls below 100 % RH). They argued that since this occurred in the second phase, it indicated that material properties were fairly correct at high moisture contents, but not necessarily correct at lower moisture contents. They then adjusted each in turn: vapor resistance factor, retention curve, and hydraulic conductivity curve. Adjusting the vapor resistance had insignificant impact. Adjusting the retention curve improved moisture content results, but not distribution profiles, whereas, adjusting the conductivity curve improved both. Hence, they argued that the largest deviations were caused by the conductivity curve. As mentioned above, the unadjusted material data originated from x-ray measurements of a capillary uptake experiment [139], whereas it was applied by Van Belleghem et al. on drying.

On the other hand, Zhao et al. [140] demonstrated that with well measured material properties, in combination with iterative adaption of the thermal transfer coefficient and with determination of the vapor transfer coefficient from experimental results, the drying process of calcium silicate and ceramic brick samples can accurately be simulated in an axial-symmetric 3D hygrothermal model.

2.1.4. Thermal conductivity

It is important to account for the moisture dependency of thermal conductivity since this can be quite significant for a range of materials [141, 142]. A temperature dependency is usually less pronounced [141], but can also be accounted for, by either simple approximation [143] or sophisticated calculation [144]. For low-hygroscopic materials, the moisture dependence becomes especially relevant for hygrothermal scenarios with capillary absorption or interstitial condensation that can significantly raise the moisture content. Highly hygroscopic materials can, on the other hand, also experience significant impact in the hygroscopic moisture region. For low density, non-capillary insulation materials, it might be limited how much moisture they can retain before drainage occurs, thus the whole moisture range might not be relevant, unless limited, localized accumulation of drained moisture is also addressed. Nevertheless, significant impact from moisture content can also be seen for such materials at moisture contents below occurrence of drainage. Hydrophobic insulation materials or materials with a closed cell pore structure might, however, remain fairly unaffected due to low moisture retention.

Fairly simple approximations are usually applied for moisture dependence in the field of building physics. For building materials, the relation to moisture content is often approximated to be linear. Table 6 shows examples of a few equivalent linear expressions with some references to where they are used.

Table 6 Equivalent thermal conductivity expressions with linear moisture dependence

$\lambda(w)=\lambda_0\left(1+b\frac{w}{\rho_s}\right)$	$\lambda(w)=\lambda_0+aw$	$\lambda(w)=\lambda_0+a\frac{w}{\rho_w}$	$\lambda(w)=\lambda_{sat}+(\lambda_0-\lambda_{sat})\frac{w_{sat}-w}{w_{sat}}$
[124]	[73, 83, 98, 145]	[116, 121]	[146]

where λ_0 [W/(m·K)] is the dry thermal conductivity, a and b are fitting parameters of varying units, λ_{sat} [W/(m·K)] thermal conductivity at saturation.

However, thermal conductivity does not necessarily have a linear relationship to moisture content. Non-linearity for some insulation materials has been shown by Jerman and Cerney [141] and Abdou and Budaiwi [147]. Liu et al. [148] discovered non-linear trends in measurements of concrete, brick, aerated concrete, and foam concrete. Furthermore, non-linear trends are seen in measurements done by Koci et al. [142] for both high performance concrete and solid clay brick, while aerated concrete shows a fairly linear trend. An even more apparent non-linearity is seen for mineral wool and EPS in that study.

It can be beneficial to have a good idea of the moisture dependence relationship one may expect for a material in order to keep the number of measurements to a minimum. For instance, when presuming a linear relationship, one only requires the dry and saturated conductivity values, whereas when presuming non-linear relationships, an increasing non-linear complexity will increase the number of needed measurements. Accuracy requirements for the moisture dependent thermal conductivity will, of course, also influence the number of measurements that the curve fitting should be compared to. Applying mathematical expressions that give smooth curves will presumably provide more realistic intermediate values compared to if one only relies on simple linear interpolation between measured values.

Simple non-linearity can be approximated by expanding to a second order expression, Eq. (22) , as done in [141, 147] for some insulation materials. Seemingly, this can also provide fairly good approximations to a range of insulation materials found in the WUFI material database [143].

$$\lambda(w) = \lambda_0 + a_1 u + a_2 u^2 \tag{22}$$

where u is either w/ρ_w or w/ρ_s, a_1 and a_2 are fitting parameters.

In contrast Liu et al. [148] assigned a power expression, Eq. (23), in simple non-linear fitting to their measurements.

$$\lambda(w) = \lambda_0 + a u^b \tag{23}$$

where b is a fitting exponent that Liu et al. [148] determined to be < 1 for all the materials they investigated.

However, not all materials or porous media follow simple trends, at least not accurately, as indicated by some materials in [40, 142, 148, 149]. In scientific disciplines other than building physics moisture dependence of thermal conductivity is addressed to a much larger extent; plausibly attributed to difficulty in measuring moisture dependent thermal conductivity in undisturbed soils or sediments, or due to limited access to equipment or measurement sites, e.g., [150]. Thus, prediction of the effective thermal conductivity (ETC) has become extensively studied. The following briefly gives a few examples.

A more advanced thermal conductivity model was provided by Ghanbarian and Daigle [149] and demonstrated on numerous porous soils over the unsaturated range. This model incorporated percolation theory in form of taking into account the critical moisture content at which the first significant continuous (high) conductive paths are established through the material. Below the critical moisture content there is less macroscopic conductivity. Furthermore, it incorporates an effective medium approximation to homogenize a heterogenous material consisting of low and high conductivity components. When formulated as saturation dependent thermal conductivity, it can be expressed as Eq. (24).

$$\theta = \frac{\left[\lambda^{1/t_s} - \lambda_{dry}^{1/t_s}\right]\left[\theta_{cr}\lambda_{sat}^{1/t_s} + (\phi - \theta_{cr})\lambda^{1/t_s}\right]}{\left[\lambda_{sat}^{1/t_s} - \lambda_{dry}^{1/t_s}\right]\lambda^{1/t_s}} \tag{24}$$

where θ_{cr} is the critical moisture content, t_s a scaling exponent. Eq. (24) needs to be solved as a second order equation and is therefore a bit cumbersome, and implementation of it might be best suited to be tabular; however, it provides more flexibility than simpler expressions for thermal conductivity. Even though this expression has a model background, it remains to be fitted to experimental data as it does not fully predict the thermal conductivity curve shape. That is, θ_{cr} and t_s become fitting parameters.

In Fig. 5 a) it can be observed that Eq. (24) can provide an alternative to Eq. (23) that may improve fitting to a couple of the materials measured by Liu et al. [148]. Measurements on wood fiber boards [40] are in Fig. 5 c) also provided with curves produced by Eq. (24). The expression is, however, a bit rigid, not able to independently of each other adjust gradients before, at, and after the critical moisture content.

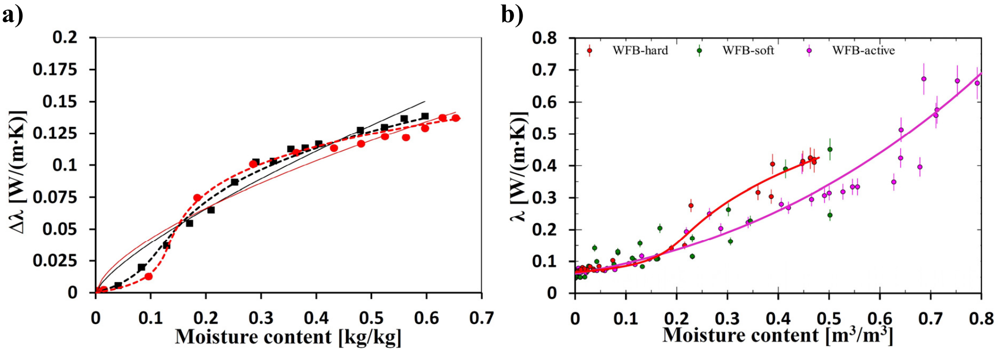

Fig. 5 a) Moisture dependent increase in thermal conductivity for foam concrete, type A (black) and B (red). Measurements and solid lines, Eq. (23), from Liu et al. [148]. Dashed lines, Eq. (24), manually fitted for demonstration, and superimposed. b) Moisture dependent thermal conductivity for wood fiber boards, type hard (red) and capillary active (pink) from [40]. Solid lines, Eq. (24), manually fitted for demonstration, and superimposed.

A plausible alternative to pure curve fitting of measurements is prediction of the unsaturated thermal conductivity, i.e., prediction of ETC. Among other approaches, numerous fractal models have been made for ETC prediction in the field of soil science, e.g., [151-153]. Nevertheless, fractal models have also been applied to, for instance, autoclaved aerated concrete [154] and concrete [155]. These apply fractal theory for materials that adhere to self-similar fractal scaling laws, and they apply fractal dimensions to represent the material structure [152]. They are further combined with different perspectives or considerations from thermo-electric models (serial and parallel resistance models) and bundle of tubes models [151, 153]. A serious drawback with some current fractal models is the seemingly over-simplistic inclusion of particle and pore scale distributions, or pore system geometry. Furthermore, although being predictive, fractal models may still rely on adjustment of parameters to improve fit to measurements.

2.2. Smart vapor barrier

In the literature, terms like smart, adaptive, moisture adaptive, or humidity dependent are found and used in combination with membrane, retarder or barrier for this kind of product [55]. What has become the most prevailing term used is smart vapor retarder (SVR), or the similar smart vapor barrier (SVB). From here onwards a distinction is applied that SVB and SVR, respectively, have a high s_d-value > or >> 10 m and a relatively low s_d-value < 10 m at dry conditions, inspired by [89].

It has been argued that SVRs could promote significant drying towards the interior in structures restricted to low or no drying towards the exterior [55]. Compact (wood frame) roofs have for this reason been subjected to much of the research into application of SVRs or SVBs, but also (compact) wood frame walls have been covered. Some of these studies are listed below for reference:

- Field testing studies of SVR in roof [156] and wood frame wall [53] configurations, and SVB in a wood frame wall [157] configuration.
- In situ investigations of SVR [158] and SVB [159, 160] in roof configurations.
- Laboratory studies with SVBs in roof [55, 161] and wood frame wall [162] configurations.

In wood frame walls it has been demonstrated that an SVR (s_d = 0.09-4.3 m) could avoid high RH or summer condensation elsewise experienced with a polyethylene vapor barrier, in the warm half of the year, although at the expense of having slightly more condensation / moisture accumulation in the wall structure during winter [53]. Dark exterior colors, to take advantage of sunshine absorption, have been proposed to increase inward drying for roofs during summer conditions [160].

In more recent years, SVBs/SVRs are also seen applied in physical studies of interior insulation of masonry. Vereecken and Roles [38] applied SVR with mineral wool in an investigation of airtightness and convective air transport to wooden beam ends. The studied masonry wall test assembly was exposed only to cold external climate and no driving rain, thereby not yielding conditions for inward drying through the retarder. No explicit assessment of the retarder function or performance was included.

Kopecky et al. [30] conducted an investigation over several years of a masonry test wall with SVR (s_d = 0.3-5 m) and mineral wool. The wall was exposed to the climate of Prague, Czech Republic, in addition to an artificial driving rain event due to the low driving rain load of the local climate. After the artificial rain event (mid-July) the wall had approximately 1.5 months of warm weather before the colder autumn and winter. The study did not include any similar wall assembly to compare SVR performance, and the SVR impact was not assessed.

De Mets et al. [31] monitored a masonry test wall with SVR or SVB? (s_d = 0.3-20 m, limits not reached under normal conditions) and mineral wool, exposed to the climate of Limelette, Belgium, with a total driving rain load 447 mm/m^2. Specific effect of the SVR was not addressed. Nevertheless, comparing mineral wool with SVR to capillary active insulation, a small positive benefit was seen using the latter. The choice of insulation solution was by itself deemed insufficient to ensure moisture safe conditions for wooden beam ends, thereby promoting the need for additional measures.

Keskküla et al. [25] applied SVR (s_d = 0.3-5 m) between two layers of 50 mm reed panels interior of a masonry fire wall that included a ventilated air cavity. The climate exposure was in Tartu, Estonia, during a particularly warm winter. However, the in situ study was complemented with hygrothermal simulations. It was concluded that the reed panel solution could not be used without SVR after comparing to results from such a setup.

Martel et al. [26] conducted an in situ study of a masonry wall with SVB (s_d < 14 m?) in combination with polyurethane foam insulation. The climate exposure was Herefordshire, UK, over 8 years. The study compared the insulation solution with and without exterior hydrophobic brick cream treatment. Considerably lower moisture contents were seen in the treated part of the wall. Performance of the SVB was not specifically assessed.

An issue exists that studies including SVBs/SVRs often lack clarity concerning the measurement conditions in determination of physical properties [163]. In order to arrive at property functions of SVBs or SVRs, extensive testing is needed to cover a reasonable range of the RH conditions that can be encountered.

Fechner and Meißner [164] measured 5 samples for 14 different RH gradients with some measurements done for two flow directions. Olaoye et al. [165] measured 5 samples each for 4 dry-cup and 4 wet-cup tests, resulting in measurements at 8 RH levels, enough to generate a vapor resistance curve for the SVB between 20 – 85 % RH [166]. Yoshinaga [163] measured 4 SVBs, two at 11 levels of RH and two at 6 levels of RH for two flow directions, with three or more samples tested at each RH condition. It was argued that the change in vapor resistance could be understood by measurements at 6 RH levels; however, it was also concluded more data was needed on vapor resistance in the range 60 – 70 % RH, where large changes in resistance occur.

In simulation studies, the RH conditions that are experienced by the SVR/SVB are usually either simplified to be the mean RH of the RH at both sides when the resistance is modeled as an interface resistance [164], or the range of RH spanning it when modeled as a physical layer with meshing, e.g., [166, 167].

Fechner and Meißner [164] proposed that a model for calculating s_d-values should take into account the RH gradient, not only a weighted arithmetic average RH. Consequently, they arrive at a two-part function where the second part is a curve-fitted second order polynomial function of the gradient. Olaoye et al. [165] suggested adjusting the design vapor resistance curve $\mu(\phi)$ by comparing the harmonic mean of the design vapor resistance curve (over the cup-test RH interval) to the experimental resistance result, from several instances of cup-tests, until the resistances align. Since the humidity continuously varies across the SVB the vapor diffusion will encounter the whole range of vapor resistance corresponding to the range of RH between the boundary RH-values. In this way, the SVB can be modeled as a physical layer included in model meshing, which was demonstrated by Olaoye et al. [166].

Yoshinaga [163] argued for considering directional dependence in the vapor resistance of SVBs, demonstrating that directional difference could be quite substantial. If the SVB has directional dependence, the vapor flow direction should meet highest resistance during winter and lowest resistance during summer [163].

2.3. Hygrothermal modeling of masonry composite

Due to the complexity in analyzing performance of interior insulation retrofit of masonry (see Section 1.1.1 and 1.1.2) application of hygrothermal simulation models have over the last 25 years gradually become widespread. An issue with simulation models is that they are simplifications of reality. Sometimes greater simplifications can be adequate, for instance, applying a 1D model to what can be assessed to be a fairly 1D scenario with 1D transfer mechanisms. Other times, a 2D model or even a 3D model might be necessary to capture multidimensional mechanisms. For brick masonry, which is a brick-mortar composite where brick and mortar can have widely different properties, including anisotropic properties, then moisture transport can be three-dimensional. Nevertheless, depending on the overall masonry configuration (e.g., of structure layers) and whether localized moisture distribution or holistic moisture performance is sought, different degrees of simplification can be deemed adequate. Furthermore, there are still limitations to software and computational capacity that make 3D models less accessible. 2D models, and sometimes 1D models are, therefore, still mostly utilized. A 1D model is, however, only able to capture successive layers across a wall, whereas a 2D model can capture some of the parallel interaction between brick and mortar crossing the wall, either as a vertical or horizontal cross section. Masonry structures including a beam end detail cannot be simplified to 1D but can to some extent be simplified to 2D.

Among 2D studies it has become common to simulate interior insulated masonry with interface resistances between brick and mortar, e.g., [17, 21, 70]. Nevertheless, resistances are just as often neglected or omitted, e.g., [32, 49, 168]. Effects of a brick-mortar interface on moisture transport along the interface are, however, not found having been included in any simulation studies, except for at smaller geometric scales [169]. The presence and effect of interface resistance are nevertheless somewhat unclear, especially regarding at what conditions (absorption, drying) it operates [48, 170], whether it is directional (material A→B or B→A) [168, 170], and whether it is dependent on the moisture driving potential (e.g., varying with capillary pressure) [168]. Furthermore, determination of the resistance value is a difficult issue. Several studies have investigated modeling of interface resistance between brick and mortar [48, 67-69, 125, 168, 171, 172].

Regarding other moisture transport mechanisms, Kehl et al. [57] modeled interior insulated masonry with and without laminar air diffusion. Additionally, potential air diffusion or convection around the beam end has been a concern in some studies [38, 173, 174].

2D modeling of interior insulated bare brick masonry can be found in a few studies, typically 1.5- to 2-brick-thick walls, [17, 21, 32, 70], whereas 3D modeling of bare brick masonry including mortar joints has not been found. However, 3D modeling has been applied on bare homogeneous brick masonry [175] and for masonry with external render [49, 176], or additionally, including air transport but without driving rain exposure [174].

Regarding modeling hydrophobization as a measure that lowers the capillary absorption of masonry, Hansen et al. [177] modeled the effect of hydrophobization surface treatment in 1D by replacing the outer 5 mm of a brick with an altered material having $A_w/15$ to that of the brick, in order to replicate difference from hydrophobization seen in Karsten tube results. Similarly, Soulios et al. [178] modeled a hydrophobized layer of 2.4 mm at the brick exterior in 1D with adjusted A_w and μ values, reduced and increased with a factor of 356 and 1.15, respectively, from the untreated brick. Whereas Jensen et al. [32] reduced the A_w-value with a factor of 1000 for the exterior 10 mm of the masonry.

Most studies investigate retrofit scenarios not the masonry modeling itself; however, there are a few studies specifically investigating the modeling of masonry, e.g., [48, 49, 169].

Vereecken and Roels [48] investigated the impact of representing masonry as a homogenous brick layer. They compared such a representation to masonry composite representations including head and bed joints, with and without brick-mortar interface resistance. The different modeling setups resulted in changes in moisture distribution, with bed joints without interface resistance acting like a buffer for moisture absorption along the brick during imbibition, whereas with interface resistance the moisture front in the brick closely resembled that of homogenous brick. With interface resistance, head joints had larger impedance on the moisture front. A homogeneous simplification resulted in a faster moisture front.

In contrast to imbibition simulation, an alternating wetting and drying simulation following a real weather sequence showed that a homogeneous simplification would underestimate moisture stored and distributed inwardly in the mortar bed joints [48]. This was attributed to slower drying performance of mortar in addition to it promoting redistribution along the bed joint. In contrast, a homogenous brick layer would allow easier drying between rain events. In an alternating wetting and drying setting, interface resistance adds negligible overall impact on moisture response, i.e., even though the resistance ensured less moisture transfer from brick to mortar, it also resulted in more difficult drying from the mortar joint. The modeling by Vereecken and Roels did not address potential increased moisture transport along the brick-mortar interface. In perspective, regarding an in situ study, Hansen et al. [42] argued a homogeneous lime mortar layer better represented masonry performance than a homogeneous brick layer in 1D simulations, when comparing to measurements and 2D simulation.

Zhou et al. [49] compared simplified 2D and 3D masonry modeling to more detailed 2D modeling. The structure investigated was a 1.5-brick-thick wall with exterior render and a continuous collar joint located 0.5 bricks from the exterior. It also included a beam end inserted 0.5 bricks into the masonry from the interior. The simplified models consisted of modeling the masonry with vertical layers of render and mortar (collar joints), respectively, and neglecting horizontal bed joints. They found the simplified 2D and 3D models were reasonably close to the detailed 2D model in results, and they concluded that 2D simulation could be a suitable alternative to 3D for predicting mold risk at beam ends.

For bare brick masonry, Gutland et al. [169] compared modeling including a fracture pathway for moisture along the brick-mortar interface to modeling the brick-mortar composite with bulk properties only. With the fracture, effects on moisture transport both along and across the fracture could be included. They demonstrated that fracture inclusion could increase both absorption and drying. The fracture modeling was approached by transforming Navier-Stokes flow between plates to liquid conductivity assigned to a fictive fracture material. The retention curve was assigned with help of the Young-Laplace equation identifying the capillary pressure at which the fracture would retain moisture. Additionally, the vapor resistance was assumed to be as stagnant air. Various interface resistance values were applied between the brick/mortar materials and the fracture. With this modeling approach, Gutland et al. set out to meet some general issues of earlier fracture modeling, which are:

1. Too demanding regarding material geometric analysis and model discretization for application to larger wall sections.
2. Applied only to fractures in homogeneous materials, not between materials.
3. Focused on wetting absorption, thereby not including drying.

3. Research questions and relation between articles

The enclosed articles are categorized as laboratory investigations, hygrothermal modeling, and physics model derivation. The relation between the articles, including the progression of the research, is illustrated in Fig. 6, and it is further elaborated in Section 3.1 - 3.4 together with more introduction of the articles.

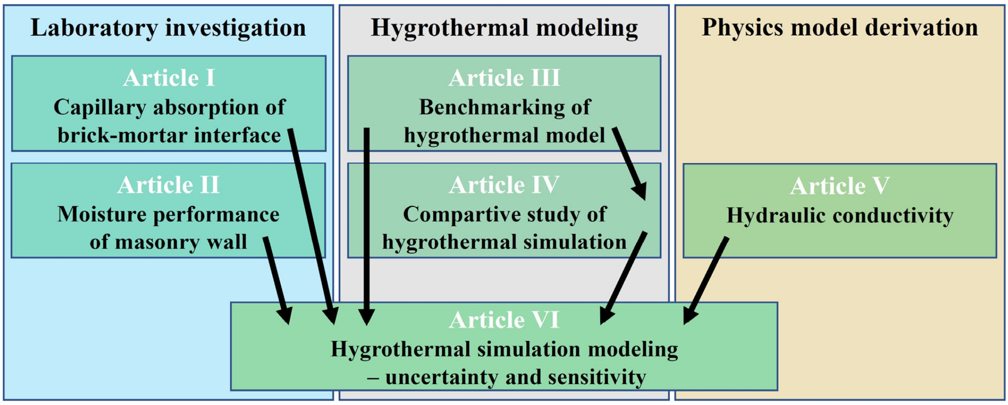

Fig. 6 Relation between articles

The research questions that are provided in each journal article are summarized in Table 7. The questions provide insight into the research objectives of the articles. For the full account of the investigations into these research questions and the conclusions made, the reader is referred to the articles. Table 7 contributes as context to the following introduction of the articles and their relation, provided in Section 3.1 - 3.4. The conference articles do not have directly articulated research questions on such a form, and they are therefore not represented in Table 7.

Table 7 Research questions covered by the journal articles

Topic	Research questions	Article
Moisture performance of masonry wall	1) To what extent will masonry variations, in brick type and masonry thickness, influence moisture uptake and drying performance?	II
	2) Will inclusion of a SVB significantly improve drying performance?	II
Hydraulic conductivity	3) Is it feasible to predict the capillary conductivity at capillary saturation?	V
	4) Can the Scheffler-Plagge model for $K(p_c)$ be simplified by scaling to conductivity at capillary saturation instead of at saturation?	V
	5) Can the overall procedure for determining $K(p_c)$ be simplified and made more practically feasible, for when only a necessary minimum of material property test data is available.	V

	6) For such a model, how is the prediction performance for $K(p_c)$ when assessing a wide range of porous building materials described in previous studies?	V
Hygrothermal simulation modeling	7) When applying modelled hydraulic conductivity what are the consequences of uncertainty regarding the following material properties? • Capillary absorption coefficient • Retention curve	VI
	8) What impact do modeling choices or simplifications have on simulation results? Aspects that herein will be investigated are: • Reading position of results in simulation model compared to sensor location in physical experiment. • Isotropic vs. anisotropic wood properties for beam end. • Including increased permeability along the brick-mortar interface in mortar properties during rain events. • Presence of a particularly “leaky” mortar joint, due to lower brick-mortar interface quality, and distance of such a joint to the sensor. • 2D simplification compared to simulating in 3D.	VI
	9) What effect is seen from modeling a smart vapor barrier compared to no barrier or traditional barrier?	VI

3.1. Laboratory experiments

Article I investigates water absorption in brick, mortar, and the composite of the two. One objective was to investigate a hypothesis of a relation between the water absorption coefficient and shear strength; however, shear strength is not a focus of this thesis and is not addressed any further. The important aspect from Article I that has further been utilized is the theory on identifying the absorption coefficient. Article I became a springboard for further laboratory work (Section 4.2) identifying absorption coefficients for bricks and mortar joints, and mortar joint interaction with bricks by the brick-mortar interface. The work that started with Article I culminated in material properties listed in Table 2 and Section 2.2. of Article II and material description in Article VI, Appendix A, used for hygrothermal simulation. The A_W-values are further used as input in the capillary conductivity model of Article V, utilized in Article VI.

Article II investigates wetting and drying behavior of masonry wall segments of different configurations, with the objective to investigate how different configurations affect this behavior. In addition to its standalone objective, it provides an experiment dataset for comparing hygrothermal simulations to, which is pursued in Article VI.

3.2. Hygrothermal modeling

Article III addresses the potential of hygrothermal modeling and simulation in 3D using COMSOL. It describes the basics of moisture and heat transport equations as PDEs, and it presents results of applying the 3D model to Hamstad benchmark I and II. Article III served as a steppingstone to Article IV model-wise. Although Article III applies an early version of the COMSOL model and is thereby outdated on the benchmarking, it serves as a demonstration of the 3D potential, a potential which is further demonstrated in Article VI.

Article IV presents a comparison between using a model in COMSOL and WUFI for a complete climate exposure using a moisture design reference year (MDRY). Thus, sub-models for shortwave and longwave radiation were included in the COMSOL model. Nevertheless, radiation models are on the side of the thesis topic and are only summarized in Appendix A.7.3. The key aspect of Article IV is the solution of more efficiently dealing with issues of RH as a dependent variable. Similar to the solution of modeling capillary pressure, which is spanning several orders of magnitude, on a logarithm format, to avoid these orders of magnitude, the RH can be modeled on a logarithm format to overcome the issue of many decimal places of RH when approaching saturation. This is of particular importance when dealing with driving rain absorption. Article VI applies the logarithmic expression for modified RH, proposed in Article IV. Furthermore, the COMSOL model version of Article IV includes modeling of humid air properties in the air cavity in the beam end pocket, which is also included in the model version used in Article VI. Modeling of the SVB is, however, different in Article IV and Article VI, with the latter modeled dependent on RH on both sides, while the former modeled dependent on local RH and modeled together with the interior gypsum board for simplicity. Modeling with RH on each side is more directly relatable to laboratory testing of the SVB, and hence assumed preferable.

Article VI investigates the impact of different modeling choices. It incorporates information gathered from Article I and II to approach modeling of increased rain absorption through mortar joints, compared to what the mortar itself allows for. The hydraulic conductivity model from Article V is applied to generate hydraulic conductivity curves for brick and mortar. Furthermore, Article VI builds further on the learnings from the work of Article III and IV, in improving modeling in COMSOL.

3.3. Capillary absorption

Article V investigates modeling of the hydraulic conductivity, with capillary conductivity approached with a bundle of tubes model. The article demonstrates prediction of the capillary conductivity at capillary saturation, which is used as basis for scaling the rest of the capillary conductivity curve. The approach outlined in Article V provides a more realistic curve than when transforming a liquid diffusivity curve to a liquid conductivity curve. That is, one assures a monotonically increasing curve with increasing moisture content. The method in Article V is applied for input data in the simulations of Article VI.

3.4. Hygrothermal simulations

Article VI highlights uncertainty caused by both unknown material properties and modeling choices, and the article explores the impact of this uncertainty. Often one is unable to completely map all material properties and one thereby has to supplement measured properties with properties that are taken from standards, estimated, modeled, or found from similar materials. Examples of this are investigated with regard to sensitivity when having non-measured retention curves and hydraulic conductivity curves. Regarding modeling choices, this includes choices on result reading positions compared to sensor location and extents, modeling mortar joints to account for increased absorption along brick-mortar interfaces, presence of leaky joints, isotropic vs. anisotropic beam end properties, and 3D vs. 2D representation of the beam end. Furthermore, the effect of SVB is investigated compared to no vapor barrier and traditional vapor barrier. Article VI draws from the experience gathered in all the foregoing articles, Article I-V, in establishing the study.

4. Research methodology and procedural account

The purpose of this chapter is not to repeat the methodology described in each article. Instead, it is to supplement the information found in the articles with additional background information and additional information not having been included in the articles or which has not been possible to publish in additional separate articles. The chapter may also cast light on reasons for the direction of the research. Furthermore, a shift in research direction is addressed in Section 4.2. Additionally, the chapter goes a step further than the articles in documenting the quality and thoroughness of the research methodology.

There are potentially several ways to classify articles according to research methodology. However, in the present thesis, one can differ between empirical (Article I, II) and conceptual (Article III, IV, V, VI).

4.1. Review of literature (Article II, V, VI, and Thesis)

Literature reviews can fulfill several purposes, to which different review forms can be categorized. However, term definitions vary in the literature body, and purpose and practice are debated. A distinction is often made between systematic literature review (SLR) and non-systematic. From one point of view, systematic reviews follow a disclosed review procedure or protocol to make the review transparent and repeatable, whereas a non-systematic review is a subjective process of discovery, evaluation, and selection, formed by exposure and experience [179]. Different forms of review focus can be organized under these two overarching approaches. However, in a more nuanced view SLR does not have a sole claim on being systematic, see [180]. Being systematic does not necessarily imply procedures, protocols, and repeatability. With a looser perspective on systematic, one may list some different literature review forms as done below. Still, many more obscure forms and variations arguably exists [181].

- Traditional literature review, i.e., state-of-the-art review for identifying research gaps and needs [180].
- Systematic literature reviews in search of addressing specific research questions [180].
- Scoping literature review, i.e., mapping body of literature on a topic in terms of extent, nature, and characteristics [182].
- Descriptive review, i.e., summarizing and clarifying knowledge of a "recent" development [181]
- Critical review, i.e., scrutinization of relevant and significant research (e.g. ideas, arguments, findings), including highlighting revision needs, supported by clear argumentation [183].

Following this list, for the current research, a traditional literature review in form of state-of-the-art has been the dominant approach; however, elements of a "systematic" literature review, in addressing specific research questions, and a descriptive and critical literature review have also been applied. Neither the thesis nor the articles further specify or distinguish between the forms having been used in different review sections.

The process of reviewing literature has involved searching for relevant keywords on the topics worked on in scientific literature search engines. Subsequent of finding relevant sources (articles, book chapters, and doctoral theses) two additional steps have systematically been taken: 1) going through the reference lists of these sources to identify additional relevant sources, 2) identifying scientific literature where these sources have been referenced later on. Additionally, the overall body of published research by some researchers has been identified when deemed relevant.

Before utilizing references to relevant literature, the quality has been considered, including consideration of publishing level and scientific merit or standing. The extent of consideration has been adapted to the end-use application of each reference, with extra scrutiny for references that affect research outcome and conclusion.

4.2. Laboratory testing – small scale

This section deals with material measurements, including individual bricks, mortar joints, and brick-mortar composed pillar samples.

4.2.1. Statistical treatment – general remarks

In experimental investigation, statistical treatment or analysis is in general important in order to determine whether or not correlations according to some hypotheses exist. Basically, this deals with the risk of rejecting a true null hypothesis (no correlation), a Type I error, or accepting a non-true null hypothesis while there actually is a correlation, a Type II error. Additionally, statistical treatment can be used to analyze data distributions and to decide statistical parameters describing distribution spread or skew, and so on, for instance, deciding standard deviation.

When addressing statistical treatment aimed at testing hypotheses, then sample size is a central issue. A too small sample size will limit sensitivity for correlation detection, causing failure to detect weak correlations. Furthermore, a sample size can be too small for viability of statistical treatment all together. A too large sample size is, on the other hand, unnecessarily resource demanding or too excessive to provide any additionally useful sensitivity, or it risks detection of noise from aspects or factors not benefitting the hypothesis investigation. Nevertheless, too large sample size is not an issue in the present work. Rather, the issue is whether one is able to arrive at sample sizes adequate for statistical treatment.

Statistical treatment could have been relevant for the experimental work and subsequent analysis in Article I and II; however, neither of these involve enough samples (specimens or sensor readings) for statistical treatment. Hence the focus regarding statistical treatment will be relevant for the following documentation of work presented here in the thesis, and which is not included in the articles. Furthermore, this is addressed to document that this issue was considered and to provide learnings for future research.

4.2.2. Sample size considerations

There is no generalized minimum value for the number of samples needed for statistical analysis. The number of samples one should seek depends on: type of statistical analysis, intended confidence levels, and sought accuracy level.

For the laboratory work encompassed by this thesis the minimum number of samples needed were considered from three angles: 1) Perspective of the t-distribution, 2) Kolmogorov-Smirnov test for normality [184], and 3) Central limit theorem. With 1) the number can vary depending on sought confidence and accuracy, as described in [185], while for 2) it becomes a question of necessary resolution for the test, where a resolution of ≥ 20 samples are preferable from a practical perspective, whereas for 3) the assumption of normality in general requires ≥ 30 samples.

Considering the practical issues of sample preparation, 30 samples was deemed too demanding, while 20 samples could be achieved in certain cases. Otherwise, a minimum of 10 samples were sought, after assessing [185], to have reasonable confidence in the mean and to calculate a meaningful standard deviation, within the theory of the t-distribution.

Cases of sample preparation:

- Brick properties (Thesis Section 4.2.3 and Article II): **20 samples** (for each of 3 brick types, hence 3x20 samples).
- Mortar (joint) properties (Thesis Section 4.2.3): **4 samples** (for each of 4 variants, hence 4x4 samples, 8 for each mortar type, see Table 8).
- Mortar (joint) properties (Article II): **10 samples** (less than 20 due to complicated production procedure, see Fig. 7 c), and needed to be made for two brick types, i.e., 2x10 samples).
- Brick-mortar interaction properties and correlation detection: aimed at 20 samples, but resulted in fewer, see Section 4.2.3.
- Vapor permeability: **5 samples** according to EN ISO 12572 [186].
- Sorption: **5 samples** (minimum 3 according to EN ISO 12571 [187].

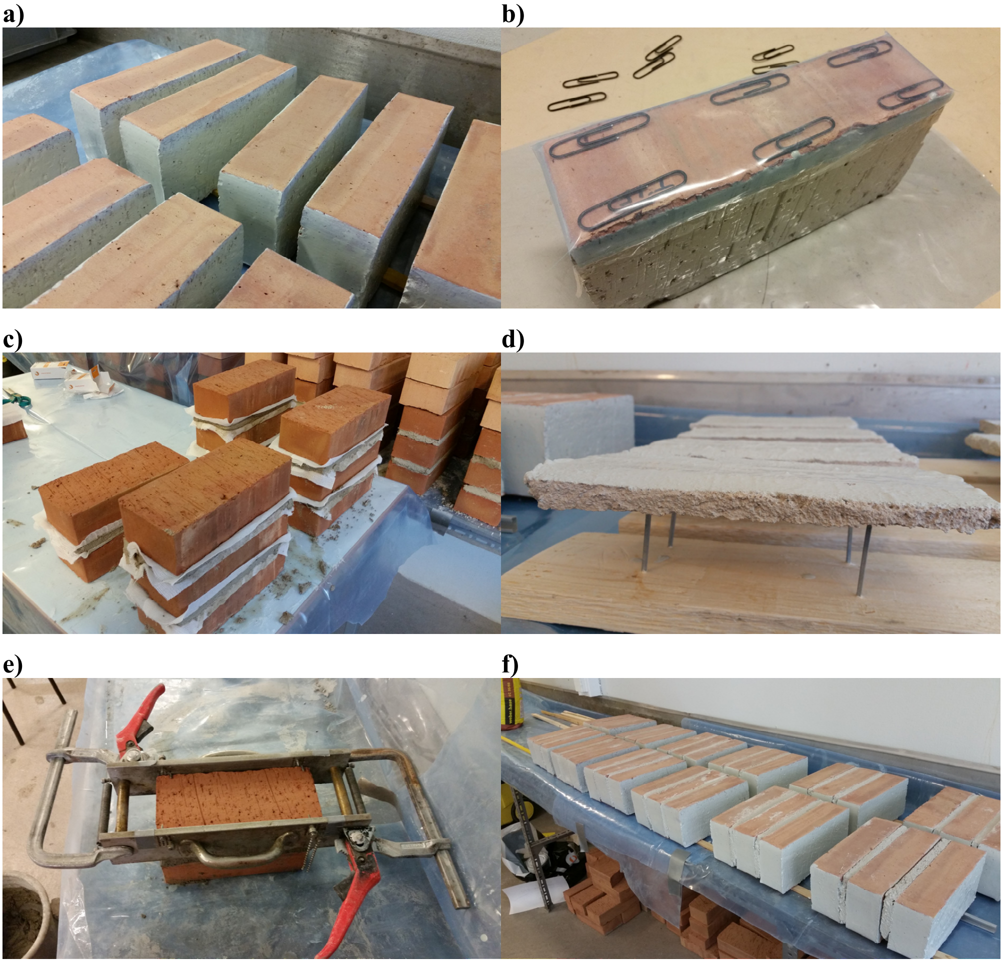

Fig. 7 Sample preparation, a) bricks with epoxy paint, b) brick with perforated plastic cover at an ensured distance to brick surface, c) mortar joints produced between cotton bandages and bricks, d) mortar joints with epoxy paint drying, e) pillar construction with tool to ensure constant joint thickness (Set 3), f) pillar specimens with epoxy paint.

4.2.3. Investigations of the brick-mortar interface and absorption (Article I and Thesis)

The laboratory study reported in Article I was supposed to act as a preliminary study, to be followed by further investigation. This laboratory work was conducted by two master students who started an investigation into a plausible correlation between the capillary absorption coefficient and shear strength, measured on a masonry pillar consisting of three bricks with bed mortar joints in between. This work was ongoing before the current PhD work became involved. However, with this preliminary laboratory result available, but not published, it became an opportunity to incorporate it into the PhD work, and to further build on it. First by writing a conference paper on the matter, before following up on the work and learnings with additional laboratory investigation.

The writing of the conference paper involved reanalyzing all the results of the preliminary laboratory study in a more precise spread-sheet setup, taking into account the theoretical framework of Bomberg et al. [188]. These updated results were then presented in the conference paper (Article I).

Although the results of Article I were implying there could be a correlation between the capillary absorption coefficient and shear strength of masonry, the results were based on too few samples for statistical analysis. Also, a severe weakness was that perforated bricks had been used instead of solid bricks (see Fig. 8 a) and b)), creating inaccuracy and large uncertainty in whether the results could be trusted. Furthermore, there were a few lessons from the preliminary laboratory work which should be improved upon.

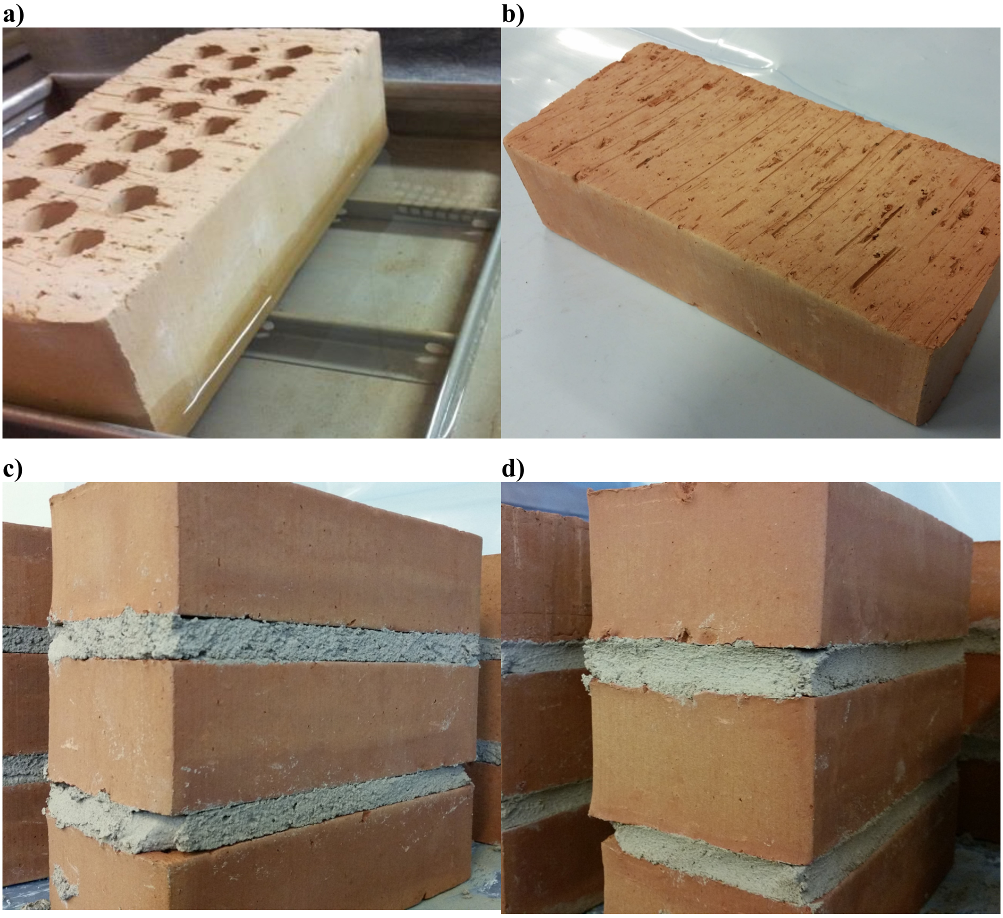

Fig. 8 Examples of a) perforated brick, b) solid brick, c) flush joint, d) concave joint.

A new laboratory investigation was undertaken to increase number of samples tested, and to improve the experiment procedure to reduce sources of error, unreliability, and inaccuracy. Improvements that were made were: 1) using solid bricks only, 2) prewetting of the bricks, 3) adding punctured plastic cover on top surface and more carefully adding epoxy paint on the sides to avoid evaporation loss during testing, see Fig. 7 b), 4) conducting the brick laying more carefully. A selection of pictures from sample preparation are provided in Fig. 7.

In addition, weight measurements were done at shorter time intervals after the specimens were lowered into the water. Furthermore, more accurate geometric measurements were taken. Observations of the moisture front permeation of the opposite surface were also noted down.

Materials applied were a high initial rate of absorption (IRA) brick (IRA of 4.5 kg/(m^{2}min) declared, 5.1 kg/(m^{2}min) measured), a lime mortar (CAL 148), and a lime-cement (LC) mortar (LC 35/65, % of lime and cement, respectively). Measured material properties are given in Table 8. Capillary absorption was not tested for a long enough time to determine w_{cap} for the mortar joints. Vapor permeability was not tested for the mortar joints; however, it was tested for the brick. Mortar joints were given two different finishes, i.e., half was given flush and concave finish, respectively (see Fig. 8 c) and d)). Flush implies a non-compacted, straightly smoothed surface finish, while concave implies a compacted finish, formed as a concave channel in the joint exterior.

Table 8 Material properties. Measured average and standard deviation. Based on 20 samples for brick, 4 samples each for flush and concave mortar joints, for both mortar types.

Material	Brick			CAL 148		LC 35/65	
	Average	Std.		Average	Std.	Average	Std.
Weight [g]	2481.98	17.88		-	-	-	-
Density [kg/m^3]	1760.91	8.37	Flush joints	1771.53	10.94	1806	5
A_w [kg/(m^2·s$^{1/2}$)][a]	0.267	0.026		0.0168	0.00231	0.0130	0.00097
W_{cap} [kg/m^3][b]	284.6	4.04		-	-	-	-
δ_v [kg/(m·s·Pa)][c]	1.963E-11	3.636E-13		-	-	-	-
Weight [g]				-	-	-	-
Density [kg/m^3]			Concave joints	1768.21	5.54	1832	8
A_w [kg/(m^2·s$^{1/2}$)][a]				0.0168	0.00184	0.0100	0.00165
W_{cap} [kg/m^3][b]				-	-	-	-
δ_v [kg/(m·s·Pa)][c]				-	-	-	-

[a] Refer EN ISO 15148 [189] (measured through brick face). [b] Taken as the hypothetical transition between capillary absorption and diffusion of trapped air. [c] EN ISO 12572 [186]

Unfortunately, several specimens were lost due to poor bonding, even with brick prewetting and more careful brick laying. These specimens fell apart after curing, during preparation and testing. This complicated arriving at a number of specimens sufficient for analysis. To arrive at a number of specimens that could be analyzed, three rounds of masonry pillar production was undertaken, giving three sets of specimens, summarized in Table 9. Given the laborious task of making specimens, and the space and time requirements for storing and testing them, the number is nevertheless low for statistical analysis and too low for proper statistical analysis.

After Set 1 it was decided the number of variations should be limited, to only further focus on LC mortar and flush joint execution. This finally resulted in 14 intact specimens from 3 production sets.

Table 9 Sets and number of specimens

Mortar type	Joint type	Number of specimens (lost specimens)		
		Set 1	Set 2	Set 3
Lime mortar (Cal 148)	Flush	6 (1)	0	0
	Concave	6 (1)	0	0
LC-mortar (LC 35/65)	Flush	6 (3)	6 (5)	10 (0)
	Concave	6 (2)	0	0

An imbibition investigation included several measurements of the pillars. The thinking was that not only the absorption coefficient but also the seep-through process of moisture could reveal possible poor brick-mortar interfaces, which could be compared to shear-testing results and observations on type of failure mechanism and on location of fracture surface. Furthermore, it was hypothesized regarding whether mortar remnant on the fracture surface could have correlation to shear strength. The following were therefore measured:

- Weight measurements at different times during partial submerging, Fig. 9 a).
- Identifying time of 1st, 2nd, 3rd, etc., up to 6th seep-through of damp patches on the opposite surface.
- Identifying location of seep-throughs, (at which mortar joint, which brick-mortar interface, or at which brick), Fig. 9 b).
- Shear strength, Fig. 9 c).
- Fracture location and mortar mud deposit, Fig. 9 d).

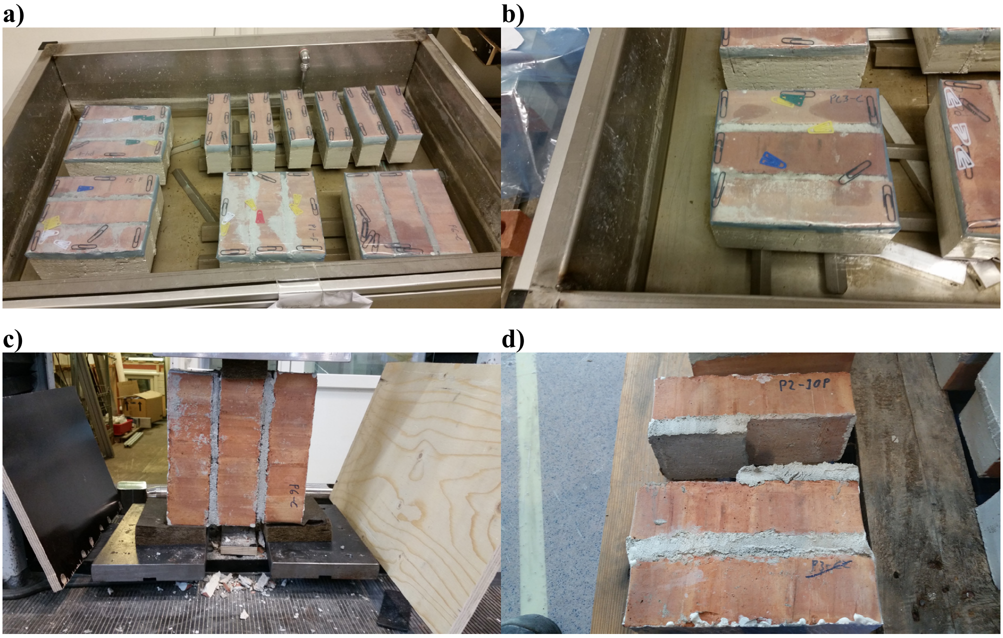

Fig. 9 Testing of brick-mortar pillar specimens. a) absorption testing, b) seep-through observation, c) shear strength testing, d) observation of fracture location and form.

4.2.4. Results and summary on absorption and shear strength (of the brick-mortar interface)

Results from investigating the potential relation between the absorption coefficient and shear strength for specimens are plotted in Fig. 10. No particular correlations are discernable in either Fig. 10 a) or b). However, it can be said the specimens with the highest shear strengths do not have the highest absorption coefficients. For lime mortar with flush joint, Fig. 10 a), one could easily plot a correlation; however, that would be highly questionable since all those specimens only have minor changes in shear strength, and the specimens for lime mortar with concave joints show no trend. In Fig. 10. b), it can be pointed out that a relatively low shear strength is observed for both the lowest and highest A_w-values, or in other words, the whole range of A_w-values are observed for specimens with low shear strength.

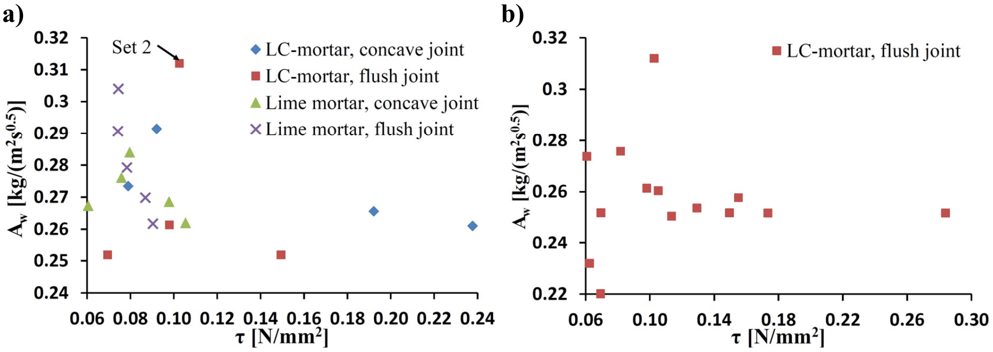

Fig. 10 Specimens plotted for A_w-τ relation: a) set 1 and 2, b) all 14 LC-mortar, flush joint specimens from set 1-3.

Seep-through observations from Set 3 are provided in Fig. 11, together with performance in terms of absorption coefficient and shear strength. Such accurate observations of seep-through were only done for Set 3. It was not possible to find any correlation between observation of seep-through location at joint interface, time of seep-through, and A_w from Fig. 11. Specimen 5 and 8, which have relatively low A_w-values, do show a late full seep-through time. However, so does specimen 7 with a moderate A_w. Furthermore, specimen 4 and 6 with relatively high A_w-values do not show a particularly quick, full seep-through, although specimen 4 has the earliest seep-through, but this is in the brick. Specimen 4 has very low shear strength, but so do specimens 5 and 8, which have low A_w-values. The highest shear strength is seen in specimen 2, which performs moderately in terms of seep-through occurrences.

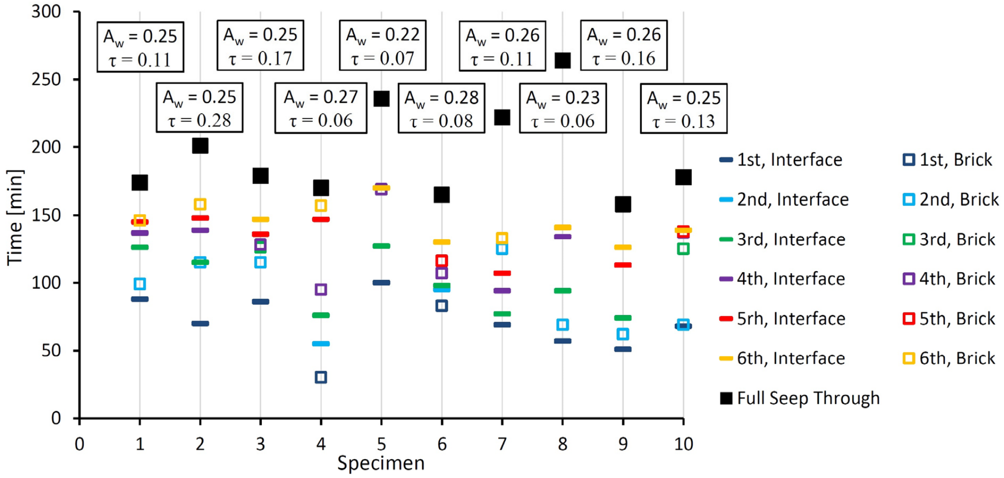

Fig. 11 Overview of seep-through location (joint interface or brick) with times of occurrence. A_w [kg/(m^{2}s$^{0.5}$)] and τ [N/mm²] of each sample are provided for correlation assessment.

No correlation is seen between fracture location and observed location of seep-through (Fig. 12). In fact, most fracture locations did not show any seep-through, with only 4 of 10 fractures locations (including specimen P2-1OP, see Fig. 9 d)) showed seep-through. However, those 4 fracture locations do correspond to the first seep-through times of those specimens.

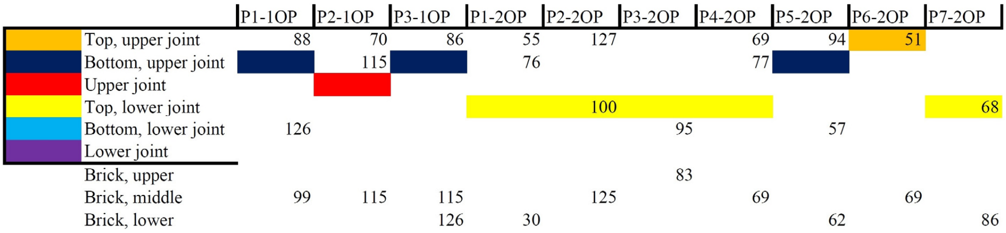

		P1-1OP	P2-1OP	P3-1OP	P1-2OP	P2-2OP	P3-2OP	P4-2OP	P5-2OP	P6-2OP	P7-2OP
🟧	Top, upper joint	88	70	86	55	127		69	94	🟧 51	
🟦	Bottom, upper joint	🟦	115	🟦	76			77	🟦		
🟥	Upper joint		🟥								
🟨	Top, lower joint				🟨	🟨 100	🟨	🟨			🟨 68
🔷	Bottom, lower joint	126					95		57		
🟪	Lower joint										
	Brick, upper						83				
	Brick, middle	99	115	115		125		69		69	
	Brick, lower			126	30				62		86

Fig. 12 Fracture location (color) vs. first 3 seep-through times and location for Set 3 (numbers in min).

Correlation between extent of mortar mud deposit left on the fractured surface, Fig. 13, and shear strength was investigated with Fig. 14. Mortar mud deposits were qualitatively classified from subjective assessment of observed fracture surfaces by assigning classes (marginal, moderate, heavy) and values (scale 1-9) as presented on the y-axis in Fig. 14. No apparent correlation was found.

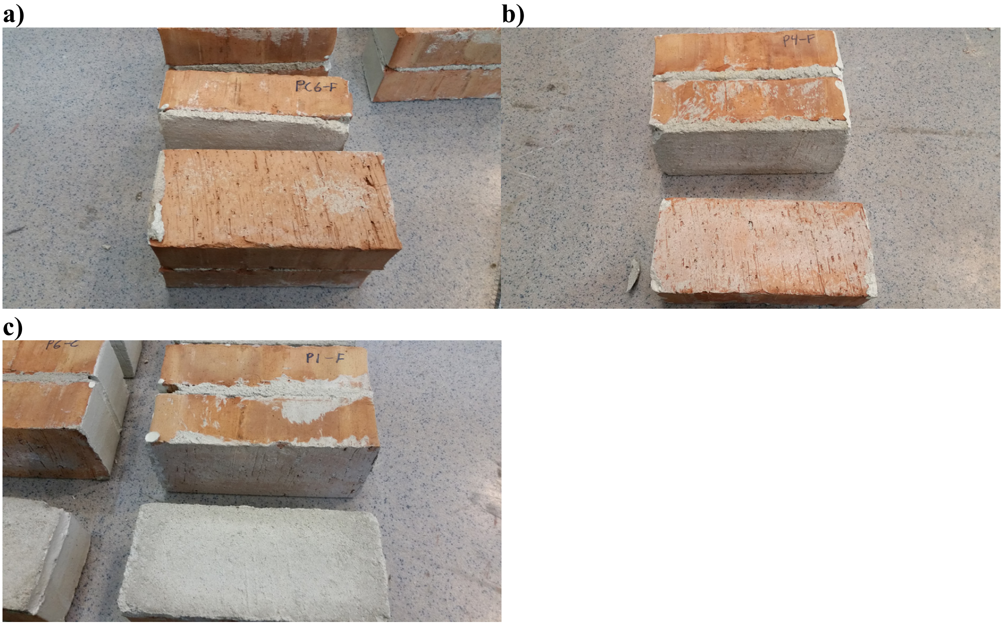

Fig. 13 Degree of mortar mud deposit on fracture surface of bricks after shear testing. Examples a) marginal (1), b) moderate (5), c) heavy (8)

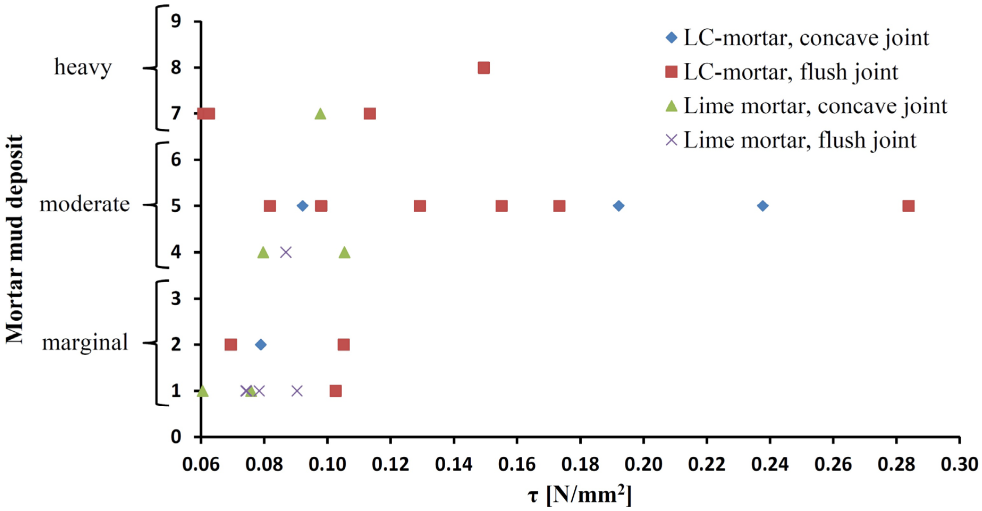

Fig. 14 Observed mortar mud deposit extent vs. shear strength results.

Finally, the results are summarized in Table 10, including fracture locations. Overall, no correlations were detected from comparing fracture location and range in shear strength in Table 10.

Table 10 Overview of fracture location in pillar specimens, associated number of specimens, shear strength range, mortar mud deposit amount on fracture surface, and absorption coefficient range.

Fracture location	Number	τ-range [N/mm^2]	Mortar mud deposit [-]	A_w-range [kg/(m^{2}s$^{0.5}$)]
Top, upper joint	3	0.074-0.192	Marginal – moderate (1-5)	0.258-0.304
Bottom, upper joint	8	0.069-0.173	Marginal – heavy (1-7)	0.250-0.279
Neither top not bottom, upper joint	1	0.284	Moderate (5)	0.252
Top, lower joint	14	0.061-0.238	Marginal - heavy (1-8)	0.220-0.312
Bottom, lower joint	2	0.080-0.098	Moderate (4-5)	0.261-0.284
Neither top not bottom, lower joint	0	-	-	-

4.2.5. Conclusion of investigation on brick-mortar interface

The following conclusions were made:

- No correlation between the water absorption coefficient and shear strength was found.
- No correlation between visual observation of seep-through, through interface or brick respectively, and shear strength was found.
- No correlation between seep-through location and fracture location (and fracture form) was found.

- No clear correlation between seep-through times, including locations, and absorption coefficients was found.
- The brick-mortar interaction significantly increases the water absorption rate compared to the absorption rate estimated from an area-averaged absorption of the two materials. This supports a hypothesis of additional moisture absorption along the brick-mortar interface.

If there is a correlation between the water absorption coefficient and shear strength, the correlation signal is weak and is easily drowned by the variability of water absorption in the brick. Thus, if such a correlation should be investigated again, it is paramount that the individual bricks are tested for their absorption coefficients and sorted in categories by value of those coefficients. This to ensure that all bricks used, to compose brick-mortar pillars in a set, have equal or comparable absorption performance, to eliminate noise, uncertainty, and incomparability.

It might also be plausible that the mortar used, operates over a too low and short interval of shear strength capacity for there to be an observable correlation. As seen in Fig. 10, most results gather in the lower range of shear strength, and these are shear strength values that are rather low in general, when compared to more cement-based mortars. Thus, different or nuancing findings might be plausible with a higher-strength mortar.

Due to the conclusions made, and with the work and results considered unsuited and insufficient to be published, further work on this topic was terminated. This research thus became a dead-end in terms of the thesis. It would have been too risky (uncertain) for the PhD project to tread further down this research path. Consequently, focus was shifted towards testing masonry wall segments with interior insulation in a climate simulator.

4.2.6. Investigation of material properties

During the laboratory work several material properties were measured. Listed in Table 11, for reference, the basic material properties were measured in accordance with relevant standards.

Table 11 Standards applied for measurements

Property	Symbol in thesis	Standard	Comment
Volume (net)		EN 772-3:1999	Used for calculating the net dry density
Density (net dry)	ρ_s	EN 772-13:2000 / EN 1015-10:2000	
Initial rate of absorption	IRA	EN 772-11:2011	
Capillary absorption coefficient	A_w	EN ISO 15148:2003	
24 h water absorption	(w_{sat})	EN 772-21:2011	Was found to be unreliable approximation of saturated moisture content, presumably due to significant amount of entrapped air.
Sorption	$w(\phi)$	EN ISO 12571:2013	
Vapor permeability	δ_v	EN ISO 12572:2001	Only the wet-cup was measured due to the practice in the laboratory, although the dry-cup is more suitable for applicability in hygrothermal simulation models.
Shear strength	τ	EN 1052-3:2002	

4.3. Large-scale testing of masonry wall segments in climate simulator (Article II)

This section will summarize the large-scale laboratory experiment setup and methods. The description will try not to be a direct repeat of what is found in Article II. Instead, it will provide a more superficial description, but which is supplemented with some additional perspectives on the experiment design, aims, methodology, and uncertainty over what is found in the article. For more specific details on materials, construction, structure, instrumentation, and climate sequence the reader is referred to Article II.

4.3.1. General

A test wall composed of nine individual masonry wall segments, Fig. 15 a), was constructed to investigate differences in hygrothermal performance from variation in masonry and interior insulation system configuration. The nine segments were given configurations so that there always were at least two segments only having one varying parameter. The exception is Seg. 2, which acted as a non-insulated reference segment that consequently was without an interior insulation system. Two series of the experiment were planned with two intentions in mind: 1) investigate experiment repeatability, and 2) focus on mineral wool in Series 1 and other insulation materials in Series 2. Although both series were run, and data gathered, it was unfortunately not possible to address the other insulation materials in the work on this thesis.

The reasons for this were that analysis of segment performance turned out to be more complicated than anticipated, repeatability between series was difficult to achieve, and because the topic of Article V was stumbled upon in the meantime, thereby leading to a shift in research priority. Therefore, the other insulation materials, which were aerogel blanket and phenolic foam board products will not be addressed in this thesis.

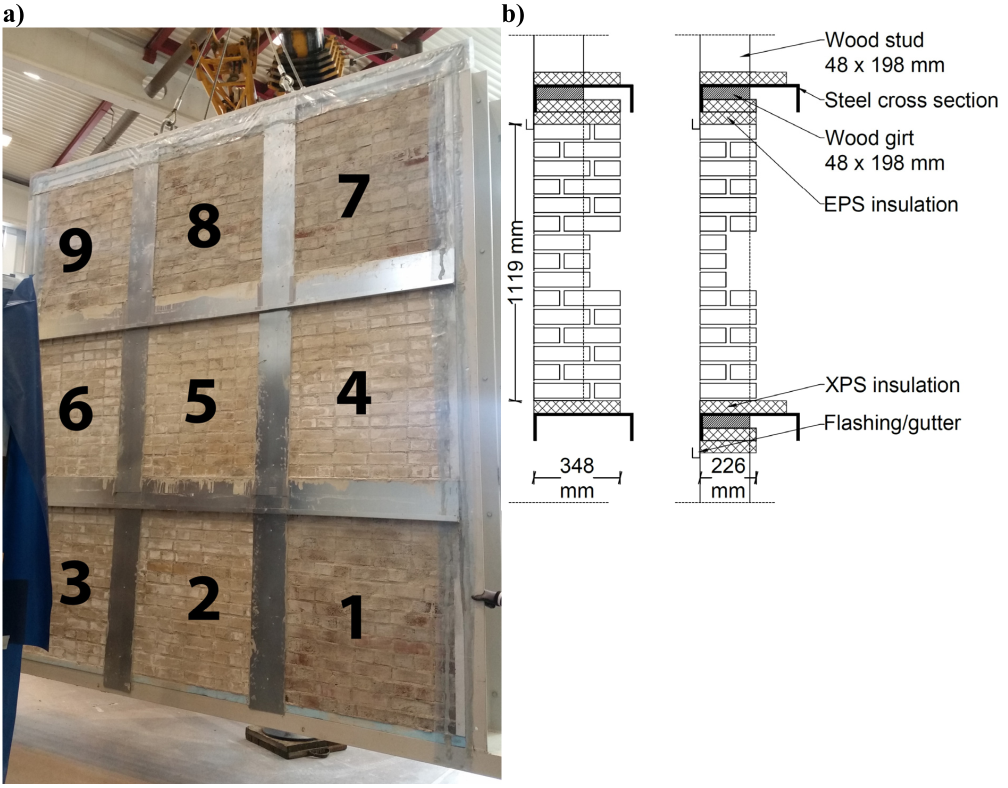

Fig. 15 a) Test wall divided into 9 wall segments, b) cross sections of brick wall segments of 1.5- and 1-brick thickness, respectively.

4.3.2. Design, objectives, and time constraints

The experiment was designed as a parameter sensitivity investigation, with parameters varied being:

- Brick type – varying between a high IRA brick, perceived to resemble brick qualities of existing bricks from times prior to 1950, and a moderate IRA brick representing modern brick design for better handling weather exposure.
- Masonry thickness – 1-brick-thick and 1.5-brick-thick.
- Insulation thickness – varying between 50, 100 and 150 mm.
- Vapor barrier – SVB and traditional vapor barrier in polyethylene.

The experiment would make use of a climate simulator that can create exterior and interior climate exposure. The insides of the climate simulator chambers are pictured in Fig. 16. Further description is provided in Article II.

Fig. 16 Climate simulator consisting of two chambers, a) exterior side with water spray nozzles and lamps, b) interior side with space for monitoring equipment. Also showing ventilation systems at the ceilings.

The intention, in addition to studying the impact of the parameter variations above, was to investigate the drying potential towards the interior. This included investigation of the drying potential regarding embedded beam ends, with the presumption that beam ends represent one of the most moisture-critical types of elements in interior insulation retrofit.

To enable clear detection of SVB contribution to inward drying, the thinking was that the masonry should undergo severe wetting, thereby ensuring high RH exterior of the SVB when warm exterior temperature was imposed for drying to take place. Then the SVB functionality should ensure low vapor resistance. Although this thinking generally should hold, it turned out that heterogeneity in the masonry obscured this, as the wall segment with traditional vapor barrier, which was to work as a comparison, from sensor readings, seemingly distributed much less moisture to the interior than the SVB-fitted counterparts.

With the experiment designed with severe rain wetting, this would become an issue for the 1.5 thick wall segments. Although it was known from previous work in the laboratory [39] that heavily wetted masonry takes long time to dry out, it was believed the time could be shortened by drying the masonry after construction and between series by keeping it inside the climate simulator at a high temperature (35 and 30 °C, exterior and interior respectively). However, even this took long time and pressed the allotted time with the climate simulator. Thus, how long the drying period of the experiment series could be run was limited. The climate sequence had a duration of 3340 h or 146 days. After brick laying, the curing and subsequent drying took almost 7 months; nevertheless, there was indication from the poor repeatability between Series 1 and 2 that an initial moisture content likely had been present for Series 1. Consequently, Series 1 might not have started completely dry as intended. Thus, a lesson from this experiment is that no less than a year should have been scheduled for the preparation and running of Series 1 after construction. This relates to the segments of 1-brick thickness. For the 1.5-brick thickness, even longer times would be required, including a longer drying period in the climate sequence. The 1.5-brick-thick segments did not dry out in time for Series 2. This especially affected Seg. 1, and therefore Seg. 1 did not participate in Series 2.

4.3.3. Configurations, structures, and materials

Nine wall segments were constructed into a large steel frame. Fig. 15 a) shows the final product. Cross sections of the 1- and 1.5-thick segments and their placement into the steel frame structure are seen in Fig. 15 b). Wood girts and studs fix in place the segments that are in a row, with insulation removing heat bridge influence from the steel on the masonry. Configurations of the parameters previously listed are provided in Table 12, with configuration changes in Series 2 listed in Table 13 for reference and clarification, even though the different insulation materials in Series 2 are not addressed in this thesis.

For both the moderate and high IRA segments a LC mortar was used (LC 50/50/610 with numbers corresponding to lime/cement/aggregate mass ratios of binder content). It has been pointed out, the importance of finding a mortar that compliments the brick for good brick-mortar bonding [65]. This was not attempted here. Instead, a common LC mortar was used, but which still should resemble mortar properties of existing buildings more than newer masonry mortars or pure cement mortars.

Table 12 Configuration overview of wall segment characteristics in Series 1

Segment	1	2	3	4	5	6	7	8	9
Moderate IRA brick	✓	-	-	-	-	-	✓	✓	✓
High IRA brick	-	✓	✓	✓	✓	✓	-	-	-
Wall thickness [bricks]	1.5	1	1.5	1	1	1	1	1	1
Reference segment	-	✓	-	-	-	-	-	-	-
Insulation thickness [mm]	50	-	50	50	50	150	50	100	150
Interior gypsum board finish	✓	-	✓	✓	✓	✓	✓	✓	✓
Polyethylene vapor barrier	-	-	-	-	✓	-	-	-	-
SVB	✓	-	✓	✓	-	✓	✓	✓	✓

Table 13 Altered configuration overview of wall segments in Series 2

Segment	1	2	3	4	5	6	7	8	9
Mineral wool batt	-	-	-	-	✓	-	-	-	-
Phenolic foam board	-	-	-	✓	-	-	✓	✓	-
Aerogel blanket	-	-	✓	-	-	✓	-	-	✓
Insulation thickness [mm]	-	-	20	50	50	40	50	50	60
Interior gypsum board finish	-	-	✓	✓	✓	✓	✓	✓	✓
Smart vapor barrier	-	-	✓	✓	✓	✓	✓	-	✓

4.3.4. Instrumentation and construction

The segments were equipped with Sahlen sensors, RH sensors, and beam end resistance moisture meters. The Sahlen sensor contains a thermistor and a resistance moisture meter based on birch wood. It is a practical sensor for monitoring moisture conditions in the high RH interval, where RH sensors are unreliable, or in structures where moisture conditions are expected in the over-hygroscopic region. A drawback with the Sahlen sensor is that when placed inside the masonry, its result is difficult to compare to hygrothermal simulations. This because, in practice, one needs to include a Sahlen sensor dummy (sensor geometry and material properties) in the simulation model for result reading (this has not been attempted in the current thesis). Otherwise, one will miss the delay that occurs in the experiment, due to not having capillary contact between the birch wood and the mortar. An additional issue is the conversion of results by aligning the retention curves of birch wood and mortar, to identify moisture content of mortar. This process gives rise to some uncertainty due to retention curve uncertainty of the respective materials. RH sensors provide limited usefulness when built into the masonry since they are unreliable close to vapor saturation and provide low to indistinguishable variation in result when very close to saturation. Thus, what they detect will be the arrival of over-hygroscopic conditions with rain events. Additionally, they become useful again (although sometimes fail) when the drying closes in on or enters hygroscopic conditions.

Sensor placement during brick laying for both Sahlen and RH sensors is depicted in Fig. 17 c) and d), whereas Fig. 18 shows an overview of all sensor locations.

Prewetting of the high IRA bricks had been found important (Section 4.2.3) for improving brick-mortar bonding, and it presumably limits infiltration along the brick-mortar interfaces. Consequently, the high IRA bricks were prewetted for 10 min before bricklaying, Fig. 17 a). In contrast, the moderate IRA bricks were only brushed with water, i.e., each course was brushed with water before next one was laid upon it. Fig. 17 b) shows brick laying of the high IRA bricks before final brushing of the mortar to make a smooth finish. Fig. 17 c) and d) show brick laying of moderate IRA segments. Beam end pockets are visible in Fig. 17 e). Brushed surface of high and moderate IRA segments are shown in Fig. 17 f) and g), respectively, with the final finish of high IRA segments, after having dried, seen in Fig. 17 h).

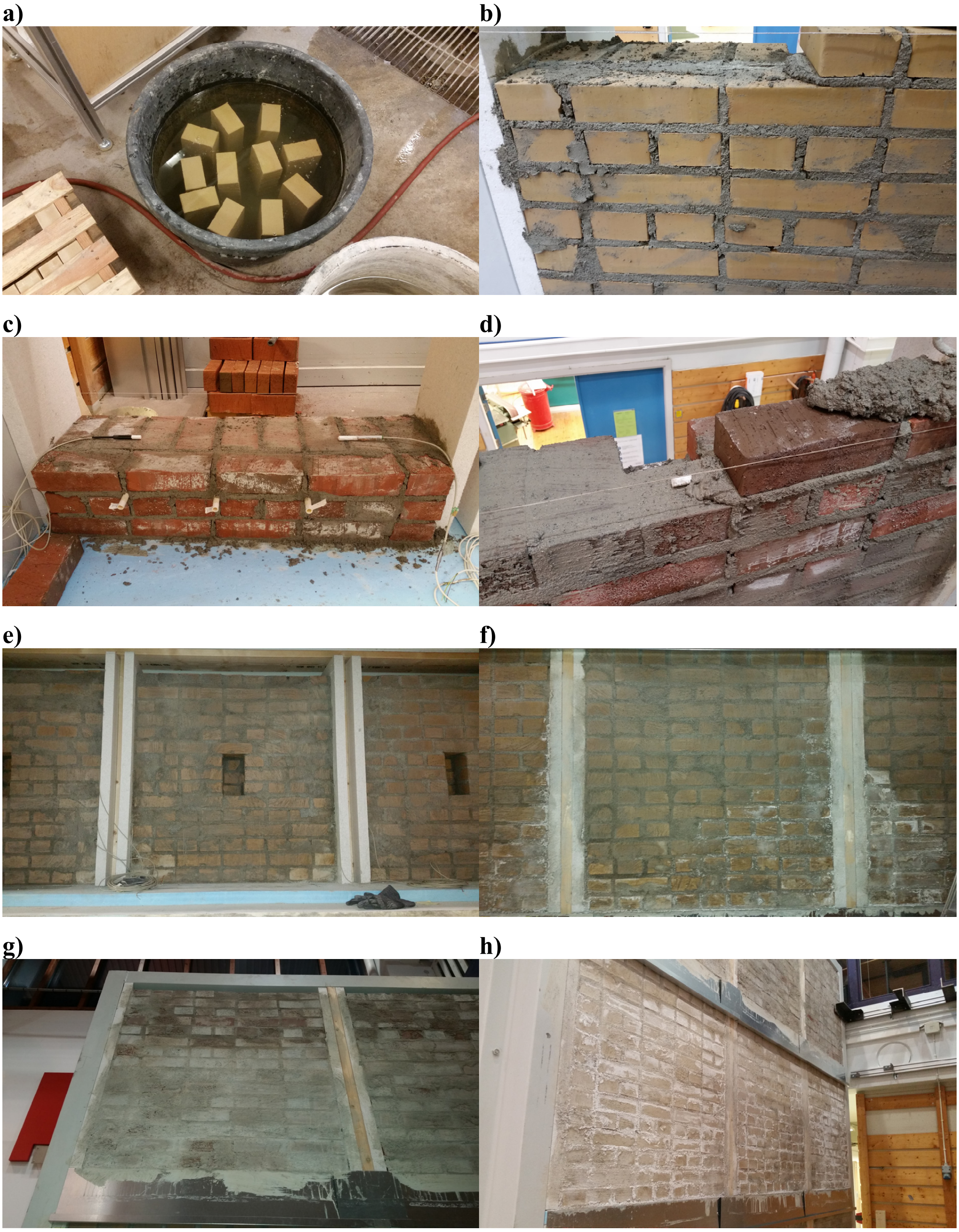

Fig. 17 a) prewetting of high IRA bricks, b) brick laying of high IRA brick segment, c,d) brick laying of moderate IRA segment, with c) Sahlen and RH sensor placement and d) Sahlen sensor placement outside beam end pocket, e) interior finish of high IRA masonry with beam end pockets, f) exterior finish of high IRA masonry, g) exterior finish of moderate IRA masonry, h) exterior with mounted gutters between rows.

After finishing a wall segment, it was covered with polyethylene plastic to prevent evaporation to the surroundings. All segments were finished after 10 days, including a three-day-weekend pause, after which they were left curing for one month. To ensure that the mortar had sufficient access to moisture during curing, wall surfaces were sprayed once a week with water, approximately 150 ml/m^2. After the one month, the plastic was removed to allow for drying to the climate of a large laboratory test hall. The hall held a temperature of approximately 18 °C for the entire period. For the first two months of drying, the hall held a low level of RH, < 30 %, due to the cold winter conditions outside at the time.

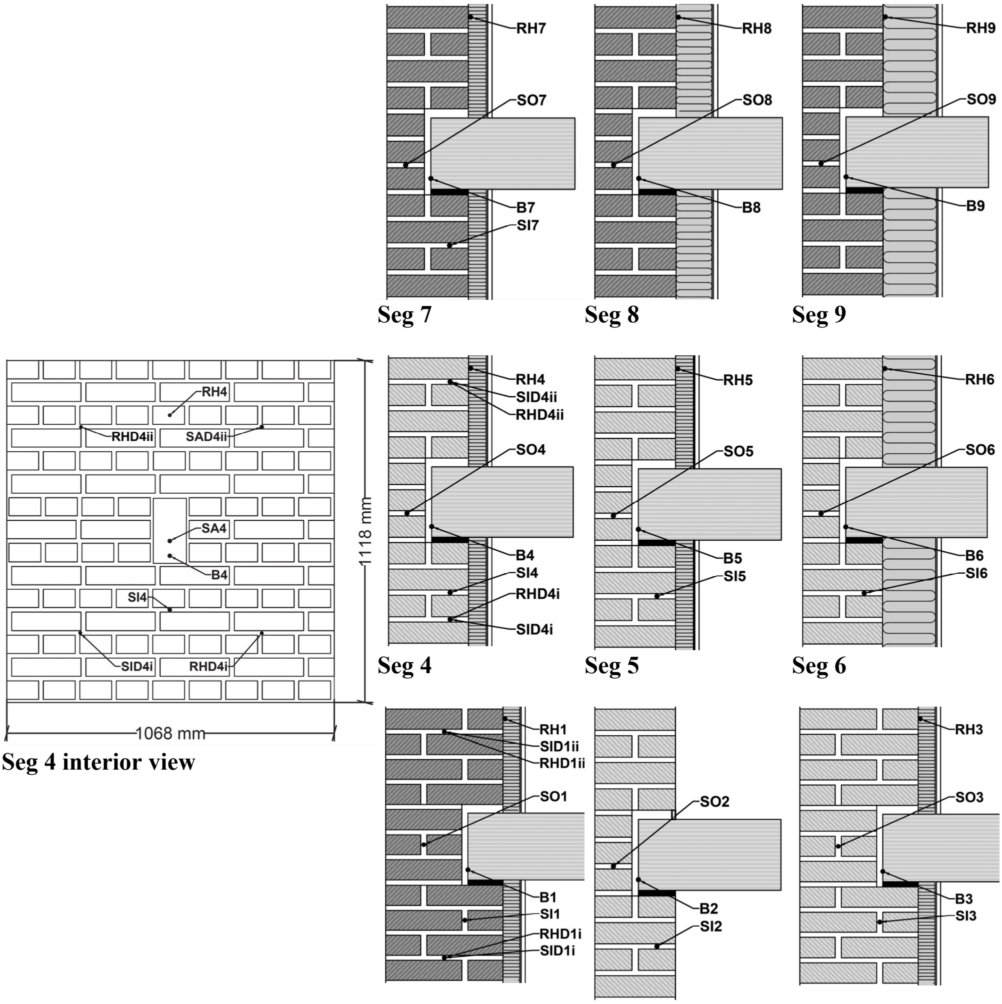

Seg 7 Seg 8 Seg 9

Seg 4 interior view

Seg 4 Seg 5 Seg 6

Seg 1 Seg 2 Seg 3

Fig. 18 Interior view of Seg. 4 and cross section overview of segments including sensor locations.

Spruce beam ends were inserted into the beam end pockets Fig. 19 a), with an asphalt sill gasket underneath to act as a capillary break. A 10-20 mm thick airgap was ensured between the beam end and the rear of the pocket. The distance variation is due to the uneven surface inside of the pocket. Thus, the distance is at least 10 mm. Airtightness was particularly important to achieve due to the ventilation mixing conditions inside of the climate chamber. The chamber attempts to create a well-mixed atmosphere to create uniform conditions. Therefore, the airflows exterior and interior of the wall segments become rather windy. However, no air pressure difference was imposed. Airtightness was approached by sealing the SVB to the beam ends with tape, and with clay filling, ensuring no gap between the gypsum board and beam end.

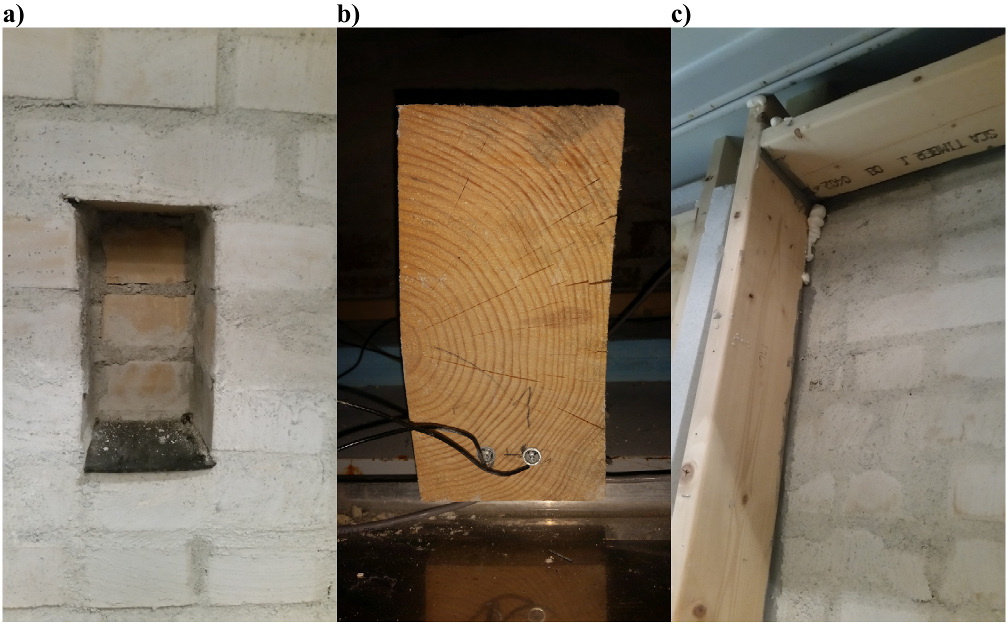

Fig. 19 Close up of a) beam end pocket, b) exterior side of spruce beam end, with mounted resistance moisture meter pins, c) frame around insulation with sealant between frame and masonry for airtightness.

4.3.5. Conditions, events, and observations while running the experiment

To supplement the information and observations mentioned and discussed in Article II and VI more pictures are provided in Fig. 20. A view of the rain events is provided in Fig. 20 a), to give an impression of the water mist conditions that are generated due to water spray nozzle functionality. The water spray provides a fine droplet spray that is not typical in real world rain events.

During Series 2 there occurred some malfunctions that created near 100 % RH conditions in the interior climate chamber. These occurrences produced heavy condensation on metal surfaces in general, since those surfaces held the lowest temperatures, Fig. 20 b). Although condensation was not particularly seen on the wall segments, RH sensors in Series 2 clearly registered these occurrences (see Article II).

After rain events, spread water droplets could be seen for a (short) while on the bricks, Fig. 20 c). Limited absorption capability is thereby indicated at local positions on the bricks.

With Article VI addressing moisture permeation along the brick-mortar interface, Fig. 20 d) and e) give two additional pictures of this occurrence with the masonry in Seg. 2.

a)

b)

c)

d)

e)

Fig. 20 A selection of pictures showing conditions, events, and observations while running the experiment: a) rain events creating a water mist in exterior chamber, b) malfunction causing 100% humidity and severe condensation on metal surfaces in the interior climate chamber (prior to Series 1), c) water droplets visible on exterior surface of high IRA bricks after 1st 20 min rain event, d) and e) darker areas outline moisture permeation in Seg. 2 after 1st 40 min rain event.

4.3.6. Uncertainties with the climate exposure

In the climate simulator 16 water spray nozzles are located 1 m from the exterior surface of the wall. The nozzles are arranged to create a relatively uniform wetting of the wall surface; however, nozzles will have different alignments towards each of the nine segments. An equal uniform wetting of each segment can therefore not be guaranteed, although a posteriori investigation found no transparent correlation between nozzle locations and sensor results. Droplet sizes are in the range of 15-35 μm. Degree of runoff is outside the research scope and has not been measured. It can therefore not be assumed that the applied intensity, i.e., the water flux, is fully absorbed by the masonry.

A temperature buffer is required by the simulator to prevent frost issues with its components; therefore, it will not allow water spray to be turned on when the temperature in the exterior chamber is below 10 °C. If the climatic sequence operates with lower temperatures than this the temperature must be raised above 10 °C for each rain event.

The temperature of the water spray is not controlled. The water comes from an intermediate water tank between the simulator and the laboratory building water system, which results in a water temperature that starts at the same indoor temperature as that of the laboratory hall (18 °C) and falls as the cold water of the water system is mixed into the water tank. Thus, for short rain events the rain temperature will keep an indoor temperature, while for long rain events it will fall over time towards the temperature of the water system.

For exterior climatic sequence temperatures that are kept below 11 °C, regular daily defrosting of the ventilation system is needed, a process which interrupts the climatic sequence for, normally, less than half an hour.

4.3.7. Other uncertainties

Article II gives a discussion on uncertainties and possible causes for the poor repeatability between the experiment series. This will not be repeated; however, in general there is often a lingering uncertainty regarding human error somewhere along the experiment procedure, which can manifest itself as repeatability issues. For instance, this can be failing to time the duration of rain events properly; however, there is no specific suspicion of this having been the case.

Other issues that may have resulted in an increased variation in masonry performance is the consistency of craftmanship during bricklaying; however, the bricklaying was done by an experienced mason to reduce such uncertainty. Nevertheless, the mortar compaction in joints may vary, especially for head joints and collar joints. Prewetting of bricks may also result in some uncertainty as the moisture uptake during prewetting can vary due to entrapped air and variation in pore structure, even though the prewetting duration was fixed. Furthermore, the prewetting may not have been substantial enough, since it only resulted in an average moisture uptake barely reaching the lowest moisture content advised by Brocken [67], see Article II.

A shortcoming of the experiment in the climate chamber was that there was no collection and weighing of runoff water during rain events. Such a measurement would have been of great help to assess the moisture absorption of the masonry, control potential differences between the experiment series, and evaluate the degree of conservativeness of simulation efforts (Article VI).

4.4. Analytical work

4.4.1. Analysis (Article II)

Analysis of the laboratory results on the masonry wall segments showed to be much more complicated than anticipated. The results showed a large spread, and result-correlations to the parameters being varied were to a large degree not apparent or could be doubted. With a low sample size (number of segments compared) a correlation needs to be highly convincing (consistent) to not be drawn into doubt. Thus, a more comprehensive and thorough quantitative analysis was needed in addition to the mere visual and qualitative comparison of segments performance, visualized through graphs.

Due to the low sample size, traditional statistics was ruled out. Instead, a semi-quantitative approach was chosen, involving ranking segment performances through indexes. The benefit would be to identify relative overperformance and relative underperformance among the segments. This could more objectively reveal and document potential correlation trends than what subjective interpretation of graphs could.

Indexes were made, inspired by the FIRGRA (Fire Growth Rate) index [190] used for classifying reaction to fire of building materials and products, in the field of fire safety engineering of buildings. The essence of the FIGRA index is to reveal information about two threat-conditions: I) A large fire is worse than a small fire, and II) a rapid fire growth is worse than a slow fire growth [191].

Similarly in the case of a masonry performance, regarding wetting, Iw) more wetting is worse than less wetting, and IIw) rapid wetting is worse than slow wetting. Additionally, regarding drying, Id) more drying is better than less drying, and IId) rapid drying is better than slow drying.

This resulted in the development of what was named the Moisture Growth Rate Index (MGRI) and the Moisture Decline Rate Index (MDRI), as described in Article II.

4.4.2. Model development (Article V)

The origin of work described in Article V can be summarized as follows:

1) Applying the standard approach of calculating the liquid conductivity from mathematical transformation of liquid diffusivity showed to have an issue, i.e., the resultant conductivity trend becomes unphysical when close to saturation (see article).
2) As an alternative the model of Scheffler [84] on modeling capillary conductivity was deemed of interest; however, it required the over-capillary saturated conductivity, which was unknown for the materials in question, and a coefficient determined from iterative hygrothermal simulation of absorption experiments. Thus, the model was not readily applicable.
3) This led to an idea that the capillary conductivity at capillary saturation perhaps could be predicted just like the capillary diffusivity at capillary saturation can be predicted, i.e., predicted from the capillary absorption coefficient.
4) However, to achieve this there needs to be established a correlation between the capillary absorption coefficient and the capillary conductivity at capillary saturation. This led to an investigation into analytical expressions for the capillary absorption coefficient and the capillary conductivity (summarized in the article).

The model development approach consisted mainly of four parts: 1) Establishing understanding of the physics, and the model-simplifications of the physics that are involved, to ensure correct implementation. 2) Ensuring sound mathematical derivation, i.e., follow each derivational step to ensure that the mathematical operations are correctly executed and that nothing is lost in the process. 3) Running the model in a spread sheet to evaluate model behavior, and the feasibility and correctness of the conductivity curve results against curves reported in the scientific literature. 4) Debugging and correcting the model when irregularities were detected.

Additionally, a consideration was given limitations, in support of limiting the number of influential factors and model complexity.

4.5. Hygrothermal simulation

This section addresses the process and methodology in developing the simulation model.

4.5.1. Reasons for choice of software

The path towards landing on a software and model to use has to some extent come into existence as it has been traveled. Back in the spring of 2014, with COMSOL being easily available at the university and with local introduction courses into COMSOL, there was an interest in the research group to become familiar with COMSOL's potential for hygrothermal building physics modeling. WUFI was the only other hygrothermal simulation software being used at the research group at the time, and it was deemed to have too little access to the physics expressions to give high research flexibility. DELPHIN was a considered alternative to COMSOL; however, it was not yet acquired by the research group at the time. In retrospect, DELPHIN would have been an easier choice than COMSOL, especially since DELPHIN over time has had the most extensive utilization and development in the scientific community within building physics. In 2014, COMSOL did not have a ready module for building physics. Such a module was included in COMSOL a couple of years later; however, when it was included, it was not optimized for driving rain. Therefore, a hygrothermal model built in COMSOL from scratch, through the COMSOL PDE interface, was continued for the current thesis research. With WUFI being most familiar, the modeling in COMSOL was approached following [124] with RH as the dependent variable. Choosing RH as the dependent variable led to a series of complications that had to be solved. RH as the dependent variable is inconvenient when addressing highly capillary cases, such as driving rain scenarios in particular, since the true driving potential is capillary pressure. Hence, capillary pressure would have been a more direct variable for operation with high moisture content and rapid rain wetting, which is the direction the research moved. The direction the research would take was, however, not known when work on the COMSOL model began.

4.5.2. Development of the hygrothermal simulation model

A model development process may ideally for instance follow something along the lines of the v-model [192, 193], where overall functionality specification (addressing end use purpose of model), sub-model functionality specification, and component specification are established as having links to their verification and validation counterparts.

In the present work, the process of establishing design specifications has unfortunately not been that systematic. Instead, the model has been developed continuously with more functionality included as more simulation scenarios have been sought undertaken. Results of early design and design aims have lingered throughout the development. This, for instance, is the explanation for why the model has kept RH as the physical dependent moisture variable instead of capillary pressure, and furthermore, why it was continued down that line. To better accommodate heavy driving rain, this led to the making of an artificial natural logarithm expression of RH as the dependent variable numerically solved for (Article IV and thesis Appendix A.6), instead of adopting the more common approach with natural logarithm of capillary pressure.

Table 14 Stages of model development (model derived and explained in Appendix A)

Stage	Functionality specification established	Utilization scenarios
1	Basic hygrothermal model coupling heat and moisture transfer.	In general
2	Three dimensionality.	Hamstad#1 and #2 benchmarks in 3D (Article III)
3	Driving rain absorption (capillary conductivity based).	Hamstad#4 benchmark
4	Driving rain absorption (capillary diffusion based).	Comparative simulation study (Article IV)
5	Smart vapor barrier (based on average experienced RH).	Comparative simulation study (Article IV)
6	Humid air gap (behind beam end), humid air properties.	Comparative simulation study (Article IV)
7	Shortwave and longwave radiation models (Section A.7.3).	Comparative simulation study (Article IV)
8	Air diffusion, i.e., coupling heat, air and moisture transfer (Section A.3).	Hamstad#3 benchmark
9	Improved driving rain absorption (hydraulic conductivity based).	Simulation study (Article VI), based on Article V.
10	Smart vapor barrier (based on dual sided RH exposure).	Simulation study (Article VI)
11	Allow for unphysical supersaturation of humid air (expanded range of RH), as a simple approach to avoid dealing with surface condensation. (Section A.6.2)	Simulation study (Article VI)

During the whole process, algorithms had to be revised and updated several times to incorporate new understanding, remove errors in algorithms, or to improve faulty or insufficient performance of algorithms.

4.5.3. Verification and validation of the simulation model (Article III, IV, and Thesis)

In the development of a simulation model, one requires verification of the model's logical, mathematical, and numerical correctness, and validation that it is meeting its intended predictive performance. Simulations only provide value if their results can be trusted [194]. Therefore, confidence in a model must be established. This can be achieved through documenting the verification and validation of the model. The verification and validation procedure is of utmost importance for successful numerical modeling [195].

Verification involves checking that model equations are solved correctly and accurately, that coupling of the physics functions correctly, that model algorithms adhere to the intended and correct logic, that the algorithms are implemented correctly in the model system, and that numerical solving of the model system operates correctly and accurately [194, 196, 197]. While verification approaches the mathematics and coding, validation approaches the physics [194].

Validation addresses whether the model physics appropriately replicate nature [198], i.e., whether it accurately represents the real world, with respect to the intended use of the model [199]. Validation ultimately involves comparing model predictions to experimental results and observations [194, 197, 198].

An important perspective of model validation is that it does not reveal whether a model works properly. Instead, a validation test reveals whether a model works improperly [195, 196]. Accumulatively passing validation tests generates trust in a model, due to the tests not rejecting it [198]. Validation should be done simultaneously with model building, which is an iterative process [200]. Statistical tests should ideally be applied in validation; however, if not realistic, graphical plots can, for instance, instead be used [200]. Several validation techniques are presented by Sargent [200]. Since validation techniques are problem dependent [200], only the perceived relevant ones from Sargent are summarized below:

- Tracing: behavior of a model entity is traced / followed through the model to determine whether it is correctly handled, and that necessary accuracy is obtained.
- Historical methods:
    - Rationalism: logical deduction of a valid model from model assumptions.
    - Empiricism: every assumption and outcome must be empirically verified.
    - “Positive Economics”: some future must be predicted by the model.
- Multistage validation: a combination sequence of historical methods.
- Parameter variability (sensitivity): Ensuring that the same sensitivity or response is seen in the model as expected in the real system.
- Comparison to other models: comparing to other already validated models.
- Predictive validation: model is used to predict system behavior, and the two are then compared.
- Sub-model testing: validation of sub-models.

Of these validation techniques, comparison to other models is mainly used in the present work. Sub-model testing and parameter variability, although not capable of fully validating model performance in the present work, have in the work presented in Article VI been used indicative of reasonable model performance.

Verification of the model has been done by repeated and meticulous debugging and double-checking of model algorithms, including their derivation. Equations and algorithms have been checked in spread sheet format to check that they produce the expected trends and values, when compared to the known functions and values of the physical variables and material properties they describe. This applies, for instance, to all the material property functions listed in Appendix B, to check that their temperature dependence works as intended. Furthermore, generated solutions of equations and algorithms have been sampled from the simulation results to verify that the solutions have arrived at realistic values.

Validation of the simulation model has been done through:

1) Benchmarking the Hamstad Benchmarks 1-5. Appendix C presents the benchmarking of Hamstad #1 – #5 benchmarks. (A benchmarking of the Hamstad #1 and #2 benchmarks with an early model version was presented in Article III, with only partial success, see Section 4.5.4.)
2) Comparative simulation study in Article IV, where the COMSOL model was compared to the WUFI model.

Note that, from some perspectives, benchmarking is perceived to fall under the realm of verification since it does not involve comparison to experiments that the model is intended to be used for, e.g., [197].

Specifically regarding hygrothermal simulation models, they should not only be validated for RH since RH is a temperature dependent parameter; thus, validation for RH should always be accompanied with validation for temperature [201]. Although, Article VI is not a validation article, the principle of assessing RH and temperature in combination is followed there.

Extensive or specific validation of all model functionality has not been possible within the scope of the thesis work. For instance, specific validation with scenarios involving humid air voids or a smart vapor barrier is not included. Nevertheless, verification that the mathematics and algorithms calculate as intended is conducted.

4.5.4. Correction of a model mistake present in Article III and IV

A mistake was unfortunately present in the model version applied in Article III and IV. In conversion of the time-derivative of the moisture content, the temperature dependence of the capillary pressure was overlooked.

That is, in Article III and IV the derivative of the moisture content was calculated as Eq. (25) with the moisture content differentiated directly for RH. This would only be valid for an isothermal situation.

Differentiation for a non-isothermal case must, however, also differentiate for temperature as a variable [202]. Therefore, following Eq. (26), the moisture content is expressed as a function of capillary pressure, with the latter a function of both RH and T.

$$\frac{dw_w}{dt}=\frac{dw_w}{d\phi}\frac{d\phi}{dt} \tag{25}$$

$$\frac{dw_w}{dt}=\frac{dw_w\left(p_c\right)}{dt}=\frac{dw_w}{dp_c}\frac{dp_c\left(\phi,T\right)}{dt}=\frac{dw_w}{dp_c}\left(\frac{dp_c\left(\phi\right)}{d\phi}\frac{d\phi}{dt}+\frac{dp_c\left(T\right)}{dT}\frac{dT}{dt}\right) \tag{26}$$

This is further expanded on in Appendix A.4.1, including for a more complex moisture content function, being a function of both RH and capillary pressure. The benchmarks presented in Article III have been repeated with the corrected model. Consequently, the fluctuations seen in Article III benchmark 1 disappear, and the results shift somewhat, when respectively comparing

Fig. 3 and 4 in Article III with Fig. C.1.2 and Fig. C.1.12. It was also discovered that the simulation result of benchmark 1 is highly sensitive to timestep size. Therefore, compared to Article III, smaller timesteps are applied for results in Appendix C.1.

4.5.5. Analysis by hygrothermal simulation (Article VI)

Analysis by means of hygrothermal simulation is the methodology applied in Article VI. The analysis approaches uncertainty and sensitivity related to modeling choices by varying choice alternatives. Additionally, some sensitivity analysis is included related to material property uncertainty in order to assess the range of result variation from such uncertainty. The study includes additional reflection through a discussion on some other sources of uncertainty related to the simulation effort. Finally, a broad discussion is included on conservativeness in such modeling, as a method to provide and promote perspectives that may trigger ideas among researchers for further research and development of modeling approaches for hygrothermal simulation.

5. Main findings

This section is limited to the journal articles, since the conference articles are more like steppingstones towards the journal articles and are deemed not to constitute main findings.

5.1. Large-scale experiment, Article II

In Article II, the impact of parameters, such as masonry thickness, brick type, insulation thickness, and vapor barrier solution, is experimentally investigated.

Masonry thickness and insulation thickness will not be given emphasis since the findings on those parameters were fairly in line with expectations and confirm findings from other studies: specifically that lower RH and moisture content, respectively, are experienced at the masonry interior and at beam ends with thicker masonry, e.g., [18, 21, 203], and slower dry out is experienced with increased insulation thickness, as expected considering the increased vapor resistance and slightly lower masonry temperature [32]. For instance, increased insulation thickness slightly worsens a mold index in [21].

Emphasis will, however, be given to brick type and SVB. Relative performance among masonry segments is summarized in Table 15. The calculation of the values is explained in Article II and is not vital to repeat here; however, what is important is their relative difference in terms of overperformance (white), underperformance (black) and average (gray). Overperformance respectively indicates lower and slower wetting, or larger and faster drying, while underperformance indicates the opposite. One can clearly see a difference between brick types, with more overperformance for the moderate IRA brick (Seg. 7-9) and with more underperformance for the high IRA brick (Seg. 4-6). One exception is the wetting experienced by the RH sensor on the interior of the masonry, which were more severe for the moderate compared to the high IRA segments. Beam end wetting (B sensor) also did not show a consistent difference between moderate and high IRA segments. Regarding drying internally in the masonry (SO and SI sensors), virtually no difference was detected between the moderate and high IRA segments; however, a weakness with this observation was the lack of SI sensors in Seg. 8 and 9. Drying on the interior of the masonry and at the beam ends was however much better for the moderate IRA segments than for the high IRA segments.

There were some surprises in the results, especially the combination of the relatively high moisture uptake experienced in the masonry itself (SO and SI sensors) for Seg. 5 while the same segment showed relatively low wetting at the masonry interior and at the beam end. Since the only design difference between Seg. 4 and 5 was the former having SVB and the latter a traditional polyethylene barrier, this complicated evaluation of SVB performance. Complicating it further, the drying (moisture decline) rate at the masonry interior and at the beam end showed to be greater for Seg. 5 than for Seg 4. Thus, SVB performance could not be determined from evaluating Series 1.

Table 15 Relative performance of segments: black represents underperformance, white overperformance, gray fairly average

	Segments	4	5	6	7	8	9
wetting	SO moisture cont.	0.98	1.15	1.23	0.93	0.65	1.06
	SO growth rate	1.00	1.23	1.34	0.87	0.44	1.12
	SI moisture content	1.30	1.25	1.22	0.73	X	X
	SI growth rate	1.51	1.46	1.42	0.54	X	X
	B moisture cont.	1.14	0.96	0.98	1.09	0.94	0.90
	B growth rate	1.33	0.86	0.96	1.30	0.79	0.76
	RH moisture cont.	1.01	0.84	1.03	1.06	1.03	1.04
	RH growth rate	0.96	0.77	1.05	1.10	1.06	1.07
drying	SO decline rate	0.99	1.01	0.96	0.98	1.00	1.05
	SI decline rate	0.98	0.98	0.84	1.00	X	X
	B decline rate	0.46	0.69	0.38	1.31	1.29	1.88
	RH decline rate	0.66	0.73	0.21	1.66	1.46	1.28

Smart vapor barrier performance was evaluated further by comparing Series 1 with Series 2 of the experiment. With Series 2 having replaced the traditional polyethylene barrier with SVB for Seg. 5, a clear comparison was expected. Unfortunately, however, repeatability discrepancies between Series 1 and 2 made such a comparison highly uncertain. (Description and discussion of the repeatability issues will not be repeated here, refer to Article II.) Comparison between the polyethylene barrier and SVB is given in Fig. 21, by showing sensor readings for the RH sensor and beam end sensor, refer Section 4.3.4 and Fig. 18. Climate simulator malfunctions in Series 2 unfortunately obscured the comparison even further, making it impossible to compare Series 1 and 2 for the wetting of Seg. 5, or for SVB performance in the cold period. For the drying period after the onset of higher temperature, the RH curve of Series 2 is seen to lie much lower than that of Series 1. However, this cannot be ascribed to the SVB because of the repeatability issues. Nevertheless, a somewhat similar drying trend is seen in both RH4 and RH5^{2nd}, both showing an (early) sharper drying trend than RH5. Thus, it is somewhat likely this could be ascribed the SVB. A similar trend is hard to see for the beam end, although there is a slightly sharper drying trend in B4 and B5^{2nd} than in B5 towards the end of the warm period.

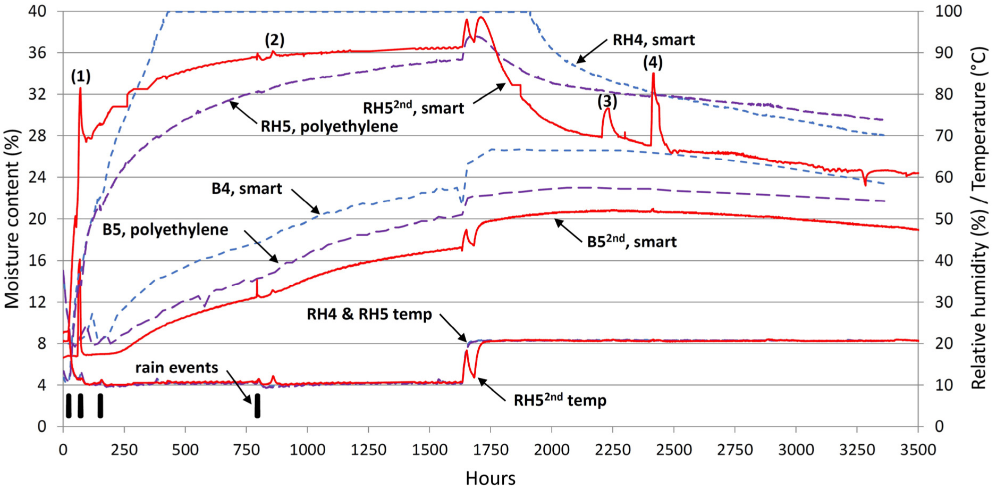

Fig. 21 RH and beam end sensor readings for Seg. 4 Series 1 (SVB) and Seg. 5 Series 1 and 2 (polyethylene and SVB respectively). Numbers (1)-(4) identify climate simulator malfunctions (Series 2 only), where interior RH briefly approached or touched 100 %. Before it was corrected, an incorrect setting also caused the temperature to fall again after the onset of the warm period in Series 2.

5.2. Hydraulic conductivity modeling, Article V

In Article V a methodology for generating hydraulic conductivity curves is established.

The findings of Article V show that it is possible to simplify the capillary conductivity model of Scheffler and Plagge [79], expressed in Eq. (20), by implementing the capillary absorption coefficient instead of measurements of effective conductivity at saturation. However, with simplification there is loss of accuracy and increased uncertainty. Thus, a simplification needs to be beneficial in terms of balancing reduction in resource demand and complexity, with loss in accuracy and certainty. Furthermore, such loss needs to be acceptable for what the simplified model is applied to. In addition to the simplification, it is shown that the Scheffler and Plagge model can be expanded to include a film conductivity model. In the article a film model by Lebeau and Konrad [109] is applied.

The following, including Fig. 22, summarizes the findings in terms of what is achieved with the simplified model when comparing to the Scheffler and Plagge model.

Scheffler and Plagge model	**Proposed model**
Capillary conductivity at capillary saturation	
	New derived/proposed expression
$K_{c,cap} = f_l\left(w_{cap}\right)\eta_{cap}K_{eff,sat}$	$K_{c,cap} = \frac{A_w^2}{2\rho_w}\int_0^{\theta_{c,cap}} \frac{1}{p_c^2}d\theta_c \left[\int_0^{\theta_{c,cap}} \frac{1}{p_c^{1/2}}d\theta_c\right]^{-2}$
Input: w_{cap}, w_{sat}, $K_{eff,sat}$, η_{sp}, η_{cap}	Input: w_{cap}, A_w, $\theta_c(p_c)$
Capillary conductivity	
	New proposed simplification
$K_c = f_l\eta_{cap}K_{eff,sat}K_{rel}$	$K_c = \frac{f_l}{f_l\left(w_{cap}\right)}K_{c,cap}K_{rel}$
Total input: w_{sat}, $\theta(p_c)$, $K_{eff,sat}$, η_{sp}, η_{cap}	Total input: w_{cap}, w_{sat}, $\theta_c(p_c)$, A_w , η_{sp}
Hydraulic conductivity	
	New expression to include film conductivity
$K = K_{hyg} + K_c$	$K = \left(1-\phi^{\eta_\phi}\right)K_{hyg} + \phi^{\eta_\phi}\left(K_{film} + K_c\right)$
Input: K_{hyg}, K_c	Input: K_{hyg}, K_{film}, K_c, η_ϕ,

Fig. 22 Overview comparison between the Scheffler and Plagge model and the proposed simplified model

Main benefits of the proposed model are:

- Replaces $K_{eff,sat}$ with A_w, with the latter easier to measure.
- Avoids η_{cap}, a scaling coefficient that is identified through iterative simulation of capillary absorption experiments.
- Includes film conductivity.

Main drawbacks of the proposed model are:

- Less accurate determination of $K_{c,cap}$.
- Needs to distinguish between retained moisture θ and capillary retained moisture θ_c to attribute correct moisture content to film and capillary conductivity.
- Introduces an additional coefficient η_ϕ to shift contributing weight of K_{hyg} and K_{film} + K_c in the hygroscopic region.

Overall Article V describes and presents the methodology of generating hydraulic conductivity curves. This can be summarized with Fig. 23, which shows that from an input of w_{cap}, w_{sat}, A_w, $w(p_c)$, and three $\mu(\phi)$-values one can generate a hydraulic conductivity curve prediction/approximation. It was found that this methodology was on par with the method of calculating the capillary conductivity from transformation of the common simple prediction of capillary diffusivity. Nevertheless, compared to the diffusivity approach, it is believed the proposed model generates more consistent curves avoiding unphysical behavior in materials having strong non-uniform pore scales.

Brick – Derluyn model dataset

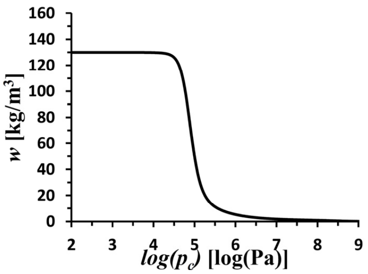

w_{cap} = 130 kg/m^3, w_{sat} = 209 kg/m^3

A_w = 0.1032 kg/(m^{2}s$^{1/2}$)

$\mu(\phi=0.33)$ = 31.5, $\mu(\phi=0.7)$ = 27.9, $\mu(\phi=0.91)$ = 11.5

Source [139]

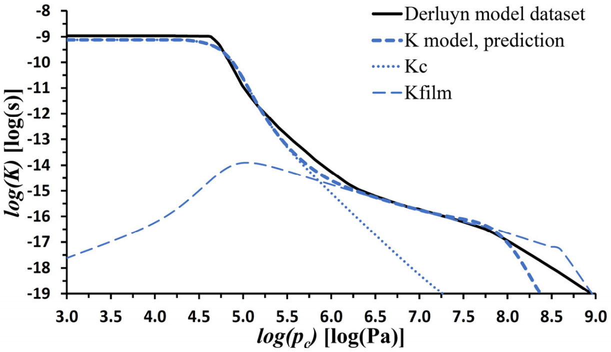

Fig. 23 Input to the model (left) and generated, predicted curve (right) compared to the curve reported in the source.

5.3. Hygrothermal simulation uncertainty, Article VI

In Article VI, a study is presented that highlights modeling uncertainty and sensitivity to hygrothermal modeling choices. The study applies a 2D hygrothermal simulation model to bare brick masonry with interior insulation retrofit, which includes an embedded beam end and SVB. Only the findings deemed most interesting in light of the thesis (sub-)objectives are further addressed here. Refer to Article VI for the full account.

A conservative approach is taken to the driving rain, only limiting the rain absorption to the minimum of rain flux and the absorption capacity of brick and mortar. Additionally, the model incorporates lumping of mortar properties and the expected increased absorption along the brick-mortar interface. The intention with such a conservative approach was to arrive at results enveloping experiment results, since the experiment results have a large spread in behavior. Thus, the modeling did not try to replicate specific results with a low error of deviation. Nevertheless, conservative results were not achieved when focusing on the early response to rain events of RH sensors on the interior of the masonry, seen from the experiment, Fig. 24. Neither the long dry out time of beam ends seen in the experiment were seen from the conservative modeling approach. However, at the same time, the conservative model did arrive at a moisture content in the masonry that was higher than in the experiment, thus underestimating and not replicating a distinct drying trend seen in the experiment. From observations of rapid rain permeation, an implementation of modeling with "leaky" mortar joints did, however, approach the rapid RH sensor response seen in experiments. Furthermore, applying a 3D model instead of a 2D model significantly delayed the drying of the beam end, Fig. 25, thereby giving a conservative enveloping result, and additionally a more matching trend, when comparing to the experiment. This indicated that the rain absorption in general could be too severe while simultaneously leak-like intrusions were underestimated in the 2D base model without "leaky" joints.

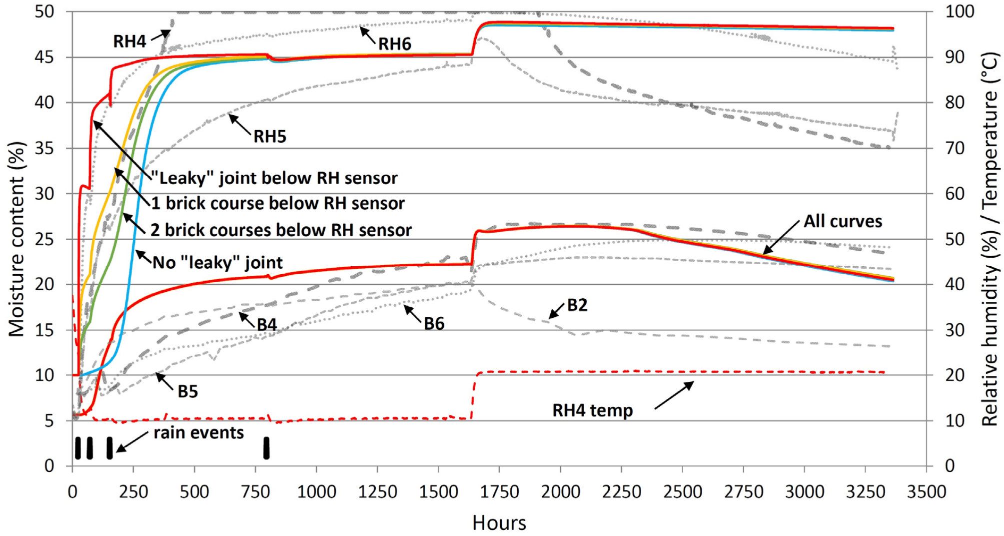

Fig. 24 Inclusion of a "leaky" joint. With a "leaky joint" a more rapid response is seen for the RH sensor. RH drying trend is underestimated. Dry-out time of the beam end is underestimated in this 2D simulation. Experiment results as grey dashed curves, simulations as colored lines.

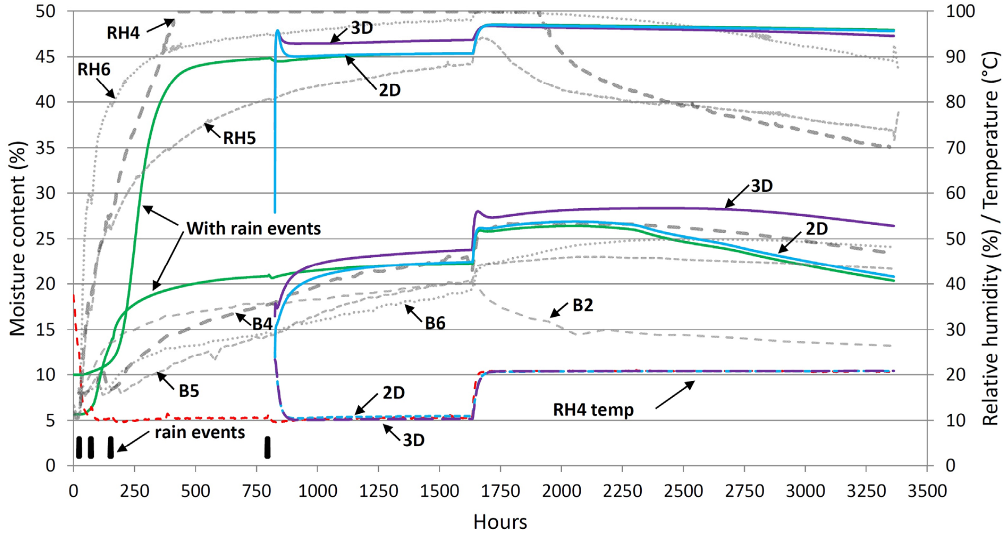

Fig. 25 Comparison between 2D and 3D simulation with initial conditions after final rain event. In 3D, a higher moisture content is seen in the beam end, in addition to a longer dry-out time, now being conservative.

SVB performance was also investigated. Simulation with SVB was compared with simulations with highly decreased and increased vapor resistance, respectively performing like no-vapor barrier and a traditional vapor barrier. As seen in Fig. 26, the RH reading shows a significant impact of the SVB, while the beam end reading shows an insignificant impact with only a minor difference at the end of the warm period. This corresponds with the findings of Article II.

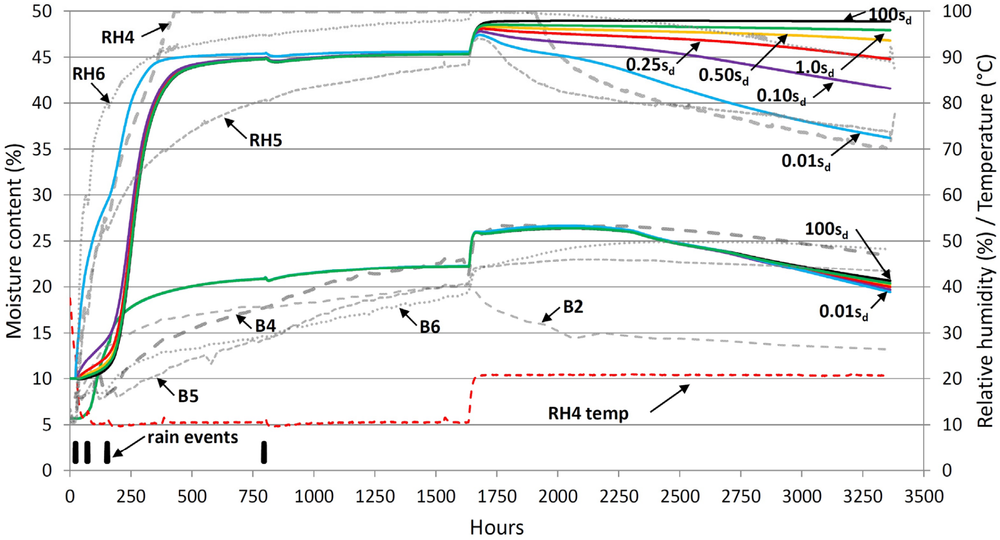

Fig. 26 SVB performance comparing different reinforcements of the vapor resistance, i.e., $1.0s_d$ implies expected SVB performance, $100s_d$ acts like a traditional polyethylene barrier and $0.01s_d$ acts like no vapor barrier.

[This page is left blank]

6. Discussion

6.1. Quality issues / significant limitations

This section discloses and discusses some quality issues and/or limitations of the different studies presented in Article II, Article V, and Article VI.

6.1.1. Large-scale laboratory experiment

In retrospect, there are some shortcomings with the setup of the large-scale experiment. The heterogeneous behavior of the bare brick masonry structure under heavy rain exposure was clearly underestimated in the planning of the experiment. Thus, too much attention was given parameter variation in the experiment design, thereby ending up with too many configurations, instead of limiting the experiment to a narrower focus on a few parameters. Consequences of this resulted in: 1) results of parameter variation were obscured by noise from the moisture transport behavior of the masonry, 2) the investigation of parameter variation suffered from poor correlatability since the compared configurations had none or too few equal copies to more substantially confirm or disconfirm correlations or reliability of findings, and 3) sensors were squandered on configurations and measurements that did not fit into, or only played a minor role in, the final focus and analysis of Article II and VI.

Additionally, the largely failed repeatability between Series 1 and 2 of the experiment complicated the intended comparison and investigation, which then partially contributed to a shift of focus, abandoning further investigation of Series 2.

It is perceived that rain exposure of bare brick masonry exacerbated the complexity of such an experiment due to the unpredictability of localized moisture infiltration and distribution that such masonry can experience. Thus, a study without or with less severe rain exposure, or with external render, could have fared better. Nevertheless, also the inclusion of 1.5-brick-thick masonry was in retrospect misplaced due to the long dry-out times and the limited available run-time of each experiment series.

Lessons learned from the shortcomings:

- Keep number of parameter variations to a few, also ensuring comparison of equally configured samples.
- Expect large variation in masonry behavior for bare brick masonry segments under severe rain exposure.
- Ensure sensor redundancy, i.e., several sensors distributed over the masonry of a wall segment, intended to measure the same but which can detect the variability of the masonry behavior.
- Plan for extra run-time for experiment series, to give a substantial buffer for potentially encountered long dry-out times, especially for thicker wall structures.

6.1.2. Hydraulic conductivity model

The assessment of the hydraulic model in Article V shows a fair predictive performance of the model for certain materials while showing rather bad predictive performance for a few others. However, the prediction performance is highly dependent on the range of saturation level or capillary pressure that is in focus. A discussion of the prediction performance at capillary saturation and possible reasons for cases of poor prediction at capillary saturation is provided in Article V, and it will not be repeated. However, a discussion will be provided on prediction performance at low saturation (high capillary pressure). As mentioned in Article V regarding film flow, no compensation/correction is provided for nanoscale. However, this is an issue for liquid transport at nanoscale in general. At nanoscale, the material hydrophilicity or hydrophobicity, liquid confinement in pores and pore crevices, and pore surface roughness can affect molecule orientation, structuring of the fluid, adhesion forces, no-slip tendency at pore wall, and, not at least, the fluid properties such as density and viscosity, and possibly also surface tension and contact angles, see, for instance, [204-206]. As mentioned in Article V, Nikitsin and Backiel-Brzozowska [207] propose a correction factor for viscosity for $r < 1$ μm. Lebeau and Konrad [109] (origin of the film model) separate calculation of the film conductivity into two expressions, one for film thicknesses $\delta \geq 10$ nm and another for $\delta < 10$ nm, in order to accommodate effects on the viscosity in nano-thin films. In contrast, the model proposed in Article V partially circumvents this issue with the hygroscopic correction model of Scheffler [79, 84], which applies calculation of liquid conductivity from decrease in vapor resistance values at higher RH compared to that at low RH values. This approach is, however, not always easy since three vapor resistance measurements at different RHs are rare in material testing studies. Furthermore, there is also uncertainty from the fact that scatter in measurements is often seen among different samples and different laboratories [208]. There is also uncertainty regarding the transition from the hygroscopic correction model to the film model, which has not been investigated in Article V.

The aforementioned becomes significant for materials that are highly hygroscopic, i.e., retain much moisture in the hygroscopic RH range (e.g., capillary pressure range $\log(p_c) > 6$, and especially $\log(p_c) > 7$). This, for instance, applies to cement- or lime-based materials like mortar, concrete, aerated concrete, and sand-lime bricks, see Article V, as well as low porosity stones. In Article V it can be seen that especially the mortar, concrete, and aerated concrete are poorly predicted at low to moderate saturation, while, simultaneously, prediction at capillary saturation is rather good. The sand-lime bricks are a bit harder to interpret with varying results among the two versions.

On the other hand, at low saturation, the low hygroscopic materials, i.e., clay brick, calcium silicate (insulation), and limestone, show in Article V much better prediction.

A related issue is the differentiation between film moisture content and capillary moisture content. The methodology in Article V is somewhat crude in identifying the contribution to moisture retention of each. With the article mainly focusing on predicting conductivity at capillary saturation, and the scaling of unsaturated conductivity to this, determination of film-associated moisture for the film model was not extensively investigated nor developed for high accuracy. With an incorrect distinguishment of film moisture and capillary moisture, the conductivity prediction will also suffer. Thus, much can probably be done to expand and improve this part of the model to better approach reality.

Another issue that has not been addressed is corner flow, which in some way can be seen as a hybrid of film and capillary flow, where increased film thickness in a corner is promoted by capillary menisci forces. This occurs in corners or crevices of the pore, of specific interest along the length of capillaries when approaching flow conductivity. For non-cylindrical pore shapes with relatively prominent angles, for instance ≤ 90 °, substantial corner flow can be expected, see [113, 136]. From this, corner flow can in cases be suspected to substantially add to the normal film flow. However, for both film flow and corner flow, surface roughness might also be expected to alter the overall flow conductivity [113]. Thus, corrections for roughness might be needed in such a model framework. This warrants further study on the basis of methodology described in [113, 136]. Overall, there might therefore be an improvement potential by including corner flow and surface roughness to the film flow contribution to hydraulic conductivity.

6.1.3. Hygrothermal simulations – Scenario and modeling choices

The hygrothermal simulation focus is, in terms of results, addressed quite holistically. That is, sensor locations are mainly limited to be the interior of the masonry and the beam end. Thus, investigation of moisture distribution throughout the brick-mortar system has not been given focus. By not comparing to moisture distribution measurements, realities, and uncertainty and accuracy issues, remain unknown regarding the liquid conductivities, interface resistances, and vapor diffusivities. In contrast, Vereecken et al. [48] demonstrated simulation differences on moisture distribution with and without interface resistances. Zhou et al. [168] compared simulation results along different paths in the masonry with moisture distribution profile measurements, in analysis of interface resistance values and capillary pressure conditions. Ramirez et al. [125] compared simulations with interface resistances to imbibition experiments to match capillary absorbed water uptake, and furthermore, demonstrated simulation differences between brick-mortar models of different sophistication. Studies like these are useful to better understand the realism of the moisture transport mechanisms and material properties that are involved.

Instead of addressing interface resistances, the current work focused on the increased capillary conductivity along the brick-mortar interface. However, only an approach of lumping the increased moisture transport with the capillary transport property of the mortar joint was attempted. In contrast, Gutland et al. [169] demonstrated an approach of modeling fractures like a thin material domain between the brick and the mortar joint to account for the increased moisture absorption. The benefit of this is that the rest of the mortar joint behaves with bulk mortar joint properties, not necessarily raising significant issues with anisotropic behavior. The lumped properties of the current work did not address the anisotropic issue, and thus had too high moisture transport across the joint during rain events when the lumped properties kicked in. The practical effect of this warrants more investigation.

The Gutland approach [169] also had the benefit of increasing the vapor diffusivity. Both Hens [209] and Vereecken et al. [210] reported decreased vapor resistance in a masonry composite, compared to the individual materials, thereby indicating the need for including some modeling mechanism for increased vapor diffusion along the brick-mortar interface. This was not attempted in the current work.

The investigated scenario involved quite severe rain exposure. For many practical interior insulation retrofit cases, such a scenario may become unrealistic for drawing correlations to real weather exposure. For instance, the understanding of severe rain infiltration is that the nearby masonry has to have reached high saturation before the brick-mortar interface will facilitate infiltration to the interior masonry [211]. This also applies to the exterior surface of the masonry, in order for a liquid (runoff) film to occur that facilitates infiltration [212]. Thus, for cyclic weather where high saturation is not reached and where the masonry dries out between rain events, increased moisture absorption along the brick-mortar interface may be a non-issue. Nevertheless, there are indications that walls can perform quite well with yearly weather exposures of low to normal wind driven rain loads but get into trouble with one severe rain event. For instance, Kopecky et al. [30] imposed one severe artificial summer rain event that significantly worsened moisture conditions for the duration of the subsequent cold season in a field-test wall. However, this was with exterior render, thus not capturing the issue with brick-mortar interfaces of bare brick masonry.

6.2. Uncertainty

Categorically, Article VI only investigates a very limited set of uncertainties related to hygrothermal simulation analysis. In perspective, Zhao et al. [46] categorize uncertainty into four groups with uncertainty related to enclosure, scenario, modeling, and numerical solving. Inspired by the categorization given by [46, 213], Table 16 is established to provide an overview of uncertainty related to hygrothermal simulation. It reveals that Article VI only partially investigates two sub-groups of what contributes to uncertainty, namely, *material properties and material interactions*, and *transport mechanisms*. The aim with Table 16 is to put Article VI into a larger context on uncertainty. According to Zhao et al. [46] uncertainty related to the *Numerical* group and what is here the *Algorithms* sub-group, can be controlled by model validation and numerical design. A precision regarding this, is that the sub-group *Algorithms* benefits from both verification and validation. In COMSOL, the sub-group *Numerical methods* is only influenced by configuration of setup menus, while the methods and schemes themselves are hard-coded. However, these settings are important to whether the simulation runs altogether or runs smoothly. Experience from the simulation work supports that tolerance settings, related to *Numerical methods*, see A.8.1, and *Discretization*, are important regarding validation efforts.

Table 16 Uncertainty categorization

Group	Sub-group	Description examples
Scenario	Climate	• Weather climate • Indoor climate and occupancy loads
	Exposure	• Environmental shielding from weather • Surface transfer- and absorption-coefficients
Structure	Material properties and material interactions	• Variability • Moisture and temperature dependence
	Geometry and as-built conditions	• Geometric dimensions • Structural idealization
Modeling	Transport mechanisms	• Simplification of phenomenon (including dimensional simplification, 1D, 2D, or 3D) • Simplifications, assumptions, or guestimates related to mechanism models
	Algorithms	• Simplifications of physics • Accuracy of expressions
Numerical	Discretization	• Temporal resolution • Spatial resolution
	Numerical methods	• Numerical discretization methods • Iterative-convergence schemes

6.3. Verification and validation

6.3.1. Hydraulic conductivity model

Verification of the model suffers from the difficulty of direct experimental verification of hydraulic conductivity at unsaturated conditions. Most datasets available in the research literature for hydraulic conductivity are only based on measurements at over-capillary saturation, i.e., measurements of K_{sat}. This is documented in Table 2 of Article V. Regarding model design, the model builds on other previous model approaches reported in the literature, and some changes are proposed. These changes are of course open for scrutiny. Nevertheless, throughout Article V, the model derivation includes arguments for the logic and reason behind these changes, as well as highlighting of similarities. Verification of the mere functional operation of the model is provided by the generation of hydraulic conductivity graphs for comparison to datasets in Article V and for application in Article VI.

Model validation is indirect and comparative in nature by comparing to datasets. These datasets are from studies that have conducted comparisons between experiments and hygrothermal simulations in order to validate incorporation of these datasets in simulation models. Consequently, the model is indirectly backed by experimental validation. Nevertheless, these experimental validations are very specific, particularly on absorption testing. Hence validating the hydraulic conductivity function as a whole over the whole moisture range is lacking. Validation implies checking that the model meets the needs of its end use, which requires extensive application in hygrothermal simulation cases that are compared with experiments. It is also a question of whether certain aspects have been oversimplified in the current model; however, this is also somewhat subjective dependent on preferences regarding what the model is used for. Future studies on what accuracy level is needed for different applications are therefore of interest. The model would then need to be validated against such accuracy needs.

6.3.2. COMSOL model

Ideally model validation should have involved more comparison to experimental results and observations than what has been possible in the present work. The large experiment (Article II) was difficult to apply for validation purposes due to the many parameters and aspects influencing wall segment performance, as can be seen by the large spread in results and the challenging repeatability. Experiments used for validation should thus be more specific, simpler in terms of less influential parameters being involved, and with proven repeatability. Heterogeneous behavior of brick and mortar, including their interface interaction, especially complicates model validation. The present thesis has a too holistic perspective to deeply approach any model validation of masonry performance. For these reasons no validation was attempted in Article VI on the interior insulated masonry simulation model.

Model validation has for the most part been limited to benchmark-comparison to other validated models, which is a common approach [101, 214, 215]; however, it limits the scope and reach of the validation. That is, the model is not particularly validated for scenarios including mechanisms not covered by the comparison benchmarks. Article IV also provides a comparative validation; however, it is not that extensive. Unfortunately, time-constraints have prevented the study from being revisited with a more thorough investigation using the latest version of the COMSOL model.

6.4. Objective achievement

Main objective: *Provide contribution to* ***modeling techniques in support of hygrothermal simulation****. Furthermore, provide* ***insight that highlights modeling uncertainty****, and which guides the ability to more confidently predict experimental results of bare brick masonry exposed to driving rain.*

The main objective is pursued by the enclosed work, mainly with Article V, addressing the first underlined part of the above objective, and Article VI, addressing the second underlined part. The other articles have more of a supporting role to the main objective, with Article II providing results that are used as a substrate for realistic evaluation of uncertainty and sensitivity in Article VI. The thesis provides additional context and nuance to the objective, by adding extra depth to details on property modeling, material measurements, and model verification and validation.

It furthermore summarizes and systematizes information on the sub-objectives, in support of the main objective. The sub-objectives are assessed in the following.

6.4.1. Smart vapor barrier

The literature overview in Section 2.2 reveals few to no studies have investigated the specific impact of SVBs applied to interior insulation retrofit of masonry. The studies that include SVB or SVR do not encompass relevant structures for comparison (structure with traditional vapor barrier), or they don't include a warm weather exposure, thereby never utilizing the SVB mechanism for drying. Neither do they go into assessment of SVB or SVR performance in detail. More studies, however, exist for structures such as compact roofs and wooden frame walls.

A couple of studies provide suggestions for how to generate and apply resistance curve(s) for the SVB. Olaoye et al. [165] proposes a harmonic mean method to determine a single curve. Values from this curve are then used to solve the resistance as function of RH at any infinitesimal segment of the SVB cross section, as there is a RH range spanning it. Fechner and Meißner [164] suggest a function dependent on two inputs, i.e., the RH level on each side of the SVB. This function is applied as a contact condition, i.e., a function governing the resistance between two material layers in the model.

In contrast to these suggestions, the current work (Article VI) has generated a 2D matrix from where resistances are interpolated at any combination of RH on the SVB's two sides. This matrix applies the measurements found for the RH boundary conditions used in testing of the SVB, provided by the product declaration. However, since the test measurements in the product declaration have low resolution, in addition to some conflicting results, there is need of comprehensive curve fitting to fully fill in the matrix. In the model the SVB is modeled as a material layer having scaled-up thickness, with a constant s_d-resistance found from the matrix by reading out from RH values from each side of the SVB. This approach is verified to function well; however, it requires more validation through comparison between modeling and laboratory testing of the SVB performance with varying RH levels.

An issue concerning modeling the SVB as a material layer (geometry scaled or non-scaled), in contrast to a contact resistance, is that it also requires other material properties [164], such as the specific heat capacity and moisture storage function. These properties are not reported having been tested for SVB. Modeling SVB as a contact condition only requires vapor resistance and thermal resistance.

Sub-objective: *Gather more* ***information on the performance of SVB*** *through experiment and simulation efforts.*

This thesis has gathered some data on SVB performance through Article II and VI. Although results on SVB performance are gathered, the results are tied to the laboratory experiment scenario that generated very specific wetting and drying conditions. The results are therefore difficult to extrapolate to interior insulation retrofit of masonry in real buildings under the hourly climate exposure of an MDRY. Thus, more realistic studies are needed to discern the performance benefit of applying SVB in retrofit scenarios.

An important indication from the results (Article II and VI) is the insignificant effect of SVB compared to traditional vapor barrier on beam end drying. This might imply it is unlikely that the moisture issue for beam ends becomes solved with SVB. Limiting the moisture exposure or improving or safeguarding the drying potential of the beam end, may therefore require several measures, where SVB can be one measure to improve the drying potential. Other measures that are proposed in the literature are, for instance, hydrophobization of the exterior masonry surface [178], keeping a wall area around the beam end free of insulation [21, 70], and adding an intentional metal heat bridge to increase the temperature at the beam end [29, 71]. An SVB can provide an important function in combination with such measures by avoiding interstitial condensation, possibly contributing to airtightness, and providing an inward drying potential. Hygrothermal simulation efforts into such measure combinations could provide interesting insight.

6.4.2. Brick-mortar interface

Sub-objective: *Determine contribution to* ***moisture uptake by the brick-mortar interface*** *in bare brick masonry.*

From reviewing scientific literature, it has become apparent there is a lack of studies focusing on the increased absorption along the brick-mortar interface. Most studies are focusing on the transverse interface resistance, not conditions along the interface. This is in line with literature review findings of [211]. In the present study the absorption, in terms of the capillary absorption coefficient, has been determined for brick-mortar pillars, thus enabling insight into the increased absorption through the brick-mortar interfaces, when comparing to the area averaged absorption of the brick and mortar constituents. Nevertheless, this is a macroscopic perspective in contrast to a microscopic one, not revealing much of the porous microstructure and flow conditions along the brick-mortar interface. Furthermore, the absorption is highly impacted by brick-mortar compatibility, workmanship, and curing conditions, which induce great uncertainty regarding actual absorption in a masonry wall. This uncertainty is further highlighted by the findings of Article II and VI. In Article II, great variation is seen in masonry behavior among wall segments constructed the same way, even though improved brick-mortar bonding had been attempted with prewetting of the bricks before brick laying. In Article VI, this was further investigated by assessing the impact of lumping interface properties and normal mortar properties, and additionally with inclusion of “leaky” joints, in order to increase absorption through mortar joints during rain events. With this, the complexity of modeling bare brick masonry is very much brought to awareness. A question thus arises on how to take this into account in modeling of masonry. In Section 2.3, it was seen that many studies have focused on inclusion of interface resistance; however, agreement on the topic is not yet reached. That topic is not investigated in this thesis; however, with the arrived-at moisture content in Article VI being too conservative (too slow drying), it is perceivable that not having included interface resistances partially could be a reason for this. Regarding increased absorption along the interface, Gutland et al. [169] propose an interesting fracture modeling simplification, which is an alternative to the lumping of properties done in Article VI. Nevertheless, the modeling approach of Gutland et al. does require higher mesh resolution and is thus more numerically demanding. Additionally, choice or determination of appropriate fracture widths remains an issue. In contrast, lumping of properties (as in Article VI) have other issues. In masonry one has the whole range of mortar joint performance, from joints performing with bulk mortar properties, to joints having severe moisture permeation along the interface. Additionally, the lumped properties approach should be applied anisotropically on the joint according to joint orientation, with lumped properties only along the joint while transverse properties are unchanged. This was not investigated in Article VI with the joints only modeled as isotropic. Furthermore, with the lumped properties spanning the whole joint, moisture distribution in the joints or throughout the mortar joint system becomes unrealistic. Whether these inaccuracies can be accepted has not been studied in the present research.

A severe rain event where the interfaces provide large impact on moisture absorption may also be an infrequent occurrence. Studies with realistic weather exposure are therefore needed to assess how the interfaces affects the masonry under varying real climate exposures.

6.4.3. Hygrothermal modeling

Sub-objective: *Establish a **hygrothermal simulation model** in a multi-physics software, providing the option of controlling all hygrothermal physics formulas, climate boundary formulas, and material property formulas.*

A hygrothermal simulation model was achieved built in a multi-physics software environment. The software provides excellent flexibility in controlling model physics and model algorithms. However, the numerical solver settings can be difficult to optimize, or be limited in providing solutions to encountered numerical instability. In 2D, the implementation of severe rain absorption was satisfactorily achieved. However, in 3D, implementing rain exposure on bare brick masonry was not achieved. It is suspected this was caused by the 3D interaction between material properties of brick and mortar, because rain was successfully implemented on a 3D layered geometry in Hamstad benchmark 4. In the benchmark the geometry had only consecutive layers, in contrast to parallel exposed material domains of bare brick masonry.

Hygrothermal simulation studies in 3D of the beam end detail are scarce, with only three recent studies found to explicitly have had such a focus. Ruisinger and Kautsch [176] modeled the masonry as homogeneous masonry around the beam end, and with external render. Their results, based on two-year climate exposure of Graz, Austria, gave close resemblance in results between 2D and 3D, for both temperature and humidity readings in the air layer exterior of the beam end, and for wood moisture content taken 10 mm into the beam end. Thus, they concluded that both 2D and 3D simulations are able to reproduce beam end measurements; although, the 3D simulation did provide slightly more accurate results. Zhou et al. [49] modeled the 3D masonry to be layered in terms of subsequent brick-mortar-brick-mortar-brick layers traversing the wall, with brick-mortar-brick-mortar layers exterior to the embedded beam end and air layer. The structure additionally had external render. The climate exposure was taken as the MDRY of Zurich, Switzerland. Their results showed relatively small differences in humidity and temperature between 2D and 3D simulations, and they thus concluded that 2D models could suitably substitute 3D models for predicting mold risk at beam ends. They did, however, point out that local active heating measures (and heat bridge measures presumably) would need 3D models, otherwise risk overpredicted heating effects in 2D. Zhao et al. [175] investigated the impact of anisotropic wood properties while additionally comparing 2D to 3D modeling of the beam end. The masonry was modeled as homogeneous bare brick (1.5-brick-thick) exposed to a test reference year of Hamburg, Germany. Their results for an interior insulation solution of mineral wool and vapor retarder (s_d = 4.3 m) showed significant increases in RH in 3D compared to 2D at the beam end.

The findings of Article VI differ from the first two forementioned sources (Ruisinger and Kautsch, and Zhou et al.) by showing significant deviation between 2D and 3D simulations, whereas the findings are in line with the latter (Zhao et al.) in this regard. From this it can be stated that more simulation studies in 3D are needed for bare brick masonry with the full complexity of the brick-mortar system. Especially studies with realistic climate exposure of bare brick masonry are of interest to determine necessity of 3D simulations for practical application. The simulation study of the present work only provides limited insight into heavily wetted one-brick-thick bare brick masonry. Furthermore, the beam end is rather exposed with only a half-a-brick-thick leaf protecting the beam end pocket. Still, the risk of infiltration and interpenetration of moisture along brick-mortar interfaces in thicker masonry structures, also constitute an interesting topic that lacks attention. Related to this is the impact of climate change and the possibly worsening magnitude or increased frequency of sudden heavy rain events that might make rain infiltration scenarios more likely.

Sub-objective: *Assess **determination of the liquid transport property** of masonry materials, as input for hygrothermal modeling, when direct measurements are not an available option.*

The liquid transport property of masonry materials is often of special significance in scenarios of interior insulation retrofit of masonry. For instance, Calle and Bossche [216] conducted a probabilistic sensitivity analysis on decay criteria by, among other parameters, varying brick properties (1D masonry representation). Among the material properties it was the capillary absorption coefficient that had the largest influence on the hygrothermal performance in terms of freeze-thaw cycles and beam end wood decay. Thus, for hygrothermal simulation, it is important to have adequate determination of the hydraulic conductivity, which is the basic property for liquid transport in connection to the true driving potential that is capillary pressure.

The complexity of accurate determination of the hydraulic conductivity by measurements has led to different approaches on simplified determination, such as (simplified) modeling, iterative calibration, parametric sweep to “goodness of fit”, or selecting similar materials through clustering techniques, see Section 1.2.3. Regarding simplified modeling, the simplest approach is determining the hydraulic conductivity through prediction of the liquid diffusivity as described in Section 2.1.3. However, as pointed out in Article V, this method has some inaccuracies. Scheffler [84] developed a method to model the hydraulic conductivity directly, a method that should be classified as more advanced and accurate than the approach of calculation from predicted diffusivity. Still, it is less complex than the more advanced network models, e.g. [115, 133]. Nevertheless, the Scheffler model is relatively demanding by requiring measurement of liquid conductivity at (over-capillary) saturation, and iterative calibration of two coefficients, respectively for absorption and drying, through comparison between experiments and simulations. What makes the approach of calculation from predicted diffusivity significantly simpler is the utilization of the capillary absorption coefficient instead of the liquid conductivity, due to the simpler experimental determination of the former. In Article V, a model, which is a simplification of the Scheffler model, was therefore derived to model the capillary conductivity at capillary saturation directly based on the capillary absorption coefficient. This simultaneously removed one of the iteratively identified coefficients of the Scheffler model, thus providing another simplification. Nevertheless, with simplification the accuracy is also reduced. Hence the new model is in an accuracy category lower than the Scheffler model. The new model should therefore be understood as an alternative to the approach of calculation from predicted diffusivity. They both require the capillary absorption coefficient and the retention curve as input. In Article V, these two methods are compared, and it was found that the new model was overall on par with the approach of calculation from predicted diffusivity. Nevertheless, for the upper moisture range, the new model performed somewhat better. Also of interest is that the new model can avoid some unphysical trends in the conductivity curve, which can be experienced by the approach of calculation from predicted diffusivity, i.e., falling conductivity with increasing moisture content, due to plateaus in the retention curve, see Article V.

Overall, the work (Article V) thus provides a contribution to simplified determination of the liquid transport property.

[This page is left blank]

7. Conclusion

7.1. Concluding main objective

The focus on modeling techniques has mainly been on hygrothermal simulation model input in the realm of material properties. Specifically, the hydraulic conductivity (liquid permeability) has in the present work been the focal point for simplified modeling techniques. This is in more detail concluded upon in Section 7.2.3. Furthermore, hygrothermal modeling with a smart vapor barrier has been given some attention, thereby providing some contrasts and an alternative to other suggestions in the research literature on how to describe smart vapor barriers in hygrothermal simulation models. Additionally, hygrothermal modeling in general is described (Article III, IV, VI, and Appendix A, with the addition of property expressions in Appendix B) for a moisture driving potential given as RH (or more precisely, a logarithmic expression of RH). Although a driving potential on RH-form is not anything new, the information presented does provide some nuances, alternative perspectives, and expression alternatives, that in total, as systematically summarized in this thesis, differ somewhat to what has been done before.

It has been demonstrated that modeling choices are a source of uncertainty to which results can have a significant sensitivity. The transport mechanism that is moisture infiltration along the brick-mortar interface has been especially highlighted in this regard. This adds to other uncertainties from climate exposure, bulk material properties, interface resistances, and boundary coefficients, that which typically have been given most attention in the research field thus far, when it comes to uncertainty analysis of interior insulation retrofit of masonry.

7.2. Concluding sub-objectives

7.2.1. Smart vapor barrier (SVB)

Compared to a traditional polyethylene vapor barrier:

- SVB significantly improves the drying rate at the masonry interior surface.
- SVB keeps lower RH at the interior masonry surface during warm exterior temperatures.
- Indication is seen that SVB can avoid summer condensation at the barrier.
- SVB provides minor to insignificant improvement in the drying rate of a beam end, when embedded in masonry that is severely wetted from rain events.

7.2.2. Brick-mortar interface

The brick-mortar interface accommodates, on a joint-area-averaged basis, a substantial increase in the A_w-value of the mortar joint. The (high IRA) brick and LC-mortar combination that is analyzed indicates a joint-area-averaged tenfold increase of A_w-value for the joint, compared to the bulk joint-mortar itself. Nevertheless, the scatter in the results is also substantial, thereby creating large uncertainty.

For bare one-brick-thick masonry, leak-like moisture permeations are observed during severe rain events, locally indicating even more prominent absorption along the brick-mortar interface than the increased joint-area-averaged A_w would indicate.

7.2.3. Hygrothermal modeling

A hygrothermal simulation model has been established, thus having enabled hygrothermal investigations of the interior insulation retrofitted masonry structure in the present research. The model has been validated against the Hamstad benchmarks in 3D and it appears to be a useful tool in analyzing bare brick masonry exposed to severe rain events. Although, the model worked well for rain absorption in 2D, it fell short in handling severe rain wetting of the brick-mortar composition in 3D. However, the Hamstad 4 benchmark, which consists of layered geometry, and which includes heavy rain exposure, was handled in 3D without issues. This thus indicates that layered geometry with layers parallel to the wall plane is easier to handle numerically in 3D, than exposed brick-mortar interfaces that transverse the wall. However, this issue requires more investigation than what the present work encompasses. In 3D, the model was therefore only utilized to analyze the aftermath of the rain events and the subsequent drying, with the beam end embedded in the masonry in focus. This revealed a significant deviation between the 2D and 3D simulation of the beam end conditions when embedded in heavily wetted masonry.

It has been demonstrated that simplifications can be made to the hydraulic conductivity determination in the bundle of tubes framework, now by allowing prediction of the conductivity at capillary saturation from the capillary absorption coefficient and the retention curve. However, with simplifications, reduced accuracy should be expected. Nevertheless, the model was found to be overall on par with a common simplified method of calculating the hydraulic conductivity from moisture diffusivity prediction. For the higher intermediate moisture content range, the new model performs somewhat better, and it does not get unphysical trends in the conductivity curve, which can occur with calculation from the diffusivity approach. In conclusion, the new model enables wider engineering applicability of the bundle of tubes modeling approach when accuracy requirements are not very strict, or when the consequent uncertainty can be dealt with. This can be useful for generation of liquid conductivity input data for hygrothermal models.

7.3. Contribution and significance

The work attempts to bring some new perspectives and understanding of the assumptions and simplifications behind material property modeling methods. Additionally, the findings may be used as guidance that may help navigate some of the difficulties and uncertainties that exist in hygrothermal modeling of bare brick masonry exposed to severe rain events. This may help practitioners and scientists to further scrutinize such modeling, and thus heightening modeling quality, or help in selection and further development of models that are appropriate for a certain intended application.

7.4. Further research needs

Regarding what has been investigated by the current work, several aspects warrant further research. A selection of aspects includes:

- Regarding hydraulic conductivity, an improvement of film-model inclusion requires more investigation on the combination with, and transition to, hygroscopic correction and capillary conductivity models. There is also plausible improvement from including contribution from corner flow, impact of surface roughness, and corrections for effects in sub-micro sized pores.
- Probabilistic handling of moisture infiltration along the brick-mortar interface is a topic of interest. It is plausible that this can, more adequately, represent such moisture transfer mechanisms in probabilistic uncertainty and sensitivity analysis. With a probabilistic approach to this, one might avoid failing to capture mechanisms that seriously affect the initiation limit state and subsequent serviceability limit state regarding moisture related damage.
- Hygrothermal simulation modeling in 3D could be of interest for representation of bare brick masonry, with focus on the brick-mortar system. Studies comparing such simulation to experiments could be useful in assessing whether one is capable of replicating the masonry performance regarding moisture distribution.
- Additional studies are of interest, spanning both in situ investigation and simulation efforts on SVB performance, for instance, focusing on quantification of the drying potential for different masonry structures over a variety of MDRY climate exposures.

[This page is left blank]

Appendix A Physics derivation and formulations for hygrothermal simulation model

This appendix will present the physical expressions applied in the hygrothermal model, including their derivation. It will follow the phenomenological approach, focusing on the physical mechanisms in a macroscopic perspective [217]. The description will nevertheless be kept brief since extensive similar, related, or equivalent descriptions have been provided elsewhere, e.g., [100, 124, 218].

A.1 Vapor transport

Vapor transport occurs in two forms, either as vapor diffusion or as vapor transported by air flow.

A.1.1 Vapor diffusion

Fick's diffusion, although originally related to mass concentration, can be written with the use of vapor pressure as the potential due to the proportionality between mass concentration and vapor pressure according to the ideal gas law [124]. The vapor diffusion flux [kg/(m^{2}s)] is given as Eq. (27).

$$g_{v,\mathrm{diff},j} = -\delta_v \frac{dP_v}{dx_j} \tag{27}$$

where δ_v [kg/(m^{2}sPa)] is the vapor permeability in Eq. (8), P_v [Pa] vapor pressure.

By using RH (ϕ) as a driving potential, Eq. (27) is transformed:

$$g_{v,\mathrm{diff},j} = -\delta_v \left(P_{sat} \frac{d\phi}{dx_j} + \phi \frac{dP_{sat}}{dx_j} \right) \tag{28}$$

where P_{sat} is the saturated vapor pressure, which is temperature dependent. Thus, with ϕ and T as driving potentials, Eq. (28) becomes:

$$g_{v,\mathrm{diff},j} = -\delta_v \left(P_{sat} \frac{d\phi}{dx_j} + \phi \frac{dP_{sat}}{dT} \frac{dT}{dx_j} \right) \tag{29}$$

A.1.2 Vapor transport by air flow

The following derivation is inspired by Hens [219] where mass ratio is related to dry air, but adapted to be in accordance with the description of humid air, as in Tsilingiris [220], where mass ratio is related to humid air. Whereas the approach of Hens is a simplification limited to lower temperatures, where the vapor pressure is small compared to the air pressure, the approach of Tsilingiris is not limited in such a way. Vapor flux can be related to flux of humid air by a mass ratio of vapor to humid air, Eq. (30).

$$g_{v,a,j} = g_{a(\text{humid air}),j} Y_{v,ha} \tag{30}$$

The mass ratio is derived as follows:

1. Following the ideal gas law, the density of a mixture can be identified. $PV = nRT \Leftrightarrow PV = \frac{\rho V}{MW}RT \Leftrightarrow P = \rho R_{MW}T$

   $\Rightarrow \rho = \frac{P}{R_{MW}T}$

   where n [mol] is number of moles, MW [g/mol] mol weight, R [J/(mol·K)] universal gas constant, R_{MW} [J/(kg·K)] the specific gas constant.

2. As partial constituents of a mixture, the vapor and dry air can be written as:

   $$\rho_v = \frac{P_v}{R_w T} \quad and \quad \rho_{a,dry} = \frac{P_{a,dry}}{R_{a,dry}T} = \frac{P_{atm} - P_v}{R_{a,dry}T}$$

   where the densities and pressures now are partial densities and pressures, respectively.

3. The mass ratio can then be presented as ratio of partial densities.

   $$\begin{aligned} Y_{v,ha} &= \frac{\rho_v}{\rho_{ha}} = \left(\frac{P_v}{R_w T}\right) \Big/ \left(\frac{P_{atm} - P_v}{R_{a,dry}T} + \frac{P_v}{R_w T}\right) = \frac{P_v}{R_w}\left(\frac{P_{atm} - P_v}{R_{a,dry}} + \frac{P_v}{R_w}\right)^{-1} \\ &= \frac{P_v}{R_w}\left(\frac{R_w\left(P_{atm} - P_v\right) + R_{a,dry}P_v}{R_{a,dry}R_w}\right)^{-1} = P_v\left(\frac{R_w\left(P_{atm} - P_v\right) + R_{a,dry}P_v}{R_{a,dry}}\right)^{-1} \\ &= P_v\left(\frac{R_w P_{atm} + P_v\left(R_{a,dry} - R_w\right)}{R_{a,dry}}\right)^{-1} = P_v\left(\frac{MW_a}{MW_w}P_{atm} + \left(1 - \frac{MW_a}{MW_w}\right)P_v\right)^{-1} \end{aligned}$$

   Thus the mass ratio can be expressed as Eq. (31).

$$Y_{v,ha} = \frac{P_v}{\frac{MW_a}{MW_w}P_{atm} + \left(1 - \frac{MW_a}{MW_w}\right)P_v} \tag{31}$$

A.1.3 Total vapor transport

Combining vapor diffusion and vapor transport by air flow gives:

$$g_{v,j} = g_{v,\text{diff},j} + g_{v,a,j} \tag{32}$$

A.2 Capillary transport

Transport of liquid water in porous materials can be expressed by Darcy’s law accordingly:

$$g_{w,j} = -K_l\left(\frac{dP_w}{dx_j} - f_i\right) = -\frac{k_l \rho_w}{\mu_w}\left(\frac{dP_w}{dx_j} - f_j\right) \tag{33}$$

where K_l [kg/(m·s·Pa)] or [s] is the liquid conductivity, P_w [Pa] liquid water pressure, k_l [m^2] liquid permeability, ρ_w [kg/m^3] density of water, μ_w [kg/m s] dynamic viscosity, f_j [N/m^3] body force in j-direction.

If the liquid pressure gradient is only caused by capillary suction, i.e. when the pressure difference over a liquid-air interface in the pores is the driving mechanism, expressed by $P_c = P_a\text{-}P_w$, then consequently P_w in Eq. (33) can be replaced with $P_a\text{-}P_c$. Here P_a is the air pressure and P_c the capillary pressure. Inserted in Eq. (33), it will respectably be the gradients in air and suction pressure that become of interest. Normally, the air pressure gradient is neglected compared to the suction pressure gradient. An exception under is conditions where moisture transport in fairly saturated porous materials can be caused by air pressure gradient (relatively low P_c values and low P_c gradient, compared to the air pressure gradient). Though, when the air pressure gradient is neglected, the result becomes:

$$g_{w,j} = \frac{k_l \rho_w}{\mu_w}\left(\frac{dP_c}{dx_j} + f_j\right) \tag{34}$$

Applying the Kelvin equation, Eq. (35) and the Young-Laplace equation, Eq. (36), enables the Darcy's equation to be expressed with RH and temperature as driving potentials in Eq. (37). A similar procedure has been described by Künzel [124], except for the inclusion of the body force.

$$\frac{P_v}{P_{sat}} = \phi = exp\left[\frac{-2\sigma\, cos(\alpha)}{\rho_w R_w T \cdot r}\right] \tag{35}$$

$$P_c = \frac{2\sigma\, cos(\alpha)}{r} \tag{36}$$

where σ [N/m] water surface tension, α [rad] water – pore wall attachment angle, r [m] pore radius. Note that the surface tension, and possibly the contact angle, as well as solute effects on the surface tension [221], are temperature dependent. Since the liquid conductivity is determined at a reference temperature for laboratory conditions, a simple correction for the temperature dependence will be added to the liquid conductivity at a later stage.

$$g_{w,j} = -\frac{k_l \rho_w}{\mu_w}\left(\rho_w R_w \frac{d\left(ln(\phi)T\right)}{dx_j} - f_j\right) \tag{37}$$

Eq. (37) when expanded becomes:

$$g_{w,j} = -\frac{k_l \rho_w}{\mu_w}\left[\rho_w R_w \left(\frac{T}{\phi}\frac{d\phi}{dx_j} + ln(\phi)\frac{dT}{dx_j}\right) - f_j\right] \tag{38}$$

A.2.1 Body forces

In normal building physics applications, the body force vector only contains contribution from gravity. It can then be substituted with $f_j = \rho_w \cdot [0, 0, -g]$. This gives:

$$g_{w,j} = -\frac{k_l \rho_w}{\mu_w} \left[\rho_w R_w \left(\frac{T}{\phi} \frac{d\phi}{dx_j} + ln(\phi) \frac{dT}{dx_j} \right) + \rho_w g \cdot \overrightarrow{e_z} \right] \tag{39}$$

where g [N/kg] is the gravity constant, e_z unit vector for z-dimension.

A.2.2 Diffusive transport coefficient

As explained by Künzel [124] it is possible to present the liquid transport on a mass diffusion form, as it shows the same characteristic progression in a porous material with respect to time as that of diffusion, even though capillary transport is a liquid flow.

$$g_{w,j} = -D_w \frac{dw_w}{dx_j} \tag{40}$$

where D_w [m^2/s] is a liquid diffusion coefficient with respect to water concentration. Eq. (40) can be transformed to RH as a driving potential:

$$g_{w,j} = -D_w \frac{dw}{d\phi} \frac{d\phi}{dx_j} = -D_\phi \frac{d\phi}{dx_j} \tag{41}$$

where D_ϕ [kg/(m·s)] is a liquid diffusion coefficient with respect to an RH driving potential. Comparing Eq. (41) to Eq. (38), a relation between D_ϕ, D_w, K_l and k_l becomes:

$$D_\phi = D_w \frac{dw}{d\phi} = \frac{k_l \rho_w^2 R_w}{\mu_w} \frac{T}{\phi} = K_l \rho_w R_w \frac{T}{\phi} \tag{42}$$

Thus, with relation Eq. (42) one can rewrite Eq. (39) to:

$$g_{w,j} = -D_\phi \left[\left(\frac{d\phi}{dx_j} + \frac{\phi}{T} ln(\phi) \frac{dT}{dx_j} \right) + \frac{1}{R_w} \frac{\phi}{T} g \cdot \overrightarrow{e_z} \right] \tag{43}$$

A.2.3 Correction for temperature dependence

The liquid diffusion coefficients and the liquid conductivity have a temperature dependence through a temperature dependency of the surface tension σ_w, viscosity μ_w, and density ρ_w of water [221, 222]. The temperature dependency through σ_w is minor compared to that of μ_w [124], whereas the temperature dependency for the density is insignificant in the typical temperature intervals of building physics but is more pronounced at higher temperatures.

Temperature correction can conveniently be applied to the liquid conductivity since it is a common form of presenting the liquid transport material property, although this does not account for material temperature dependence. The latter dependence can also be significant [223]. The alternative would be to measure or determine the liquid conductivity at different temperatures, which would be demanding [222]. Therefore, typically a scaling correction is used to determine liquid conductivity at different temperatures. This implies using property reference values at T_{ref}, corresponding to typical laboratory temperature conditions at which $K_{l,ref}$ (or $D_{w,ref}$) was determined. Evaluating Darcy's law, Eq. (33), the liquid conductivity is inversely proportional to the viscosity [224]. Also, it is proportional with the water density, but this relation is neglected in the following. The relation to surface tension is less apparent, and there is also a related effect of temperature dependency for contact angles. However, in a simplified approach, it can be recognized that the capillary absorption coefficient is often predicted with an expression proportional to the square root of surface tension [223]. Furthermore, the capillary conductivity at capillary saturation is proportional to the square of the capillary absorption coefficient (see Article V). Therefore, simplified the conductivity can be assumed to be proportional to the surface tension. Consequently Eq. (44) can be used as a temperature correction:

$$K_l(T) = \frac{\sigma_w(T)}{\sigma_{w,ref}} \frac{\mu_{w,ref}}{\mu_w(T)} K_{l,ref} \tag{44}$$

The liquid diffusivity to be used in Eq. (43) is then given as:

$$D_\phi(T) = K_l(T) \rho_w R_w \frac{T}{\phi} \tag{45}$$

A.3 Air transport

Flow of air is either on diffusion or convection form. While air diffusion becomes a rather simple product of a permeability coefficient and acting pressure gradient, the air convection requires a known velocity field or a velocity field to be solved.

A.3.1 Air diffusion

When dealing with materials that do not allow for convective air transport (non-high porosity), it is convenient to look at diffusive air transport. Just like the vapor diffusion, air diffusion is governed by a potential of pressure differences; however, now it is the air pressure difference and not the vapor pressure difference that is working. Applying Fick's law, now for air instead of vapor, gives Eq. (46).

$$g_{a,j,\text{diff air flux}} = -\delta_a \frac{dP_a}{dx_j} \tag{46}$$

where δ_a [kg/(m·s·Pa)] is an air permeability coefficient, which should be understood to be that of humid air, i.e., both temperature and humidity dependent. An air diffusion coefficient D_a [m^2/s] can be transformed to an air permeability coefficient δ_a by $\delta_a = D_a/(R_{a,\text{humid}}T)$, which can be simplified to $\delta_a = D_a/(R_aT)$ at low temperatures where the vapor pressure is much less than the air pressure.

The air pressure gradient can either be manually defined or solved for. Manually defining the air pressure gradient is the simplest approach. It can be assigned to isotropic materials in one-dimensional problems, i.e., where a pressure gradient only exists in one direction. Looking at the specific pressure drops over different material layers due to the contribution of the resistance of each layer, is a possible simplification for multilayered problems. In other words, as there is a total pressure drop over the whole structural element, a part of this pressure drop is taken by each material layer according to the diffusive resistance of the layer. The gradient of the pressure then becomes the pressure difference over a layer divided by the thickness of the layer.

$$g_{a,\text{diff air flux}} = -\delta_{a,layer} \frac{\Delta P_{layer}}{\Delta x_{layer}} = -\delta_{a,layer} \frac{dP_{layer}}{dx_{layer}} \tag{47}$$

Solving for the air pressure gradient will only be described in the most simplified form. Sometimes, as a simplification, air diffusion is decoupled from its dependence to pore structure and moisture filling of the pore structure. In such a case, solving for the pressure gradient can be done by plugging Fick's law into the continuity equation.

$$\frac{d\rho_a}{dt} = \frac{d}{dx_j}\left(\delta_a \frac{dP_a}{dx_j}\right) \tag{48}$$

Assuming that the vapor pressure is much less than the air pressure, applying the ideal gas law to Eq. (48) and expanding it to P_a and T as driving potentials gives:

$$\frac{d\left(\frac{P_a}{R_a T}\right)}{dt} = \frac{1}{R_a}\left(\frac{1}{T}\frac{dP_a}{dt} - \frac{P_a}{T^2}\frac{dT}{dt}\right) \tag{49}$$

Applying Eq. (49) in Eq. (48), and moving the time-derivative of T from the left to the right of the equality sign, a partial differential equation having the air pressure as driving potential is fully revealed:

$$\frac{1}{R_a T}\frac{dP_a}{dt} = \frac{d}{dx_j}\left(\delta_a \frac{dP_a}{dx_j}\right) + \frac{1}{R_a T^2}\frac{dT}{dt} P_a \tag{50}$$

Eq. (50) can be readily applied in COMSOL as a PDE for solving the air pressure across a structure. It allows for air pressure changes due to changes in air permeability and temperature, including changes in boundary conditions of air pressure and temperature. However, it is not coupled with moisture dependence, i.e., solving of the moisture content and its effect on air permeability are not accounted for.

This approach can be used in the Hamstad 3 benchmark, since the temperature changes in that benchmark are not so pronounced that it, with (Eq. (50)), impacts much on the simple design pressure-gradient of the benchmark.

A.3.2 Air convection

For highly porous materials or air cavities it is most accurate to model convective air transport. This however requires solving for a velocity field, i.e., from the Navier-Stokes equations. The equations can typically be somewhat simplified due to the low viscosity of air and with an assumption of laminar flow. This is generally acceptable in building physics unless severe conditions are investigated. That being said, air convection, approached by solving the Navier-Stokes, will not be further described in this thesis. Alternatively, in some cases it might be that a laminar diffusive air velocity is specified to readily be inserted into a hygrothermal model. In either case Eq. (51) can implement air flow from known air velocities.

$$g_{\mathrm{a,j,conv\ air\ flux}} = \psi_a \rho_a u_{a,j} \tag{51}$$

where ψ_a [-] is the porosity (pore volume ratio) available for air.

A.4 Moisture balance

To describe the mass balance for moisture transport, one can utilize the continuity equation, assuming incompressible flow. The continuity equation addresses the conservation of mass in a control volume, and it is expressed as:

$$\frac{dw_w}{dt} + \frac{dg_{(w+v),j}}{dx_j} = 0 \tag{52}$$

where w_w [kg/m^3] is the moisture content, and g_{w+v} [kg/(m^{2}s)] overall flux of liquid moisture and vapor.

Behind Eq. (52) there is actually a set of two mass balances, one each for vapor and liquid [100]:

$$\begin{aligned} \frac{dw_v}{dt} &= -\frac{dg_{v,j}}{dx_j} + G_v \\ \frac{dw_w}{dt} &= -\frac{dg_{w,j}}{dx_j} + G_w \end{aligned} \tag{53}$$

where w_v [kg/m^3] is the vapor content, G_v [kg/(m^{3}s)] evaporated moisture, G_w [kg/(m^{3}s)] condensed moisture. However, since $G_v = -G_w$, i.e., the source of evaporation is liquid and the source of condensation is vapor, the sum of the two equations (Eq. (53)) becomes Eq. (52) when dw_v/dt is assumed negligible compared to dw_w/dt. This assumption usually holds acceptable accuracy except for highly porous materials, at combined high temperatures and high RH saturation.

Expanding and rearranging Eq. (52) gives:

$$\frac{dw_w}{dt} = -\frac{d}{dx_j}\left(g_{w,j} + g_{v,j}\right) \tag{54}$$

A.4.1 Time differential (left side of Eq. (54))

Left hand side needs to be expanded to become time differentials of the applied driving potential(s). This also depends on the retention function that is to be applied. With Eq. (5) being applied, one can separate it into two parts $w_w = w_{w,\phi}(\phi) + w_{w,pc}(p_c)$.

$$\frac{dw_w}{dt} = \frac{d}{dt}\left(w_{w,\phi} + w_{w,p_c}\right) = \frac{dw_{w,\phi}}{d\phi}\frac{d\phi}{dt} + \frac{dw_{w,p_c}}{dp_c}\frac{dp_c}{dt} \tag{55}$$

With $p_c = \rho_w R_w T \ln(\phi)$, Eq. (55) needs to be expanded to partial differentials with respect to RH and T:

$$\frac{dw_w}{dt} = \left(\frac{dw_{w,\phi}}{d\phi} + \frac{dw_{w,p_c}}{dp_c} \frac{dp_c}{d\phi} \right) \frac{d\phi}{dt} + \frac{dw_{w,p_c}}{dp_c} \frac{dp_c}{dT} \frac{dT}{dt} \tag{56}$$

where $dp_c/d\phi = \rho_w R_w T/\phi$ and $dp_c/dT = \rho_w R_w \ln(\phi)$. In Eq. (56) the differentials as result of Eq. (5) are given as Eq. (57) and (58):

$$\frac{dw_{w,\phi}}{d\phi} = w_{lim} n_{w,0} \phi^{\left(n_{w,0}-1\right)} \tag{57}$$

$$\frac{dw_{w,p_c}}{dp_c} = \left(w_{cap} - w_{lim}\right) \sum_{i=1}^{N=4} \left(l_{w,i} \left(\frac{1-n_{w,i}}{n_{w,i}} \right) \left[1 + \left(c_{w,i} P_c\right)^{n_{w,i}} \right]^{\left(\frac{1-n_{w,i}}{n_{w,i}} -1 \right)} n_{w,i} \left[c_{w,i} P_c \right]^{\left(n_{w,i}-1\right)} c_{w,i} \right) \tag{58}$$

A.4.2 Flux differentials (right side of Eq. (54))

The fluxes are given by Eq. (32) for vapor transport, with Eq. (29) for vapor diffusion, and Eq. (30) and (46) for vapor transport by air flow (diffusion chosen due to Hamstad 3 benchmark), and furthermore with Eq. (43) for liquid transport.

$$\begin{aligned} -\frac{d}{dx_j}\left(g_{w,j} + g_{v,j}\right) = \; & \frac{d}{dx_j} \Bigg(D_\phi \left[\left(\frac{d\phi}{dx_j} + \frac{\phi}{T} ln(\phi) \frac{dT}{dx_j} \right) + \frac{1}{R_w} \frac{\phi}{T} g \cdot \vec{e_z} \right] \\ & + \delta_v \left[P_{sat} \frac{d\phi}{dx_j} + \phi \frac{dP_{sat}}{dT} \frac{dT}{dx_j} \right] + \delta_a \frac{dP_a}{dx_j} Y_{v,ha} \Bigg) \end{aligned} \tag{59}$$

Sorted on driving potential Eq. (59) becomes:

$$\begin{aligned} -\frac{d}{dx_j}\left(g_{w,j} + g_{v,j}\right) = \; & \frac{d}{dx_j} \Bigg(\left[\delta_v P_{sat} + D_\phi \right] \frac{d\phi}{dx_j} + \left[\delta_v \phi \frac{dP_{sat}}{dT} + D_\phi \frac{\phi}{T} ln(\phi) \right] \frac{dT}{dx_j} \\ & + D_\phi \frac{1}{R_w} \frac{\phi}{T} g \cdot \vec{e_z} + \delta_a \frac{dP_a}{dx_j} Y_{v,ha} \Bigg) \end{aligned} \tag{60}$$

A.4.3 COMSOL PDE form

The COMSOL PDE is written on the form:

$$e_a \frac{d^2\Omega}{dt^2} + d_a \frac{d\Omega}{dt} + \nabla \cdot \left(-c\nabla\Omega - \alpha\Omega + \gamma \right) + \beta\nabla\Omega + a\Omega = f \tag{61}$$

where Ω is the dependent variable, e_a (mass coefficient), d_a (damping or mass coefficient), c (diffusion coefficient), α (conservative flux convection coefficient), γ (conservative flux source), β (convection coefficient), a (absorption coefficient), f (source term) are expressions, (where descriptive names in parenthesis follow from COMSOL).

Note that the dependent variable applied in COMSOL is ϕ_{mod} (see Section A.6), thus $d\Omega = d\phi_{mod}$ and $d\phi = (d\phi/d\phi_{mod})\cdot d\phi_{mod}$. This results in α and a of Eq. (61) are not applicable, and expressions with ϕ are placed in γ (or applicable in f).

Sorting Eq. (56) and Eq. (60) into the form of (61) produces:

$$\begin{aligned}
d_a &= \frac{dw_{w,\phi}}{d\phi} - \rho_w R_w \frac{dw_{w,p_c}}{dp_c}\frac{T}{\phi} \\
c &= \delta_v P_{sat} + D_\phi \\
\gamma &= -\left[\delta_v \phi \frac{dP_{sat}}{dT} + D_\phi \frac{\phi}{T} ln(\phi)\right]\frac{dT}{dx_j} - D_\phi \frac{1}{R_w}\frac{\phi}{T} g\cdot\vec{e_z} - \delta_a \frac{dP_a}{dx_j} Y_{v,ha} \\
f &= \frac{dw_{w,p_c}}{dp_c}\rho_w R_w \, ln\,\phi \frac{dT}{dt}
\end{aligned} \tag{62}$$

If changes in the vapor moisture content were to be included, d_a and f need to be supplemented with additional terms. The derivation is deemed too excessive and too remote of the thesis scope to be included here; however, derivation including similar consideration (dw_v/dt in Eq. (68), leading to Eq. (75)), is present in the derivation of the enthalpy equation, which is more elaborate, see Section A.5.3 and consider comments in Section A.5.4.

Suffice to say, only the resultant expressions are therefore provided for reference. That is, the d_a and f expressions in Eq. (62) can be expanded to:

$$\begin{aligned}
d_a &= \frac{dw_{w,\phi}}{d\phi} - \rho_w R_w \frac{dw_w}{dp_c}\frac{T}{\phi} \\
&\quad + P_{sat}\left(\frac{w_{sat} - w_w}{\rho_w R_w T} - \frac{\phi}{\rho_w R_w T}\frac{dw_{w,\phi}}{d\phi} + \frac{dw_{w,p_c}}{dp_c}\right) \\
f &= \frac{dw_{w,p_c}}{dp_c}\rho_w R_w \, ln\,\phi \frac{dT}{dt} - \left(\frac{w_{sat} - w_w}{\rho_w R_w}\left[\frac{1}{T}\frac{dP_{sat}}{dT} - \frac{P_{sat}}{T^2}\right] + P_{sat}\frac{dw_{w,p_c}}{dp_c}\frac{ln\,\phi}{T}\right)\phi\frac{dT}{dt}
\end{aligned} \tag{63}$$

Analyzing the above, within a temperature range up to 100 °C and for normal atmospheric pressures, we can see the following:

$$\begin{aligned}
P_{sat}\frac{dw_{w,p_c}}{dp_c} &\ll \rho_w R_w \frac{dw_{w,p_c}}{dp_c}\frac{T}{\phi} \\
\frac{P_{sat}\phi}{\rho_w R_w T}\frac{dw_{w,\phi}}{d\phi} &\ll \frac{dw_{w,\phi}}{d\phi} \\
P_{sat}\frac{dw_{w,p_c}}{dp_c}\frac{ln\,\phi}{T}\phi\frac{dT}{dt} &\ll \frac{dw_{w,p_c}}{dp_c}\rho_w R_w \, ln\,\phi \frac{dT}{dt}
\end{aligned}$$

The closest that any of the left terms come constitutes 0.000582 of the right terms at 100 °C and 100 % RH. Thus negligible. Hence, we finally have:

$$
\begin{aligned}
d_a &= \frac{dw_{w,\phi}}{d\phi} - \rho_w R_w \frac{dw_w}{dp_c}\frac{T}{\phi} + P_{sat}\frac{w_{sat}-w_w}{\rho_w R_w T} \\
f &= \frac{dw_{w,p_c}}{dp_c}\rho_w R_w \ln\phi \frac{dT}{dt} - \frac{w_{sat}-w_w}{\rho_w R_w}\left[\frac{1}{T}\frac{dP_{sat}}{dT} - \frac{P_{sat}}{T^2}\right]\phi\frac{dT}{dt}
\end{aligned}
\tag{64}
$$

A.5 Heat balance and enthalpy equation

Similar to Eq. (53), the species mass balance equations [100, 218, 225] (omitting convective air flow in contrast to [218]), when addressing net gain or net loss, are given as:

$$
\begin{aligned}
I_B \quad & \frac{dw_w}{dt} = -\frac{d}{dx_j}\left(g_w\right) + G_w \\
II_B \quad & \frac{dw_v}{dt} = -\frac{d}{dx_j}\left(g_v\right) + G_v \\
III_B \quad & \frac{dw_a}{dt} = -\frac{d}{dx_j}\left(g_a\right)
\end{aligned}
\tag{65}
$$

where w_a [kg/m^3] is air content.

A.5.1 Derivation of the applied enthalpy equation

The general enthalpy equation, without convection, can be described and derived accordingly with respect to specific enthalpy (h [J/kg]), following Tariku [218]:

$$
\frac{d}{dt}\left(\rho h\right) = -\frac{dq_\lambda}{dx_j} - \frac{d}{dx_j}\left(gh\right) + \dot{Q}
$$

$$
\frac{d}{dt}\left(\rho_s h_s + w_w h_w + w_v h_v + w_a h_a\right) = -\frac{dq_\lambda}{dx_j} - \frac{d}{dx_j}\left(g_w h_w + g_v h_v + g_a h_a\right) + \dot{Q}
$$

$$
\begin{aligned}
&\rho_s\frac{dh_s}{dt} + \left(w_w\frac{dh_w}{dt} + h_w\frac{dw_w}{dt} + w_v\frac{dh_v}{dt} + h_v\frac{dw_v}{dt} + w_a\frac{dh_a}{dt} + h_a\frac{dw_a}{dt}\right) \\
&= -\frac{d}{dx_j}\left(-\lambda_{eff}\frac{dT}{dx_j}\right) - \left(g_w\frac{dh_w}{dx_j} + h_w\frac{dg_w}{dx_j} + g_v\frac{dh_v}{dx_j} + h_v\frac{dg_v}{dx_j} + g_a\frac{dh_a}{dx_j} + h_a\frac{dg_a}{dx_j}\right) + \dot{Q}
\end{aligned}
$$

$$
\begin{aligned}
&\rho_s\frac{dh_s}{dt} + w_w\frac{dh_w}{dt} + w_v\frac{dh_v}{dt} + w_a\frac{dh_a}{dt} \\
&+h_w\frac{dw_w}{dt} + h_v\frac{dw_v}{dt} + h_a\frac{dw_a}{dt} \\
&= \frac{d}{dx_j}\left(\lambda_{eff}\frac{dT}{dx_j}\right) - g_w\frac{dh_w}{dx_j} - g_v\frac{dh_v}{dx_j} - g_a\frac{dh_a}{dx_j} \\
&-h_w\frac{dg_w}{dx_j} - h_v\frac{dg_v}{dx_j} - h_a\frac{dg_a}{dx_j} + \dot{Q}
\end{aligned}
\tag{66}
$$

where subscript s refers to solid, λ [W/(m·K)] thermal conductivity, $\dot{Q}$ [J/(m^{3}s)] heat source term.

Sorting the terms from Eq. (66) by species and identifying expression I$_B$, II$_B$ and III$_B$ from Eq. (65) provides:

$$\begin{aligned}
&\rho_s \frac{dh_s}{dt} + w_w \frac{dh_w}{dt} + w_v \frac{dh_v}{dt} + w_a \frac{dh_a}{dt} \\
&+h_w \underbrace{\left(\frac{dw_w}{dt} + \frac{dg_w}{dx_j} \right)}_{=G_W} + h_v \underbrace{\left(\frac{dw_v}{dt} + \frac{dg_v}{dx_j} \right)}_{=G_V} + h_a \underbrace{\left(\frac{dw_a}{dt} + \frac{dg_a}{dx_j} \right)}_{=0} \\
&= \frac{d}{dx_j}\left(\lambda_{eff} \frac{dT}{dx_j} \right) - g_w \frac{dh_w}{dx_j} - g_v \frac{dh_v}{dx_j} - g_a \frac{dh_a}{dx_j} + \dot{Q}
\end{aligned} \tag{67}$$

With G$_W$ = -G$_V$, then Eq. (67) can be shortened and grouped (I to IV) to become:

$$\begin{aligned}
&\overbrace{\rho_s \frac{dh_s}{dt} + w_w \frac{dh_w}{dt} + w_v \frac{dh_v}{dt} + w_a \frac{dh_a}{dt}}^{I} \\
&= \overbrace{\frac{d}{dx_j}\left(\lambda_{eff} \frac{dT}{dx_j} \right)}^{II} + \overbrace{\left(-g_w \frac{dh_w}{dx_j} - g_v \frac{dh_v}{dx_j} - g_a \frac{dh_a}{dx_j} \right)}^{III} \\
&\overbrace{+\left(h_w - h_v \right) \left(\frac{dw_v}{dt} + \frac{dg_v}{dx_j} \right)}^{IV} + \dot{Q}
\end{aligned} \tag{68}$$

A.5.2 Enthalpy

By international convention the zero points for the internal energy is arbitrarily set at the triple point (T$_0$ = 273.16 K) [226]. We define a relative position with a temperature at 0.01 °C (triple point convention) to write the enthalpy expressions, e.g. [37] [218].

$$\begin{aligned}
&i && h_s = h_{s0} + c_{ps}\left(T - T_0 \right) \\
&ii && h_w = h_{w0} + c_{pw}\left(T - T_0 \right) \\
&iii && h_v = \underbrace{h_{w0} + h_{vap}\left(T_0 \right)}_{=h_{V0}} + c_{pv}\left(T - T_0 \right) \\
&iv && h_a = h_{a0} + c_{pa}\left(T - T_0 \right)
\end{aligned} \tag{69}$$

The derivatives of Eq. (69) consequently become:

$$\begin{aligned}
&i' && dh_s = c_{ps} dT \\
&ii' && dh_w = c_{pw} dT \\
&iii' && dh_v = c_{pv} dT \\
&iv' && dh_a = c_{pa} dT
\end{aligned} \tag{70}$$

And the $h_w - h_v$ term in IV in Eq. (68) has the relation

$$h_w - h_v = -h_{vap}\left(T_0\right) + \left(c_{pw} - c_{pv}\right)\left(T - T_0\right) = -h_{vap}\left(T\right) \tag{71}$$

A.5.3 Analyzing each of the enthalpy eq. parts I-IV of Eq.(68)

In part I we contract the terms for vapor and dry air into a single term for humid air in the non-moisture filled porosity, and furthermore apply relations in Eq. (70):

$$\begin{aligned}
I \quad & \rho_s \frac{dh_s}{dt} + w_w \frac{dh_w}{dt} + w_v \frac{dh_v}{dt} + w_a \frac{dh_a}{dt} \\
& = \rho_s \frac{dh_s}{dt} + w_w \frac{dh_w}{dt} + w_{ha} \frac{dh_{ha}}{dt} \\
& = \rho_s c_{ps} \frac{dT}{dt} + w_w c_{pw} \frac{dT}{dt} + \frac{w_{sat} - w_w}{\rho_w} \rho_{ha} c_{pha} \frac{dT}{dt} \\
& = \rho_s \left(c_{ps} + \frac{w_w}{\rho_s} c_{pw} \right) \frac{dT}{dt} + \frac{w_{sat} - w_w}{\rho_w} \rho_{ha} c_{pha} \frac{dT}{dt}
\end{aligned} \tag{72}$$

The humid air properties ρ_{ha} and c_{pha} follow the method of Tsilingiris [220]; however, the correction factors therein can be neglected since those are fairly insignificant.

Term II can be applied directly; however, for clarification, an example of expanding the efficient conductivity is provided. Usually only a linear trend with moisture content is applied; nevertheless, for instance, for insulation materials, a second order function might be a more suitable approximation. See Section 2.1.4 for alternatives.

$$\begin{aligned}
II \quad & \frac{d}{dx_j}\left(\lambda_{eff} \frac{dT}{dx_j} \right) \\
& = \frac{d}{dx_j}\left(\underbrace{\left[\lambda_s + \lambda_{b1} \frac{w_w}{\rho_w} + \lambda_{b2} \left(\frac{w_w}{\rho_w} \right)^2 \right]}_{\lambda_{eff}} \frac{dT}{dx_j} \right)
\end{aligned} \tag{73}$$

Addressing the air transport in III as humid air instead of dry air:

$$
\begin{aligned}
III \quad & -g_w \frac{dh_w}{dx_j} - g_v \frac{dh_v}{dx_j} - g_a \frac{dh_a}{dx_j} \\
& = -g_w \frac{dh_w}{dx_j} - g_v \frac{dh_v}{dx_j} - g_{ha} \frac{dh_{ha}}{dx_j} \\
& = D_\phi \left(\frac{d\phi}{dx_j} + \underbrace{\frac{\phi}{T} ln(\phi) \frac{dT}{dx_j}}_{\text{usually negligible}} + \frac{1}{R_w} \frac{\phi}{T} g \cdot \overrightarrow{e_z} \right) c_{pw} \frac{dT}{dx_j} \\
& \underbrace{+ \delta_v \left(P_{sat} \frac{d\phi}{dx_j} + \phi \frac{dP_{sat}}{dT} \frac{dT}{dx_j} \right)}_{negligible} c_{pv} \frac{dT}{dx_j} \\
& + \delta_{ha} \frac{dP_a}{dx_j} c_{pha} \frac{dT}{dx_j} \\
& \\
& = D_\phi \left(\frac{d\phi}{dx_j} + \frac{1}{R_w} \frac{\phi}{T} g \cdot \overrightarrow{e_z} \right) c_{pw} \frac{dT}{dx_j} \\
& + \delta_{ha} \frac{dP_a}{dx_j} c_{pha} \frac{dT}{dx_j}
\end{aligned}
\tag{74}
$$

In IV we insert Eq. (71), the temperature dependent heat of vaporization. We furthermore expand the terms. Here we let the vapor content in the pore volume, that is not occupied by liquid moisture, change with liquid moisture content. Hence, we assume the humid air is freely vented as liquid takes up or leaves the space.

$$
\begin{aligned}
IV \quad & \left(h_w - h_v \right) \left(\frac{dw_v}{dt} + \frac{dg_v}{dx_j} \right) \\
& = -h_{vap} \left[\frac{d}{dt} \left(\frac{w_{sat} - w_w}{\rho_w} \frac{\phi P_{sat}}{R_w T} \right) \right. \\
& \left. + h_{vap} \frac{d}{dx_j} \left(-\delta_v \left[P_{sat} \frac{d\phi}{dx_j} + \phi \frac{dP_{sat}}{dT} \frac{dT}{dx_j} \right] - \delta_{ha} Y_v \frac{dP_a}{dx_j} \right) \right]
\end{aligned}
$$

IV continued:

$$
\begin{aligned}
IV \quad & = -h_{vap}\left(\frac{w_{sat}-w_w}{R_w\rho_w}\frac{d}{dt}\left(\frac{\phi P_{sat}}{R_w T}\right)-\frac{\phi P_{sat}}{\rho_w R_w T}\left[\frac{dw_{w,\phi}}{dt}+\frac{dw_{w,p_C}}{dt}\right]\right) \\
& -h_{vap}\frac{d}{dx_j}\left(-\delta_v\left[P_{sat}\frac{d\phi}{dx_j}+\phi\frac{dP_{sat}}{dT}\frac{dT}{dx_j}\right]-\delta_{ha}Y_v\frac{dP_a}{dx_j}\right) \\
& = h_{vap}\left(-\frac{w_{sat}-w_w}{\rho_w R_w}\left[\frac{P_{sat}}{T}\frac{d\phi}{dt}+\phi\left(\frac{1}{T}\frac{dP_{sat}}{dT}\frac{dT}{dt}-\frac{P_{sat}}{T^2}\frac{dT}{dt}\right)\right]\right. \\
& \left. +\frac{\phi P_{sat}}{\rho_w R_w T}\left[\frac{dw_{w,\phi}}{d\phi}\frac{d\phi}{dt}+\frac{dw_{w,p_C}}{dp_c}\frac{d}{dt}\underbrace{\left(-\rho_w R_w T\, ln\,\phi\right)}_{p_C}\right]\right) \\
& +\frac{d}{dx_j}\left(h_{vap}\delta_v\phi\frac{dP_{sat}}{dT}\frac{dT}{dx_j}+h_{vap}\left[\delta_v P_{sat}\frac{d\phi}{dx_j}+\delta_{ha}Y_v\frac{dP_a}{dx_j}\right]\right) \\
& = h_{vap}\left(-\frac{w_{sat}-w_w}{\rho_w R_w}\left[\frac{P_{sat}}{T}\frac{d\phi}{dt}+\phi\left(\frac{1}{T}\frac{dP_{sat}}{dT}\frac{dT}{dt}-\frac{P_{sat}}{T^2}\frac{dT}{dt}\right)\right]\right. \\
& \left. +\frac{\phi P_{sat}}{\rho_w R_w T}\frac{dw_{w,\phi}}{d\phi}\frac{d\phi}{dt}-\frac{\phi P_{sat}}{\cancel{\rho_w R_w} T}\frac{dw_{w,p_c}}{dp_c}\cancel{\rho_w R_w}\left[\frac{T}{\phi}\frac{d\phi}{dt}+ln\,\phi\frac{dT}{dt}\right]\right) \\
& +\frac{d}{dx_j}\left(h_{vap}\delta_v\phi\frac{dP_{sat}}{dT}\frac{dT}{dx_j}+h_{vap}\left[\delta_v P_{sat}\frac{d\phi}{dx_j}+\delta_{ha}Y_v\frac{dP_a}{dx_j}\right]\right)
\end{aligned}
$$

Sorted:

$$
\begin{aligned}
IV \quad & \left(h_w-h_v\right)\left(\frac{dw_v}{dt}+\frac{dg_v}{dx_j}\right) \\
& = -h_{vap}\left(\frac{w_{sat}-w_w}{\rho_w R_w}\phi\left[\frac{1}{T}\frac{dP_{sat}}{dT}-\frac{P_{sat}}{T^2}\right]+P_{sat}\frac{dw_{w,p_C}}{dp_c}\frac{\phi\, ln\,\phi}{T}\right)\frac{dT}{dt} \\
& -h_{vap}P_{sat}\left(\frac{w_{sat}-w_w}{\rho_w R_w T}-\frac{\phi}{\rho_w R_w T}\frac{dw_{w,\phi}}{d\phi}+\frac{dw_{w,p_C}}{dp_c}\right)\frac{d\phi}{dt} \\
& +\frac{d}{dx_j}\left(h_{vap}\delta_v\phi\frac{dP_{sat}}{dT}\frac{dT}{dx_j}+h_{vap}\left[\delta_v P_{sat}\frac{d\phi}{dx_j}+\delta_{ha}Y_v\frac{dP_a}{dx_j}\right]\right)
\end{aligned}
\qquad (75)
$$

A.5.4 COMSOL PDE form

Repeating Eq. (61), the COMSOL PDE is written on the form:

$$
e_a\frac{d^2\Omega}{dt^2}+d_a\frac{d\Omega}{dt}+\nabla\cdot\left(-c\nabla\Omega-\alpha\Omega+\gamma\right)+\beta\nabla\Omega+a\Omega=f
$$

where Ω is the dependent variable, e_a (mass coefficient), d_a (damping or mass coefficient), c (diffusion coefficient), α (conservative flux convection coefficient), γ (conservative flux source), β (convection coefficient), a (absorption coefficient), f (source term) are expressions, (where descriptive names in parenthesis follow from COMSOL).

Sorting Eq. (72) - (75) in the form of Eq. (61) gives:

$$\begin{aligned}
d_a &= \rho_s\left(c_{ps}+\frac{w_w}{\rho_s}c_{pw}\right)+\frac{w_{sat}-w_w}{\rho_w}\rho_{ha}c_{pha}\\
&\quad +h_{vap}\left(\frac{w_{sat}-w_w}{\rho_w R_w}\phi\left[\frac{1}{T}\frac{dP_{sat}}{dT}-\frac{P_{sat}}{T^2}\right]+P_{sat}\frac{dw_{w,p_c}}{dp_c}\frac{\phi\, ln\,\phi}{T}\right)\\
c &= \lambda_{eff}+h_{vap}\delta_v\phi\frac{dP_{sat}}{dT}\\
\gamma &= -h_{vap}\left[\delta_v P_{sat}\frac{d\phi}{dx_j}+\delta_{ha}Y_v\frac{dP_a}{dx_j}\right]\\
\beta &= -D_\phi\left(\frac{d\phi}{dx_j}+\frac{1}{R_w}\frac{\phi}{T}g\cdot\vec{e_z}\right)c_{pw}-\delta_{ha}\frac{dP_a}{dx_j}c_{pha}\\
f &= -h_{vap}P_{sat}\left(\frac{w_{sat}-w_w}{\rho_w R_w T}-\frac{\phi}{\rho_w R_w T}\frac{dw_{w,\phi}}{d\phi}+\frac{dw_{w,p_c}}{dp_c}\right)\frac{d\phi}{dt}\\
&\quad +\dot{Q}
\end{aligned}\tag{76}$$

Usually all the terms including $(w_{sat}-w_w)/\rho_w$, $dw_{w,\phi}$ and $dw_{w,pc}$ are neglected, i.e., expressions that come from the heat capacity of the humid air and from changes in the vapor content in the porous volume due to changes in volume occupied by liquid moisture (assuming air becomes vented out of the material), in addition to temperature changes and the temperature dependency of vapor saturation pressure. However, in certain scenarios with highly porous materials with combined high temperature and high RH they may become significant.

A.6 Numerical-related practical setup of physics

A.6.1 Setup in Article IV

In Article IV, a practical solution is presented for continuing to use RH as the dependent variable when dealing with heavy driving rain. It involves converting the dependent variable into a modified RH representation, ϕ_{mod}, given by Eq. (77), which can be converted back to ϕ by Eq. (78). With this modified RH, one would have a variable that does not need the same level of accuracy during numerical solving as ϕ itself. This is relevant when approaching capillary saturation where ϕ values may operate in a range of 0.999 to 0.9999999, equivalent to p_c values ranging from 1.3E5 to 1.3E1 respectively. Instead, ϕ_{mod} will here range from ≈ 11.51 to 2.3, respectively. This simplifies numerical handling of the dependent variable in COMSOL.

$$\phi_{mod}=ln\left(\left[1-\phi\right]10^8\right)\tag{77}$$

$$\phi = 1 - \frac{exp\left[\phi_{mod}\right]}{10^8} \tag{78}$$

Gradients of ϕ are simply represented using the chain rule.

$$\frac{d\phi}{dt} = \frac{d\phi}{d\phi_{mod}} \frac{d\phi_{mod}}{dt}, \quad \frac{d\phi}{dx_j} = \frac{d\phi}{d\phi_{mod}} \frac{d\phi_{mod}}{dx_j} \tag{79}$$

where:

$$\frac{d\phi}{d\phi_{mod}} = -\frac{exp\left[\phi_{mod}\right]}{10^8} \tag{80}$$

A.6.2 Setup in Article VI

The approach using Eq. (77) to (80) works fine for porous materials. However, in a simulation scenario involving humid air, there is a question on how to handle condensation. Condensation occurs mostly as surface condensation, i.e., water droplets form on surfaces colder than the humid air, as the vapor saturation pressure is exceeded. This is most prominent on surfaces of materials that have very low hygroscopicity and absorptivity. Another form of condensation is heterogeneous condensation on particles suspended in the air. However, this requires knowledge about “dust” particles in the air. The condensation process is relevant for accurate heat balance and temperature calculation since condensed water releases its latent heat of evaporation. Also, condensed water could also move by surface runoff or as precipitation.

Nevertheless, hygrothermal simulation models usually do not account for surface condensation or heterogeneous condensation. Instead, an approach to avoid this issue all together is to create and manipulate a retention curve for air, thus, making air artificially capable of obtaining moisture at very low capillary pressures, that is, pressures that are lower than those active in retention curves of solid materials. Then the moisture is not lost, nor displaced by incorrect redistribution, and the excess moisture in the air can be absorbed by the materials over time.

Another approach is to allow for unphysical supersaturation. Supersaturation only occurs in extreme environments that are never experienced in building-physics conditions; however, mathematically it can be used to store moisture related to surface condensation. The model thereby accounts for the moisture but without including sub models for surface condensation. This can be justified for the scenario addressed in this thesis (Article VI) since it does not involve surface condensation to any significant degree. There is only a brief period of a few hours where surface condensation would have taken place on the asphalt sill gasket in contact with the air gap behind the beam end. It was found that the asphalt, which was modeled without moisture uptake and transport, was prone to surface condensation conditions; however, if replaced by mortar the issue of condensation was not observed.

The following describes the expanding of ϕ_{mod} to allow for supersaturation, i.e., $S \geq 1$, where S is equivalent to ϕ but where $\phi \leq 1$. However, it should be noted that with the following approach, efficient running of the model was not achieved during the surface condensation event. That is, the method worked, but the model ran with extremely small timesteps during peaks of heavily fluctuating timesteps.

We let ϕ_S be a ϕ equivalent variable, which spans the whole range of ϕ and S, i.e., allows for supersaturation. To expand ϕ_{mod} by keeping the essence of Eq. (77) one can make the ϕ_{mod} function approximately inversely symmetrical over $\phi_S = 1$ as done with Eq. (81).

$$\phi_S = 1 + \frac{\left(-exp\left(\phi_{mod}\right) + exp\left(-\phi_{mod}\right)\right)}{10^8} \tag{81}$$

$$\frac{d\phi_S}{d\phi_{mod}} = \frac{\left(-exp\left(\phi_{mod}\right) - exp\left(-\phi_{mod}\right)\right)}{10^8} \tag{82}$$

Solving Eq. (81) for ϕ_{mod}:

$$\begin{aligned}
&\left(1-\phi_S\right)10^8 = exp\left(\phi_{mod}\right) - exp\left(-\phi_{mod}\right) \\
&\text{with: } \frac{exp\left(\phi_{mod}\right) - exp\left(-\phi_{mod}\right)}{2} = sinh\left(\phi_{mod}\right) \\
&\rightarrow \frac{\left(1-\phi_S\right)10^8}{2} = sinh\left(\phi_{mod}\right) \\
&\text{with: } ar\,sinh\left(x\right) = ln\left(x + \sqrt{x^2+1}\right) \\
&\rightarrow ar\,sinh\left(\frac{\left(1-\phi_S\right)10^8}{2}\right) = ln\left(\frac{\left(1-\phi_S\right)10^8}{2} + \sqrt{\left[\frac{\left(1-\phi_S\right)10^8}{2}\right]^2 + 1}\right)
\end{aligned} \tag{83}$$

Solving the arsinh function requires the natural logarithm of a second order polynomial where one cannot take the logarithm of a negative number. The expression thereby loose one of its solutions. However, it turns out the other solution is the negative of the logarithm. Thus, the overall expression for ϕ_{mod} becomes:

$$\begin{aligned}
\phi_{mod} \quad &= if\left(\phi_S < 1\right) ln\left(\frac{\left(1-\phi_S\right)10^8}{2} + \sqrt{\left[\frac{\left(1-\phi_S\right)10^8}{2}\right]^2 + 1}\right) \\
&-\left(1 - if\left(\phi_S < 1\right)\right) ln\left(\frac{\left(1-\phi_S\right)10^8}{2} + \sqrt{\left[\frac{\left(1-\phi_S\right)10^8}{2}\right]^2 + 1}\right)
\end{aligned} \tag{84}$$

Eq. (84) is inverse symmetric about $\phi_{mod} = 0$, meaning ϕ_{mod} goes into negative values as $\phi_S > 1$. Having both positive and negative values might presumably create some scaling issues in COMSOL. Therefore, a solution is to shift the ϕ_{mod} variable so that it can be consistently scaled. Shifting too much may create accuracy issues in solving ϕ_{mod}, while shifting too little does not provide a good consistent scaling. With these considerations, an arbitrary shift of 50 seems relatively sufficient. Eq. (81), (82) and (84) rewritten become:

$$\phi_S = 1 + \frac{\left(-exp\left(\phi_{mod} - 50\right) + exp\left(-\left[\phi_{mod} - 50\right]\right)\right)}{10^8} \tag{85}$$

$$\frac{d\phi_S}{d\phi_{mod}} = \frac{\left(-exp\left(\phi_{mod}-50\right)-exp\left(-\left[\phi_{mod}-50\right]\right)\right)}{10^8} \tag{86}$$

$$\begin{aligned} \phi_{mod} \quad &= 50 + if\left(\phi_S < 1\right) ln\left(\frac{\left(1-\phi_S\right)10^8}{2} + \sqrt{\left[\frac{\left(1-\phi_S\right)10^8}{2}\right]^2 + 1}\right) \\ &-\left(1-if\left(\phi_S < 1\right)\right) ln\left(\frac{\left(1-\phi_S\right)10^8}{2} + \sqrt{\left[\frac{\left(1-\phi_S\right)10^8}{2}\right]^2 + 1}\right) \end{aligned} \tag{87}$$

A.7 Boundary expressions

A.7.1 Moisture balance – boundary expressions

The PDE for moisture balance has the following boundary expressions, interior and exterior respectively:

$$\begin{aligned} g_i &= g_{vi,sor} + g_{avi,sor} \\ g_e &= g_{ve,sor} + g_{ave,sor} + g_{le,sor} \end{aligned} \tag{88}$$

where i interior, e exterior, v vapor, sor source, a air flow, l liquid

$$\begin{aligned} g_{vi,sor} &= \beta_{p,i}\left(p_{v,i} - p_{sat}\phi\right) \\ g_{ve,sor} &= \beta_{p,e}\left(p_{v,e} - p_{sat}\phi\right) \end{aligned} \tag{89}$$

Vapor supplement from air transport is dependent on air-flow direction, i.e., whether the vapor content is determined from the boundary conditions or from the model surface. Since the “sor”, i.e., source, implies source to the model surface, then properties for positive sor-terms are determined at (ambient) boundary conditions, while a negative sor-term implies transport from a model surface, so that properties are determined at surface conditions.

$$\begin{aligned} g_{avi,sor} \quad &= \left(g_{ai,sor} > 0\right) g_{ai,sor} \frac{p_{vi}}{\left(\frac{MW_a}{MW_w}\right)P_{atm} + \left(1 - \frac{MW_a}{MW_w}\right)p_{vi}} \\ &+ \left(g_{ai,sor} < 0\right) g_{ai,sor} \frac{\phi p_{sat}}{\left(\frac{MW_a}{MW_w}\right)P_{atm} + \left(1 - \frac{MW_a}{MW_w}\right)\phi p_{sat}} \\ g_{ave,sor} \quad &= \left(g_{ae,sor} > 0\right) g_{ae,sor} \frac{p_{ve}}{\left(\frac{MW_a}{MW_w}\right)P_{atm} + \left(1 - \frac{MW_a}{MW_w}\right)p_{ve}} \\ &+ \left(g_{ae,sor} < 0\right) g_{ae,sor} \frac{\phi p_{sat}}{\left(\frac{MW_a}{MW_w}\right)P_{atm} + \left(1 - \frac{MW_a}{MW_w}\right)\phi p_{sat}} \end{aligned} \tag{90}$$

where the fraction in Eq. (90) is the vapor fraction of moist air Y_v, Eq. (31). With air flow, Eq. (91), under the presumption of only air flow in x-direction, and with a requirement that the exterior normal points towards the negative x-direction and the interior normal points towards the positive x-direction (i.e., exterior and interior at respectively left and right side of model).

The air flux boundary expressions are taken as:

$$g_{ae,sor,x} = -\delta_a \frac{dP_{atm}}{dx}$$
$$g_{ai,sor,x} = \delta_a \frac{dP_{atm}}{dx} \tag{91}$$

which is a consequence of the approach described in Section A.3.1.

Finally, the rain flux source is given as:

$$g_{le,sor} = min\left[g_l, -D_{\phi,cap}\left(\frac{\phi - \phi_{acc}}{b_{l,min}} + ln\,\phi \frac{\phi}{T} \frac{T - T_{r,e}}{b_{l,min}} \right) \right] \tag{92}$$

where g_l is the (impinging) rain flux, which is only non-zero when it rains, ϕ_{acc} artificial RH (RH_{acc} = RH accuracy) in a fictitious exterior water film layer that is arbitrarily set to 0.99999, which corresponds to p_c = 1351 Pa at 20 °C; $T_{r,e}$ is the rainwater temperature, which in a non-laboratory environment can be simplified and set equal to the exterior air temperature, $T_{a,e}$, due to the rainwater temperature usually being unknown; $b_{l,min}$ is the thickness of the exterior mesh boundary layer of the model. Eq. (92) is an approximation to Eq. (93) [73], an effective maximum moisture flux a material can absorb. The reason for the approximation is further addressed in Section A.8.3. Surface runoff is not addressed. Excess rainwater implicitly disappears in the model.

$$g_{l,eff} = min\left[g_l, K_{c,cap} \frac{dp_c}{dx} \right] \tag{93}$$

The capillary pressure gradient has to be positive in Eq. (93).

A.7.2 Heat balance – boundary expressions

The PDE for heat balance has the following boundary conditions, interior and exterior respectively, separated into source and impedance terms:

$$\begin{aligned} q_{i,sor} &= q_{i,sor} + q_{iv,sor} + q_{avi,sor} + q_{ai,sor} \\ q_{i,imp} &= q_{i,imp} + q_{iv,imp} + q_{avi,imp} + q_{ai,imp} \\ q_{e,sor} &= q_{e,sor} + q_{ev,sor} + q_{el,sor} + q_{ave,sor} + q_{ae,sor} \\ q_{e,imp} &= q_{e,imp} + q_{ev,imp} + q_{el,imp} + q_{ave,imp} + q_{ae,imp} \end{aligned} \tag{94}$$

where; i interior, e exterior, v vapor, a air flow, l liquid, imp impedance, sor source

Impedance terms are in COMSOL multiplied with the dependent variable (here T), which is solved for in numerical iterations. Therefore, the impedance term is given without the dependent variable as seen, for instance, in Eq. (95).

The convective thermal heat transfer is given as:

$$\begin{aligned} q_{i,sor} &= \alpha_{ai} T_{eq,i} \\ q_{i,imp} &= \alpha_{ai} \\ q_{e,sor} &= \alpha_{ae} T_{eq,e} \\ q_{e,imp} &= \alpha_{ae} \end{aligned} \tag{95}$$

The heat transfer by vapor diffusion is under the assumption that the vapor lost from the model surface is heated or cooled by the air and not the surface. In contrast, the heat of evaporation affects the surface as the vapor is either evaporated or condensed at the surface with it going directly out of or into the liquid moisture content calculation of the surface material.

$$\begin{aligned} q_{vi,sor} &= g_{vi,sor} h_{vap} + \left(g_{vi,sor} > 0\right) g_{vi,sor} c_{pv,i} T_{ai} \\ q_{vi,imp} &= \left(g_{vi,sor} > 0\right) g_{vi,sor} c_{pv,i} \\ q_{ve,sor} &= g_{ve,sor} h_{vap} + \left(g_{ve,sor} > 0\right) g_{ve,sor} c_{pv,e} T_{ae} \\ q_{ve,imp} &= \left(g_{ve,sor} > 0\right) g_{ve,sor} c_{pv,e} \end{aligned} \tag{96}$$

where c_{pv} is the specific heat capacity of vapor. As a simplification, the heat capacity is in a consistent manner evaluated at boundary temperature instead of an average value of boundary and surface temperature. This also applies to the following.

Heat transfer by rain absorption:

$$\begin{aligned} q_{el,sor} &= g_{le,sor} c_{pw,e} T_{r,e} \\ q_{el,imp} &= g_{le,sor} c_{pw,e} \end{aligned} \tag{97}$$

Heat transfer by vapor content in air flow:

$$\begin{aligned} q_{avi,sor} &= g_{avi,sor} h_{vap} \\ q_{avi,imp} &= 0\left[W/\left(m^2 K\right)\right] \\ q_{ave,sor} &= g_{ave,sor} h_{vap} \\ q_{ave,imp} &= 0\left[W/\left(m^2 K\right)\right] \end{aligned} \tag{98}$$

Heat transfer by (humid) air flow Eq. (99) under the assumption that air leaving the model surface is heated or cooled by the air and not the surface.

$$\begin{aligned}
q_{ai,sor} &= \left(g_{ai,sor} > 0\right) g_{ai,sor} c_{pha,i} T_{ai} \\
q_{ai,imp} &= \left(g_{ai,sor} > 0\right) g_{ai,sor} c_{pha,i} \\
q_{ae,sor} &= \left(g_{ae,sor} > 0\right) g_{ae,sor} c_{pha,e} T_{ae} \\
q_{ae,imp} &= \left(g_{ae,sor} > 0\right) g_{ae,sor} c_{pha,e}
\end{aligned} \tag{99}$$

where c_{pha} is the specific heat capacity of humid air, $g_{ai,sor}$ and $g_{ae,sor}$ are given in Eq. (91).

A.7.3 Longwave and shortwave boundary expressions (Article IV)

Including longwave and shortwave radiation is done by expanding Eq. (94) to:

$$\begin{aligned}
q_{e,sor} &= q_{e,sor} + q_{ev,sor} + q_{el,sor} + q_{ave,sor} + q_{ae,sor} + q_{er\_long,sor} + q_{er\_short,sor} \\
q_{e,imp} &= q_{e,imp} + q_{ev,imp} + q_{el,imp} + q_{ave,imp} + q_{ae,imp} + q_{er\_long,imp}
\end{aligned} \tag{100}$$

Longwave radiation from the surroundings to a surface is calculated according to principles of Hens [219] p.79. Eq. (101) [219] is the net heat flux $\dot{q}''$ [W/m^2] to the surface, calculated as the sum of heat exchange between a surface (subscript s) and, respectively, the terrestrial environment (e) and the sky (sk).

$$\dot{q}''_{rse} + \dot{q}''_{rssk} \approx \varepsilon_{Ls}\sigma\left[\left(F_{se}F_{Tse} + F_{ssk}F_{Tssk}\right)\left(T_e - T_s\right) - 21F_{ssk}F_{Tssk}\left(1 - f_c\right)\right] \tag{101}$$

where subscript se is surface-environment, ssk surface-sky, ε_{Ls} [-] longwave emissivity of surface, σ [W/(m^{2}K^4)] Stefan-Boltzmann's constant, F_{se} and F_{ssk} [-] view-factors of respectively environment and sky for the surface, F_{Tse} and F_{Tssk} [K^3] scaling radiation-temperature factors given as $F_{Tij}=4[(T_i+T_j)/2]^3$, T_e and T_s [K] temperature of environment and surface respectively, f_c [-] cloud factor between 0 and 1. The view factors F_{se} and F_{ssk} are in sum always equal to 1. They are both equal to 0.5 for a vertical wall, close to a plane ground-level, with an unobstructed view of the horizon. The sky temperature is assumed to be 21 degrees lower than the air (environment) temperature [219], hence the value 21 in Eq. (101). The cloud factor is given by MDRY data (often in interval 0-100, thus, having to be scaled by 1/100).

Thus, from Eq. (101) we have the long wave contributions to Eq. (100):

$$\begin{aligned}
q_{er\_long,sor} &= \varepsilon_{Ls}\sigma\left[\left(F_{se}F_{Tse} + F_{ssk}F_{Tssk}\right)T_e - 21F_{ssk}F_{Tssk}\left(1 - f_c\right)\right] \\
q_{er\_long,imp} &= \varepsilon_{Ls}\sigma\left(F_{se}F_{Tse} + F_{ssk}F_{Tssk}\right)
\end{aligned} \tag{102}$$

The shortwave radiation model was never fully developed and verified for accuracy in the work on Article IV. Therefore, the shortwave model should be approached with care.

Shortwave radiation is separated into direct solar radiation, diffuse solar radiation and possible solar reflection by the environment.

$$q_{er\_short,sor} = E_{direct} + E_{diffuse} + E_{reflective} \tag{103}$$

Direct and diffuse radiation are given in MDRY data as radiation flux to a horizontal plane; thus, respectively, they have to be reconstituted and reangled. Angular reflection from highly reflective surfaces, like reflective building facades or bodies of water, will not be addressed.

Instead, we assume diffuse reflectance of the direct solar radiation from the environment, in addition to diffuse reflection of diffuse radiation. Then the view factor of the wall to the reflective environment can simply be expressed with a cosine expression.

$$E_{reflective} = \rho_e \left(E_{direct,hor} + E_{diffuse,hor} \right) \frac{\left(1 - cos\left(k_{tilt,wall}\right)\right)}{2} \tag{104}$$

where ρ_e [-] is the reflectance coefficient of the environment, subscript $_{hor}$ refers to flux measured in the horizontal plane, $k_{tilt,wall}$ [rad] is the angle between the ground and the wall, i.e. > π/2 leaning outward over the ground, and < π/2 leaning backward towards the sky, where $k_{tilt,wall} = 0$ indicates a horizontal surface having a view factor of the sky that equals unity.

Similar, the diffusive radiation is expressed as:

$$E_{diffuse} = E_{diffuse,hor} \frac{\left(1 + cos\left(k_{tilt,wall}\right)\right)}{2} \tag{105}$$

Direct solar radiation is the most complex one since it is dependent on the position of the sun in the sky. Additionally, a direct path of sight must exist between the surface and the sun. This requires knowledge of the sun position in the sky over the course of day and year. Thus, a sun position algorithm is necessary. Many algorithms for calculating the position of the sun exist in the literature. These algorithms can, for instance, be categorized based on complexity, accuracy, and year-interval of validity, where, of course, there is a strong connection between the first one and the latter two of these properties. It follows that the decision on what algorithm to use should be based on the interval of years needed, what accuracy is sufficient for the use in question, and what computational complexity that can be accepted.

The direct solar radiation is reconstituted from what is detected at the horizontal plane to what is detected by the wall plane:

$$E_{direct} = \frac{E_{direct,hor}}{sin\left(\alpha_h\right)} cos\left(\alpha_i\right) \quad for\ 0 < \alpha_h \le \frac{\pi}{2}, \quad 0 \le \alpha_i \le \frac{\pi}{2} \tag{106}$$

where α_h [rad] is the sun elevation angle, i.e., the vertical angle between the horizon and the sun, and α_i [rad] is the angle of incidence, i.e., incoming sun rays relative to the wall normal. The angle ranges imply that for $\alpha_h \le 0$ sun has set, and angles above π/2 are not possible, whereas $\alpha_i > \pi/2$ gives sun positions behind the wall, i.e., the wall is in the shade, while $\alpha_i < 0$ should not occur in the calculation.

The sun elevation angle over the horizon is calculated as [227]:

$$\alpha_h = arcsin\left[sin\left(\delta_{sun}\right) sin\left(B_{lat}\right) - cos\left(\delta_{sun}\right) cos\left(B_{lat}\right) cos\left(asi_{sun}\right) \right] \tag{107}$$

where δ_{sun} [rad] is the sun declination angle, B_{lat} [rad] is the latitude, asi_{sun} [rad] is the sun azimuth angle.

Whereas, the angle of incidence is calculated as [227]:

$$\alpha_i = arccos\left[cos\left(\alpha_h\right)cos\left(j_{asi}\right)sin\left(k_{tilt,wall}\right) + sin\left(\alpha_h\right)cos\left(k_{tilt,wall}\right)\right] \tag{108}$$

where $j_{asi} = asi_{sun}(t) - asi_{wall}$ [rad] is the angular difference between the sun and wall azimuths.

The following applies that the azimuth angle is the eastward angle from the north, i.e., direction north is 0° and south is 180°. Both the sun and the wall are given azimuth angles, i.e., respectively, asi_{sun} and asi_{wall} [rad]. However, while the wall angle is fixed, the sun angle is a function of time that follows a sun position algorithm. When the azimuth angles of the wall and sun are equal, then the wall normal aligns with the horizontal component of the vector of sunshine towards the wall.

The azimuth angle of the sun can in a crude fashion (low accuracy) be calculated as:

$$asi_{sun} = \left(t - \left[N_{day} - 1\right]24\frac{h}{day}\cdot 3600\frac{s}{h}\right)\frac{1}{3600s}\left(\frac{15}{360}\right)2\pi \tag{109}$$

where N_{day} is the day-number in the year, the 15/360 is the angular ratio per hour, i.e., 24 h x 15°/h = 360°.

Eq. (109) ensures that each and every midnight $asi_{sun} = 0$; however, this is not accurate.

The declination angle δ_{sun} [rad] can be estimated as:

$$\delta_{sun} = -23.44\left(\frac{2\pi}{360}\right)cos\left(\frac{2\pi}{365}\left[N_{day} - 10\right]\right) \tag{110}$$

where 23.44 [deg] is the axis tilt of the earth, $2\pi/360$ is conversion from deg to rad, while the cosine expression ensures the yearly change in sun declination for the northern hemisphere with a maximum on June 21st (172nd day), and a minimum on December 21 (355th day). Eq. (109) and (110) are extremely crude expressions for calculating the sun position. It is recommended to apply a more accurate sun position algorithm.

A.8 COMSOL setup

A.8.1 Tolerance settings

Table A.1 Applied tolerance settings

Setting location	Name tag	Value	Method
Step 1: Time dependent – Study settings	Relative tolerance	0.001	
Time dependent solver – Absolute tolerance	Tolerance factor	0.1	Scaled
	Tolerance (dependent variable phim)	1e-3	Scaled
	Tolerance for time derivatives (dependent variable phim)	1e-3	Scaled
	Tolerance (dependent variable T)	1e-3	Scaled
	Tolerance for time derivatives (dependent variable T)	1e-3	Scaled
Segregated – General	Tolerance factor	0.1	
Segregated step phim – Method and Termination	Tolerance factor	1e-3	
Segregated step T – Method and Termination	Tolerance factor	1e-3	

A.8.2 Time-stepping

Deciding maximum timesteps is important for balancing simulation runtime efficiency and simulation correctness and accuracy. The COMSOL model has been set up with steps taken by the solver to be «free», that is, COMSOL decides the time step size taken to approach converging iteration, while adhering to tolerance requirements. Additionally, maximum timesteps need to be specified. Ideally, to shorten simulation runtimes as large timesteps as possible would be desired. However, a range of practical considerations must be made.

- The largest timestep is limited by desired simulation result resolution.
- Timesteps at times of changing boundary conditions cannot be larger than boundary condition resolution.
- Timesteps at times with rapid changes that are numerically hard to solve should be rather small (e.g., rain events to give reasonable solving of moisture front progression).
- COMSOL updates timestep only before initiating a new timestep; therefore, there is need of a margin of small timesteps between large timesteps and when small timesteps are required. If not, due to the «free» steps taken by the solver, one risks a shift in

timesteps, in worst case resulting in an overstepping of events or boundary condition changes up to the size of the large timestep.

It was found most practical to define maximum timesteps in form of a table defining timesteps at any time during the simulation. A function f(t) is then used to call for such a table in the *maximum time* setting under *Time Stepping* in the *Time-Dependent solver*. Refer also to Article VI for more information on practical handling of maximum timesteps in relation to rain events.

A.8.3 Relaxation expressions for the rain boundary condition

The rain boundary condition can induce significant numerical hardship or instability that results in COMSOL applying so small timesteps that the simulation runtime becomes unacceptably long. During work on the model, a few remedies were discovered that can alleviate this issue. The findings are summarized below to possibly be of help for others who run into similar problems. However, these findings should be approached with care, and should undergo specific verification for any setting they are applied.

It was found that the timestep parameter that is defined in COMSOL could be useful to distinguish situations with small timesteps taken by the solver. Basically, *timestep* is the numerical timestep during numerical solving (chosen freely by the solver for the BDF method (Backward Differentiation Formula) applied in COMSOL). It can then be put into expressions.

A list of tried boundary algorithm expression for the driving rain load is given in Table A.2.

Table A.2 List of tried boundary algorithm expressions (parameter explanations are given after table)

Type	Expression	Assessment
Source term / load	$min\left[g_l, D_\phi \frac{d\phi}{d\phi_m}\frac{d\phi_m}{dx}\right]$	Fails
Source term / load	$min\left[g_l, \left(\frac{d\phi_m}{dx}<0\right)\left(-D_\phi \frac{(\phi-\phi_{acc})}{b_{l,min}}\right) + \left(1-\left(\frac{d\phi_m}{dx}<0\right)\right)D_\phi \frac{d\phi}{d\phi_m}\frac{d\phi_m}{dx}\right]$	Fails
Source term / load	$min\left[g_l, -D_\phi \frac{(\phi-\phi_{acc})}{b_{l,min}}\right]$ where bl$_{min}$ is smallest mesh boundary layer thickness, i.e., the mesh boundary layer furthest out on the exterior.	Works in combination with reduction terms
Source term / load	$min\left[g_l, -D_{\phi,max} \frac{(\phi-\phi_{acc})}{b_{l,min}}\right]$	Works in combination with reduction terms

Reduction (exponential)	$\left[(timestep < 0.1timestep_0)\left(\frac{timestep}{timestep_0}\right)^{coeff} + (timestep > 0.1timestep_0) + (timestep == 0.1timestep_0)\right]$	Works for large enough coeff and timestep$_0$. Loses significant source contribution.
Reduction (linear)	$\left[1-(timestep < timestep_0)\frac{(timestep_0 - timestep)}{timestep_0}\right]$	Works for large enough timestep$_0$. Loses minimal source contribution.
Criteria (abrupt)	$(\phi_{mod} > \phi_{mod,acc})$	Not clear
Criteria (abrupt)	$(\phi_{mod} > \phi_{mod,acc})\left(\left(w_w + \frac{dw_w}{d\phi}\frac{d\phi}{d\phi_{mod}}\frac{d\phi_{mod}}{dt}\right) < w_{w,sat}\right)$	Not clear
Criteria (linear)	$[\phi_{mod} > \phi_{mod,acc}] + \left([\phi_{mod} < \phi_{mod,acc}] \cdot [\phi_{mod} > \phi_{mod,acclim}]\left[1-\frac{(\phi_{mod,acc} - \phi_{mod})}{(\phi_{mod,acc} - \phi_{mod,acclim})}\right]\right)$	Not clear, but allows model to operate rain wetting to lower p_c values.

After assessment it was found that the most suited combination from Table A.2 was as follows:

$$
\begin{aligned}
g_{le,sor} = &\Bigg([\phi_{mod} > \phi_{mod,acc}] + [\phi_{mod} < \phi_{mod,acc}] \\
&\cdot [\phi_{mod} > \phi_{mod,acclim}]\left[1-\frac{(\phi_{mod,acc} - \phi_{mod})}{(\phi_{mod,acc} - \phi_{mod,acclim})}\right]\Bigg) g_{le\_term}
\end{aligned}
\tag{111}
$$

where $\phi_{mod,acc} = \phi_{mod}(\phi_{acc})$, $\phi_{mod,acclim} = \phi_{mod}(\phi_{acclim})$, where ϕ_{acc} is arbitrarily set to 0.99999 and ϕ_{acclim} to 0.9999999 which, respectively, correspond to p_c = 1351 Pa and 13.51 Pa at 20 °C. The benefit of the linear criteria in Eq. (111) is not utilized in the following so it is basically redundant, but it could be of benefit if ϕ_{acc} is replaced with ϕ_{acclim} in Eq. (112), if materials with retention curves that go to such low p_c values are addressed. The g_{le_term} is given as:

$$
\begin{aligned}
g_{le\_term} &= min\left[g_l \cdot f_1(timestep), -D_{\phi,max}\left[\frac{(\phi-\phi_{acc})}{b_{l,min}} + \frac{\phi\, ln(\phi)}{T}\frac{(T-T_{r,e})}{b_{l,min}}\right] \cdot f_2(timestep)\right] \\
f_1(timestep) &= \left[1-(timestep < 0.2timestep_0)\frac{(0.2timestep_0 - timestep)}{0.2timestep_0}\right] \\
f_2(timestep) &= \left[1-(timestep < timestep_0)\frac{(timestep_0 - timestep)}{timestep_0}\right]
\end{aligned}
\tag{112}
$$

where timestep_0 has been set to 0.1 s; however, larger values might also be acceptable, but more rainwater will be lost from the model during numerical hardship if substantially larger values are used.

A.8.4 Principles for material properties functions

There are some principles or preferences that preferably should be met with property expressions for simple and stable implementation into hygrothermal simulation models, while at the same time providing realistic property behavior.

- Smooth and continuous retention curve with dependence to capillary pressure. (The curve must account for hygroscopic sorption also).
- Analytically differentiable retention curve expression.
- Smooth and continuous curve for vapor permeability with dependence to moisture content.
- Smooth and continuous curve for liquid conductivity with dependence to capillary pressure or moisture content.
- Smooth and continuous curve for thermal conductivity with dependence to moisture content.

These principles are adhered to with the expressions described, suggested, and applied in Article V and Article VI. See also Section 2.1. Curves can either be described through expressions or be tabulated. With tabulated property descriptions, values are interpolated between entries, and the resolution needs to be high enough not to needlessly lose accuracy in the property curve shapes.

[This page is left blank]

Appendix B Property functions

Following are the (basic) temperature dependent property functions applied in the COMSOL model. Refer to Section 2.1, Article V and Article VI for the moisture dependent ones. Formulas for humid air will not be repeated here; refer to Tsilingiris [220] and [228].

B.1 Water and water vapor properties

Specific heat capacity of vapor [220]

$$c_{pv} = c_0 + c_1\left(T - T_0\right) + c_2\left(T - T_0\right)^2 \quad \left[J / kgK\right] \tag{113}$$

where c_0 = 1869.10989, c_1 = -0.2578421578, c_3 = 0.01941058941, T_0 = 273.15 K

Comment: There seems to be some differences between values generated from Eq. (113) and the IAPWS reported properties [229] for saturated vapor pressures. Furthermore, there is also the issue of what the heat capacity of vapor is for unsaturated vapor pressures, something not addressed in [220].

A remedy for the latter is given by the following function.

Specific heat capacity of vapor (saturated and unsaturated) [230]

Function is applicable within temperature range 273.15-473.15 K. Less accuracy above 373.15 K for increasing vapor pressures; nevertheless, still less than 1 % deviation except at the highest end.

$$c_{pv} = A_E + B_E\left(T - T_0\right) + C_E\left(T - T_0\right)^2 + \frac{p_v - p_t}{A_F + B_F\left(T - T_0\right) + C_F\left(T - T_0\right)^2} \quad \left[J / kgK\right] \tag{114}$$

where p_t = 611.657 Pa

for T <= 323.15 K; A_E = 1877.2, B_E = -0.49545, C_E = 8.1818E-3, A_F = 22.537, B_F = 0.49321, C_F = 0.048927

for T > 323.15 K; A_E = 1856.1, B_E = 0.28056, C_E = 6.9444E-4, A_F = 22.537, B_F = 0.49321, C_F = 0.048927

Comment: Although [230] claims to follow IAPWS, the values at saturation generated by (114) do not seem to align to the IAPWS reported properties [229].

However, with a modification to the constants, a reasonable approximate alignment is achieved:

for T <= 323.15 K; A_E = 1888.2, B_E = -0.49545, C_E = 8.1818E-3, A_F = 42.537, B_F = 0.45321, C_F = 0.046227

for T > 323.15 K; A_E = 1868.1, B_E = 0.28056, C_E = 6.9444E-4, A_F = 30.537, B_F = 0.508, C_F = 0.049927

Nevertheless, there is uncertainty related to the specific heat capacity of vapor, especially unsaturated vapor, and the corresponding values of specific heat capacity of humid air, with the uncertainty of the latter reported by [228]. It is outside the scope of the present thesis work to further investigate this issue.

Specific heat capacity of water [231]

Function is applicable within the temperature range 273.15-373.15 K at atmospheric pressure, with very good accuracy below 363.15 K.

$$c_{pw} = a + b\left(T - T_0\right) + c\left(T - T_0\right)^{1.5} + d\left(T - T_0\right)^2 + e\left(T - T_0\right)^{2.5} \quad \left[J/\left(kg \cdot K\right)\right] \tag{115}$$

where a = 4217.4356, b = -5.6181625, c = 1.2992528, d = 0.11535353, e = 4.14964E-03, T_0 = 273.15K

Comment: since two of the temperature exponents are non-integers, T cannot be less than 273.15 K. Therefore, such a criterion must be included within all the temperature terms, to avoid error and model crash if a calculation is attempted for T < 273.15 K.

Specific enthalpy of vaporization of water [232]

Function is applicable within a temperature range between the triple point (also allow 0 °C) and the critical point.

$$h_{vap} = h_t \left[\frac{T_c - T}{T_c - T_t}\right]^{Z_c^2\left[\left(T - T_t\right)/\left(T_c - T_t\right)\right] + Z_c} \quad \left[J/kg\right] \tag{116}$$

where h_t = 2500920 J/Kg (heat of vaporization at triple point), T_c = 647.096 K (temperature at critical point), T_0 = 273.16 K (temperature at triple point), Z_c = 0.292 (universal critical ratio)

Dynamic viscosity of water [233]

Function is applicable within the temperature range 273.15-643.15 K with maximum error of 2.5 %.

$$\mu_w\left(T\right) = a \cdot 10^{\frac{b}{T-c}} \quad \left[kg/\left(m \cdot s\right)\right] \tag{117}$$

where a = 2.414E-5 N·s/m^2, b = 247.8 K, c =140 K

Surface tension of water [234]

Function is applicable for temperatures between the triple point (also allows for 0 °C) and the critical point.

$$\sigma_w\left(T\right) = aX^{5/4} + bX^{9/4} + cX^{13/4} \quad [10^{-3}\ N/m] \tag{118}$$

where X = (T_c-T)/T_c, with T_c = 647.126 K (at which surface tension is zero), a = 232.713514, b = -140.18645, c = -4.890098

B.2 Air properties

Specific heat capacity [220]

Function is valid for a temperature range -23 °C to 777 °C

$$c_{pa} = \left(c_0 + c_1 T + c_2 T^2 + c_3 T^3 + c_4 T^4\right) \cdot 10^3 \quad \left[J/\left(kg \cdot K\right)\right] \tag{119}$$

where c_0 = 1.03409, c_1 = -0.284887E-3, c_2 = 0.7816818E-6, c_3 = -0.4970786E-9, c_4 = 0.1077024E-12

B.3 Air-vapor properties

Saturation pressure [235]

Function is applicable for the whole range of temperatures given that the saturated vapor pressure is on a vapor-liquid water interface. Nevertheless, the expression has been derived with hydrometeorological applications in mind, and the verification covered the interval -40 to 50 °C. At temperatures approaching 100 °C the accuracy decreases.

$$P_{sat} = P_0 \cdot exp\left[24.921 \cdot \left(1 - \frac{T_0}{T}\right)\right]\left(\frac{T_0}{T}\right)^{5.06} \quad \left[Pa\right] \tag{120}$$

where P_0 = 611.657 Pa, T_0 = 273.16 K (saturation pressure and temperature at triple point respectively)

Saturation pressure gradient (differentiated from the above)

$$\frac{dP_{sat}}{dT} = P_0 \cdot exp\left[24.921 \cdot \left(1 - \frac{T_0}{T}\right)\right]\left(\frac{T_0}{T}\right)^{5.06} \cdot \left[-5.06\frac{1}{T} + 24.921\frac{T_0}{T^2}\right] \quad \left[Pa/K\right] \tag{121}$$

Vapor permeability in air [118, 144, 236]

Range of applicability is not known to the author.

$$\delta_{v,a} = \frac{2.306 \cdot 10^{-5}}{R_w T}\frac{P_0}{P}\left(\frac{T}{T_0}\right)^{1.81} \quad \left[kg/\left(m \cdot s \cdot Pa\right)\right] \tag{122}$$

where P_0 and P are the standard (P_0 = 101325 Pa) and acting atmospheric pressure, respectively, T_0 = 273.15[K].

[This page is left blank]

Appendix C Verification and validation of the COMSOL model

Verification of the COMSOL model involves checking the correctness of the physics code-implementation, design functionality of algorithms, and accuracy to benchmark standards. Validation involves checking and assessing whether the model satisfies end use application and performance needs.

All the Hamstad benchmarks [121] have been run in 3D since the 3D functionality is numerically hardest to simulate. Hence, what works in 3D should run easier for lower dimensions. Still, all the Hamstad benchmarks are 1D benchmarks, i.e., their boundary conditions and geometry functionality are strictly 1D. Therefore, the benchmarks do not actually test heat, air, and moisture transport performance in 3D, only the physics and algorithm functionality for 3D. Complete description of benchmarks is found in the Hamstad benchmark report [121], which encompasses setups, inputs, and expected results.

Benchmarks 1 and 2 are already addressed in Article III; however, since the COMSOL model algorithms have been corrected for a mistake and updated to accommodate driving rain, also these benchmarks are repeated.

C.1 Hamstad 1 benchmark (Drying under seasonal and daily weather variation)

Provides a scenario of a two-layer roof structure with an exterior load bearing layer and an interior insulation layer. The load bearing layer is capillary active while the insulation layer is non-capillary. A moisture membrane prevents vapor exchange at the exterior. Climate exposure involves daily external temperature and interior vapor pressure variation over a year on an hourly basis. It includes interstitial condensation between the two material layers [73]. Large temperature fluctuations occur in the load bearing layer during summer times due to the large external temperature variation. The scenario runs for five years from a high initial moisture content to slowly decrease year by year by drying towards the interior.

The scenario tests model accuracy and consistency over long times, as well as the handling of large temperature fluctuations.

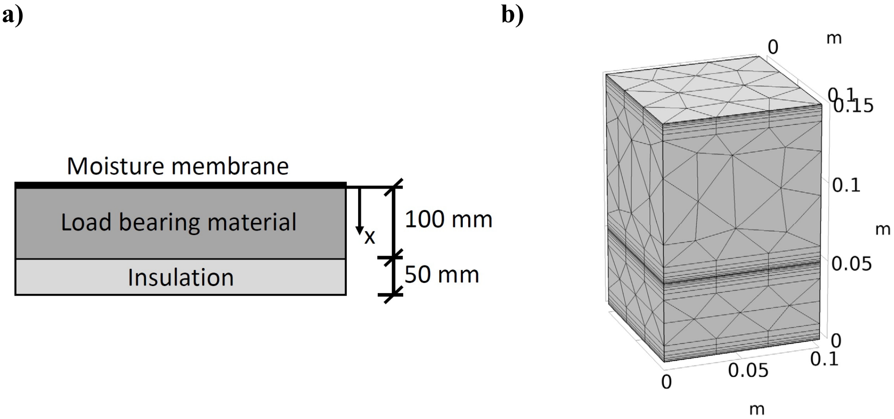

Fig. C.1.1 a) Benchmark object b) Geometry and mesh setup, including boundary layers at all interfaces.

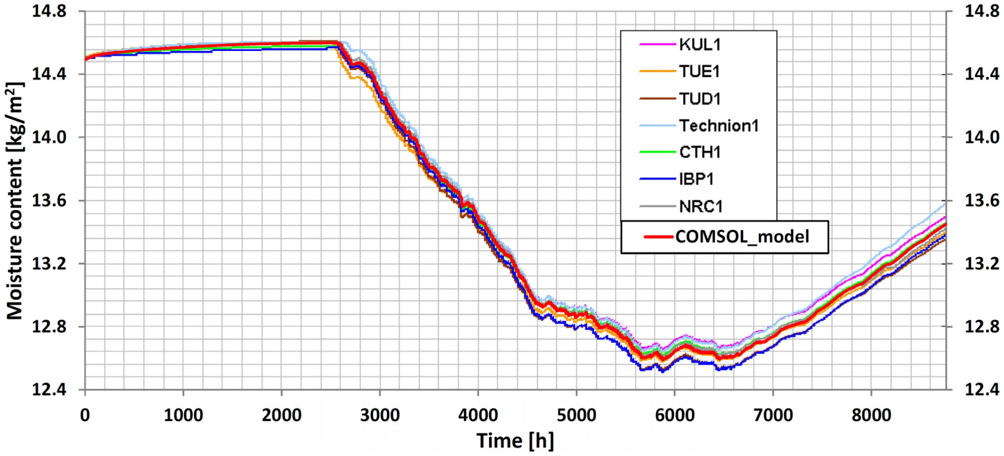

Fig. C.1.2 Average moisture content in the load bearing layer 1st year

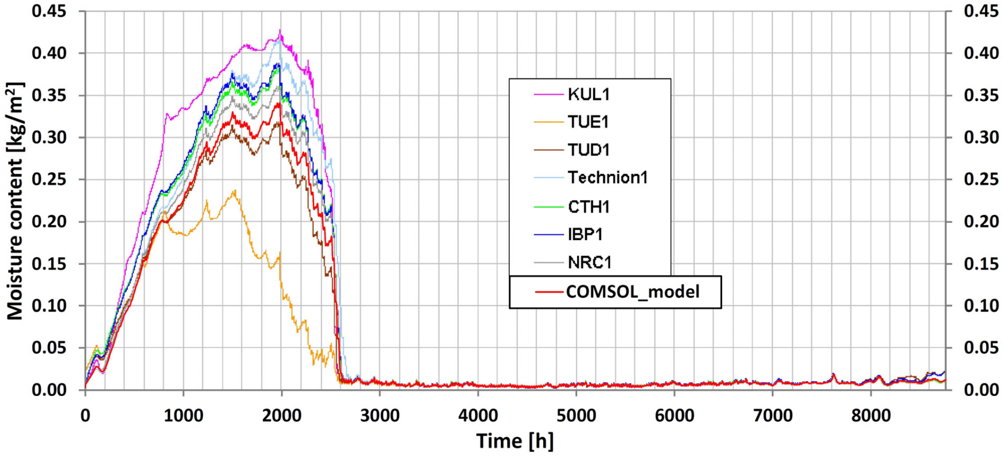

Fig. C.1.3 Average moisture content in insulation 1st year

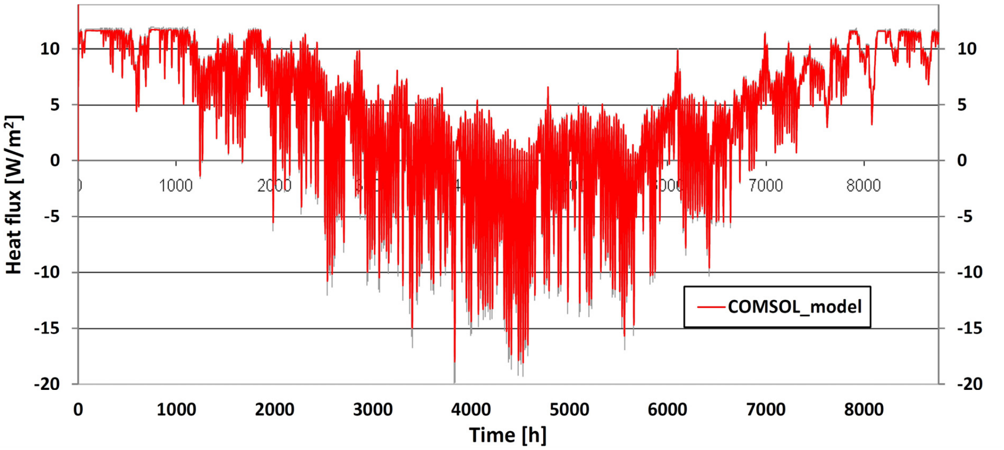

Fig. C.1.4 Average of calculated heat flows from interior to the ceiling, 1st year

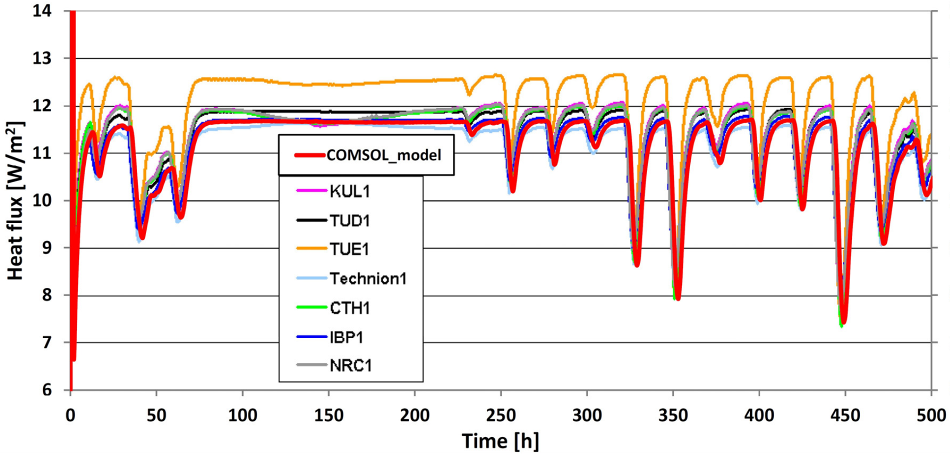

Fig. C.1.5 Heat flow from interior to the ceiling, 1st year, first 500 h

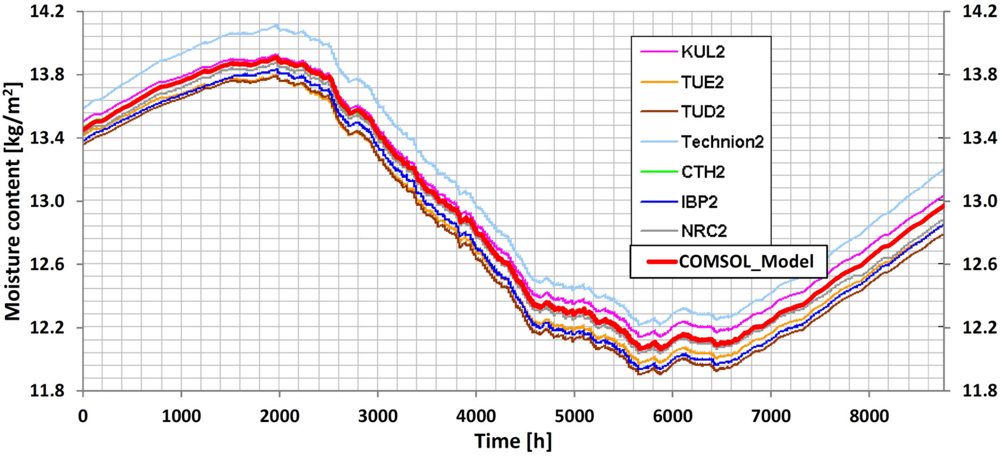

Fig. C.1.6 Average moisture content in the load bearing layer 2nd year

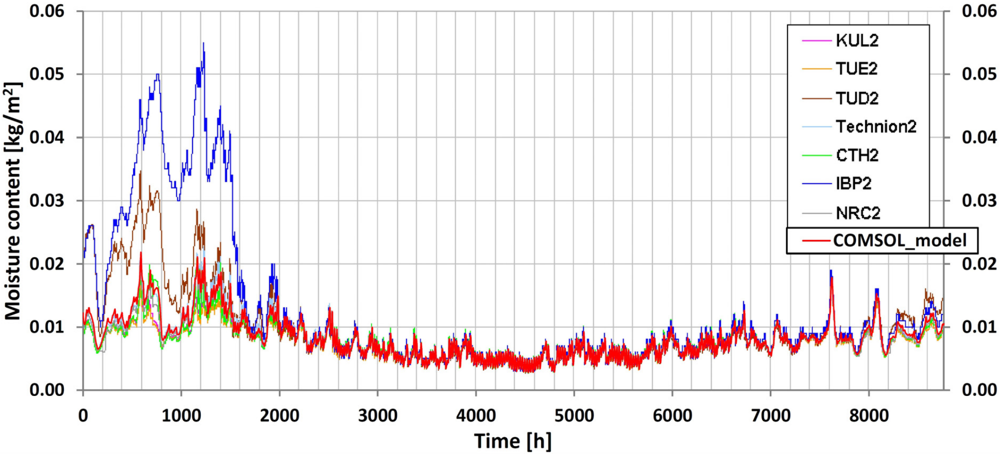

Fig. C.1.7 Average moisture content in insulation 2nd year

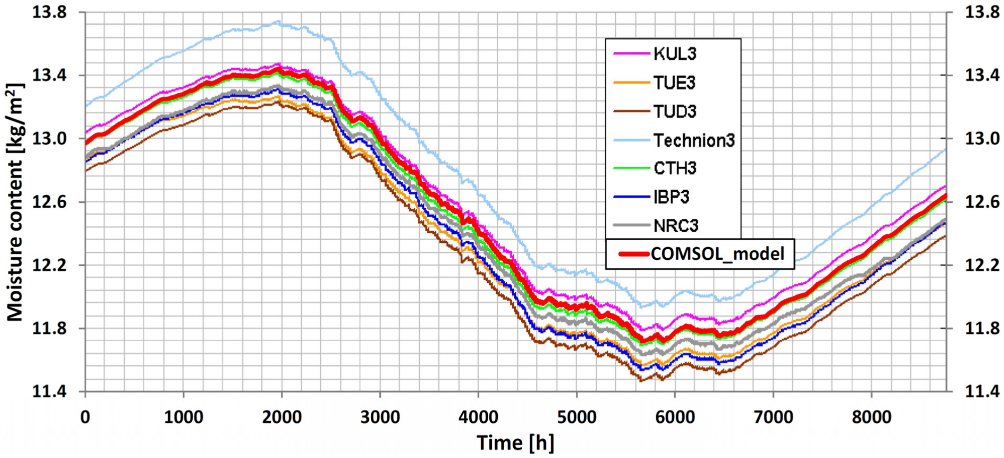

Fig. C.1.8 Average moisture content in the load bearing layer 3rd year

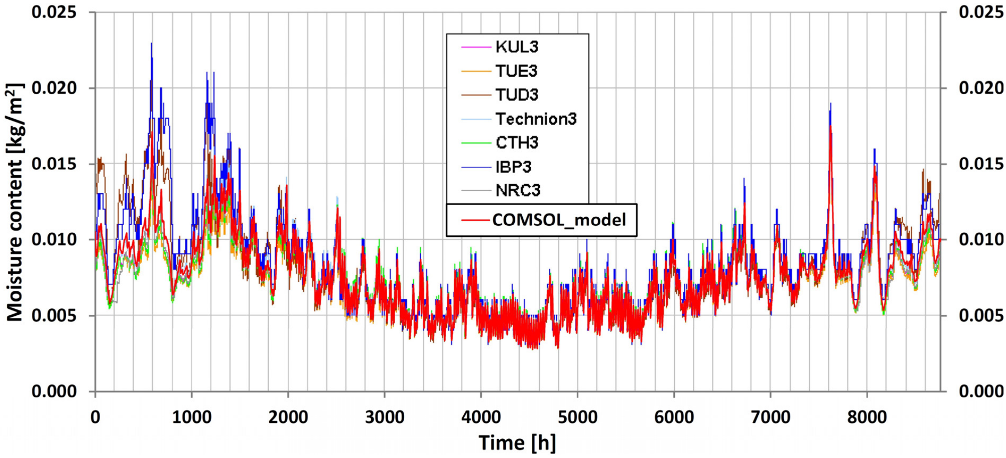

Fig. C.1.9 Average moisture content in insulation 3rd year

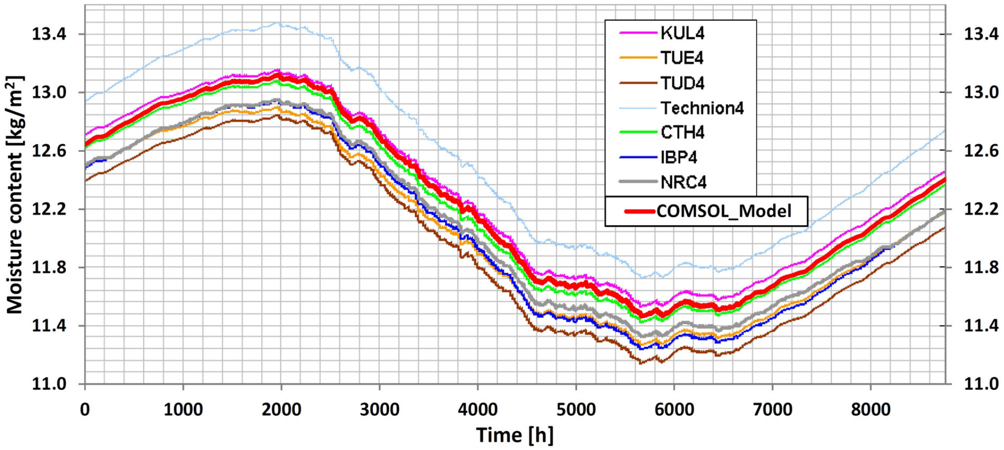

Fig. C.1.10 Average moisture content in the load bearing layer 4th year

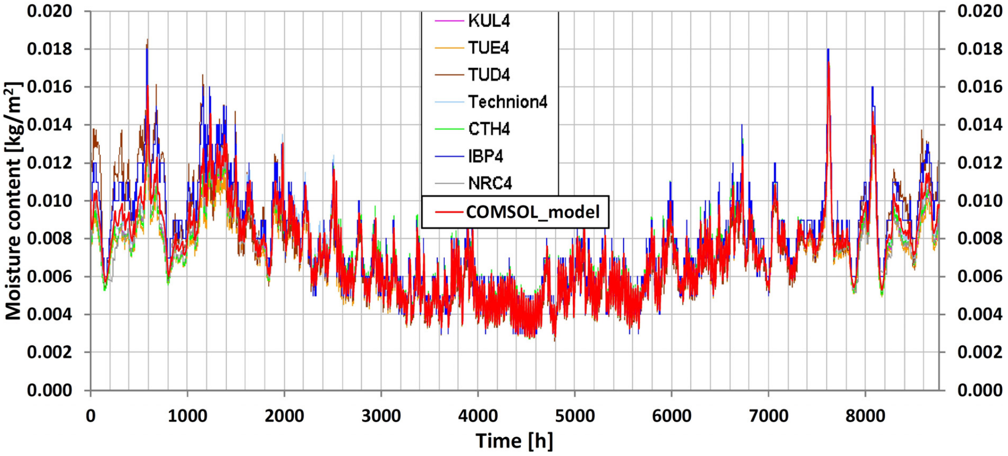

Fig. C.1.11 Average moisture content in insulation 4th year

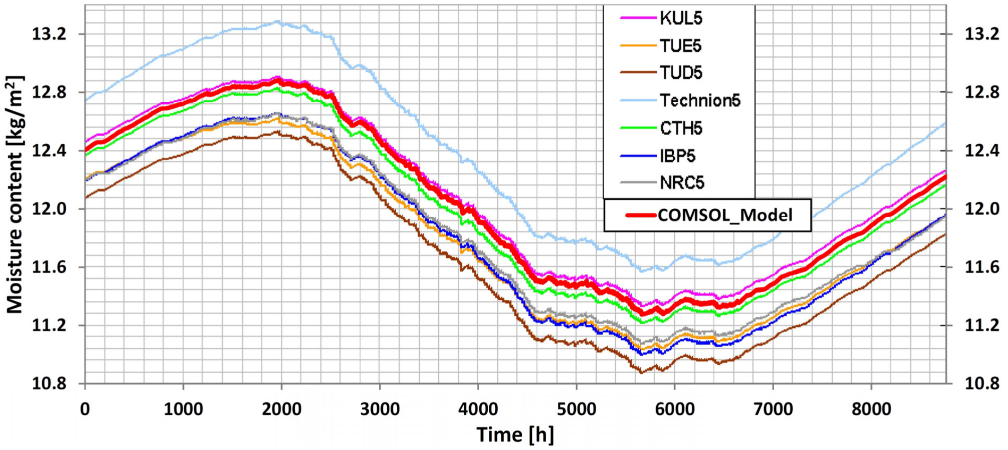

Fig. C.1.12 Average moisture content in the load bearing layer 5th year

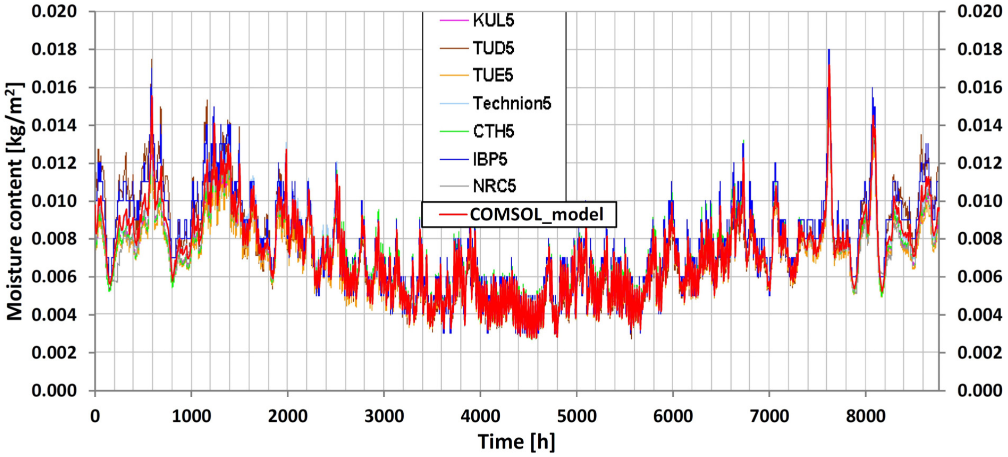

Fig. C.1.13 Average moisture content in insulation 5th year

Comments on this benchmark:

- The benchmark is sensitive to the timestep-size taken. Since the simulation lasts five years, it is tempting to use large timesteps; however, a timestep-size of 3600 s, equal to the boundary condition time-resolution, becomes inaccurate, leading to the result diverging over time. A considerably smaller timestep is thus necessary. A timestep of 360 s provides a result in line with the benchmark.
- This realization is important in simulations involving 3D due to the associated numerical load. To keep simulation time low, as large timesteps as possible are preferred. However, this implies that a timestep-size close to the boundary condition time-resolution is not feasible for keeping accuracy over long duration scenarios.

C.2 Hamstad 2 benchmark (Isothermal drying)

Provides a scenario of a wall layer under fictitious isothermal conditions (altered enthalpy of vaporization). From an initial high moisture content, the layer will dry out due to a constant lower relative humidity at the exterior and interior. With exterior and interior relative humidity being unequal, a distinct non-symmetric moisture profile forms. The scenario has an analytical solution.

This benchmark is the simplest of the five benchmarks and tests the moisture storage and transport PDE, independent of temperature.

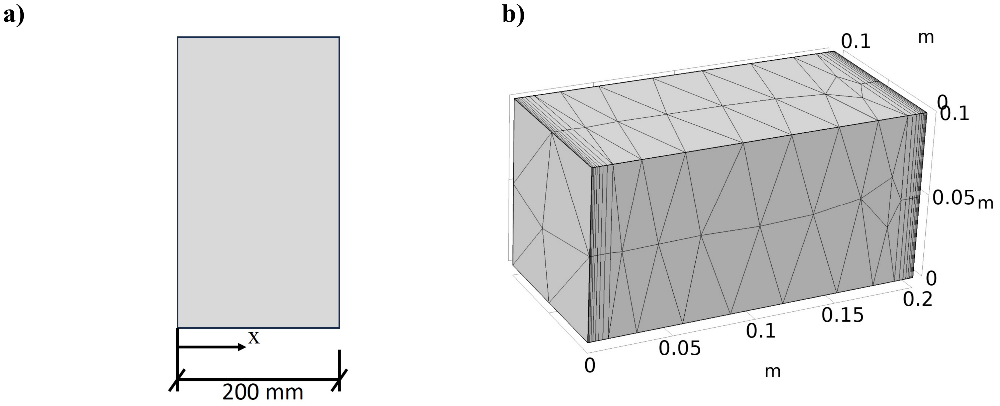

Fig. C.2.1a) Benchmark object b) Geometry and mesh setup, including boundary layers at all interfaces.

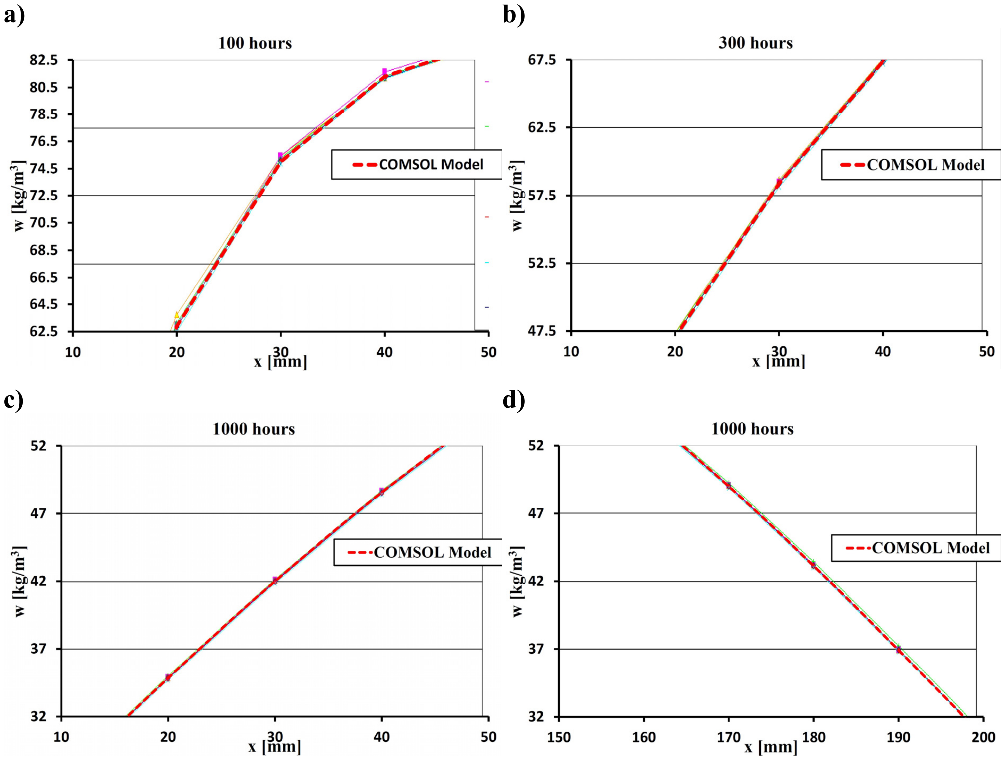

Fig. C.2.2 Moisture content at a) 100 h, b) 300 h, c) 1000 h, over x-interval 0-5 cm and d) 1000h at x-interval 15-20 cm.

C.3 Hamstad 3 benchmark (Air diffusion)

Provides a scenario of a lightweight wall subjected to an air pressure potential that switches from an interior over-pressure to under-pressure. The scenario first ensures moisture deposition in the wall before subsequent drying.

Although air diffusion is not part of the current thesis, air diffusion has been included in the COMSOL model to demonstrate its versatile functionality.

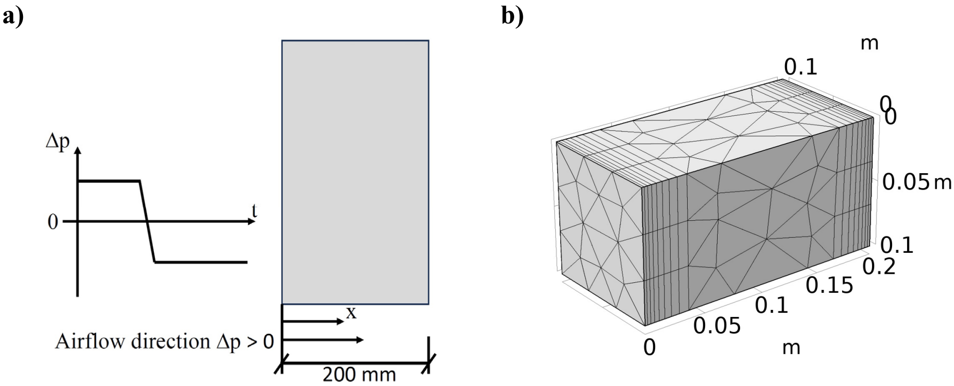

Fig. C.3.1 a) Benchmark object and air pressure scenario, b) Geometry and mesh setup, including boundary layers at all interfaces.

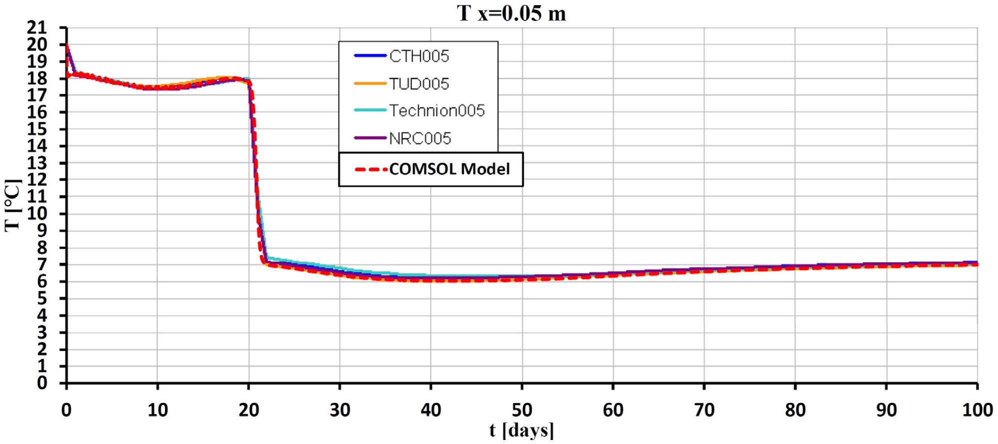

Fig. C.3.2 Temperature evolution at x = 0.05 m

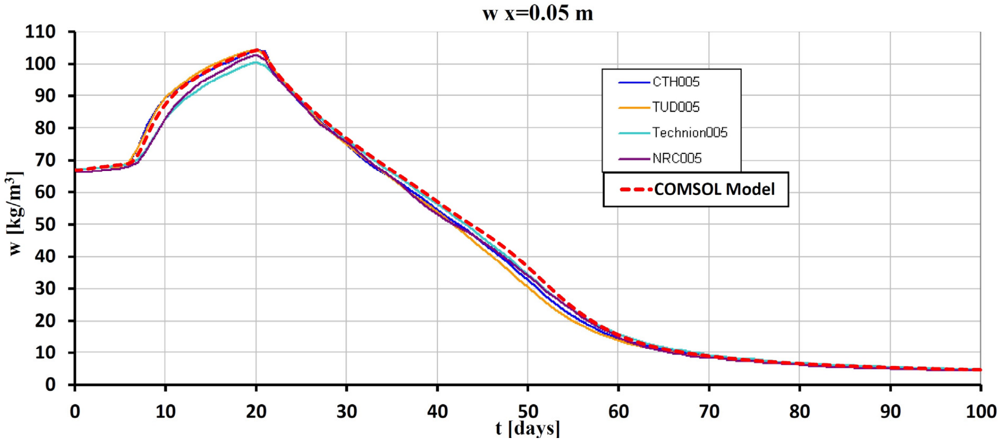

Fig. C.3.3 Moisture content evolution at x = 0.05 m

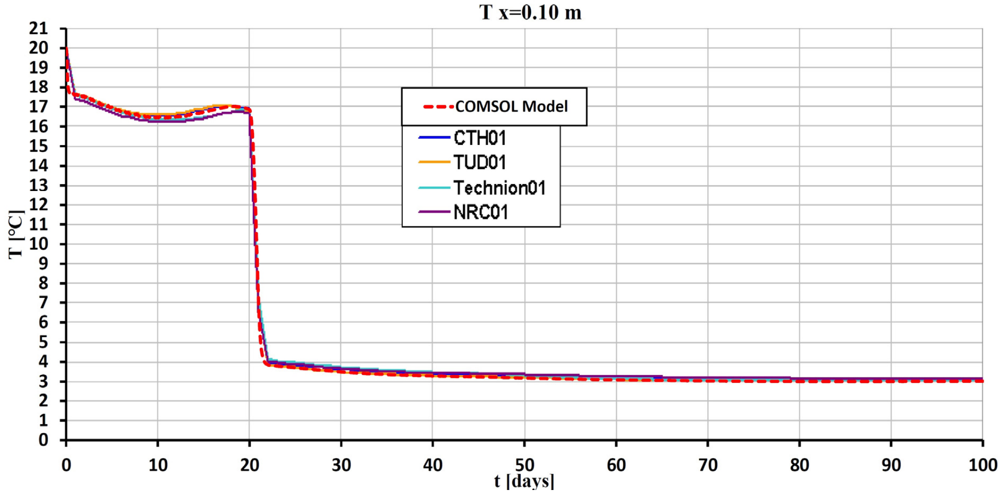

Fig. C.3.4 Temperature evolution at x = 0.1 m

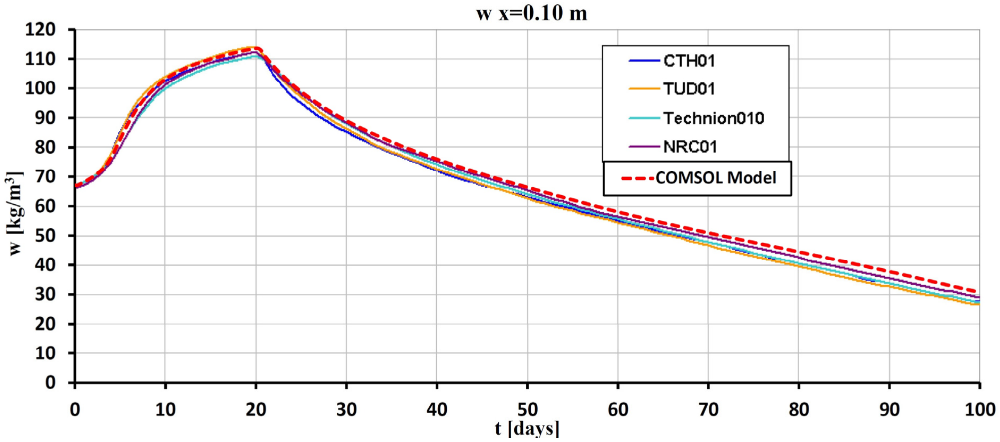

Fig. C.3.5 Moisture content evolution at x = 0.1 m

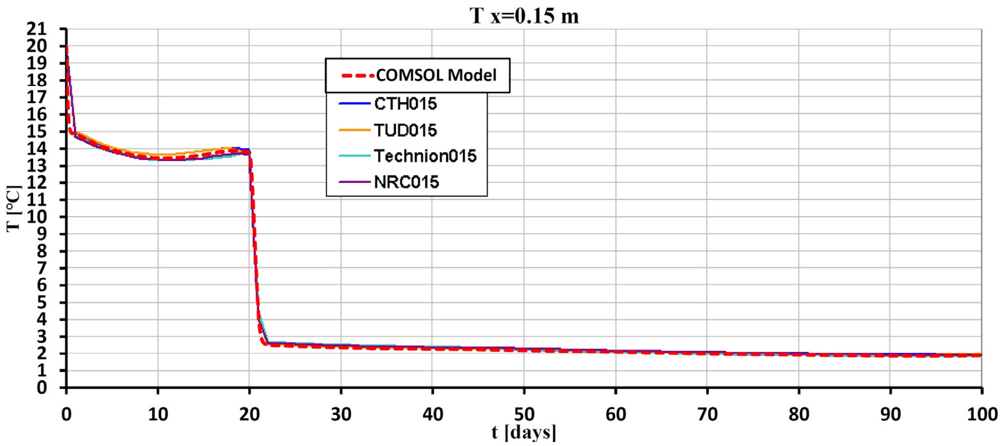

Fig. C.3.6 Temperature evolution at x = 0.15 m

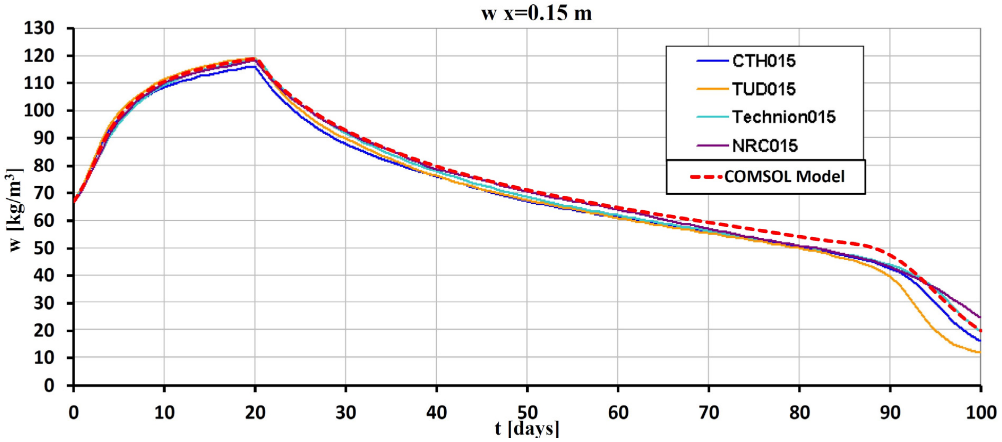

Fig. C.3.7 Moisture content evolution at x = 0.15 m

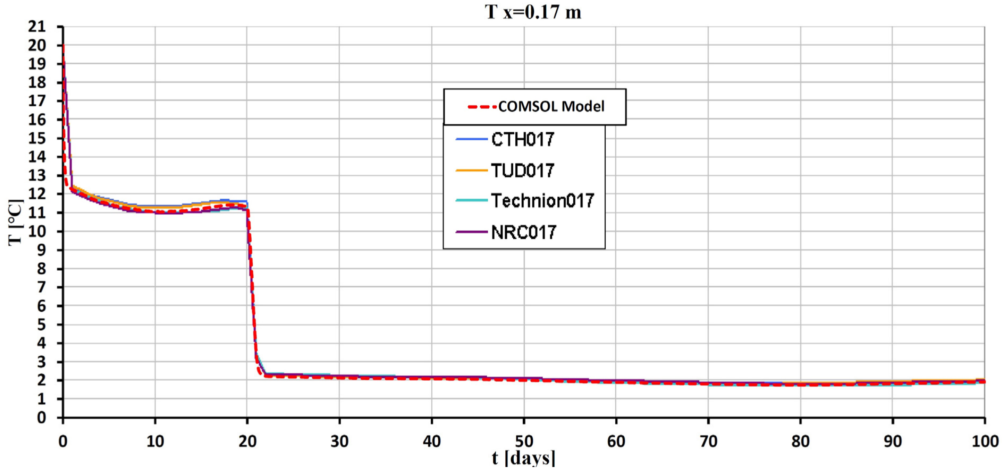

Fig. C.3.8 Temperature evolution at x = 0.17 m

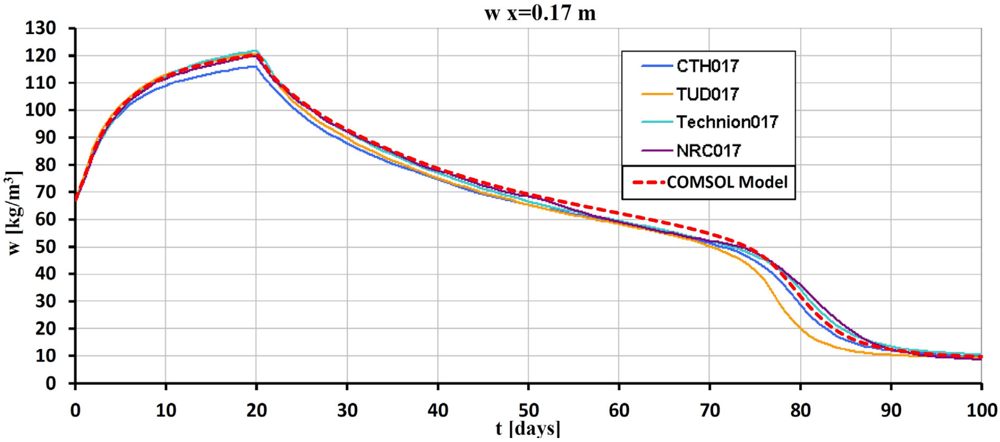

Fig. C.3.9 Moisture content evolution at x = 0.17 m

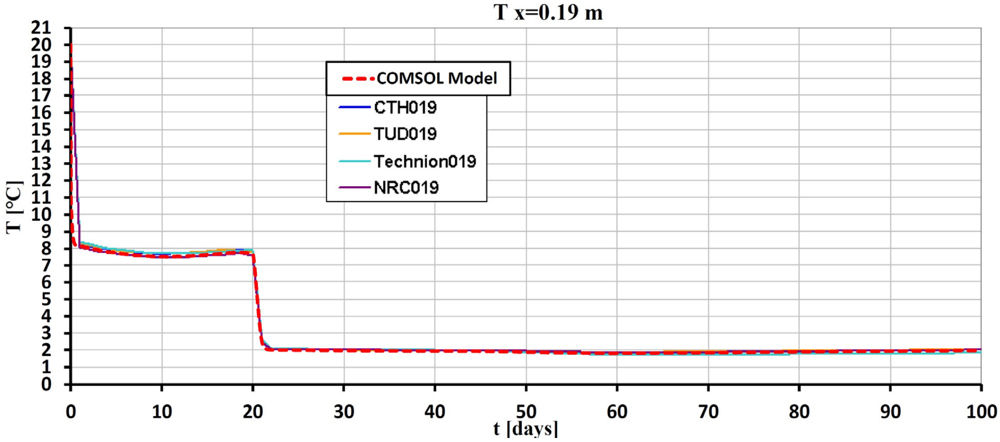

Fig. C.3.10 Temperature evolution at x = 0.19 m

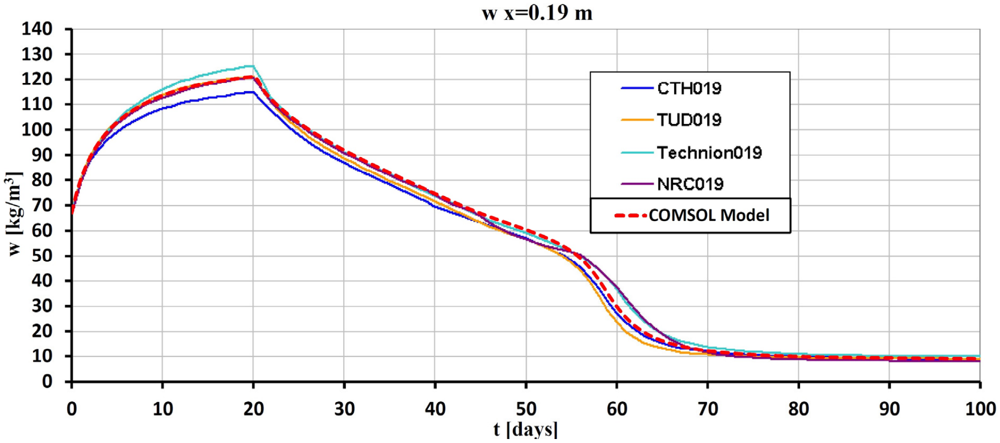

Fig. C.3.11 Moisture content evolution at x = 0.19 m

Comment on this benchmark:

- This benchmark can be somewhat sensitive to how the humid air properties in detail are described and modeled for the air flow.

C.4 Hamstad 4 benchmark (Driving rain absorption)

Provides a scenario of a two-layer wall exposed to a sequence of exterior driving rain events and high temperature fluctuations. Interior there is a varying vapor pressure representing a moisture load. The climate exposure is severe, including moisture condensation, alternating rapid wetting and drying, as well as moisture redistribution across the interface between the two material layers [73]. Furthermore, the exterior layer has very high hydraulic conductivity.

Due to its driving rain inclusion, this benchmark is important for hygrothermal models intended to handle driving rain. Thus, it is central for testing the COMSOL model of this thesis.

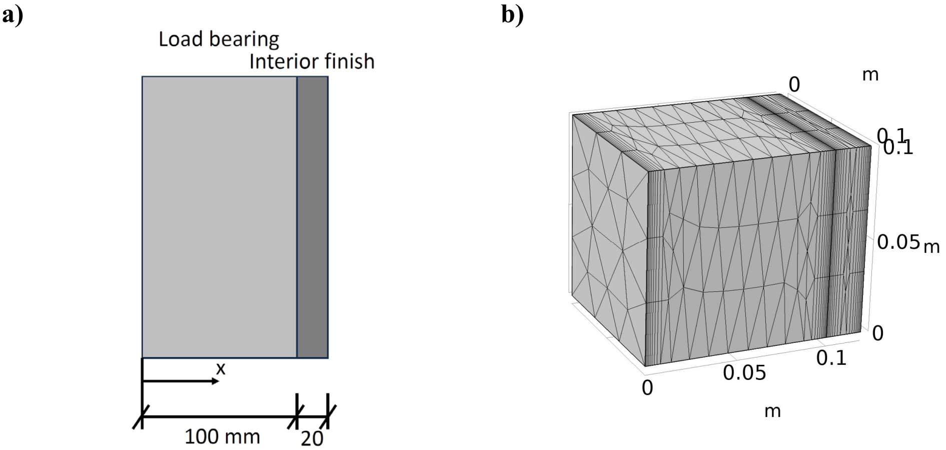

Fig.C.4.1 a) Benchmark object, b) Geometry and mesh setup, including boundary layers at all interfaces.

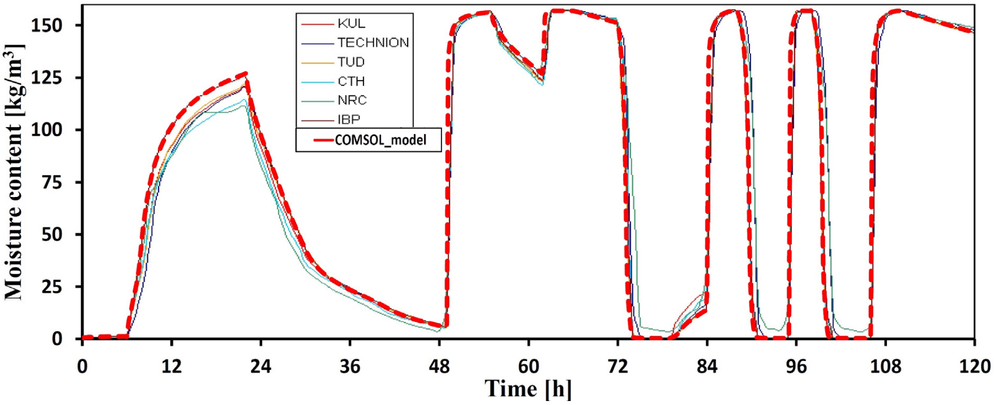

Fig.C.4.2 Moisture content on outer surface

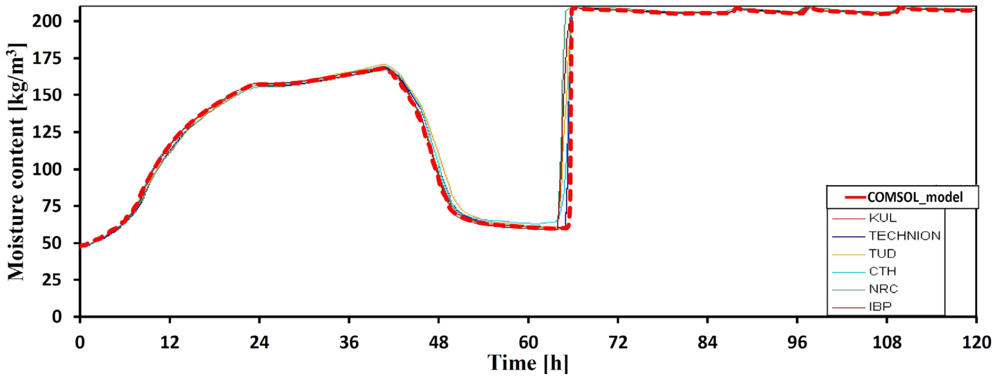

Fig.C.4.3 Moisture content on inner surface

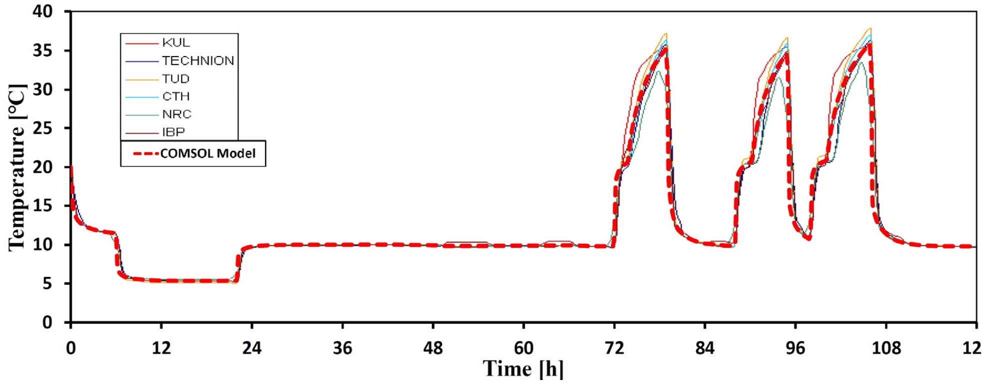

Fig.C.4.4 Temperature on outer surface

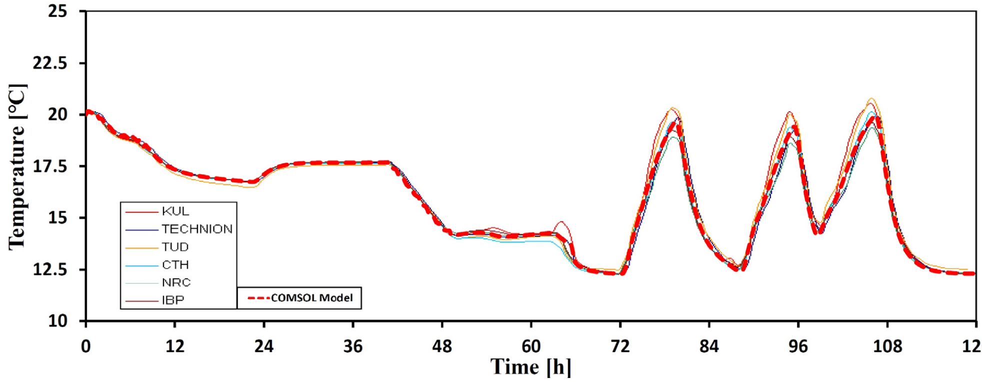

Fig.C.4.5 Temperature on inner surface

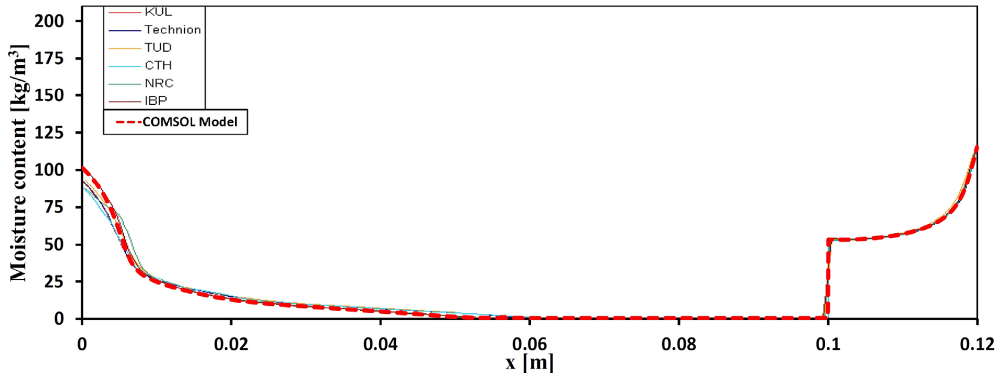

Fig.C.4.6 Moisture profile at 12 hours

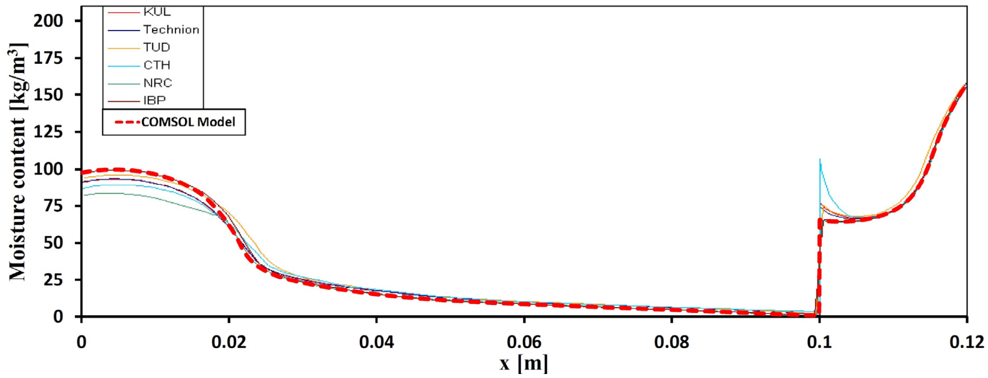

Fig.C.4.7 Moisture profile at 24 hours

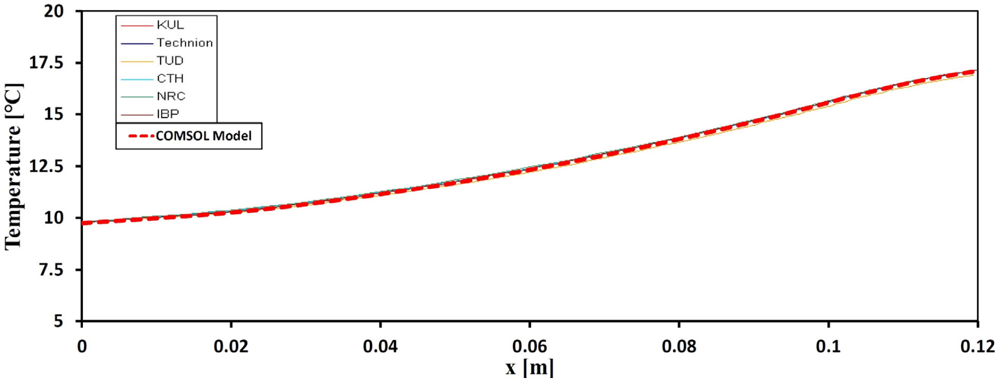

Fig.C.4.8 Temperature profile at 24 hours

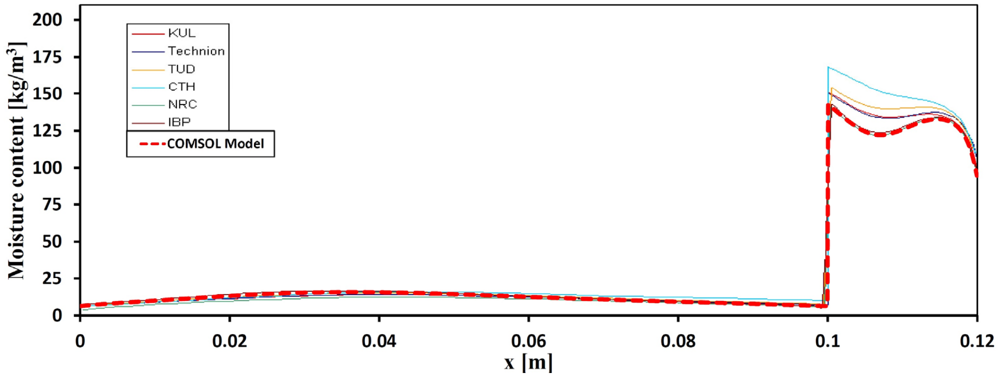

Fig.C.4.9 Moisture profile at 48 hours

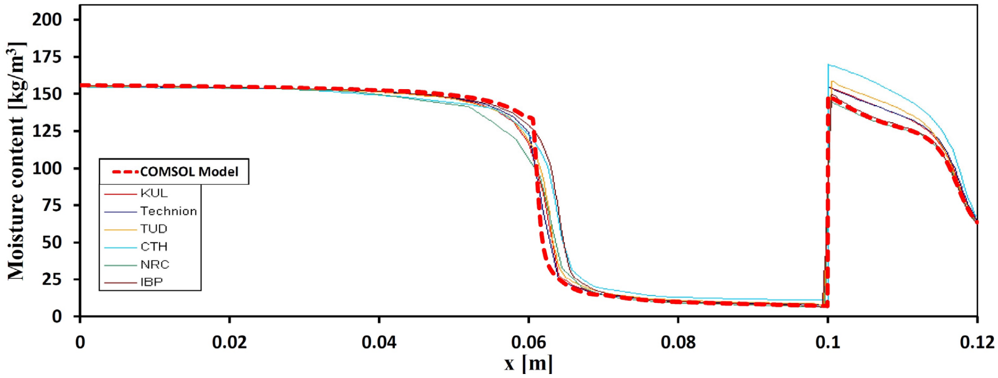

Fig.C.4.10 Moisture profile at 54 hours

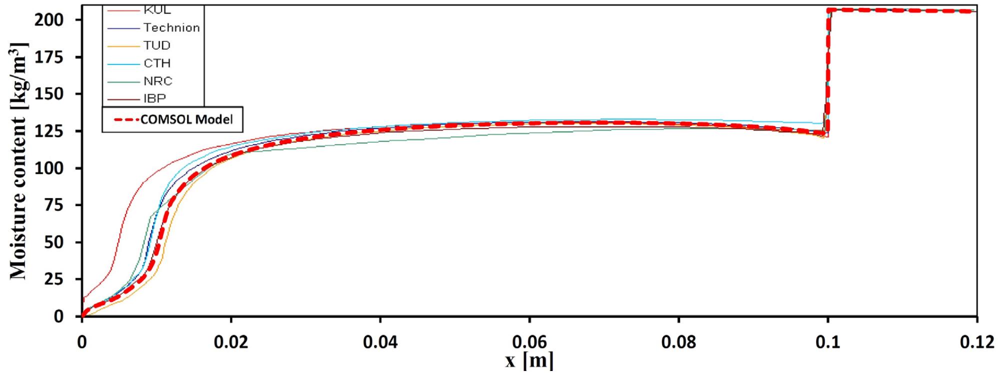

Fig.C.4.11 Moisture profile at 78 hours

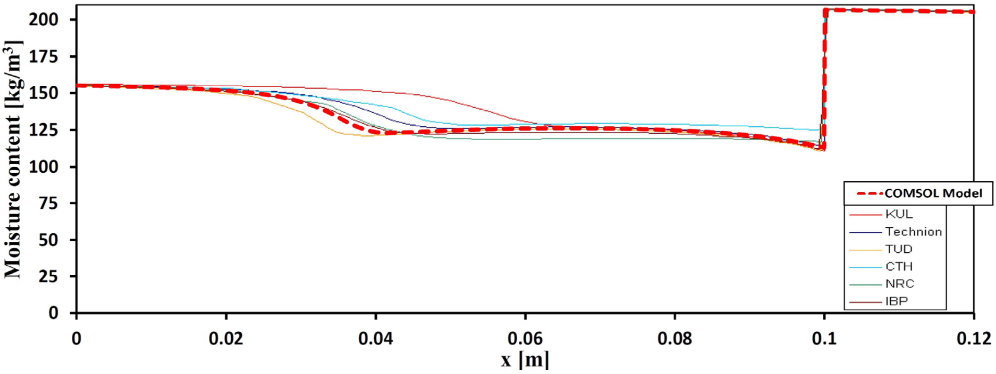

Fig.C.4.12 Moisture profile at 96 hours

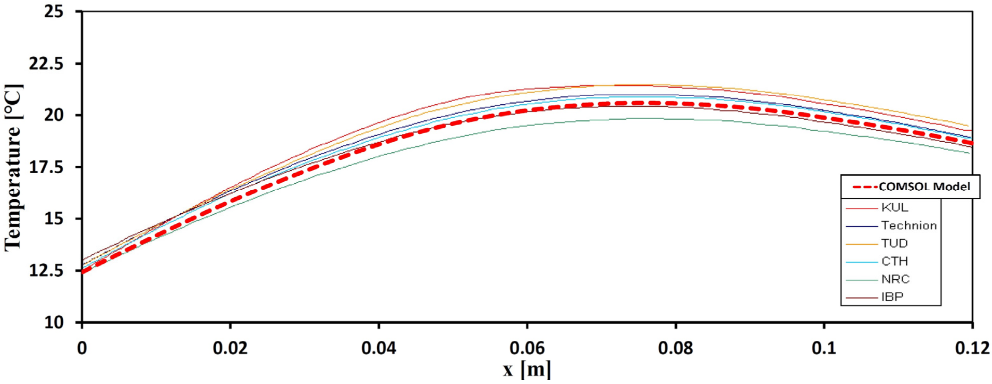

Fig.C.4.13 Temperature profile at 96 hours

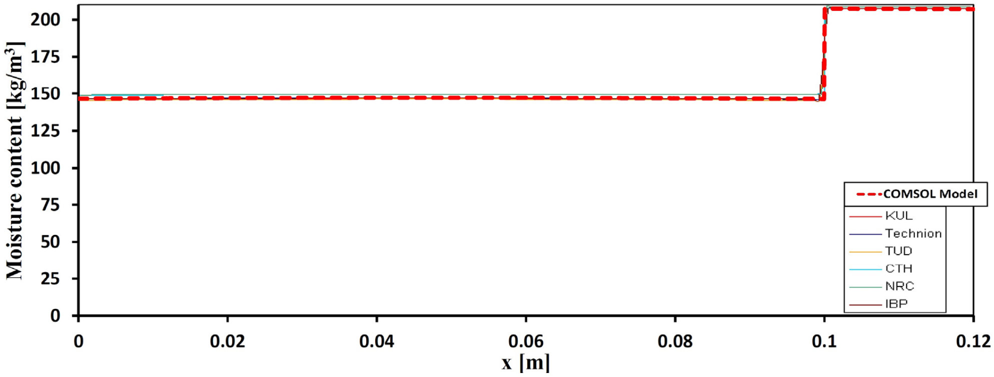

Fig.C.4.14 Moisture profile at 120 hours

Comment on this benchmark:

- Timesteps during rain events need to be rather small to achieve the result of Fig.C.4.10. Otherwise, the moisture front progression will be underestimated. Timesteps smaller than 120 s provide a more reasonable fit, while for instance 360 s gives clear underestimation. Furthermore, the result of Fig.C.4.10 is also sensitive to mesh resolution.

C.5 Hamstad 5 benchmark (Capillary active interior insulation)

Provides a scenario of brick masonry with capillary active interior insulation. Being vapor open, condensation occurs in the wall, and the capillary properties of the insulation ensures some moisture distribution towards the interior. With constant boundary conditions, the scenario concept is simple, with a transition in moisture content profile over time from an initial condition.

Presenting a masonry structure with interior insulation makes this benchmark very relevant for the COMSOL model, by testing the combined vapor and capillary transport functionality and performance.

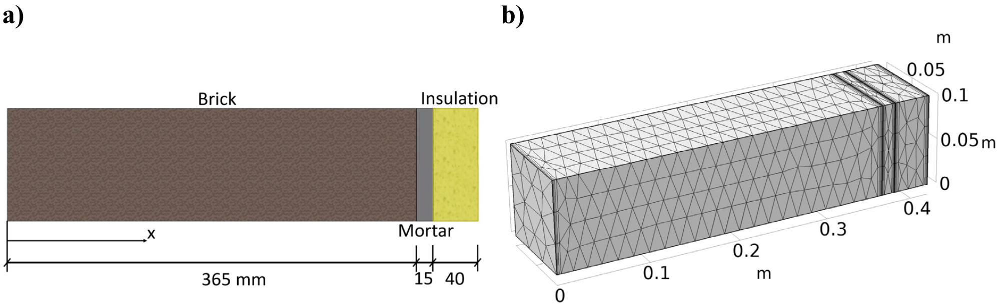

Fig. C.5.1 a) Benchmark object, b) Geometry and mesh setup, including boundary layers at all interfaces.

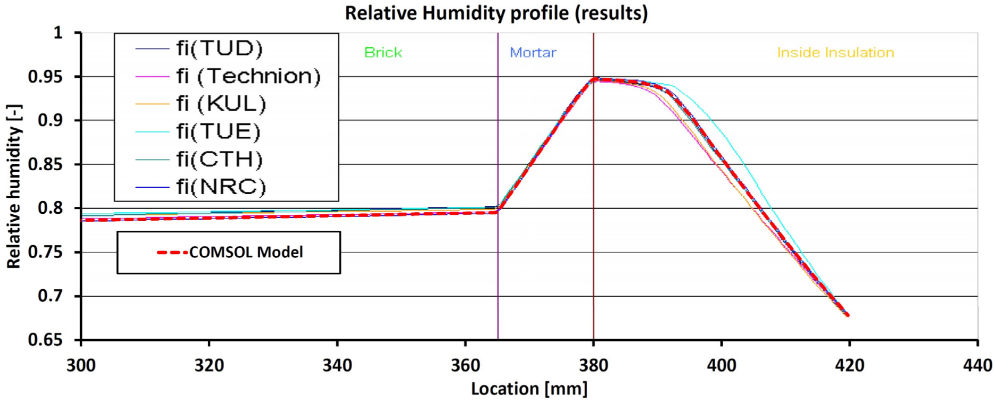

Fig. C.5.2 Relative humidity at end of day 60. Superposition of COMSOL model results over solutions from [121].

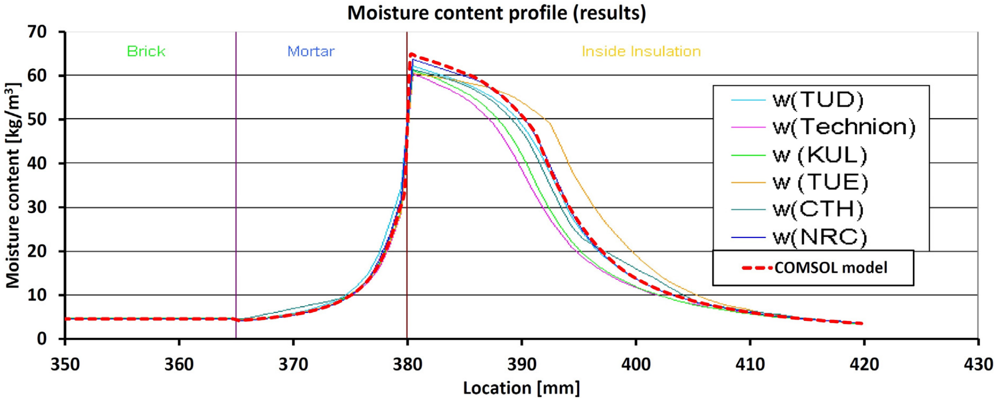

Fig. C.5.3 Moisture content at end of day 60. Superposition of COMSOL model results over solutions from [121].

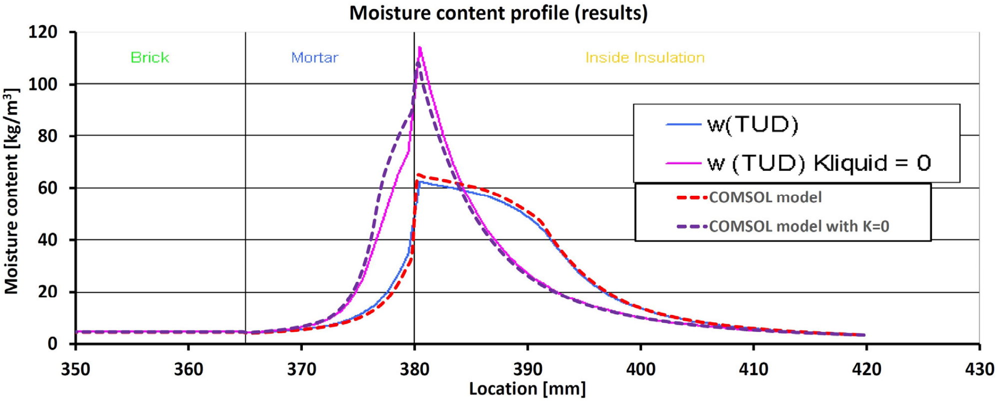

Fig. C.5.4 Moisture content with and without acting capillary conductivity for insulation layer at end of day 60. Superposition of COMSOL model results over solutions from [121].

References

[1] A. Brand, L. Allen, M. Altman, M. Hlava, J. Scott, Beyond authorship: attribution, contribution, collaboration, and credit, Learned Publishing 28(2) (2015) 151-155.

[2] Elsevier, CRediT author statement, 2019. https://www.elsevier.com/authors/policies-and-guidelines/credit-author-statement. (Accessed 12. Jan. 2022).

[3] P. Tuominen, K. Klobut, A. Tolman, A. Adjei, M. de Best-Waldhober, Energy savings potential in buildings and overcoming market barriers in member states of the European Union, Energy and Buildings 51 (2012) 48-55.

[4] L.C. Felius, F. Dessen, B.D. Hrynyszyn, Retrofitting towards energy-efficient homes in European cold climates: a review, Energy Efficiency 13(1) (2020) 101-125.

[5] T. Odgaard, S.P. Bjarløv, C. Rode, Interior insulation – Characterisation of the historic, solid masonry building segment and analysis of the heat saving potential by 1d, 2d, and 3d simulation, Energy and Buildings 162 (2018) 1-11.

[6] A. Blumberga, R. Freimanis, D. Blumberga, I. Veidenbergs, E.J. de Place Hansen, T.K. Hansen, G. Du, E. Stöcker, H. Sontag, P. Freudenberg, H. Janssen, S. Roels, E. di Gíuseppe, M. D'Orazio, A. Gianangeli, G. Maracchini, E. Quagliarini, E.B. Møller, C.M. Capener, L. Lång, P. Johansson, S. Lasvaux, M. Giorgi, D. Favre, P. Padey, G. Wagner, Written guidelines for decision making concerning the possible use of internal insulation in historic buildings, RIBuild, Robust Internal Thermal Insulation of Historic Buildings, 2020.

[7] M. Harrestrup, S. Svendsen, Full-scale test of an old heritage multi-storey building undergoing energy retrofitting with focus on internal insulation and moisture, Building and Environment 85 (2015) 123-133.

[8] E.D. Giuseppe, M. D'Orazio, C. Favi, M. Rossi, S. Lasvaux, P. Padey, D. Favre, K. Wittchen, G. Du, A. Nielsen, A. Blumberga, E. Kamendere, Report and tool: Probability based Life Cycle Impact Assessment, RIBuild, Robust Internal Thermal Insulation of Historic Buildings, 2019.

[9] P. Johansson, P. Wahlgren, Deterioration in brick buildings: hygrothermal performance and measures to save them, 12th Nordic Symposium on Building Physics (NSB 2020), E3S Web of Conferences, EDP Sciences, Tallinn University of Technology, Tallinn, Estonia, 2020.

[10] P. Freudenberg, Monitoring Data Basis of European Case Studies for Sound Performance Evaluation of Internal Insulation Systems Under Different Realistic Boundary Conditions, RIBuild, Robust Internal Thermal Insulation of Historic Buildings, 2019.

[11] V. Marincioni, V. Gori, E.J. de Place Hansen, D. Herrera-Avellanosa, S. Mauri, E. Giancola, A. Egusquiza, A. Buda, E. Leonardi, A. Rieser, How Can Scientific Literature Support Decision-Making in the Renovation of Historic Buildings? An Evidence-Based Approach for Improving the Performance of Walls, Sustainability 13(4) (2021) 2266.

[12] W.B. Rose, Should the Walls of Historic Buildings Be Insulated, APT Bulletin: The Journal of Preservation Technology 36(4) (2005) 13-18.

[13] X. Zhou, D. Derome, J. Carmeliet, Hygrothermal modeling and evaluation of freeze-thaw damage risk of masonry walls retrofitted with internal insulation, Building and Environment 125 (2017) 285-298.

[14] S. Sahyoun, H. Ge, M.A. Lacasse, M. Defo, Reliability of Existing Climate Indices in Assessing the Freeze-Thaw Damage Risk of Internally Insulated Masonry Walls, Buildings 11(10) (2021) 482.

[15] J. Straube, C. Schumacher, Interior Insulation Retrofits of Load-Bearing Masonry Walls in Cold Climates, Journal of Green Building 2(2) (2007) 42-50.

[16] H.M. Künzel, Effect of interior and exterior insulation on the hygrothermal behaviour of exposed walls, Materials and Structures 31(2) (1998) 99-103.

[17] M. Morelli, S. Svendsen, Investigation of interior post-insulated masonry walls with wooden beam ends, Journal of Building Physics 36(3) (2013) 265-293.

[18] X. Zhou, J. Carmeliet, D. Derome, Influence of envelope properties on interior insulation solutions for masonry walls, Building and Environment 135 (2018) 246-256.

[19] A.A. Hamid, P. Wallentén, Hygrothermal assessment of internally added thermal insulation on external brick walls in Swedish multifamily buildings, Building and Environment 123 (2017) 351-362.

[20] K. Ueno, J.W. Lstiburek, P. Eng, Field Monitoring of Embedded Wood Members in Insulated Masonry Walls in a Cold Climate, in: M. Bomberg, D. Yarbrough, J. Kosny (Eds.) Fourth BEST Conference Building Enclosure Science & Technology, The National Institute of Building Sciences, Kansas City, MO, United States, 2015.

[21] M. Harrestrup, S. Svendsen, Internal insulation applied in heritage multi-storey buildings with wooden beams embedded in solid masonry brick façades, Building and Environment 99 (2016) 59-72.

[22] T. Odgaard, S.P. Bjarløv, C. Rode, Interior insulation – Experimental investigation of hygrothermal conditions and damage evaluation of solid masonry façades in a listed building, Building and Environment 129 (2018) 1-14.

[23] R. Walker, S. Pavía, Thermal and moisture monitoring of an internally insulated historic brick wall, Building and Environment 133 (2018) 178-186.

[24] P. Wegerer, T. Bednar, Evaluating the hygrothermal performance of wooden beam heads in 19th century town houses using in-situ measurements, 7th International Building Physics Conference, IBPC2018, Syracuse, NY, USA, 2018.

[25] K. Keskküla, T. Aru, M. Kiviste, M.-J. Miljan, Hygrothermal Analysis of Masonry Wall with Reed Boards as Interior Insulation System, Energies 13(20) (2020) 5252.

[26] T. Martel, E. Rirsch, A. Simmonds, C. Walker, The monitoring of wall moisture in a property retrofitted with Internal Wall Insulation, Case Studies in Construction Materials 14 (2021) e00520.

[27] T. De Mets, A. Tilmans, X. Loncour, Hygrothermal assessment of internal insulation systems of brick walls through numerical simulation and full-scale laboratory testing, Energy Procedia 132 (2017) 753-758.

[28] N.F. Jensen, S.P. Bjarløv, C. Rode, T.R. Odgaard, Hygrothermal assessment of internally insulated solid masonry walls fitted with exterior hydrophobization and deliberate thermal bridge, ce/papers 2(4) (2018) 79-87.

[29] T. Odgaard, S.P. Bjarløv, C. Rode, Influence of hydrophobation and deliberate thermal bridge on hygrothermal conditions of internally insulated historic solid masonry walls with built-in wood, Energy and Buildings 173 (2018) 530-546.

[30] P. Kopecký, K. Staněk, M. Bureš, J. Richter, P. Ryparová, J. Tywoniak, Experimental investigations of wooden beam ends in masonry with interior insulation: Measured data in real-scale experimental walls exposed to semi-continental climatic conditions, Journal of Building Physics 43(3) (2019) 147-170.

[31] T. De Mets, A. Tilmans, Evaluation of the risk of decay of wooden beams embedded in internally insulated walls by long-term measurements, in: J. Kurnitski , T. Kalamees (Eds.) 12th

Nordic Symposium on Building Physics, E3S Web of Conferences, EDP Sciences, Tallinn, Estonia, 2020, p. 01002.

[32] N.F. Jensen, S.P. Bjarløv, C. Rode, E.B. Møller, Hygrothermal assessment of four insulation systems for interior retrofitting of solid masonry walls through calibrated numerical simulations, Building and Environment 180 (2020) 107031.

[33] N.F. Jensen, S.P. Bjarløv, C. Rode, B. Andersen, E.B. Møller, Hygrothermal performance of six insulation systems for internal retrofitting solid masonry walls, Journal of Building Physics 44(6) (2021) 539-573.

[34] X. Zhou, D. Derome, J. Carmeliet, Robust moisture reference year methodology for hygrothermal simulations, Building and Environment 110 (2016) 23-35.

[35] T. Van den Brande, B. Blocken, S. Roels, Rain water runoff from porous building facades: Implementation and application of a first-order runoff model coupled to a HAM model, Building and Environment 64 (2013) 177-186.

[36] E. Vereecken, S. Roels, Capillary active interior insulation systems for wall retrofitting: a more nuanced story, International Journal of Architectural Heritage 10(5) (2016) 558-569.

[37] H.L.S.C. Hens, Combined heat, air, moisture modelling: A look back, how, of help?, Building and Environment 91 (2015) 138-151.

[38] E. Vereecken, S. Roels, Wooden beam ends in combination with interior insulation: An experimental study on the impact of convective moisture transport, Building and Environment 148 (2019) 524-534.

[39] P. Johansson, S. Geving, C.-E. Hagentoft, B.P. Jelle, E. Rognvik, A.S. Kalagasidis, B. Time, Interior insulation retrofit of a historical brick wall using vacuum insulation panels: Hygrothermal numerical simulations and laboratory investigations, Building and Environment 79 (2014) 31-45.

[40] V. Kočí, M. Jerman, Z. Pavlík, J. Maděra, J. Žák, R. Černý, Interior thermal insulation systems based on wood fiberboards: experimental analysis and computational assessment of hygrothermal and energy performance in the Central European climate, Energy and Buildings 222 (2020) 110093.

[41] V. Kočí, J. Kočí, J. Maděra, Z. Pavlík, X. Gu, W. Zhang, R. Černý, Thermal and hygric assessment of an inside-insulated brick wall: 2D critical experiment and computational analysis, Journal of Building Physics 41(6) (2018) 497-520.

[42] T.K. Hansen, S.P. Bjarløv, R.H. Peuhkuri, M. Harrestrup, Long term in situ measurements of hygrothermal conditions at critical points in four cases of internally insulated historic solid masonry walls, Energy and Buildings 172 (2018) 235-248.

[43] E. Vereecken, S. Roels, Capillary active interior insulation: do the advantages really offset potential disadvantages?, Materials and Structures 48(9) (2015) 3009-3021.

[44] A. Martín-Garín, J.A. Millán-García, J. Terés-Zubiaga, X. Oregi, I. Rodríguez-Vidal, A. Baïri, Improving Energy Performance of Historic Buildings through Hygrothermal Assessment of the Envelope, Buildings 11(9) (2021) 410.

[45] E. Vereecken, L. Van Gelder, H. Janssen, S. Roels, Interior insulation for wall retrofitting – A probabilistic analysis of energy savings and hygrothermal risks, Energy and Buildings 89 (2015) 231-244.

[46] J. Zhao, J.J. Zhang, J. Grunewald, S. Feng, A probabilistic-based method to evaluate hygrothermal performance of an internally insulated brick wall, Building Simulation 14(2) (2021) 283-299.

[47] H. Janssen, P. Freudenberg, A. Tijskens, T. Hou, Basic probabilistic analysis of hygrothermal performance of interior insulation, RIBuild, Robust Internal Thermal Insulation of Historic Buildings KU Leuven, Leuven, Belgium, 2019, p. 108.

[48] E. Vereecken, S. Roels, Hygric performance of a massive masonry wall: How do the mortar joints influence the moisture flux?, Construction and Building Materials 41 (2013) 697-707.

[49] X. Zhou, J. Carmeliet, D. Derome, Assessment of moisture risk of wooden beam embedded in internally insulated masonry walls with 2D and 3D models, Building and Environment 193 (2021) 107460.

[50] M. Gutland, S. Bucking, M. Santana Quintero, Hygrothermal modelling of historic rubble masonry walls: Accounting for geometric and compositional variability, Journal of Building Engineering 48 (2022) 103929.

[51] H. Stopp, H. Fechner, P. Strangeld, P. Häupl, The Hygrothermal Performance of External Walls with Inside Insulation 2001.

[52] J. Zhao, J. Grunewald, U. Ruisinger, S. Feng, Evaluation of capillary-active mineral insulation systems for interior retrofit solution, Building and Environment 115 (2017) 215-227.

[53] S. Gatland, A. Karagiozis, C. Murray, K. Ueno, The hygrothermal performance of wood-framed wall systems using a relative humidity-dependent vapor retarder in the Pacific Northwest, ASHRAE Transaction (2007) 1-8.

[54] D. Derome, S. Saneinejad, Inward vapor diffusion due to high temperature gradients in experimentally tested large-scale wall assemblies, Building and Environment 45(12) (2010) 2790-2797.

[55] S. Geving, M. Stellander, S. Uvsløkk, Smart vapour barriers in compact wood frame roofs, American Society of Heating, Refrigeration, and Air-Conditioning Engineers (ASHRAE) (2013).

[56] P. Häupl, J. Grunewald, U. Ruisinger, Hygrothermal analysis of external walls within the reconstruction of the Rijksmuseum Amsterdam, WIT Transactions on The Built Environment 83 (2005).

[57] D. Kehl, U. Ruisinger, J. Plagge, J. Grunewald, Wooden beam ends in masonry with interior insulation - A literature review and simulation on causes and assesment of decay, in: A. Mahdavi, B. Martens (Eds.) 2nd Central European Symposium on Building Physics, Vienna University of Technology, Vienna, Austria, 2013, pp. 299-304.

[58] P. Johansson, B. Time, S. Geving, B.P. Jelle, A. Sasic Kalagasidis, C.-E. Hagentoft, E. Rognvik, Interior insulation retrofit of a brick wall using vacuum insulation panels: design of a laboratory study to determine the hygrothermal effect on existing structure and wooden beam ends, 12th International Conference on Thermal Performance of the Exterior Envelopes of Whole Buildings, ASHRAE, Clearwater, FL, USA, 2013.

[59] P. Häupl, K. Jurk, H. Petzold, Inside thermal insulation for historical facades, Second International Building Physics Conference, In-house publishing, Leuven, Belgium, 2003.

[60] J. Grunewald, U. Ruisinger, P. Häupl, The Rijksmuseum Amsterdam–hygrothermal analysis and dimensioning of thermal insulation, in: P. Fazio, H. Ge, J. Rao, G. Desmarais (Eds.) 3rd international building physics conference—research in building physics and building engineering, CRC Press, Montreal, Canada, 2006.

[61] P. Klõšeiko, E. Arumägi, T. Kalamees, Hygrothermal performance of internally insulated brick wall in cold climate: A case study in a historical school building, Journal of Building Physics 38(5) (2015) 444-464.

[62] M. Guizzardi, J. Carmeliet, D. Derome, Risk analysis of biodeterioration of wooden beams embedded in internally insulated masonry walls, Construction and Building Materials 99 (2015) 159-168.

[63] G.R. Finken, S.P. Bjarløv, R.H. Peuhkuri, Effect of façade impregnation on feasibility of capillary active thermal internal insulation for a historic dormitory – A hygrothermal simulation study, Construction and Building Materials 113 (2016) 202-214.

[64] J. Knarud, S. Geving, T. Kvande, Hygrothermal simulations of internally insulated massive masonry walls exposed to driving rain in cold climate, in: J. Arfvidsson, L.-E. Harderup, A. Kumlin, B. Rosencrantz (Eds.) 10th Nordic Symposium on Building Physics, LTH, Lund University: Lund, Sweden, 2014, pp. 1141-1148.

[65] C.J.W.P. Groot, J.T.M. Gunneweg, The influence of materials characteristics and workmanship on rain penetration in historic fired clay brick masonry, HERON 55 (2) (2010) 141-153.

[66] B. Blocken, D. Derome, J. Carmeliet, Rainwater runoff from building facades: A review, Building and Environment 60 (2013) 339-361.

[67] H.J.P. Brocken, Moisture transport in brick masonry: the grey area between bricks, Department of the Built Environment, Technische Universiteit Eindhoven, Eindhoven, Netherlands, 1998.

[68] H. Derluyn, H. Janssen, J. Carmeliet, Influence of the nature of interfaces on the capillary transport in layered materials, Construction and Building Materials 25(9) (2011) 3685-3693.

[69] H. Janssen, H. Derluyn, J. Carmeliet, Moisture transfer through mortar joints: A sharp-front analysis, Cement and Concrete Research 42(8) (2012) 1105-1112.

[70] M. Morelli, G.A. Scheffler, T.R. Nielsen, S. Svendsen, Internal insulation of masonry walls with wooden floor beams in northern humid climate, 11th International Conference on Thermal Performance of the Exterior Envelopes of Whole Buildings, ASHRAE, Clearwater Beach, FL, USA, 2010, pp. 89-100.

[71] K. Ueno, Masonry Wall Interior Insulation Retrofit Embedded Beam Simulations, Building Enclosure Science & Technology (BEST3) Conference, Building Science Press, Atlanta, GA, USA, 2012.

[72] T. Defraeye, B. Blocken, J. Carmeliet, Influence of uncertainty in heat–moisture transport properties on convective drying of porous materials by numerical modelling, Chemical Engineering Research and Design 91(1) (2013) 36-42.

[73] C.-E. Hagentoft, A.S. Kalagasidis, B. Adl-Zarrabi, S. Roels, J. Carmeliet, H. Hens, J. Grunewald, M. Funk, R. Becker, D. Shamir, Assessment method of numerical prediction models for combined heat, air and moisture transfer in building components: benchmarks for one-dimensional cases, Journal of thermal envelope and building science 27(4) (2004) 327-352.

[74] J. Zhao, R. Plagge, N.M. Ramos, M.L. Simões, J. Grunewald, Application of clustering technique for definition of generic objects in a material database, Journal of Building Physics 39(2) (2015) 124-146.

[75] J. Zhao, R. Plagge, N.M.M. Ramos, M. Lurdes Simões, J. Grunewald, Concept for development of stochastic databases for building performance simulation – A material database pilot project, Building and Environment 84 (2015) 189-203.

[76] S. Panico, M. Larcher, V. Marincioni, A. Troi, C. Baglivo, P.M. Congedo, Identifying key parameters through a sensitivity analysis for realistic hygrothermal simulations at wall level supported by monitored data, Building and Environment 229 (2023) 109969.

[77] J. Grunewald, P. Häupl, M. Bomberg, Towards an Engineering Model of Material Characteristics for Input to Ham Transport Simulations - Part 1: An Approach, Journal of Thermal Envelope and Building Science 26(4) (2003) 343-366.

[78] J. Carmeliet, H. Janssen, H. Derluyn, An improved moisture diffusivity model for porous building materials, in: P. Häupl, J. Roloff (Eds.) Proceedings of 12th Symposium for Building Physics, Dresden, Germany, 2007.

[79] G.A. Scheffler, R. Plagge, A whole range hygric material model: Modelling liquid and vapour transport properties in porous media, International Journal of Heat and Mass Transfer 53(1) (2010) 286-296.

[80] D. Derome, A. Kubilay, T. Defraeye, B. Blocken, J. Carmeliet, Ten questions concerning modeling of wind-driven rain in the built environment, Building and Environment 114 (2017) 495-506.

[81] I. Vandemeulebroucke, L. Kotova, S. Caluwaerts, N. Van Den Bossche, Degradation of brick masonry walls in Europe and the Mediterranean: Advantages of a response-based analysis to study climate change, Building and Environment 230 (2023) 109963.

[82] P. Johansson, L. Lång, C.-M. Capener, How well do mould models predict mould growth in buildings, considering the end-user perspective?, Journal of Building Engineering 40 (2021) 102301.

[83] X. Zhou, D. Derome, J. Carmeliet, Analysis of moisture risk in internally insulated masonry walls, Building and Environment 212 (2022) 108734.

[84] G. Scheffler, Validation of hygrothermal material modelling under consideration of the hysteresis of moisture storage, Faculty of Civil Engineering, Dresden University of Technology, Dresden, Germany, 2008.

[85] C. Feng, H. Janssen, Hygric properties of porous building materials (VII): Full-range benchmark characterizations of three materials, Building and Environment 195 (2021) 107727.

[86] NS-EN 772-11, Methods of test for masonry units - Part 11: Determination of water absorption of aggregate concrete, autoclaved aerated concrete, manufactured stone and natrual stone masonry units due to capillary action and the initial rate of water absorption of clay masonry units, European Committee for Standardization (CEN), Brussels, Belgium, 2011.

[87] I. Vandemeulebroucke, S. Caluwaerts, N. Van Den Bossche, Decision framework to select moisture reference years for hygrothermal simulations, Building and Environment 218 (2022) 109080.

[88] S. Kim, D. Zirkelbach, H.M. Künzel, Review of Methods to Create Meteorological Data Suitable for Moisture Control Design by Hygrothermal Building Envelope Simulation, Energies 16(7) (2023) 3271.

[89] S. Geving, J. Holme, Vapour retarders in wood frame walls and their effect on the drying capability, Frontiers of Architectural Research 2(1) (2013) 42-49.

[90] T.R. Odgaard, Challenges when retrofitting multi-storey buildings with interior thermal insulation, Department of Civil Engineering, Technical University of Denmark Lyngby, Denmark, 2019.

[91] T.K. Hansen, Hygrothermal performance of internal insulation in historic buildings, Department of Civil Engineering, Technical University of Denmark, Lyngby, Denmark, 2019.

[92] U. Ruisinger, Das hygrothermische Verhalten von Balkenköpfen bei innen gedämmten Gebäuden, Institut für Hochbau, Technischen Universität Graz, Dresden, Germany, 2019.

[93] K. Calle, Renovation of historical facades: The rescue or the kiss of death?, Faculteit Ingenieurswetenschappen en Architectuur, Vakgroep Architectuur en Stedenbouw, Ghent University, Ghent, Belgium, 2020.

[94] V. Marincioni, A probabilistic approach for the moisture risk assessment of internally insulated solid walls, Institute for Environmental Design and Engineering, UCL (University College London), London, UK, 2020.

[95] N.F. Jensen, Robust solutions for internal retrofitting solid masonry walls in historic buildings with regards to hygrothermal performance, Department of Civil Engineering, Technical University of Denmark, Lyngby, Denmark, 2021.

[96] V. Soulios, Hygrothermal Performance of Hydrophobized Brick and Mortar: Energy Renovation Through Internal Insulation-Can Hydrophobization Improve the Moisture Safety?, Department of the Build Environment, Aalborg University, Aalborg, Denmark, 2021.

[97] M.J. Gutland, Evaluating Uncertainty in Hygrothermal Modelling of Heritage Masonry Buildings, Carleton University, Ottawa, Canada, 2022.

[98] P. Klõšeiko, Hygrothermal Performance of Masonry Walls Retrofitted with Interior Insulation in Cold Climate, Department of Civil Engineering and Architecture, Tallinn University of Technology, Tallinn, Estonia, 2022.

[99] W. Zheng, C. Shen, L.-P. Wang, Y. Jin, An empirical soil water retention model based on probability laws for pore-size distribution, Vadose Zone Journal 19(1) (2020) e20065.

[100] C. Hagentoft, HAMSTAD–WP2 Modeling, Report R-02: 9, Building Physics, Chalmers University of Technology, Gothenburg, Sweden 2002.

[101] Q. Li, J. Rao, P. Fazio, Development of HAM tool for building envelope analysis, Building and Environment 44(5) (2009) 1065-1073.

[102] M.T. Van Genuchten, A closed-form equation for predicting the hydraulic conductivity of unsaturated soils, Soil Science Society of America Journal 44(5) (1980) 892-898.

[103] W. Durner, Hydraulic conductivity estimation for soils with heterogeneous pore structure, Water Resources Research 30(2) (1994) 211-223.

[104] T.K.D. Weber, W. Durner, T. Streck, E. Diamantopoulos, A Modular Framework for Modeling Unsaturated Soil Hydraulic Properties Over the Full Moisture Range, Water Resources Research 55(6) (2019) 4994-5011.

[105] H. Janssen, Comment on Cabrera et al. A User-Friendly Tool to Characterize the Moisture Transfer in Porous Building Materials: FLoW1D. Appl. Sci. 2020, 10, 5090, Applied Sciences 12(3) (2022) 1123.

[106] J. Carmeliet, S. Roels, Determination of the Moisture Capacity of Porous Building Materials, Journal of Thermal Envelope and Building Science 25(3) (2002) 209-237.

[107] A. Revil, N. Lu, Unified water isotherms for clayey porous materials, Water Resources Research 49(9) (2013) 5685-5699.

[108] C. Feng, H. Janssen, C. Wu, Y. Feng, Q. Meng, Validating various measures to accelerate the static gravimetric sorption isotherm determination, Building and Environment 69 (2013) 64-71.

[109] M. Lebeau, J.-M. Konrad, A new capillary and thin film flow model for predicting the hydraulic conductivity of unsaturated porous media, Water Resources Research 46(12) (2010) W12554.

[110] K. Chen, F. Liang, C. Wang, A fractal hydraulic model for water retention and hydraulic conductivity considering adsorption and capillarity, Journal of Hydrology 602 (2021) 126763.

[111] A. Peters, Simple consistent models for water retention and hydraulic conductivity in the complete moisture range, Water Resources Research 49(10) (2013) 6765-6780.

[112] N. Lu, Generalized Soil Water Retention Equation for Adsorption and Capillarity, Journal of Geotechnical and Geoenvironmental Engineering 142(10) (2016) 04016051.

[113] W. Zheng, X. Yu, Y. Jin, Considering surface roughness effects in a triangular pore space model for unsaturated hydraulic conductivity, Vadose Zone Journal 14(7) (2015) vzj2014. 09.0121.

[114] F. Stanić, P. Delage, I. Tchiguirinskaia, P.-A. Versini, Y.-J. Cui, D. Schertzer, A New Fractal Approach to Account for Capillary and Adsorption Phenomena in the Water Retention and Transfer Properties of Unsaturated Soils, Water Resources Research 56(12) (2020) e2020WR027808.

[115] J. Carmeliet, S. Roels, Determination of the isothermal moisture transport properties of porous building materials, Journal of Building Physics 24(3) (2001) 183-210.

[116] A. Fang, Y. Chen, L. Wu, Modeling and numerical investigation for hygrothermal behavior of porous building envelope subjected to the wind driven rain, Energy and Buildings 231 (2021) 110572.

[117] J. Grunewald, P. Häupl, Ein Modell zur Beschreibung der feuchteabhängigen Dampfleitfähigkeit kapillarporöser Materialien, 11th Symposium on Building Climatology, Technische Universität Dresden, Dresden, Germany, 2002, pp. 286-294.

[118] R. Schirmer, Die Diffusionszahl von Wasserdampf-Luft-Gemischen und die Verdampfungsgeschwindigkeit, VDI-Verlag, Beiheft VDI-Zeitschrift, Verfahrenstechnik, 1938, pp. 170-177.

[119] G. Scheffler, R. Plagge, P. Häupl, Hygrische Materialmodellierung und ihre Abhängigkeit vom Prozess und der Prozessdynamik, Bauphysik 29(3) (2007) 164-177.

[120] J. Zhao, R. Plagge, Characterization of hygrothermal properties of sandstones—Impact of anisotropy on their thermal and moisture behaviors, Energy and Buildings 107 (2015) 479-494.

[121] C.-E. Hagentoft, HAMSTAD, Final report: Methodology of HAM-modeling, Chalmers University of Technology, Gothenburg, Sweden, 2002.

[122] J. Carmeliet, H. Hens, S. Roels, O. Adan, H. Brocken, R. Cerny, Z. Pavlik, C. Hall, K. Kumaran, L. Pel, Determination of the Liquid Water Diffusivity from Transient Moisture Transfer Experiments, Journal of Thermal Envelope and Building Science 27(4) (2004) 277-305.

[123] F. Descamps, Continuum and discrete modelling of isothermal water and air transfer in porous media, Building physics laboratory, Katholieke Universiteit Leuven, Leuven, Belgium, 1997.

[124] H.M. Künzel, Simultaneous heat and moisture transport in building components, Fraunhofer IRB-Verlag, Stuttgart, Germany, 1995.

[125] R. Ramirez, B. Ghiassi, P. Pineda, P.B. Lourenço, Simulation of moisture transport in fired-clay brick masonry structures accounting for interfacial phenomena, Building and Environment 228 (2023) 109838.

[126] I. Gómez, J.M. Sala, J.A. Millán, Characterization of Moisture Transport Properties for Lightened Clay Brick — Comparison Between Two Manufacturers, Journal of Building Physics 31(2) (2007) 179-194.

[127] K.M. Graczyk, M. Matyka, Predicting porosity, permeability, and tortuosity of porous media from images by deep learning, Scientific Reports 10(1) (2020) 21488.

[128] T. Bandai, T.A. Ghezzehei, Physics-Informed Neural Networks With Monotonicity Constraints for Richardson-Richards Equation: Estimation of Constitutive Relationships and Soil Water Flux Density From Volumetric Water Content Measurements, Water Resources Research 57(2) (2021) e2020WR027642.

[129] Y. Mualem, A new model for predicting the hydraulic conductivity of unsaturated porous media, Water Resources Research 12(3) (1976) 513-522.

[130] A.G. Hunt, R.P. Ewing, R. Horton, What's Wrong with Soil Physics?, Soil Science Society of America Journal 77(6) (2013) 1877-1887.

[131] J. Carmeliet, F. Descamps, G. Houvenaghel, A Multiscale Network Model for Simulating Moisture Transfer Properties of Porous Media, Transp Porous Med 35(1) (1999) 67-88.

[132] P. Van Marcke, B. Verleye, J. Carmeliet, D. Roose, R. Swennen, An Improved Pore Network Model for the Computation of the Saturated Permeability of Porous Rock, Transp Porous Med 85(2) (2010) 451-476.

[133] M. Islahuddin, H. Janssen, Pore-Structure-Based Determination of Unsaturated Hygric Properties of Porous Materials, Transp Porous Med 130(3) (2019) 675-698.

[134] S. Roels, J. Carmeliet, H. Hens, Modelling Unsaturated Moisture Transport in Heterogeneous Limestone, Transp Porous Med 52(3) (2003) 333-350.

[135] N.T. Burdine, Relative permeability calculations from pore size distribution data, Petroleum Transactions, AIME 198 (1953) 71-78.

[136] E. Diamantopoulos, W. Durner, Physically-based model of soil hydraulic properties accounting for variable contact angle and its effect on hysteresis, Advances in Water Resources 59 (2013) 169-180.

[137] M. Bianchi Janetti, H. Janssen, Effect of dynamic contact angle variation on spontaneous imbibition in porous materials, Transp Porous Med 142(3) (2022) 493-508.

[138] M. Van Belleghem, M. Steeman, H. Janssen, A. Janssens, M. De Paepe, Validation of a coupled heat, vapour and liquid moisture transport model for porous materials implemented in CFD, Building and Environment 81 (2014) 340-353.

[139] H. Derluyn, P. Moonen, J. Carmeliet, Moisture transfer across the interface between brick and mortar joint, in: C. Rode (Ed.) Proceedings of the 8th symposium on building physics in the nordic countries, Technical University of Denmark, Copenhagen, Denmark, 2008, pp. 865-872.

[140] J. Zhao, S. Feng, J. Grunewald, F. Meissner, J. Wang, Drying characteristics of two capillary porous building materials: Calcium silicate and ceramic brick, Building and Environment 216 (2022) 109006.

[141] M. Jerman, R. Černý, Effect of moisture content on heat and moisture transport and storage properties of thermal insulation materials, Energy and Buildings 53 (2012) 39-46.

[142] V. Kočí, E. Vejmelková, M. Čáchová, D. Koňáková, M. Keppert, J. Maděra, R. Černý, Effect of moisture content on thermal properties of porous building materials, Int J Thermophys 38(2) (2017) 28.

[143] Fraunhofer, WUFI 2D 4.2, Fraunhofer IBP, Germany, 2019.

[144] F. Ochs, W. Heidemann, H. Müller-Steinhagen, Effective thermal conductivity of moistened insulation materials as a function of temperature, International Journal of Heat and Mass Transfer 51(3–4) (2008) 539-552.

[145] E. Vereecken, S. Roels, A numerical study of the hygric performance of a masonry wall, 9th International Masonry Conference, Universidade do Minho, International Masonry Society, Guimaraes, Portugal, 2014.

[146] Q. Li, Development of a hygrothermal simulation tooil (HAM-BE) for building envelope study, Building, Civil and Environmental Engineering, Concordia University, Montreal, Quebec, Canada, 2008.

[147] A. Abdou, I. Budaiwi, The variation of thermal conductivity of fibrous insulation materials under different levels of moisture content, Construction and Building Materials 43 (2013) 533-544.

[148] Y. Liu, C. Ma, D. Wang, Y. Wang, J. Liu, Nonlinear Effect of Moisture Content on Effective Thermal Conductivity of Building Materials with Different Pore Size Distributions, Int J Thermophys 37(6) (2016) 56.

[149] B. Ghanbarian, H. Daigle, Thermal conductivity in porous media: Percolation-based effective-medium approximation, Water Resources Research 52(1) (2016) 295-314.

[150] A. Revil, Thermal conductivity of unconsolidated sediments with geophysical applications, Journal of Geophysical Research: Solid Earth 105(B7) (2000) 16749-16768.

[151] X. Qin, J. Cai, P. Xu, S. Dai, Q. Gan, A fractal model of effective thermal conductivity for porous media with various liquid saturation, International Journal of Heat and Mass Transfer 128 (2019) 1149-1156.

[152] Y. Shen, P. Xu, S. Qiu, B. Rao, B. Yu, A generalized thermal conductivity model for unsaturated porous media with fractal geometry, International Journal of Heat and Mass Transfer 152 (2020) 119540.

[153] Z. Chu, G. Zhou, R. Li, Enhanced fractal capillary bundle model for effective thermal conductivity of composite-porous geomaterials, International Communications in Heat and Mass Transfer 113 (2020) 104527.

[154] H.-Q. Jin, X.-L. Yao, L.-W. Fan, X. Xu, Z.-T. Yu, Experimental determination and fractal modeling of the effective thermal conductivity of autoclaved aerated concrete: Effects of moisture content, International Journal of Heat and Mass Transfer 92 (2016) 589-602.

[155] Y. Wang, C. Ma, Y. Liu, D. Wang, J. Liu, A model for the effective thermal conductivity of moist porous building materials based on fractal theory, International Journal of Heat and Mass Transfer 125 (2018) 387-399.

[156] C. Langerock, A. Tilmans, T. De Mets, X. Loncour, E. Nguyen, S. Charron, B. Michaux, Hygrothermal behaviour of compact roofs in wood frame constructions through on-site measurements, Energy Procedia 132 (2017) 813-818.

[157] M. Steeman, N. Van Den Bossche, K. Calle, Drying potential of wood frame walls subjected to accidental water infiltration, in: C. Serrat, J.R. Casas, V. Gibert (Eds.) XV International Conference on Durability of Building Materials and Components (DBMC 2020), International Center for Numerical Methods in Engineering (CIMNE), Barcelona, Spain, 2020, pp. 945-952.

[158] K.G. Wakili, T. Frank, A humidity dependent vapour retarder in non-ventilated flat roofs. In situ measurements and numerical analysis, Indoor and Built Environment 13(6) (2004) 433-441.

[159] N.S. Bunkholt, L. Gullbrekken, S. Geving, T. Kvande, Compact wooden roofs with smart vapour barrier–Pilot project experiences, 12th Nordic Symposium on Building Physics (NSB 2020), E3S Web of Conferences, EDP Sciences, Tallinn University of Technology, Tallinn, Estonia, 2020, p. 07010.

[160] N.S. Bunkholt, L. Gullbrekken, B. Time, T. Kvande, Pitched unventilated wood frame roof with smart vapour barrier – field measurements, Journal of Physics: Conference Series 2069(1) (2021) 012007.

[161] S. Geving, E. Thorsrud, S. Uvsløkk, The performance of unventilated wooden roofs with smart vapour barriers during winter conditions, in: J. Arfvidsson, L.-E. Harderup, A. Kumlin, B. Rosencrantz (Eds.) Proceedings of the 10th Nordic Symposium on Building Physics (NSB 2014), LTH, University of Lund, Lund, Sweden, 2014, pp. 207-14.

[162] F. Tariku, W. Maref, B. Di Lenardo, S. Gatland, Hygrothermal performance of RH-dependent vapour retarder in Canadian coastal climate, 12th Canadian Conference of Building Science and Technology Montreal, QC, Canada, 2009.

[163] M. Yoshinaga, Performance of smart vapor retarders under hot and humid summer conditions, Building and Environment 218 (2022) 109163.

[164] H. Fechner, F. Meißner, Advanced modelling of vapor resistance of moisture dependent vapor retarder, Energy Procedia 132 (2017) 201-206.

[165] T.S. Olaoye, M. Dewsbury, H. Künzel, Laboratory Measurement and Boundary Conditions for the Water Vapour Resistivity Properties of Typical Australian Impermeable and Smart Pliable Membranes, Buildings 11(11) (2021) 509.

[166] T.S. Olaoye, M. Dewsbury, L. Wallis, H. Küenzel, Hygrothermal Modelling of the Differences between Single versus Variable Relative Humidity Vapour Diffusion Resistivity Properties of Pliable Membranes, CivilEng 3(3) (2022) 687-716.

[167] S.J. Chang, S. Wi, S.G. Kang, S. Kim, Moisture risk assessment of cross-laminated timber walls: Perspectives on climate conditions and water vapor resistance performance of building materials, Building and Environment 168 (2020) 106502.

[168] X. Zhou, G. Desmarais, P. Vontobel, J. Carmeliet, D. Derome, Masonry brick–cement mortar interface resistance to water transport determined with neutron radiography and numerical modeling, Journal of Building Physics 44(3) (2020) 251-271.

[169] M. Gutland, S. Bucking, M. Santana Quintero, A methodology for hygrothermal modelling of imperfect masonry interfaces, Journal of Building Physics 44(6) (2021) 485-509.

[170] R. Ramirez, B. Ghiassi, P. Pineda, P.B. Lourenço, Experimental characterization of moisture transport in brick masonry with natural hydraulic lime mortar, Building and Environment 205 (2021) 108256.

[171] H. Janssen, H. Derluyn, J. Carmeliet, Moisture transfer through mortar joints: interface resistances or hygric property changes, Proceedings to the 12th Symposium for Building Physics Dresden University at Technology, Institute of Building Climatology, Dresden, Germany, 2007, pp. 808-815.

[172] K. Calle, T. De Kock, V. Cnudde, N. Van den Bossche, Liquid moisture transport in combined ceramic brick and natural hydraulic lime mortar samples: Does the hygric interface resistance dominate the moisture transport?, Journal of Building Physics 43(3) (2019) 208-228.

[173] P. Wegerer, T. Bednar, Hygrothermal performance of wooden beam heads in inside insulated walls considering air flows, Energy Procedia 132 (2017) 652-657.

[174] M.B. Janetti, Hygrothermal Analysis of Building Components Inclosing Air Cavities: Comparison between Different Modeling Approaches and Experimental Results, Institut für Konstruktion und Materialwissenschaften, University of Innsbruck, Innsbruck, Austria, 2015.

[175] J. Zhao, S. Feng, Z. Kou, F. Meissner, U. Ruisinger, J. Grunewald, Characterization of hygrothermal properties of two wood species- the impact of anisotropy on their thermal and moisture behaviors, Construction and Building Materials 398 (2023) 132375.

[176] U. Ruisinger, P. Kautsch, Comparison of hygrothermal 2D- and 3D-simulation results with measurements from a test house, 12th Nordic Symposium on Building Physics (NSB 2020) E3S Web Conf., Tallinn University of Technology, Tallinn, Estonia, 2020, p. 08004.

[177] T.K. Hansen, S.P. Bjarløv, R. Peuhkuri, Moisture transport properties of brick–comparison of exposed, impregnated and rendered brick, International RILEM Conference on Materials, Systems and Structures in Civil Engineering, segment on Moisture in Materials and Structures, Lyngby, Denmark, 2016, pp. 351-360.

[178] V. Soulios, E. Jan de Place Hansen, R. Peuhkuri, Hygrothermal performance of hydrophobized and internally insulated masonry walls - Simulating the impact of hydrophobization based on experimental results, Building and Environment 187 (2021) 107410.

[179] S. Kraus, M. Breier, W.M. Lim, M. Dabić, S. Kumar, D. Kanbach, D. Mukherjee, V. Corvello, J. Piñeiro-Chousa, E. Liguori, D. Palacios-Marqués, F. Schiavone, A. Ferraris, C. Fernandes, J.J. Ferreira, Literature reviews as independent studies: guidelines for academic practice, Review of Managerial Science 16(8) (2022) 2577-2595.

[180] S.K. Boell, D. Cecez-Kecmanovic, On being 'systematic'in literature reviews in IS, Journal of Information Technology 30 (2015) 161-173.

[181] F. Rowe, What literature review is not: diversity, boundaries and recommendations, European Journal of Information Systems 23(3) (2014) 241-255.

[182] M.T. Pham, A. Rajić, J.D. Greig, J.M. Sargeant, A. Papadopoulos, S.A. McEwen, A scoping review of scoping reviews: advancing the approach and enhancing the consistency, Research Synthesis Methods 5(4) (2014) 371-385.

[183] M.N.K. Saunders, C. Rojon, On the attributes of a critical literature review, Coaching: An International Journal of Theory, Research and Practice 4(2) (2011) 156-162.

[184] J. Filliben, A. Heckert, Kolmogorov-Smirnov Goodness-of-Fit Test, in: C.T. Croarkin, Paul (Ed.) NIST/SEMATECH e-Handbook of Statistical Methods, NIST, 2022.

[185] J. Prins, D. McCormack, D. Michelson, K. Horrell, Sample sizes required, in: C.T. Croarkin, Paul (Ed.) NIST/SEMATECH e-Handbook of Statistical Methods, NIST, 2022.

[186] EN ISO 12572, Hygrothermal performance of building materials and products - Determination of water vapour transmission properties, European Committee for Standardization (CEN), Brussels, Belgium, 2001.

[187] EN ISO 12571, Hygrothermal performance of building materials and products - Determination of hygroscopic sorption properties, European Committee for Standardization (CEN), Brussels, Belgium, 2013.

[188] M. Bomberg, M. Pazera, R. Plagge, Analysis of Selected Water Absorption Coefficient Measurements, Journal of Thermal Envelope and Building Science 28(3) (2005) 227-243.

[189] EN ISO 15148, Hygrothermal performance of building materials and products - Determination of water absorption coefficient by partial immersion, European Committee for Standardization (CEN), Brussels, Belgium, 2003.

[190] B. Sundström, The Development of a European Fire Classification System for Building Products-Test Methods and Mathematical Modelling, Department of Fire Safety Engineering, Lund Institute of Technology, Lund University, Lund, Sweden, 2007.

[191] B. Sundström, The relantionship of the SBI test to the reference scenario, Fire Safe Products in Construction: A Benefit of the Construction Products Directive, European Commission, EGOLF (European Group Organisations for Fire Testing, Inspection and Certification) and EAFP (the European Association for Passive Fire Protection), Luxembourg, 1999.

[192] P. Isaias, T. Issa, High level models and methodologies for information systems, Springer, Birkbeck, University of London, London, UK, 2015.

[193] I. Graessler, J. Hentze, The new V-Model of VDI 2206 and its validation, at - Automatisierungstechnik 68(5) (2020) 312-324.

[194] P.J. Durst, D.T. Anderson, C.L. Bethel, A historical review of the development of verification and validation theories for simulation models, International Journal of Modeling, Simulation, and Scientific Computing 08(02) (2017) 1730001.

[195] A.C. Calder, B. Fryxell, T. Plewa, R. Rosner, L.J. Dursi, V.G. Weirs, T. Dupont, H.F. Robey, J.O. Kane, B.A. Remington, R.P. Drake, G. Dimonte, M. Zingale, F.X. Timmes, K. Olson, P. Ricker, P. MacNeice, H.M. Tufo, On Validating an Astrophysical Simulation Code, The Astrophysical Journal Supplement Series 143(1) (2002) 201.

[196] W.L. Oberkampf, T.G. Trucano, Verification and validation in computational fluid dynamics, Progress in Aerospace Sciences 38(3) (2002) 209-272.

[197] W.L. Oberkampf , T.G. Trucano , C. Hirsch Verification, validation, and predictive capability in computational engineering and physics, Applied Mechanics Reviews 57(5) (2004) 345-384.

[198] D. Sornette, A.B. Davis, J.R. Kamm, K. Ide, A General Strategy for Physics-Based Model Validation Illustrated with Earthquake Phenomenology, Atmospheric Radiative Transfer, and Computational Fluid Dynamics, in: T. Barth, M. Griebel, D. Keyes, R. Nieminen, D. Roose, T. Schlick (Eds.), Computational Methods in Transport: Verification and Validation, Springer, Berlin, Heidelberg, 2008, pp. 19-73.

[199] S. Sankararaman, S. Mahadevan, Integration of model verification, validation, and calibration for uncertainty quantification in engineering systems, Reliability Engineering & System Safety 138 (2015) 194-209.

[200] R.G. Sargent, Validation of simulation models, Institute of Electrical and Electronics Engineers (IEEE), 1979.

[201] H.E. Huerto-Cardenas, F. Leonforte, N. Aste, C. Del Pero, G. Evola, V. Costanzo, E. Lucchi, Validation of dynamic hygrothermal simulation models for historical buildings: State of the art, research challenges and recommendations, Building and Environment 180 (2020) 107081.

[202] S. Dubois, F. Lebeau, A. Evrard, Non-isothermal moisture balance equation in porous media: a review of mathematical formulations in Building Physics, Biotechnologie, Agronomie, Société et Environnement 18(3) (2014).

[203] K. Calle, N. Van Den Bossche, Sensitivity analysis of the hygrothermal behaviour of homogeneous masonry constructions: Interior insulation, rainwater infiltration and hydrophobic treatment, Journal of Building Physics 44(6) (2021) 510-538.

[204] R. Sarfati, D.K. Schwartz, Temporally Anticorrelated Subdiffusion in Water Nanofilms on Silica Suggests Near-Surface Viscoelasticity, ACS Nano 14(3) (2020) 3041-3047.

[205] D. Wang, Y. Tian, L. Jiang, Abnormal Properties of Low-Dimensional Confined Water, Small 17(31) (2021) 2100788.

[206] S. Wang, F. Javadpour, Q. Feng, Confinement Correction to Mercury Intrusion Capillary Pressure of Shale Nanopores, Scientific Reports 6(1) (2016) 20160.

[207] V.I. Nikitsin, B. Backiel-Brzozowska, Determining hydraulic radii of construction wall materials in capillary moisture transfer, International Journal of Heat and Mass Transfer 88 (2015) 558-564.

[208] C. Feng, A.S. Guimarães, N. Ramos, L. Sun, D. Gawin, P. Konca, C. Hall, J. Zhao, H. Hirsch, J. Grunewald, M. Fredriksson, K.K. Hansen, Z. Pavlík, A. Hamilton, H. Janssen, Hygric properties of porous building materials (VI): A round robin campaign, Building and Environment 185 (2020) 107242.

[209] H.S.L.C. Hens, The vapor diffusion resistance and air permeance of masonry and roofing systems, Building and Environment 41(6) (2006) 745-755.

[210] E. Vereecken, W. Van De Walle, S. Roels, A novel and flexible test setup to measure the vapour diffusion resistance of building materials and wall components, in: R. Černý, J. Kočí,

V. Kočí (Eds.) 4th Central European Symposium on Building Physics (CESBP 2019), MATEC Web of Conferences, EDP Sciences, Prague, Czech Republic, 2019.

[211] S. Kahangi Shahreza, J. Niklewski, M. Molnár, Novel water penetration criterion for clay brick masonry claddings, Construction and Building Materials 353 (2022) 129109.

[212] K. Calle, C. Coupillie, A. Janssens, N. Van Den Bossche, Implementation of rainwater infiltration measurements in hygrothermal modelling of non-insulated brick cavity walls, Journal of Building Physics 43(6) (2019) 477-502.

[213] H.J. Moon, Assessing mold risks in buildings under uncertainty, College of Architecture, Georgia Institute of Technology, Atlanta, GA, USA, 2005.

[214] F. Tariku, K. Kumaran, P. Fazio, Transient model for coupled heat, air and moisture transfer through multilayered porous media, International Journal of Heat and Mass Transfer 53 (2010) 3035-3044.

[215] A. Fang, Y. Chen, L. Wu, Transient simulation of coupled heat and moisture transfer through multi-layer walls exposed to future climate in the hot and humid southern China area, Sustainable Cities and Society 52 (2020) 101812.

[216] K. Calle, N. Van Den Bossche, Sensitivity of the hygrothermal behaviour of homogeneous masonry constructions: from Sobol indices to decision trees, 12th Nordic Building Physics Conference (NSB 2020) E3S Web of Conferences, EDP Sciences, Tallinn University of Technology, Tallinn, Estonia, 2020, p. 07001.

[217] H. Janssen, B. Blocken, J. Carmeliet, Conservative modelling of the moisture and heat transfer in building components under atmospheric excitation, International Journal of Heat and Mass Transfer 50(5–6) (2007) 1128-1140.

[218] F. Tariku, Whole building heat and moisture analysis, Department of Building, Civil and Environmental Engineering, Concordia University, Montreal, Quebec, Canada, 2008.

[219] H. Hens, Building Physics–Heat, Air and Moisture, Fundamentals and Engineering Methods with Examples and Exercises, Ernst & Sohn A Wiley, ISBN 978-3-433-01841-5, 2007.

[220] P.T. Tsilingiris, Thermophysical and transport properties of humid air at temperature range between 0 and 100 °C, Energy Conversion and Management 49(5) (2008) 1098-1110.

[221] H. Gao, M. Shao, Effects of temperature changes on soil hydraulic properties, Soil and Tillage Research 153 (2015) 145-154.

[222] M. Guizzardi, D. Derome, J. Carmeliet, Water uptake in clay brick at different temperatures: Experiments and numerical simulations, Journal of Building Physics 39(4) (2016) 373–389.

[223] N. Karagiannis, M. Karoglou, A. Bakolas, A. Moropoulou, Effect of temperature on water capillary rise coefficient of building materials, Building and Environment 106 (2016) 402-408.

[224] R.J. Gummerson, C. Hall, W.D. Hoff, Water movement in porous building materials—II. Hydraulic suction and sorptivity of brick and other masonry materials, Building and Environment 15(2) (1980) 101-108.

[225] P. Häupl, J. Grunewald, H. Fechner, H. Stopp, Coupled heat air and moisture transfer in building structures, International Journal of Heat and Mass Transfer 40(7) (1997) 1633-1642.

[226] W. Wagner, A. Pruß, The IAPWS Formulation 1995 for the Thermodynamic Properties of Ordinary Water Substance for General and Scientific Use, Journal of Physical and Chemical Reference Data 31(2) (2002) 387-535.

[227] M. Schubnell, H. Ries, Velocity-controlled tracking of the sun, Solar Energy Materials 21(2) (1990) 207-212.

[228] P.T. Tsilingiris, Review and critical comparative evaluation of moist air thermophysical properties at the temperature range between 0 and 100°C for Engineering Calculations, Renewable and Sustainable Energy Reviews 83 (2018) 50-63.

[229] H.-J. Kretzschmar, W. Wagner, IAPWS Industrial Formulation 1997 for the Thermodynamic Properties of Water and Steam, in: H.-J. Kretzschmar, W. Wagner (Eds.), International Steam Tables: Properties of Water and Steam based on the Industrial Formulation IAPWS-IF97, Tables, Algorithms, Diagrams, Springer, Berlin, Heidelberg, 2019, pp. 7-150.

[230] M. Vestfálová, P. Šafařík, Dependence of the isobaric specific heat capacity of water vapor on the pressure and temperature, in: P. Dancova, M. Vesely (Eds.) EPJ Web of Conferences, EDP Sciences, Prague, Czech Republic, 2016, p. 02133.

[231] C.O. Popiel, J. Wojtkowiak, Simple Formulas for Thermophysical Properties of Liquid Water for Heat Transfer Calculations (from 0°C to 150°C), Heat Transfer Engineering 19(3) (1998) 87-101.

[232] A.G. Meyra, V.A. Kuz, G.J. Zarragoicoechea, Universal behavior of the enthalpy of vaporization: an empirical equation, Fluid Phase Equilibria 218(2) (2004) 205-207.

[233] Y.A. Cengel, J.M. Cimbala, Fluid mechanics - Fundamentals and Applications, Second ed., Tata McGraw-Hill Education, 2010.

[234] G.R. Somayajulu, A generalized equation for surface tension from the triple point to the critical point, Int J Thermophys 9(4) (1988) 559-566.

[235] D. Koutsoyiannis, Clausius–Clapeyron equation and saturation vapour pressure: simple theory reconciled with practice, European Journal of physics 33(2) (2012) 295.

[236] S. Geving, J.V. Thue, Håndbok 50 - Fukt i bygninger, Norges byggforskningsinstitutt, Oslo, Norway, 2002.

[This page is left blank]

Research Articles

Article I

Experimental investigation of capillary absorption along mortar-brick interface plane

J. I. Belghaug Knarud, T. Kvande, S. Geving

Proceedings CESBP 2016 BauSIM 2016, Central European Symposium on Building Physics / BauSIM, Fraunhofer IRB Verlag, Dresden, Germany (2016) 117-124 ISBN (E-Book): 978-3-8167-9798-2

EXPERIMENTAL INVESTIGATION OF CAPILLARY ABSORPTION ALONG MORTAR-BRICK INTERFACE PLANE

J. I. Belghaug Knarud[1], T. Kvande[1], and S. Geving[1]
[1]Department of Civil and Transport Engineering, NTNU, Trondheim, Norway

Corresponding author. Tel.: +47 90675937.
E-mail address: jon.knarud@ntnu.no

ABSTRACT

Interfaces between brick and mortar in masonry structures have in hygrothermal modeling often been given a resistance on the moisture transport across them. However, interfaces may also have some impact on transport of moisture along the interface planes themselves.

In this paper experimental investigation has been conducted on how capillary absorption coefficients, when tested for parallel to the mortar joint plane, are influenced by the mortar and the mortar-brick interface of the joint. The coefficients are compared to the shear strength capacities of the respective specimens in order to investigate any connection between water absorption and mortar joint quality.

INTRODUCTION

Brick masonry has long been popular when constructing buildings, even though the masonry design and function have changed over the years. In many older buildings the brick masonry forms the load bearing structure, also including exterior walls. Masonry makes out a major bulk of the exterior wall cross section, running originally more or less continuously from the exterior to the interior side. However, as times change the use and expected performance of buildings change as well. Old factories and workshops may be redesigned to become offices or residential apartments, and older residential buildings, with low comfort and high heating costs, may be upgraded to meet new standards. To achieve this, exterior walls may be retrofitted to new criteria such as higher heat insulation and air tightness. If the exterior facade is wanted preserved the retrofit is done on the interior side. From a building physics point of view interior retrofit gives challenges on avoiding moisture problems and damages, and more detailed analysis of the wall is often necessary to ensure that the retrofitting is safe. At this point the performance of the masonry becomes important; how severely is it wetted from driving rain or condensation?, how quickly does it dry out after it has become wet?, how fast, where and how does the moisture travel in the masonry?, are examples of questions which might be needed answered. Many factors influence on this; however the present paper will be limited to capillary absorption, a parameter having great influence on the transport of moisture, and wetting of masonry. More specifically, it is of interest to look at how the interface between brick and mortar influences on the capillary absorption when the process occur along the interface plane. Many researchers have been looking at the interface's significance in masonry before, for instance in relation to the bonding strength of the masonry (e.g. Groot (1993)), or to the moisture transport across it (e.g Brocken (1998)); however, it does not seem that nearly as much have been done on moisture transport along the interface plane.

Our investigations on this topic are still at an early stage, and laboratory testing is and will be ongoing. However, we will take the opportunity to present some results and lessons we made from initial investigations done in connection with a master thesis at our laboratory.

Capillary absorption

Water absorption development of bricks, in addition to some other materials, can be expressed as a volumetric cumulative water absorption through the area of contact with free water by the following equation (Hall, 1977)

$$i = St^{1/2} \tag{1}$$

i = cumulative absorption [m]; S = sorptivity [$m/s^{1/2}$]; t = time [s]

In Equation (1) the square root of time originate from similar mathematics to that of diffusion theory for a semi-infinite solid (Vejmelková et al., 2009, Crank, 1975). The sorptivity is analogous to the square of diffusivity. Measuring water absorption is however usually done by weighing the material at different times during the absorption process and it is therefore more convenient to relate water absorption to unit mass. Furthermore, equation (1) is purely theoretical for strict ideal boundary conditions where the liquid diffusion starts from the boundary surface, where it is in contact with free water, and at which the material needs to show same isotropic behavior as further inside. In practice these ideal conditions at the boundary are difficult to obtain as the test specimen for practical reasons have to be placed with some immersion depth to ensure free water contact with the whole surface, which may not be completely smooth. The immersion depth causes a small pressure, corresponding to the water head, and alters the conditions (see Bomberg et al. (2005)). Furthermore for a porous material with non-smooth surface, large pores, voids, and surface roughness might contribute to higher initial absorption due to larger effective surface area than what is used for calculation. It is therefore necessary to address initial absorption. Hence, equation (1) is expanded to the following (Bomberg et al., 2005)

$$I = A_0 + A_w\sqrt{t} \qquad (2)$$

I = cumulative absorption [kg/m^2]; A_0 = initial water uptake [kg/m^2]; A_w = water absorption coefficient [kg/m^2·s$^{1/2}$]

Equation (2) applies to the region named "theory-following absorption" in Figure 1, and A_0 is then a constant value at t = 0 where the linear trend of the region meets the y-axis. Hence A_0 is not measured, but found by extending the line of that region. The initial region must as a consequence be excluded from the readings used to establish the line of the theory-following region. For instance, for certain clay bricks described by Bomberg et al. (2005) this initial region spans 225s.

The water absorption testing need to be done at isothermal conditions since the temperature dependency of both surface tension and dynamic viscosity of water would otherwise influence the process. With isothermal conditions it is however possible to compare results of sorptivity or water absorption coefficient found at different temperatures (see Gummerson et al. (1980)).

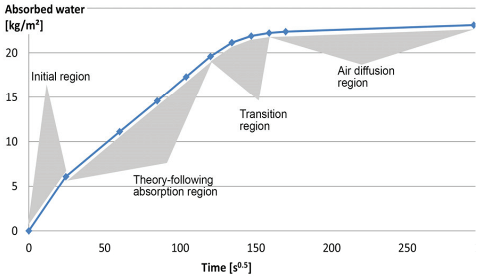

Figure 1: Development in cumulative water absorption with respect to square root of time. Division into regions of different trends.

After the theory-following region the waterfront of the absorption has reached the other side of the test specimen and semi-infinite boundary conditions no longer apply. At this point there will be a transition region where the rest of the smaller pores are filled, and where the overall pore space is filled by capillary saturation. The moisture content after the transition to the air diffusion region is, by definition, the capillary moisture content w_{cap} (Roels et al., 2004).

During capillary absorption some air is trapped in the process, and this air will over time dissolve in the liquid water and diffuse out of the specimen (e.g. Janssen et al. (2015)), thereby giving a small slope in the air diffusion region of Figure 1. For a hypothetical material with homogeneous pore size, having a steep waterfront which fill all pores simultaneously as it progresses through the specimen (indicating the capillary saturation is quickly reached after or almost at the waterfront), there would be no transition region to the air diffusion region. For some test specimens differing much from this hypothetical case, quite long transitions regions may exist, and it is plausible air diffusion already is taking place, having substantial impact on the absorption development. By identifying the slope of the capillary region and that of the air diffusion region, the intersection of the lines can be identified as a transition comparable to the hypothetical case. The accumulated water at the intersection can be a good estimate of the capillary moisture content. In the present studies the average of the moisture content at this intersection and at the first trustworthy identified measurement in the air diffusion region is used as the capillary moisture content.

EXPERIMENT

Selected materials

A solid brick was initially intended for the experimental work; however, due to complications in the delivery, a perforated brick (< 25 volume % perforation) ended up being used instead. This had some implications on the evaluation of the experiment results as discussed later. Dimensions of the brick were L x W x H of 226 x 104 x 60 mm. The brick type was chosen for its high initial absorption rate (IRA), assumed to be similar to that of historical bricks often encountered in retrofitting and renovation projects. Product information given by the producer include: average weight per brick, 2.0 kg; net density of solid, 1750 kg/m^3, a density class with accuracy ± 10 %; IRA, 4.5 kg/m^2·min; water absorption, 25-vol %. Considering weight, density, total brick volume as well as the weight given by the producer for a solid version of the brick type, the perforation voids make out approximately 20 - 23 % of the brick volume. Some additional data given by the producer is given in the appendix table.

Properties of 11 bricks were measured for comparison with the product information. Net density (NS-EN 772-13) and net volume (NS-EN 772-3) were respectively measured to be 1702 kg/m^3, with a standard deviation of 14.1 kg/m^3, and 0.00108 m^3, with standard deviation of 0.00001 m^3. The percentage of voids (perforations not included) were found to be 29 % with a standard deviation of 0.9 %.Water absorption, in accordance with NS-EN 772-21, was measured to be 17.1 % mass, with a standard deviation of 0.7 %. IRA was measured in accordance with IRA definition of NS-EN 772-11. An immersion depth of 10 mm was used instead of the 5 mm described in NS-EN 772-11. The measured values should therefore be considered as extra conservative. Measurements were done both normal to the brick bed and face. For the brick bed the IRA was found to be 4.2 kg/m^2·min with a standard deviation of 0.3 kg/m^2·min, while for the face it was found to be 3.8 kg/m^2·min with a standard deviation of 0.2 kg/m^2·min.

Four types of commercially available mortars were tested in combination with the brick. These included two prescribed LC-mortars; LC 50/50/610 and LC 35/65/520, numbers corresponding to lime/cement/aggregate mass ratios of binder content, and two design mortars classified M5 in accordance with NS-EN 998-2. The two M5 mortars are further addressed as M5A and M5B, where M5A is a general mortar while M5B is specially designed for bricks with relatively high IRA values (up to 3.5 kg/m^2·min). The aggregate of all the mortars is natural sand with grain diameters 0-2 mm.

Test specimens

Three types of specimens were tested; i) individual bricks, ii) brick pillars, and iii) mortar joints taken from the pillars after the pillars had been tested for shear strength.

Pillars, of three bricks height, was laid using a specially design aluminum form, as shown in Figure 2, in order to consistently achieve 15 mm mortar bed joints. A total of 26 pillar specimens were made as shown in Table 1. Most of the specimens were given concave joints (-C); however, KC50-F was given a flush joint (-F) at the face side for comparison. The making of a concave joint finish is expected to compact and smooth the joint surface, possibly giving smaller surface pore openings which then will affect the water absorption rate. With the exception of M5A-CW no prewetting of the bricks was undertaken. Prewetting of bricks before laying them has for a long time been a common practice in order to reduce the water loss of the mortar joint, due to high suction from the bricks, during initial curing

Some specimens had to be scrapped due to poor bonding between the mortar and brick during curing, causing KC50-F and M5A-C only having 3 specimens. The specimens were left curing at room temperature of 22 °C for 25 days under a polyethylene sheet cover. The function of the cover was to retain a relative humidity (RH) for the curing process, higher than the 29 % RH of the room, to prevent dry-out. Before the testing of water absorption coefficient the cover was removed in order to condition the specimens to the room conditions. The room RH of 29 % was lower than the prescribed RH of 40 to 60 % of NS-EN ISO 15148.

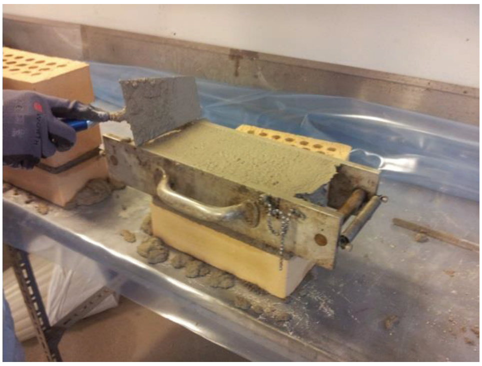

Figure 2: The brick laying and the tool used to ensure constant joint thickness.

Table 1: List of pillar and mortar joint specimen series.

NAME	MORTAR	FEATURE	# SPECIM.
KC50-F	KC 50/50	Flush joint	3
KC50-C	KC 50/50	Concave joint	5
KC35-C	KC 35/65	Concave joint	5
M5A-C	M5 A	Concave joint	3
M5A-CW	M5 A	Concave joint, pre-wetted brick	5
M5B-C	M5 B	Concave joint	5

Experimental setup - water absorption

The experimental setup was in accordance with NS-EN ISO 15148. A tank with automatic readjustment of the water level was used; however the one tank did not provide sufficient space for all the specimens, so four tanks with manual readjustment of water level were also used. The test specimens were placed in the tanks on supports to keep them off the bottom. The water level was set at 10 mm, a deviation from NS-EN ISO 15148 having 5 ± 2 mm, in order to keep it equal for all the specimens since the concave joints required a higher water level. The pillars (Figure 3), the single bricks and the mortar joints (Figure 4) were placed in the water with the face down.

The pillar specimens were weighed at 10 min, each hour in the interval 1-8 hours and at 24 hours. Weighing of the mortar joint specimens was done at 15 min, each hour in the interval 4-11 hours and at 24 hours. This gave 10 measured values to be plotted for both specimen types.

After shear strength testing of the pillars, the remaining intact mortar joint of each pillar were chiseled or, when bonding appeared to strong, sawn out of the pillars to become the mortar joint specimens. When chiseled the mortar joints kept some mortar bumps where the brick perforations had been located, as can be seen in Figure 4. However these bumps only appear on the side being the lower one of the joint in relation to the brick laying. The cause of only one side having these bumps can be found from the use of the tool shown in Figure 2, which prevented the new laid brick from being pushed into the mortar to such an extent that the mortar would be pressed up in the perforation holes. As a consequence the joints cross section became non-constant, with somewhat increased cross section area at the bumps.

Figure 3: Absorption testing of pillar specimens, KC50-C. Tray with manually regulated water level.

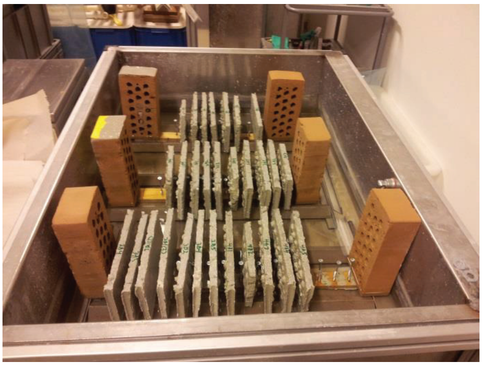

Figure 4: Absorption testing of joint specimens. Tray with automatic water level regulation.

Experimental setup – initial shear strength

For measuring the initial shear strength a procedure similar to that of NS-EN 1052-3 was used. There were three differences to that of the standard. First, no lateral precompression load was applied; second, instead of steel roller bearings, wood fiber pads were used under the steel supports to ensure good contact to the specimen; third, instead of 9 only 3 or 5 specimens were tested in the different series. Due to the first and third difference, no plot of initial shear strength to precompression stress could be made for result evaluation in accordance with NS-EN 1052-3. However, since the aim of the shear testing was to investigate whether a correlation existed between water absorption rate and the mortar joint quality, it was deemed that a detailed analysis of shear strength was unnecessary. Inclusion of the precompression would also have required a much higher number of specimens, which would not have been possible within the cost and time constraints of the experiments. The shear test setup is shown in Figure 5.

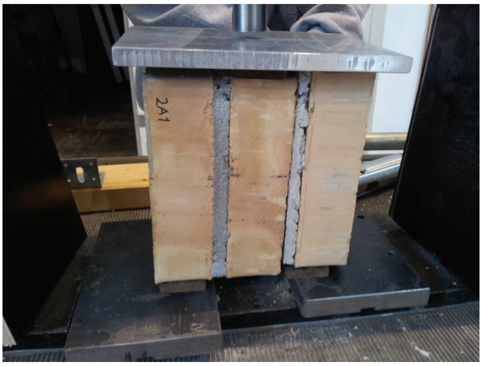

Figure 5: Shear testing of pillar specimen KC35-C. Failure in top interface of lower joint.

ANALYSIS AND DISCUSSION OF THE RESULTS

It is clear from the results plotted in Figure 6 that most of the pillars show an absorption trend that is much more curving than that of the ideal theoretical trend described in the introduction. Downward curving trend can be seen in some materials having very coarse pore structure, where the gravitational effect becomes comparable to the capillary suction (Hall and Tse, 1986, Hall, 1989). However, this is not likely to be the case in the present study, since the pores are not coarse enough for gravitational effect to become substantial. In other words, gravitational effects are negligible as long as the specimen height is much smaller than potential capillary rise in the material (Bomberg et al., 2005).

Furthermore, the curving trend is not present for the bricks or for M5A-CW, also excluding that the perforations in the bricks are the cause. On the other hand, the perforations make the cross sectional area varying up through the specimen. A varying cross section is in conflict with the unidirectional flow conditions used in the derivation of equation(1), even though the results for the bricks and M5A-CW seem to follow the theory quite well. It is possible the theory-following region of the absorption development is just limited by the volume flow passing through the smallest cross section area at the plane cutting through the center of the perforations. In such case it might be misleading to use the gross cross sectional area of the specimens to determine A_w if one should compare the value to that of a solid brick. Another aspect, which is also later addressed, is that some mortar has pressed into the perforations making the actual absorption situation more obscured.

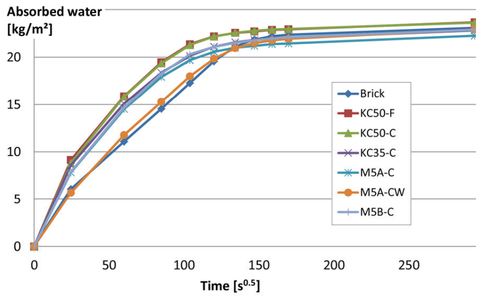

Figure 6: Absorption development of brick and pillar speciemens. All values are averages of the test series.

Moisture evaporation from the specimen may also explain the long transition region, as the laboratory relative humidity was low and no measure was taken to reduce the contribution from evaporation. Bomberg et al. (2005) suggests for instance placing a plastic cover over the specimen to reduce evaporation, as long as pressure equalization to the room atmosphere is ensured.

Table 2: Brick – water absorption coefficient, A_w [$kg/m^2 \cdot s^{1/2}$], at 22 °C. Measured from 11 specimens. Standard deviation is that of samples, i.e. using n-1 for reduction in degrees of freedom.

MEAN	MIN / MAX	STAND. DEV.
0.1410	0.1206 / 0.1549	0.0111

Table 3: Brick – capillary saturation water content, W_{cap} [kg/m^3], measured from 11 specimens. Standard deviation is that of samples, i.e. using n-1 for reduction in degrees of freedom (n-2 for combined).

	MEAN	MIN / MAX	STAND. DEV.
Theoretical ideal graph regime transition	203.48	194.24 / 211.47	5.28
First trustable point of air diffusion regime	205.02	195.50 / 213.16	5.40
Above perspectives' combined average	204.25	194.24 / 213.16	5.40

Due to tight schedule when testing the mortar joint specimens, the water absorption was not measured up to capillary saturation, and no value for capillary moisture content could therefore be found. However, the absorption development up to 24 hours can be seen in Figure 7. An estimate on the water content at capillary saturation was attempted by subtracting the average saturated water content of the bricks (Table 3) from the pillar capillary water content, leaving the mortar joint water content at capillary saturation. The result of this attempt is given in Table 5, but as can be seen the values have a high spread indicating their trustworthiness is low. The volume of mortar is for instance unknown and hard to estimate due to some mortar having pushed into the perforation of the bricks. The resulting net density and porosity of the mortar in the pillar specimens have also not been measured in this study.

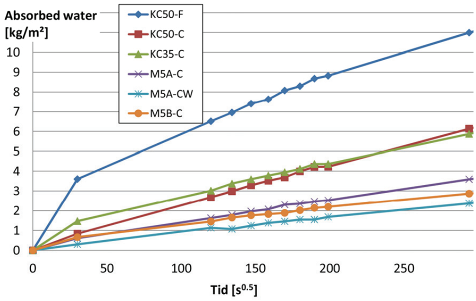

Figure 7: Absorption development of mortar joint types. All values are averages of the test series.

Table 4: Mortar joint specimen series - water absorption coefficients, A_w [$kg/m^2 \cdot s^{1/2}$], at 22 °C.

SERIES	MEAN VALUE	MIN / MAX VALUES
KC50-F	0.0297	0.0270 / 0.0365
KC50-C	0.0206	0.0129 / 0.0283
KC35-C	0.0173	0.0144 / 0.0214
M5A-C	0.0118	0.0093 / 0.0180
M5A-CW	0.0083	0.0065 / 0.0127
M5B-C	0.0091	0.0071 / 0.0134

Table 5: Mortar joint specimen series – capillary saturation water content, W_{cap} [kg/m^3]. Estimated from pillar specimens at time of capillary saturation (average of theoretical and first trustable point of air diffusion regime).

SERIES	MEAN VALUE	MIN / MAX VALUES
KC50-F	258.79	231.96 / 287.82
KC50-C	265.21	239.65 / 293.90
KC35-C	199.71	137.75 / 256.16
M5A-C	163.20	133.85 /189.05
M5A-CW	182.21	159.29 / 206.99
M5B-C	208.76	181.14 / 258.94

Due to the curving trend in Figure 6 least square linear regression was used to determine the absorption coefficient from the curves. The curve region presumably representing the theory-following region in Figure 1 was, in lack of a better procedure, visually evaluated after best understanding and determined by comparing different linear regression lines having taking into account different number of measurement points.

The mean values for the water absorption coefficient of the pillar series, given in Table 6, are all higher than the max value of the brick from Table 2. Only a few specimens of KC35-C and M5A-CW have lower values than the brick maximum, and these are then quite close. Since the A_w values for the mortar joints (Table 4) are much lower than that of the bricks, while the joint seemingly reach capillary saturation very slowly (Figure 7), this is a strong indication of extra moisture movement along the brick-mortar interface. With the exception of M5A-CW, the pillars appear to reach capillary saturation sooner than the bricks, respectively at a time ~ 130 $s^{1/2}$ compared to ~ 160 $s^{1/2}$, as seen in Figure 6.

Table 6: Pillar specimen series - water absorption coefficients, A_w [kg/m^2·s$^{1/2}$], at 22 °C.

SERIES	MEAN VALUE	MIN / MAX VALUES
KC50-F	0.1744	0.1640 / 0.1813
KC50-C	0.1760	0.1667 / 0.1828
KC35-C	0.1631	0.1512 / 0.1728
M5A-C	0.1687	0.1599 / 0.1749
M5A-CW	0.1599	0.1531 / 0.1704
M5B-C	0.1734	0.1621 / 0.1797

The values for KC50-F and KC50-C do not differ significantly in Table 6 and no conclusion on the effect of the mortar joint finish (flush vs. concave) can be made from these numbers alone. However, when looking at the results for only the joints (Table 4) there is a significant difference between the two, giving indication that the concave joint give lower water absorption. A possible explanation for why the pillars do not benefit from this might be that the bricks, having higher capillary transport potential, become dominant on supplying water to the mortar joint. Also, the concave from of the joints may create a higher inflow of water by creating two-dimensional inflow at the brick edge along the joint, and further upholding the absorption rate of the pillar by circumventing the joint compacted finish. When looking at the values for KC35-C, these explanations seem insufficient or incorrect. KC35C show in comparison low water absorption both for the joint and pillar specimens. It might be as simple as the KC50-F number of specimens is too limited to give statistical validity. Still, Figure 8 show lower shear strength capacity for the KF50 concave joints than the flush joints, indicating poorer brick-mortar interface bonding of the former. Overall the shear strength capacities of KF35-C show to be better than those of KF50-C.

Increased water absorption may originate from higher interface porosity or void presence caused by poor brick - mortar bonding. However, the presented data in Figure 8 encompass too few specimen measurements to calculate any statistical probability for this causality. Interestingly though; observations during the testing gave notice of water seeping through on the upper pillar surface for some of the specimens after a test period of 2 hours. This was especially the case for the middle brick. Comparing 2 hours (84.9 $s^{1/2}$) with the absorption development for the brick (Figure 6) shows that this is a much earlier time than that of the expected seep through, which lie in the interval between ~ 120 $s^{1/2}$ and 150 $s^{1/2}$ for the different bricks (values taken at the approximate start of the transition region defined in Figure 1). This seems odd unless the mortar joints influence by giving increase to the waterfront velocity. Since the mortar joints themselves did not show any fast absorption towards capillary saturation, an explanation points strongly to the influence of the brick mortar interface. M5A-CW did not show this early water seep through, and as can be seen from Figure 6 its average absorption development followed that of the brick.

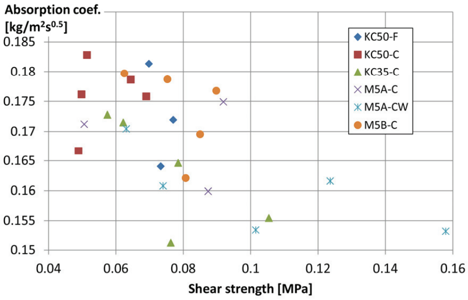

Figure 8: Water absorption coefficients plotted to specimens corresponding shear strengths.

All the shear testing failures occurred at the brick-mortar interface. The shear strength capacity was overall lower than expected for these types of mortar, and, for comparison, most specimens failed at lower capacities than 0.1 MPa, i.e. the lowest listed initial shear strength in NS-EN 1996-1-1. This indicates there have been factors influencing the bonding between brick and mortar in a negative sense. A likely cause is that the high water suction of the bricks draws too much water out of the mortar in the initial time after laying the brick, thereby having less than optimal water content in the mortar for the curing process, or having a changed mortar composition at the interface as fine particles are transported by the flow. This is supported by the pre-wetted brick specimens (M5A-CW) performing better in the shear testing. Still, not even the pre-wetted bricks ensured high shear strength in all the specimens. Another possible cause of negative influence might be the tool (Figure 2), used to ensure constant joint thicknesses. When using it the brick laying went slower, increasing risk with mortar stiffening and drying before next brick is laid in place. Surprisingly many of the specimens failed at the top of the lower joint of the laying order, while none failed at the top of the upper joint, perhaps indicating some unknown procedural problem with the brick laying. Only M5A-CW and M5B-C had a different location of failure, with three failures each at the bottom of the upper joint. It was checked whether the latter failure occurred at higher shear strengths, and it was found that the specimen with the lowest shear capacity corresponded to failure of the first kind, but no conclusion or credible indication could be obtained as failure of the first kind also had one occurrence at a higher shear strength for both mortars. There were too few specimens to do any statistical evaluation. The tool does have some available adjustment so that more compression of the mortar can be achieved when laying the top brick, which perhaps can ensure better contact and bonding between mortar and brick. Trying such adjustment can be undertaken in further studies.

CONCLUSION

Water absorption coefficients were investigated for a brick type, having high suction capabilities (high IRA value), in combination with several mortar types. When tested with the face down, it was found that pillar specimens (consisting of three bricks with mortar joints) had higher water absorption coefficients than the individual bricks, for all test series. Saturated capillary moisture content was reached sooner for the pillars than for the individual bricks. Most of the pillars series had absorption developments showing strong curving trends making determination of water absorption coefficients and saturated capillary water contents difficult and more uncertain. The pillar series with closest trend to that of the bricks had used prewetted bricks during brick laying in contrast to the other pillar series. Taking into account that the mortar joints themselves had much lower water absorption rate than the bricks, the mortar joint interfaces appear the most likely cause of increased water absorption rate for the pillars. Comparing tested shear strength capacities of the pillars with their respective water absorption coefficients it was found indications of a connection between high absorption coefficients and low shear strength capacities. In conclusion the results give a strong indication that poor mortar-brick bonding at the joint interfaces give higher water absorption rates and faster water front velocity close to these interfaces. However, the number of specimens tested was not high enough to give any statistical analysis on this. In addition, aspects like mentioned in the lessons learned, given below, give rise to uncertainties in the results.

A few lessons were made during the study.

- The bricks should be pre-wetted in order to achieve better bonding between brick and mortar, and thereby more reasonable initial shear strength capacities.
- The tool used (Figure 2) may have interfered with the bonding between brick and mortar on the top of the joints, according to laying order, and more testing both with and without this tool should be conducted in order to see its effect. If used, care should be taken to ensure good contact between the brick and mortar, and effects of different tool adjustments can be investigated.
- The transition region of the pillar series, except for M5A-CW, begins quite early. Although there are indications of poor interfaces giving rise to this, it will be important to remove other uncertainties caused by other aspects influencing on this. Inaccuracies caused by the procedure of specimen making and testing should be limited even more; (i) perforated bricks should be avoided as this give rise to challenges and uncertainties, especially since the cross sectional area varies and since mortar press into the perforations; (ii) care should be taken to avoid mortar stiffening or dry-out during the brick laying; (iii) evaporation from specimens' top surface during testing should be limited.

A new study which incorporates the understanding made from these lessons, and especially avoids the unfortunate use of perforated brick, has been planned and is under way.

ACKNOWLEDGEMENT

Great appreciation is given the former master students Jonas Lundli Buan and Dilush Dennis Joseph for their contribution of gathering experimental data in this study at our laboratory.

REFERENCES

BOMBERG, M., PAZERA, M. & PLAGGE, R. 2005. Analysis of Selected Water Absorption Coefficient Measurements. *Journal of Thermal Envelope and Building Science,* 28**,** 227-243.

BROCKEN, H. J. P. 1998. *Moisture transport in brick masonry: the grey area between bricks.* Technische Universiteit Eindhoven.

CRANK, J. 1975. *The Mathematics of Diffusion: 2d Ed*, Clarendon Press.

GROOT, C. J. W. P. 1993. *Effects of water on mortar-brick bond*, TU Delft, Delft University of Technology.

GUMMERSON, R. J., HALL, C. & HOFF, W. D. 1980. Water movement in porous building materials—II. Hydraulic suction and sorptivity of brick and other masonry materials. *Building and Environment,* 15**,** 101-108.

HALL, C. 1977. Water movement in porous building materials—I. Unsaturated flow theory and its applications. *Building and Environment,* 12**,** 117-125.

HALL, C. 1989. Water sorptivity of mortars and concretes: a review. *Magazine of Concrete Research,* 41**,** 51-61.

HALL, C. & TSE, T. K.-M. 1986. Water movement in porous building materials—VII. The sorptivity of mortars. *Building and Environment,* 21**,** 113-118.

JANSSEN, H., VEREECKEN, E. & HOLÚBEK, M. 2015. A Confrontation of Two Concepts for the Description of the Over-capillary Moisture Range: Air Entrapment versus Low Capillarity. *Energy Procedia,* 78**,** 1490-1494.

NS-EN 772-3 1999. Methods of test for masonry units - Part 3: Determination of net volume and percentage of voids of masonry units by hydrostatic weighing. Brussels, Belgium: European Committee for Standardization (CEN).

NS-EN 772-11 2011. Methods of test for masonry units - Part 11: Determination of water absorption of aggregate concrete, autoclaved aerated concrete, manufactured stone and natrual stone masonry units due to capillary action and the initial rate of water absorption of clay masonry units. Brussels, Belgium: European Committee for Standardization (CEN).

NS-EN 772-13 2000. Methods of test for masonry units - Part 13: Determination of net and gross dry density of masonry units (except for natural stone). Brussels, Belgium: European Committee for Standardization (CEN).

NS-EN 772-21 2011. Methods of test for masonry units - Part 21: Determination of water absorption of clay and calsium silicate masonry units by cold water absorption. Brussels, Belgium: European Committee for Standardization (CEN).

NS-EN 998-1 2010. Specification for mortar for masonry - Part 1: Rendering and plastering mortar. Brussels, Belgium: European Committee for Standardization (CEN).

NS-EN 998-2 2010. Specification for mortar for masonry - Part 2: Masonry mortar. Brussels, Belgium: European Committee for Standardization (CEN).

NS-EN 1745 2012. Masonry and masonry products - Methods for determining thermal properties. Brussels, Belgium: European Committee for Standardization (CEN).

NS-EN 1996-1-1 2005+A1:2012+NA:2013. Eurocode 6: Design of masonry structures - Part 1-1: General rules for reinforced and unreinforced masonry structures. Brussels, Belgium: European Committee for Standardization (CEN).

ROELS, S., CARMELIET, J., HENS, H., ADAN, O., BROCKEN, H., CERNY, R., PAVLIK, Z., HALL, C., KUMARAN, K., PEL, L. & PLAGGE, R. 2004. Interlaboratory Comparison of Hygric Properties of Porous Building Materials. *Journal of Thermal Envelope and Building Science,* 27**,** 307-325.

VEJMELKOVÁ, E., PAVLÍKOVÁ, M., JERMAN, M. & ČERNÝ, R. 2009. Free Water Intake as Means of Material Characterization. *Journal of Building Physics,* 33**,** 29-44.

Appendix: Mortar properties specified by producer and the standards the producer refers to

MORTAR	AIR CONTENT	COMPRESSIVE STRENGTH	WATER ABSORPTION	THERMAL CONDUCTIVITY	VAPOR PERMEABILITY
LC 50/50	8 – 14%	CS II (1.5 – 5.0 N/mm^2)^a	W 0 (not specified)^a	0.82 W/m·K^c	15/35^c
LC 35/65	-	CS III (3.5 - 7.5 N/mm^2)^a	W 0 (not specified)^a	0.82 W/m·K^c	15/35^c
M5 A	14 – 20 %	> 5 MPa (28 days)	< 0.6 kg/m^2·min$^{0.5}$	0.82 W/m·K^c	15/35^c
M5 B	14 – 20 %	5 MPa^b	< 0.6 kg/m^2·min$^{0.5}$	0.82 W/m·K^c	15/35^c

^{a} in accordance with NS-EN 998-1

^{b} in accordance with NS-EN 998-2

^{c} in accordance with NS-EN 1745. All values are decided based on a density of 1800 kg/m^3. Corresponding specific heat capacity is given as 1000 J/kg·K.

Article II

Moisture performance of interior insulated brick wall segments subjected to wetting and drying – A laboratory investigation

J. I. Knarud, S. Geving, T. Kvande

Building and Environment 188 (2021) 107488 https://doi.org/10.1016/j.buildenv.2020.107488

Building and Environment 188 (2021) 107488

Contents lists available at ScienceDirect

Building and Environment

journal homepage: http://www.elsevier.com/locate/buildenv

Moisture performance of interior insulated brick wall segments subjected to wetting and drying – A laboratory investigation

Jon Ivar Knarud [*], Stig Geving, Tore Kvande

Department of Civil and Environmental Engineering, Norwegian University of Science and Technology, NO-7491, Trondheim, Norway

ARTICLE INFO

Keywords:
Interior insulation
Masonry wall
Wooden beam ends
Smart vapor barrier
Laboratory climatic simulator

ABSTRACT

Hygrothermal challenges are introduced when equipping facades of existing masonry buildings with interior insulation. If not addressed, moisture damages to the building envelope may follow. Many measures for overcoming reduction in drying potential have been proposed and studied. Still, more understanding is needed regarding effects of measures.

This paper investigates wetting and drying behavior of masonry wall segments mounted in a large-scale building envelope climate simulator, exposing them to a climatic sequence including driving rain. Equipped with interior insulation and embedded wooden beam ends, most wall segments are applied with a smart vapor barrier. This should allow for inward drying during warm exterior climate, while under cold climate, prevent interstitial condensation.

A variety in masonry wetting and drying behavior among segments of same brick type was found to partly obscure effects of other parameters such as insulation thickness, brick type and vapor barrier type. Compared to high IRA (initial rate of absorption) brick segments, moderate IRA brick segments show higher drying rates at beam ends and at the interface between interior masonry surface and insulation. During wetting, results were found to be inconsistent. An increased drying of the interface between interior masonry surface and insulation was found to correlate to decreasing insulation thickness and application of a smart vapor barrier over a traditional polyethylene barrier. A similar but less pronounced trend is also detected at beam ends. A smart vapor barrier seemingly improves the drying potential, but it likely needs to be accompanied by other measures.

1. Introduction

Interior insulation retrofit is an intriguing measure in renovation of existing masonry buildings, where exterior facades should be preserved for their aesthetics and historical or cultural heritage value. Such an insulation measure can lower an otherwise excessive heating requirement in a cold temperate climate. Furthermore, it can improve indoor comfort by increasing the interior surface temperature and air tightness of the building envelope. Nevertheless, interior insulation retrofit also presents challenging issues by changing the hygrothermal conditions of the exterior walls [1]. Primarily, both overall temperature and the temperature gradient over the external masonry cross section will become substantially lowered. Consequently, outwards heat flow through the wall decrease, lowering the capacity for evaporation to exterior surroundings. Furthermore, added interior insulation retrofit provides increased vapor resistance, reducing inward drying. With impaired drying potential, interior insulated walls become vulnerable towards moisture sources. Embedded beam ends become particularly vulnerable [2]. Driving rain is one of the main moisture sources, especially critical for unprotected bare masonry which quickly may absorb large amounts of water. Through literature review Kehl et al. [3] found lack of protection against wind driven rain to be one of the main reasons for decay of wooden beam ends, the others being different sources of leaks. For protection from driving rain, external render is the typical go-to measure. A render with low capillary absorption rate, and which is relatively open for vapor diffusion is typically to prefer [4,5]. For protected bare brick facades, external render is not an option. Hydrophobation is among possible measures, although the effectiveness to driving rain events have not always been found straight forward [6,7]. Rainwater moisture uptake depends on a number of masonry properties, not only the material properties of the brick and mortar as separate materials, but also essential, is the result of brick-mortar interaction during brick laying. Groot and Gunneweg [8] attributed an open brick-mortar interface as the main cause of water leakage through one of

---

[*] Corresponding author.
E-mail address: jon.knarud@ntnu.no (J.I. Knarud).

https://doi.org/10.1016/j.buildenv.2020.107488
Received 20 September 2020; Received in revised form 24 November 2020; Accepted 25 November 2020

their test walls, and indicated a more compatible mortar to the applied brick could have decreased the leakage. Suction properties of the brick were by Groot and Larbi [9] found important in the formation of the interface microstructure. Similarly, linking it to interface microstructure, Slapø et al. [7] found a correlation between fresh mortar water content and driving rain penetration of masonry, where low water content resulted in higher water penetration. Prewetting of bricks can reduce water loss from mortar [10]; however, this also affects mortar porosity and moisture transport properties [11].

Interface conditions could also be an explanation to why Johansson et al. [12] found a clear discrepancy between numerical simulations and laboratory results, stating the brick and mortar must have been more capillary active than assumed for the simulation. However, a more severe climatic exposure than assumed was also pointed out as a possible cause.

In order to limit interstitial condensation, airtightness around beam ends is suggested being an important measure. In Graz, Austria, monitoring interior insulation solutions applied to a historic masonry wall running past an attic floor, Ruisinger [13] demonstrated significantly reduced relative humidity (RH) at beam ends with sealing compared to non-sealed counterparts. Despite high RH at beam end for the unsealed solution, wood moisture in the beam ends did not exceed dangerous levels. With a masonry wall exposed to stable artificial winter conditions Vereecken and Roels [14] found lower RH at wooden beam ends when airtight sealing was provided, compared to no airtight sealing and tape only sealing. Kopecký et al. [15] investigated sealing around beam ends and concluded that airtight sealing did not ensure a robust moisture-safe solution for the case in question under climatic conditions of Prague, Czech Republic, although it improved the microclimate at the beam ends compared to an unsealed solution.

Other measures have also been proposed and studied. Use of capillary active insulation has received extensive focus [16], as it provides a possibility for increased inward drying by means of capillary transfer of moisture having reached the inner part of the brick layer. Allowing an increased heat flux throughout the wall around beam ends, by keeping a gap in the insulation [2,17] or by inserting a thermal bridge material [6], has also been investigated.

Smart vapor barriers (SVBs), or retarders (SVRs) have long been proposed as a solution for balancing water uptake and drying of building components [18]. With humidity-dependent vapor resistance the SVB can utilize the different conditions it operates under, which are mainly caused by yearly climatic changes. For a masonry wall with relatively vapor open interior insulation, cold exterior conditions ensure low RH at the exterior side of the barrier due to the temperature gradient over the insulation. Given the interior RH neither is too high (e.g. not above 50–60% [18,19] depending on the barrier product), this will cause the vapor barrier to significantly inhibit or reduce outward vapor diffusion. With warmer exterior conditions, the temperature gradient over the insulation will decrease or potentially even become reversed. If much moisture then persists in the masonry, significant vapor pressure increase will occur exterior of the barrier. Such conditions will cause the barrier to allow for inward vapor diffusion, given indoor RH is not too low for the SVB to stay open (e.g. not below 30–40%). With wall exterior exposed to sun radiation, inward vapor diffusion can be further amplified. A study of wet brick-clad walls has demonstrated that a vapor open interior finish will reduce vapor buildup in the insulation compared to a vapor tight finish [20]. Solar driven inward vapor flux has also been found to generate risk for biological materials present on the exterior side of a polyethylene vapor barrier in field studies [21]. Use of SVBs might therefore provide needed additional drying capability for masonry structures. However, there are only a few studies which combine interior insulation of masonry with a SVB or SVR. (Here we apply a distinction between the two; a barrier and retarder respectively having relatively high s_d - value, e.g. $s_d >$ or $\gg 10$ m, and relatively low s_d - value, e.g. $s_d < 10$ m. [22], at realistic but low RH.) Vereecken and Roels [14] applied a SVR to a mineral wool insulated test wall where they investigated airtightness and convective moisture transport to wooden beam ends. The study did not include driving rain, and only included a cold external climate, thereby not providing favorable conditions for inward drying through the retarder. Beyond being assessed to constitute a rather vapor tight system, neither the retarder function nor performance was addressed explicitly any further. Kopecký et al. [15] exposed an interior mineral wool insulated wall having a SVR ($s_d = 0.3$–5 m) to intense artificial driving rain (1.7 $L/(m^2 min) = 102\ mm/(m^2 h)$) for 40 min. The wall was part of a test façade exposed to several years of Prague, Czech climate, which in that time had low driving rain load. Artificial driving rain was applied mid of July giving approximately 1.5 months of warm weather before a colder autumn and winter. It was concluded the artificial rain worsened hygrothermal conditions in joist pockets. Still, the study did not include any similar wall for comparison which did not have a SVR. Retarder impact was not explored. De Mets et al. [23] monitored a test wall insulated on the interior with mineral wool and supplied with a SVR ($s_d = 0.3$–20 m, limits not reached at normal conditions). The wall was exposed to Limelette, Belgium climate, having wind driven rain load of 447 mm/m^2 over the three years in question. Comparing different insulation solutions, there was found a small positive impact of using capillary active insulation over the mineral wool + SVR solution; however, the choice of insulation material was deemed insufficient by itself, without other measures, to provide a moisture safe solution in combination with wooden beams. Specific impact of retarder was not addressed.

To better understand potential usefulness of SVBs, or SVRs, more studies and data are needed. Noticed lacking, are studies applying SVBs, having high s_d - values at low RH. Such barriers can potentially further limit interstitial condensation during winter conditions.

The objective of this study is to investigate how different configurations of interior insulated masonry affect moisture uptake and drying over a simple climatic sequence including driving rain. Investigation of, and elaborating on, the drying potential is given a special focus, with a Nordic climate in mind. For this reason, most configurations include a SVB to enable a significant potential (hypothesis) for inward drying. Embedded beam ends are included since these presumably compose the most moisture critical detailing related to interior insulation retrofit, when excluding corrosion and frost damage issues. However, assessment of hygrothermal performance regarding moisture tolerance and potential material damage or decay is not addressed in the study. The study- and monitoring design represents a rather holistic approach, assessing wetting and drying performance of whole interior insulated masonry wall segments. Hence, influence of brick-mortar interaction, interface conditions and microstructure on masonry behavior is not directly investigated.

In extent of the objective the following research questions are addressed; 1) to what extent will masonry variations, in brick type and masonry thickness, influence moisture uptake and drying performance? 2) will inclusion of a SVB significantly improve drying performance?

An aim is to enable results from the study to be used as data sets in benchmarking of hygrothermal simulation models, particularly set up for masonry structures addressing the comprehensive variety in material/structure behavior. Furthermore, the results may contribute to outline a range in structure performance, potentially for comparison to probabilistic hygrothermal simulation studies. Methodology for such studies have become further refined in recent years; [24–26]. Additionally, the results might possibly provide samples for neural network learning [27].

2. Materials and methods

2.1. General overview

A test wall composed of 9 masonry segments (Fig. 1(a)) has been constructed with various segment configurations. Influence from varying brick type, masonry thickness, interior insulation thickness and

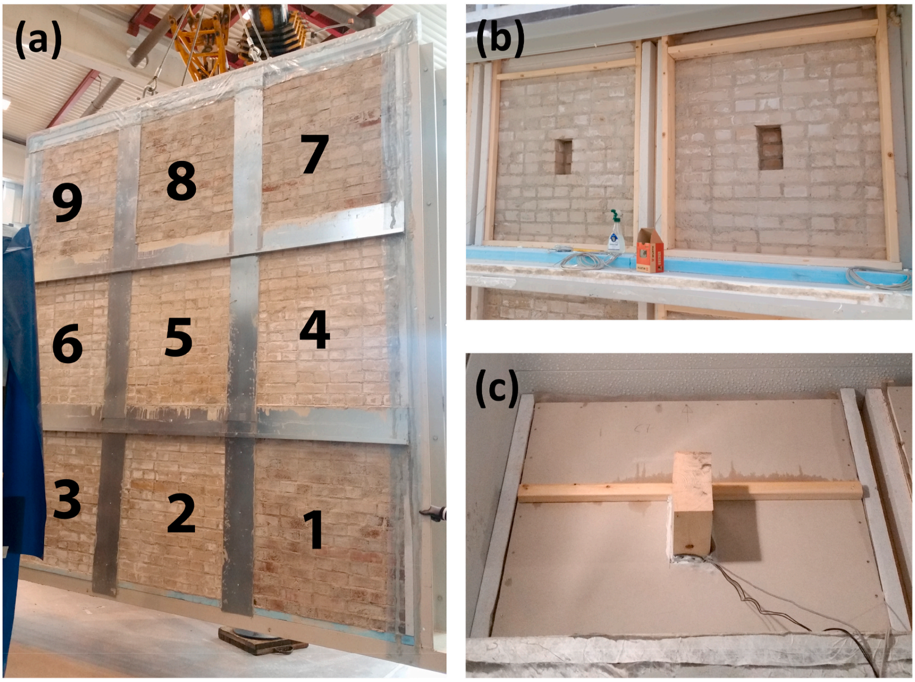

Fig. 1. (a) Test wall. Exterior face with flashings/gutters mounted. Each segment numbered. (b) Interior view of seg. 5 and 6 before insulation was mounted. (c) Interior view of seg. 7 after completed. Transverse wooden board only to fix beam end.

application of a SVB is studied. In an envelope climate simulator (Fig. 2) the wall is exposed to a climatic sequence, first ensuring wetting through cold climate rain events, before ensuring drying in relatively warm climate conditions. The exterior surface consists of exposed bare brick. Two experiment series, with equal climatic sequence, but with different interior insulation configurations, were completed in the work; however, the current paper is mostly limited to the first series. Following subchapters describe in detail; wall construction, instrumentation, experiment setup, climatic sequence and sensor data treatment.

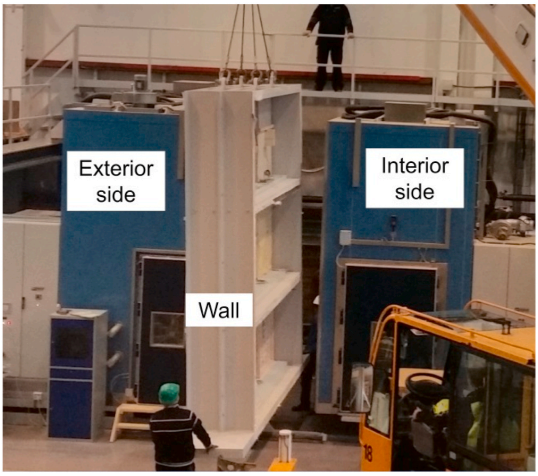

Fig. 2. Test wall lifted into the building envelope climate simulator.

2.2. Masonry materials

Two brick types were selected; one with moderate initial rate of absorption (IRA) and one with high IRA, both with specified dimensions LxWxH of 226 × 104 × 60 in mm. IRA follows definition of initial (1st min) rate of water absorption found in EN 772-11 [28]. Product information given by the producer are listed for each brick type in Table 1. Including a high IRA brick type was motivated by an assumption that this would resemble absorption behavior of typical brick types found in older buildings (late-19th to mid-20th century). Johansson and Whalgren [29] reported for instance a water flow rate three times higher in an investigated historic brick compared to modern bricks. The high IRA brick in the current study has an almost identical capillary absorption coefficient (A_w, Table 2) to that reported by Guizzardi et al. [30] being similar with bricks commonly found in existing older buildings. In contrast, Odgaard et al. [6] and Jensen et al. [31] applied a brick with a higher capillary absorption coefficient (0.278 $kg/(m^2 \cdot s^{1/2})$) to resemble brick found in Danish buildings from 1850 to 1950. A moderate IRA brick type is typically of more modern design, specifically designed to withstand harsher weather exposure. Table 2 summarizes data measured for the masonry products in the current study, with capillary absorption coefficient (A_w), capillary moisture content (W_{cap}) and vapor permeability (δ_v) being some central properties affecting moisture movement. A prescribed LC-mortar; LC 50/50/610, was used, where the

Table 1
Producer product data for the two brick types used.

Brick type	Moderate IRA	High IRA
Weight per brick [kg]	2.9	2.6
Brick density [kg/m^3]	2150	1750
IRA [kg/(m^2·min)]	1.5	4.5
Water absorption [vol-%]	10	25

Table 2
Material properties. Measured average and standard deviation, based on 20 samples each (5 samples for vapor permeability). Mortar joint samples were made between bricks of respective type (moderate IRA bricks brushed with water and high IRA bricks prewetted as in bricklaying of segments described in subchapter 2.3).

Material	Brick				Mortar			
Type/(between)	Moderate IRA		High IRA		(moderate IRA)		(high IRA)	
	Average	Std.	Average	Std.	Average	Std.	Average	Std.
Weight [kg]	3.05	0.06	2.46	0.02	–	–	–	–
Density [kg/m^3]	2166	60	1723	12	1788	27	1823	30
A_w [kg/(m^2·s$^{1/2}$)][a]	0.044	0.028	0.188	0.016	–	–	–	–
W_{cap} [kg/m^3][b]	116.67[c]	29.8[c]	255.74	8.2	–	–	–	–
δ_v [kg/(m·s·Pa)][d]	4.75E-12	6.2E-13	1.45E-11	6.50E-13	1.21E-11	6.59E-13	1.03E-11	6.21E-13

[a] Refer EN ISO 15148 [32] (measured through brick face).
[b] Taken as the hypothetical transition between capillary absorption and diffusion of trapped air.
[c] One sample omitted since a glassy surface prevented water absorption.
[d] Wet cup, EN ISO 12572 [33].

numbers correspond to lime/cement/aggregate mass ratios of binder content. Not all mortar properties have been tested explicitly or extensively for the current study (left empty in Table 2). From rudimentary testing A_w of the mortar is believed to be in the range 0.01–0.04 kg/(m^2·s$^{1/2}$). W_{cap} was not tested for the mortar; however, from indirect findings, W_{cap} between 167 kg/m^3 and 294 kg/m^3 are quite plausible.

A larger relative diversity in property values was seen among moderate IRA bricks than among high IRA bricks (Table 2). The latter behaved more predictable from specimen to specimen than the former when tested for water absorption. This difference among moderate IRA bricks can stem from the burning of the bricks. Support for this comes from observations that some bricks had a glassier surface, having undergone vitrification, and that the same bricks showed considerably lower water absorption.

2.3. Brick wall construction

The wall consists of 9 brick wall segments built into a steel frame having internal measurements 3600 mm × 3925 mm; refer Fig. 1(a). Steel decks, being part of the frame, support each level making out a row of segments, while two-inch-thick wood studs separate segments vertically. The brick segments were built on a 50 mm layer of XPS boards, giving insulation, and disconnecting the brick from the steel deck heat bridge. Refer Fig. 1(b). A metal flashing/gutter profile was mounted from top of the XPS, covering and rainproofing the exterior transition between the segment rows. Each segment was fitted between 50 mm EPS boards, one on each side (Fig. 1(c)). Seven segments were built one brick thick (226 mm), while the two remaining were built 1.5 brick thick (348 mm). Except for vertical collar joints separating the wythes being 18 mm thick due to brick dimensions, a joint thickness of 15 mm was otherwise used. Each segment was fitted with a centered beam pocket to be used for an embedded beam end. The pockets are half a brick plus a mortar joint thickness deep (104 + 18 mm). Consequently; 1.5 brick thick segments have 1 brick thick masonry between the beam end pocket and the exposed exterior surface, while 1 brick thick segments only have 0.5 brick in-between (see Fig. 3). Metal flashings were mounted vertically to cover and rainproof segment transitions on a row.

Brick laying was done by an experienced senior mason. To avoid too much water being drawn from the mortar during brick laying, high IRA bricks were prewetted before use. Prewetting consisted of submerging bricks with the end down for precisely 10 min. On average this resulted in a moisture content of 181 kg/m^3, which equals 71% of capillary moisture content, just above the 70% advised by Brocken [34] as a minimum to affect amount of extracted water from the mortar. Moderate IRA bricks were used directly without prewetting; however, to possibly reduce drying of the mortar, top of each course was brushed with water. A masonry brush was used. The mortar was mixed from just over 4.5 L of water per 25 kg of dry mortar. Flush joints were applied for the masonry, and all surfaces were brushed with heavily wetted mortar to create a rugged surface finish were the brick color could be seen through a very thin mortar coating/film.

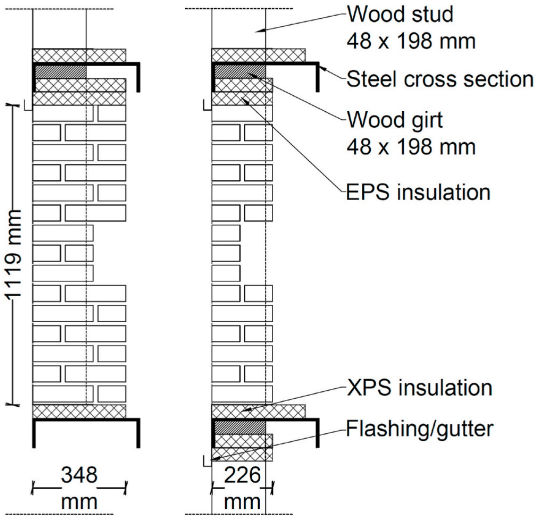

Fig. 3. Cross sections of brick segments. To the left 1.5 brick thick and to the right 1 brick thick.

2.4. Interior structure

Configurations of mineral glass wool insulation (0.035 W/(m·K) thermal conductivity), a vapor barrier and a 13 mm thick gypsum board finish were mounted on the interior of the wall segments as listed in Table 3. Segment 2 was left free of any interior structure to act as a non-retrofitted reference for comparison of two test series. The configurations listed in Table 3 (test series 1) were chosen in order to always have at least two segments for comparison with only one changing parameter.

A SVB, consisting of a humidity active membrane with protective polypropylene felt on each side, was applied interior to the insulation. Segment 5 is the exception, which for comparison was given a traditional polyethylene vapor barrier ($s_d \approx 50$ m). The SVB has a declared s_d - value span from 0.05 to 30 m, with lowest value at close to dew point conditions, and highest value at relatively low RH conditions, plausible during winter conditions. Vapor resistance testing data, referred to by a technical approval document for the SVB, implies that with an interior RH of 50% and a RH above 75% exterior to the barrier, s_d - values fall below 1.4 m. The following trend seemingly follow an exponential decay

Table 3
Configuration overview of wall segment characteristics for the 9 wall segments of test series 1.

Segment	1	2	3	4	5	6	7	8	9
Moderate IRA brick	✓	–	–	–	–	–	✓	✓	✓
High IRA brick	–	✓	✓	✓	✓	✓	–	–	–
Wall thickness [bricks]	1.5	1	1.5	1	1	1	1	1	1
Reference segment	–	✓	–	–	–	–	–	–	–
Insulation thickness [mm]	50	–	50	50	50	150	50	100	150
Interior gypsum board finish	✓	–	✓	✓	✓	✓	✓	✓	✓
Polyethylene vapor barrier	–	–	–	–	✓	–	–	–	–
SVB	✓	–	✓	✓	–	✓	✓	✓	✓
Dry U-value[a] [W/m^{2}K]	0.454	1.722	0.424	0.468	0.468	0.197	0.491	0.285	0.201
s_d-value[b] [m]	0.143	0	0.143	0.143	0.143	0.273	0.143	0.208	0.273
s_d - value masonry[c] [m]	10.08	3.22	5.04	3.22	3.22	3.22	6.66	6.66	6.66

[a] Segment calculated in accordance with EN ISO 6946 [35], masonry as inhomogeneous layers. Masonry products' thermal conductivities from EN 1745 [36]. Thermal bridge of beam end not considered.

[b] Approximate s_d - value of interior structure (insulation layer + gypsum board), vapor barrier excluded.

[c] Masonry calculated as inhomogeneous layers from brick and mortar vapor permeabilities.

function as it approaches a s_d - value of 0.18 m at 94% RH exterior to the barrier. However, scattering in the data suggests there is some uncertainty to these s_d - values. In series 2 segment 5 was given the same configuration as segment 4 in series 1. Series 2 otherwise focused on comparing different insulation materials exchanging mineral wool with aerogel and phenolic foam products. Thermal resistance was for the most part kept approximately the same, while the vapor resistance changed with insulation material. With exception of seg. 5, series 2 will not be addressed in the current paper, other than providing comparison for repeatability and performance assessment sensitivity.

Spruce wooden beam ends (Fig. 1(c)), 400 mm long and W x H dimensions of 107 mm × 213 mm, were placed into beam end pockets at a distance of 10 mm from pocket rear end. The spruce beam ends are taken from one log cut in Norway, being not particularly fast-grown, having a dry density of approximately 449 kg/m^3 (1 sample measured). An asphalt sill gasket was used as a capillary break between bottom of the beam end and masonry. The vapor barrier was taped around the beam end. To ensure that vapor could not circumvent the gypsum vapor resistance along the beam, the gap between the beam end and the gypsum finish was sealed with a sealant clay product. Clay in combination with the tape presumably provide a better vapor- and airtight solution than tape alone. Similarly, the gap between the beam and the masonry interior surface of segment 2 was sealed with clay to make it vapor- and airtight.

Presumably there is low probability of any air leak through the wall since no atmospheric pressure difference is imposed between the interior and exterior. Nevertheless, the climate simulator air conditioning system is equipped with powerful fans creating a well-mixed atmosphere and rather windy conditions, which could make air washing of the interior structure and beam end pocket plausible. However, with sealing of the vapor barrier to the beam end (tape and clay), in addition to mounting of the gypsum board with densely placed screws along the segment perimeter, air washing becomes unlikely.

2.5. *Instrumentation*

A total of 20 Sahlen sensors, 21 RH sensors and 9 beam end resistance moisture meters were used. All Sahlen sensors and 4 RH sensors were built into the masonry during brick laying. The built-in RH sensors were shielded by a layer of vapor open wind barrier fabric to mitigate capillary connection to the masonry.

The RH sensors, of type E + E Elektronik E0E06-FT1A1, have a working range of 0–100% RH and −40 °C–60 °C. Accuracies are ±3% RH, range 0–90% RH and ±5% RH, range 90–100% RH, and < ± 0.4 °C in the operating temperature interval of the experiment. A Sahlen sensor includes a thermistor and a resistance moisture meter (based on birch as wood species). It has a working range 8–65 weight-% moisture content and −20 °C–60 °C. The Sahlen sensor is a cylindric plastic tube with a small piece of birch wood encapsulated in vapor open plastic foam. The wood has electrodes embedded to measure the moisture content through electrical resistance. With a sorption isotherm for the birch the RH can be (roughly) estimated. One advantage over ordinary RH-sensors, which are more accurate at RH levels below 95%, is the Sahlen sensor measurement robustness for periods with saturated conditions. Fig. 4 shows a Sahlen sensor being placed in a mortar joint. Beam end resistance moisture meters consist of two non-insulated screws, 25 mm apart as recommended in Ref. [37]. Measuring lowest resistance between the screws along their depth, it is presumed the measured result represents moisture content at the surface, where moisture content is expected being highest. Accuracies of the wood sensors (Sahlen and the beam end resistance moisture meter) are addressed in Appendix B and subchapter 4.1 and 4.4.

The sensor thickness almost fills out the width of a mortar joint. When placed in the masonry, sensors were typically in physical contact with the lower brick, but no measures were taken to ensure contact when or after mortar was added to form the joint. It should be noted that Sahlen sensors, although placed in the masonry, do not measure actual moisture content in the masonry materials, but instead, due to different hygric properties, rather moisture content in the birch sensors; refer Fig. 14 and discussion in subchapter 4.4. Hence, a Sahlen sensor is a material-indirect measuring probe in contrast to for instance a time-domain reflectometer (TDR) sensor [38] or an electrical conductivity sensor [30,39] which can give measurements for porous masonry materials they span. Fig. 5 shows sensor placements. Name tags have been allocated each sensor; SO (Sahlen, outer), SI (Sahlen inner), SID (Sahlen inner diagonal), B (beam), RH (relative humidity), RHD (relative humidity diagonal). Numbers refer to segment number, while i and ii refers respectively to the lower and upper sensor of a diagonal pair. With exception of diagonal sensors which are diagonally opposing each other, (well) within segment extents, all sensors are located at a centered

Fig. 4. Placement of Sahlen sensor in segment 5.

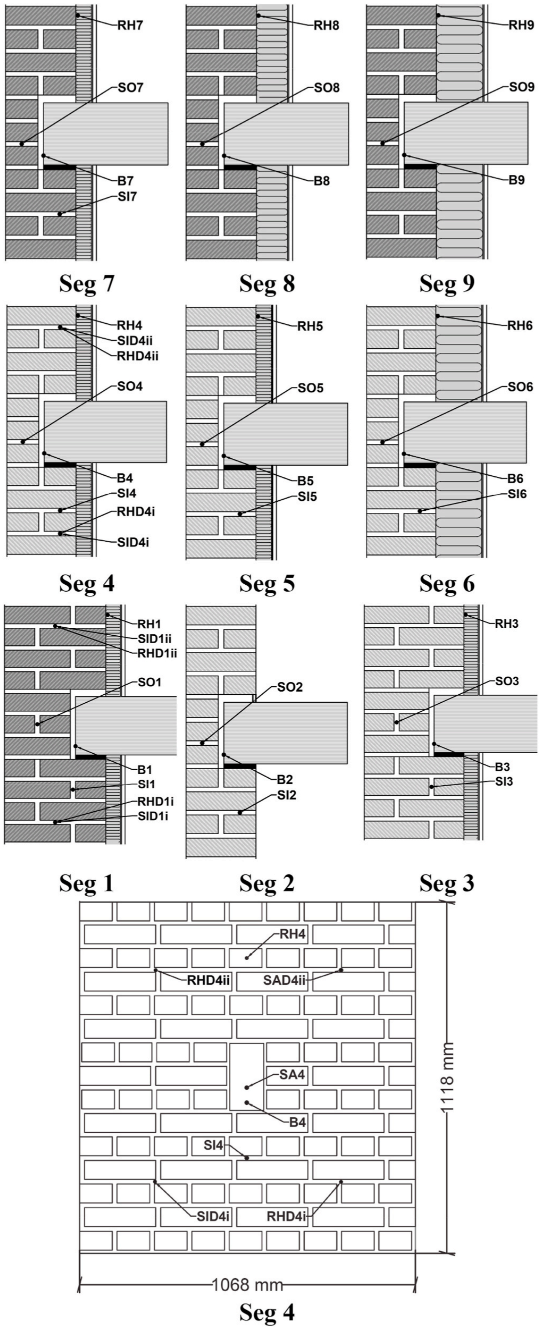

Fig. 5. Cross sectional overview of the 9 wall segments, including sensor locations. Moderate IRA segments shown in dark color. Below, Seg. 4 with projected sensor locations seen from interior.

vertical plane through their respective segment. Diagonal sensors are included to investigate moisture distribution in the segment, i.e. degree of evenness over the wall plane.

2.6. *Experiment setup*

The brick wall was installed in the large-scale building envelope climate simulator shown in figure Fig. 2. Consisting of an exterior climate chamber and an interior climate chamber, the climate simulator is able to generate controlled dynamic conditions on building envelope wall elements. In the exterior climate chamber, there are options for controlling temperature, humidity, water spray (rain) and light radiation (solar radiation), while the interior climate chamber has options of temperature, humidity and atmospheric pressure. Temperature at the exterior can be varied between −20 °C and 80 °C and at the interior between 5 °C and 50 °C.

The RH on both sides of the wall can theoretically be varied the full range of 5–100%, supported by experience with the simulator; however, the recommended range in the user manual is 20–95%. Rate of change in temperature and RH is limited to 0.5 °C/min and 5%/min respectively.

A fixed water spray rate of approximately 47 mm/m^{2}h can be turned on and off. The applied rain load intensity is relatively high compared to maximum intensities given in Ref. [40], calculated from observation station data relevant for comparison. Since focus has been to ensure sufficient masonry wetting for subsequent drying, invoking involvement of the SVB, resembling real wind driven rain weather has not been sought.

2.7. *Preparation (drying)*

The wall was dried fully assembled at conditions shown in Appendix A until all sensors, except for seg. 1 and 3, showed dry conditions in the masonry, i.e. Sahlen sensor moisture contents approximately below 10%. The 1.5 brick segments dried out too slowly to arrive at such low moisture contents. Seg. 3 was close with SO3 at 10.4% and SI3 at 12.5%, and presumably reasonably dry. For seg. 1 SID1i was the worst sensor showing 25.5%, while SO1, SI1 andSID1i all showing between 14 and 15%.

2.8. *Climatic sequence*

A climatic sequence, of which an overview is presented in Fig. 6, was designed to investigate wetting and drying of the wall segments. A more detailed description and explanation can be found in Appendix A.

Unfortunately, the climatic sequence was introduced to some "noise" in series 2 due to malfunctioning equipment, and at one occasion the overlooking of an incorrect setting. A valve, governing steam generation for the interior side, broke down a few times, and an actuator became worn out. The malfunctioning equipment resulted in high interior RH, close to or at 100% RH. Resulting impact is shown as spikes in RH in Fig. 12 at 69, 793, 2207 and 2407 h, marked (1)–(4). The incorrect setting resulted in a drop in exterior temperature, after the warm period was implemented, at 1656 h.

2.9. *Sensor data treatment*

Treatment of data gathered from Sahlen and beam end sensors are addressed in detail in Appendix B.

3. Results

Results are presented with two different approaches; 1) comparison of moisture development over time between relevant segments, 2) identification of under- and overperformance of each segment 4–9 (seg. 1–3 not included due to different thickness/sensor locations, or lack of interior insulation, making sensor result comparison problematic).

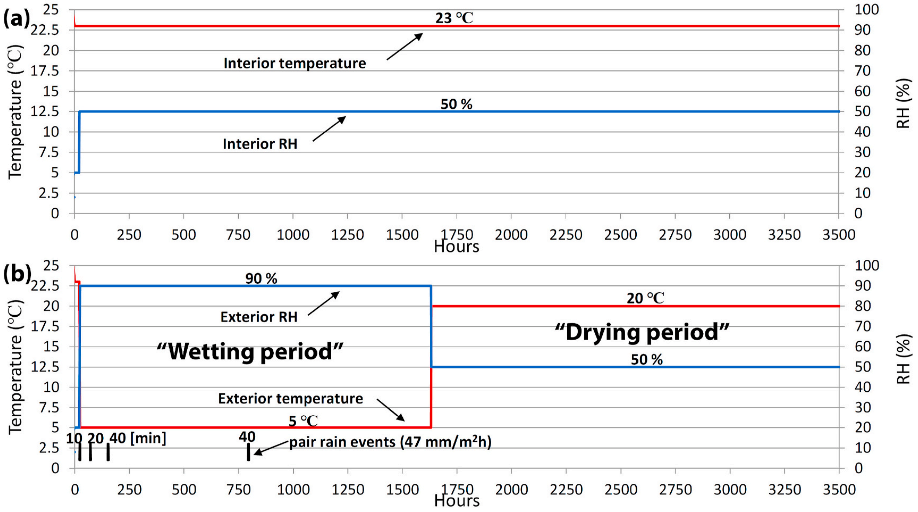

Fig. 6. Climate sequence overview; (a) interior climate, (b) exterior climate. Wetting period will denote the cold climate period and drying period the warm period, refer Appendix A for explanation.

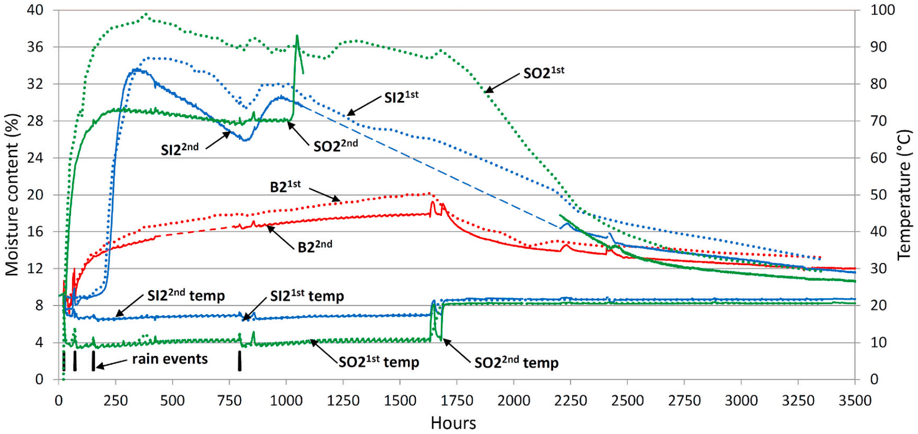

Fig. 7. Reference segment for both experiment series (1st and 2nd). Dashed lines indicate presumed trend for lost data due to logger malfunction. Trend of lost data for SO2^{2nd} remains non-presumed, as the spike in moisture content before the missing data may indicate a sensor/logger malfunction or interference.

Performance is presented through assessment criteria, applied to each segment and made relative to the average (criterion) of segments. Overperformance implies less/slower moisture uptake during wetting period (Fig. 6) and higher/faster drying during drying period, and vice versa for underperformance. Appendix C addresses in detail how segment performance has been assessed. Table 4 summarizes result from comparing performance of moderate IRA segments to that of high IRA segments. Relative performances of series 1 are given in Table 5. Table 6 summarizes results from comparing change in performance of each brick type from series 1 to 2, in order to look for repeatability issues between series, further addressed in subchapter 4.1 and 4.2.

With regard to graph-containing figures (Fig. 7 - Fig. 12 + Fig. 15) the temperature graphs have the same line type and color as the corresponding RH/moisture graphs which are easier distinguishable, higher up in the same figure diagram.

3.1. Reference segment

Segment 2 is used as a reference segment to compare repeatability over the two series. Fig. 7 shows SO2, SI2 and B2 sensor readings for each series. SO2 readings from series 2 are significantly lower than from series 1. Furthermore, there appear a sharp spike in the readings, just before logger malfunctioned, for which no explanation has been found. Due to the clear discrepancy to that of series 1, actual trend of SO2 in series 2 remains unclear. While the moisture content readings for SI2 and B2 in series 2 are lower by a few % moisture content, their trends hold up to series 1. Since series 2 has been logged with a data logger those readings have finer resolution. Especially the small temporary jump in moisture content of B2 series 2, at start of the warm period, would not be visible in the resolution of series 1.

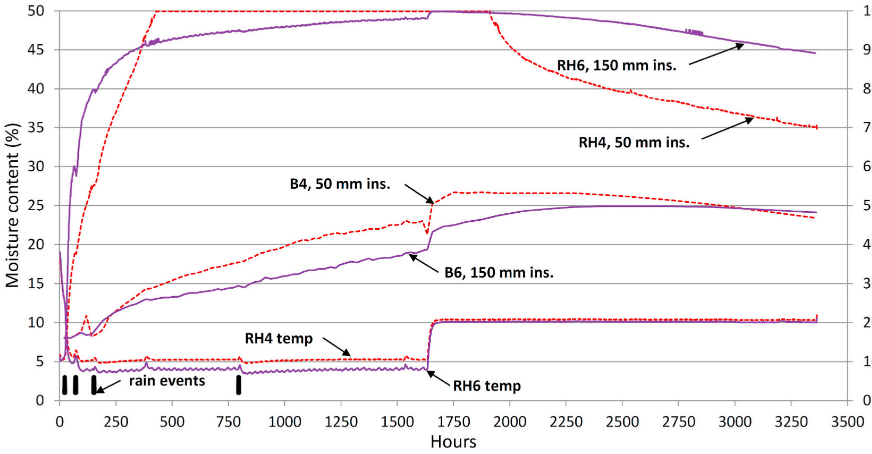

Fig. 8. High IRA. RH and beam end readings for seg 4 (50 mm insulation) and seg 6 (150 mm insulation).

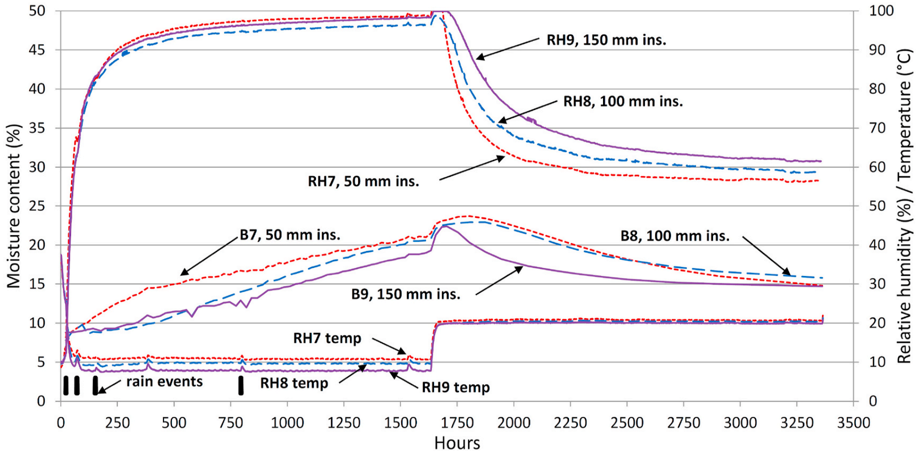

Fig. 9. Moderate IRA. RH and beam end readings for seg 7 (50 mm insulation), seg 8 (100 mm) and seg 9 (150 mm).

3.2. *Insulation thickness*

For higher insulation thickness RH sensor readings decrease slower; refer Fig. 8 and Fig. 9. Beam end and SO sensors show a more complex picture according to Table 5. Here SO8 (100 mm ins.) overperform while B7 (50 mm ins.) underperform in the wetting period. Whereas for the drying period, B9 (150 mm ins.) has the highest moisture decline index; although, as seen in Fig. 9 this is amplified by a stronger temporary jump in moisture content at the beam end at initiation of the warm period. RH6 (150 mm ins.) has significant underperformance in moisture decline rate index compared to both segment 4 and 5 (both series) (50 mm ins.); refer Table 5. However, Fig. 8 shows RH6 has a different drying development than all comparable segments; seg. 4–5 (Figs. 8 and 12) and 7-9 (Fig. 9). RH6 also underperforms somewhat with the moisture growth rate index, but not to the same extent. Segment 6 otherwise performs more or less in line with the other moderate IRA segments 4 and 5.

3.3. *Brick type*

Fig. 10 shows a clear difference between moderate IRA and high IRA segments for beam end moisture content, when entering the warm period. B7 and B9 fall rapidly compared to their counterparts B4 and B6. B8 has a similar trend as B7, as seen in Fig. 9, but is not included in Fig. 10 since it does not have a high IRA counterpart with same insulation thickness. Table 5 also indicates a systematic overperformance of the moderate IRA segments (Seg. 7–9) during the warm period for beam and RH sensor types. During the cold period, there is both under- and overperformance among both moderate and high IRA segments; thereby no clear, consistent picture. Among 1.5 brick thick segments, seg. 1 (moderate IRA) has for the most part (Fig. 11), a lower RH and beam end moisture content than seg. 3 (high IRA).

3.4. *Masonry thickness*

Substantially slower drying rate is seen in the 1.5, brick thick segments 1 and 3 than in the 1 brick thick segments 4 and 7; refer Fig. 11. Interior insulation, SVB and gypsum had to be removed in the middle of

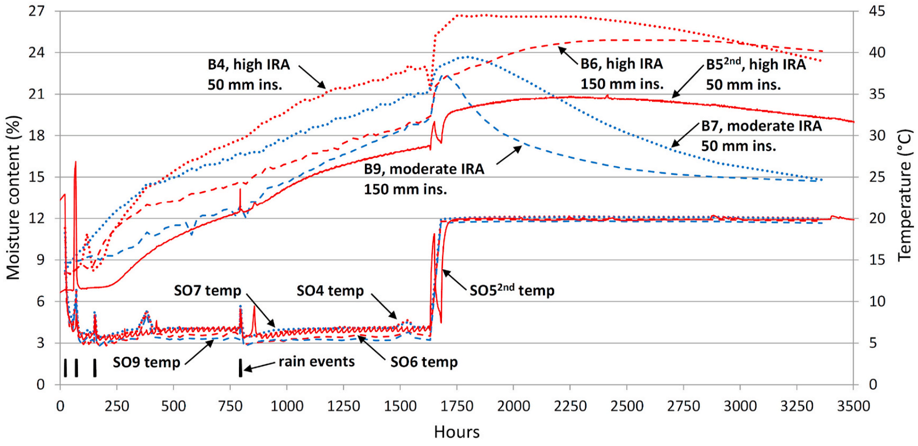

Fig. 10. Beam end measurements for high and moderate IRA segments having 50 mm insulation (B4, B5 and B7 respectively) and 150 mm insulation (B6 and B9 respectively). Temperature readings, included for reference, are taken from the SO sensors. SO temperatures are in the cold period substantially lower than that at the beam end (not measured); refer Fig. 5 for sensor locations.

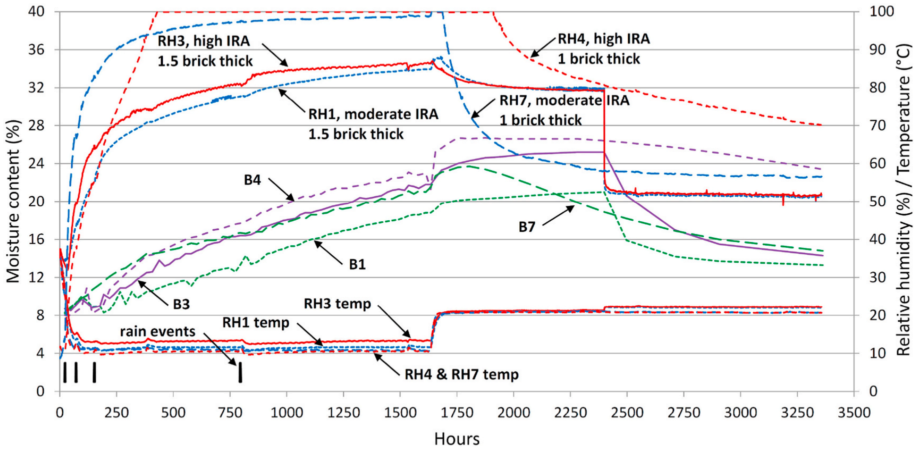

Fig. 11. RH and beam end sensor results for seg. 1 and 3 (1.5 brick thick) and seg. 4 and 7 (1 brick thick). Line color sorted on IRA: moderate IRA seg 1 and 7; high IRA seg. 3 and 4. Removal of inner structure causes sharp drop in graphs for seg. 1 and 3 at 2378 h. (For interpretation of the references to color in this figure legend, the reader is referred to the Web version of this article.)

the drying period for the thick segments 1 and 3 of series 1, as the masonry otherwise would not dry out in time for the scheduled series 2 (segment 1 did not dry out in time and was left uninsulated in series 2). Consequently, there is a sharp drop in moisture readings at 2378 h progressed.

RH readings show a lower maximum RH level for segments 1 (88% RH) and 3 (87% RH) compared to 4 and 7, which reach 99.89 and 100% RH respectively. The RH level of segment 7 drops almost immediately after the warm period starts, while segment 4 drops 228 h later. While RH1 and RH3 show a small initial drop after the warm period begins, only slow further decrease is seen.

Beam ends for segment 1 and 3 have a lower moisture increase in the cold period compared to their 1 brick thick counterparts of same IRA brick type. With the onset of the warm period, B7 shows initial increase before substantial drying takes place. The moisture content increases initially for B1, B3 and B4. For B4 it flattens out until 2280 h progressed before slowly decreasing, whereas it continues to increase for B1 and B3 until insulation is removed.

3.5. *Vapor barrier*

In Fig. 12, Seg. 5, equipped with polyethylene vapor barrier (RH5), has a slower rate of wetting in the cold period compared to seg. 4 (RH4), equipped with a SVB. Since RH5^{2nd} is influenced by malfunction (1), no information can be drawn from it in the cold period. However, in the warm period more rapid drying is seen for RH5^{2nd} than for RH5, respectively having smart and polyethylene vapor barrier. Also, RH4 has a sharper decline than RH5. Sensor B5^{2nd} has consistently lower moisture content than both B5 and B4, with the latter being the highest. A slightly more pronounced downward slope can be seen at the end of the drying period for B4 and B5^{2nd} (SVB), compared to B5 (polyethylene vapor barrier). With exception of SO sensors, Table 5 indicates seg. 4 having a slightly higher moisture content than seg. 5.

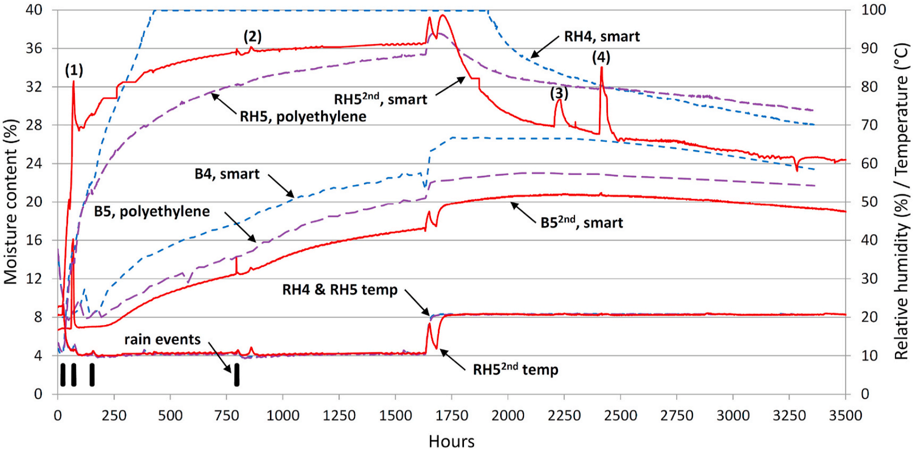

Fig. 12. RH and beam end sensor readings for seg 4 series 1 (SVB) and seg 5 series 1 and 2 (polyethylene and SVB respectively). Numbers (1)–(4) identify climate simulator malfunctions (series 2 only), where interior RH briefly approached or touched 100%.

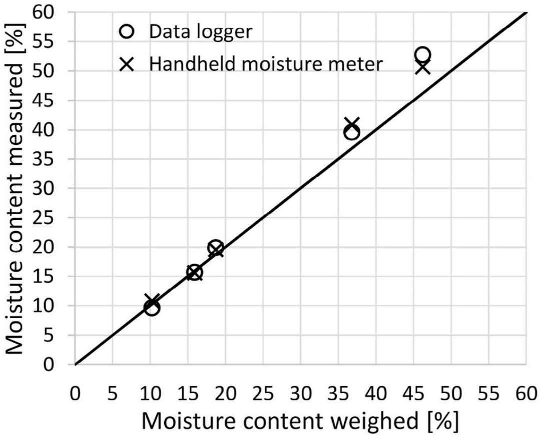

Fig. 13. Moisture measurement methods, applied tangentially/radially to growth rings in a 5 cm thick beam end cutting, compared to weighed moisture content. Handheld moisture meter and data logger respectively used in series 1 and 2.

4. Discussion

Before discussing the results there are some weaknesses with use of the MGRI and MDRI criteria, detailed in Appendix C, which should be understood. Although MGRI nicely address rate of wetting and whether a relatively high moisture content is achieved quickly, it will hardly say much about the final moisture level at end of the cold period. Regarding MDRI, rapid drying is favored, which might conceal that a sensor drying out slowly at first, could finally end up dryer than sensors it is compared to.

4.1. Series repeatability issues

Repeatability were not accurately achieved when comparing the reference segment of the two series shown in Fig. 7. It is not known why the moisture content of series 2 is lower. Sensor SO2 shows considerably lower moisture content in series 2; however, the cause of the spike in moisture content just before the logger malfunctioned have not been identified and it may be some malfunction or interference with how the sensor/logger operated. Therefore, the SO2 result in series 2 is questionable. An exercise was undertaken to investigate the possibility of systematic change from series 1 to 2, in order to assess possible reasons for the difference seen with seg. 2. A similar lower SO level was also the case for the other SO sensors. Although not shown explicitly in current paper, the trend is summarized in Table 6. To clarify, without going too much into series 2, it is of interest that for the SO sensors the moisture content is consistently lower for all segments of series 2, except for segment 8 where it remains lower until the last rain event, whereon after it exceeds series 1. A drop was also seen in several of the SI sensors, but some exceptions with higher moisture level among those makes that less consistent. Remaining sensors do not show consistent change from series 1 to 2, refer Table 6. Of course, segments of series 2, with exception of the reference segment, have other interior insulation solutions, and the moisture content would be expected to differ between the two series, especially over the course of time, due to different dry-out conditions. However, when limiting the view to wetting associated with the rain events, detected by the SO sensors, which are furthest out in the masonry, a close response similarity between the two series would be expected. This is found not to be the case, both verified by visual comparison of graphs between series for each segment (not shown in current paper) and comparison of the calculated moisture growth rate index, summarized in Table 6. Regarding the beam end sensor B2 in Fig. 7, it also lies a bit lower for series 2, but the same is not consistent for the other segments (not shown in current paper). However, both the time of equipment malfunction, mark (1) in Fig. 12, and impact of the different insulation solutions of series 2, may have impacted beam end sensors more than the case is for SO sensors. Furthermore, beam end moisture content may have a relatively slow response to rain events [41]. Consequently, series comparison for beam sensors are less compelling than for SO sensors.

Plausible causes for fall in SO sensor moisture content from series 1 to 2 may include; 1) small discrepancies in rain event durations and rainwater temperature, 2) unequal initial masonry moisture contents, 3) different measurement equipment/method 4) movement of fine particles, minerals and salts affecting masonry sensors or water uptake, 5) durability of Sahlen sensors. Having assessed these plausible causes, 2) unequal initial moisture content, is perceived as the likely dominant cause. However, non could be completely disregarded having influence; 1) is believed to be insignificant, while 4) and 5) lack sufficient

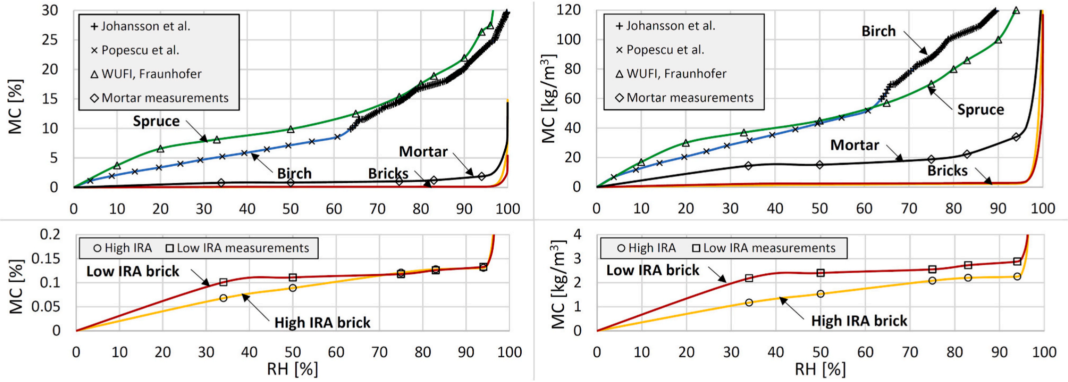

Fig. 14. Adsorption curves for key materials in the study. Left; moisture content (MC) as weight %. Right; MC as kg water per m^3. Lower graphs zoom in on the brick. Birch (Sahlen sensor) values are taken from Johansson et al. [12] and expanded with the reference adsorption curve from Popescu et al. [44]. Spruce values are taken from the Fraunhofer WUFI material database [45]. Measurements refer to testing conducted in connection with current study, following EN ISO 12571 [46]. Continuation of curves after 94% RH (last measurement point) is only indicative of trend towards the capillary absorption limit and has not been measured.

Table 4
Directional change (trend) in performance criteria between brick types; seg 7–9 (moderate IRA) compared to 4–6 (high IRA). Criteria average sorted on series.

		Series 1	Series 2
Wetting	SO moisture cont.	Lower/indet.	Lower/indet.
	SO growth rate	Lower/indet.	Lower/indet.
	B moisture cont.	Indeterminate	Indeterminate
	B growth rate	Indeterminate	Indeterminate
	RH moisture cont.	Indeterminate	Indeterminate
	RH growth rate	Same/higher	Indeterminate
Drying	SO decline rate	Similar	Similar
	B decline rate	Cleary higher	Higher
	RH decline rate	Cleary higher	Higher/indet.

Table 5
Segment relative performance to criteria average. Overview of sensors for series 1. Black represents underperformance, white overperformance, gray fairly average. Criteria average sorted on series 1.

	Segments	4	5	6	7	8	9
wetting	SO moisture cont.	0.98	1.15	1.23	0.93	0.65	1.06
	SO growth rate	1.00	1.23	1.34	0.87	0.44	1.12
	SI moisture content	1.30	1.25	1.22	0.73	X	X
	SI growth rate	1.51	1.46	1.42	0.54	X	X
	B moisture cont.	1.14	0.96	0.98	1.09	0.94	0.90
	B growth rate	1.33	0.86	0.96	1.30	0.79	0.76
	RH moisture cont.	1.01	0.84	1.03	1.06	1.03	1.04
	RH growth rate	0.96	0.77	1.05	1.10	1.06	1.07
drying	SO decline rate	0.99	1.01	0.96	0.98	1.00	1.05
	SI decline rate	0.98	0.98	0.84	1.00	X	X
	B decline rate	0.46	0.69	0.38	1.31	1.29	1.88
	RH decline rate	0.66	0.73	0.21	1.66	1.46	1.28

Table 6
Directional change (trend) in performance criteria from series 1 to 2. Criteria average sorted on brick type.

		Seg 4-6 High IRA	Seg 7-9 Moderate IRA
Wetting	SO moisture cont.	Falls clearly	Falls
	SO growth rate	Falls clearly	Falls
	B moisture cont.	Indeterminate	Rise clearly
	B growth rate	Indeterminate	Rise clearly
	RH moisture cont.	Rise clearly	Indeterminate
	RH growth rate	Rise clearly	Same/rise
Drying	SO decline rate	Indeterminate	Indeterminate
	B decline rate	Rise	Indeterminate
	RH decline rate	Rise	Indeterminate

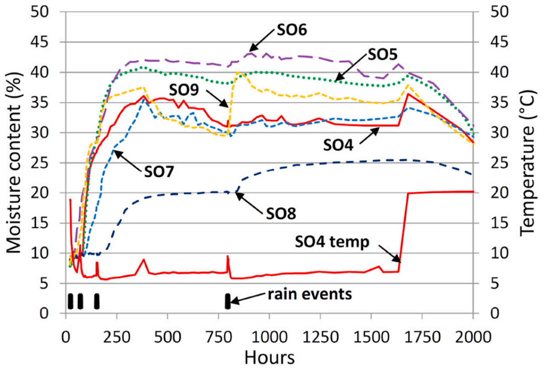

Fig. 15. Comparison of SO sensors. Temperature of SO4 included for reference to climatic sequence temperature change.

information to be properly assessed. 3) was investigated, finding good correlation (Fig. 13) between measurement methods and actual moisture content, in line with expectation arising from accuracy margins reported in Ref. [42].

4.2. RH wetting criteria

Results in Table 6 related to RH wetting criteria were found misleading due to a clear correlation between malfunction (1) in Fig. 12 and a higher moisture content and growth rate criteria for series 2. This was the case for both moderate and high IRA brick; however, for moderate IRA brick a lower overall RH level for series 2 in seg. 7 and 8 conceals the impact on the criteria (this is not shown in present paper; only mentioned to explain Table 6). No apparently significant impact is seen from the malfunction on other sensor types; however, since presumed malfunction-caused moisture uptake would take time to reach these sensors, impact on sensor readings would nevertheless be low compared to moisture impact from rain events. RH wetting criteria trends in Table 6 should therefore be disregarded. Related, it should be noted that the equipment malfunctions marked (3) and (4) in Fig. 12 affect the criteria for the RH sensors of series 2 by showing less drying than would otherwise be the case. RH6 of series 2 are strangely affected by this and becomes hard to interpret. Nevertheless, results in Table 6 are believed to remain unaffected by these malfunctions.

4.3. Insulation thickness

It appears insulation thickness has a clear impact on the masonry-insulation interface drying rate, as seen both for high and moderate IRA bricks (Figs. 8 and 9); however, the puzzling shape of the RH6 curve warrant some skepticism to the sensor trustworthiness (RH sensors sometimes show irregular performance after exposure to 100% RH). The effect on beam ends are more subtle, although minor improved drying rates are seen at the end of the warm period for B4 and B7 (50 mm ins.) respectively compared to B6 (150 mm ins.) and B8 (100 mm ins.). It strengthens the picture that both B4 and B7 respectively start with a higher moisture content than B6 and B8 at the initiation of the warm period. However, the low moisture content experienced in B9 (150 mm ins.) after the cold period, and its rapid drying in the warm period, shows other factors except change in insulation thickness influence beam end performance.

4.4. Brick type

Differences between moderate and high IRA segment performance seem apparent. Tables 4 and 5 show clear beam and RH drying criteria overperformance for the moderate IRA segments 7–9 compared to the average of segments 4–9 for series 1 and also, but to less extent, series 2. Hence, the high IRA segments 4–6 underperform. Since moderate IRA bricks have both a lower capillary diffusivity and a capillary moisture content (Table 2), one may suspect less water from the rain events have been absorbed in the moderate IRA segments, resulting in a smaller quantity of water needed to dry out compared to the high IRA segments. Coupled with a lower vapor permeability for the moderate IRA brick, less vapor might be driven off the masonry towards the interior, after the interior masonry surface falls below the over-hygroscopic range. This might explain why there is no over- or underperformance in drying rate found for the SO and SI sensors, as vapor diffusion will go slower in moderate IRA segments, thereby counteracting a presumed lower water content. It might however be worth contemplating Fig. 14. As seen, the adsorption of the two brick types neither differ much nor change much over the range 70–94% RH, which correspond to birch (Sahlen) moisture contents below 23%. In fact, moderate IRA bricks have higher adsorption than high IRA bricks in absolute terms (kg/m^3), over the whole range below 94% RH. Presumed equal Sahlen sensor levels for the different IRA brick type segments; if more moisture is taken up by high IRA brick, compared to moderate IRA brick, it only has that capacity at RH over 94%, or more likely, in the over-hygroscopic range as one approach the capillary moisture content. Point being, although most of the Sahlen sensors indicate moisture contents in this region after the rain events, investigation of this region of the adsorption curves have not been attempted in the current study, thereby limiting what conclusions can be drawn here. From Fig. 15 it can be noted that only SO8 is at or below 25% moisture content for the entire time. Some of the SI and SID sensors operate for longer times in the region below 23%; however, the moderate IRA segments have too few of these for comparison. Also noteworthy; in Fig. 14 for RH below 94%, it is actually the mortar joints which holds most of the moisture in the masonry (kg/m^3), not the bricks. Since the sensors are embedded in the mortar joints and not the bricks, this might have implications regarding sensor response time compared to occurrence of changes in the moisture content in bricks as they dry out. Furthermore, response time behavior of the Sahlen sensors are unknown; although a “plug sensor” product, which might be somewhat similar to a Sahlen sensor, have been reported to have long response times (up to 150–200 h) [43], making it most suitable for seasonal wetting and drying and not rapid phenomena. There might therefore be a delay in SO, SI and SID results compared to actual moisture content in surrounding masonry after rapid changes in the climatic sequence.

Regarding wetting, high IRA segments seem to have a higher rate of moisture uptake in the masonry (SO and SI sensors Table 5); however, also segment 9 shows relatively high rate, and there are unfortunately no SI sensors in segment 8 and 9 to substantiate further. Segment 8 shows the lowest SO moisture uptake rate, significantly lower than the other segments. Beam and RH wetting criteria show no clear difference between moderate and high IRA segments. For the 1.5 brick thick segments, it can be seen in Fig. 11 that the moderate IRA RH1 lags a bit behind at a lower level during wetting than the high IRA RH3. Although it is difficult to say, this difference could partly stem from a higher brick-mortar/mortar-brick interface resistance at the collar joint, associated with dry cured compared to wet cured mortar reported by Derluyn et al. [11] (in current study respectively as relatively dry moderate IRA bricks seg. 1 and prewetted high IRA bricks seg. 3). However, both the mortar density and vapor permeability given in Table 2 have the opposite correlation to curing condition to that reported in Ref. [11], which may indicate that the high-IRA prewetting was far from sufficient to establish truly wet curing conditions. Also, B1 increases less than B3, even though there is no continuous collar joint in the path of rain penetration. Therefore, the difference in capillary transport coefficient between the two brick types may nevertheless be the dominant cause, if not differences among the segments in the horizontal brick-mortar interface porosity also plays a significant part.

4.5. Masonry thickness

The 1.5 brick thick masonry shows a slower or more limited wetting of RH and beam end sensors than those in the 1 brick thick segments. Similar, lower RH was reported by Zhou et al. [5] for simulated 3 wythes compared to 2 wythes thick masonry, crediting it to larger moisture storage capability. Except for the increased masonry volume available for rainwater deposit, and the increased thickness to overcome by capillary diffusion, it can also be understood by the barrier effect of the collar joint [8] being present in each course of the 1.5 brick thick masonry compared to every other course in the 1 brick thick masonry. Still, the 1.5 brick thick masonry shows poor drying capabilities. Assessing sensors embedded in the masonry there is insignificant to very limited drying before insulation is removed for seg. 1 and 3. Also the beam end sensors B1 and B3 show an increase in moisture content after onset of the warm period until insulation is removed; however, comparing B3 of series 1 to that of series 2 (not shown in present paper), although with a different insulation material, a drying trend could have been expected shortly after if the insulation had not been removed. A plausible explanation of the slow drying performance of the thick segments is the extra thickness which outward drying needs to overcome. Moisture having accumulated deep into the masonry towards the interior will have impeded drying towards the exterior, due to the thickness and because it needs to pass back through collar joints; hence, more inward drying is relied upon to arrive at dryer conditions. Especially for seg. 1; extra initial moisture, compared to other segments, may also have impacted the results, diminishing result trustworthiness.

4.6. Smart vapor barrier

Assessing the results (Fig. 12), it is not possible to conclude on SVB influence during the cold period. Although B5^{2nd} has a lower moisture content trend than B5, it cannot be ascribed the SVB, due to inconsistencies in repeatability from series 1 to 2. Furthermore, the SVB would not promote inward drying in the cold period since the vapor pressure gradient opposes drying and since the barrier s_d - value in this period is quite high. If any, the SVB (s_d - value under these conditions crudely estimated to $s_d \approx 20–30$ m) would promote a larger outbound vapor flux than the polyethylene barrier ($s_d \approx 50$ m). Given this vapor would meet a saturation vapor pressure in a rain wetted masonry, additional moisture, although presumably relatively insignificant, would be deposited in the masonry with the SVB compared to with the polyethylene barrier. In perspective, the wooden beam end constitutes along its total length of 400 mm the weakest vapor resistance, with a $s_d = 1.72$ m if the longitudinal vapor resistance factor of 4.3 found in the WUFI material database [45] is applied. The beam end cross-sectional area only constitutes 1.9% of the segment's surface area, the vapor barrier covering the rest; however, the beam has a direct path to the beam end sensor. Furthermore, wood cracks in beam ends could also be influencing on effective vapor resistance. Especially beam end results could consequently be sensitive to differences in wood quality. Although the beam ends originate from the same log, different occurrence of wood cracks and knots has naturally been observed. For the drying period, RH5^{2nd} is seen to decline faster than RH5. Had it not been for RH4 which also surpasses the drying of RH5, it could have been a repeatability issue. However, since both RH4 and RH5^{2nd} have a similar drying trend, something which also barely can be seen comparing B4 and B5^{2nd} to that of B5, it gives an indication the SVB provides increased drying for the segments. If in fact the SVB can be ascribed the large difference in drying rate between RH5 and RH5^{2nd}, it provides great improvement at the interface between masonry and insulation. The beam end seems to have less pronounced improvement. From Fig. 12 it is worth noting how sensitive RH5^{2nd} is to the spikes in indoor RH caused by the malfunctions.

After series 1 the wall was set to dry at an exterior and interior temperature of 35 and 30 °C respectively. Consequently, a negative vapor pressure gradient formed towards the interior. When, under these conditions, the polyethylene vapor barrier of seg. 5 was removed, condensed moisture was observed on the side facing the insulation. No condensed moisture was observed on the SVBs. This could point to the SVB possessing beneficial performance in cases of inward solar driven vapor flux.

5. Conclusions

Interior insulated brick masonry wall segments have been investigated, undertaking wetting and drying. Large variety in masonry behavior, and hence segment performance, is seen from results. This despite favorable interaction between mortar and brick was attempted through relatively extensive prewetting of high IRA bricks during construction. Whether the cause is variety in mortar-brick interface quality or brick properties remains unknown. Large variety in masonry behavior was also seen among moderate IRA segments, made with non-prewetted bricks; however, this brick type had larger relative variety in capillary absorption, likely due to varying occurrence of face vitrification.

Moderate IRA segments consistently showed better drying performance than high IRA segments at the masonry-insulation interface and at beam ends. There is indication that high IRA segments are more prone to increased wetting; however, results are inconclusive. Less insulation thickness improved drying at the masonry-insulation interface, but only minor improvement was indicated at beam ends, for both brick types.

Compared to 1 brick thick masonry a thickness of 1.5 shows lower RH at the brick-insulation interface, and lower moisture content at the beam end. Slower masonry drying is also observed.

The investigation gives indication of improved drying having a smart vapor barrier instead of a traditional polyethylene vapor barrier; however, the effect was obscured by repeatability issues and variety in masonry behavior among the segments. The minor improvement in beam end drying seen from a smart vapor barrier, may imply additional measures often will be needed to ensure a sufficient beam end drying potential.

Declaration of competing interest

The authors declare that they have no known competing financial interests or personal relationships that could have appeared to influence the work reported in this paper.

Acknowledgement

The authors gratefully acknowledge the financial support by The Research Council of Norway and several partners through the Centre for Research-based Innovation "Klima 2050" (Grant No 237859) (www.klima2050.no). Lab-engineer Ole Aunrønning is acknowledged for an invaluable contribution with wall and equipment assembly, material property testing and measurement monitoring.

Appendix A. Climatic sequence

A climatic sequence (Table A.1) was designed to promote wetting and subsequent drying of the wall segments. Driving rain events are responsible for most of the wetting during a wetting period.

For the wetting period a cold exterior climate of 5 °C and 90% RH was chosen for its resemblance of Nordic late autumn or early spring conditions. For the drying period a warm exterior climate of 20 °C and 50% RH was chosen, resembling relatively high temperature Nordic summer conditions. Both the cold and warm climates were kept constant for their respective periods and thereby do not represent any realistic real-world climate. The climates were chosen in their form to constitute a simplistic climate test sequence for enabling conditions for wetting and subsequently drying of the wall. Although the term wetting is used on the cold period, a wetting is not exclusively taking place, as some drying of the masonry takes place outside of the rain events, especially for the reference segment. Nevertheless, as are seen, for most segments the beam end and RH sensors experience increasing moisture ("wetting"), and therefore the term wetting is chosen.

The rain events were decided to start with a short duration to observe how the wall segments would perform and how the moisture sensors would respond. This in order to avoid risk of exaggerated wetting of the wall. The rain events were conducted in pairs, with 2–2.67 h between the events of a pair. If a pair of rain events did not give sufficient response in the moisture sensors over a couple of days, in the perspective of showing enough moisture build up in the masonry to enable significant drying to the interior, the event duration was doubled and a new event pair was scheduled. This procedure resulted in three rain event pairs in the beginning of the climatic sequence leading up to events with duration of 40 min. A cold climate was then kept 640 h or almost 27 days. After this time is was seen that the RH at the interior of the masonry was not at a level in which sufficient utilization of the smart vapor barrier could be guaranteed. A final rain event pair of 40 min duration was therefore included to wet the wall segments even more. After that a cold climate was enacted for 834 h or almost 35 days. Following the cold climate, a warm climate period was initiated to investigate the drying performance of the wall segments. This period lasted 1729 h or 72 days.

The interior climate was kept constant at 23 °C and 50% RH for the whole duration of the study. No atmospheric pressure difference was implemented over the wall.

Table A.1
Climatic sequence used in the climate simulator for the laboratory study.

Description	Time of activation (h)	Number of hours (h)	Number of min (min)	Exterior side			Interior side	
				Rain (mm/h)	Temperature (°C)	RH (%)	Temperature (°C)	RH (%)
Drying	–	–	–	–	39	8	35	8
Acclimatization	0.00	21.00	–	–	23	20	23	20
Cold climate	21.00	1.25	–	–	5	90	23	50
Rain	22.25	0.17	10	47	11	90	23	50
Cold climate	22.42	2.00	–	–	5	90	23	50
Rain	24.42	0.17	10	47	11	90	23	50
Cold climate	24.58	45.83	–	–	5	90	23	50
Rain	70.42	0.33	20	47	11	90	23	50
Cold climate	70.75	2.67	–	–	5	90	23	50
Rain	73.42	0.33	20	47	11	90	23	50
Cold climate	73.75	76.87	–	–	5	90	23	50
Rain	150.62	0.67	40	47	11	90	23	50
Cold climate	151.28	2.33	–	–	5	90	23	50
Rain	153.62	0.67	40	47	11	90	23	50
Cold climate	154.28	640.05	–	–	5	90	23	50
Rain	794.33	0.67	40	47	11	90	23	50
Cold climate	795.00	2.33	–	–	5	90	23	50
Rain	797.33	0.67	40	47	11	90	23	50
Cold climate	798.00	834.37	–	–	5	90	23	50
Warm climate	1632.37	1729.55	–	–	20	50	23	50

Appendix B. Sensor data treatment

In the first series the Sahlen and beam end sensors were logged manually with a handheld moisture meter (Multifunction Moisture Meter FME from PCE instruments), directly giving moisture content, with input settings of wood species and temperature. Spruce, Nordic (Picea Abies) was used as wood specie also on measurements of the birch Sahlen sensors, since the correct birch (Betula Pendula) was not included in the moisture meter; however, a correction to birch from spruce was done as post processing. The temperature was found with a handheld ohmmeter, through use of an in-laboratory calibrated resistance-temperature chart. In the second series both the Sahlen thermistor resistance and the wood resistance were logged by use of data-loggers, the latter with use of Material Moisture Gigamodules from Scanntronik. Logging frequency in the second series was per hour, whereas the frequency of the manual logging of the first series were adapted to correspond to expected and observed rate of change in sensor data; per few hours after rain events, per once a day to per once a week approaching the end of the climatic sequence. The Steinhart-Hart equation [47] has been used to calculate the temperature from the thermistor resistance for both series. For the logged resistance moisture meter data, equation (B.1), a linearized representation of resistance as function of moisture content [48], has been used.

$$\log[\log(R)+1]=A\cdot u+B \tag{B.1}$$

where R is resistance (MOhm), u is moisture content (mass %) and A and B are wood species dependent constants. Forsèn and Tarvainen [49] have found values for the constants from an ample amount of wood samples tested; spruce (Nordic): A = −0.038, B = 1.067; birch (Nordic): A = −0.039, B = 1.032. Expression (B.1) will, due to the mathematical implication of the logarithm of the bracket, be limited to resistance values above 0.1 MOhm; however, the lower practical resistance limit must be even higher, since; 1) this form of expression has not been fitted for high moisture contents, for instance limited to below 18% in Ref. [49] and 25% in Ref. [48], 2) resistance measurements become inaccurate and unreliable in identifying moisture contents above the fiber saturation point (FSP) [50]. The FSP is hard to determine conclusively due to variations in definition details and measuring approaches [51]; however, for reference, typical values reported are in the range 30–40% [52].

The resistance-moisture relation is also influenced by temperature, making a proper temperature correction needed. Although the temperature correction is species dependent [48], this has not been included due to lack of credible data on this dependence. Instead, expression (B.2), a general temperature correction from Ref. [48], which is adjusted from Ref. [53] (based on North American wood species), has been used:

$$u_{corr}=\frac{u+0.567-0.0260\cdot x+0.000051\cdot x^2}{0.881\cdot 1.0056^x} \tag{B.2}$$

where u_{corr} is the corrected moisture content, u the moisture content from equation (B.1) and x = (θ + 28), where θ is the temperature in Celsius.

In addition to temperature, the resistance-moisture content relation has been suggested dependent on other parameters such as density, ash content, wood structure, acidity [54], lignin content [55], measurement angle to the grain or growth ring orientation [56], specimen size [57], heartwood vs. sapwood, distance between measuring pins [49] and present amount of water-soluble salts [58]. With exception of water-soluble salt, these parameters have much less pronounced influence than temperature, (e.g. Refs. [42,49,56]). Although, it should be noted there is some controversy regarding measurement direction to the grain orientation [37], where, if not accounted for, differences up to 2% moisture content have been reported by some authors; [59,60]. Nevertheless, since there is too little species-specific information available to get accurate corrections on any of these factors, such corrections have been omitted.

Appendix C. Performance criteria

Segment performance is assessed after definitions outlined in Table C.1. The performance, in a positive interpretation, is related respectively to moisture uptake avoidance and drying efficiency, relative to average performance of segments 4–9. For instance, a sensor showing a relatively high drying efficiency (more extensive or faster drying) compared to average among segments, for same sensor type, will be classified as having overperformance. Only segments 4–9 are included since these are the only segments with one brick thick masonry (same sensor locations in masonry) and with interior insulation, thereby having comparable conditions and RH sensors in all segments (excludes seg 2).

Table C.1
Defining over- and underperformance in relative terms (in table; defining low and high respectively as lower and higher than average performance among segments)

Period	Wetting period	Drying period
Parameters	Moisture uptake/moisture uptake rate	Drying efficiency
Overperformance	Low	High
Underperformance	High	Low

Assessment of segment performance has been divided into performance during a "wetting period", corresponding to the cold climate period (refer climatic sequence in Appendix A), and a drying period corresponding to the warm climate period. As performance criteria for the wetting period the time-average moisture content has been assessed in addition to a time-average moisture growth rate index (MGRI). Calculation of the latter, expression (C.1), involves; i) For each timestep (1 h); dividing the moisture content, minus an average initial level, by a modified transpired time. The modified transpired time includes an additional arbitrary 100 h to the actual transpired time, to make the index less sensitive to early increase in moisture. ii) Taking the time-average of the sum of i). Such an index will bring into light the degree of rapid moisture growth, and the quantity of moisture, i.e. rapid and high moisture growth will produce high index.

$$MGRI = \frac{1}{N_{period}} \sum_{i=1}^{N_{period}} \frac{u_i - u_{\text{average initial}}}{t_i + 100h} \tag{C.1}$$

where N_{period} is the number of timesteps taken in the wetting period (here number of hours), u_i moisture content (or RH level) at time step, and t_i transpired time at time step.

In assessment of the drying period a time-average moisture content is less credible since the segments have reached different levels of moisture during the wetting period, and thereby starts the drying period at these different levels. Instead, a moisture decline rate index (MDRI) is applied; expression (C.2). Starting from a hypothetic realistic worst-case moisture level of the sensor sample group, the difference between this level and the actual moisture level, weighted for the starting moisture of the drying period, is divided by the modified transpired time. The time-average of the sum of the aforementioned is then applied.

$$MDRI = \frac{1}{N_{period}} \sum_{i=1}^{N_{period}} \frac{u_{\text{worst initial}} - u_i/f_i}{t_i + 100h} \tag{C.2}$$

where N_{period} is the number of timesteps taken in the drying period (here number of hours), u_i moisture content (or RH level) at time step, f_i factor weighing the moisture content for the starting level, aligning it to the initial average, and which subsides linearly with time so that it becomes 1.0 at the end of the period, and t_i transpired time at time step.

For all segment sensors having same location (depth) in wall segment cross section, the performance criteria are compared to that of a hypothetical average among segments, by taking the ratio. The average performance among segments has been taken for 1) all segments of both series, 2) segments of each series separately (to look for regular differences between brick types), 3) segments of both series for each brick type separately (to look for systematic differences between series). Since the current focus is limited to segments insulated with mineral wool, 1) will be excluded from being addressed and 3) will only be addressed to highlight potential repeatability issues or shortcomings in execution of the two series. Assessing a limited number of sensors (each 3 samples of high and moderate IRA segments) there is by default limited credence to the results; nevertheless, it might indicate a trend if all 3 samples show same direction in performance.

References

[1] H.M. Künzel, Effect of interior and exterior insulation on the hygrothermal behaviour of exposed walls, Mater. Struct. 31 (2) (1998) 99–103.
[2] M. Morelli, S. Svendsen, Investigation of interior post-insulated masonry walls with wooden beam ends, J. Build. Phys. 36 (3) (2012) 265–293.
[3] D. Kehl, U. Ruisinger, J. Plagge, J. Grunewald, Wooden beam ends in masonry with interior insulation - a literature review and simulation on causes and assesment of decay, in: A. Mahdavi, B. Martens (Eds.), 2nd Central European Symposium on Building Physics, Vienna University of Technology, Vienna, Austria, 2013, pp. 299–304.
[4] M. Guizzardi, J. Carmeliet, D. Derome, Risk analysis of biodeterioration of wooden beams embedded in internally insulated masonry walls, Construct. Build. Mater. 99 (2015) 159–168.
[5] X. Zhou, J. Carmeliet, D. Derome, Influence of envelope properties on interior insulation solutions for masonry walls, Build. Environ. 135 (2018) 246–256.
[6] T. Odgaard, S.P. Bjarløv, C. Rode, Influence of hydrophobation and deliberate thermal bridge on hygrothermal conditions of internally insulated historic solid masonry walls with built-in wood, Energy Build. 173 (2018) 530–546.
[7] F. Slapø, T. Kvande, N. Bakken, M. Haugen, J. Lohne, Masonry's resistance to driving rain: mortar water content and impregnation, Buildings 7 (3) (2017) 70.
[8] C.J.W.P. Groot, J.T.M. Gunneweg, The influence of materials characteristics and workmanship on rain penetration in historic fired clay brick masonry, HERON 55 (2) (2010) 141–153.
[9] C.J.W.P. Groot, J. Larbi, The influence of water flow (reversal) on bond strength development in young masonry, HERON 44 (2) (1999) 63–78.
[10] H.J.P. Brocken, M.E. Spiekman, L. Pel, K. Kopinga, J.A. Larbi, Water extraction out of mortar during brick laying: a NMR study, Mater. Struct. 31 (1) (1998) 49–57.
[11] H. Derluyn, H. Janssen, J. Carmeliet, Influence of the nature of interfaces on the capillary transport in layered materials, Construct. Build. Mater. 25 (9) (2011) 3685–3693.
[12] P. Johansson, S. Geving, C.-E. Hagentoft, B.P. Jelle, E. Rognvik, A.S. Kalagasidis, B. Time, Interior insulation retrofit of a historical brick wall using vacuum insulation panels: hygrothermal numerical simulations and laboratory investigations, Build. Environ. 79 (2014) 31–45.
[13] U. Ruisinger, Long-term measurements and simulations of five internal insulation systems and their impact on wooden beam heads, in: A. Mahdavi, B. Martens (Eds.), 2nd Central European Symposium on Building Physics, Vienna University of Technology, Vienna, Austria, 2013, pp. 313–319.
[14] E. Vereecken, S. Roels, Wooden beam ends in combination with interior insulation: an experimental study on the impact of convective moisture transport, Build. Environ. 148 (2019) 524–534.
[15] P. Kopecký, K. Staněk, M. Bureš, J. Richter, P. Ryparová, J. Tywoniak, Experimental investigations of wooden beam ends in masonry with interior insulation: measured data in real-scale experimental walls exposed to semi-continental climatic conditions, J. Build. Phys. 43 (3) (2019) 147–170.
[16] E. Vereecken, S. Roels, Capillary active interior insulation: do the advantages really offset potential disadvantages? Mater. Struct. 48 (9) (2015) 3009–3021.

[17] M. Harrestrup, S. Svendsen, Internal insulation applied in heritage multi-storey buildings with wooden beams embedded in solid masonry brick façades, Build. Environ. 99 (2016) 59–72.

[18] H.M. Kunzel, The Smart Vapor Retarder: an Innovation Inspired by Computer Simulations, ASHRAE Annual Meeting, ASHRAE Transactions, Toronto, Canada, 1998, pp. 903–907.

[19] H.M. Künzel, Flexible vapor control solves moisture problems of building assemblies—smart retarder to replace the conventional PE-film, J. Therm. Envelope Build. Sci. 23 (1) (1999) 95–102.

[20] D. Derome, S. Saneinejad, Inward vapor diffusion due to high temperature gradients in experimentally tested large-scale wall assemblies, Build. Environ. 45 (12) (2010) 2790–2797.

[21] A.A. Hamid, P. Wallentén, Hygrothermal assessment of internally added thermal insulation on external brick walls in Swedish multifamily buildings, Build. Environ. 123 (2017) 351–362.

[22] S. Geving, J. Holme, Vapour retarders in wood frame walls and their effect on the drying capability, Front. Architect. Res. 2 (1) (2013) 42–49.

[23] T. De Mets, A. Tilmans, Evaluation of the risk of decay of wooden beams embedded in internally insulated walls by long-term measurements, in: J. Kurnitski, T. Kalamees (Eds.), 12th Nordic Symposium on Building Physics, E3S Web of Conferences, EDP Sciences, Tallinn, Estonia, 2020, 01002.

[24] L. Van Gelder, H. Janssen, S. Roels, Probabilistic design and analysis of building performances: methodology and application example, Energy Build. 79 (2014) 202–211.

[25] E. Vereecken, L. Van Gelder, H. Janssen, S. Roels, Interior insulation for wall retrofitting – a probabilistic analysis of energy savings and hygrothermal risks, Energy Build. 89 (2015) 231–244.

[26] V. Marincioni, G. Marra, H. Altamirano-Medina, Development of predictive models for the probabilistic moisture risk assessment of internal wall insulation, Build. Environ. 137 (2018) 257–267.

[27] A. Tijskens, S. Roels, H. Janssen, Neural networks for metamodelling the hygrothermal behaviour of building components, Build. Environ. 162 (2019) 106282.

[28] NS-EN 772-11, Methods of Test for Masonry Units - Part 11: Determination of Water Absorption of Aggregate Concrete, Autoclaved Aerated Concrete, Manufactured Stone and Natrual Stone Masonry Units Due to Capillary Action and the Initial Rate of Water Absorption of Clay Masonry Units, European Committee for Standardization (CEN), Brussels, Belgium, 2011.

[29] P. Johansson, P. Wahlgren, Interior insulation retrofit of a brick wall using super insulation materials: design of a field testing in an industrial brick building, in: J. Zhang (Ed.), 7th International Building Physics Conference, IBPC, Syracuse, NY, United States, 2018, pp. 265–270.

[30] M. Guizzardi, D. Derome, J. Carmeliet, Water uptake in clay brick at different temperatures: experiments and numerical simulations, J. Build. Phys. 39 (4) (2016) 373–389.

[31] N.F. Jensen, C. Rode, B. Andersen, S.P. Bjarløv, E.B. Møller, Internal insulation of solid masonry walls – field experiment with Phenolic foam and lime-cork based insulating plaster, in: J. Kurnitski, T. Kalamees (Eds.), 12th Nordic Symposium on Building Physics, E3S Web of Conferences, 2020, 01003. Tallinn, Estonia.

[32] EN ISO 15148, Hygrothermal Performance of Building Materials and Products - Determination of Water Absorption Coefficient by Partial Immersion, European Committee for Standardization (CEN), Brussels, Belgium, 2003.

[33] EN ISO 12572, Hygrothermal Performance of Building Materials and Products - Determination of Water Vapour Transmission Properties, European Committee for Standardization (CEN), Brussels, Belgium, 2001.

[34] H.J.P. Brocken, Moisture Transport in Brick Masonry: the Grey Area between Bricks, Department of the Built Environment, Technische Universiteit Eindhoven, Eindhoven, Netherlands, 1998.

[35] EN ISO 6946, Building Components and Building Elements - Thermal Resistance and Thermal Transmittance - Calculation Methods, European Committee for Standardization (CEN), Brussels, Belgium, 2017.

[36] EN 1745, Masonry and Masonry Products - Methods for Determining Thermal Properties, European Committee for Standardization (CEN), Brussels, Belgium, 2012.

[37] J. Straube, D. Onysko, C. Schumacher, Methodology and design of field experiments for monitoring the hygrothermal performance of wood frame enclosures, J. Therm. Envelope Build. Sci. 26 (2) (2002) 123–151.

[38] Z. Suchorab, D. Majerek, V. Kočí, R. Černý, Time Domain Reflectometry flat sensor for non-invasive monitoring of moisture changes in building materials, Measurement 165 (2020).

[39] M. Guizzardi, D. Derome, R. Vonbank, J. Carmeliet, Hygrothermal behavior of a massive wall with interior insulation during wetting, Build. Environ. 89 (2015) 59–71.

[40] J.P. Rydock, A look at driving rain intensities at five cities, Build. Environ. 41 (12) (2006) 1860–1866.

[41] K. Ueno, J.W. Lstiburek, P. Eng, Field monitoring of embedded wood members in insulated masonry walls in a cold climate, in: M. Bomberg, D. Yarbrough, J. Kosny (Eds.), Fourth BEST Conference Building Enclosure Science & Technology, The National Institute of Building Sciences, Kansas City, Mo, United States, 2015.

[42] M. Fredriksson, L. Wadsö, P. Johansson, Small resistive wood moisture sensors: a method for moisture content determination in wood structures, Eur. J. Wood and Wood Prod. 71 (4) (2013) 515–524.

[43] K. Ueno, J. Straube, Laboratory calibration and field results of wood resistance humidity sensors, in: D. Onysko, M. Bomberg (Eds.), First BEST Conference Building Enclosure Science & Technology, The Building Enclosure Technology and Environment Council, Minneapolis, MN, United States, 2008.

[44] C.-M. Popescu, C.A.S. Hill, S. Curling, G. Ormondroyd, Y. Xie, The water vapour sorption behaviour of acetylated birch wood: how acetylation affects the sorption isotherm and accessible hydroxyl content, J. Mater. Sci. 49 (5) (2014) 2362–2371.

[45] W.U.F.I. Fraunhofer, 2D 4.2, Fraunhofer IBP, Germany, 2019.

[46] EN ISO 12571, Hygrothermal Performance of Building Materials and Products - Determination of Hygroscopic Sorption Properties, European Committee for Standardization (CEN), Brussels, Belgium, 2013.

[47] J.S. Steinhart, S.R. Hart, Calibration curves for thermistors, Deep-Sea Res. Oceanogr. Abstr. 15 (4) (1968) 497–503.

[48] A. Samuelsson, Resistanskurvor För Elektriska Fuktkvotsmätare, TräteknikCentrum, Trätek, Stockholm, Sweden, 1990.

[49] H. Forsén, V. Tarvainen, Accuracy and Functionality of Hand Held Wood Moisture Content Meters, VTT Publications; 420, Espoo, Finland, 2000. VTT Technical Research Centre of Finland.

[50] B. Kasal, G. Lear, Moisture measurement, in: B. Kasal, T. Tannert (Eds.), In Situ Assessment of Structural Timber, Springer, Netherlands, 2011, pp. 99–104.

[51] M. Babiak, J. Kúdela, A contribution to the definition of the fiber saturation point, Wood Sci. Technol. 29 (3) (1995) 217–226.

[52] S.L. Zelinka, S.V. Glass, J.E. Jakes, D.S. Stone, A solution thermodynamics definition of the fiber saturation point and the derivation of a wood–water phase (state) diagram, Wood Sci. Technol. 50 (3) (2016) 443–462.

[53] F. Pfaff, P. Garrahan, New temperature correction factors for the portable resistance-type moisture meter, For. Prod. J. 36 (3) (1986) 28–30.

[54] Q.P. Du, A. Geissen, D. Noack, Widerstandskennlinien einiger Handelshölzer und ihre Meßbarkeit bei der elektrischen Holzfeuchtemessung, Holz als Roh- Werkst. 49 (7) (1991) 305–311.

[55] A. Venkateswaran, The interdependence of the lignin content and electrical properties of wood, Wood Fiber Sci. 6 (1) (1974) 46–52.

[56] A.J. Stamm, The electrical resistance of wood as a Measure of its moisture content, Ind. Eng. Chem. 19 (9) (1927) 1021–1025.

[57] M. Fredriksson, J. Claesson, L. Wadsö, The influence of specimen size and distance to a surface on resistive moisture content measurements in wood, Math. Probl Eng. 2015 (2015).

[58] S.V. Glass, S.L. Zelinka, Moisture relations and physical properties of wood, in: R. J. Ross (Ed.), Wood Handbook: Wood as an Engineering Material, US Dept. of Agriculture, Forest Service, Forest Products Laboratory, Madison, WI, United States, 2010, pp. 4.1–4.19.

[59] F.C. Beall, Relative humidity and moisture content instrumentation, in: H. N. Rosen, W.T. Simpson, E.M. Wengert (Eds.), Symposium on Wood Moisture Content - Temperature and Humidity Relationships, US Dept. of Agriculture, Forest Service, Forest Production Laboratory, Blacksburg, VA, United States, 1979, pp. 47–54.

[60] W.L. James, Electric Moisture Meters for Wood, U.S. Forest Servise Research Note, US Dept. of Agriculture, Forest Service, Forest Products Laboratory, Madison, WI, United States, 1963.

Article III

Implementation and benchmarking of a 3D hygrothermal model in the COMSOL Multiphysics software

J. I. Knarud, S. Geving

6th International Building Physics Conference, IBPC 2015, Energy Procedia 78 (2015) 3440-3445 http://dx.doi.org/10.1016/j.egypro.2015.12.327

Available online at www.sciencedirect.com

ScienceDirect

Energy Procedia 00 (2015) 000–000

Energy Procedia

www.elsevier.com/locate/procedia

6th International Building Physics Conference, IBPC 2015

Implementation and benchmarking of a 3D hygrothermal model in the COMSOL Multiphysics software

Jon Ivar Knarud[a,]*, Stig Geving[a]

[a]Department of Civil and Transport Engineering, Norwegian University of Science and Technology, Høgskoleringen 7A, 7491 Trondheim, Norway

Abstract

Many buildings physics problems are difficult to evaluate properly without looking at the problem in three dimensions. For instance, it can be difficult to assess moisture transport in a brick masonry wall segment as it consists of a relatively complex system of brick and mortar. Still, most hygrothermal simulations are likely done in 1D or 2D, but development in computer hardware and software makes 3D simulations easier accessible. This paper looks into benchmarking of a hygrothermal simulation model created in the COMSOL Multiphysics software. The results show COMSOL to have promising applicability for 3D hygrothermal simulations.

Keywords: Hygrothermal, 3D simulation, COMSOL, Hamstad Benchmark

1. Introduction

In building physics, hygrothermal simulations are required in a number of different evaluative tasks, such as when evaluating structural performance with regard to transfer, absorption and release of heat and moisture, often with a final aim of looking for unwanted condensation and moisture damage. Hygrothermal simulations have mainly in the past been limited to 1D or 2D application, often with the use of dedicated software with limited or no user access to the mathematical equations describing the physics involved. However, a combination of development in computer processing capacity and the developing of so called multiphysics software have in the recent years made it

---

* Corresponding author. Tel.: +47 90675937.
E-mail address: jon.knarud@ntnu.no

Nomenclature

$c_{p,v}$	specific heat capacity of vapour [J/(kg K)]	R_w	specific gas constant H_2O [J/(kg K)]
$c_{p,w}$	specific heat capacity of water [J/(kg K)]	T	Temperature [K]
D_ϕ	capillary transport coefficient [kg/(m s)]	w_w	water moisture content [kg/m^3]
g	gravity constant [m/s^2]		
$g_{v,j}$	water vapour mass flux vector [kg/(m^{2}s)]	Greek letters	
$g_{w,j}$	liquid water mass flux vector [kg/(m^{2}s)]	δ_v	vapour diffusion coefficient [kg/(m s Pa)]
h_w	enthalpy of evaporation [J/kg]	ρ_s	dry density of solid material [kg/m^3]
K_l	liquid permeability coef. [kg/(m s Pa)]	ρ_w	water density [kg/m^3]
P_{sat}	vapour saturation pressure [Pa]	ϕ	relative humidity [-]

possible to conduct even 3D hygrothermal simulations with a complete user access to the mathematical equations describing the physics. The COMSOL Multiphysics software [1] have shown great promise in this regard, already having been applied by several researchers [2-9] in solving hygrothermal simulations. Except for [2, 7], this has been limited to 1D and 2D. Tariku [5] applied COMSOL, as part of his own created HAMfit model, existing in both a 1D and 2D version, on all the Hamstad Benchmarks [10] with good results. Hygrothermal 3D models in COMSOL has not been found, however, to previously been benchmarked.

In this paper implementation for COMSOL 3D modeling of heat and moisture transport is described. The heat and moisture transport mechanisms of the COMSOL model has been verified by applying the mathematical model on two benchmarks, namely Hamstad benchmark #1 and #2 [10]. The Hamstad benchmarks are all 1D benchmarks, meaning the heat, air and moisture transport is one-directional. However, the benchmarks are still valid in a 3D model given that the boundary conditions allow no heat and mass exchange over the boundaries normal to the two other directions. Further work will however be necessary to stress test the full 3D-functionality of the model on problems with results known to be correct, either in the form of benchmarks or results from laboratory tests.

2. Mathematical description of modeled physics

2.1. Moisture transport

Transport of moisture in porous materials is usually divided into three mechanisms; vapour diffusion due to gradients in vapour pressure, capillary suction due to gradients in suction pressure and vapour transfer by air transport due to gradients in air pressure. In order to implement the three mechanisms into a single partial differential equation (PDE) the mechanisms needs to become a part of a transient moisture balance having a common dependent variable. Traditionally this dependent variable has been either moisture content or relative humidity, where the latter is used here due to its benefit of being continuous over interfaces between materials having different moisture sorption capabilities. The following describe the mathematical expression for vapour diffusion and capillary suction.

Vapour diffusion can be expressed by Fick's law, i.e the negative product of a diffusivity constant δ and the gradient of vapour pressure, which with the vapour pressure expanded for, and having relative humidity (RH) as dependent variable, gives the following flux in direction j=1,2,3 [11]

$$g_{v,j} = -\left(\delta \cdot P_{sat} \frac{d\phi}{dx_j} + \delta \cdot \phi \frac{dP_{sat}}{dT} \frac{dT}{dx_j} \right) \tag{1}$$

Capillary suction is commonly based on Darcy's law, which with the use of a liquid permeability coefficient K_l becomes [6]

$$g_{w,j} = -K_l\left[\rho_w R_w\left(\frac{T}{\phi}\frac{d\phi}{dx_j} + \ln(\phi)\frac{dT}{dx_j}\right) + \rho_w g\cdot\vec{e_z}\right] \tag{2}$$

Inserting expressions (1) and (2) in the continuity equation for moisture content, expanding the transient term as well as writing the terms in (2) with a capillary transport coefficient D_ϕ [kg/(m^2 s)] instead of K_l [kg/(m s Pa)], and finally rearranging the terms according to occurrence of ϕ gives the following PDE for moisture transport.

$$\frac{dw_w}{d\phi}\frac{d\phi}{dt} = \frac{d}{dx_j}\left(\left[\delta_v P_{sat} + D_\phi\right]\cdot\frac{d\phi}{dx_j} + \left[\left(\delta_v\frac{dP_{sat}}{dT} + D_\phi\frac{1}{T}\ln(\phi)\right)\frac{dT}{dx_j} + \frac{D_\phi}{R_w}\frac{1}{T}g\cdot\vec{e_z}\right]\cdot\phi\right) \tag{3}$$

2.2. Heat transport

The PDE for heat transport is based on the enthalpy equation on conservative form. The heat storage term is modified for a porous material, taking into account both the porous solid and the water content at any given time, while neglecting the contribution of any vapour located inside the pores.

$$\rho_s c_{p,eff}\frac{d(T)}{dt} = \frac{d}{dx_j}\left(\lambda\frac{dT}{dx_j} - \left[c_{p,w}g_{w,j} + c_{p,v}g_{v,\mathrm{j}}\right]T - h_v g_{v,\mathrm{j}}\right) \tag{4}$$

where

$$c_{p,eff} = \left(c_{p,s} + \frac{w_w}{\rho_s}c_{p,\mathrm{w}}\right)$$

3. Benchmarks

3.1. Description of the Hamstad #1 benchmark

In the Hamstad benchmark #1 two material layers, which share an interface that experience condensation when the surrounding conditions call for it, are involved in a long term drying process of one of the material layers. The benchmark shall resemble a roof structure, as seen in figure 1a, where a loadbearing material is insulated by another material layer on the inside while having a water and vapour tight membrane layer on the exterior side. The loadbearing material layer, with a thickness of 100 mm, has an initial moisture content of 145 kg /m^3 (≈99 % RH) while the insulating material layer, with a thickness of 50 mm, has an initial moisture content of 0.065 kg /m^3 (≈56 % RH). Initial temperature is 20 °C for both layers, and 20 °C is also the constant value of the interior temperature. The interior vapour pressure as well as the exterior temperature is given by a table which gives varying values for a whole year. Although the benchmark covers 5 years, it uses the same boundary conditions for all the years. Exterior vapour pressure is also given, but the values are irrelevant due to the vapour tight exterior surface. Heat transfer coefficients for the interior and exterior are given as 7 W/(m^{2}K) and 25 W/(m^{2}K) respectively, and the interior vapour transfer coefficient is given as 2·10-8 s/m. Material properties for the two materials and more detailed description of the benchmark are given by [10].

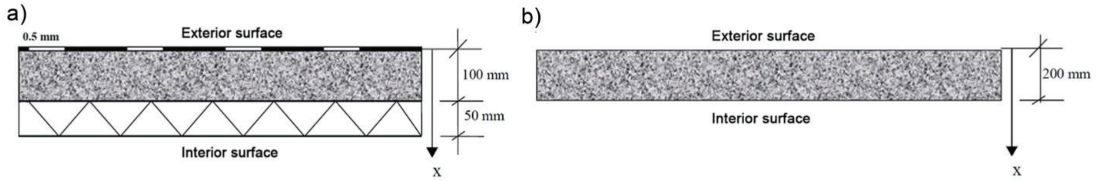

Fig. 1. (a) Benchmark #1, a two layer roof structure [10]; (b) Benchmark #2, a single material layer [10].

3.2. Description of the Hamstad #2 benchmark

The Hamstad benchmark #2 is a test which looks at the redistribution of moisture as the external and internal relative humidity, are suddenly changed from the initial situation, all while behaving as an isothermal case. An analytical solution exists for this test, assuming isothermal behavior [6]. The geometry consists of a single, perfectly airtight, 200 mm material layer, as seen in figure 1b. Initial conditions of the material include a relative humidity of 95 % and a temperature of 20 °C. When time starts running, boundary conditions of 45 % RH external and 65 % RH internal are imposed. As the benchmark case is isothermal, the boundary temperature is 20 °C. However, in order to keep the material temperature more or less constant at 20 °C the latent heat of evaporation has been set to 56.8 J/kg, which is considerably less than the usual value of 2500000 J/kg. The heat and vapour transfer coefficients at both surfaces are 25 W/(m^2K) and 1·10-3 s/m respectively. Material properties for the two materials and more detailed description of the benchmark are given by [10].

3.3. Methodology of benchmark implementation in COMSOL

The COMSOL model is built up around the PDEs for moisture and heat transport. These PDEs have been user defined in COMSOL, to become equal to equation (3) and (4), by using the so-called *coefficient form PDE* from the physics interface available in the software. A 3D geometry of the benchmark cases has been built as shown in figure 2, with dimension values in meters. Benchmark #1 and #2 are respectively having the x shown in figure 1 as a vertical and horizontal directional variable, i.e. z and x directions respectively in the PDEs. Each material layer is defined as a domain. The PDEs automatically call up the material properties of the material for the domain in question during the numerical solving. Meshes are generated as seen in figure 2, with eight layered boundary layers on surfaces and internal interfaces.

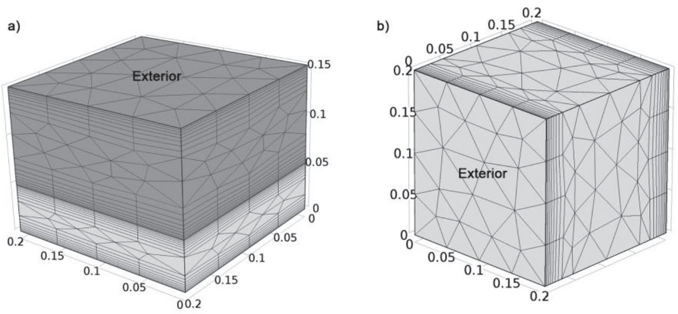

Fig. 2. The benchmark geometry and mesh including boundary layers at all interfaces. Values in meters. (a) Benchmark #1; (b) Benchmark #2.

The results from benchmark #1 are given as the hourly average of the moisture content in the loadbearing material. As shown in figure 3 and 4 the results for the first and fifth of a total of five years of benchmark #1 shows a rather good correlation to the benchmark solutions. The results are seen in the figures to more or less follow the benchmark solution given by Technion. However, the results also show more hourly fluctuations compared to the benchmark solutions. It has not been established whether this is caused by the 3D dimensionality of the model, the integration technique which was used to get average values, or some other aspect of the model.

The results of benchmark #2 can be seen in figure 5a and b, which show a very good fit with the benchmark solutions. It should be mentioned that the lines marked "results from Hamstad" on figure 5 consist of several lines lying more or less on top of each other. For more details on the results supplied by the Hamstad benchmark refer to [10].

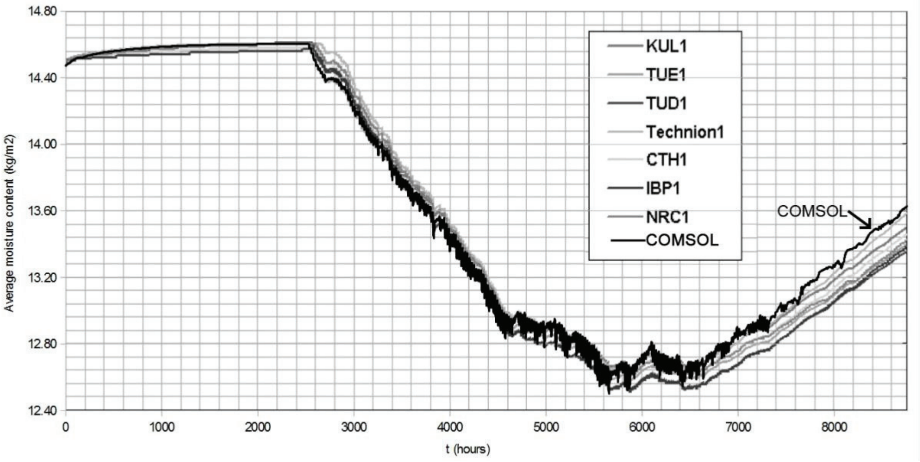

Fig. 3. Benchmark #1, superposition of average moisture content, COMSOL result, over solutions from [10] for year 1 of the benchmark.

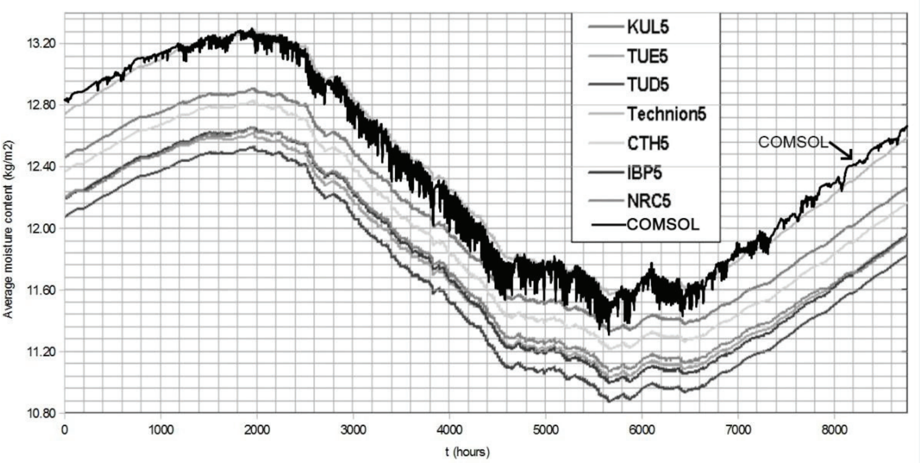

Fig. 4. Benchmark #1, superposition of average moisture content, COMSOL result, over solutions from [10] for year 5 of the benchmark.

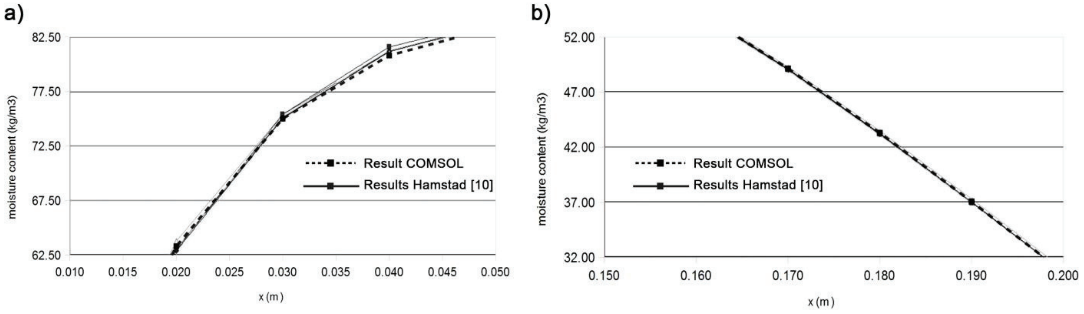

Fig. 5. Benchmark #2, superposition of COMSOL moisture content result over solutions from [10] at x(m); (a) 100 hours; (b) 1000hours.

4. Conclusion

The application of COMSOL for 3D hygrothermal simulation seems promising after running through Hamstad benchmark #1 and #2, where the results showed good agreement with the benchmark solutions. However, these two benchmarks only include moisture and heat transport where the only boundary exposure is varying vapour pressure and temperature. Further benchmarking is needed to be done on benchmarks including air transport and liquid water uptake, in order to evaluate the applicability, as well as the full functionality and performance, of COMSOL for 3D hygrothermal simulation.

References

[1] COMSOL. Sweden: COMSOL Inc.; 2015 [cited 2015 11.02]. Available from: http://www.comsol.se/.
[2] Schijndel AWM. HAM Construction modeling using COMSOL with MatLab Modeling Guide version 1.0. COMSOL Users Conference; Eindhoven 2006.
[3] Schijndel AWM. Heat and Moisture Modeling Benchmark using COMSOL. Proceedings of the COMSOL Users Conference; Hannover 2008.
[4] Schellen H, Schijndel Av, Briggen P, editors. The use of COMSOL for Building Constructions Engineering regarding Heat and Moisture transport. European COMSOL Conference, Frankfurt; 2008.
[5] Tariku F. Whole building heat and moisture analysis: Concordia University; 2008.
[6] Tariku F, Kumaran K, Fazio P. Transient model for coupled heat, air and moisture transfer through multilayered porous media. International Journal of Heat and Mass Transfer. 2010;53(15–16):3035-44.
[7] Janetti MB, Ochs F, Feist W. 3D Simulation of Heat and Moisture Diffusion in Constructions. Comsol Conference; Stuttgart 2011.
[8] Nusser B, Teibinger M. Coupled Heat and Moisture Transfer in Building Components-Implementing WUFI Approaches in COMSOL Multiphysics. Proceedings of the COMSOL Users Conference; Milan 2012.
[9] Janetti MB, Ochs F, Feist W. On the conservation of mass and energy in hygrothermal numerical simulation with COMSOL Multiphysics. Building Simulation Conference; Chambery 2013.
[10] Hagentoft C-E. HAMSTAD–Final report: Methodology of HAM-modeling. Report R-02. 2002;8.
[11] Künzel HM. Simultaneous heat and moisture transport in building components: IRB-Verlag Stuttgart; 1995.

Article IV

Comparative study of hygrothermal simulations of a masonry wall

J. I. Knarud, S. Geving

11th Nordic Symposium on Building Physics, NSB2017, 11-14 June 2017, Trondheim, Norway, Energy Procedia 132 (2017) 771-776 https://doi.org/10.1016/j.egypro.2017.10.027

Note:

Provided with a corrected page addendum for page 774.

Available online at www.sciencedirect.com

ScienceDirect

Energy Procedia 132 (2017) 771–776

Energy Procedia

www.elsevier.com/locate/procedia

11th Nordic Symposium on Building Physics, NSB2017, 11-14 June 2017, Trondheim, Norway

Comparative study of hygrothermal simulations of a masonry wall

Jon Ivar Knarud[a],*, Stig Geving[a]

[a]*Department of Civil and Transport Engineering, Norwegian University of Science and Technology, Høgskoleringen 7A, 7491 Trondheim, Norway*

Abstract

With increasing requirements on reducing heat consumption and improving comfort levels of existing buildings, interior insulation retrofit is a hot topic for many masonry buildings. However, as the drying potential of the wall is lowered as a consequence, interior insulation of massive masonry walls increases the risk of moisture related problems. Therefore, carefulness is needed when approaching such solutions. A useful approach on evaluating moisture risks, when deciding the interior insulation design, is the use of hygrothermal simulations. In the present study a 2D numerical hygrothermal study has been conducted on an internally insulated masonry wall with a smart vapor barrier. The focus has been on comparing and discussing the options available in, and the challenges faced with, COMSOL Multiphysics and WUFI for this purpose.

Peer-review under responsibility of the organizing committee of the 11th Nordic Symposium on Building Physics.

Keywords: Hygrothermal; 2D simulation; COMSOL 5.2; WUFI 2D 3.4; Masonry

---

1. Introduction

Over the last couple of decades an increasing focus has been given lowering energy consumption of the existing building stock. Especially older masonry buildings have been, and still are, a challenge in this regard since the facades of these buildings often are protected for their historical and aesthetic values, limiting insulation retrofitting to the interior side. From a building physics point of view interior insulation creates extra concerns as it lowers the masonry temperature, increases risk of indoor moisture condensing in the wall, as well as reducing the drying capacity of the wall. Especially driving rain may be difficult to dry out again. In this perspective hygrothermal

---

* Corresponding author. Tel.: +47 90675937.
E-mail address: jon.knarud@ntnu.no

1876-6102 © 2017 The Authors. Published by Elsevier Ltd.
Peer-review under responsibility of the organizing committee of the 11th Nordic Symposium on Building Physics
10.1016/j.egypro.2017.10.027

Nomenclature

$c_{p,v}$	specific heat capacity of vapor [J/(kg K)]
$c_{p,w}$	specific heat capacity of water [J/(kg K)]
D_ϕ, D_w	capillary transport coefficient [kg/(m s)]
e_z	unit vector z-direction
g	gravity constant [m/s^2]
$g_{v,j}$	water vapor mass flux vector [kg/(m^{2}s)]
$g_{w,j}$	liquid water mass flux vector [kg/(m^{2}s)]
h_w	enthalpy of evaporation [J/kg]
K_l	liquid permeability coef. [kg/(m s Pa)]
P_{sat}	vapor saturation pressure [Pa]
R_w	specific gas constant H_2O [J/(kg K)]
T	Temperature [K]
w_w	water moisture content [kg/m^3]
Greek letters	
δ_v	vapor diffusion coefficient [kg/(m s Pa)]
λ	thermal conductivity [W/(m K)]
ρ_s	dry density of solid material [kg/m^3]
ρ_w	water density [kg/m^3]
ϕ	relative humidity [-]

simulations ensure great means to analyze how different exterior and interior climatic conditions may influence different structural designs, including alternative interior insulation design solutions. Hygrothermal simulation software has existed for a while now; nevertheless, there is still a development in this software, and new possibilities arise with this development and the evolution of computational capacity. Over the last decade multiphysics software has gained increasing interest for possibilities to combine all kinds of physics and for options which gives the user great flexibility in designing and optimizing physics models on one's own. For an internally insulated masonry wall; especially 3D functionality and the option of adding different physics to different parts of the structure may make such software interesting. For instance, including models for convection and radiation in air cavities or gaps could be of interest, but it is a vast land of possibilities. Even though adding great benefits, multiphysics software may demand more of the user, as additional mistakes or pitfalls may be stumbled into compared to the dedicated hygrothermal software. The latter has usually been carefully validated against benchmarks, and has a more documented and fixed stepwise procedure for the user to follow.

In this paper the objective has been to address the use of COMSOL Multiphysics [1] for a 2D hygrothermal simulation, and to do a comparison with WUFI [2]. As a simulation case a masonry wall structure with interior insulation, exposed to climatic conditions representable for the Nordics, has been chosen.

2. Mathematical description of moisture and heat transport

Transport of moisture in porous materials ordinarily encompasses vapor diffusion, due to gradients in vapor pressure, and capillary suction, due to gradients in suction pressure. If needed, vapor transport by air flow, due to gradients in air pressure, may also be included. In the current study only vapor diffusion and capillary suction have been included as mechanisms for moisture transport, since air flows are not present in the case looked at. A basis has been taken in using relative humidity (RH) as the dependent moisture transport variable. Moisture transport is in terms of a partial differential equation (PDE) given as (1), which is derived from the continuity equation.

$$\frac{dw_w}{d\phi}\frac{d\phi}{dt} = \frac{d}{dx_j}\left(\left[\delta_v P_{sat} + D_\phi\right]\cdot\frac{d\phi}{dx_j} + \left[\left(\delta_v \frac{dP_{sat}}{dT} + D_\phi \frac{1}{T}\ln(\phi)\right)\frac{dT}{dx_j} + \frac{D_\phi}{R_w}\frac{1}{T} g\cdot\overrightarrow{e_z}\right]\cdot\phi\right) \tag{1}$$

Although many researchers have written publications on the use of COMSOL for building physics applications, few have explained in detail how they have set up COMSOL to solve the PDEs for a dependent variable of relative humidity, suction pressure or vapor pressure. One exception is van Schijndel [3] who described how the PDE were solved for the logarithm of the suction pressure. Such a solution effectively limits the span of orders of magnitude the suction pressure appears in during the numerical solving, and thereby improves the numerical solving situation greatly. For COMSOL this solution is a necessity in order for the numerical solver to function at high relative humidities in the capillary range. For a PDE based on relative humidity, the same challenge appear; however, instead of spanning orders of magnitude the relative humidity needs to be solved accurately as phi values approach unity, i.e. a phi value of 0.9999, or even 0.99999, needs to be dealt with accurately, due to the large impact small changes in phi in this region have on water content and capillary transport properties for many porous materials. Such a high accuracy in phi values approaching unity can be quite a challenge or time consuming for numerical solving. Gradients with respect to phi can also become very large and span orders of magnitude in this RH region. In order to get around this in COMSOL the transport equations have been altered to be solved for a logarithmic representation of phi named phi_{mod}, a modified variable for phi. Expression for Phi_{mod} is given in (2) ensuring phi values up to 0.9999999 can be approached with acceptable accuracy. Phi_{mod} will for phi values between 0.01 and 0.9999999 consequently stay in the interval between 18.41 and 2.30 respectively. The alteration of the transport equations have been done by applying the chain rule to the derivatives of phi giving $d\phi/dt = d\phi/d\phi_{mod}\cdot d\phi_{mod}/dt$ and $d\phi/dx_j = d\phi/d\phi_{mod}\cdot d\phi_{mod}/ dx_j$, where $d\phi/d\phi_{mod} = -\exp(\phi_{mod})/10^8-1$. One should note there is no scientific derivation from physics that leads to Phi_{mod}. It is only a convenient mathematical alteration made for making the COMSOL model work. The alteration has no impact on the physics, only the numerical solving.

$$\phi_{\text{mod}} = \ln\left[10^8\left(1-\phi\right)\right] \tag{2}$$

Transport of heat is taken care of by applying a PDE (3) based on the enthalpy equation on conservative form.

$$\rho_s c_{p,eff}\frac{d\left(T\right)}{dt} = \frac{d}{dx_j}\left(\lambda\frac{dT}{dx_j} - \left[c_{p,w}g_{w,j} + c_{p,v}g_{v,\text{j}}\right]T - h_v g_{v,\text{j}}\right) \tag{3}$$

Where $g_{w,j}$ and $g_{v,j}$ are the capillary and vapor diffusive transport terms found from Darcy's law and Fick's law, which are also included in (1), easily identified by D_ϕ and δ_v respectively. The heat storage in the porous material, which is partially filled with a water content, is taken care of with $c_{p,eff} = (c_{p,s}+w_w/\rho_s\cdot c_{pw})$.

3. Case description

As a case for the comparative study an interior insulated one-brick thick wall with an embedded wooden beam was chosen. See table 1, Fig 1. This is a typical design which may experience too high RH in the wooden beam end, i.e. RH which gives rise to wood degradation. A smart vapor barrier is used to enable some inward drying at times when RH in the nearest wall structure becomes high, typically in the summer when the outside temperature is high. At the same time the vapor barrier prevents vapor from the inside to diffuse into the wall structure at times when the relative humidity in the nearest wall structure is low, typically in the winter. Table 4 gives the correlation between RH and vapor resistance value for the smart vapor barrier.

The exterior climate has been chosen as the moisture design reference year (MDRY) of Værnes in Norway. The wall orientation is towards south. No obstacles are influencing the shortwave and longwave radiation, or the driving rain, received by the wall. The driving rain has been modeled by the ASHRAE Standard 160-2009 "Criteria for Moisture Control Design Analysis in Buildings", since this is an option in WUFI. The explicit longwave calculation has been enabled in the WUFI model, while the COMSOL model calculate longwave radiation exchange with the simple method described by Hens [4] in his chapter on applying radiation calculation for outside environment. Shortwave radiation contributions include reflectance from environment, but the COMSOL model does not yet include complete accuracy for the time the sun passes over the sky. The shortwave radiation thereby occur a bit earlier than it should, and the angles of incoming sunshine are a bit off. For the interior climate the approach found in annex C of NS-EN 15026 [5] for a normal occupancy has been used.

The masonry consists of solid clay brick and prescribed lime-cement mortar, LC 35/65/520 where the numbers corresponding to lime/cement/aggregate mass ratios of binder content, while the embedded beam is made of spruce with longitudinal properties. The air gap between the beam end and the masonry has been modeled in both models with the simplified method of approximation described in the WUFI help file, for a 20 mm gap, although the model gap is 18 mm. This implies that the vapor diffusion coefficient and the heat conductivity are modified in order to account for convection, as well as radiation for the latter.

Sorption curves for the different materials can be found from expression (4), in table 1, with moisture content at saturation found in table 2, and with the listed coefficients in table 3. Vapor diffusion coefficients have been calculated from expression (5) with coefficients found in table 2. Liquid permeability is given by expression (6), with exception of mineral wool which does not give rise to capillary transport. Dw is given by expression (7), based on water absorption coefficients (Aw) found in table 2, with exception of the spruce where logarithmic interpolation and extrapolation was done on the basis of dw = 1.8E-12 at w = 030 and dw = 5.0E-10 at w = 600. dw/dPsuc can be found from derivation of (4). For the smart vapor barrier tabulated Sd-values, as function of relative humidity, are given in table 4. The values are not for a specific product on the market, but give one realistic trend one can find for a typical smart vapor barrier. The interior gypsum board is only modeled as a vapor and thermal resistance.

Table 1. Wall cross section and expressions for material properties

<table>
<tr><th>Fig. 1. Wall cross section</th><th>Expressions (4) and (6), respectively</th><th>Expressions (5) and (7), respectively</th></tr>
<tr><td rowspan="2">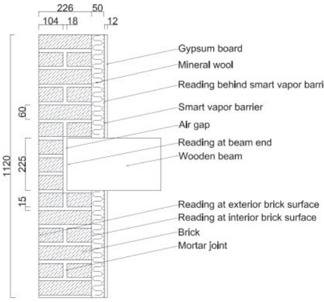
</td>
<td>$w = w_{sat} \cdot \sum_i \left(lw_i \left[1 + \left(cw_i \cdot P_{suc} \right)^{nw_i} \right]^{\left(\frac{1-nw_i}{nw_i} \right)} \right)$</td>
<td>$\delta_v = \frac{1}{R_w T} \frac{26.1 \cdot 10^{-6}}{c_\delta} \frac{\left(1 - \frac{w}{w_{sat}} \right)}{0.503 \left(1 - \frac{w}{w_{sat}} \right)^2 + 0.497}$</td></tr>
<tr><td>$K_l = D_w \frac{dw}{dP_{suc}} = D_w \frac{d\phi}{dP_{suc}} \frac{dw}{d\phi}$</td>
<td>$D_w = 3.8 \left(\frac{A_w}{w_{sat}} \right)^2 \cdot 1000^{\left(\frac{w}{w_{sat}} - 1 \right)}$</td></tr>
</table>

Table 2. Material properties and coefficients.

Material	w_{sat} [kg/m^3]	Aw [kg/m^{2}s$^{1/2}$]	c_δ	λ [W/(m·K)]	c_p [J/(kg·K)]	ρ [kg/m³]
Brick	276	0.265	9.675	0.47	850	1761
LC mortar	130	0.01372	48.99	0.82	850	1806
Spruce	600	-	4.213	0.23	1500	455
Mineral wool	60	-	1.3	0.037	850	60

Table 3. Coefficients for sorption curves, expression (6).

Material	lw1	lw2	lw3	lw4	cw1	cw2	cw3	cw4	nw1	nw2	nw3	nw4
Brick	0.4	0.8	-0.1	-0.1	8.340E-6	6.672E-7	1.876E-7	2.502E-7	1.65	2.5	2.8	2.2
LC mortar	0.9	0.5	-0.2	-0.2	1.626E-6	9.174E-9	7.645E-8	5.838E-9	1.34	3.6	1.244	4.7
Spruce	0.6	0.5	0.4	-0.5	1.807E-4	2.502E-5	1.737E-6	1.737E-7	1.23	1.11	1.38	1.0785
Mineral wool	1	0	0	0	2.085E-6	-	-	-	1.79	-	-	-

Table 4. Sd-values [m] for smart vapor barrier.

RH [-]	0	0.125	0.195	0.39	0.436	0.585	0.624	0.70	0.79	0.901	0.957	0.975	1
Sd [m]	105	102.5	98.3	53.6	37.6	7.0	4.196	1.412	0.412	0.084	0.038	0.029	0.024

4. Results

Starting the first hour of January, the simulations cover two years. The second year thereby has a more reasonable starting moisture content. Fig. 2 shows the RH at the different locations indicated as readings in Fig. 1.

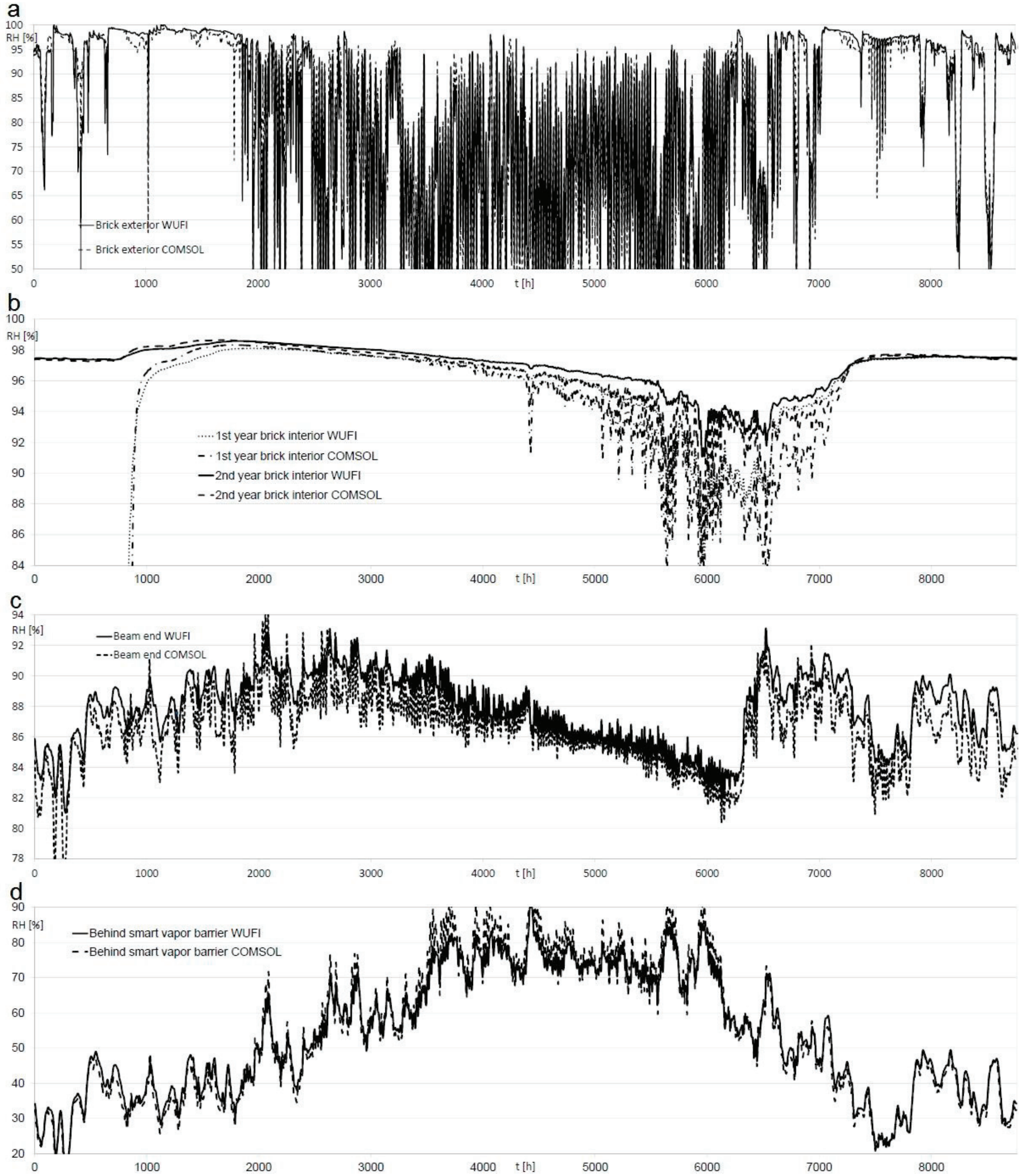

Fig. 2. Relative humidity (RH) developments the second year at the (a) brick exterior surface; (b) brick interior surface; (c) beam end; (d) behind the smart vapor barrier as perceived from the indoors.

5. Discussion and conclusion

As can be seen from Fig. 2 the results match quite well; however, there are some deviations. A spreadsheet analysis of the results, with comparison to the weather exposure, was undertaken to investigate this closer. However, before addressing this it should be noted that the results in Fig. 2 are not taking into account that driving rain will be in the form of driving snow, and thereby not taken up by the wall, when the outdoor temperature is below zero degrees. Excluding precipitation in the form of snow was initially part of the COMSOL model, but had to be turned off since WUFI did not exclude snow in this manner. WUFI help indicates the rain deposition factor should account for snow or hail, by applying lower factors. In Nordic climates, snow frequently constitute a large part of the precipitation during the winter half of the year; however, the weather may also frequently shift between rain and snow. Consequently this would require the overall simulation to be divided into several simulation steps having different factor values. For convenience snow consideration was therefore excluded from the COMSOL model.

When looking at the RH values, plotted in Fig. 2a, in combination with the exterior climate data it was discovered that WUFI often ended up with higher RH from rain absorption than COMSOL. It was first suspected that an explanation could be found in that WUFI states different functions for the ASHRAE Standard 160-2009 driving rain in the WUFI help file and in the WUFI 2D software itself. In the WUFI help file the function includes, as in the standard itself, a reduction for the angle to the wall of the incoming rain to that of the normal, while in the software this is not exclusively included in the function given below the relevant input fields. However, a simulation with COMSOL taking out this angular reduction was then conducted, and the RH levels were seen to become higher than that of the WUFI model. The cause might therefore be something else. From the readings of the interior brick RH levels one could perhaps suspect that the COMSOL model more rapidly transport moisture inward in the masonry, as the RH level surpasses that of WUFI in the periods when driving rain is relatively high, see Fig. 2b. However, this should not really be the case as long as both models include the same material properties. Furthermore, no reduction in capillary transport is included for capillary redistribution of moisture compared with capillary uptake, for either model. Consequently, the cause of the deviation in brick exterior RH due to rainwater uptake remains undetermined and needs to be studied further than what has been done in this paper.

Another cause for deviations between the results was seen to be the radiation models. As mentioned the radiation models applied in COMSOL are not equal to that of WUFI, and the models have not yet been fully optimized for accuracy. Nevertheless, especially the shortwave radiation was seen contributing largely to the deviations. The COMSOL model shows a higher susceptibility towards temperature increase, due to direct shortwave radiation, than WUFI. As a result, in times of shortwave radiation, the brick exterior RH in COMSOL has higher fluctuations towards lower values. It must be analyzed further whether there are some errors or inaccuracies in the COMSOL model in this regard.

In conclusion, a hygrothermal model made in COMSOL has been shown to give similar RH results to that of WUFI. However, the results deviate somewhat as discussed above. The COMSOL model needs to be validated further, as there probably are parts to improve or correct for the better. Especially the models applied for longwave and shortwave radiation could benefit from further development in increasing their accuracy. With that in mind, COMSOL has shown great potential to function as a hygrothermal simulation tool.

References

[1] COMSOL. COMSOL Multiphysics Sweden: COMSOL Inc.; 2017 [cited 2017 03.02]. Available from: https://www.comsol.com/.

[2] Fraunhofer. WUFI, 2D Germany: Fraunhofer IBP; 2017 [cited 2017 05.02]. Available from: https://wufi.de/en/software/wufi-2d/.

[3] Schijndel AWM. Heat and Moisture Modeling Benchmark using COMSOL. Proceedings of the COMSOL Users Conference; Hannover 2008.

[4] Hens H. Building Physics–Heat, Air and Moisture, Fundamentals and Engineering Methods with Examples and Exercises, Ernst & Sohn A Wiley. ISBN 978-3-433-01841-5, 2007.

[5] NS-EN 15026. Hygrothermal performance of building components and building elements. Assessment of moisture transfer by numerical simulation. Brussels, Belgium: European Committee for Standardization (CEN); 2007.

Correction for page 774

Sorption curves for the different materials can be found from expression (4), in table 1, with moisture content at saturation found in table 2, and with the listed coefficients in table 3. Vapor diffusion coefficients have been calculated from expression (5) with coefficients found in table 2. Liquid permeability is given by expression (6), with exception of mineral wool which does not give rise to capillary transport. Dw is given by expression (7), based on water absorption coefficients (Aw) found in table 2, with exception of the spruce where logarithmic interpolation and extrapolation was done on the basis of Dw = 1.8E-12 at w = 30 kg/m^3 and Dw = 5.0E-10 at w = 600 kg/m^3. dw/dPsuc -can be found from derivation of (4). For the smart vapor barrier tabulated Sd-values, as function of relative humidity, are given in table 4. The values are not for a specific product on the market, but give a realistic trend one can find for a typical smart vapor barrier. The interior gypsum board is only modeled as a vapor and thermal resistance. Heat and vapor transfer coefficients are as follows on the exterior and interior boundary respectively: $\alpha_{a,e} = 25$ W/m^{2}K, $\alpha_{a,i} = 8$ W/m^{2}K, $\beta_{p,e}=2\cdot10^{-7}$ s/m, $\beta_{p,i} = 3\cdot10^{-8}$ s/m.

Table 1. Wall cross section and expressions for material properties

Fig. 1. Wall cross section	Expressions (4) and (6), respectively	Expressions (5) and (7), respectively
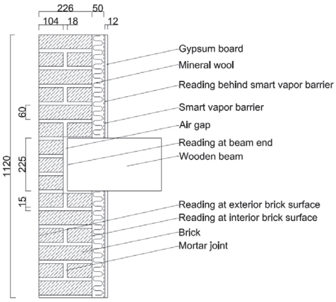	$w = w_{sat} \cdot \sum_i \left(lw_i \left[1 + \left(cw_i \cdot P_{suc}\right)^{nw_i} \right]^{\left(\frac{1-nw_i}{nw_i}\right)} \right)$	$\delta_v = \frac{1}{R_w T} \frac{26.1\cdot10^{-6}}{c_\delta} \frac{\left(1-\frac{w}{w_{sat}}\right)}{0.503\left(1-\frac{w}{w_{sat}}\right)^2+0.497}$
	$K_l = -D_w \frac{dw}{dP_{suc}} = -D_w \frac{d\phi}{dP_{suc}} \frac{dw}{d\phi}$	$D_w = 3.8\left(\frac{A_w}{w_{sat}}\right)^2 \cdot 1000^{\left(\frac{w}{w_{sat}}-1\right)}$

Table 2. Material properties and coefficients.

Material	w_{sat} [kg/m^3]	Aw [kg/m^{2}s$^{1/2}$]	c_δ	λ [W/(m·K)]	c_p [J/(kg·K)]	ρ [kg/m^3]
Brick	276	0.265	9.675	0.47	850	1761
LC mortar	130	0.01372	48.99	0.82	850	1806
Spruce	600	-	4.213	0.23	1500	455
Mineral wool	60	-	1.3	0.037	850	60

Table 3. Coefficients for sorption curves, expression (4).

Material	lw1	lw2	lw3	lw4	cw1	cw2	cw3	cw4	nw1	nw2	nw3	nw4
Brick	0.4	0.8	-0.1	-0.1	8.340E-6	6.672E-7	1.876E-7	2.502E-7	1.65	2.5	2.8	2.2
LC mortar	0.9	0.5	-0.2	-0.2	1.626E-6	9.174E-9	7.645E-8	5.838E-9	1.34	3.6	1.244	4.7
Spruce	0.6	0.5	0.4	-0.5	1.807E-4	2.502E-5	1.737E-6	1.737E-7	1.23	1.11	1.38	1.0785
Mineral wool	1	0	0	0	2.085E-6	-	-	-	1.79	-	-	-

Table 4. Sd-values [m] for smart vapor barrier.

RH [-]	0	0.125	0.195	0.39	0.436	0.585	0.624	0.70	0.79	0.901	0.957	0.975	1
Sd [m]	105	102.5	98.3	53.6	37.6	7.0	4.196	1.412	0.412	0.084	0.038	0.029	0.024

4. Results

Starting the first hour of January, the simulations cover two years. The second year thereby has a more reasonable starting moisture content. Fig. 2 shows the RH at the different locations indicated as readings in Fig. 1.

Article V

Modelling hydraulic conductivity for porous building materials based on a prediction of capillary conductivity at capillary saturation

J. I. Knarud, T. Kvande, S. Geving

International Journal of Heat and Mass Transfer 186 (2022) 122457
https://doi.org/10.1016/j.ijheatmasstransfer.2021.122457

International Journal of Heat and Mass Transfer 186 (2022) 122457

Contents lists available at ScienceDirect

International Journal of Heat and Mass Transfer

journal homepage: www.elsevier.com/locate/hmt

Modelling hydraulic conductivity for porous building materials based on a prediction of capillary conductivity at capillary saturation

Jon Ivar Knarud[a,*], Tore Kvande[a], Stig Geving[b]

[a] *Department of Civil and Environmental Engineering, Norwegian University of Science and Technology, NO-7491 Trondheim, Norway*
[b] *Department of Architecture, Materials and Structures, SINTEF Community, NO-7465 Trondheim, Norway*

ARTICLE INFO

Article history:
Received 23 October 2021
Revised 10 December 2021
Accepted 19 December 2021

Keywords:
Liquid conductivity
Moisture diffusion
Thin film surface diffusion
Capillary absorption coefficient

ABSTRACT

Liquid moisture transport plays a key role in performance of many building assemblies. For hygrothermal simulation models, used to assess such assemblies, it is important to include realistic liquid transport properties for the specific porous building materials involved. Unfortunately, comprehensive experimental and modeling methods associated with determining the hydraulic conductivity limit widespread application of material-specific determination. To ease applicability, this paper investigates how to simplify conductivity prediction and modeling by building on a bundle of tubes approach. Incorporating a new expression variant for the capillary absorption coefficient (A_w), a novel prediction expression for the conductivity at capillary saturation ($K_{c,cap}$) is derived. modeling of unsaturated capillary conductivity (K_c) can thus be scaled to $K_{c,cap}$ instead of the traditional approach of scaling to conductivity at over-capillary saturation (K_{sat}), avoiding some complexity and concerns one traditionally has faced. Hence, in contrast to most models for K_c, which apply K_{sat}, this paper applies $K_{c,cap}$ as reference to scale the conductivity at unsaturated conditions. To model the hydraulic conductivity (K) for the full moisture range, K_c is coupled with a thin film model (K_{film}) and a hygroscopic correction model (K_{hyg}). The prediction model is evaluated against a wide range of porous building material datasets found in literature as well as compared to a common alternative approach, with reasonable results. The findings of this study can help for better understanding of challenges in analytical calculation of A_w and of why bundle of tube models have accuracy issues in predicting K_c, with the study suggesting remedies for some of these issues.

1. Introduction

Hygrothermal simulation has become an important tool for assessing the hygrothermal performance of building details or parts, either it concerns new designs or retrofits, renovations or improvements to existing buildings. When involving capillary moisture transport, it is important that capillary properties of porous materials are realistically captured. Of key interest is the moisture retention curve and the hydraulic conductivity curve. Of these the latter is the most challenging, as it is difficult to experimentally determine in the unsaturated region [1], and relatively resource intensive to determine (accurately) in the saturated region. Usually, one of two approaches are used to identify the hydraulic conductivity for the full range of moisture contents: 1) modeling which usually include scaling to the saturated conductivity, or 2) calculation from the moisture diffusivity. Although the moisture diffusivity is relatively easier to determine over unsaturated capillary conditions it is still resource intensive, traditionally involving experimentally determining moisture profiles and for instance applying the Boltzmann transform method to determine the moisture diffusivity function, e.g. [2]. Thus, for practical applications it is not obvious that the diffusivity approach is realistic to utilize [1]. Regarding modeling, hydraulic conductivity has often been modeled by bundle of tubes models, with the most well-known model contributions, originally developed for petroleum and soil science, being Burdine [3], Mualem [4] and Van Genuchten [5]. An alternative to bundle of tubes models have been the more advanced network models, which incorporate percolation theory [6, 7].

Although bundle of tubes models are not without flaws, with their oversimplification of the pore system and flow paths (e.g. [6]), their relative simplicity provides an approach less laborious and easier accessible to utilize than their network model alternatives [7]. Bundle of tubes models are commonly scaled from measured capillary conductivity at saturation K_{sat} or at zero capillary pressure K_0; however, these have shown to be difficult to determine accurately [8]. Furthermore, it has been reported difficulty

---

* Corresponding author.
E-mail address: jon.knarud@ntnu.no (J.I. Knarud).

https://doi.org/10.1016/j.ijheatmasstransfer.2021.122457

Nomenclature (excluding Table 1)

A	area (m^2)
$A_{int,v}$	cross sectional area of internal voids per unit area (m^2/m^2)
A_w	capillary absorption coefficient (kg/(m^2 s$^{1/2}$))
B_A, B_c, B_f	area, curvature and flow rate correction factors due to pore shape irregularity (-)
$C_{int,v}$	circumference of internal voids per unit area (m/m^2)
D_w	diffusion coefficient (m^2/s)
$f_{curvature}$	film curvature correction factor (-)
f_d	factor of deviation (-)
f_l	mechanistic scaling function (-)
j	moisture flux (kg/(m^2 s))
K	hydraulic conductivity (kg/(m s Pa))
L	length (m)
l_w, c_w, n_w	coefficients for retention curve expression, (-), (Pa^{-1}), (-) respectively
m	mass (kg)
m''	mass uptake per unit area (kg/m^2)
$\dot{m}''$	mass rate per unit area (kg/(m^2 s))
n	cumulative pore number (-)
p	pressure (Pa)
r	capillary pore radius (m)
r_0, r_{eff}, r_{ae}	average, effective and average/effective pore radius (m)
R_w	gas constant for water (J/(kg K))
S_{wi}, S_{wf}	wetting phase saturation, initial and behind imbibition front respectively (-)
t	time (s)
T	temperature (K)
V	volume (m^3)
$\dot{V}$	volumetric flow rate (m^3/s)
$\dot{V}'$	volumetric flow rate per unit length (m^3/(m s))
V''	absorbed volume per unit area (m^3/m^2)
w	moisture content (kg/m^3)
x	spatial coordinate (m)

Greek symbols

α	correction factor (-)
α_p	dimensionless pressure (-)
δ	film thickness (m)
δ_v	vapor diffusion coefficient (kg/(m s Pa))
ε	porosity (-)
η_Aw, η_cap	various scaling factors (-)
η_sp, η_ϕ	various exponents (-)
θ	moisture content (m^3/m^3)
μ	vapor diffusion resistance (-)
μ_w	dynamic viscosity water (kg/(m s))
Π, Π_e, Π_m,	disjoining pressure, with electrostatic and molecular components (Pa)
ρ_w	density water (kg/m^3)
σ_w	surface tension water (N/m)
τ	tortuosity (-)
φ	contact angle (°)
ϕ	relative humidity (%)

Subscripts

a	air
abs	absorption
ad	adsorbed
c	capillary
cap	capillary saturation
dry	dry cup measurement
Dw	diffusion coefficient based
eff	effective
film	adsorbed moisture film
g	gas
hyg	hygroscopic
l	liquid
lim	limiting
mod	modified
nom	nominal
p	pore
red	redistribution
ref	reference
rel	relative
sat	saturation
tot	total
v	vapor
w	water
wet	wet cup measurement

with scaling to the saturated conductivity, when saturation is set equal to total porosity, because the moisture retention curve is ill-defined in the over capillary region close to saturation [9].

Nevertheless, to accommodate an engineering need for less resource intensive predictions of hydraulic conductivity, bundle of tubes models are still of interest. With a bundle of tubes model as the foundation, Scheffler and Plagge [7] proposed a whole moisture range hydraulic conductivity model. Although this model is intriguing, it relies on a couple of material dependent parameters which require iterative post-processing through simulation to be determined properly. Furthermore, the model still relies on scaling to an effective conductivity at over-capillary saturation, which needs to be determined experimentally. Equipment for, and experience with, such experimental determination is not particularly available for wide practical application.

In the present paper the aim has been to develop a model, inspired by the Scheffler and Plagge model, but which is easier to apply, by removing reliance on iterative post-processing and reducing reliance on material property data which is particularly resource intensive to acquire.

Specifically, the objective of this study is to derive and investigate an alternative approach to predict hydraulic conductivity as function of capillary pressure, $K(p_c)$, not relying on comprehensive testing of K (or K_{sat}) in contrast to existing approaches.

From initial, inspirational ideas research questions were formulated to substantiate the objective. The following questions are explored in our study: 1) Is it feasible to predict the capillary conductivity at capillary saturation? 2) Can the Scheffler-Plagge model for $K(p_c)$ be simplified by scaling to conductivity at capillary saturation instead of at saturation? 3) Can the overall procedure for determining $K(p_c)$ be simplified and made more practically feasible, for when only a necessary minimum of material property test data is available. 4) For such a model, how is the prediction performance for $K(p_c)$ when assessing a wide range of porous building materials described in previous studies?

The focus of this paper is categorically limited to bundle of tubes models, in description of the hydraulic conductivity, in contrast to network models. Hysteresis effects are not addressed. Furthermore, needed information on the pore size distribution will be estimated from the retention curve, and it has been outside the scope of the work to assess whether direct use of a measured pore size distribution would improve predictions. The study does not include a comparative evaluation of how realistic physics are represented in comparable, alternative prediction approaches; however, a quantitative comparative evaluation of prediction performance is included.

The paper is outlined as follows: First the model is derived and presented. Then procedure for its application and evaluation is introduced. After follows results and result assessments, followed by further discussion and finally a summary and conclusion.

2. Hydraulic conductivity model

Several hydraulic conductivity models for the whole moisture range have previously been proposed, e.g., within field of building physics [7, 10] and soil science [11, 12]. In contrast to the former the latter include models for thin film flow to the overall hydraulic conductivity. With thin film flow models seemingly having benefitted conductivity modeling at low moisture contents in soil science, it is possible similar benefits can be introduced to application in building physics. Thin film flow will therefore be incorporated in the overall hydraulic model presented in the following sections. In this study we will limit the hydraulic conductivity model to liquid conductivity, with the presumption that vapor transport is addressed separately in hygrothermal simulation software. Hence, vapor transport (vapor conductivity) is not included.

In the following sections we go through the sequential steps of deriving the hydraulic conductivity model. First we introduce the bundle of tube model based on Grunewald et al. [10]. Then theory on predicting the capillary absorption coefficient is introduced followed by a proposed new prediction expression. Next, this enables forming a prediction expression for the capillary conductivity at capillary saturation. Further, the Sceffler and Plagge model [7] is rearranged for scaling to conductivity at capillary saturation. Thereafter follows a thin film model based on Lebeau and Konrad [11] and a correction model for the hygroscopic region based on the Sceffler and Plagge model [7]. The overall hydraulic model is then established. Finally, a procedure for incorporating the retention curve into the model is given.

2.1. Capillary conductivity

The Hagen-Poiseuille equation describes the volumetric laminar flow in a cylindrical pore (tube) of radius r along the tube path of length L. However, pores in porous media usually never meet the ideal of cylindrical geometry [13]. Therefore, a flow rate correction factor B_f is included to account for impact of irregular geometry (non-cylindrical), on the volumetric flow rate. In contrast to Cai et al. [13], which relates a correction factor α directly to r, B_f is here related to the volumetric flow rate; hence, B_f equates to α^4 in [13]. The Hagen-Poiseuille equation thus take the form:

$$\dot{V}(r) = -B_f \frac{\pi r^4}{8\mu_w} \frac{dp_l}{dL} \tag{1}$$

where μ_w is the dynamic viscosity of water and p_l the liquid pressure. With capillary pressure $p_c = p_g - p_l$ and presumed constant gas (air) pressure p_g, dp_l is simply substituted with $-dp_c$. Here, for convenience, positive values for p_c are applied throughout, although p_c alternatively can be written as negative pressure (suction). r represents an equivalent cylindric radius, in practical terms, half of a hydraulic diameter, or the radius of an inscribed circle for regular polygons. Flow in capillaries may be perceived to follow tortuous streamlines [13, 14]. Consequently, the flow path length dL is greater than a more relatable dimension dx, of a control volume. This can be addressed by introducing the tortuosity τ, which from a macroscopic perspective represents the ratio of effective capillary path length to length dx (thickness of a control volume). That is; $dL = \tau \bullet dx$, see e.g. [15]. With these changes, Eq. (1) transforms to:

$$\dot{V}(r) = B_f \frac{\pi r^4}{8\mu_w} \frac{1}{\tau} \frac{dp_c}{dx} \tag{2}$$

The volumetric flow rate in a bundle of capillaries can be found by integrating Eq. (2) over the pore size distribution density [7, 10], i.e. integrating with respect to radius the product of volumetric flow rate and corresponding incremental number of pores at respective radius. Adapted from [7, 10] the capillary moisture flux then becomes:

$$j_{w,x} = \rho_w \int_R \dot{V}(r) \frac{dn(r)}{dr \cdot dA} dr \tag{3}$$

where j_w is the moisture flux, and dA indicates unit area $dA = dydz$ of a control volume $dV = dxdydz = 1\ \mathrm{m}^3$.

The expression for the incremental number of pores can be established as follows:

$$dn(r) = \frac{\Delta V(r)}{A_p(r)\tau dx} = \frac{\Delta\theta_c \cdot dV}{B_A \pi r^2 \tau dx} = \frac{dA}{B_A \pi r^2 \tau} \frac{d\theta_c(r)}{dr} dr \tag{4}$$

where $dn(r)$ is the increment number of pores at a radius, $\Delta V(r)$ change in moisture filled capillary volume as function of r, $A_p(r)$ pore cross section, θ_c volumetric capillary retained moisture content. B_A area correction factor for non-circular cross section $B_A = A_p/A_{p,cylindrical}$ (e.g. $B_A = 1.27$ square, $B_A = 1.65$ equilateral triangle). Including the factor B_A is important to account for the "extra" water in each pore which is not included in the inscribed circle which r represents. For non-circular cross sections, not including B_A will overestimate the number of pores. Rearranging Eq. (4) we have:

$$\frac{dn(r)}{dr \cdot dA} = \frac{1}{B_A \pi r^2 \tau} \frac{d\theta_c(r)}{dr} \tag{5}$$

Note that by including B_A and τ, Eqs. (4) and (5) differs from the approach in [7, 10]. Inserting Eqs. (2) and (5) into Eq. (3) and integrating over all radii involved at a capillary moisture content θ_c:

$$j_{w,x} = \frac{B_f}{B_A} \frac{\rho_w}{8\mu_w \tau^2} \int_0^{\theta_c} r(\theta_c)^2 d\theta_c \frac{dp_c}{dx} \tag{6}$$

Eq. (6) is similar to what is reported in [7], but with the additional inclusion of tortuosity and the factors B_f and B_A. The radius can be related to the capillary pressure through the Young-Laplace equation, which when given by Eq. (7) includes a correction factor B_c for pore shape irregularity [13, 16]. This irregularity affects the meniscus curvature, see [17].

$$p_c = \frac{2\sigma_w \cos(\varphi)}{r/B_c} \tag{7}$$

where σ_w is the surface tension of water and φ the contact angle. Following Wong et al. [17] the general Young-Laplace equation can be arranged:

$$p_c = \frac{\sigma}{r} \nabla \cdot \hat{\boldsymbol{n}} \rightarrow \frac{rp_c}{\sigma} \equiv \alpha_p = \nabla \cdot \hat{\boldsymbol{n}} \tag{8}$$

where α_p is a dimensionless pressure and $\nabla \bullet \boldsymbol{n}\hat{}$ is the dimensionless mean curvature.

B_c can then be defined as:

$$B_c = \frac{\alpha_{p,actual}}{\alpha_{p,cylindrical}} \tag{9}$$

Considering Eqs. (8) to (7), $\alpha_p = 2cos(\varphi)$ for a cylindrical pore. Assuming 0° contact angle; for a cylindrical pore $\alpha_p = 2$ (Eq. (9): $B_c = 1.0$), for an equilateral triangle shaped pore $\alpha_p = 1.7776$ [17, 18] ($B_c = 0.8888$), and for a square shaped pore $\alpha_p = 1.8862$ [17, 18] ($B_c = 0.9431$). Note that the correction factor assigned by Cai et al. [13] as α, would here equate to $\alpha = B_f^{1/4} = 1/B_c$. For an equilateral triangle $\alpha = 1.186$ and a square $\alpha = 1.094$ [13] (α can be found from assessing calculated analytical solutions of Hagen-Poiseuille flow for respective pore shapes). These α-values coincide with $\alpha = B_f^{1/4} \neq 1/B_c$. Thus, in [13] the two correction factors, respectively for the Hagen-Poiseuille and Young-Laplace equation, are incorrectly conflated into one and the same.

Inserting Eq. (7) solved for r into Eq. (6) gives:

$$j_{w,x} = \frac{B_f B_c^2}{B_A}\frac{\rho_w \sigma_w^2 \cos^2(\varphi)}{2\mu_w \tau^2}\int_0^{\theta_c}\frac{1}{p_c(\theta_c)^2}d\theta_c \frac{dp_c}{dx} \tag{10}$$

with the capillary conductivity in Eq. (10) being:

$$K_c = \frac{B_f B_c^2}{B_A}\frac{\rho_w \sigma_w^2 \cos^2(\varphi)}{2\mu_w \tau^2}\int_0^{\theta_c}\frac{1}{p_c(\theta_c)^2}d\theta_c \tag{11}$$

K_c becomes $K_{c,cap}$, i.e. capillary conductivity at capillary saturation, when integrated up to $\theta_c = \theta_{c,cap}$. By including pore shape correction factors and tortuosity Eq. (11) distinctly differs traditional approaches. Although, it is not particularly useful since B_f, B_c and B_A are still unknown factors. However, $K_{c,cap}$ has previously been suggested to be predicted from the capillary absorption coefficient A_w [19], as $K_{c,cap} = 10^{-8}\eta_{Aw}A_w^2$, where η_{Aw} being a material dependent coefficient reported to be in the interval 0.95 – 16.0. This expression is neither specifically sophisticated in its intuitiveness (non-correct or hidden units) nor convincingly related to physical characteristics of the material and fluid. Furthermore, with a coefficient spanning over one order of magnitude prediction accuracy suffers without experience in choosing the coefficient.

Nevertheless, if assuming $K_{c,cap}$ could be predicted from A_w, a dimensional analysis of K through the Rayleigh method [20] reveals that an expression of K could be a function of A_w^2 divided by a density characteristic, units [kg/m^3], and a pressure characteristic, unit [Pa]. (This does not necessarily exclude other possibilities of physical parameters.) Guessing the correct appearance however would not necessarily be straight forward, risking becoming heavily reliant on a nonsensical coefficient. A plausible approach is to presume more information is needed regarding A_w to understand the relation to K.

2.2. Capillary absorption coefficient

An expression for A_w was derived by Beltran et al. [21] to be:

$$A_w = \rho_w\left(\frac{\sigma_w}{\mu_w}\right)^{1/2}\frac{\varepsilon_{cap}}{\tau}r_0^{1/2}\left(\frac{\cos\varphi}{2}\right)^{1/2} \tag{12}$$

where ε_{cap} is the capillary porosity and r_0 is an average pore radius. Eq. (12) can also be directly derived from the early Handy imbibition model [13, 22], with the liquid permeability $k_w = \varepsilon_{cap} r_0^2/(8\tau)$ [21, 23]. As seen, Eq. (12) does not include correction for pore shape irregularity; however a similar expression by Benavente et al. [24], has one such correction included.

$$A_w = B_c^{1/2}\rho_w\left(\frac{\sigma_w}{\mu_w}\right)^{1/2}\frac{\varepsilon}{\tau^{1/2}}r_{eff}^{1/2}\left(\frac{\cos\varphi}{2}\right)^{1/2} \tag{13}$$

where ε is the porosity and r_{eff} is an effective radius which requires to be calculated by Newton's iteration method, see [24]. Hypothetically, with measurement of A_w one can thereby estimate B_c. Unfortunately, Eq. (13) suffers from some shortcomings, including; incorrect handling of the tortuosity, not including a correction factor in the Hagen-Poiseuille equation and not addressing the wetting liquid saturation [13]. A further developed expression can be found from an imbibition model derived by Cai et al. [13]:

$$A_w = \alpha^{3/2}\rho_w\left(\frac{\sigma_w}{\mu_w}\right)^{1/2}\frac{\varepsilon\left(S_{wf}-S_{wi}\right)}{\tau}r_{ae}^{1/2}\left(\frac{\cos\varphi}{2}\right)^{1/2} \tag{14}$$

where S_{wf} is the wetting phase saturation behind the imbibition front, S_{wi} the initial wetting phase saturation, and r_{ae} an average/effective pore radius. If assuming S_{wf} equals capillary saturation and S_{wi} is negligible, i.e. for an initially dry material or for a relatively non-hygroscopic material, then $\varepsilon(S_{wf} - S_{wi}) \approx \varepsilon_{cap}$. Even though Eq. (14) is a considerable improvement from Eq. (12) it also has its issues. As previously mentioned, the correction factors for the Hagen-Poiseuille and Young-Laplace equations have incorrectly been conflated in α. Furthermore, for materials having a pore structure of highly varying pore size it is difficult to assess r_{ae}.

Thereby, to accommodate these issues a revised derivation approach to A_w is warranted.

2.3. Proposed new A_w-expression

In the following an expression for A_w is derived with derivation steps from Cai et al. [13] coupled with approaches from Section 2.1.

Specifically addressing imbibition where a face of a porous material is put in contact with a free water surface, and assuming sharp-front theory of capillary absorption [25], there will be a sharp moisture front which moves through the material. We furthermore assume dealing with materials and a setting which follow linear cumulative absorption with respect to square root of time, i.e., $m'' = A_w\sqrt{t}$, where m'' is cumulative liquid mass absorption per unit area. Proportionality to $\sqrt{t}$ corresponds to a specific time-dependent imbibition regime in which neither inertia nor gravitational forces are significant. A thorough review of the imbibition regimes is provided by Dejam et al. [26].

In Eq. (1) dp_l is replaced with $-dp_c$ as before, but with dL now the distance L (pore length) the imbibition moisture front has traveled. Similar to [13], p_c is furthermore replaced with Eq. (7). Consequently, the volumetric flow rate of one pore can be expressed as:

$$\frac{dV_p}{dt} = B_f B_c \frac{\pi r^3}{4\mu_w}\frac{\sigma_w \cos(\varphi)}{L} \tag{15}$$

Assuming Eq. (15) only addresses capillary pores, initially being dry, which through the imbibition process becoming fully saturated between the free liquid surface and the moisture front, we have $V_p = L \bullet A_p$. Substituting L in Eq. (15) with V_p/A_p enables Eq. (15) to be integrated with regard to V_p and t. Integrating limits are; for $t = 0$, $V_p = 0$, and for $t = t$, $V_p = V_p$. Hence:

$$\frac{1}{2}V_p^2 = B_f B_c \frac{\pi r^3}{4\mu_w}\sigma_w \cos(\varphi) A_p t \tag{16}$$

The absorbed volume of water V_p can be integrated over the bundle of capillaries involved by repeating the same approach as in Eq. (3). Solving Eq. (16) for V_p and integrating over the pore size distribution density:

$$V'' = \int_R\left[B_f B_c B_A \frac{\pi^2 r^5}{2\mu_w}\sigma_w \cos(\varphi) t\right]^{1/2}\frac{dn(r)}{dr\cdot dA}dr \tag{17}$$

Applying Eq. (5), Eq. (17) becomes:

$$V'' = \int_0^{\theta_{c,cap}}\left[\frac{B_f B_c}{B_A}\frac{r}{2\mu_w}\sigma_w \cos(\varphi) t\right]^{1/2}\frac{1}{\tau}d\theta_c \tag{18}$$

Multiplying Eq. (18) with the water density, and rearranging:

$$m'' = \frac{B_f^{1/2}B_c^{1/2}}{B_A^{1/2}}\rho_w\left(\frac{\sigma_w}{\mu_w}\right)^{1/2}\left(\frac{\cos\varphi}{2}\right)^{1/2}\frac{1}{\tau}\int_0^{\theta_{c,cap}} r^{1/2}d\theta_c \cdot t^{1/2} \tag{19}$$

From Eq. (19) it follows that:

$$A_w = \frac{B_f^{1/2}B_c^{1/2}}{B_A^{1/2}}\rho_w\left(\frac{\sigma_w}{\mu_w}\right)^{1/2}\frac{1}{\tau}\int_0^{\theta_{c,cap}} r^{1/2}d\theta_c\left(\frac{\cos\varphi}{2}\right)^{1/2} \tag{20}$$

Comparing Eqs. (20) to (14) one can see $\alpha^{3/2}$ is recovered if one allows the incorrect conflation $\alpha = B_f^{1/4} = 1/B_c$ previously addressed. In derivation of Eq. (20) it is assumed $\varepsilon S_{wf} = \varepsilon_{cap} = \theta_{c,cap}$, and S_{wi} is through the integral step to Eq. (16) implicitly assumed to be negligible ($S_{wi} = 0$). Both can be included by multiplying Eqs. (17)-(20) with $\varepsilon(S_{wf} - S_{wi})/\varepsilon_{cap}$. Nevertheless, the biggest difference to Eq. (14) is the treatment of the pore structure, in Eq. (20) with the integral of pore radii involved in capillary absorption over the interval of saturation up to capillary saturated moisture content $\theta_{c,cap}$.

Replacing r by means of the Young-Laplace equation, Eq. (7), Eq. (20) finally becomes:

$$A_w = \frac{B_f^{1/2} B_c}{B_A^{1/2}} \frac{\rho_w \sigma_w}{\mu_w^{1/2}} \frac{\cos(\varphi)}{\tau} \int_0^{\theta_{c,cap}} \frac{1}{p_c^{1/2}} d\theta_c \tag{21}$$

2.4. Proposed novel prediction of conductivity at capillary saturation

Taking the square of Eq. (21), solving for the unknown correction factor product $B_f B_c^2 B_A^{-1}$ and inserting into Eq. (11), $K_{c,cap}$ can finally be predicted by:

$$K_{c,cap} = \frac{A_w^2}{2\rho_w} \int_0^{\theta_{c,cap}} \frac{1}{p_c^2} d\theta \left[\int_0^{\theta_{c,cap}} \frac{1}{p_c^{1/2}} d\theta_c \right]^{-2} \tag{22}$$

Eq. (22) satisfies the dimensional analysis previously mentioned with the density characteristic revealed to be the density of water and the pressure characteristic expressed as a relation of two integrals both of functions of p_c.

2.5. Capillary model

With $K_{c,cap}$ being the capillary conductivity at capillary saturation the capillary model for saturations $0 \leq \theta_c \leq \theta_{c,cap}$ can follow the capillary model of Scheffler and Plagge [7]; $K_c = f_l \eta_{cap} K_{eff,sat} K_{rel}$, in where $f_l(w_{cap})\eta_{cap} K_{eff,sat}$ equals $K_{c,cap}$. η_{cap} is a scaling parameter to scale K_c to a measured effective (over-capillary) saturation $K_{eff,sat}$. Since $K_{c,cap}$ in the present work is predicted directly and not reliant on scaling by η_{cap} the model of Scheffler and Plagge is rewritten to Eq. (23).

$$K_c = \frac{f_l}{f_l(w_{cap})} K_{c,cap} K_{rel} \tag{23}$$

f_l, Eq. (24), being the scaling function of the mechanistic serial-parallel pore model described by Scheffler and Plagge [7], following the principles of Grunewald et al. [10], and $f_l(w_{cap})$ being f_l evaluated at w_{cap} (moisture content at capillary saturation).

$$f_l = \frac{\left(\frac{w}{w_{sat}}\right)^{\eta_{sp}}}{\left(\frac{w}{w_{sat}}\right)^{\eta_{sp}} + \left(1 - \frac{w}{w_{sat}}\right)^2 \left(1 - \left(\frac{w}{w_{sat}}\right)^{\eta_{sp}}\right)} \tag{24}$$

where η_{sp} is a parameter to adjust the serial-parallel relation, by modifying the volumetric fraction that is parallel pore domain in the mechanistic model [7], and w_{sat} is moisture content at saturation. K_{rel} being the relative capillary conductivity [7, 10] given as:

$$K_{rel} = \frac{\int_0^{\theta_c} p_c^{-2} d\theta_c}{\int_0^{\theta_{c,cap}} p_c^{-2} d\theta_c} \quad for\ \theta_c \leq \theta_{c,cap} \tag{25}$$

In contrast to [7, 10] the upper integral limit below the fraction line is $\theta_{c,cap}$, instead of $\theta_{eff,sat}$. The η_{sp} parameter is material dependent [19]; however, we will argue it is also dependent on boundary conditions, i.e. dependent on whether it is absorption, redistribution or drying of moisture, or a combined representation of these, which is in focus when determining capillary conductivity (see Section 4.3). For a hypothetical pure parallel flow behavior $\eta_{sp} = 0$; however, usually it resides in the interval up in lower single digits.

2.6. Thin film model

Surface diffusion is a liquid transport mechanism which is important in pores not available for capillary transport, due to too low moisture filling for capillary menisci to form. Thin film flow is an approach to account for surface diffusion. We apply parts of the model approach described by Lebeau and Konrad [11]. Integration of a velocity distribution, arrived from Navier-Stokes equations, over a film thickness yields the volumetric flow rate per unit length of film cross section [11]. Adopted from [11], the thin film equation assuming no-slip at pore wall and negligible shear between liquid and air becomes:

$$\dot{V}' = \frac{\delta^3}{3\mu_w} \frac{dp_c}{dx} \tag{26}$$

where δ is the film thickness, which can be expressed as function of capillary pressure. Positive value for p_c gives Eq. (26) without minus sign in contrast to [11].

Multiplying Eq. (26) with the water density and the pore system void circumference over a cross section of the control volume gives the moisture flux:

$$j_{film} = \frac{\rho_w \delta^3}{3\mu_w} C_{\text{int},v} \frac{dp_c}{dx} \tag{27}$$

where $C_{\text{int},v}$ is the circumference of internal voids not capillary filled as function of p_c, with $C_{int,v} = C_{int,v,tot} - C_{int,v,c}$, where $C_{int,v,tot}$ is the total circumference of internal voids and $C_{int,v,c}$ is the circumference of filled capillary pores. Ideally $C_{int,v,c}(p_c)$ should be found from a pore size distribution; however, if relying on the retention curve, as is done in the current paper, it can be calculated as:

$$C_{\text{int},v,c} = \int_R 2\pi r \frac{dL}{dx} \frac{dn(r)}{dr \cdot dA} dr \overset{eq.(5)}{=} \frac{2}{B_A} \int_0^{\theta_c} \frac{1}{r} d\theta_c \tag{28}$$

$$C_{\text{int},v,tot} = \frac{2}{B_A} \int_0^{\theta_{c,cap}} \frac{1}{r} d\theta_c \tag{29}$$

Note that Eqs. (28) and (29) provide the inscribed circle circumference of the capillaries, thereby constituting a simplification to film flow. The radius in Eqs. (28) and (29) is solved from Eq. (7), where B_c needs to be approximated by comparing measured A_w to Eq. (21). In lack of detailed information about the pore shapes, B_f, B_c and B_A are unknown. If values for B_f and B_A are chosen, based on simple assumptions, a value for B_c can be identified and Eqs. (28) and (29) can be calculated. We here assume film in over-capillary pores (not filled at capillary saturation) has negligible contribution to hydraulic conductivity, due to a relative low total circumference of such pores. These are therefore not included in the calculation. Furthermore, for the integration in Eqs. (28) and (29) we do not allow accumulated circumference for pores with radius below twice the diameter of a water molecule (diameter of a water molecule ≈ 3E-10 m) as no efficient film flow will allow to form for smaller pore sizes.

From Eq. (27) the film contribution to the hydraulic conductivity can be identified as:

$$K_{film} = \frac{\rho_w \delta^3}{3\mu_w} C_{\text{int},v} \tag{30}$$

According to [11] the film thickness is involved in two relations of disjoining pressure components. The overall disjoining pressure is given as [11]:

$$\Pi(\delta) = \Pi_e(\delta) + \Pi_m(\delta) \tag{31}$$

where Π_e is the ionic-electrostatic component and Π_m the molecular component.

$$\Pi_e(\delta) = \frac{\varepsilon_r \varepsilon_0}{2} \left(\frac{\pi k_B T}{eZ} \right)^2 \frac{1}{\delta^2} \tag{32}$$

Table 1
Parameters for Eq. (32) and (33) adopted from [11].

Parameter	Description	Value
A_{svl} (J)	Hamaker constant	-6.0×10^{-20}
e (C)	Electron charge	1.60218×10^{-12}
k_B (J/K)	Boltzmann constant	1.38065×10^{-23}
T (K)	Temperature	293.15
Z (-)	Valence charge	1
ε_0 (C^2/(J m))	Permittivity of free space	8.85419×10^{-12}
ε_r (-)	Relative permittivity of water	80.23

$$\Pi_m(\delta) = -\frac{A_{svl}}{6\pi\delta^3} \tag{33}$$

with parameters summarized in Table 1, assessed at 293.15 K.

The disjoining pressure Eq. (31) is related to liquid pressure [11]:

$$\Pi(\delta) = p_g - p_l \tag{34}$$

Relating Eq. (34) to the capillary pressure which is also defined $p_c = p_g$ - p_l one have that the disjoining pressure is analog to capillary pressure.

Since Eqs. (32) and (33) are functions of δ^{-2} and δ^{-3} respectively, it is inconvenient to analytically solve for δ. Instead, for simplicity we propose calculating $\Pi(\delta)$ for a range of δ and then plot $\log(\delta)$ as function of $\log(\Pi(\delta))$. From such a plot a simple 2nd degree polynomial function can be fitted. Following this approach δ can be approximated with:

$$\delta_{film} = 10^{0.0116\cdot(\log|p_c|)^2 - 0.5535\cdot\log|p_c| - 5.7810} \tag{35}$$

Eq. (35) has up to ± 5% deviation to the actual film thickness over the range $10^0 < |p_c| < 10^9$ Pa. The film model, Eq. (30), could seemingly model hydraulic conductivity in the hygroscopic region for non-filled pores. However, with its background stemming from the rather macroscopic perspective of solving Navier-Stokes, it lacks in handling complexity associated with very thin films at nanoscale. For very thin films, measuring in a low number of water molecule layers, limiting aspects, physical conditions, material properties and pore wall characteristics will impact film existence and behavior. For instance, 1) water molecule diameter limits lowest film thickness and smallest pores that are effectively accessible to water, 2) material hydrophilicity or hydrophobicity, temperature, film confinement, and pore wall roughness affect water molecule orientation, structuring of the fluid, adhesion forces, no-slip tendency at pore wall and fluid properties such as density and viscosity, e.g. [23, 27].

Therefore, there is need for corrections to the film model, or a more advanced film model altogether, to address nanoscale properly. However, instead of adding complexity to the film model, such as to some extent is done in [11], we circumvent the issue with two simple/practical correctional steps; 1) the film thickness cannot be thicker than what the adsorbed water content in the material allows for. Hence, the overall film moisture content (adsorbed part of retention curve) divided by the product of water density and the pore system surface area of non-filled capillaries gives an upper bound. 2) in the lower to middle hygroscopic region we keep the hygroscopic model from Scheffler and Plagge, described in next subchapter, with a smooth transition from the hygroscopic model to the film model as function of relative humidity (RH). By taking these two steps the modeling is kept simpler, but at a cost of realism and accuracy.

With step 1), resulting film thickness to be applied in Eq. (30) becomes:

$$\delta = \min\left(\delta_{film}(p_c), \frac{w(p_c) - w_c(p_c)}{\rho_w C_{\text{int},v}(p_c)}\right) \tag{36}$$

Or

$$\delta = \min\left(\delta_{film}(p_c), \frac{w(p_c) - \rho_w B_A A_{\text{int},v,c}}{\rho_w C_{\text{int},v}(p_c)}\right)$$

where w_c is the capillary retained moisture content occupying filled capillaries, and $A_{int,v,c}$ the cumulative inscribed circle cross sectional area of filled capillaries given by Eq. (37), derived in same way as Eq. (28).

$$A_{\text{int},v,c} = \frac{1}{B_A}\int_0^{\theta_c} d\theta_c \tag{37}$$

2.7. Hygroscopic correction model

Scheffler and Plagge [7] propose accounting for liquid conductivity in the hygroscopic region by assessing the difference in vapor diffusion between dry cup and wet cup measurements. Herein they assume a negligible liquid transport contribution included in the vapor conductivity K_v (Eq. (38) [1]) for the dry cup measurement. The difference; wet cup – dry cup, Eq. (39), approximates the liquid transport fraction K_{hyg} acting during the wet cup measurement. They propose three vapor diffusion measurements are needed to enable logarithmic interpolation and extrapolation: one dry cup and two different wet cup measurements. Eq. (38) arise from relating vapor diffusion to a driving potential on the form of capillary pressure.

$$K_v = \frac{\delta_{v,a}}{\mu}\cdot\frac{\phi p_{v,sat}}{\rho_w R_w T} \tag{38}$$

where $\delta_{v,a}$ is the vapor diffusion coefficient of air, μ the vapor diffusion resistance factor, $p_{v,sat}$ the saturated vapor pressure.

$$K_{hyg}(\theta_{wet}) = \left(\frac{\phi(\theta_{wet})_{wet}}{\mu_{wet}} - \frac{\phi_{dry}}{\mu_{dry}}\right)\delta_{v,a}\frac{p_{v,sat}}{\rho_w R_w T} \tag{39}$$

where θ_{wet} is the associated volumetric moisture content at which K_{hyg} is determined, μ_{wet} and μ_{dry} are vapor diffusion resistance coefficients from wet and dry cup measurements, and ϕ_{wet} and ϕ_{dry} effective RH associated with respective resistance coefficient. Commonly $\phi_{wet} = 0.715$ and $\phi_{dry} = 0.25$ since μ_{wet} and μ_{dry} are respectively found at standardized conditions 50/93% and 0/50% RH [28].

Unfortunately, usually only a single wet or dry vapor diffusion resistance (in Europe commonly defined by [28]) is sought. Rarely more than one of these is reported in a study. Carmeliet and Roels [1] is one of few exceptions explicitly having reported three measurements (one dry cup and two wet cup). Therefore, three measurements need to be preplanned with determining K_{hyg} in mind. If only one of the resistance coefficients is available, for instance the dry cup, then the other one associated with $\phi_{wet} = 0.715$ could be subjected to a guesstimate. For materials having very low hygroscopicity, i.e., relatively small difference in sorption between 25% and 71.5% RH, one can assume μ_{wet} and μ_{dry} to be rather similar. If only one or two values are available one can adopt K-values from the thin film model at relatively high RH values, as long as these are larger values than the one or two values of the liquid part of vapor conductivity which are available. If the thin film model gives larger μ-equivalent values (Eq. (38) solved for μ from K_{film}) than μ_{dry} we recommend setting successively slightly lower vapor diffusion resistance factors for the two wet cup calculations of Eq. (39), (e.g. $\mu_{wet} = \mu_{dry} - 0.1$). Then, logarithmic interpolation still can be achieved.

A 2nd degree Lagrange logarithmic interpolation, incorporating an arbitrary third liquid conductivity point; $K_{hyg}(\phi_{dry}) = 10^{-2}K_{v,dry}$, could be a practical and reasonable approach for interpolation.

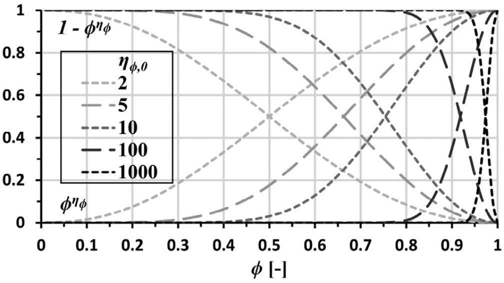

Fig. 1. Influence of $\eta_{\phi,0}$ on the transition between hygroscopic correction model and film/capillary models.

2.8. Proposed hydraulic conductivity model

The resulting model is in general a combination of the liquid conductivity model from Scheffler and Plagge [7] and the thin film model of Lebeau and Konrad [11]. However, it includes a significant key alteration by having replaced $K_{eff,sat}$, i.e. measured effective saturated conductivity, with the prediction expression for $K_{c,cap}$, which instead requires measurement of A_w. Saturated capillary conductivity measurements are relatively more complicated than measurements of the capillary absorption coefficient. Furthermore, the scaling parameter η_{cap} of the Scheffler and Plagge model is avoided, which significantly simplifies the calculation procedure, since this parameter is determined iteratively by simulation of water absorption experiments [7]. The new overall model is given as:

$$K = (1 - \phi^{\eta_\phi})K_{hyg} + \phi^{\eta_\phi}\left(K_{film} + K_c\right) \tag{40}$$

where η_ϕ is a fitting exponent function, which we have arbitrarily given the form $\eta_\phi = \eta_{\phi,0}(1 - \phi)$, where $\eta_{\phi,0} \geq 0$. Setting $\eta_{\phi,0} = 0$ would remove impact of the hygroscopic correction model and would require a more sophisticated thin film model as discussed in Section 2.6. Fig. 1 illustrates the impact of the function depending on $\eta_{\phi,0}$. With $\eta_{\phi,0} = 5$ a rather balanced transition within the upper hygroscopic region is achieved between the hygroscopic correction model and the film/capillary models, whereas higher values will ensure the hygroscopic correction model overrides more of the hygroscopic region. Note that Eq. (40) needs to be supplemented with a criterion which ensures K increases or remains constant as the capillary pressure decrease in order to avoid potential cases where the transition from the hygroscopic correction model to the film and capillary models results in a fall in hydraulic conductivity. Relevant for some materials where the film model provides lower predictions than the hygroscopic correction model.

Eq. (40) ensures that K_{hyg} is phased-out while K_{film} is phased-in as ϕ increase. Furthermore, since K_{film} is dependent on $C_{int,v}$, which subsides as capillary pores are filled, the capillary model takes over for K_{film} as this happens. Since both ϕ and θ can be expressed as functions of p_c Eq. (40) can readily be applied to generate a $\log(p_c)$ – $\log(K)$ table for implementation by logarithmic interpolation in hygrothermal simulation models (equal to the setup of the Hamstad 4 benchmark [29]).

2.9. Retention curve

The retention curve consists of an adsorptive and a capillary contribution, w_{ad} and w_c respectively:

$$w = w_{ad} + w_c \tag{41}$$

It is of interest to separate the two contributions to separately control the adsorbed and capillary related moisture contents for implementation in hydraulic conductivity sub-models. Different models have been proposed for the retention curve contributions of Eq. (41) in the literature, e.g. [11, 12, 30]; however, these become difficult to apply in the present work. In [11] one rely on an unknown adsorbed moisture content (hypothetical bound film in both capillary filled and non-filled pores) θ_0 at a matric head of −1 m. From our experience it is difficult to determine θ_0 from retention curve data and to get the function it resides to fit the retention curve of certain materials, even though the overall procedure in [11] for determining w_{ad} and w_c is elegant. In [12] and [30] the adsorbed moisture content is not replaced by capillary filling, which would cause underestimation of w_c at higher moisture contents. Since we base the capillary conductivity on Hagen-Poiseuille equation, we require the initially adsorbed moisture content on pore walls to be transformed into capillary moisture content as capillary menisci are formed, filling the entire cross section with moisture as capillaries become saturated. Consequently, we have had to choose a different approach.

The approach for handling the retention contributions depend on whether the pore size distribution or only the retention curve is available. With the pore size distribution available, one can estimate the adsorbed moisture content as the product of the film thickness, the non-capillary-filled pore surface area and the water density, accounting for moisture reduction due to film curvature. If only relying on the overall retention curve, which is the case in the current work, we propose the following approximation approach.

For implementation of the current model a retention expression proposed by Carmeliet and Roels [31] was made multimodal; resulting in Eq. (42). The expression is based on the Van Genuchten expression [5] proposed to be used multimodal by Durner [9], and extended with a Freundlich type expression [32].

$$w = w_{\lim}\left[\exp\left(-\frac{p_c}{\rho_w R_w T}\right)\right]^{n_{w,0}} + (w_{cap} - w_{\lim}) \cdot \sum_{i=1}^{N=4}\left(l_{w,i}\left[1 + (c_{w,i} \cdot p_c)^{n_{w,i}}\right]^{\left(\frac{1-n_{w,i}}{n_{w,i}}\right)}\right) \tag{42}$$

where w_{lim} would be the limiting, critical water content between the hygroscopic and over-hygroscopic region (however, the actual w_{lim} value could be expected to deviate from the critical moisture content, being a more arbitrary fitting parameter [31]), $n_{w,0}$ fitting exponent, $l_{w,i}$ weighing coefficient equal to share of pore volume associated with corresponding inflection point in a cumulative pore size distribution, i.e. $\Sigma\ l_{w,i} = 1$, $c_{w,i}$ inverse of p_c at inflection point, $n_{w,i}$ fitting exponent.

In Eq. (42), the Freundlich term associated with w_{lim} is intended to provide the adsorptive contribution at low to intermediate RH-values, before capillary filling becomes significant, while the Van Genuchten term associated with w_{cap} - w_{lim} being the multimodal expression for capillary retained moisture. Of course, this is an over-simplification where in reality adsorbed moisture would be present at higher moisture contents in pores not yet capillary filled, whereas part of the initial adsorbed moisture content would become part of capillary filled pores. Furthermore, some materials, for instance concrete, have such a small pore structure that both film adsorption and capillary filling are significant at intermediate RH-values. Hence, respectively associating the Freundlich term and Van Genuchten terms to adsorptive and capillary moisture is not feasible in a general approach for all materials.

We therefore apply an iterative procedure:

1. Integrate all sub model integrals over θ instead of θ_c, with θ derived from Eq. (42) as $\theta = w/\rho_w$.
2. Calculate $\delta_{film}(p_c)$ Eq. (35) and $C_{int,v} = C_{int,v,tot} - C_{int,v,c}$ with Eqs. (43) and (44), which now include a curvature correction factor $f_{curvature} = (\pi r^2 - \pi(r-\delta)^2)/(2\pi r\delta)$ for $\delta < r$ and $f_{curvature} = \pi r^2/(2\pi r\delta)$ for $\delta \geq r$.

Table 2
Description details on model datasets.

	Input data availability			Hydraulic model dataset derived from a combination of			
Material [source]	Sorption curve	Retention curve	Vapor resistance measurements	Direct measurements	Modeled	Adjusted from indirect measurements	Post-processed from simulation
Brick [19]	yes	yes[a]	1 reported	K_{sat} only	yes	yes	yes
Sand-lime brick [19]	yes	yes[a]	1 reported	K_{sat} only	yes	yes	yes
Aerated concrete [19]	yes	yes[a]	1 reported	K_{sat} only	yes	yes	yes
Calcium silicate insulation [19]	yes	yes[a]	1 reported	K_{sat} only	yes	yes	yes
Brick [1]	yes	yes	3 reported	K_{sat} only	yes	yes[c]	no
Sand-lime brick [1]	yes	yes	3 reported	K_{sat} only	yes	yes[c]	no
Brick [33]	no	yes	1 reported, 3 K_v plotted	yes[b]	no	yes[c]	no
Cement mortar (wet cured) [33]	no	yes	1 reported, 3 K_v plotted	yes[b]	no	yes[c]	no
Calcium silicate insulation [34]	yes	yes	1 reported	K_{sat} only	yes	no	no
Limestone [35]	no	function	1 reported	no	yes	yes	no
Concrete [36, 37]	yes	yes	none	K_{sat} only	yes	no	no

[a] retention curve for adsorption is in the source presumed from measured retention curve for desorption.
[b] x-ray measurement data.
[c] only hygroscopic region.

3. Calculate $w_{ad}(p_c) = \rho_w C_{int,v} \delta_{film}$ as an approximation of film bound moisture.
4. Calculate $w_c(p_c) = \max(0, w - w_{ad})$ with w from Eq. (42).
5. Recalculate all integrals with $\theta_c = w_c/\rho_w$

$$C_{int,v,c} = \frac{2}{B_A}\int_0^{\theta_c} f_{curvature}\frac{1}{r}d\theta_c \tag{43}$$

$$C_{int,v,tot} = \frac{2}{B_A}\int_0^{\theta_{c,cap}} f_{curvature}\frac{1}{r}d\theta_c \tag{44}$$

3. Application and evaluation procedure

3.1. Datasets

Datasets are chosen from the literature to assess the model and alternative approaches for comparison. The datasets include: brick, sand-lime brick, aerated concrete and calcium silicate insulation from Scheffler [19], ceramic brick and calcium silicate brick (sand-lime brick) from Carmeliet and Roels [1], brick and wet cured cement mortar from Derluyn et al. [33], calcium silicate insulation from Häupl et al. [34], limestone from Cabrera et al. [35], and concrete (labeled 65DI) from Leech [36, 37]. It is important to point out that these datasets are not purely experimental datasets, rather they provide hydraulic conductivity curves derived from varying degree of being modeled and fitted to direct or indirect experimental data of a material's hydraulic conductivity. Therefore, they will henceforward be referred to as model datasets. In their respective sources, the model datasets have gone through some experimental validation on absorption [1, 33-35, 37] and drying [1]. Generally, only model datasets which include necessary input data; retention curve (adsorption), capillary absorption coefficient (or sorptivity), vapor resistance coefficient (or vapor diffusion coefficient), and a proposed model/dataset for the hydraulic conductivity have been chosen. However, concrete is also included even though the source does not include vapor resistance data. Hence, for concrete, only the capillary conductivity will be assessed. Table 2 includes additional details on the model datasets. Of the models datasets, those of Scheffler [19] give hydraulic conductivity which is intended to be valid both for absorption and drying, whereas the rest address absorption only. It should also be noted that the retention curves from Scheffler do not stem from direct measurements for the most part, rather Scheffler estimated them from experimentally determined desorption retention curves and assessment of material pore structure [19].

Table 3
Tortuosity values.

Material	N	τ [-]	ε [%]	Ref.
Brick	15	1.6–5.4	18.8–39.0	[39]
	1	2.654	26	[40]
Aerated concrete	8	1.4965–1.7818	72.4–83.8	[41]
Calcium silicate insulation	–	1.092[a]	90	–
Sand-lime brick	1	2.085	33	[40]
Limestone	2	1.27,1.47	24.3,32.1	[42]
Cement mortar	1	2.875	15.6	[40]
Concrete	1	3.536	13.4	[40]

[a] calculated from tortuosity expression derived by Yu and Li [38], based on 90% porosity.

3.2. Practical implementation of the hydraulic model

The relation between p_c and θ for each material is given by the retention curve accompanying each dataset. Since it is rather inconvenient to solve p_c from Eq. (42), integration of integrals containing p_c is done numerically after ensuring sufficiently high resolution in values of w being evaluated. For instance, in a spread sheet, enough values of w need to be calculated to accurately capture the shape of p_c as function of θ. The retention curves have been generated from Eq. (42) with input parameters which can be found in Appendix A, and give approximately identical retention curves to what accompanying the datasets.

In addition to input obtained from dataset sources, material tortuosity is needed to solve Eq. (21) (without the correction factors, see Section 2.6). Approximations to tortuosity can be found from values reported in the literature. Some values are summarized in Table 3, with the average (Table 4) applied in present work (except with exclusion of the highest outlier of brick). Although there is a distinction between geometric, electrical, diffusive and hydraulic tortuosity [14], such a distinction has not be addressed in the present work. The uncertainty and inaccuracy of applying literature values for tortuosity to specific materials is assumed to be greater than the distinction between the different definitions of tortuosity. The distinction becomes more important if the tortuosity is measured specifically for respective materials. A correlation to porosity is often attributed the tortuosity [14], however we have not differentiated the tortuosity by porosity for the materials of the same type, e.g. brick. In absence of tortuosity values a geometrical tortuosity model derived by Yu and Li [38] can be used as an approximation. It has the benefit of not requiring any empirical parameters or physical characteristics, except the porosity. However, it does not represent any natural porous material [14].

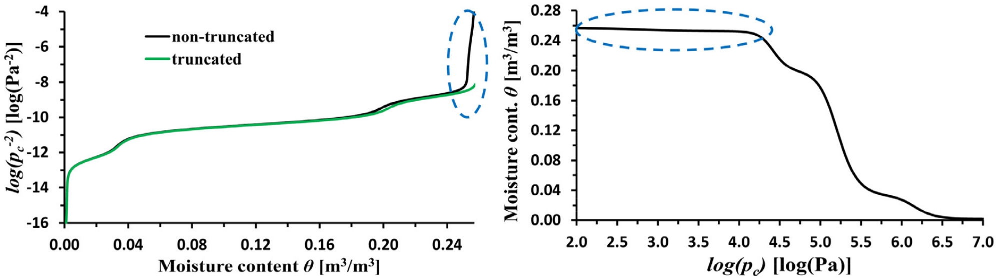

Fig. 2. Left: principle of truncated area under the curve for brick (Scheffler). Encircled region highlights the area under the curve in which p_c rapidly decrease over the last few % of retained moisture content. Right: corresponding retention curve, with the challenging region encircled.

Table 4
Chosen values for parameters not available from dataset sources.

Material	τ	B_f	B_A	η_{sp} [a]	$\eta_{\phi,0}$
Brick Derluyn	2.7	1.43	1.27	1	5
Brick Carmeliet	2.7	1.43	1.27	1	5
Brick Scheffler	2.7	1.43	1.27	2[b]	5
Sand-lime brick Carmeliet	2.1	1.43	1.27	1	5
Sand-lime brick Scheffler	2.1	1.43	1.27	2	5
Calcium silicate Scheffler	1.1	1.43	1.27	1	5
Calcium silicate Häupl	1.1	1.43	1.27	1	5
Limestone	1.4	1.43	1.27	1	5
Aerated concrete	1.7	1.43	1.27	2	5
Cement mortar	2.9	1.43	1.27	1	5
Concrete	3.5	1.43	1.27	1	5

[a] The choice of η_{sp} is discussed in subchapter 4.3.
[b] a value of 2.8 is specified in [7]; however, this value seemingly becomes too high, see Section 4.1 and 4.3.

For simplicity we have chosen a square pore shape for the correction factors B_f and B_A. A square pore shape provides a perceived middle ground between an unrealistic ideal of cylindrical pore shape and more irregular pore shapes. Ideally the representative pore shape of each material should be assessed individually; however, this is left outside the scope of the current study.

The serial-parallel exponent η_{sp} of the mechanistic scaling function, Eq. (24), has been simply chosen as follows: $\eta_{sp} = 2$ for comparison to the model datasets from Scheffler [19], since these incorporate drying data. Exception is calcium silicate for which the model dataset correlates very well with perceived absorption behavior. For the rest of the datasets $\eta_{sp} = 1$. The choice of η_{sp} is made after experience with the model and with an aim to demonstrate the model from simple generalized inputs and not involve material dependent adjustment. Further assessment of η_{sp}-optimalization is addressed in Section 4.3.

Finally, for practical reasons the integrals of $p_c^{-1/2}$ and p_c^{-2}, Eqs. (21) and (22), have been truncated at a slightly lower moisture content than $\theta_{c,cap}$. The reason for this can best be explained with Fig. 2, where p_c^{-2} is plotted against moisture content. For the last few % of moisture content the function increases dramatically. Since the scale is logarithmic, an integration of the area under the curve will easily be heavily influenced by this area. Comparing to the retention curve, this moisture content corresponds to the last filling of large-scale capillary pores as the retention curve slope flattens out towards w_{cap}. As this occurs p_c-values decrease dramatically with only little change in moisture content. We will argue that this span in p_c-values is a poor representation of acting p_c associated with capillary absorption because:

- The large pores (pore volume) this moisture content represents have a high probability of being insufficient to represent continuous capillaries through the material.
- Certain materials have larger isolated pores which may be detected in measurements of retention curve or pore size distribution due to small scale samples, while for larger material scales the pores are not continuous through the material.

A similar discussion is given by Durner [8, 9] for the asymptotic slope of the retention curve near saturation for models including over-capillary retention. Although Durner [9] relates part of the issue to difficulty and uncertainty in determining the retention curve in the over-capillary region close to saturation, the high sensitivity of bundle of tubes K-models to low capillary pressures associated with the retention curve at high saturations remains an issue also here. For these reasons the integrals are truncated at a $\theta_{c,cap}$ cut-off value. For most materials this cut-off is above 97% of $\theta_{c,cap}$, with the brick (Carmeliet) at 95.7% due to a presumed lower precision in its retention curve compared to the other materials. The procedure has been kept simple, cutting the curve off where it starts turning upwards for the almost vertical increase (Fig. 2). Each integral is then divided by the cut-off value (e.g., if 98% then divided by 0.98). The resulting area under the curve is given by the truncated curve in Fig. 2.

3.3. Alternative approaches for comparison

A common alternative approach is that of calculating the hydraulic conductivity from the moisture diffusivity (e.g. [43, 44])

$$K_{Dw} = D_w \frac{dw}{dp_c} \tag{45}$$

The notation $_{Dw}$ in K_{DW} is here just applied to distinguish the hydraulic conductivity in Eq. (45) from Eq. (40). A much used empirical model for D_w is that of Künzel [45]:

$$D_{w,abs} = 3.8\left(\frac{A_w}{w_{cap}}\right)^2 1000^{\frac{w}{w_{cap}}-1} \tag{46}$$

The first part of Eq. (46); $3.8(A_w/w_{cap})^2$, is with the value 3.8 presumably a generalization of an integral of the area under a moisture penetration profile, see [46]. Several non-generalized expressions also exists, e.g. [46, 47]; however, these require a material dependent parameter. Note that Künzel [45] and Kruβ [48] distinguish between absorption and redistribution/drying, with $D_{w,red}$, based on experimental support, often presumed equal to $10^{-1}{\cdot}D_{w,abs}$.

An unfortunate consequence of Eq. (45) is the decrease of K when the retention curve flattens out over an interval of p_c. Carmeliet et al. [43] noted there is need for a correction to the resulting curve of K at low p_c-values to avoid a decrease in K which would be unphysical. They state K should monotonically increase with decreasing p_c (increasing moisture content) and propose to keep K constant after its highest value for successive decrease in

p_c. However, it is not only at low p_c-values decrease in K can occur with Eq. (45). It can also occur at intermediate p_c-values with retention curves for materials with a pore size distribution including distinctly different scales. See resulting graphs in Section 4.1. We therefore propose an algorithm for a modified calculation of the K_{Dw} curve:

$$K_{Dw,\text{ mod },i+1} = \begin{cases} K_{Dw,i+1} & for\ K_{Dw,i+1} \geq K_{Dw,\text{ mod },i} \\ K_{Dw,\text{ mod },i} & for\ K_{Dw,i+1} < K_{Dw,\text{ mod },i} \end{cases} \tag{47}$$

with i being an increment number representing the position in the resolution N of increasing moisture content, from $w = 0$ with $i = 1$ to $w = w_{cap}$ with $i + 1 = N$. Both K_{Dw}, Eq. (45), and $K_{Dw,mod}$, Eq. (47), are included for comparison, respectively referred to as *K(*D_w *absorption) standard* and *K(*D_w *absorption) modified* in graph legends.

The empirical prediction expression $K_{c,cap} = 10^{-8}\eta_{Aw}A_w{}^2$ reported by Scheffler [19], coupled with the overall hydraulic model through Eqs. (23) and (40), is also included for comparison. Since the material-specific η_{Aw} is unknown, the reported lower and upper bound of 0.95 and 16 respectively are both applied. The resulting hydraulic conductivity models are denoted *K model, empirical low* and *K model, empirical high.*

4. Results and assessment

4.1. Comparisons to datasets

Fig. 3, a) to k), presents the approaches to predict the material model datasets. Material input properties to the hydraulic model are given to the left while the results are compared to the model dataset on the right. Results of the hydraulic model proposed in this paper is labeled *K model, prediction*. For view on a log*(K)* – log*(*p_c*)* relation refer to Appendix B. Note that model dataset graphs of Fig. 3b), d) and j) also contain contribution from K_v while the prediction approaches do not. For the materials addressed in Fig. 3d) and j) particularly, which retain significant moisture in the hygroscopic region, comparison assessments at lower moisture contents are thus not viable.

Note that the results demonstrate the proposed prediction model with relatively generalized choices for input parameters (Table 4). Optimal fitting of these parameters for each material has not been a priority in this study. Nevertheless, a simple assessment of η_{sp} and $\eta_{\phi,o}$ is given in Section 4.3 and 4.4.

The *K(Dw absorption) standard* approach will not be addressed, as it is only included to illustrate the issue described in Section 3.3, while *K(Dw absorption) modified* is its replacement. The *K model, empirical low and high* are seen to vary greatly in their ability to align with the model datasets. The *low* only relatively close for sand-lime brick and calcium silicate, in Fig. 3e) and g) respectively. Whereas the *high* reasonable for all the three bricks, calcium silicate, and limestone in Fig. 3a), b), c), f) and h) respectively. For sand-lime brick, cement mortar and concrete both are far off (Fig. 3d) j) and k) respectively). Overall, in the expression $K_{c,cap} = 10^{-8}\eta_{Aw}A_w{}^2$ the material dependence is clearly not fully taken care of by $A_w{}^2$ alone; however, also the interval of η_{Aw} is insufficient and even lower values are needed to make it encompass cement mortar and concrete. Due to the unknown material dependent η_{Aw} from an a-priori perspective the *K model, empirical* approaches are not addressed any further.

In the remainder only *K model, prediction* and *K(Dw absorption) modified* are assessed.

Interestingly for both brick and sand-lime brick of the Carmeliet model datasets both approaches overestimate $K_{c,cap}$. This could indicate that the respective retention curves at high moisture contents encompass filling of pores which are rather isolated and not suitable to be included in the bundle of tubes model integral. However, for brick (Carmeliet) the retention curve also converges with a gentle slope towards w_{cap} over a longer interval of p_c compared to the other two bricks, which makes it more difficult to determine the truncation of the integrals for this material. The same issue is seen for aerated concrete. If for sand-lime brick (Carmeliet) the largest pores had not been included in the integrals (truncated at lower moisture content or with an adjusted retention curve) a better prediction of $K_{c,cap}$ could have been achieved. For sand-lime brick (Scheffler) and calcium silicate (Scheffler) it might be that Scheffler's estimate of the retention curves at low p_c-values provides too gentle slopes, when comparing to the desorption retention curves in [19]; however, the $K_{c,cap}$ prediction deviation could also be that the largest pores are too spatially sparce to resemble continuous capillaries.

One clear observation is how the *K model, prediction* given $\eta_{sp} = 1.0$ has a tendency to follow *K(Dw absorption) modified* for all materials. Due to the relative simplicity of the film model and the hygroscopic correction model, including increased uncertainty regarding the dataset models in the corresponding moisture region, as some are post-modified in this region, while others are not or seemingly not properly modeled in this region, it is hard to provide a concise and meaningful visual assessment of the figures in the hygroscopic region. However, it is included in a quantified assessment in the next section.

4.2. Quantified assessment

An attempt is made to quantify the prediction accuracy of the proposed hydraulic conductivity model to that of the model datasets. We introduce a factor of deviation f_d which will describe the average deviation from the reference model dataset. By average deviation a graph y_i will on average follow the notional relation $y_i = f_d{}^{\pm 1} y_{ref}$, where y_i and y_{ref} are respectively the y-values of the graph that is compared and of the reference graph it is compared to (i.e., the model dataset). The ±1 exponent indicates the function y_i can both overshoot and undershoot function y_{ref}. To what extent under- or overshooting occurs is not divulged by the factor itself. Since the curves have a strong exponential nature, spanning many orders of magnitude, it is necessary to evaluate them in form of logarithms. The factor of deviation is given as Eq. (48). Note that the ±1 exponent mentioned above is linked to taking the absolute value of the logarithmic difference.

$$f_d = 10^{\int_{\theta_{rel}} \left|\log(y_i) - \log(y_{ref})\right| d\theta_{rel}} \tag{48}$$

where $\theta_{rel} = \theta/\theta_{cap}$ is relative moisture content, i.e., relative to capillary saturated moisture content. If $f_d = 1.0$ the curves would be a perfect match; however. such a case would be highly unlikely. Although dependent on accuracy preference, values of $f_d \leq 2$ and $f_d > 2$ might respectfully be regarded as reasonable and not so reasonable predictions, with in mind the exponential nature of the capillary conductivity curve. Values of $f_d < 1.5$ might be regarded as reasonably good.

Only the *K model, prediction* and *K(*D_w *absorption) modified* are assessed, since the former being the proposed hydraulic model and the latter is the likely (or common) contender. Overall, after assessing Fig. 3, the other approaches show to be less sophisticated and have less reliable performance. Factors of deviation are summarized in Table 5

Table 5 reveals the following. Hydraulic conductivity at capillary saturation is predicted better by *K model, prediction* in 5 materials, while better by *K(Dw absorption) modified* in 6 materials. For aerated concrete the two are almost equal, for limestone and cement mortar the two have both good predictions with rather high precision. Also, calcium silicate is similar for the two with fair precision, while for brick Carmeliet the two are similarly poor predic-

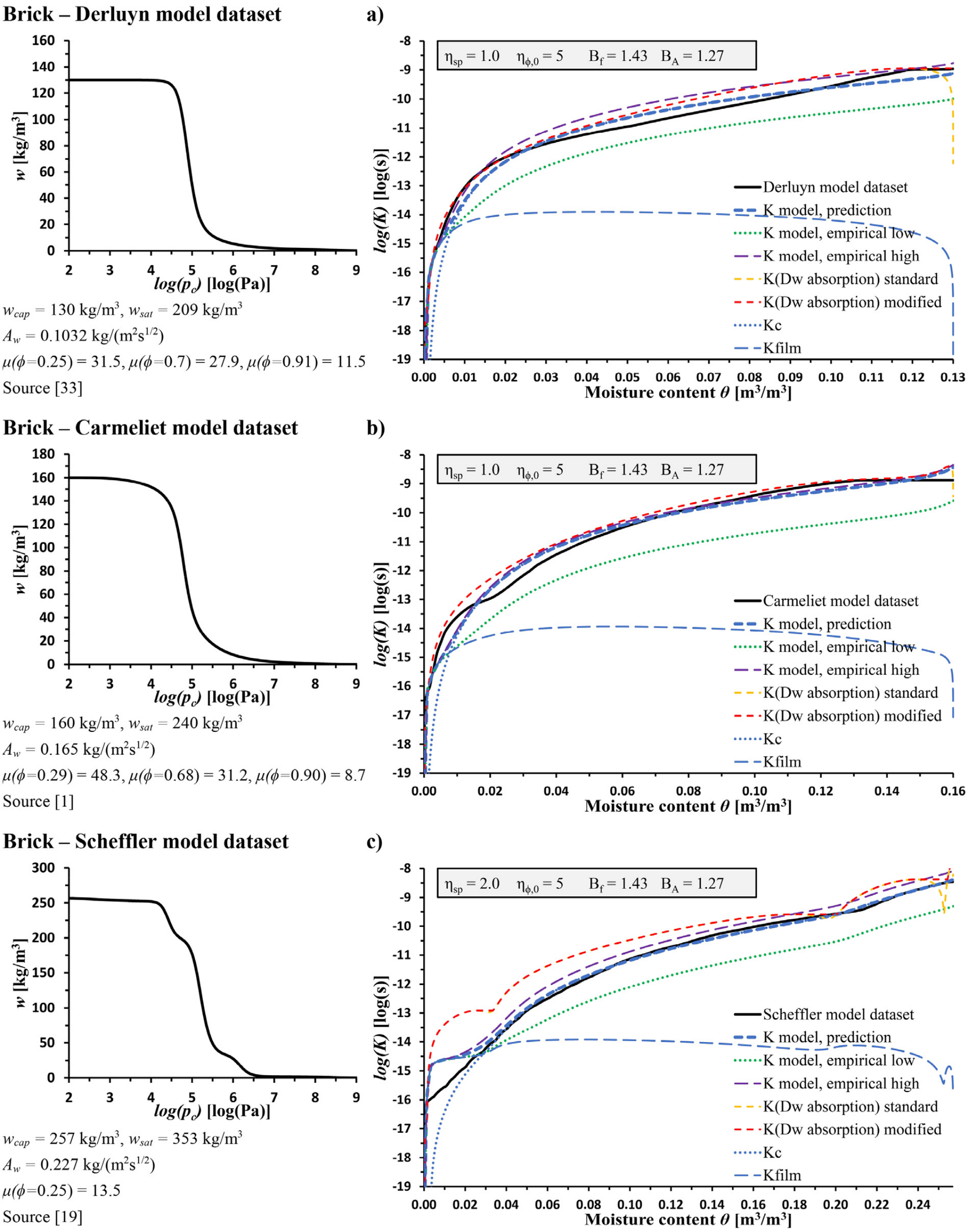

Fig. 3. Left: retention curves, reproduced with Eq. (42), and basic properties used as input in the hydraulic model. Right: hydraulic conductivity; different modeling approaches compared to datasets.

tions. Overall *K model, prediction* and *K(Dw absorption) modified* respectively have 8 and 7 reasonable predictions ($f_d \leq 2$), while both have 6 for reasonably good ($f_d \leq 1.5$).

Excluding the three materials at which *K(Dw absorption) modified* is at a disadvantage, each predict 4 materials better than the other over the whole moisture content interval. Furthermore, *K model, prediction* has 5 reasonably predictions while *K(Dw absorption) modified* has 6. For $\theta_{rel} \leq 0.5$, the numbers are 3 and 4 respectively while for $0.5 < \theta_{rel}$ 5 for both. Interestingly, there is only one reasonably good predictions for $\theta_{rel} \leq 0.5$, with *K model, prediction* only reaching the threshold value for Limestone, whereas for $0.5 < \theta_{rel}$ *K model, prediction* has 4 and *K(Dw absorption) modified* has 2. Summarized, *K(Dw absorption) modified* shows higher precision for a few more materials in $K_{c,cap}$ prediction, although the

Sand-lime brick – Carmeliet model dataset

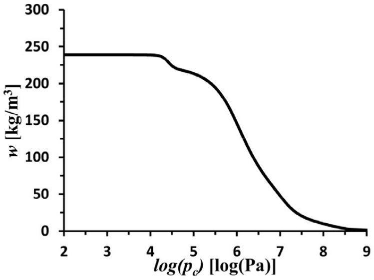

w_{cap} = 239 kg/m³, w_{sat} = 319 kg/m³

A_w = 0.043 kg/(m²s$^{1/2}$)

$\mu(\phi=0.3)$ = 23, $\mu(\phi=0.7)$ = 12, $\mu(\phi=0.92)$ = 3

Source [1]

d)

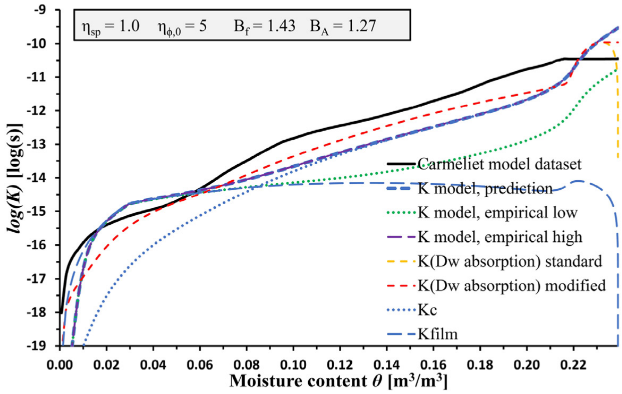

Sand-lime brick – Scheffler model dataset

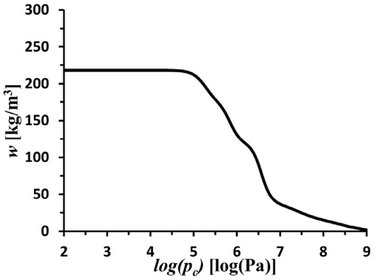

w_{cap} = 218 kg/m³, w_{sat} = 345 kg/m³

A_w = 0.052 kg/(m²s$^{1/2}$)

$\mu(\phi=0.25)$ = 40

Source [19]

e)

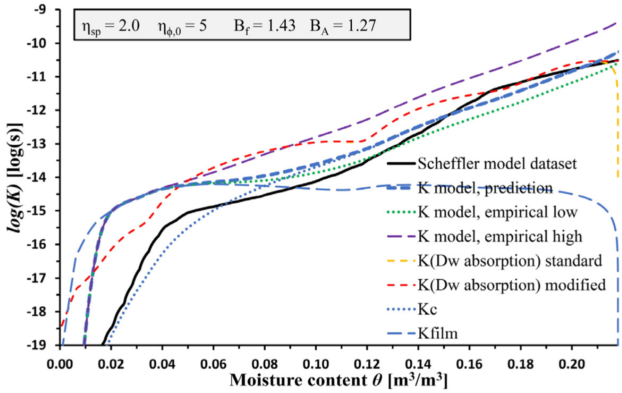

Calcium silicate – Scheffler model dataset

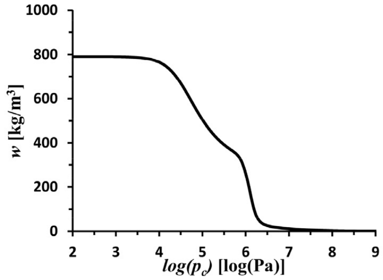

w_{cap} = 790 kg/m³, w_{sat} = 900 kg/m³

A_w = 1.11 kg/(m²s$^{1/2}$)

$\mu(\phi=0.25)$ = 4

Source [19]

f)

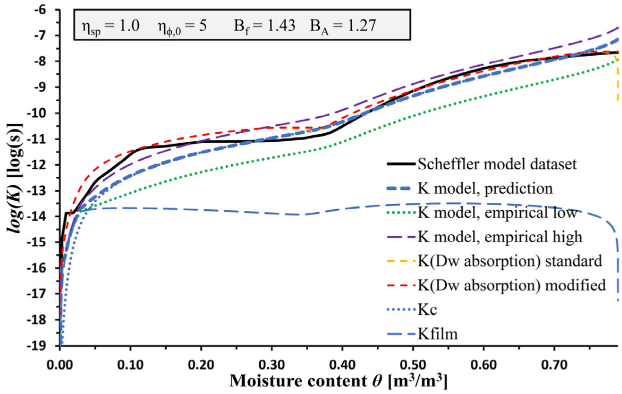

Fig. 3. Continued

Calcium Silicate – Häupl model dataset g)

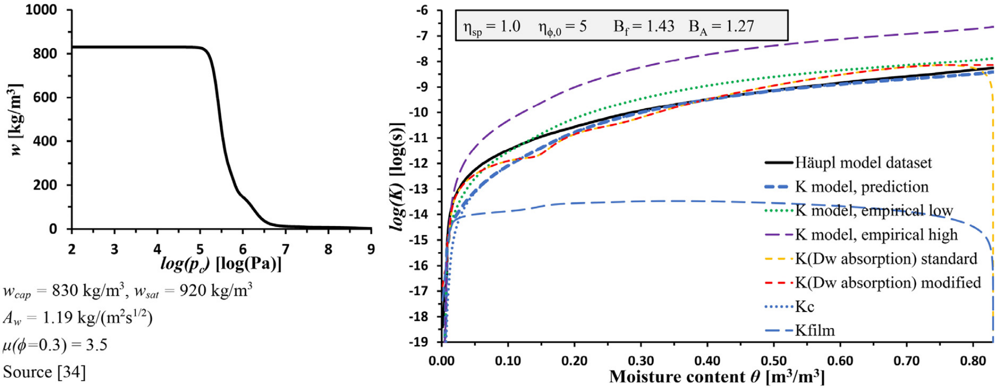

w_{cap} = 830 kg/m^3, w_{sat} = 920 kg/m^3

A_w = 1.19 kg/(m^{2}s$^{1/2}$)

$\mu(\phi$=0.3) = 3.5

Source [34]

Limestone– Cabrera model dataset h)

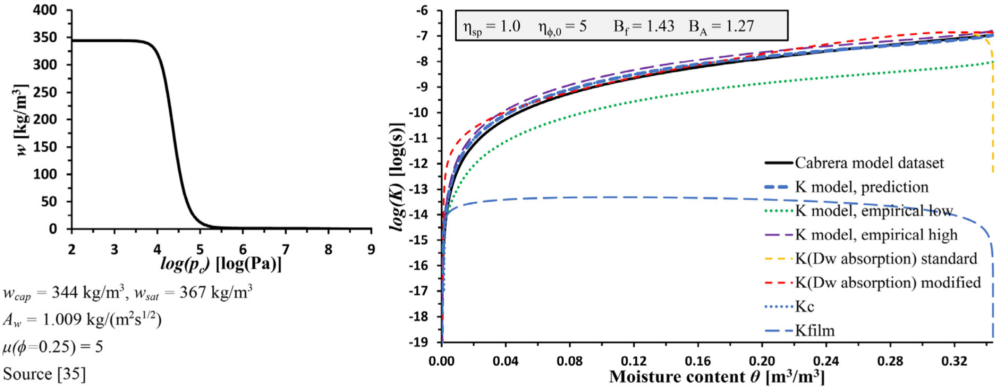

w_{cap} = 344 kg/m^3, w_{sat} = 367 kg/m^3

A_w = 1.009 kg/(m^{2}s$^{1/2}$)

$\mu(\phi$=0.25) = 5

Source [35]

Aerated concrete – Scheffler model dataset i)

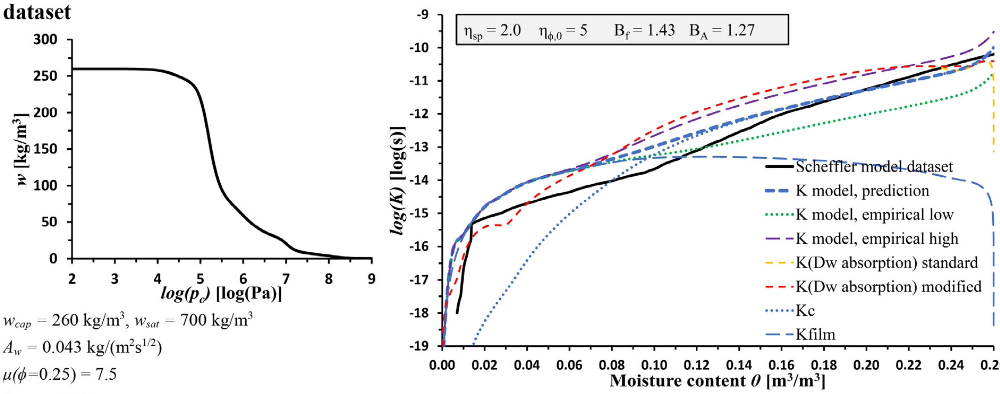

w_{cap} = 260 kg/m^3, w_{sat} = 700 kg/m^3

A_w = 0.043 kg/(m^{2}s$^{1/2}$)

$\mu(\phi$=0.25) = 7.5

Source [19]

Fig. 3. Continued

difference is not great. On the other hand, *K model, prediction* provides higher precision for a few more materials in the upper moisture range. Even with these two distinctions in performance the two different approaches have similar overall performance, neither distinguish itself as especially better or worse compared to the other.

4.3. The η_{sp} parameter

The way the η_{sp} parameter influence the mechanistic serial-parallel pore model of [7] can be roughly be summarized as follows; With $\eta_{sp} \rightarrow 0$, hypothetically, the model becomes purely parallel, i.e. the capillaries involved in capillary transport are filled

Cement mortar – Derluyn model dataset

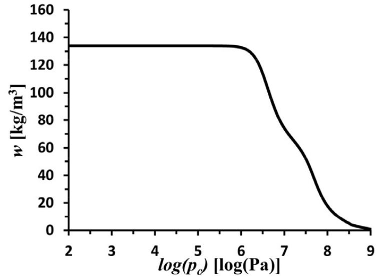

w_{cap} = 134 kg/m³, w_{sat} = 158 kg/m³

A_w = 0.0154 kg/(m²s$^{1/2}$)

$\mu(\phi=0.25)$ = 379, $\mu(\phi=0.7)$ = 279, $\mu(\phi=0.91)$ = 45.3

Source [33]

j)

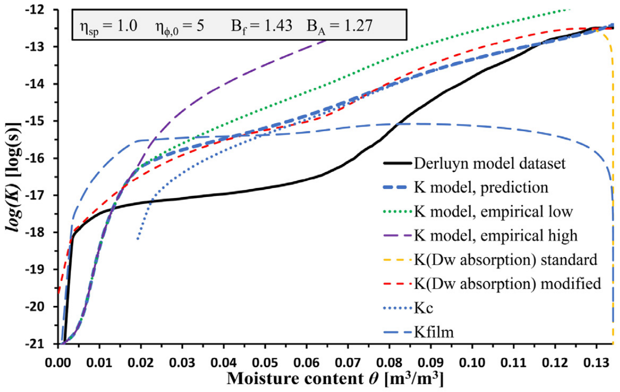

Concrete – Leech model dataset

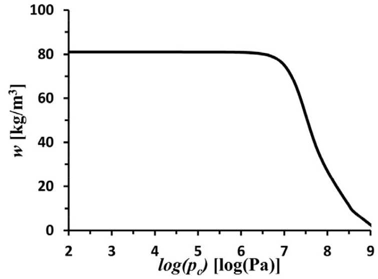

w_{cap} = 81 kg/m³, w_{sat} = 127 kg/m³

A_w = 0.00357 kg/(m²s$^{1/2}$)

$\mu(\phi=0.25)$ = ? (only capillary dataset)

Source [36, 37]

k)

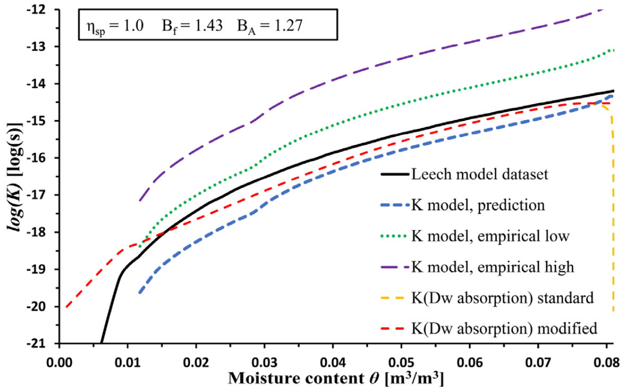

Fig. 3. Continued

Table 5
Quantified factors of deviation f_d, Eq. (48). Lowest deviation values in bold. Parentheses indicate where the *K(Dw absorption) modified* is at a disadvantage, i.e. model datasets adapted for drying.

	K model, prediction				K(D_w absorption) modified			
θ_{rel} integral interval	$0 < \theta_{rel} \leq 1$	$0 < \theta_{rel} \leq 0.5$	$0.5 < \theta_{rel} \leq 1$	$\theta_{rel} = 1$	$0 < \theta_{rel} \leq 1$	$0 < \theta_{rel} \leq 0.5$	$0.5 < \theta_{rel} \leq 1$	$\theta_{rel} = 1$
Brick Derluyn	**1.64**	1.75	**1.53**	1.44	1.93	**1.70**	2.18	**1.04**
Brick Carmeliet	**1.60**	**1.96**	**1.30**	**2.72**	1.77	2.32	1.35	3.03
Brick Scheffler	**(1.45)**	**(1.73)**	**(1.21)**	1.18	(5.20)	(12.63)	(2.14)	4.24
Sand-lime brick Carmeliet	4.51[a]	3.63[a]	5.60	8.17	**2.85**[a]	**2.71**[a]	**3.00**	**3.06**
Sand-lime brick Scheffler	**(5.34)**	**(17.60)**	**(1.62)**	1.81	(7.23)	(22.69)	(2.30)	**1.06**
Calcium silicate Scheffler	1.98	2.71	1.45	3.15	**1.62**	**2.12**	**1.23**	**1.08**
Calcium silicate Häupl	**1.57**	2.11	**1.17**	1.44	1.88	**1.96**	1.80	**1.29**
Limestone	**1.29**	**1.50**	**1.11**	**1.01**	1.76	1.75	1.77	1.28
Aerated concrete	**(2.60)**	**(4.68)**	**(1.45)**	**1.57**	(4.15)	(4.77)	(3.60)	1.60
Cement mortar	11.25[a]	27.99[a]	**4.52**	1.19	**8.69**[a]	**13.61**[a]	5.55	1.05
Concrete	3.11	4.80	2.40	**1.38**	**1.68**	**1.94**	**1.54**	2.11
# predictions $f_d \leq 2$	5 (6)	3 (4)	5 **(8)**	**8**	**6**	**4**	5	7
# predictions $f_d \leq 1.75$	**4 (5)**	2 **(3)**	**5 (8)**	7	2	2	3	7
# predictions $f_d \leq 1.5$	**1 (2)**	**1**	**4 (6)**	6	0	0	2	6
# predictions $f_d \leq 1.25$	0	0	**2 (3)**	3	0	0	1	**4**

[a] are significantly influenced by that the model dataset includes K_v contribution while prediction approach does not.

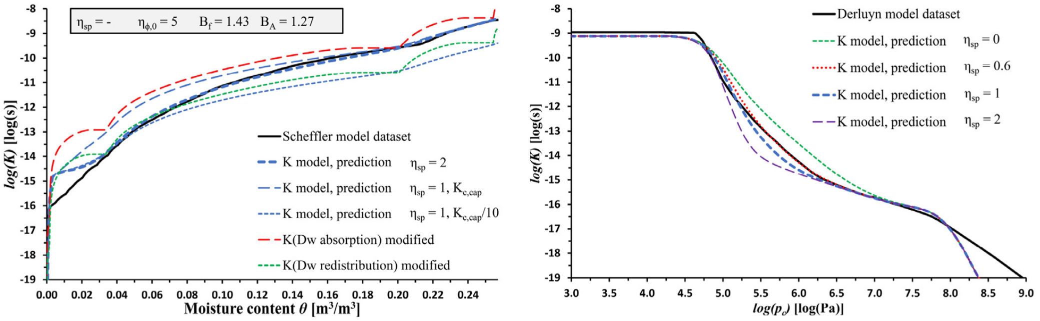

Fig. 4. η_{sp} parameter. Left: For brick (Scheffler), demonstration on how the η_{sp} parameter relates to absorption and redistribution. Right: For brick (Derluyn), demonstration of impact of variation in η_{sp}.

with continuous liquid towards some moisture front similar to an ideal imbibition model. With $\eta_{sp} = 1$ the model has a serial-parallel relation as function of *w/wsat*, Eq. (24), without diminishment or reinforcement though the exponent. Fig. 4 demonstrates the impact of the η_{sp} parameter. For datasets which unite absorption and drying data in one graph the result for brick (Scheffler) (Fig. 4 left) shows a value of $\eta_{sp} = 2$ is in good agreement; whereas, lime-sand brick (Scheffler) and aerated concrete are even better described by $\eta_{sp} = 3$ (not shown). Hence the results of Fig. 3 and Table 5 could be improved for these latter two materials updated with $\eta_{sp} = 3$. Consequently, based on the limited number of datasets which incorporate drying experiments we find $2 \leq \eta_{\text{sp}} \leq 3$ to best represent these. For the pure absorption datasets Fig. 3 has shown relatively good agreement with $\eta_{sp} = 1$. However, the choice of $\eta_{sp} = 1$ was a generalized one, and the best fit could deviate from this. Although the best fit on each dataset has not been investigated, Fig. 4 (right) demonstrates the impact of different η_{sp} on the brick (Derluyn), where a value of η_{sp} as low as 0.6 might give the better fit at lower moisture contents, although this cause poorer fit at intermediate moisture contents. Both the calcium silicate materials also indicate improvement with $\eta_{sp} = 0.6$ (not shown), or even perhaps slightly lower to $\eta_{sp} = 0.5$ for calcium silicate (Häupl). Except for concrete, which seems to best be modeled with $\eta_{sp} = 0$, no clear support is found for η_{sp}-values lower than 0.5 for the other datasets looked at. With only small improvement, limestone indicates values of η_{sp} up to 1.3 might be used (not shown). If excluding concrete, in lack of similar, confirming observations, then, based on the limited number of absorption datasets we find $0.5 \leq \eta_{\text{sp}} \leq 1.3$ to best represent these.

4.4. The $\eta_{\phi,0}$ parameter

As mentioned in Section 2.8 the $\eta_{\phi,0}$ parameter governs how much of the hygroscopic correction model overrides the film and capillary models in the hygroscopic region. Fig. 5 demonstrate how the $\eta_{\phi,0}$ parameter can be used to override the two other models for materials which has much of the retained moisture content within the hygroscopic region. For such materials there might be a conflict between the results of the film/capillary model and vapor resistance measurements which the hygroscopic correction model is built on. This conflicting behavior resembles the issue the η_{sp} parameter is designed to resolve. After all, the vapor resistance data is not related to absorption. Rather, it stems from steady state measurements. Still, η_{sp} and $\eta_{\phi,0}$ impact the overall model from different angles. For sand-lime brick (Carmeliet) changing $\eta_{\phi,0}$ to 200 would improve the fit to vapor resistance measurements (not shown). For the rest of the datasets too few vapor resistance measurements are known to give an assessment, or the materials contain too little moisture in the hygroscopic region for the issue to be relevant. We deem it outside the scope of this paper to investigate the correctness of combining data from “non-absorption” vapor resistance measurements with a capillary absorption prediction model.

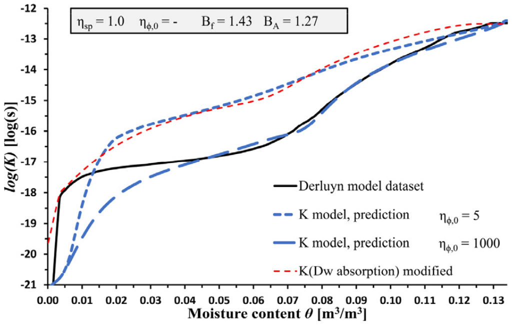

Fig. 5. Impact of the $\eta_{\phi,0}$ parameter on cement mortar. The deviation between the model dataset and the prediction with $\eta_{\phi,0} = 1000$ at low moisture contents stems from dataset including vapor conductivity (K_v).

5. Discussion

The proposed model has been demonstrated to be on par with the *K(D_W)* approach. Nevertheless, since the model is sensitive to the capillary pressure of the largest pores it is important to combine the model with an assessment of whether the largest pore sizes can actually be believed to constitute continuous pores though the material. That is, whether the largest pores can be represented with the bundle of tubes model approach or whether they behave more isolated. The *K(D_W)* approach is less sensitive on this aspect and therefore achieves better prediction of $K_{c,cap}$ for a few materials compared to the proposed model. However, at the same time the proposed model is seen to give better prediction in the higher moisture range as a whole. Consequently, there might be possible practical adjustments to the model application which can improve prediction performance, either 1) by a truncation at slightly lower moisture contents for materials with rather gentle retention curve slopes close to capillary saturation, or 2) by adjusting retention curves to become a bit more sharply rounded off at capillary saturation. Such adjustments have not been investigated in connection with the current study. It is also implicit that use of the model requires input of rather accurate retention curves. That is, retention curves for materials which do not have very uniform pore size distribution should be described by multimodal curves which capture some resolution in the pore size distribution. Still, uncertainty persists regarding these issues since the current study has not investigated accuracy issues with retention curve representation and its effect on the model prediction performance.

Whereas traditional bundle of tubes models are criticized for having a non-physics based tortuosity correction [6, 49], the current model derivation has included the tortuosity leading up to Eq. (11). Nevertheless, for the current capillary model it turns out that the tortuosity is baked into the capillary absorption coefficient and is therefore not present in the final $K_{c,cap}$ prediction, Eq. (22). Another part of the criticism of bundle of tubes models is that they fail to increase the tortuosity of flow paths when the permeability decrease as water-filled pathways become sparse at low moisture contents [6]. The mechanistic model f_l (for its principle see [7]) does however address this issue even though it does not interfere with the tortuosity directly. If assessing Eq. (11) in connection with Eq. (23) one finds that K_c is proportional to f_l/τ^2 which could partly be interpreted in terms of providing an effective tortuosity which increase with lower moisture contents, since f_l decrease with lower moisture contents.

5.1. Other correction factors

With regard to calculating capillary absorption coefficients, Nikitsin and Backiel-Brzozowska [50] argues for a need to include additional correction factors. These include K_{NW} for taking into account *"narrowing and widening of capillaries along their length"*, K_T as a temperature correction to the ratio of σ_W/μ_W, based on a description of water vapor preceding the capillary moisture front where the vapor will adsorb on the pore walls, thereby releasing heat (this in capillary absorption experiments of initially dry materials), and K_μ for correcting the viscosity for its dependence on pore radius, mainly for $r < 1$ μm [50].

Although K_{NW} has not explicitly been addressed in the present work we will argue both B_f and B_c implicitly could include such an effect. However, since the current model approach involves choosing a value for B_f, this effect is all placed in B_c when identified from comparing Eq. (21) to the experimentally determined A_W-value. Still, when estimating the pore radius with Eq. (7), the resulting r will be underestimated if B_c is significant influenced (diminished) from narrowing and widening of pores.

K_T can be calculated as $K_T = (\sigma_m\mu_0)/(\sigma_0\mu_m)$, where subscripts *0* and *m* refer to ambient and microscale temperature respectively. This factor basically accounts for a reported microscale temperature increase which lowers the surface tension and viscosity. Although, Nikitsin and Backiel-Brzozowska [50] assume a 10 K increase for their case (with reported $K_T = 1.24$) they provide too little information to confidently generalize inclusion of such a factor. For instance, in order for a significant temperature increase to take place we would assume the following prerequisites are needed: 1) completely initially dry material, thereby creating high adhesion forces; hence, preconditioning to laboratory conditions of the material before A_W measurements cannot have taken place. 2) a large pore wall circumference to cross section area ratio is needed to give high heat release per water volume heated. 3) relatively fast capillary flow rate and low bulk material thermal inertia. We deem it outside the scope of the present work to address whether or to which degree such a phenomenon exists to give an impact, hence K_T is not included.

K_μ should ideally be included, since the factor is important for calculation of A_W, which when compared to measured A_W is used to approximate B_c and pore radius for the film model. In order to keep the model conveniently simple, and its description not too long, such a correction has not been included in the present work.

6. Summary and conclusions

Modeling capillary conductivity with a bundle of tubes model has been revisited. By incorporating the experimentally determined capillary absorption coefficient a novel prediction expression for the capillary conductivity at capillary saturation has been derived. By introducing a prediction of the conductivity at capillary saturation, bundle of tubes models become more directly implementable and avoid part of the criticism such models previously have received at over-capillary saturation. The feasibility of scaling bundle of tube models to conductivity at capillary saturation has been demonstrated.

A hydraulic conductivity model for the full moisture range has been established based on the Scheffler and Plagge model [7], supplied with a film model of Lebeau and Konrad [11]. With the new model no longer requiring iterative post-processing of a parameter for scaling to conductivity at over-capillary saturation, a simplification is achieved, easing applicability of the model. The impact of an adjustment parameter in the mechanistic scaling function, as part of the Scheffler and Plagge model, has also been demonstrated more in detail, which casts light on the flexibility of the model. Value interval recommendations for this adjustment parameter are provided. An additional adjustment parameter to adjust between the film/capillary models and a hygroscopic correction model (latter also being part of the Sceffler and Plagge model) has also been introduced and demonstrated to give some additional flexibility, although no conclusion has been made regarding its determination. As a necessary step towards the prediction expression for conductivity at capillary saturation a new analytical expression for the capillary absorption coefficient has also been derived. This derivation may provide contrasting nuances to previously reported derivations of this coefficient.

The new hydraulic conductivity model, including the new prediction expression for the conductivity at capillary saturation, has been demonstrated on 11 porous material datasets with reasonable success.

The resulting model should be easier to implement than most comparable, alternative bundle of tubes models by not requiring testing of capillary conductivity, since it utilize the easier determinable capillary absorption coefficient. The new prediction is however sensitive to the retention curve close to capillary saturation which for some cases could result in inaccurate prediction.

Also, although not new information, the article reaffirms that hydraulic conductivity is dependent on the situational boundary conditions, i.e., whether the material is subjected to absorption, redistribution or drying of moisture.

There is still much unanswered regarding how to more accurately and practically incorporate models for the hygroscopic region and at modest moisture content, i.e., film and hygroscopic correction models, which highlight need for further research. Also of interest, is how to address the situational difference between absorption, redistribution and drying of moisture when calculating the hydraulic conductivity for the full moisture range. The scientific novelty of the current study only addresses absorption.

Credit author statement

Jon Ivar Knarud: Conceptualization, Methodology, Validation, Formal analysis, Investigation, Writing - Original Draft, Visualization. **Tore Kvande:** Writing - Review & Editing, Supervision. **Stig Geving:** Writing - Review & Editing, Supervision.

Declaration of Competing Interest

Acknowledgment

The authors gratefully acknowledge the financial support by The Research Council of Norway and several partners through the centre for Research-based Innovation “Klima 2050″ (Grant No 237859) (www.klima2050.no).

Appendix A. Table A.1: Input applied to Eq. (42)

Table A.1
Coefficients for retention curves.

Material	w_{lim}	$n_{w,0}$	$l_{w,1}$	$l_{w,2}$	$l_{w,3}$	$l_{w,4}$	$c_{w,1}$	$c_{w,2}$	$c_{w,3}$	$c_{w,4}$	$n_{w,1}$	$n_{w,2}$	$n_{w,3}$	$n_{w,4}$
Brick Derluyn	1.0	0.4	0.846	0.154	0	0	1.40E-05	9.02E-06	–	–	4	1.69	–	–
Brick Carmeliet	0.7	1	0.054	0.455	0.491	0	3.84E-04	2.76E-05	1.72E-05	–	1.6	1.691	4.457	–
Brick Scheffler	1.7	0.65	0.02	0.21	0.65	0.12	3.7E-03	4.00E-05	6.72E-06	7.44E-07	1.6	5	4	4
Sand-lime brick Carmeliet	9.0	0.8	0.08	0.09	0.74	0.09	4.02E-05	9.99E-06	1.34E-06	9.49E-08	6	1.7	1.74	3.2
Sand-lime brick Scheffler	16	0.35	0.25	0.25	0.4	0.1	5.91E-06	1.51E-06	2.92E-07	4.83E-08	3	4	4.2	2.3
Calcium silicate Scheffler	3	2.5	0.63	0.09	0.27	0.01	3.08E-05	1.13E-06	7.83E-07	5.25E-07	1.71	7	6.6	4
Calcium silicate Häupl	8.4	0.2	0.72	0.1	0.177	0.003	3.79E-06	1.64E-06	6.13E-07	3.51E-08	5	8	3.5	8
Limestone	1	1	0.997	0.003	0	0	4.94E-05	5.00E-05	–	–	3.14	3.32	–	–
Aerated concrete	8	1.2	0.1	0.6	0.24	0.06	4.35E-05	6.85E-06	1.42E-06	9.90E-08	2	4	2	5
Cement mortar	16	0.55	0.35	0.07	0.58	0	2.25E-08	5.49E-08	2.81E-07	–	3.2	2.8	2.8	–
Concrete	25	0.45	0.2	0.8	0	0	3.32E-08	5.18E-08	–	–	3.4	2	–	–

Appendix B. Log(K)-log(pc) graphs of materials (Fig. 3 equivalent)

a) Brick (Derluyn)

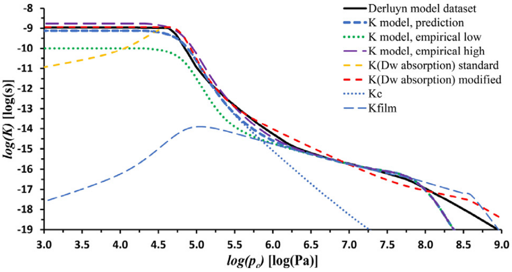

b) Brick (Carmeliet)

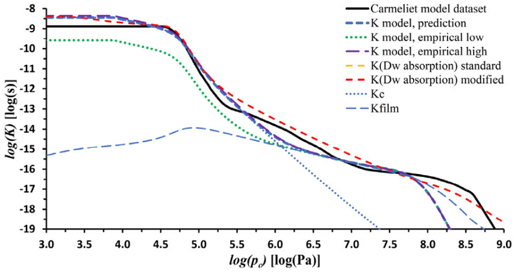

c) Brick (Scheffler)

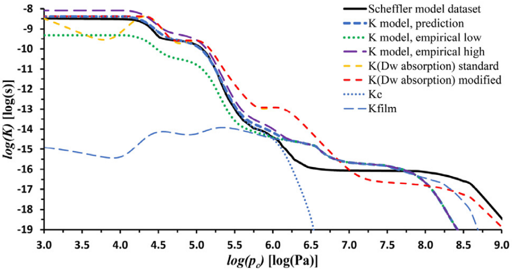

d) Sand-lime brick (Carmeliet)

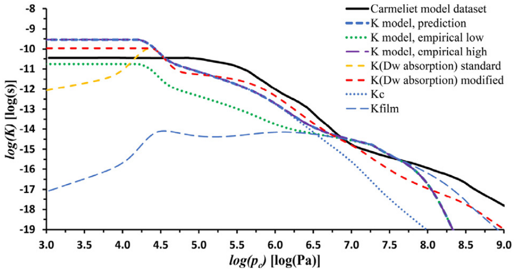

e) Sand-lime brick (Scheffler)

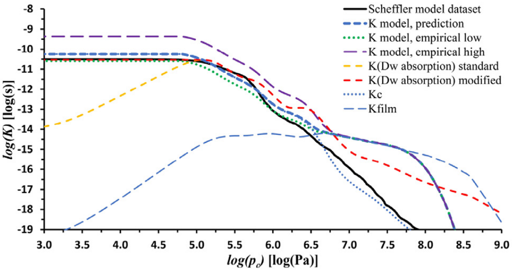

f) Calcium silicate (Scheffler)

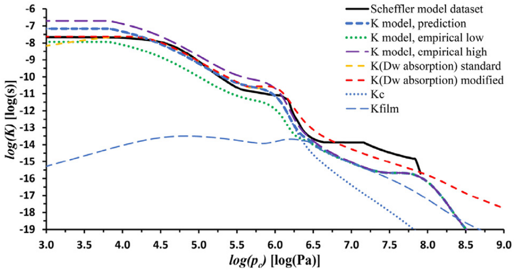

g) Calcium Silicate (Häupl)

h) Limestone

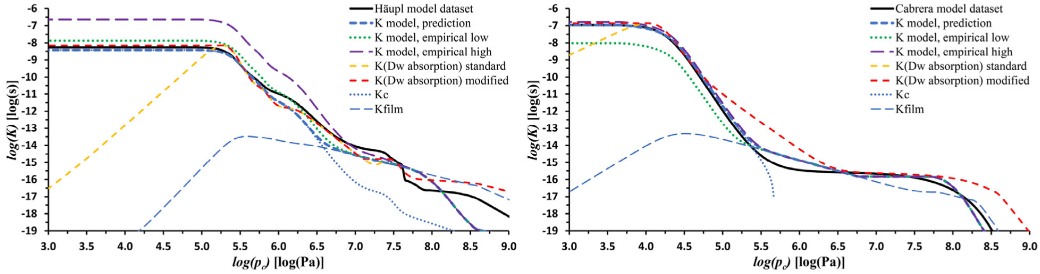

i) Aerated concrete

j) Cement mortar

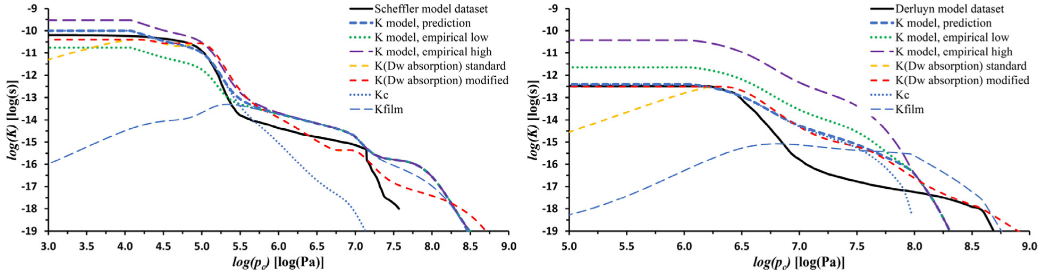

k) Concrete

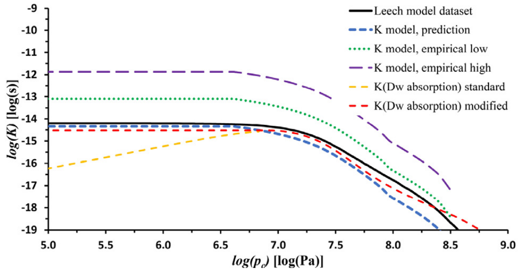

References

[1] J. Carmeliet, S. Roels, Determination of the isothermal moisture transport properties of porous building materials, J. Build. Phys. 24 (3) (2001) 183–210.

[2] F. Descamps, Continuum and Discrete Modelling of Isothermal Water and Air Transfer in Porous Media, Katholieke Universiteit Leuven, Leuven, Belgium, 1997.

[3] N.T. Burdine, in: Relative Permeability Calculations from Pore Size Distribution Data, 198, Petroleum Transactions, AIME, 1953, pp. 71–78.

[4] Y. Mualem, A new model for predicting the hydraulic conductivity of unsaturated porous media, Water Resour. Res. 12 (3) (1976) 513–522.

[5] M.T. Van Genuchten, A closed-form equation for predicting the hydraulic conductivity of unsaturated soils, Soil Sci. Soc. Am. J. 44 (5) (1980) 892–898.

[6] A.G. Hunt, R.P. Ewing, R. Horton, What's Wrong with Soil Physics? Soil Sci. Soc. Am. J. 77 (6) (2013) 1877–1887.

[7] G.A. Scheffler, R. Plagge, A whole range hygric material model: modelling liquid and vapour transport properties in porous media, Int. J. Heat Mass Transf. 53 (1) (2010) 286–296.

[8] W. Durner, Hydraulic conductivity estimation for soils with heterogeneous pore structure, Water Resour. Res. 30 (2) (1994) 211–223.

[9] W. Durner, Predicting the unsaturated hydraulic conductivity using multi–porosity water retention curves, Indirect Methods for Estimating the Hydraulic Properties of Unsaturated Soils (1992) 185–202.

[10] J. Grunewald, P. Häupl, M. Bomberg, Towards an engineering model of material characteristics for input to ham transport simulations - Part 1: an approach, J. Therm. Envelope Build. Sci. 26 (4) (2003) 343–366.

[11] M. Lebeau, J.-M. Konrad, A new capillary and thin film flow model for predicting the hydraulic conductivity of unsaturated porous media, Water Resour. Res. 46 (12) (2010).

[12] A. Peters, Simple consistent models for water retention and hydraulic conductivity in the complete moisture range, Water Resour. Res. 49 (10) (2013) 6765–6780.

[13] J. Cai, E. Perfect, C.-L. Cheng, X. Hu, Generalized modeling of spontaneous imbibition based on hagen–poiseuille flow in tortuous capillaries with variably shaped apertures, Langmuir 30 (18) (2014) 5142–5151.

[14] B. Ghanbarian, A.G. Hunt, R.P. Ewing, M. Sahimi, Tortuosity in porous media: a critical review, Soil Sci. Soc. Am. J. 77 (5) (2013) 1461–1477.

[15] M.S. Paterson, The equivalent channel model for permeability and resistivity in fluid-saturated rock—a re-appraisal, Mech. Mater. 2 (4) (1983) 345–352.

[16] A.C.M. Franken, J.A.M. Nolten, M.H.V. Mulder, D. Bargeman, C.A. Smolders, Wetting criteria for the applicability of membrane distillation, J. Memb. Sci. 33 (3) (1987) 315–328.

[17] H. Wong, S. Morris, C.J. Radke, Three-dimensional menisci in polygonal capillaries, J. Colloid Interface Sci. 148 (2) (1992) 317–336.

[18] G. Mason, N.R. Morrow, Meniscus curvatures in capillaries of uniform cross–section, J. Chem. Soc. Faraday Trans. 80 (9) (1984) 2375–2393 1: Physical Chemistry in Condensed Phases.

[19] G. Scheffler, Validation of Hygrothermal Material Modelling Under Consideration of the Hysteresis of Moisture Storage, Dresden University of Technology, Dresden, Germany, 2008.

[20] E.O. Macagno, Historico-critical review of dimensional analysis, J. Franklin Inst. 292 (6) (1971) 391–402.

[21] V. Beltran, A. Escardino, C. Feliu, M.D. Rodrigo, Liquid suction by porous ceramic materials, Brit. Ceramic Trans. J. 87 (2) (1988) 64–69.

[22] L.L. Handy, Determination of effective capillary pressures for porous media from imbibition data, Trans. AIME 219 (01) (1960) 75–80.

[23] I. Rodionova, E. Shkol'nikov, V. Volkov, The effect of fluid properties on the hydrodynamic permeability coefficient, Colloid J. (Kolloidnyi Zhurnal) 67 (4) (2005) 469–477.

[24] D. Benavente, P. Lock, M. Ángeles García Del Cura, S. Ordóñez, Predicting the capillary imbibition of porous rocks from microstructure, Transp. Porous Media 49 (1) (2002) 59–76.

[25] I. Ioannou, C. Hall, M.A. Wilson, W.D. Hoff, M.A. Carter, Direct measurement of the wetting front capillary pressure in a clay brick ceramic, J. Phys. D Appl. Phys. 36 (24) (2003) 3176–3182.

[26] M. Dejam, H. Hassanzadeh, Z. Chen, Reinfiltration through liquid bridges formed between two matrix blocks in fractured rocks, J. Hydrol. (Amst.) 519 (2014) 3520–3530.

[27] R. Sarfati, D.K. Schwartz, Temporally Anticorrelated Subdiffusion in water Nanofilms on silica suggests near-surface viscoelasticity, ACS Nano 14 (3) (2020) 3041–3047.

[28] EN ISO 12572, Hygrothermal Performance of Building Materials and Products - Determination of Water Vapour Transmission Properties, European Committee for Standardization (CEN), Brussels, Belgium, 2001.

[29] C.-E. Hagentoft, HAMSTAD, Final report: Methodology of HAM-modeling, Report R-02, Chalmers University of Technology, Gothenburg, Sweden, 2002.

[30] N. Lu, Generalized soil water retention equation for adsorption and capillarity, J. Geotech. Geoenviron. Eng. 142 (10) (2016) 04016051.

[31] J. Carmeliet, S. Roels, Determination of the moisture capacity of porous building materials, J. Therm. Envelope Build. Sci. 25 (3) (2002) 209–237.

[32] A. Revil, N. Lu, Unified water isotherms for clayey porous materials, Water Resour. Res. 49 (9) (2013) 5685–5699.

[33] H. Derluyn, P. Moonen, J. Carmeliet, Moisture transfer across the interface between brick and mortar joint, in: Proceedings of the 8th symposium on building physics in the nordic countries, Technical University of Denmark, Copenhagen, Denmark, 2008, pp. 865–872.

[34] P. Häupl, H. Fechner, H. Petzold, Interior retrofit of masonry wall to reduce energy and eliminate moisture damage: comparison of modeling and field performance, Thermal Performance of Exterior Envelopes of Whole Buildings IX: International Conference, ASHRAE, 2004.

[35] V. Cabrera, R. López-Vizcaíno, Á. Yustres, M.Á. Ruiz, E. Torrero, V. Navarro, A functional structure for state functions of moisture transfer in heritage building elements, J. Build. Eng. 29 (2020) 101201.

[36] C.A. Leech, Water Movement in Unsaturated Concrete, The University of Queensland, Brisbane, Qld, Australia, 2003.

[37] C. Leech, D. Lockington, R.D. Hooton, G. Galloway, G. Cowin, P. Dux, Validation of Mualem's conductivity model and prediction of saturated permeability from Sorptivity, ACI Mater. J. 105 (1) (2008) 44–51.

[38] Y. Bo-Ming, L. Jian-Hua, A geometry model for tortuosity of flow path in porous media, Chin. Phys. Lett. 21 (8) (2004) 1569–1571.

[39] M. Raimondo, M. Dondi, D. Gardini, G. Guarini, F. Mazzanti, Predicting the initial rate of water absorption in clay bricks, Constr. Build. Mater. 23 (7) (2009) 2623–2630.

[40] A. Merioua, A. Bezzar, F. Ghomari, Non-destructive electrical methods for measuring the physical characteristics of porous materials, J. Nondestr. Eval. 34 (2) (2015) 1–12.

[41] H. Garbalińska, M. Stasiak, M. Bochenek, G. Musielak, Assessment of a new method for determining the relationship between effective diffusivity and moisture concentration – exemplified by autoclaved aerated concrete of four density classes, Int. J. Heat Mass Transf. 124 (2018) 288–297.

[42] G.M. Laudone, C.M. Gribble, K.L. Jones, H.J. Collier, G.P. Matthews, Validated a priori calculation of tortuosity in porous materials including sandstone and limestone, Chem. Eng. Sci. 131 (2015) 109–117.

[43] J. Carmeliet, H. Hens, S. Roels, O. Adan, H. Brocken, R. Cerny, Z. Pavlik, C. Hall, K. Kumaran, L. Pel, Determination of the liquid water diffusivity from transient moisture transfer experiments, J. Therm. Envelope Build. Sci. 27 (4) (2004) 277–305.

[44] C.R. Pedersen, Combined Heat and Moisture Transfer in Building Constructions, Technical University of Denmark, Lyngby, Denmark, 1990.

[45] H.M. Künzel, Simultaneous Heat and Moisture Transport in Building Components, Fraunhofer IRB-Verlag, Stuttgart, Germany, 1995.

[46] D. Lockington, J.Y. Parlange, P. Dux, Sorptivity and the estimation of water penetration into unsaturated concrete, Mater. Struct. 32 (5) (1999) 342.

[47] J. Carmeliet, H. Janssen, H. Derluyn, An improved moisture diffusivity model for porous building materials, in: Proceedings of 12th Symposium for Building Physics, Dresden, Germany, 2007.

[48] M. Krus, Moisture Transport and Storage Coefficients of Porous Mineral Building Materials: Theoretical Principles and New Test Methods, Fraunhofer IRB Verlag, Stuttgart, Germany, 1996.

[49] R.W. Vervoort, S.R. Cattle, Linking hydraulic conductivity and tortuosity parameters to pore space geometry and pore-size distribution, J. Hydrol. (Amst.) 272 (1) (2003) 36–49.

[50] V.I. Nikitsin, B. Backiel-Brzozowska, Determining hydraulic radii of construction wall materials in capillary moisture transfer, Int. J. Heat Mass Transf. 88 (2015) 558–564.

Article VI

Hygrothermal simulation of interior insulated brick wall – Perspectives on uncertainty and sensitivity

J. I. Knarud, T. Kvande, S. Geving

Buildings 13(7) (2023) 1701 https://doi.org/10.3390/buildings13071701

buildings

Article

Hygrothermal Simulation of Interior Insulated Brick Wall—Perspectives on Uncertainty and Sensitivity

Jon Ivar Knarud [1,*], Tore Kvande [1] and Stig Geving [2]

[1] Department of Civil and Environmental Engineering, Norwegian University of Science and Technology, NO-7491 Trondheim, Norway; tore.kvande@ntnu.no
[2] Department of Architecture, Materials and Structures, SINTEF Community, NO-7465 Trondheim, Norway; stig.geving@sintef.no
* Correspondence: jon.knarud@ntnu.no; Tel.: +47-96019248

Abstract: Energy retrofit of existing masonry buildings has become attractive to meet demands for reduction in energy consumption. Retrofit may, however, introduce moisture risk that needs to be assessed. Hygrothermal simulation analysis is often conducted in this respect. Nevertheless, hygrothermal simulation of interior insulated bare brick masonry exposed to driving rain can be challenging due to the many aspects involved that determine heat- and moisture-transport behavior, and which should be addressed by an applied model. The present study highlights uncertainty encountered when establishing a hygrothermal simulation model. Furthermore, different modeling choices or simplifications are studied to determine impact on results. As a check of realism, results of 2D simulations are compared to results of a previous laboratory experiment of masonry wall segments subjected to severe rain wetting and subsequent drying. Rain absorption is modeled conservatively, attempting simulation results to envelope experiment results. Conservative results were not achieved for a relative humidity sensor placed on the masonry interior without inclusion of a "leaky" mortar joint. Simultaneously, the conservative approach underestimated drying experienced by the relative humidity sensor in two of three experiment wall segments. Regarding beam-end moisture content, the modeling approach conservatively enveloped experiment results in 3D but not in 2D.

Keywords: modeling approach; masonry wall; wooden beam ends; moisture absorption; capillary conductivity; brick–mortar interface; smart vapor barrier

Citation: Knarud, J.I.; Kvande, T.; Geving, S. Hygrothermal Simulation of Interior Insulated Brick Wall—Perspectives on Uncertainty and Sensitivity. *Buildings* **2023**, *13*, 1701. https://doi.org/10.3390/buildings13071701

Academic Editor: Chenggao Li

Received: 6 June 2023
Revised: 19 June 2023
Accepted: 29 June 2023
Published: 3 July 2023

1. Introduction

1.1. Context

In cold temperate climates, interior insulation is an important retrofit measure for older existing masonry buildings with exterior facades worth preserving. Compared to modern buildings following today's building regulations, masonry buildings from the period 1850–1950 have very high U-values. Interior insulation retrofit can by lowering U-values lower a high heating demand [1]. In combination with improving building envelope air tightness, utilizing heat recovery from ventilation, and, potentially, other measures, substantial reduction in energy consumption can be achieved [2].

Nevertheless, applying interior insulation is not without challenges since the hygrothermal conditions in the exterior wall also change. Outbound heat flow through the wall decreases, thereby lowering outward drying capacity, and the added interior insulation solution will by adding vapor resistance reduce inward drying. Hence, an interior insulated wall becomes more sensitive to moisture sources. This has instigated research focus on both how to protect from moisture sources and how to improve drying conditions, e.g., [3–7]. Problematic moisture sources are driving rain [3,8], leaks in the building envelope [4], rising moisture from the ground [9], and indoor humid air condensing in the wall where it meets the saturation temperature [6]. Protection from driving rain and leaks involves measures such as improvement of rainproofing details, repairment of mortar joints, and provision of external render or hydrophobization. Protection from indoor humid air involves applying a vapor barrier or retarder, or ensuring low indoor relative humidity (RH). Sufficient protection may not easily be achieved for protected facades with strict limitations to external render and façade appearance. Ensuring a level of drying may, therefore, also be necessary. Strategies to improve drying include, for instance, applying capillary-active insulation materials, leaving a gap in insulation at beam ends, increasing temperature in beam ends, or utilizing smart vapor barriers (SVBs) or retarders (SVRs) that allow inward drying.

1.2. Hygrothermal Modeling

Designing case-specific solutions requires knowledge of the solution performance under realistic climate exposure or exposure to a design climate. Hygrothermal simulation has become a central tool for investigating such performance, e.g., [10,11]. Nevertheless, establishing realistic simulation models does not come without challenges. There are numerous complicating aspects related to establishing a model of masonry in hygrothermal simulation software. Overall, these aspects involve issues on how to model moisture sources, material properties, and the masonry to account for interaction between brick and mortar. Modeling moisture sources involves questions of rain distribution on façade, rain impact and runoff, rain absorption, and moisture infiltration [12–14]. Modeling material properties engages uncertainty regarding anisotropic behavior [15], moisture retention and hysteresis [16], moisture-dependent liquid conductivity [17–19], and vapor diffusivity, including uncertainty from lack of property measurements. Modeling masonry involves addressing complexity of material connectivity or interface resistance [20,21], material inhomogeneity, and changing properties along interface planes between brick and mortar [22,23], including moisture penetration and infiltration pathways [24], all dependent on mortar curing and curing moisture content, brick-and-mortar properties, and craftmanship during brick laying [25].

To further elaborate on the complexity regarding masonry performance and modeling of masonry, a selection of relevant research literature findings are summarized. Brocken [22] found moisture-transport properties of mortar joints to vary significantly. It was concluded that it was not possible to discern whether interfaces had perfect or imperfect hydraulic contact. Nevertheless, Brocken discovered that by shifting part of the retention curve for mortar to lower capillary pressures a simulation with perfect hydraulic contact would give reasonable results. Ramirez et al. [15] found resistance effects during absorption to be directionally dependent on materials, with most effect detected from lime mortar to brick, attributing it to discontinuity of the finer mortar pores. Whereas, in a drying experiment, Ramirez et al. [15] could not detect any resistance effects from the experiment results themselves. Zhou et al. [23] found no directional dependence for interface resistance. Instead, the resistance was found to be strongly dependent on local capillary pressure, and that relatively small changes in resistance value had large impact on moisture-distribution profiles. Vereecken and Roels [21] investigated simulation models in 2D with and without interface resistance and concluded that interface resistance had negligible impact when the wall was subjected to alternating wetting and drying from real weather, even though it had impact on a stand-alone imbibition process.

Hens [26] investigated vapor diffusion resistance in one-stone-thick masonry leaf specimens and found the resistance to be much lower than for the brick itself, attributing it to microcracks at the brick–mortar interface and imperfect joint filling. From the results presented by Hens, the vapor resistance decreased approximately to a third, although precise comparison is difficult due to a dependence on RH throughout the material. Similarly, Vereecken et al. [27] also reported lower vapor resistance of a masonry composite than for the individual brick and mortar constituents.

Gutland et al. [28] modeled fractures along brick–mortar interfaces as a material domain with hygrothermal properties derived from a fracture model. Their simulations demonstrated increased absorption from such modeling, and under cyclic conditions significantly increased drying compared to a base model without fracture(s).

Jensen et al. [6] ran numerical simulations, varying a range of parameters after an initial automated calibration of initial moisture content, rain-exposure coefficient, and shortwave-absorption coefficient. They found less RH fluctuation in the simulation than in the experiment and pointed to this seemingly being a common issue for simulation programs reported among other studies, and it could be related to not including hysteresis effects.

Johanson et al. [29], in a comparison between experiment and simulation, found the moisture progression to be considerably faster in the experiment than in the simulation.

Findings such as the aforementioned promote discussion on how to approach hygrothermal modeling of masonry to capture realistic performance.

1.3. Objective and Scope

The objective of the current study is to highlight uncertainty in hygrothermal simulation of an interior insulated brick wall, and to study impact of some modeling choices or simplifications, by addressing several influential aspects in simulation model setup and execution. Simulations are compared to a large-scale laboratory experiment of Knarud et al. [30] as a check of realism. However, it should be made clear that this is not a validation exercise. Nor is it a calibration study. Instead, it is a study highlighting modeling uncertainty and sensitivity to modeling choices, which is accompanied with some remarks on conservativeness in hygrothermal modeling.

The investigated object is an interior insulated masonry wall segment subjected to wetting and drying in a simple climatic sequence. It is insulated with mineral wool and fitted with a smart vapor barrier (SVB) to allow for inward drying. Detailed description is provided by Knarud et al. [30]. Nevertheless, central parts of the description are summarized in Section 2.

The exterior surface of the masonry consists of bare brick. It is therefore more complicated to investigate than masonry with external render. External render acts like a capillary retarder by creating a uniform layer that almost entirely removes the chance of moisture infiltration through brick-mortar interfaces. With a wall without external render, we however face many of issues of modeling masonry.

A common challenge with conducting hygrothermal simulations is incomplete available description of material properties when, for instance, it is not possible to completely map all the properties through laboratory testing and measurements. Complete mapping of properties is a very extensive and laborious process, that requires extensive effort, e.g., [16,31,32]. In addition, for in situ studies, identification of material properties is often limited to non-destructive measurements. Therefore, many simulation studies, e.g., [6,33,34], are conducted with some properties unknown, which are then substituted with properties from presumed similar materials. However, this inserts uncertainty.

With this in mind, the objective is approached by addressing three research questions:

1 When applying modelled hydraulic conductivity what are the consequences of uncertainty regarding the following material properties?
    - Capillary absorption coefficient;
    - Retention curve.

2 What impact do modeling choices or simplifications have on simulation results? Aspects that herein will be investigated are:
    - Reading position of results in simulation model compared to sensor location in physical experiment;
    - Isotropic vs. anisotropic wood properties for beam end;
    - Including increased permeability along the brick–mortar interface in mortar properties during rain events;

- Presence of a particularly "leaky" mortar joint, due to lower brick–mortar interface quality, and distance of such a joint to the sensor;
- 2D simplification compared to simulation in 3D.

3 What effect is seen from modeling a smart vapor barrier compared to no barrier or traditional barrier?

The main novelty follows research question 2 which is not a typical focus of similar studies. Although question 1, to some extent, has been investigated in other studies [19,35], these studies focus on much more limited geometric extents, not a masonry wall envelope. Regarding question 3, SVB has not previously been given much explicit focus, even though SVR has been included in simulation studies [36,37]. SVB contribution to inward drying has not been much reported on regarding masonry with beam ends.

Magnitude of observed sensitivity will, of course, depend on what is investigated, that is, the scenario that is being studied. Direct extrapolation of sensitivity results from one studied scenario to other scenarios is, thus, challenging. Therefore, actual quantification of sensitivity will not be provided other than visual demonstration of the impact on results.

Other limitations: Rainwater runoff, splashing, and surface adherence will not be addressed. Instead, the modeling approach is simplified to seek the maximum rain absorption that the rain load and material properties allow for. Wetting of the masonry is, therefore, approached in a form of worst-case scenario; although, this does not exclude localized infiltration through leak points (interpenetration) being able to create even more severe wetting. Transverse interface resistances, between brick and mortar, that allows for impeded moisture absorption across collar joints and between bricks and bed joints in the masonry are neither included nor addressed. With the exception of retention curve and hydraulic conductivity, only average values are used for material properties involved, i.e., the sensitivity of property variability is not extensively investigated.

A question arises as to whether simulations become realistic, with strong replicability of laboratory results or conservative, providing an "on-the-safe-side" enveloping result which laboratory results are not worse than.

The present work aims to investigate the influence or sensitivity of modeling choices on results, in contrast to a traditional sensitivity analysis that samples values of properties or boundary coefficients from probability distributions. The aim is also to approach perspectives on conservativeness in modeling.

2. Case Study Description—Materials and Methods

2.1. General

The masonry structure is part of a larger experimental study of nine differently composed wall segments shown in Figure 1a. A detailed description of the experiment can be found in [30]. Of the nine segments, the current paper will address simulation of segment 4, which has 50 mm glass-wool insulation and SVB. Segments 2, 5, and 6, which all have the same brick type and masonry thickness as segment 4, will also briefly be mentioned or addressed for comparison. Each segment includes a wooden beam end inserted into a beam-end pocket in the masonry. Segments 4 and 6 are equipped with SVB while segment 5 has polyethylene vapor barrier. The wall is exposed to an exterior climate sequence ensuring first wetting of the wall through cold-climate rain events before ensuring drying in relatively warm climate conditions. The following subsections will in brief describe the masonry materials, interior structure, instrumentation, experiment setup, and climatic sequence. For more details refer to [30].

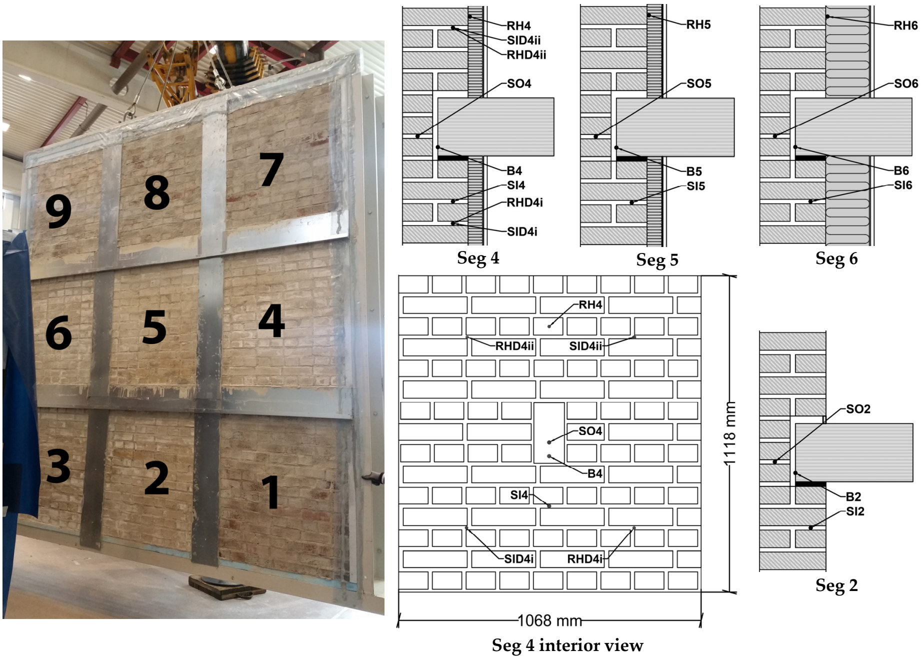

(**a**) (**b**)

Figure 1. Test wall. (**a**) Exterior face with flashings/gutters mounted. Each segment numbered. (**b**) Cross-sectional overview of the four wall segments, including sensor locations.

2.2. Masonry Materials

The brick (Figure 2) used for the addressed segments is a high-initial-rate-of-absorption (IRA) brick, which is presumed to be close in performance to typical bricks found in older buildings (late-19th to mid-20th century) [30]. The mortar is a prescribed LC-mortar; LC 50/50/610, where the numbers correspond to lime/cement/aggregate mass ratios of binder content. Material properties, masonry dimensions, and masonry construction are further described in [30]. Property values applied in the simulation model are listed in Appendix A, with further description of hydraulic conductivity in Section 4.1.

Figure 2. Close-up of bricks during brick laying.

2.3. Interior Structure

The interior structure of segment 4 consists of 50 mm interior glass-wool insulation (0.034 W/(m·K) thermal conductivity), a SVB, and an interior finish of 13 mm gypsum board. The SVB vapor-resistance properties applied in the simulation model are discussed and described in detail in Appendix B. Segments 5 and 6 are the same as segment 4 except, respectively, having a traditional polyethylene vapor barrier ($s_d \approx 50$ m) instead of a SVB and 150 mm insulation instead of 50 mm. Segment 2 has no interior structure and acted as a reference in [30]. A spruce beam end, 400 mm long, 107 mm wide and 213 mm high, is placed in the beam-end pocket on an asphalt sill gasket. There is a 10–20 mm gap between the pocket rear end and the beam end (18 mm in simulation model). The transition between beam end and vapor barrier is rendered vapor- and airtight.

2.4. Instrumentation

A number of Sahlen sensors (SO, SI, and SID), RH sensors (RH and RHD) and beam-end wood moisture electrodes (resistance moisture meters) (B) are located in the structure, as shown in Figure 1b. However, for the current paper, only RH4–RH6 and B2, B4–B6 are addressed. For more information, refer to [30].

2.5. Experiment Setup and Climate Sequence

The wall segments were tested in a large-scale building envelope climate simulator. This simulator contains both an exterior and interior climate chamber. On the exterior, the wall was exposed to dynamic conditions following a climate sequence provided in Figure 3b, whereas on the interior, the conditions were kept constant after initial conditioning, see Figure 3a. First, the wall was exposed to a cold exterior climate including four pairs of rain events (2 × 10 min, 2 × 20 min, 2 × 40 min, and 2 × 40 min), constituting a "wetting period", before it was exposed to a warm climate, constituting a "drying period". The rain exposure had a magnitude of constant 47 mm/h which is relatively high when compared to relevant real-world rain intensities [30]. The purpose of the climate sequence was to observe and compare rate of wetting and subsequent drying in differently constructed masonry wall segments, with focus on SVB and beam-end performance in this regard. A more detailed list of the climate sequence can be found in [30]. The same climate sequence was applied in the simulation model.

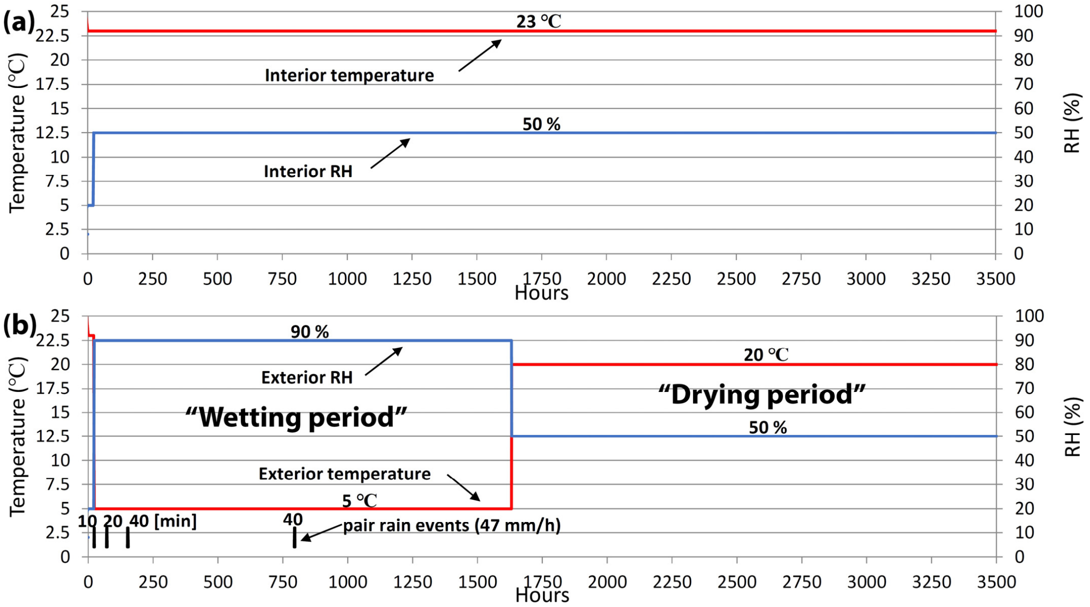

Figure 3. Climate sequence overview; (**a**) interior climate and (**b**) exterior climate. Reproduced from [30].

3. Hygrothermal Modeling

3.1. Model Physics

A model was set up to simulate the experiment scenario. The hygrothermal simulation model is an in-house physics model set up in COMSOL Multiphysics [38]. COMSOL provides a physics model builder, in the form of partial differential equations (PDEs), which were utilized in the current study to describe the balance and transport equations for moisture and heat. Furthermore, COMSOL includes numerical solvers based on the finite element method (FEM), of which the PARDISO (parallel sparse direct solver) has been employed. Previous versions of the model physics were applied in [39,40], with the current version having been developed further from these to better handle heavy rain exposure as a boundary condition. Furthermore, handling of the specific moisture capacity was corrected for non-isothermal conditions. That is, [39,40], unfortunately, did not include the temperature differential of the capillary pressure in connection to the specific moisture capacity, see Equation (1), which was the cause of the daily fluctuations experienced in benchmark 1 in [39]. The current version was also improved to more realistically represent the sorption/retention in both the hygroscopic and over-hygroscopic regions, see Equation (A1) Appendix A. Since the retention curve consists of two parts, the first part being dependent on RH (hygroscopic region) and the second part dependent on capillary pressure (over-hygroscopic region), the specific moisture capacity was split into two terms, $dw_{\phi}/d\phi$ and dw_{pc}/dp_c, in Equation (1).

$$\frac{dw}{dt} = \frac{d}{dt}\left(w_{\phi} + w_{p_c}\right) = \frac{dw_{\phi}}{d\phi}\frac{d\phi}{dt} + \frac{dw_{p_c}}{dp_c}\frac{dp_c}{dt} \tag{1}$$

where w is moisture content [kg/m^3], w_{ϕ} is the moisture retention curve term for hygroscopic region, w_{pc} is the moisture retention curve term for over-hygroscopic region, t [s] time, ϕ [-] RH, p_c [Pa] capillary pressure, and where the time-derivative of the capillary pressure is expanded as:

$$\frac{dp_c}{dt} = \frac{dp_c}{d\phi}\frac{d\phi}{dt} + \frac{dp_c}{dT}\frac{dT}{dt}$$

where T [K] is temperature.

The moisture balance is given by Equation (2), which originate from equivalent expressions derived in [41,42]. Since the scenario studied does not contain air transport, vapor transport due to air diffusion (or convection) is not included.

$$\frac{dw}{dt} = \frac{d}{dx_j}\left(\left[\delta_v P_{sat} + D_{\phi}\right]\frac{d\phi}{dx_j} + \left[\delta_v \phi \frac{dP_{sat}}{dT} + D_{\phi}\frac{\phi}{T}ln(\phi)\right]\frac{dT}{dx_j} + \frac{D_{\phi}}{R_w}\frac{\phi}{T}g \cdot \vec{e_z}\right) \tag{2}$$

where δ_v [kg/(m·s·Pa)] is vapor diffusivity, P_{sat} [Pa] saturation pressure, D_{ϕ} [kg/(m·s)] capillary diffusivity for ϕ as driving potential ($D_{\phi} = K\rho_w R_w T\phi^{-1}$), K [s] hydraulic conductivity, ρ_w [kg/m^3] water density, R_w [J/(kg·K)] specific gas constant for water vapor, g [m/s^2] gravity, and e_z unit vector for z-dimension (dimension of acting gravity, positive in the opposite direction to that of gravity).

The enthalpy balance is given by Equation (3), when omitting the contribution from change in air content and humid air vapor content in the pore structure. A similar expression is derived in [43].

$$\begin{aligned} \rho_s c_{p,eff}\tfrac{dT}{dt} \quad &= \tfrac{d}{dx_j}\left(\left[\lambda_{eff} + h_{vap}\delta_v\phi\tfrac{dP_{sat}}{dT}\right]\tfrac{dT}{dx_j} + h_{vap}\delta_v P_{sat}\tfrac{d\phi}{dx_j}\right) \\ &+ D_{\phi}\left(\tfrac{d\phi}{dx_j} + \tfrac{1}{R_w}\tfrac{\phi}{T}g \cdot \vec{e_z}\right)c_{pw}\tfrac{dT}{dx_j} \end{aligned} \tag{3}$$

where ρ_s [kg/m^3] is the density of solid material, $c_{p,eff}$ [J/(kg·K)] effective heat capacity ($c_{p,eff} = c_{ps} + c_{pw}w/\rho_s$), c_{ps} and c_{pw} specific heat capacity of solid dry material and liquid water, respectively, λ_{eff} [W/(m·K)] moisture-dependent effective thermal conductivity (temperature dependence is omitted), and h_{vap} [J/kg] specific enthalpy of evaporation (temperature dependent).

The rain boundary moisture flux is modeled as an approximation to Equation (4) [44].

$$g_{l,eff} = min\left[g_l, K_{c,cap}\frac{dp_c}{dx}\right] \tag{4}$$

where $g_{l,eff}$ and g_l [kg/(m^2·s)] are, respectively, effective boundary moisture flux and actual rain flux, and $K_{c,cap}$ [s] capillary conductivity at capillary saturation.

The approximation to Equation (4) is given by Equation (5).

$$g_{l,eff} = min\left[g_l, -D_{\phi,cap}\left(\frac{\phi - \phi_{acc}}{b_{l,min}} + ln\phi\frac{\phi}{T}\frac{T - T_e}{b_{l,min}}\right)\right] \tag{5}$$

where $D_{\phi,cap}$ is D_ϕ at capillary saturation, ϕ and ϕ_{acc}, respectively, RH of the first boundary cell and of an arbitrary set RH accuracy level assumed for moisture film at boundary (ϕ_{acc} = 0.99999, equivalent to p_c = 1351 Pa at 20 °C, well below capillary saturation of the retention curves), $b_{l,min}$ [m] thickness of the first and thinnest boundary layer cell at the exterior boundary surface (arbitrarily set to $b_{l,min}$ = 0.0005 m), and T and T_e [K], respectively, temperature of the first boundary cell and exterior temperature.

Not using Equation (5) in combination with boundary layers, but instead limiting moisture uptake on saturation only, can provide marginally higher moisture uptake. However, the fine meshing that boundary layers provide is believed to give a more accurate account of moisture content and absorption conditions at the exterior surface. Still, this issue has not been investigated extensively in the present study, and uncertainty thereby persist regarding whether the approach chosen is the most optimal approach. A relevant model algorithm validation by benchmarking is documented in Appendix C.

3.2. Limitations

There are some limitations to the model due to lack of certain information:

1. With material property data mostly available for one direction only, materials are, in general, modeled as isotropic;
2. Moisture retention and capillary conductivity as functions of capillary pressure have not been tested for in the current study. Approximate guesstimates have instead been applied, based on the materials' sorption curves and capillary absorption coefficients, and retention curves of what are believed to be similar materials;
3. Interface resistances between materials are not included, i.e., the model assumes full hydraulic contact;
4. Hysteresis has not been included. Materials are only modeled on adsorption and absorption data.

Consequences of 1.: the isotropic simplification will especially affect the bricks and the mortar joints. The spruce beam end is modelled anisotropic as default. For the bricks, the capillary transport coefficient has been measured through the brick face, which for these bricks is the surface with the finest pore structure and, presumably, the side with the highest resistance to water penetration. The brick head has similar appearance. Higher capillary transport coefficients could be expected in other directions, i.e., moisture absorption through the brick bed or stretcher (opposite face). Larger pores and cracks can especially be seen on the brick bed. Since the rain moisture exposure is one-directional with a combination of brick face and head being exposed, both the bed and stretcher directions are, presumably, less important; however, bed absorption would be important if the model were to explicitly replicate additional influx of moisture along the brick–mortar interface. More information about the specific modeling is provided in Section 3.4.

Regarding 2.: not having the exact retention and capillary conductivity curves as functions of capillary pressure for the masonry materials in question is inconvenient for a simulation case which is so heavily determined by capillary transport during and after rain absorption. Having adequately described retention and capillary conductivity functions is essential for arriving at high confidence simulation results. However, since such functions are not available for the specific materials in this study the functions had to be established from the material data being available (sorption curves in hygroscopic region and capillary absorption coefficients), together with retention curves of similar materials described in the research literature. Descriptions and details regarding applied material property functions are given in Appendix A and displayed in Sections 4.1 and 4.2.

Concerning 3.: interface resistances between different materials can significantly influence moisture transport in masonry [23], i.e., impede moisture movement between materials during absorption and redistribution conditions. Thus, not including them will allow faster moisture transport across the masonry than the actual situation. However, it can also result in different moisture distribution in the masonry compared to reality [23]. During drying conditions, insignificant influence from not including interface resistance is expected, see [15].

As for 4.: not including hysteresis is a common simplification due to the complexity of hysteresis modeling and extensiveness of required material testing. However, not including hysteresis will inherently cause uncertainty.

3.3. Key Uncertainty Regarding Material Properties

In the present study, not all material properties are available for the specific brick and mortar applied in the experiment. Basically, it was not possible within the extent of the experiment in [30] to fully measure all properties, due to limitations in laboratory resources and time. Table 1 provides an overview of necessary material properties and how they have been determined for the hygrothermal simulation. Key properties, such as the moisture retention and hydraulic conductivity ([35]), have not been measured but were taken from perceived similar materials and modelled, respectively, where, in addition, modeling of the hydraulic conductivity requires the moisture retention as input [17]. Significant uncertainties are, therefore, introduced. This provides an ample example to demonstrate typical uncertainty challenges hygrothermal simulation efforts encounter due to limited resources for complete mapping of properties. Impact of this uncertainty will be further addressed in Sections 4.1 and 4.2.

Table 1. Necessary material properties, including partial or indirect properties for the retention and hydraulic conductivity. Includes overview of determination: measured (Mea.), from standard (Sta.), from similar materials (Sim), modelled (Mod.), and estimated (Est.).

	Storage	**Determination**	**Transport**	**Determination**
General	Density, ρ_s	Mea.		
Heat	Specific heat capacity, c_p	Sta.	Thermal conductivity, λ	Sta. (dry), Sim. (wet)
Moisture	Sorption (hygroscopic), $w(\phi)$	Mea.	Vapor diffusivity, δ_v	Mea.
	Retention (over-hygroscopic), $w(p_c)$	Sim.	Hydraulic conductivity, $K(p_c)$	Mod.
	Capillary moisture content, w_{cap}	Mea. (brick)/Mea. Sim. (mortar)	Capillary absorption coefficient, A_w	Mea. (brick)/Mea. Sim. (mortar)
	Saturated moisture content, w_{sat}	Est. Sim.		

3.4. Simulation Model Design Setup

Illustration of the overall 2D model is provided in Figure 4a, where different colors indicate different materials. The model lumps the additional moisture influx along the brick–mortar interface together with that of the mortar as a simplification and, thereby, ends up with an increased capillary conductivity for the mortar during absorption. That is, lumped properties are applied only during rain events. Figure 4b illustrates how the mortar joints are modelled. Joints with a continuous brick–mortar interface from the exterior are modeled with the lumped properties (dark blue Figure 4b). Whereas mortar joints that have no brick–mortar interface continuity to the exterior are modeled with normal mortar properties (light blue–grey Figure 4b). The mortar with lumped properties arrives at a capillary absorption coefficient in the same order of magnitude as the brick, see Appendix A.

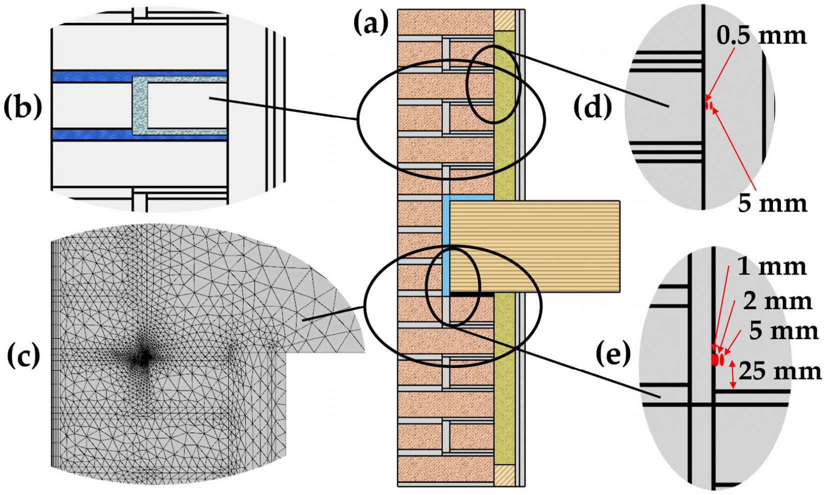

Figure 4. (**a**) Overview of simulation model. (**b**) Joint modeled in two zones; one continuous (dark blue), capturing the uninterrupted brick–mortar interface traversing the wall; the other (light blue–grey) capturing the collar joint and the mortar not having continuous interface from the exterior. (**c**) Illustration of applied mesh resolution. Reading position distances of simulation results at: (**d**) the interior of the masonry; and (**e**) the beam end.

The air cavity around the beam end is modeled as humid air according to formulas in [45], corrected for radiation and convection over a cavity width of 20 mm following the WUFI help file [46]. However, for simplicity it is only corrected for as a vertical cavity in the transverse direction; thus, neither accurate for the horizontal cavity-part above the beam end, nor correct in the vertical direction for the vertical cavity.

Description of how the SVB is modelled is provided in Appendix B.

The exterior and interior heat-transfer coefficients are both taken as 25 $W/(m^2{\cdot}K)$, whereas the vapor-transfer coefficients are both 2×10^{-7} s/m. Equal coefficients are used on both sides due to the ventilation conditions created by the climate simulator.

Model boundary conditions are given a timestep resolution of 600 s to capture the climate sequence of the experiment. The simulation is run with maximum timesteps of 30 s for rain events and the temperature jump (Figure 3) and the 20 min leading up to the events. For the temperature jump, small timesteps are applied to accommodate model algorithms of the humid air layer behind the beam end. Otherwise, temperature jumps would not be a particular issue requiring low timesteps. Timesteps of 600 s are used for approximately 2 h prior to boundary condition changes. Elsewhere, timesteps of 3600 s are used. Low timesteps in the lead-up time to events or boundary condition changes is a technical measure taken to avoid timesteps having been shifted to the point where they overstep events, which can happen in COMSOL when using free time-stepping taken by the solver in combination with maximum step size, since it only updates timestep size before initiating a new timestep. Thus, if operating with, for instance, timesteps of 600 s or 3600 s up to an event one might risk losing, respectively, up to almost 600 s or 3600 s of the event. Before this became apparent to the authors, some simulation try runs lost a rain event causing strange inconsistency between results.

Applied mesh resolution is illustrated in Figure 4c. Increasing mesh resolution further did not provide significant impact to results. The mesh includes eight boundary layers on the exterior surface that is exposed to driving rain. The thickness of the layers grows with a stretching factor of 1.3, with the outermost, and thinnest, being 0.5 mm thick. The high mesh resolution below the corner of the beam end is due to the humid air at a point in time reaches saturation and condensation conditions when in contact with the asphalt sill gasket. However, surface condensation from humid air is not included in the model. Instead, the humid air is allowed to go to unphysical supersaturation. This simplification was deemed acceptable since these conditions only happen at this location for some hours after the temperature jump initiating the warm period.

4. Results and Assessments

If not otherwise stated, the RH reading position is taken 5 mm from the interior masonry surface, and the beam-end moisture content reading is taken 2 mm into the beam end 25 mm from the bottom, see Figure 4d,e.

Note that the resistance moisture meters used to detect moisture content in the beam ends did not manage to provide reliable moisture contents below 8–10%. Furthermore, in the experiment the acclimatization time from very dry conditions was insufficient to arrive at consistent 20% RH throughout the structures. Hence, the sensors display lower RH and moisture content than the initial condition used in simulations, with the latter following the exterior and interior climate at the experiment onset. The initial conditions of the experiment and the simulations are therefore not comparable. The consequence of this should, nevertheless, be insignificant after moisture from rain events reaches the sensors or reading positions.

4.1. Uncertainty from Hydraulic Conductivity

Hydraulic-conductivity curves are modelled following a bundle-of-tubes model described in Knarud et al. [17]. Input to generate a conductivity curve includes A_w-value, retention curve, and vapor resistance. Among these inputs, uncertainty regarding impact of the A_w-value and retention curve will be assessed in this and the next section. For the brick, the A_w-value was measured [30] for enough specimens to identify standard deviation. Simulations with conductivity values generated for −2, −1, +1, and +2 std. of the A_w-value can, thereby, be assessed. Standard deviation was not given for mortar. Instead, a likely min–max range was provided. For simplicity, we here put the min as −2 std. and max as +2 std. so that hydraulic-conductivity curves can be generated in the same format for the two materials, see Figure 5a,b. As seen from Figure 6, the variation in A_w-value has a large impact on how early the RH sensor responds to increased moisture intrusion in the wall structure. The variation in mortar properties and, especially, in the lumped properties due to the large uncertainty span in A_w-values is likely a large contributor to this, whereas the variation for brick is likely of relatively low impact due to the low standard deviation for the brick. Interestingly, higher A_w-values do not increase RH in the warm period much, whereas lower A_w-values decrease the RH. This is due to changes in the saturation level at the masonry interior, where the higher A_w-values provide lasting ~100% RH at the masonry interior while lower A_w-values provide lower RH values. This reveals a downside with the conservative model setup, where little to no variation in RH reading value is possible upwards after the interior masonry reaches ~100% RH. Thus, impact of worsening material and model conditions falls into a blind spot of the RH sensor. What is left to be distinguished from the RH readings is the response rate to rain events in the first half of the cold period.

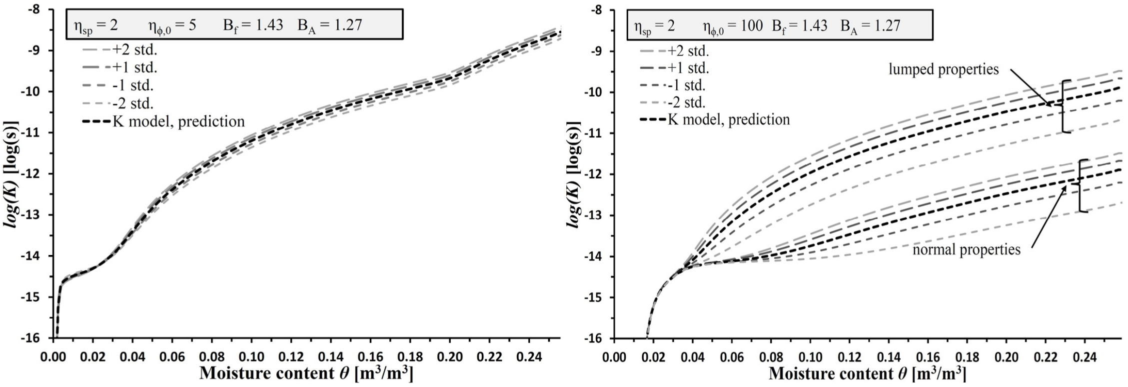

(**a**) (**b**)

Figure 5. Uncertainty regarding hydraulic-conductivity curves modeled according to [17] based on standard deviation in A_W-value [30] for (**a**) brick and (**b**) mortar. Standard deviation for the mortar is unknown; however, ±2 std. is presumed to approximately correspond to the min–max range listed in [30]. Lumped properties are explained in Section 3.4 and Appendix A.

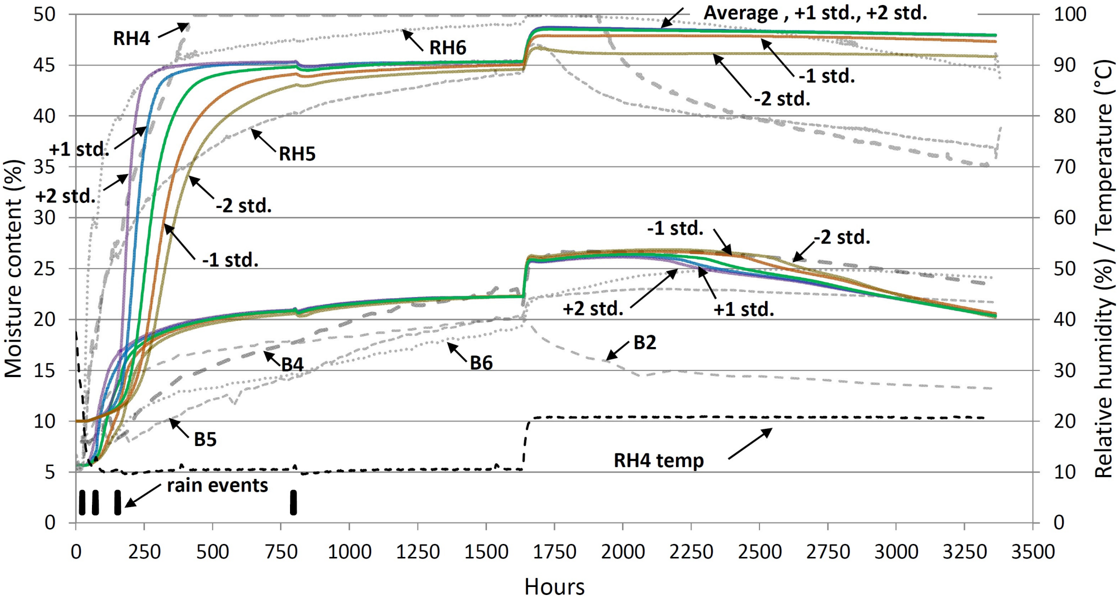

Figure 6. Result sensitivity to distribution range of A_W-values. Colored lines (green, default setup) provide RH and B simulated readings for seg. 4. Light grey dashed curves show results gathered in experiment (the same is the case in subsequent graphs showing results). Moisture content in weight-%.

For the beam end, higher conductivity curves provide earlier drying, while lower curves delay drying.

4.2. Uncertainty from Retention Curve

Regarding the uncertainty caused by not knowing the exact retention curve for the brick and mortar, impact of the retention curve is assessed. Uncertainty in the retention curve is approached by generating two extreme retention curve-"outliers", Figure 7a,c. The min- and max-retention curves, respectively, correspond to the perceived low and high end of pore sizes that are plausible for the materials. Associated hydraulic conductivity is generated with these retention curves, thus, giving corresponding min and max conductivity curves in Figure 7b,d. However, the lumped hydraulic-conductivity curve is taken as the default lumped-properties curve in Figure 5. The results, see Figure 8, display remarkably small difference between the simulations. The max setup has marginally earlier response and higher values for the RH reading, whereas the opposite is the case for the low setup. For the beam-end moisture content, the max and low setups provide, respectively, somewhat higher and lower moisture content at the onset of the warm period.

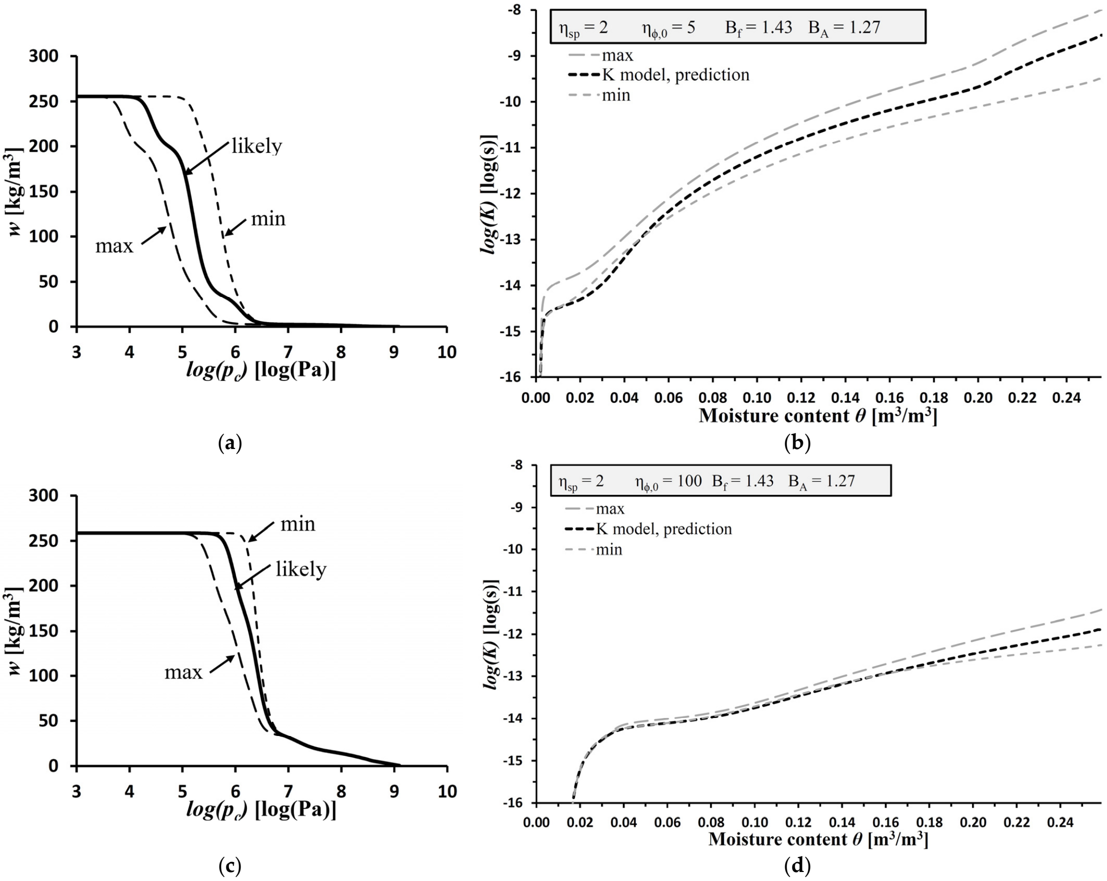

Figure 7. Variation in retention curves (**a**,**c**) to perceived outlying min/max limits, including change in hydraulic-conductivity curves (**b**,**d**), respectively, for (**a**,**b**) brick and (**c**,**d**) mortar.

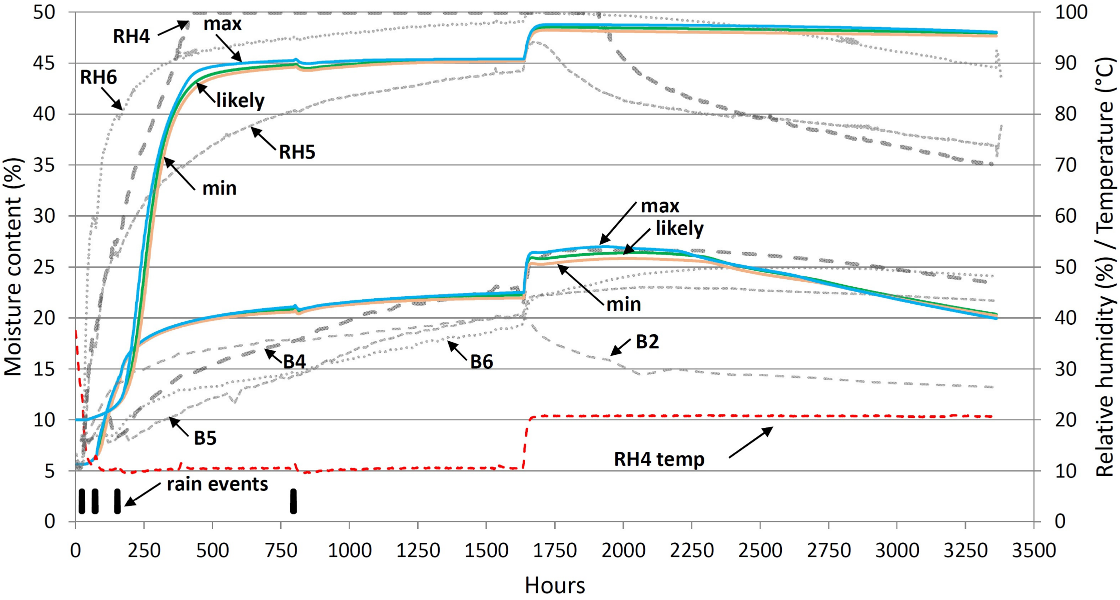

Figure 8. Sensitivity of variation in retention curves.

4.3. Reading Position

Initially, the RH reading position was assumed to align with the center of the RH sensor. With the sensor having a thickness of approximately 10 mm, the reading position in the simulation model was taken 5 mm from the masonry interior surface. However, after reconsideration, this assumption was drawn into some doubt. Especially, since the simulation results, see Figure 6, seem unable to increase the RH much above 90% in the cold period at 5 mm distance, whereas RH 4 is seen to go higher. The result difference in Figure 9 follows closely the temperature difference between 5 mm and 0.5 mm (Figure 10), correlated with the consequent temperature-dependent change in saturated vapor pressure. Assessing the situation, the simulation model is simply built up with insulation in the location of the sensor, whereas in the experiment the insulation bends around the sensor. Hence, locating the reading position at a certain distance from the masonry will effectively put it into the insulation. Even though the glass wool is rather vapor-open, the insulation still provides a thermal resistance over 5 mm, which affects effective temperature and, consequently, the RH level. Also, it might be that the RH sensor is more sensitive towards the highest RH level one side of it experiences, that is, with one side being pressed up against the masonry, higher RH may be experienced at the RH sensor openings at that side, and, effectively, influence what is measured. In Figure 9, assessing the simulation results against the experiment, a 0.5 mm distance is closer to RH4 and RH6, while 5 mm distance is partly closer to RH5 in the cold period of the experiment. However, the higher RH6 curve can be partially explained with the increased insulation thickness (150 mm) causing the RH sensor to be in colder surroundings. The jump of the RH5 curve at the start of the warm period is also seen from the simulation with 5 mm distance.

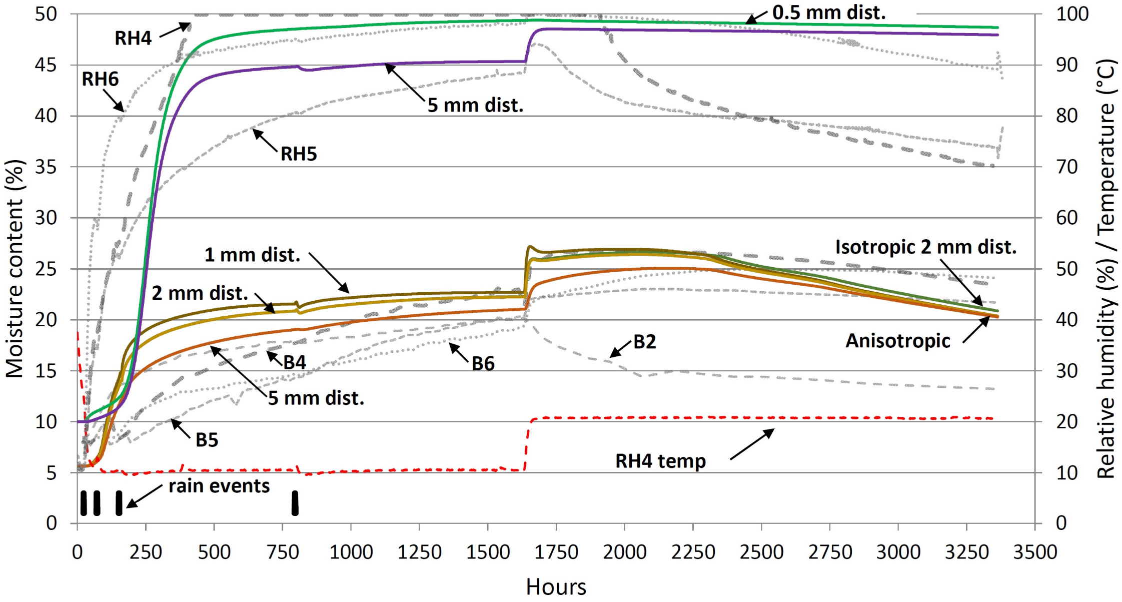

Figure 9. RH results for varying the reading-point distance from the interior masonry surface. Beam-end results for reading position, and isotropic and anisotropic beam-end properties.

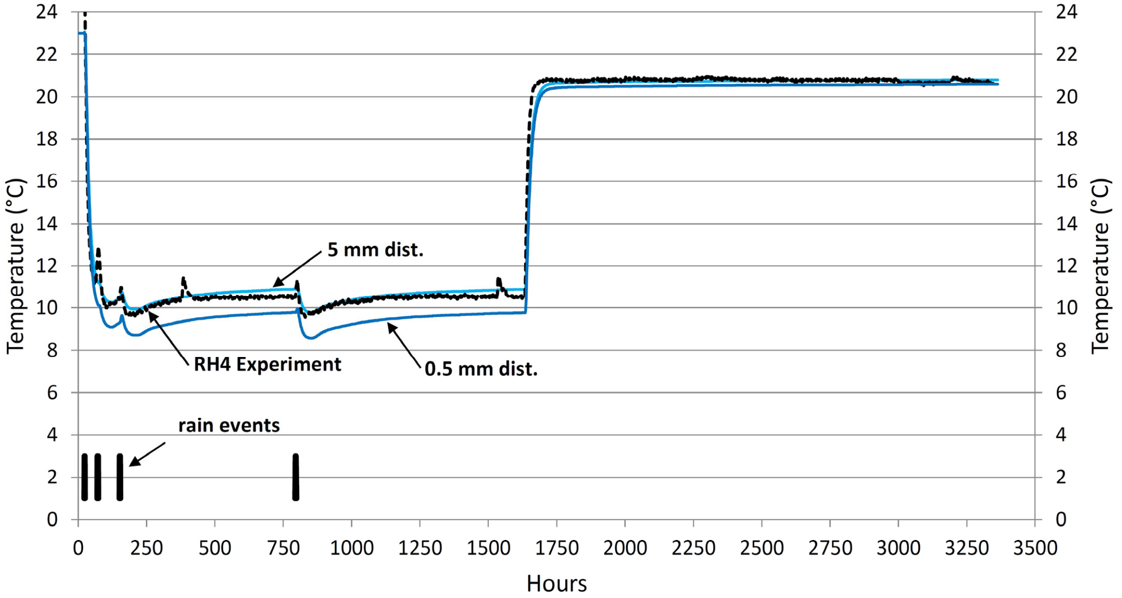

Figure 10. Temperature results. Varying reading-point distance from the interior masonry surface compared to experiment results of RH4.

Temperature reading at 0.5 mm is approximately 1.10 K lower than at 5 mm during the cold period (Figure 10), where the latter is almost a match to the measurement, but incrementally higher and lower during the cold and warm periods, respectively. Temperature peaks not aligning with rain events in the experiment results are likely due to ice accumulation and defrosting of the ventilation system in the climate simulator. In perspective, specifically addressing the cold period, both results are, respectively, well within or at the ±1 K threshold for narrower accuracy range for at least 95% of the data, suggested by Huerto-Cardenas et al. [10] for model validation. However, the strictness of such a criterion is dependent on the variation in boundary temperature, and the criterion is intended for simulation in comparison to in situ or field measurement, not a laboratory climate sequence as is the case here. From these results, see Figure 10, it is indicated that choosing a RH reading position at 0.5 mm likely underestimates the temperature and overestimates the RH somewhat during the cold period.

Beam-end moisture readings are taken at 1, 2, and 5 mm into the wood, see Figure 4e. The readings at 1 and 2 mm are close to enveloping the B4 result in the cold period and the beginning of the warm period, whereas the moisture content decreases much faster than in the experiment over the second half of the warm period. The reading at 5 mm fails to be conservative for B4; however, it succeeds in being conservative for B5 and B6 for the cold period and the beginning of the warm period. It is relatively close in following the B2 trend over the cold period. There might be a significant uncertainty regarding the electric conductivity in the wood at these depths at the beam end, as it is affected by surface roughness, cracks, and local wood density and wood ring structure. Thus, local differences in wood structure can, by contributing to measurement uncertainty, explain the large differences between the segments, in addition to uncertainty regarding masonry heterogeneity and unevenness in the air-layer thickness, which affect moisture transport, that is.

4.4. Isotropic vs. Anisotropic Beam End

Applying isotropic material properties is a common simplification in hygrothermal modeling. It is, therefore, of interest to investigate the difference arising from such a simplification. For the isotropic case, longitudinal wood properties are used in both directions. In the anisotropic case, the wood properties in the vertical direction were replaced with radial properties for capillary conductivity and with twice the vapor resistance of the longitudinal direction, instead of the radial vapor resistance; this, with the assumption that the radial vapor resistance would be too strict considering the presence of cracks and the tangential influence in the 3D wood structure not being captured well by the 2D model. A difference between isotropic and anisotropic modeling is, indeed, seen in Figure 9, although not large. With the isotropic simulation, there seems to be a greater influx of moisture into the beam end from the masonry in the vertical direction, due to longitudinal wood properties, thereby, maintaining a higher moisture content longer than for the anisotropic simulation.

4.5. Effect of Lumping Mortar Properties and Brick–Mortar Interface Properties

A simulation was also undertaken with normal mortar properties for all joints, not compensating for the brick–mortar interface. An issue of numerical instability was experienced with this simulation at the fourth rain event (second rain event pair), preventing the simulation to proceed at acceptable speed. The instability is believed to have been caused by the mesh boundary layer, presumably, due to the large difference in capillary conductivity between mortar and brick along these layers. The solution became to replace the exterior 5 mm of the mortar joint with mortar having lumped properties. The mesh boundary layer was reduced to six layers with growth governed by a stretching factor of 1.1, and joints in the exterior half of the masonry were given increased mesh resolution for smoother transition from the boundary layers. This ensured that boundary layers would be well within the exterior 5 mm of the joints. Boundary layers were kept, due to Equation (5).

As seen in Figure 11 the simulation with normal mortar property joints results in both a later RH curve in response to rain events and a lower curve for beam-end moisture content during the warm period.

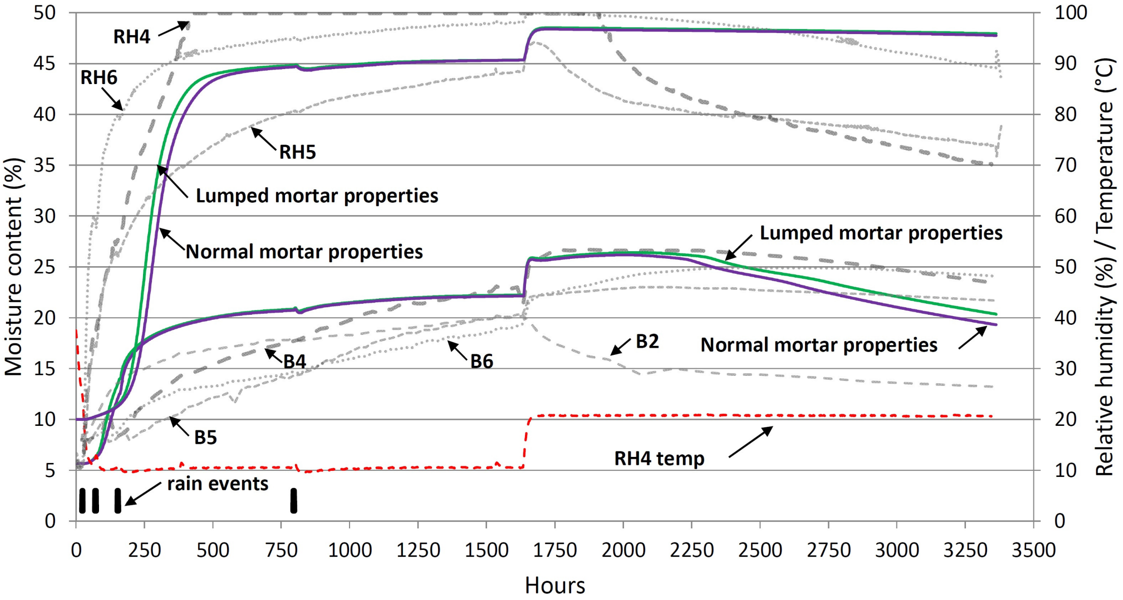

Figure 11. Difference between normal and lumped mortar properties.

4.6. Effect of "Leaky" Joint Inclusion

In the laboratory experiment, recorded video monitoring of segment 2 revealed rapid localized moisture permeation. Figure 12 shows moments from this monitoring, with the visually confirmed extent of the wetted surface area (area of dampness) outlined after the first and second 40 min rain events.

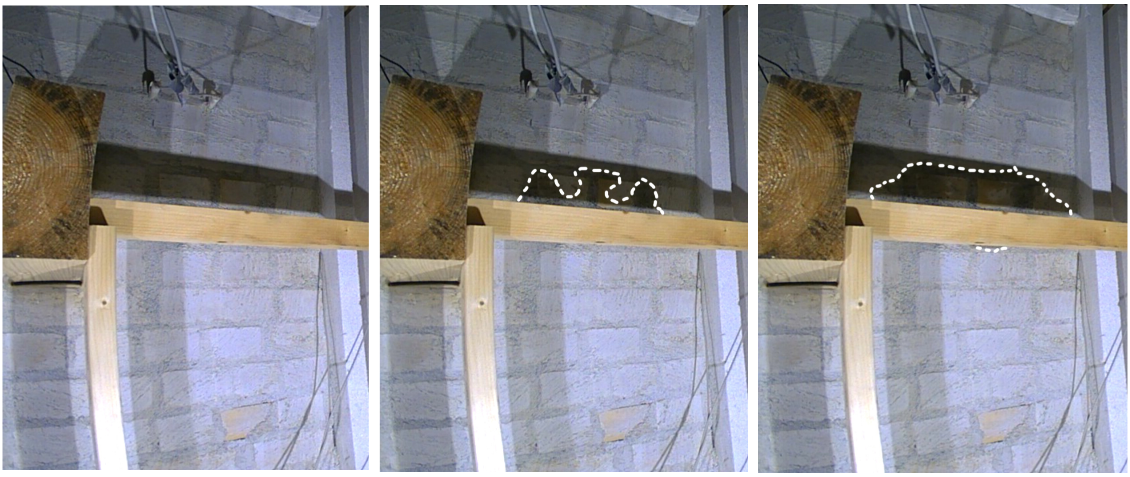
(**a**) (**b**) (**c**)

Figure 12. Segment 2 rain permeation of a mortar joint; (**a**) before rain events, (**b**) after the first 40 min rain event (initiated at 150.6 h), and (**c**) after the second 40 min rain event (initiated at 153.6 h). The extent of the wet masonry surface is outlined.

During the first 40 min rain event (at 150.6 h), the first sign of moisture permeation became visible after only 3 min. This was a very rapid permeation and would indicate a leak infiltration or interpenetration along a brick–mortar interface, capable of wetting the interior masonry surface.

Due to this observation, a "leaky" mortar joint was modeled with a 10-times higher capillary absorption coefficient (Aw-value), i.e., $A_W = 2.5\ \text{kg}/(\text{m}^2\text{s}^{1/2})$. That is, it became an extreme case of the lumped properties approach, as a simple, less mesh-intensive alternative to fracture modeling as in [28]. No effort was undertaken to calibrate this Aw-value to measurements, so it should be understood as an example value. Three simulations were then run with one "leaky" mortar joint, respectively, replacing the closest mortar joint below the interior RH sensor and the joint one brick course and two brick courses further below. The results are provided in Figure 13. Including a "leaky" mortar joint just below the sensor provided RH results that showed much faster response time, early on close to RH6. With a "leaky" joint one brick course below, the sensor response was a bit earlier than RH4. "Leaky" joint two brick courses below the sensor also showed early response but with less rapid rise than for the one brick course below.

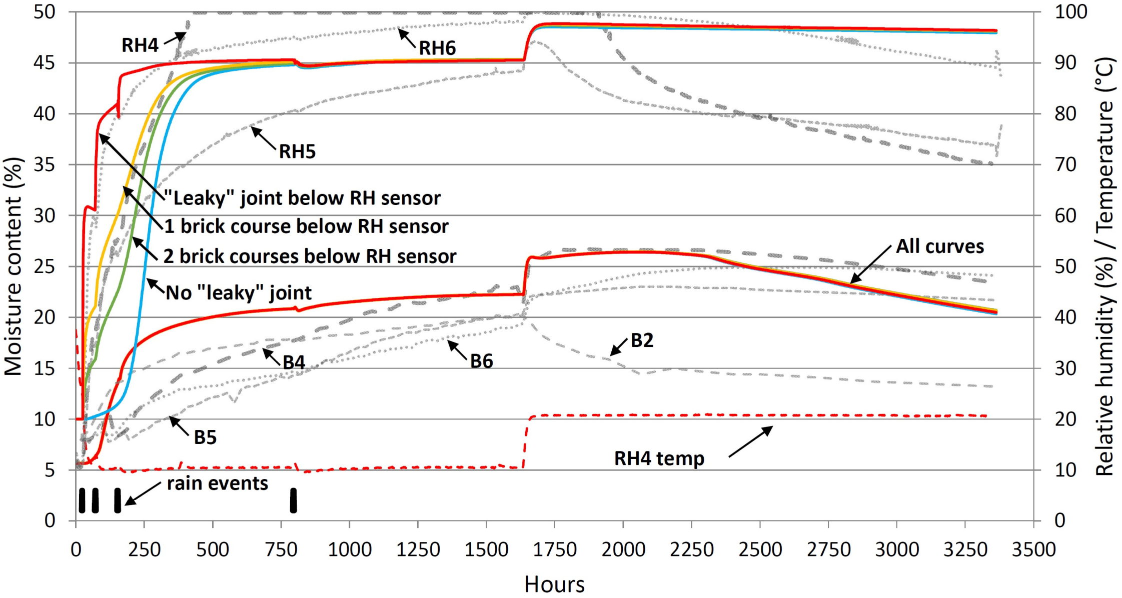

Figure 13. Inclusion of a "leaky" joint just below the sensor, and one brick and two brick courses further below, respectively.

Often the first onset of moisture permeation is observed through the head joint [24]; however, the head joints are not realistically present in a 2D model of the vertical cross-section. Hence, to see the effect of a "leaky" head joint, a 2D model of the horizontal cross-section or, more realistically, a 3D simulation, would be necessary. Permeation through head joints is also observable in Figure 12.

Overall, a "leaky" joint is a 3D occurrence since it would likely have limited extent, whereas in 2D it implicitly has unlimited extent in the missing dimension. 2D results should, therefore, be approached with some care.

4.7. 3D vs. 2D Model

Simulating 3D details like the beam end with a 2D model also introduce uncertainties. Nevertheless, not many studies have provided 3D simulation including beam end. A reason for this is the high numerical complexity and computational requirements associated with a 3D model. Thus, 3D models are usually simplified to homogeneous masonry or layers of masonry and are not of bare brick masonry exposed to rain, see [47,48].

A 3D model was built to investigate the difference compared to the 2D model. The model extents are illustrated in Figure 14a. To limit computational demand, the model takes advantage of axis-symmetry along the center of the beam. Furthermore, the extent of the model is limited around the beam at a distance that from the 2D simulation was indicated to have low impact from the heat and moisture transport occurring around the beam. Due to the limited extent of the 3D model, the RH reading position has been moved two brick courses closer to the beam end. An air layer of 13 mm thickness is present on the side of the beam end, separating it from the masonry.

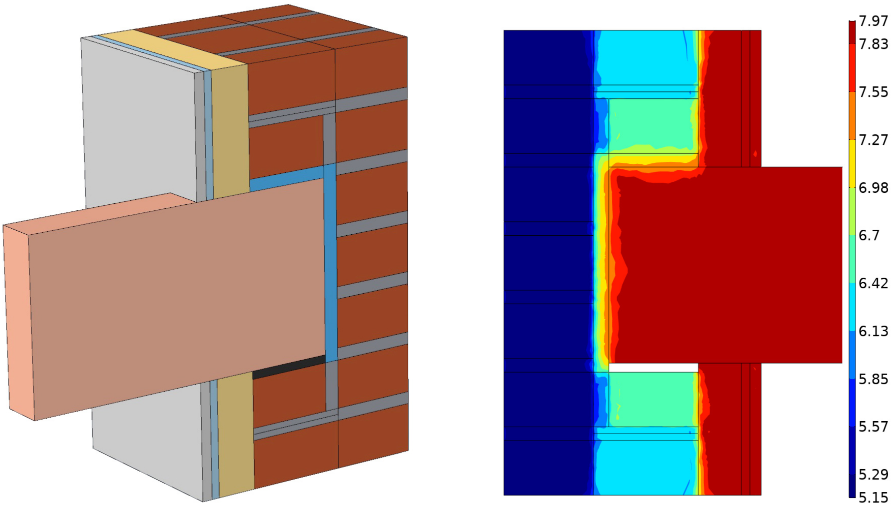

(**a**) (**b**)

Figure 14. (**a**) Extents of 3D model, and (**b**) initial moisture content distribution given as log(p_c) at 825 h. The contour plot it generated after gradients are created, thus, sharp initial jumps are smoothed out.

Stable numerical solving of the rain events was not achieved in the 3D model. To avoid simulating the rain events, moisture content after the final rain event, seen from the default 2D simulation, was provided as initial moisture content, with a simplified distribution over the masonry, for a 2D and 3D model setup starting after the final rain event. Figure 14b shows the capillary pressure distribution, applied as initial conditions to distribute the moisture content. The initial temperature was set to 23 °C for the whole structure. Due to time constraints on simulation runtime, another simplification of the 3D model involved having a lower resolution mesh than the 2D model. Somewhat lower accuracy should, therefore, be expected in 3D compared to 2D.

The results of the 2D and 3D simulations using initial moisture contents instead of rain events are given in Figure 15. A difference is seen in the RH results where the 3D simulation shows a higher curve in the cold period. This is, mostly, due to the 3D simulation predicting slightly lower temperature, see Figure 16. However, it can also have been influenced by the moisture distribution (initial or otherwise) acting differently. Furthermore, having moved the reading position closer to the beam end may be the reason for the RH curve becoming slightly lower at the end of the warm period. The default 2D simulation and the 2D simulation with initial moisture provides almost identical results. Also, for the beam end, only slight difference is seen between the two 2D simulations, whereas the 3D simulation provides large deviation to the 2D simulation at the beam end. More moisture is taken up during the cold period and a high level with slow and long dry-out is seen in the warm period. A slightly lower temperature at the beam end is seen in the 3D simulation during the cold period compared to the 2D simulation. These differences are likely due to the beam end in the 3D simulation being surrounded by moist masonry, although separated by air layers, whereas the 2D simulation implies that the beam end stretches out indefinitely in the missing dimension.

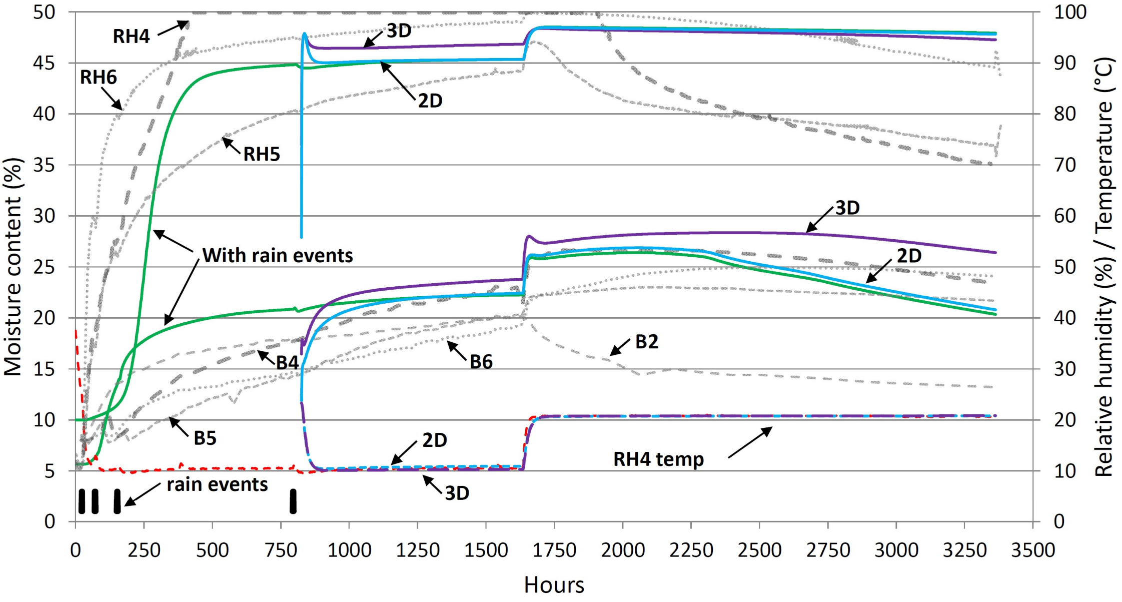

Figure 15. Comparison of 2D to 3D simulation.

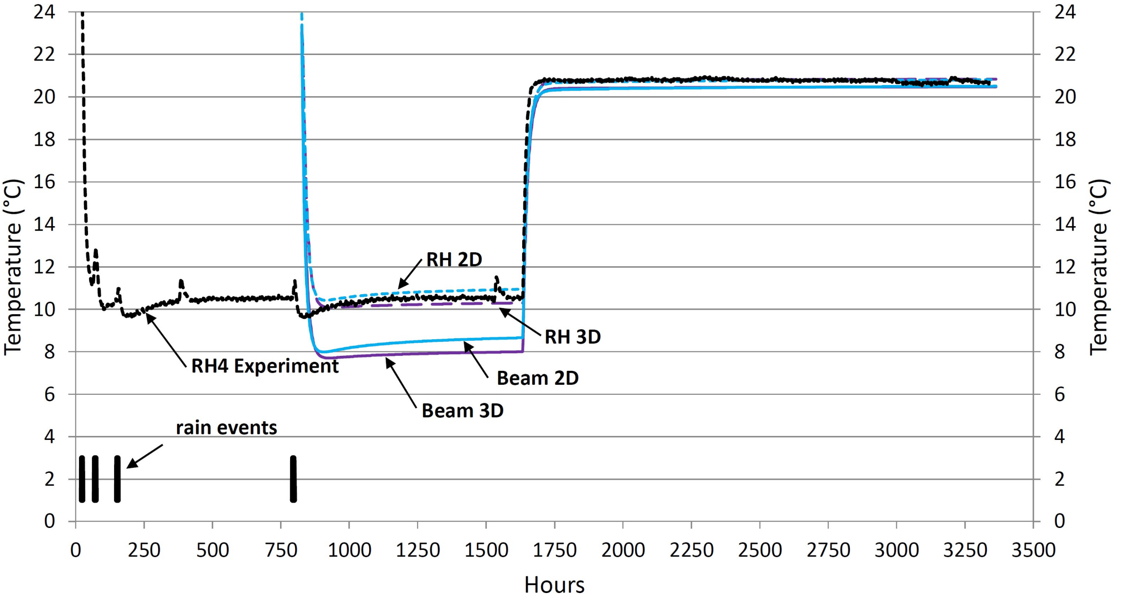

Figure 16. Comparison of 2D and 3D temperature predictions.

4.8. *Effect of SVB*

Before addressing the effect of SVB, read-out values of the SVB operating status are briefly summarized. During the cold period, the vapor resistance of the SVB decreases simultaneously as moisture from rain events intrudes into the wall. For the unaltered SVB setup, see Appendix B, the lowest it reached was about $s_d \approx 15.6$ m in the cold period (read in the SVB across the insulation from the RH sensor). In the warm period, the s_d-value slowly increased in the interval $s_d \approx 0.55$–0.57 m with the exception of the scenario with a "leaky" joint next to the sensor which experienced $s_d \approx 0.53$–0.55 m.

Uncertainty accompanies the SVB modeling due to a low resolution in the RH-dependent vapor-resistance test results provided by the SVB documentation. As described in Appendix B, the vapor-resistance values between known values are manually curve-fitted. Consequently, the values are inherently uncertain and might miss the reality.

To investigate effects of the SVB, compared to effects of no-vapor-barrier and traditional polyethylene barrier, simulations were set up with the presumed vapor resistance multiplied by a factor. That factor was given values: 100, 1, 0.5, 0.25, 0.1, and 0.01, where 1 represents the presumed behavior, 100 becomes more like a traditional polyethylene vapor barrier, and 0.01 is close to no vapor barrier. 0.5, 0.25, and 0.1 are added to show intermediate values and the response of the simulation results. Although there are limits to improvement of SVB products, i.e., product development capable of reducing vapor resistance during high RH conditions, intermediate values, at least, provide a notion of improvement potential.

As seen in Figure 17, only minimal RH difference exists between $100s_d$ and $0.10s_d$ up to the onset of warm exterior climate at 1632 h. For the case with very low resistance, i.e., $0.01s_d$, a much quicker rise in RH and a higher RH level are observed. For the drying period after 1632 h, vapor resistance of the SVB has large impact. Although the presumed performance of the applied SVB ($1.0s_d$) does not show much drying, it is, nevertheless, an improvement compared to how a traditional polyethylene vapor barrier would perform ($100s_d$). Lower s_d shows greater drying, with practically no vapor barrier ($0.01s_d$) having the fastest dry-out.

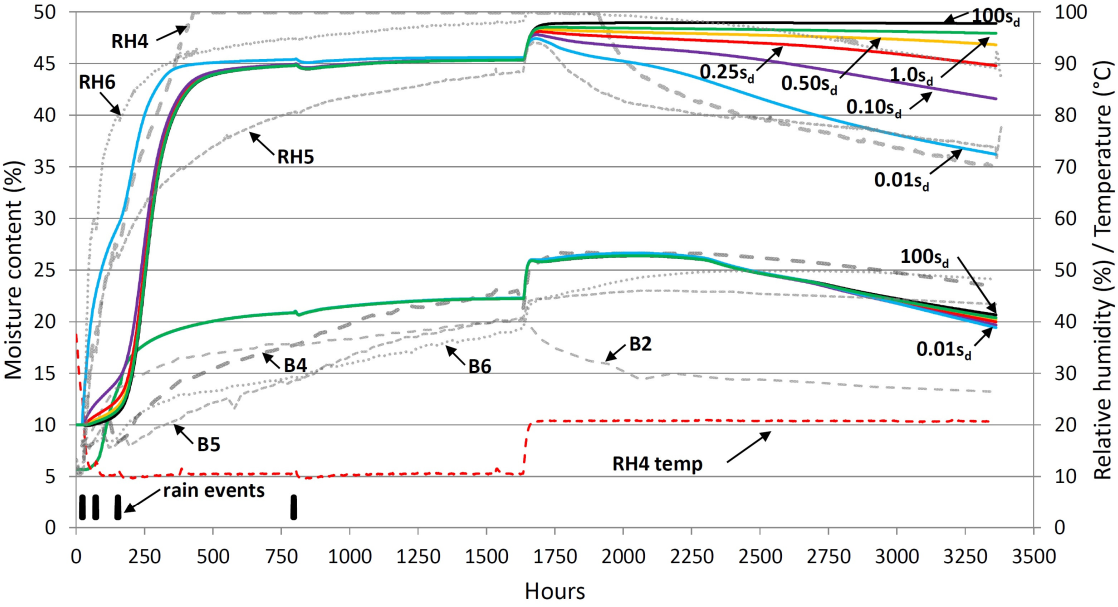

Figure 17. Effect of SVB vapor resistance; multiples of provided/presumed s_d-values, i.e., $1.0s_d$ = values in Appendix B.

In the current simulations, varying the SVB vapor resistance shows a relatively insignificant effect on beam-end drying. It supports the observation in [30] that the beam end shows no clear effect or only minor effect changing from polyethylene vapor barrier to SVB.

5. Discussion

5.1. Numerical Model Issues

Applying sudden rain flux of the magnitude of rapidly wetting the masonry to capillary saturation was found to be leading to some numerical instability. Primarily, the rain is modeled as a step function. Even though the step is given continuous second-derivative smoothing over 60 s, the numerical simulation struggles with the abruptness and magnitude of the rain load, especially when the exterior surface is relatively dry prior to the rain. Several aspects were found to have an impact on this situation.

During establishment of the model, it was discovered that the numerical stability was impacted by the retention curve, with sharp jumps giving more numerical instability than smooth retention curves. Similarly, Gutland et al. [28] reported numerical issues if the retention curve was to be modeled as a step function (the most extreme case of sharp retention curve), in the hygrothermal simulation software DELPHIN.

Janssen et al. [49] addressed oscillations observed at the toe of the moisture front, where oscillation magnitude was found to be dependent on initial moisture content and mesh discretization. They concluded that such oscillation had a limited effect on the overall result over time. Furthermore, they argued that with natural climate exposure one will rarely experience such sharp moisture fronts, making such simulations even less affected by this issue. The findings of Janssen et al. are similar to observations during the current study, although the issue has not been explicitly studied. However, oscillations localized somewhere along the moisture front toe (2D), sometimes severe, are observed. Nevertheless, the simulation quickly becomes corrected, erasing the trace of the oscillation in a relatively short time span (a few hours), compared to the overall duration of the simulation case. Still, numerical instability may be caused by such oscillation, leading to situations where the numerical iteration does not converge well.

COMSOL will, in situations where the iterative numerical solution does not converge and satisfy the tolerance criteria, try smaller and smaller timesteps. With repeated no convergence, the timesteps become untenably small.

It was found that, in some cases, a couple of measures could improve numerical solving (prevent or rein in small timesteps). The model can be relaxed with regard to the rain load when numerical convergence becomes poor (small timesteps) during absorption from rain events. This involves the rain load being relaxed linearly when at times the convergence timesteps become small, e.g., <0.02 s, so that 0.002 s timesteps only have a 1/10 of the rain load. Similarly, the masonry absorption-capacity can be relaxed linearly for timesteps, e.g., <0.1 s. These two relaxations do not occur simultaneously, with the second only applying when the exterior surface moisture content becomes close to saturation. Additionally, the rain flux can be modeled as linearly diminishing over a capillary pressure range, e.g., 1351 Pa > p_c > 13.5 Pa (0.99999 < ϕ < 0.9999999 at 20 °C), which is well below the overall moisture retention interval of capillary pressure for brick and mortar. These two measures with the aforementioned values were implemented in the simulations of the present study.

The numerical instability is believed to be caused by either or both the sharp moisture front gradient, creating oscillation with under- and overshooting at the moisture front toe, and the possible overshooting of the saturated moisture content from one timestep to the next, creating difficulties with numerical handling. This is also influenced by interaction between brick and mortar when they have very different capillary conductivities.

5.2. Capillary Model Evaluation

To assess the rain absorption of the model, a simple one-brick geometry was simulated with exposure to the rain for two hours through the brick face. From the simulation with the default hydraulic-conductivity curve a result of A_w = 0.194 kg/(m^{2}s$^{1/2}$) was calculated. This value is considered reasonably close to the measured absorption coefficient A_w = 0.188 kg/(m^{2}s$^{1/2}$), which was used as input to generate the capillary-conductivity curve applied in the model. For comparison, the max-setup (Section 4.2) provided A_w = 0.182 kg/($m^2s^{1/2}$) and the min-setup gave A_w = 0.174 kg/($m^2s^{1/2}$). Whereas the min-setup is deemed to behave logically, the max-setup gave surprisingly low value and seemed to attract some more numerical instability, possibly causing it to underestimate the absorption rate. Overall, the values indicated that the model approaches rain absorption as severely as free liquid absorption in an absorption experiment. Similarly, normal and lumped mortar properties, respectively, resulted in A_w = 0.023 kg/($m^2s^{1/2}$) and A_w = 0.22 kg/($m^2s^{1/2}$), fairly close to the 0.025 and 0.25 kg/($m^2s^{1/2}$), respectively, applied as input to generate the capillary conductivity.

Although the simulated A_w-values came close to the measured/intended values, the correctness of the hydraulic-conductivity curves is not thereby implied. For instance, Janssen [50] showed the same capillary-absorption results could be produced from different conductivity curves, including having variation in the conductivity at capillary saturation. To further evaluate accuracy, laboratory measurements of moisture front profiles would be needed for comparison to profiles from simulations. Such profiles are furthermore influenced by the retention curve which is unknown for the specific brick.

5.3. Material Properties and Model Uncertainties

The simulations show some significant deviations to the experiment results. Especially the RH sensors RH4 and RH5 show a drying trend that has not been replicated, nor attempted to be replicated, within the current study and model framework. This is partly due to the conservative approach of the simulation study, which likely overestimates the moisture uptake of the masonry. Nevertheless, uncertainty with both material properties and conservative boundary conditions impacts overestimation of moisture content. To elaborate on this, possible explanations for the observed deviations can be:

- There might be less overall rain uptake in the masonry, due to runoff, in combination with "leaky" joint interfaces enabling leak-like intrusions (infiltrations) through the masonry. This would enable the RH sensor to still show rapid response to rain, while the masonry overall would store less moisture needing to be dried out inwards through the SVB; this, plausibly in combination with interface resistances, lower acting capillary conductivities, or higher vapor diffusivities for the rest of the masonry;
- The exterior finish of the masonry having been brushed with heavily wetted mortar [30] could have closed the surface pores of the bricks, or created a surface coating, that reduces moisture absorption of the bricks;
- The interior insulation structure and mounting of the SVB in the experiment may have been less air-tight than presumed in the simulation model.

Furthermore, the drying rate of the beam end at the end of the warm period is larger in the 2D simulation than indicated in the experiment. As seen in Section 4.7, a 3D simulation shows a much more severe situation for the beam end. This result differs from the findings of [47,48], which indicated that 2D simulations were able to replicate measured results very well, with only small differences seen between 2D and 3D simulations. A reason for why these results differ is likely due to the differences in scenario, with the present study covering severe rain wetting of bare brick masonry, whereas the other studies involve lower rain severity in combination with external render and thicker masonry, including applying layered masonry models instead of modeling all mortar joints.

Regarding the SVB modeling, there is also some uncertainty. Unknown intermediate vapor resistance values for the SVB and possible, but unknown, directional dependence, rendered the modeling difficult and uncertain (see Appendix B). It is plausible that the SVB has a lower vapor resistance than what was modeled in certain RH ranges. To include SVB functionality more confidently in hygrothermal simulation models, there is a need for documentation of SVBs that provides more information and considerably higher resolution in s_d-values over the RH-range than what were available.

5.4. Conservative Modeling Philosophy

When conducting hygrothermal simulations for comparison to experiment results, one can question the intended purpose. That is, should the simulation aim at replicating specific results with low error of deviation or should it provide a conservative result that with a safety margin envelopes experiment results? This becomes an important question when acknowledging that the experiment results show a large span in behavior; in fact, behaviors differing so much that one could believe they were stemming from differently constructed masonry walls. However, it mainly confirms the diversity or heterogeneity of masonry regarding moisture transport, especially relevant for bare external masonry façades exposed to driving rain. Replicating specific results from experiments might, therefore, be unrealistic. This corresponds with; that heat, air, and moisture transport models (HAM models) have been attributed with providing good results in problems where the aim is to reproduce patterns [51].

Whether insurance of conservative results should be sought is not often addressed or pondered (we here exclude such discussions in topics on numerical methods and numerical solving). The "question of conservative" is more commonly discussed regarding selection of a moisture reference year or the use of damage indexes, e.g., mold or frost risk models. For instance, the European standard EN 15026 [52] states that a moisture reference year should reflect the most severe conditions likely to occur every 10 years. A 10-year return period has been deemed appropriate, intending that it allows moisture accumulated in "a bad year" to dry out in subsequent years [53]. Regarding mold models, Johansson et al. [54] suggests predictions should have a safety margin, i.e., the models should be conservative; although, the safety margin should not be excessive, due to the extra costs that would entail. With humidity loads often being the cause of building envelope deterioration and limited service-life, Kalamees [55] states that the common practice of neglecting safety factors in hygrothermal design deserves some criticism. Hens [56] harshly criticizes the practice of hygrothermal modeling as modeling fiction. That is, geometry, material properties, climate exposure, contact conditions, and initial conditions are not well known; nevertheless, they are modeled as well defined in deterministic models. Models should address probability and risk, not only be able to model very specific cases of extremely simplistic building parts [56]. An emerging discipline of probabilistic hygrothermal simulation-based risk assessment [36,57,58] has, to some extent, met this call for interior insulated masonry by combining hygrothermal simulation with Monte Carlo simulation. These studies assess the probabilistic sensitivity occurring from input values (e.g., properties and boundary condition coefficients) described with probability distributions. However, hygrothermal-simulation modeling choices or approaches, within the framework of probabilistic risk assessment of degrees of model reliability, are not particularly addressed. That is, less discussed is how to ensure conservative model design, or model design which does not fail to reveal conflict with the initiation or serviceability limit state. The initiation limit state is defined by ISO 13823 as "*state that corresponds to the initiation of significant deterioration of a component of the structure*" [59]. Implementation of serviceability limit state (SLS) analysis following ISO 13823 is discussed by Lacasse and Morelli [60]; herein, with focus on climate-exposure input and hygrothermal-simulation results for use in damage indexes (RHT index) in a comparative capacity. One modeling aspect is addressed by including different degrees of moisture deposition on a sill plate in a stucco-clad wood-frame wall to illustrate impact on the RHT index. Nevertheless, the modeling aspect is not particularly discussed in relation to the SLS analysis. They conclude the hygrothermal SLS approach has merit, albeit not yet fully explored [60]. As another example, rain infiltration in brick-veneer walls has, to some extent, been investigated and discussed in terms of modeling choices [13,24,61,62]. Similar insight is, however, limited in regard to historic masonry [61]. However, two studies should be mentioned. Simplifications of modeling masonry as a homogenous brick layer (1D) instead of a brick–mortar composite (2D), with and without interface resistances, were investigated by Vereecken and Roels [21]. Their study insightfully demonstrated the parts both brick and mortar played in moisture transport and distribution. Moisture transport along brick–mortar interfaces were not included. That, however, was addressed by Gutland et al. [28] who provided a modeling methodology for increased moisture transport along the brick–mortar interface and demonstrated its functionality and performance. However, these studies were rather limited in geometric extent, focusing on interaction between a few bricks and joints, and did not address performance of interior insulation retrofit in this regard. Thus, more insight is needed into whether models represent correct transfer mechanisms. The term transfer mechanisms is taken from ISO 13823 [59,63].

While the current study does not address probability distributions and probabilistic sensitivity from material properties, contact conditions, or initial conditions, the simulations have been established with an attempted conservative approach of rainwater absorption. This has been apporached by ensuring the maximum amount of rainwater absorption that material properties of brick and mortar allow for, including accounting for increased absorption of the brick–mortar interface. Nevertheless, this was not sufficient to recreate the rapid RH-response (all sensors) and the high RH levels (RH4) on the inside of the masonry during the cold period seen in the experiments. Including a "leaky" joint to resemble an infiltration leak was necessary to approach conservative RH-response results, whereas a 3D model was found necessary to provide slow dry-out of beam ends and conservative results during the warm period. Scrutiny regarding results reading position compared to sensor extents has also been shown to be useful. This should be a call for a discussion regarding how such, or similar, masonry structures should be modeled to uphold confidence of result conservativeness.

6. Conclusions

The study applies a conservative 2D simulation model to investigate and demonstrate the impact of uncertainty and modeling choices, with the simulation results compared to results of an experiment for a check of realism. The simulation model is very conservative in the aspect of allowing high rain absorption and, consequently, high moisture content in the wall. This approach is seen to underestimate the water transport of "leaky" joints. Including "leaky" joints with substantially higher moisture transport in the model is shown to produce RH response in line with the more severe laboratory results at the masonry interior surface. At the same time, the 2D model underestimates the long drying out times of the beam end. When applying a 3D model for comparison, a substantially higher moisture content and longer dry-out time is predicted for the beam end. Nevertheless, the conservative approach likely becomes too severe, failing to replicate the distinct drying trend seen in two of the RH-sensor data on the masonry interior surface. It is believed several factors, such as rain-absorption effectiveness, capillary conductivities and interface resistances in the masonry, SVB vapor resistance, and non-homogeneous material properties, affect the situation simultaneously, making the experiment drying trend less severe than the results of the basis simulation. This highlights a question of how to model correct moisture-transfer mechanism to uphold model confidence. This, especially, applies to bare brick masonry exposed to severe rain, where the rain absorption may follow infiltration pathways.

The conclusion is summarized as follows:

- Uncertainty in hydraulic conductivity curves for brick and mortar are clearly impacting results, with a large impact on response of RH sensors to rain events, and on the dry-out of beam ends. Large uncertainty regarding the mortar capillary absorption coefficient was likely the dominant cause;
- Altering the retention curves, including subsequent impact on hydraulic-conductivity curves, had moderate to minor impact on the results. However, with the model operating around the highest RH range that the RH readings could detect at the reading location, and with some uncertainty regarding numerical solving, the true impact of altering the retention curves became obscured;

- RH results are sensitive to the results reading position in the model when comparing simulation to experiment, for the experiment sensor located interior to the masonry surface at the masonry–insulation interface. Similar is the case for the beam-end moisture sensor, regarding at what depth into the modeled wood readings are conducted. Consideration should be given to sensor location and behavior in experiments when choosing reading position and when evaluating simulation results;
- Modeling wooden beam end as anisotropic instead of isotropic does influence simulation results;
- Lumping moisture transport along the brick–mortar interface with mortar properties does show more rapid RH response and slightly increased RH at interior masonry surface. It, furthermore, increases moisture content at the beam end compared to results with normal mortar properties. However, the effect is not large enough to ensure the rapid RH response seen of RH sensors to rain events;
- Inclusion of a "leaky" mortar joint, representing considerably faster moisture permeation from rain events along the brick–mortar interface provides results more in line with the rapid RH-sensor response seen in experiment. The inclusion of a "leaky" mortar joint is supported by experiment observations;
- Conservative beam-end moisture content is neither achieved with normal mortar properties nor with lumped properties in 2D simulation. In contrast, a 3D simulation is seen to give much higher moisture content in the beam end and longer dry-out times providing highly conservative results;
- Vapor resistance of SVB has low influence on results during the cold exterior climate. With warm climate, the dry-out towards the interior are highly dependent on SVB vapor resistance. If further product development could achieve lower vapor resistance of a SVB product for high RH environments, this could provide significant benefits with regard to dry-out performance;
- Vapor resistance of SVB has almost insignificant influence on beam-end dry-out under the studied conditions;
- The (conservative) modeling approach clearly overestimated moisture content in the masonry, and within the conservative model framework the distinct dry-out trend seen in two of the three experiment wall segments investigated was not replicated, the model, thus, giving indication of being too conservative in some respects.

Author Contributions: Conceptualization, J.I.K.; methodology, J.I.K.; software, J.I.K.; validation, J.I.K.; formal analysis, J.I.K.; investigation, J.I.K.; data curation, J.I.K.; writing—original draft preparation, J.I.K.; writing—review and editing, J.I.K., T.K. and S.G.; visualization, J.I.K.; supervision, T.K. and S.G. All authors have read and agreed to the published version of the manuscript.

Funding: The authors gratefully acknowledge the financial support by the Research Council of Norway and several partners through the Centre for Research-based Innovation "Klima 2050" (grant no. 237859) (www.klima2050.no).

Data Availability Statement: Data sharing is not applicable to this article.

Acknowledgments: Lab engineer Ole Aunrønning is acknowledged for an invaluable contribution with wall and equipment assembly, material property testing, and measurement monitoring.

Conflicts of Interest: The authors declare no conflict of interest.

Appendix A Hygrothermal Formulas and Material Properties

The retention curve is given by Equation (A1) which is a multimodal version of an expression proposed by Carmeliet and Roels [64]. For more details, see [17].

$$w = w_{\lim} \underbrace{\left[\exp\left(-\frac{P_c}{\rho_w R_w T}\right)\right]^{n_{w,0}}}_{=\phi} + \left(w_{cap} - w_{\lim}\right) \sum_{i=1}^{N=4} \left(l_{w,i} \left[1 + \left(c_{w,i} P_c\right)^{n_{w,i}}\right]^{\left(\frac{1-n_{w,i}}{n_{w,i}}\right)} \right) \quad \text{(A1)}$$

where $w_{\lim}$ would be the limiting, critical water content between the hygroscopic and over-hygroscopic region; however, the actual $w_{\lim}$-value could be expected to deviate from the critical moisture content, being a more arbitrary fitting parameter [64]. w_{cap} moisture content at capillary saturation, P_c capillary pressure, ρ_w density of water, R_w specific gas constant for water vapor, $n_{w,0}$ fitting exponent, $l_{w,i}$ weighing coefficient equal to the share of pores associated with the corresponding inflection point in cumulative pore-size distribution, i.e., $\Sigma l_{w,i} = 1$, $c_{w,i}$ inverse of P_c at inflection point, and $n_{w,i}$ fitting exponent. Material properties are provided in Table A1 and coefficients in Table A2.

The vapor diffusivity is taken as Equation (A2) which is a combination of Schirmer's equation [65] and the scaling expression of the serial–parallel pore model [66] accounting for liquid moisture content. The vapor-resistance coefficient μ_{dry} correlates the permeability to a porous material, with μ_{dry} determined by dry cup measurements.

$$\delta_v = \frac{1}{R_w T} \frac{2.306 \cdot 10^{-5}}{\mu_{dry}} \left(\frac{P_0}{P_a}\right) \left(\frac{T}{T_0}\right)^{1.81} \frac{\left(1 - \frac{w}{w_{sat}}\right)}{p + \left(1 - \frac{w}{w_{sat}}\right)^2 (1-p)} \quad \text{(A2)}$$

with P_0 and P_a, respectively, the standard and acting atmospheric pressure, T_0 = 273.15 K, p is the volumetric fraction that is parallel pore domain [18], p has simply been set to p = 0.497 [8,44] for all materials, although p is material-dependent [66], and using a constant for p has been disputed [18].

The moisture-dependent thermal conductivity is expressed as Equation (A3). A second-order correction for moisture content is included to better represent insulation materials. Use of Equation (A3) is a necessary simplification due to lack of conductivity measurements. In reality, a highly non-linear relationship to moisture content may exist, which is better represented with, for instance, the formulas in [67]. Coefficients and background for Equation (A3) are listed in Table A3.

$$\lambda_{eff} = \lambda + b_{w1} \frac{w}{w_{sat}} + b_{w2} \left(\frac{w}{w_{sat}}\right)^2 \quad \text{(A3)}$$

where λ [W/(m·K)] is dry thermal conductivity, and b_{w1} and b_{w2} [W/(m·K)] correction coefficients for moisture content.

From testing in our laboratory, we have found A_w-values for mortar joints when including absorption effect from the brick–mortar interfaces parallel to absorption direction to be in the range 0.14–0.44 kg/(m^{2}s$^{1/2}$). Although these values have a wide span, they can be said to be closer to the brick A_w-value of 0.188 kg/(m^{2}s$^{1/2}$) than the mortar A_w-value (0.01–0.04 kg/(m^{2}s$^{1/2}$) [30]). The highest value in the span might be unrealistic for the wall that we are simulating since measures were made to achieve a rather good-quality brick–mortar interface, more similar to test samples representing the lower range of the span. However, these samples were constructed with similar, but slightly different, bricks and mortar, thereby, introducing uncertainty. As a guesstimate, we chose to apply an A_w-value of 0.25 kg/(m^{2}s$^{1/2}$), a factor of 10 higher than the normal absorption value, for mortar joints parallel to absorption direction during rain events. Outside of rain events, the intermediate A_w-value of mortar 0.025 kg/(m^{2}s$^{1/2}$) is applied to calculate hydraulic conductivity.

Table A1. Applied material properties.

Material	w_{sat} **[kg/m^3]**	w_{cap} **[kg/m^3]**	$w_{\lim}$ **[kg/m^3]**	**A$_w$ [kg/(m^{2}s$^{1/2}$)]**	μ_{dry} **[-]**	λ **[W/(m·K)]**	c_p **[J/(kg·K)]**	ρ **[kg/m^3]**
Brick high IRA	310.8 [a]	255.74 [a]	2.5 [e]	0.188 [a]	13.36 [a]	0.45 [c]	1000 [c]	1723 [a]
LC mortar	294 [a]	258.79 [a]	18 [e]	0.025 [a]	18.81 [a]	0.82 [c]	1000 [c]	1806 [a]
Gypsum	720 [d]	353 [d]	6 [e]	0.0397 [d]	6 [b]	0.25 [b]	850 [d]	720 [b]
Spruce longitudinal	600	600 [d]	60 [e]	0.00688 [d]	4.213 [d]	0.23 [d]	1500	455 [d]
Spruce radial/tangential	600	600 [d]	60 [e]	0.000933 [d]	8.426 [f]	0.09 [d]	1500	455 [d]
Mineral wool	992 [d]	232 [d]	0.61 [e]	-	1.3 [d]	0.034 [b]	850 [d]	17 [b]
Asphalt sill gasket	-	-	-	-	-	0.553	1500	1200

[a] measured, refer [30], w$_{sat}$ a guestimate based on measurements. [b] product declaration. [c] in accordance with EN 1745 [68]. [d] WUFI material database [46]. [e] curve fitting to sorption/retention curves. [f] arbitrary choice taking into account radial and tangential directions, and occurrence of cracks.

Table A2. Coefficients for retention curves, expression (A1).

Material	$n_{w,0}$	$l_{w,1}$	$l_{w,2}$	$l_{w,3}$	$l_{w,4}$	$c_{w,1}$	$c_{w,2}$	$c_{w,3}$	$c_{w,4}$	$n_{w,1}$	$n_{w,2}$	$n_{w,3}$	$n_{w,4}$
Brick high IRA [a]	0.7	0.12	0.66	0.22	0	8.67×10^{-7}	6.72×10^{-6}	4.00×10^{-5}	-	4	4	5	-
LC mortar [b]	0.4	0.07	0.55	0.36	0.02	7.41×10^{-8}	4.20×10^{-7}	1.13×10^{-6}	2.00×10^{-5}	3	5	4	2
Gypsum [c]	1.2	0.11	0.44	0.35	0.10	1.81×10^{-7}	2.24×10^{-6}	5.52×10^{-6}	1.48×10^{-5}	2.6	6	4	1.8
Spruce [c]	0.6	0.10	0.50	0.30	0.10	7.02×10^{-8}	1.03×10^{-6}	3.43×10^{-6}	6.18×10^{-5}	2.2	5	1.8	1.6
Mineral wool [c]	4	0.13	0.51	0.36	0	2.06×10^{-6}	1.48×10^{-5}	7.40×10^{-5}	-	5	2.8	1.8	-

[a] curve fitting to a retention curve trend of a presumed similar brick, accounting for the measured sorption curve. [b] curve fitting to retention curve trend, of a presumed representative mortar, that is, shifted on the capillary pressure axis to fit with the measured sorption curve. [c] curve fitting to retention curves taken from WUFI material database [46].

Table A3. Conductivity correction coefficients.

Material	λ_{sat} **[W/(m·K)]** [a]	b_{w1} **[W/(m·K)]**	b_{w2} **[W/(m·K)]**
Brick high IRA	1.35 [b]	0.9	0
LC mortar	1.5 [b]	0.68	0
Gypsum	1.16 [b]	0.91	0
Spruce	0.7097 [b]	0.4797	0
Mineral wool	0.5975 [c]	0.0159	0.5476
Asphalt sill gasket	0.553	0	0

[a] effective conductivity at saturation. [b] inspired by WUFI material database [46]. [c] conductivity of water at 293.15 K.

Appendix B Modeling of the SVB

The SVB is modeled as a material with a notional thickness of 10 mm. Heat capacity and conductivity are scaled with factor 1/20 and 20, respectively, to account for the ratio of notional thickness to actual thickness. Sorption is set equal to mineral wool without conducting scaling, in lack of better estimates.

Vapor-diffusion resistance is modelled as dependent on RH on each side of the SVB. Table A4 provides a matrix of sd-values found from manual curve fitting to a limited set of measured values (underlined in Table A4) provided by a technical approval document for the SVB. The matrix is rendered symmetric, i.e., assuming s_d-values are independent of SVB orientation, due to lack of information or data specifying otherwise. However, directional dependence of SVBs or smart vapor retarders (SVRs) is common, e.g., [69], and, consequently, to account for directional dependence such a matrix should be non-symmetric. For visual perception, resultant curves are provided in Figure A1. One perceived outlier (s_d = 3 m at 75/25% RH) was excluded since it did not fit with the other data; however, it might be plausible that s_d = 8 m at 75/33% RH could be an outlier instead, or also, which perceivably would radically lower s_d-values in the affected region.

Table A4. SVB s_d-values (m) as function of RH at both sides of the barrier. Bold, underlined numbers are measured values originating from the technical approval document of the SVB, with one outlier (presumed wrong) placed in parenthesis.

RH\RH	**0**	**11**	**25**	**30**	**33**	**40**	**45**	**50**	**55**	**60**	**65**	**70**	**75**	**80**	**85**	**90**	**95**	**100**
0	107	104	**100**	96.8	93	82	73	63	52	42	32	22	**14**	8.6	4.4	1.4	0.43	0.26
11	104	101	97.5	94	90	79.6	70	60	50	40	30	20.5	**12**	7	3.6	1.15	**0.36**	0.22
25	**100**	97.5	92	89	86	76	66.5	57	46	37	28	19	10 (**3**)	5.4	2.6	0.82	0.29	0.174
30	96.8	94	89	86	83	73	63	53	43	34	26	17	9	4.9	1.9	0.7	0.265	0.158
33	93	90	86	83	79	68	58	**48**	38.5	30	22	14.8	**8**	3.9	1.45	0.62	0.25	0.148
40	82	79.6	76	73	68	52	40	30	23	17	11.5	7.5	4.1	2	0.92	0.46	0.22	0.127
45	73	70	66.5	63	58	40	28.5	21	15	10.5	7	4.2	2.4	1.2	0.7	0.37	0.2	0.114
50	63	60	57	53	**48**	30	21	15	10	6.9	4.4	2.65	**1.4**	0.88	0.54	0.3	**0.18**	0.102
55	52	50	46	43	38.5	23	15	10	6.8	4.8	3.1	1.7	0.96	0.65	0.42	0.25	0.16	0.091
60	42	40	37	34	30	17	10.5	6.9	4.8	3.2	2.1	1.21	0.74	0.51	0.32	0.21	0.14	0.08
65	32	30	28	26	22	11.5	7	4.4	3.1	2.1	1.42	0.9	0.58	0.4	0.26	0.18	0.12	0.07
70	22	20.5	19	17	14.8	7.5	4.2	2.65	1.7	1.21	0.9	0.65	0.45	0.31	0.22	0.155	0.105	0.06
75	**14**	**12**	10 (**3**)	9	**8**	4.1	2.4	**1.4**	0.96	0.74	0.58	0.45	0.34	0.24	**0.18**	0.13	0.09	0.052
80	8.6	7	5.4	4.9	3.9	2	1.2	0.88	0.65	0.51	0.4	0.31	0.24	0.19	0.145	0.105	0.075	0.045
85	4.4	3.6	2.6	1.9	1.45	0.92	0.7	0.54	0.42	0.32	0.26	0.22	0.18	0.145	0.115	0.085	0.06	0.04
90	1.4	1.15	0.82	0.7	0.62	0.46	0.37	0.3	0.25	0.21	0.18	0.155	0.13	0.105	0.085	0.065	0.05	0.035
95	0.43	**0.36**	0.29	0.265	0.25	0.22	0.2	**0.18**	0.16	0.14	0.12	0.105	0.09	0.075	0.06	0.05	0.04	**0.03**
100	0.26	0.22	0.174	0.158	0.148	0.127	0.114	0.102	0.091	0.08	0.07	0.06	0.052	0.045	0.04	0.035	**0.03**	0.025

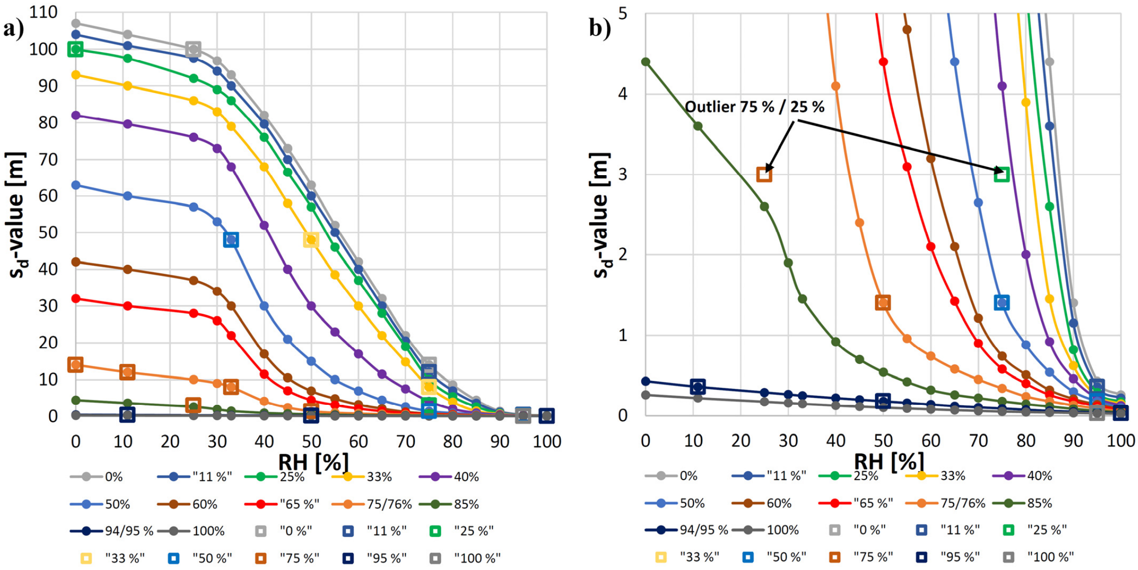

Figure A1. SVB s_d-value curves each plotted with a constant RH level on one side with varying RH on the other side; (**a**) full range on *y*-axis and (**b**) reduced range on *y*-axis. Values from Table A4 marked with dots. Measured values from technical approval document marked with squares.

Appendix C Model Algorithm Validation

Presentation of benchmark results is provided to support confidence in the hygrothermal model that is applied in the current article. The Hamstad benchmark 4 [70] has been chosen since this implements severe climate exposure, including moisture condensation, alternating rapid wetting and drying, in addition to moisture redistribution between two materials [44]. The benchmark is designed as a 1D benchmark, i.e., the heat and moisture transport are 1D directional. However, the benchmark has been run in COMSOL in 3D to verify that the model can handle 2D and 3D functionality. Still, it does not validate 3D directional heat and moisture transport per se. Full description of the benchmark can be found in [44,70] and will not be repeated.

Selected results of the benchmark validation are provided in Figure A2. The selection considers what are of particular interest for the current study; that is, validating handling of moisture front from severe rain absorption (see Figure A2e) and moisture redistribution (see Figure A2f,g).

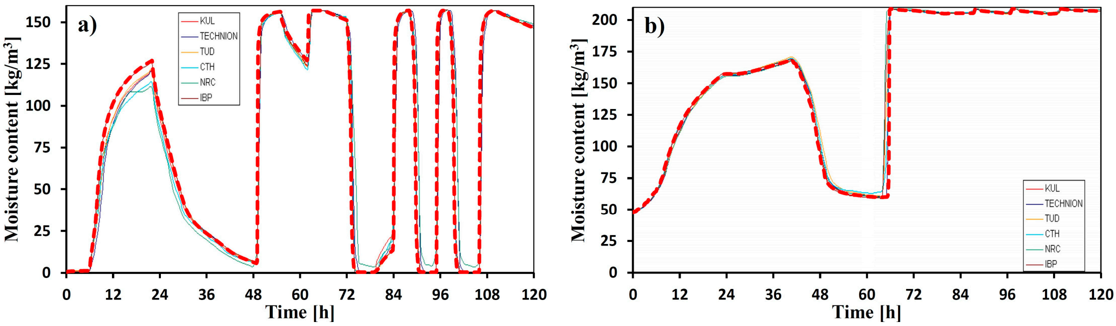

Figure A2. *Cont.*

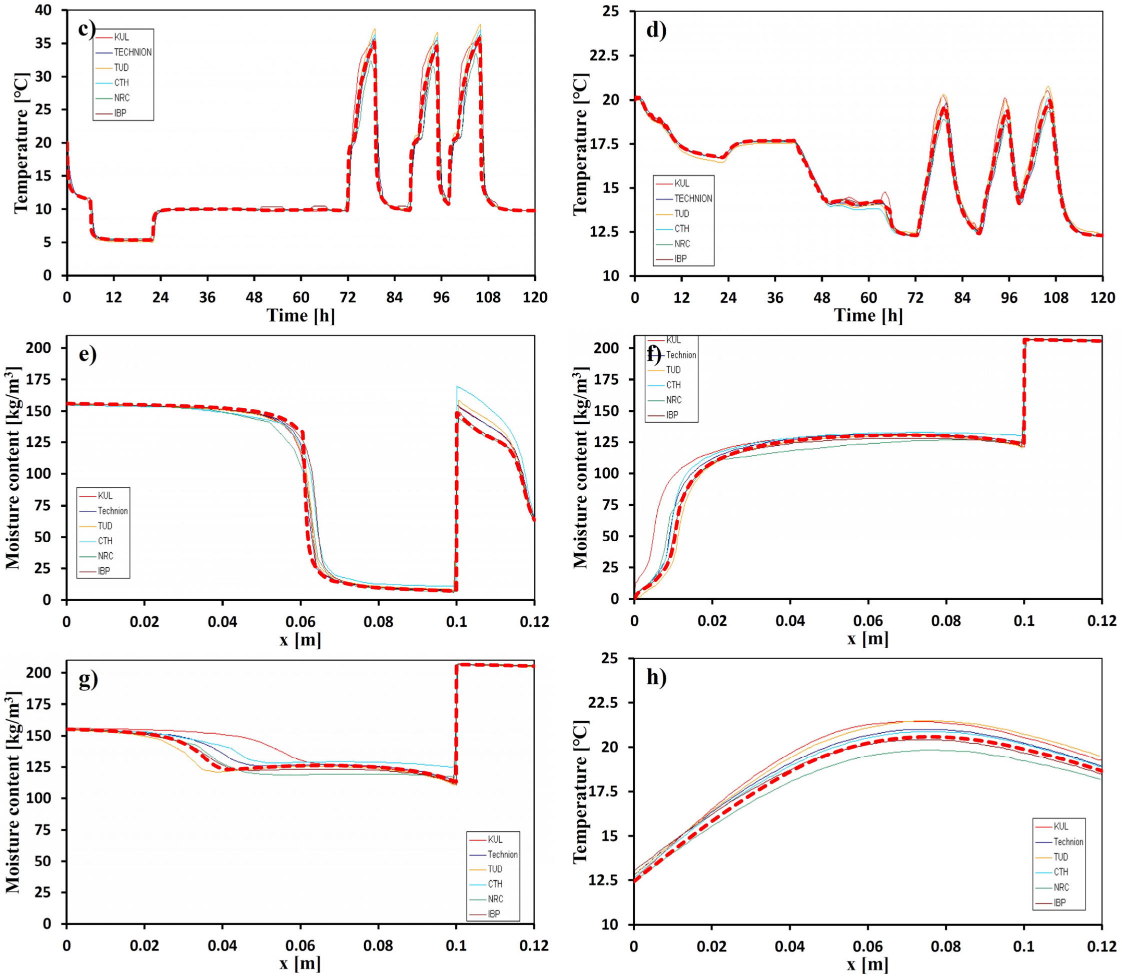

Figure A2. Model validation against Hamstad benchmark 4. Results, dashed red lines, are superimposed graphs from [70]. Moisture content (**a**) exterior surface, (**b**) interior surface, temperature (**c**) exterior surface, (**d**) interior surface, moisture profile at (**e**) 54 h, (**f**) 78 h, (**g**) 96 h, temperature profile at (**h**) 96 h.

References

1. Odgaard, T.; Bjarløv, S.P.; Rode, C. Interior insulation—Characterisation of the historic, solid masonry building segment and analysis of the heat saving potential by 1d, 2d, and 3d simulation. *Energy Build.* **2018**, *162*, 1–11. [CrossRef]
2. Harrestrup, M.; Svendsen, S. Full-scale test of an old heritage multi-storey building undergoing energy retrofitting with focus on internal insulation and moisture. *Build. Environ.* **2015**, *85*, 123–133. [CrossRef]
3. Harrestrup, M.; Svendsen, S. Internal insulation applied in heritage multi-storey buildings with wooden beams embedded in solid masonry brick façades. *Build. Environ.* **2016**, *99*, 59–72. [CrossRef]
4. Zhou, X.; Carmeliet, J.; Derome, D. Influence of envelope properties on interior insulation solutions for masonry walls. *Build. Environ.* **2018**, *135*, 246–256. [CrossRef]
5. Vereecken, E.; Roels, S. Wooden beam ends in combination with interior insulation: An experimental study on the impact of convective moisture transport. *Build. Environ.* **2019**, *148*, 524–534. [CrossRef]
6. Jensen, N.F.; Bjarløv, S.P.; Rode, C.; Møller, E.B. Hygrothermal assessment of four insulation systems for interior retrofitting of solid masonry walls through calibrated numerical simulations. *Build. Environ.* **2020**, *180*, 107031. [CrossRef]

7. Martel, T.; Rirsch, E.; Simmonds, A.; Walker, C. The monitoring of wall moisture in a property retrofitted with Internal Wall Insulation. *Case Stud. Constr. Mater.* **2021**, *14*, e00520. [CrossRef]
8. Zhou, X.; Derome, D.; Carmeliet, J. Analysis of moisture risk in internally insulated masonry walls. *Build. Environ.* **2022**, *212*, 108734. [CrossRef]
9. Johansson, P.; Wahlgren, P. Deterioration in brick buildings: Hygrothermal performance and measures to save them. In Proceedings of the 12th Nordic Symposium on Building Physics (NSB 2020), Tallinn, Estonia, 6–9 September 2020.
10. Huerto-Cardenas, H.E.; Leonforte, F.; Aste, N.; Del Pero, C.; Evola, G.; Costanzo, V.; Lucchi, E. Validation of dynamic hygrothermal simulation models for historical buildings: State of the art, research challenges and recommendations. *Build. Environ.* **2020**, *180*, 107081. [CrossRef]
11. Martín-Garín, A.; Millán-García, J.A.; Terés-Zubiaga, J.; Oregi, X.; Rodríguez-Vidal, I.; Baïri, A. Improving Energy Performance of Historic Buildings through Hygrothermal Assessment of the Envelope. *Buildings* **2021**, *11*, 410. [CrossRef]
12. Blocken, B.; Derome, D.; Carmeliet, J. Rainwater runoff from building facades: A review. *Build. Environ.* **2013**, *60*, 339–361. [CrossRef]
13. Calle, K.; Coupillie, C.; Janssens, A.; Van Den Bossche, N. Implementation of rainwater infiltration measurements in hygrothermal modelling of non-insulated brick cavity walls. *J. Build. Phys.* **2019**, *43*, 477–502. [CrossRef]
14. Kubilay, A.; Zhou, X.; Derome, D.; Carmeliet, J. Moisture modeling and durability assessment of building envelopes—Recent advantages. In *Building Performance Simulation for Design and Operation*, 2nd ed.; Jan, L.M.H., Roberto, L., Eds.; Routledge: London, UK, 2019; pp. 270–314.
15. Ramirez, R.; Ghiassi, B.; Pineda, P.; Lourenço, P.B. Experimental characterization of moisture transport in brick masonry with natural hydraulic lime mortar. *Build. Environ.* **2021**, *205*, 108256. [CrossRef]
16. Scheffler, G. *Validation of Hygrothermal Material Modelling under Consideration of the Hysteresis of Moisture Storage*; Dresden University of Technology: Dresden, Germany, 2008.
17. Knarud, J.I.; Kvande, T.; Geving, S. Modelling hydraulic conductivity for porous building materials based on a prediction of capillary conductivity at capillary saturation. *Int. J. Heat Mass Transf.* **2022**, *186*, 122457. [CrossRef]
18. Scheffler, G.A.; Plagge, R. A whole range hygric material model: Modelling liquid and vapour transport properties in porous media. *Int. J. Heat Mass Transf.* **2010**, *53*, 286–296. [CrossRef]
19. Van Belleghem, M.; Steeman, M.; Janssen, H.; Janssens, A.; De Paepe, M. Validation of a coupled heat, vapour and liquid moisture transport model for porous materials implemented in CFD. *Build. Environ.* **2014**, *81*, 340–353. [CrossRef]
20. Derluyn, H.; Janssen, H.; Carmeliet, J. Influence of the nature of interfaces on the capillary transport in layered materials. *Constr. Build. Mater.* **2011**, *25*, 3685–3693. [CrossRef]
21. Vereecken, E.; Roels, S. Hygric performance of a massive masonry wall: How do the mortar joints influence the moisture flux? *Constr. Build. Mater.* **2013**, *41*, 697–707. [CrossRef]
22. Brocken, H.J.P. *Moisture Transport in Brick Masonry: The Grey Area between Bricks*; Technische Universiteit Eindhoven: Eindhoven, The Netherlands, 1998.
23. Zhou, X.; Desmarais, G.; Vontobel, P.; Carmeliet, J.; Derome, D. Masonry brick–cement mortar interface resistance to water transport determined with neutron radiography and numerical modeling. *J. Build. Phys.* **2020**, *44*, 251–271. [CrossRef]
24. Kahangi Shahreza, S.; Niklewski, J.; Molnár, M. Novel water penetration criterion for clay brick masonry claddings. *Constr. Build. Mater.* **2022**, *353*, 129109. [CrossRef]
25. Groot, C.J.W.P.; Gunneweg, J.T.M. The influence of materials characteristics and workmanship on rain penetration in historic fired clay brick masonry. *Heron* **2010**, *55*, 141–153.
26. Hens, H.S.L.C. The vapor diffusion resistance and air permeance of masonry and roofing systems. *Build. Environ.* **2006**, *41*, 745–755. [CrossRef]
27. Vereecken, E.; Van De Walle, W.; Roels, S. A novel and flexible test setup to measure the vapour diffusion resistance of building materials and wall components. In Proceedings of the 4th Central European Symposium on Building Physics (CESBP 2019), Prague, Czech Republic, 2–5 September 2019.
28. Gutland, M.; Bucking, S.; Santana Quintero, M. A methodology for hygrothermal modelling of imperfect masonry interfaces. *J. Build. Phys.* **2021**, *44*, 485–509. [CrossRef]
29. Johansson, P.; Geving, S.; Hagentoft, C.-E.; Jelle, B.P.; Rognvik, E.; Kalagasidis, A.S.; Time, B. Interior insulation retrofit of a historical brick wall using vacuum insulation panels: Hygrothermal numerical simulations and laboratory investigations. *Build. Environ.* **2014**, *79*, 31–45. [CrossRef]
30. Knarud, J.I.; Geving, S.; Kvande, T. Moisture performance of interior insulated brick wall segments subjected to wetting and drying—A laboratory investigation. *Build. Environ.* **2021**, *188*, 107488. [CrossRef]
31. Zhao, J.; Plagge, R. Characterization of hygrothermal properties of sandstones—Impact of anisotropy on their thermal and moisture behaviors. *Energy Build.* **2015**, *107*, 479–494. [CrossRef]
32. Feng, C.; Janssen, H. Hygric properties of porous building materials (VII): Full-range benchmark characterizations of three materials. *Build. Environ.* **2021**, *195*, 107727. [CrossRef]
33. Hansen, T.K.; Bjarløv, S.P.; Peuhkuri, R.H.; Harrestrup, M. Long term in situ measurements of hygrothermal conditions at critical points in four cases of internally insulated historic solid masonry walls. *Energy Build.* **2018**, *172*, 235–248. [CrossRef]

34. Andreotti, M.; Bottino-Leone, D.; Calzolari, M.; Davoli, P.; Dias Pereira, L.; Lucchi, E.; Troi, A. Applied Research of the Hygrothermal Behaviour of an Internally Insulated Historic Wall without Vapour Barrier: In Situ Measurements and Dynamic Simulations. *Energies* **2020**, *13*, 3362. [CrossRef]
35. Defraeye, T.; Blocken, B.; Carmeliet, J. Influence of uncertainty in heat–moisture transport properties on convective drying of porous materials by numerical modelling. *Chem. Eng. Res. Des.* **2013**, *91*, 36–42. [CrossRef]
36. Vereecken, E.; Van Gelder, L.; Janssen, H.; Roels, S. Interior insulation for wall retrofitting—A probabilistic analysis of energy savings and hygrothermal risks. *Energy Build.* **2015**, *89*, 231–244. [CrossRef]
37. De Mets, T.; Tilmans, A.; Loncour, X. Hygrothermal assessment of internal insulation systems of brick walls through numerical simulation and full-scale laboratory testing. *Energy Procedia* **2017**, *132*, 753–758. [CrossRef]
38. COMSOL Inc. *COMSOL Multiphysics*; COMSOL Inc.: Stockholm, Sweden, 2021.
39. Knarud, J.I.; Geving, S. Implementation and Benchmarking of a 3D Hygrothermal Model in the COMSOL Multiphysics Software. *Energy Procedia* **2015**, *78*, 3440–3445. [CrossRef]
40. Knarud, J.I.; Geving, S. Comparative study of hygrothermal simulations of a masonry wall. *Energy Procedia* **2017**, *132*, 771–776. [CrossRef]
41. Künzel, H.M. *Simultaneous Heat and Moisture Transport in Building Components*; Fraunhofer IRB-Verlag: Stuttgart, Germany, 1995.
42. Tariku, F.; Kumaran, K.; Fazio, P. Transient model for coupled heat, air and moisture transfer through multilayered porous media. *Int. J. Heat Mass Transf.* **2010**, *53*, 3035–3044. [CrossRef]
43. Tariku, F. *Whole Building Heat and Moisture Analysis*; Concordia University: Montreal, QU, Canada, 2008.
44. Hagentoft, C.-E.; Kalagasidis, A.S.; Adl-Zarrabi, B.; Roels, S.; Carmeliet, J.; Hens, H.; Grunewald, J.; Funk, M.; Becker, R.; Shamir, D. Assessment method of numerical prediction models for combined heat, air and moisture transfer in building components: Benchmarks for one-dimensional cases. *J. Therm. Envel. Build. Sci.* **2004**, *27*, 327–352. [CrossRef]
45. Tsilingiris, P.T. Thermophysical and transport properties of humid air at temperature range between 0 and 100 °C. *Energy Convers. Manag.* **2008**, *49*, 1098–1110. [CrossRef]
46. *Fraunhofer WUFI 2D 4.2*; Fraunhofer IBP: Stuttgar, Germany, 2019.
47. Ruisinger, U.; Kautsch, P. Comparison of hygrothermal 2D- and 3D-simulation results with measurements from a test house. *E3S Web Conf.* **2020**, *172*, 08004. [CrossRef]
48. Zhou, X.; Carmeliet, J.; Derome, D. Assessment of moisture risk of wooden beam embedded in internally insulated masonry walls with 2D and 3D models. *Build. Environ.* **2021**, *193*, 107460. [CrossRef]
49. Janssen, H.; Blocken, B.; Carmeliet, J. Conservative modelling of the moisture and heat transfer in building components under atmospheric excitation. *Int. J. Heat Mass Transf.* **2007**, *50*, 1128–1140. [CrossRef]
50. Janssen, H. Comment on Cabrera et al. A User-Friendly Tool to Characterize the Moisture Transfer in Porous Building Materials: FLoW1D. *Appl. Sci.* **2020**, *10*, 5090, *Appl. Sci.* **2022**, *12*, 1123.
51. Piaia, J.C.Z.; Cheriaf, M.; Rocha, J.C.; Mustelier, N.L. Measurements of water penetration and leakage in masonry wall: Experimental results and numerical simulation. *Build. Environ.* **2013**, *61*, 18–26. [CrossRef]
52. *NS-EN 15026*; Hygrothermal Performance of Building Components and Building Elements. Assessment of Moisture Transfer by Numerical Simulation. Norwegian Standards: Oslo, Norway, 2007.
53. Zhou, X.; Derome, D.; Carmeliet, J. Robust moisture reference year methodology for hygrothermal simulations. *Build. Environ.* **2016**, *110*, 23–35. [CrossRef]
54. Johansson, P.; Lång, L.; Capener, C.-M. How well do mould models predict mould growth in buildings, considering the end-user perspective? *J. Build. Eng.* **2021**, *40*, 102301. [CrossRef]
55. Kalamees, T. *Hygrothermal Criteria for Design and Simulation of Buildings*; Tallinn University of Technology: Tallinn, Estonia, 2006.
56. Hens, H.S. Modeling the heat, air, and moisture response of building envelopes: What material properties are needed, how trustful are the predictions? *J. ASTM Int.* **2007**, *4*, 1–11. [CrossRef]
57. Marincioni, V.; Marra, G.; Altamirano-Medina, H. Development of predictive models for the probabilistic moisture risk assessment of internal wall insulation. *Build. Environ.* **2018**, *137*, 257–267. [CrossRef]
58. Janssen, H.; Freudenberg, P.; Tijskens, A.; Hou, T. *Basic Probabilistic Analysis of Hygrothermal Performance of Interior Insulation*; KU Leuven: Leuven, Belgium, 2019; p. 108.
59. *ISO 13823*; General Principles on the Design of Structures for Durability. ISO: Geneva, Switzerland, 2008.
60. Lacasse, M.A.; Morelli, M. A Systematic Method of Assessing the Durability of Wood-Frame Wall Assemblies: Towards the Limit-States Design Approach. In Proceedings of the Thermal Performance of the Exterior Envelopes of Whole Buildings XIII International Conference, Clearwater, FL, USA, 4–8 December 2016; pp. 235–245.
61. Lacasse, M.A.; Van Den Bossche, N.; Van Linden, S.; Moore, T.V. A brief compendium of water entry results derived from laboratory tests of various types of wall assemblies. In Proceedings of the 4th Central European Symposium on Building Physics (CESBP 2019), Prague, Czech Republic, 2–5 September 2019.
62. Nath, S.; Dewsbury, M.; Künzel, H.; Watson, P. Mould Growth Risks for a Clay Masonry Veneer External Wall System in a Temperate Climate. *Atmosphere* **2022**, *13*, 1755. [CrossRef]
63. Lacasse, M.A.; Ge, H.; Hegel, M.; Jutras, R.; Laouadi, A.; Sturgeon, G.; Wells, J. *Guideline on Design for Durability of Building Envelopes*; National Research Council (NRC) of Canada: Ottawa, ON, Canada, 2018.

64. Carmeliet, J.; Roels, S. Determination of the Moisture Capacity of Porous Building Materials. *J. Therm. Envel. Build. Sci.* **2002**, *25*, 209–237. [CrossRef]
65. Schirmer, R. *Die Diffusionszahl von Wasserdampf-Luft-Gemischen und Die Verdampfungsgeschwindigkeit*; Springer: Berlin/Heidelberg, Germany, 1938; pp. 170–177.
66. Grunewald, J.; Häupl, P.; Bomberg, M. Towards an Engineering Model of Material Characteristics for Input to Ham Transport Simulations—Part 1: An Approach. *J. Therm. Envel. Build. Sci.* **2003**, *26*, 343–366. [CrossRef]
67. Ghanbarian, B.; Daigle, H. Thermal conductivity in porous media: Percolation-based effective-medium approximation. *Water Resour. Res.* **2016**, *52*, 295–314. [CrossRef]
68. *EN 1745*; Masonry and Masonry Products—Methods for Determining Thermal Properties. CEN: Brussels, Belgium, 2012.
69. Yoshinaga, M. Performance of smart vapor retarders under hot and humid summer conditions. *Build. Environ.* **2022**, *218*, 109163. [CrossRef]
70. Hagentoft, C.-E. HAMSTAD, Final report: Methodology of HAM-modeling. In *Report R-02*; Chalmers University of Technology: Gothenburg, Sweden, 2002.

ISBN 978-82-326-7688-0 (printed ver.)
ISBN 978-82-326-7687-3 (electronic ver.)
ISSN 1503-8181 (printed ver.)
ISSN 2703-8084 (online ver.)

NTNU
Norwegian University of
Science and Technology